



Southern African Universities Power Engineering Conference

SAUPEC 2013

31 January and 1 February 2013
North-West University, Potchefstroom, South Africa

It all starts here



PROCEEDINGS OF THE 21ST
SOUTHERN AFRICAN UNIVERSITIES POWER
ENGINEERING CONFERENCE – DIGITAL EDITION

SAUPEC 2013

North-West University, Potchefstroom, South Africa
31 January and 1 February 2013

Review: Authors were invited to submit full papers to the broad subject “Electrical engineering”. Each paper was peer reviewed by at least two specialist reviewers. In the case where the reviewers did not agree, a third review was done to decide the outcome. Final acceptance was based on the contribution, scientific and technical merit of the paper.

Disclaimer: Authors are responsible for the contents of their papers.

Published by Southern African Universities Power Engineering Conference

School of Electrical, Electronic and Computer Engineering, Private Bag X6001, Potchefstroom,
2520, South Africa

Tel: +27 18 299 1976

ISBN 978-1-86822-631-3

Acknowledgements

Organising Committee:

JA De Kock, AJ Grobler, APJ Rens, PA van Vuuren, G van Schoor, KR Uren, W Steenkamp (NWU)

Web site:

S Geldenhuys (NWU)

Welcome address:

T Eloff (Vice-Chancellor of the North-West University)

Keynote address:

JJ Roos (President of the Association of Municipal Electricity Undertakings)

Technical Reviewers:

Cape Peninsula University of Technology

G Atkinson - Hope
WC Stemmet
M Adonis

CTLAB

CH Marais

Durban University of Technology

GF D'almaine

Nelson Mandela Metropolitan University

W Phipps
RT Harris
AG Roberts

North-West University

G Van Schoor
APJ Rens
JA De Kock
KR Uren
R Gouws
T Seiphetlho
H Marais
PA Van Vuuren
SR Holm

Stellenbosch University

HJ Vermeulen
H du T Mouton
JP Holtzhausen
MJ Kamper
R-J Wang
HC Reader
PJ Randewijk
N Gule

University of Cape Town

MA Khan
C De Beer
CT Gaunt
P Barendse
R Herman
KA Folly
J de la Bat
R Solomon
DT Oyedokun
KO Awodele

University of Johannesburg

AF Mulaba-Bafubiandi
DC Pentz

University of KwaZulu-Natal

L Chetty
AK Saha

University of South Africa

S Du

University of Pretoria

MN Gitau

University of Witwatersrand

IW Hofsajer
JM Van Coller
IR Jandrell
KJ Nixon
JI Braid
WA Cronje
MV Shuma-lwisi

Foreword

It is a privilege to welcome you to the 21st Southern African Universities Power Engineering Conference, to be hosted at the North-West University, Potchefstroom campus. We hope that the papers presented will generate some stimulating conversations and that all involved will experience some academic growth.

We would like to thank all the reviewers for their huge contribution to the success of the conference. Thank you for the excellent feedback you gave the authors as well as the timely fashion in which you completed the reviews. Your time and efforts are greatly appreciated. Only papers that were accepted by two reviewers are published in the proceedings. Discussion papers were not reviewed and are used to present work in progress. Digital copies are included on the USB storage devices.

The welcome address by Dr Theuns Eloff, Vice-Chancellor of the NWU is definitely a highlight. Your support for this conference and engineering at the NWU is greatly appreciated. We would also like to thank Hannes Roos for delivering the keynote address as the President of the Association of Municipal Electricity Undertakings. The organising committee would also like to thank the NWU for making their facilities available.

Enjoy Potchefstroom and SAUPEC 2013!

SAUPEC 2013 organising committee.

Table of contents

Topic A: Control and applications

1

AN AUTOMATED SYSTEM APPROACH FOR CENTRE PIVOT FIELD IRRIGATION

F Adlam, R.J. Oberholster and B. Swart

2

MEASUREMENT METHODOLOGY FOR THE INVESTIGATION OF HOME ENTERTAINMENT CONSOLES

A.J. Bredekamp and G. Atkinson-Hope

8

MULTI-TERMINAL HVDC VOLTAGE SOURCE CONVERTER OPEN LOOP TRANSFER FUNCTIONS

W.M. Phetha and L. Chetty

16

TABLET BASED WIRELESS MEASUREMENTS FOR POWER APPLICATIONS

H.L. Brummer, C.W.I. McAfee and K.J. Nixon

22

Topic B: Electromagnetics

28

CALCULATIONS OF GEOMAGNETICALLY INDUCED CURRENTS (GICs) IN THE NAMIBIAN TRANSMISSION NETWORK

M.N. Simon, D.T. Oyedokun and C.T. Gaunt

29

SMALL ENCLOSURE SHIELDING EFFECTIVENESS TESTING

J. A. Andriambeloson, H. C. Reader and, G. C. M. Coetzer

33

TESTING THE RESPONSE OF LABORATORY BENCH TRANSFORMERS TO GEOMAGNETICALLY INDUCED LIKE CURRENTS

H.K. Chisepo, C.T. Gaunt and D.T. Oyedokun

37

Topic C: High voltage

43

A REVIEW OF FACTORS THAT AFFECT CORONA ELECTROPORATION OF IN-VITRO SAMPLES IN A HIGH VOLTAGE POINT-PLANE GAP TEST APPARATUS

N. K. Chetty and L. Chetty

44

AN INVESTIGATION INTO THE PROBABILITIES OF 66kV and 132kV BUSHING FAILURES AND MITIGATING AGAINST THE ASSOCIATED RISKS.

E. Russell, R.T. Harris, W. Phipps, A.G. Roberts

51

AN OVERVIEW OF THE ELECTRICAL TREEING PHENOMENA IN SOLID DIELECTRICS

D.R. Cornish and C. Nyamupangadengu

57

IN SERVICE CONDITION MONITORING OF SURGE ARRESTERS WITHIN ETHEKWINI ELECTRICITY

M. Gumede and G. F. d'Almaine

62

MOBILE MULTI-VOLTAGE ARTIFICIAL POLLUTION TESTING CHAMBER FOR HIGH VOLTAGE INSULATORS

J. A. Almeida, N. D. Smit and K. J. Nixon

69

PROPOSED OPTIMISATION OF HVDC LINES

R.G. Stephen and C.T. Gaunt

75

SENSITIVITY ANALYSIS OF Z-SOURCE BREAKER

Y. Singh and L. Chetty

80

Topic D: Machines	85
A REVIEW OF CONDITION MONITORING TECHNIQUES AND TYPICAL FAILURE MODES WITH REGARDS TO LARGE ROTATING ELECTRICAL MACHINES	
W. Doorsamy and W. Cronje	86
DESIGN OF A NON-INTRUSIVE CABLE CONDITION MONITORING TECHNIQUE BY MEANS OF PARTIAL DISCHARGE	
H. van Jaarsveldt and R. Gouws	92
DESIGN CONSIDERATIONS IN THE IMPLEMENTATION OF AN ELECTROMAGNETIC BRAKE FOR A 15 KW PM WIND GENERATOR	
J.H.J. Potgieter and M.J. Kamper	98
DESIGN OF A PROTOTYPE POWER LINE INSPECTION ROBOT	
N. du Plessis and R. Gouws	104
EVALUATION OF RELUCTANCE SYNCHRONOUS MACHINE ROTOR TOPOLOGIES FOR POSITION SENSORLESS CONTROL	
W.T. Villet and M.J. Kamper	110
PERFORMANCE EVALUATION OF A CENTRIFUGAL PUMP SYSTEM UNDER VARIABLE SPEED OPERATION	
C. Kühn and P.J. Randewijk	116
PERFORMANCE COMPARISON OF INDUCTION MOTOR AND LINE START PM MOTOR FOR COOLING FAN APPLICATIONS	
C. Mutize and R-J. Wang	122
TRANSMISSION LINE MONITORING SYSTEM FOR A POWER LINE INSPECTION ROBOT	
T.C. Visser and R. Gouws	127
UPGRADE OF THE ANTIQUATED 3TM2500 TRANSFORMER SCHEME TO PROVIDE IMPROVED TRANSFORMER PROTECTION	
M. Sandt, R.T Harris, W. Phipps and A.G. Roberts	133
Topic E: Power electronics	139
MINIATURE INTEGRATED CO-AXIAL CURRENT SHUNT FOR HIGH FREQUENCY SWITCHING POWER ELECTRONICS	
A.L.J. Joannou and D.C. Pentz	140
POWER LOSS ANALYSIS OF TWO-LEVEL AND NPC THREE-LEVEL VOLTAGE SOURCE INVERTERS	
A. Khan, M.A. Khan and P. Barandse	146
THE IMPACT OF THE CONVERTER MODES ON THE DISTRIBUTION OF ACTIVE HARMONIC POWERS	
N.P. Bokoro and J.H.C. Pretorius	152
Topic F: Power systems	156
A Steady-state Long Transmission Line Performance Analysis of UHVDC Power Systems	
F.M. Kasangala and G. Atkinson-Hope	157
AN OVERVIEW OF APPLIANCE MONITORING USING POWER SIGNATURE	

M.B. Shabalala and M.V. Shuma-lwisi	163
Component model and network model validation in power system studies	
S. Mvuyana, J.M. Van Coller and T. Modisane	169
CONVERTING CONVENTIONAL HIGH VOLTAGE AC TRANSMISSION LINES INTO A DIRECT CURRENT TRANSMISSION SYSTEM	
M.J. Matabaro, W.C. Stemmet and G. Atkinson-Hope	176
DESIGN AND DEVELOPMENT OF MEDIUM VOLTAGE OPEN RACK HARMONIC FILTERS FOR DISTRIBUTION NETWORKS	
A.M. Meru and G. Atkinson-Hope	182
EFFICIENCY PLAN FOR A DISTRIBUTION NETWORK UNDER CONTINGENCY CONDITIONS	
N. Ntshamba and K. Awodele	188
GRID PARAMETER ESTIMATION AT THE POINT OF COMMON COUPLING: IMPLEMENTATION AND EVALUATION OF A METHOD IN LITERATURE	
M. I. Naude, W.A. Cronje and M.V. Shuma-lwisi	194
IMPACT OF A NETWORK'S COMPONENT FAILURE MODEL ON THE PERCEPTION OF ITS RELIABILITY	
M. Edimu, R. Herman and C.T. Gaunt	200
INFLUENCE OF TEMPERATURE ON TIME DOMAIN REFLECTOMETRY IN SHIELDED POWER CABLES	
L.S. Ndlovu S. Munilal and C. Nyamupangedengu	206
INTRODUCTION OF A MORE DETAILED CALCULATION OF GEOMAGNETICALLY INDUCED CURRENTS IN TRANSMISSION NETWORKS	
D.T. Oyedokun, M.N. Simon, C.T. Gaunt	211
INVESTIGATING THE PERFORMANCE OF FACTS DEVICES (SVCs) IN THE ESKOM NETWORK	
L. Mataka and A.K. Saha	216
INVESTIGATION INTO THE PERFORMANCE OF PHASOR MEASUREMENT UNITS FOR POWER SYSTEM STABILITY APPLICATIONS – PRELIMINARY INVESTIGATIONS	
B.W.D. Berry and K.J. Nixon	222
PROBABILISTIC METHODS APPLIED TO LOAD MODELLING IN RELIABILITY AND CUSTOMER INTERRUPTION COSTS EVALUATION	
N.F.S. Ip Cho, K.O. Awodele and R. Herman	228
REVIEW OF BARE CONDUCTORS FOR OVERHEAD POWER TRANSMISSION	
L.P. Luhlanga and A.K. Saha	234
SHORT TERM LOAD FORECASTING FOR A LARGE INSTITUTION USING SUPPORT VECTOR REGRESSION	
R. Clark and W.A. Cronje	240
TRANSMISSION GRID EXPANSION IN UGANDA: A PROPOSED PLANNING PROCESS	
S. Mugisa and C.T. Gaunt	245
Topic G: Renewable and alternative energy	251

ASSESSING THE ECONOMIC VIABILITY OF THE MOLTEN SALT POWER TOWER CONCENTRATED SOLAR POWER (CSP) WITH THE NATIONAL ENERGY REGULATOR OF SOUTH AFRICA (NERSA) RENEWABLE ENERGY FEED-IN TARIFF (REFIT) SCHEME	252
C. Chukwuka and K. A. Folly	
DESIGN OF A PROTOTYPE ULTRA-CAPACITOR SOLAR PANEL STREET LIGHT	258
A.E. van Niekerk and R. Gouws	
FLY ASH RESISTIVITY PROFILING FOR COAL FIRED POWER STATIONS TO OPTIMIZE ELECTROSTATIC PRECIPITATOR EFFICIENCY	264
G. Chauke and R. Gouws	
OPERATIONAL STUDY ON LOW TEMPERATURE AND HIGH TEMPERATURE PEM FUEL CELLS	270
C. de Beer, P. Barendse, P. Pillay, B. Bullecks and R. Rangeswamy	
PROBABILISTIC METHODS FOR RENEWABLE ENERGY SOURCES SUPPLYING VARIABLE LOADS – ADDITION OF GRID CONNECTION	275
E. Namanya and C.T. Gaunt	
RECONFIGURABLE SOLAR ARRAY FOR IMPROVING EFFICIENCY OF A POWER CONVERTER	281
M.R. Looi, M.M. Wu and J.I. Braid	
SOUTH AFRICAN COAL AND ITS ABRASIVENESS INDEX DETERMINATION: AN ACCOUNT OF CHALLENGES	288
N. Tshiongo and A.F. Mulaba-Bafubiandi	
THE CHALLENGES OF SUSTAINABLE ENERGY DEVELOPMENT IN DEVELOPING NATION– A CASE STUDY OF NIGERIA.	294
O.A. MAFIMIDIWO and A.K. SAHA	
Index	301

Topic A

Control and applications

AN AUTOMATED SYSTEM APPROACH FOR CENTRE PIVOT FIELD IRRIGATION

F Adlam*, R.J. Oberholster** and B. Swart***

*Department of Electrical Engineering, Nelson Mandela Metropolitan University, Port Elizabeth 6031, South Africa E-mail: frank.adlam@nmmu.ac.za

** Department of Electrical Engineering, Nelson Mandela Metropolitan University, Port Elizabeth 6031, South Africa E-mail: s207003291@live.nmmu.ac.za

***Department of Electrical Engineering, Nelson Mandela Metropolitan University, Port Elizabeth 6031, South Africa E-mail: s207019268@live.nmmu.ac.za

Abstract: This paper describes the design, development, installation and commissioning of a prototype automated centre pivot field irrigation system. Most South African farmers use basic centre pivot irrigation systems creating a market opportunity for fully automated systems. Weather prediction, soil type, soil moisture content and penetration depth of water in the soil are parameters taken into consideration to control irrigation optimally. It is computer controlled and wireless networked to provide angular mechanical in-line tower monitoring, real-time alarms, remote access and human machine interface. SCADA provides control, recipe selection, historical data logging, system animation and user interface. The initial project phase results are encouraging and the project is in its second phase.

Keywords: centre pivot field irrigation, soil, control system, automation, HMI, networking.

1. INTRODUCTION

Irrigation is an important factor in commercial agriculture to ensure profitable crop yield. Investing in a suitable irrigation system contributes to sustainable crop profitability [1].

Centre pivot field irrigation, as in figure 1, is a popular form of irrigation due to the efficiency of irrigating large areas. It consists of a single water pipe and electrical cable running underground to the centre of the field to be irrigated where it serves as a base for tower connections [2]. A tower consists of an arced pipe with sprinklers hanging from it, as well as electrical driven wheels used for pivot rotation.

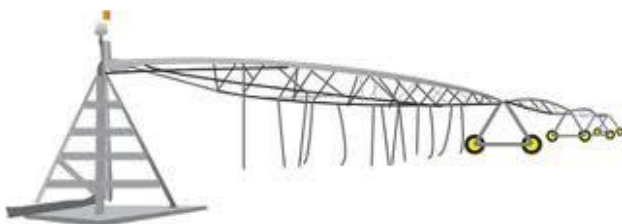


Figure 1: Centre pivot field irrigation

The system is modular and scalable by adding or removing towers [2]. Soil types and moisture content are important factors in optimum irrigation [3].

2. EXISTING BASIC CENTRE PIVOT SYSTEMS

Basic centre pivot systems are widely used in agriculture but do not use resources optimally in contributing to increased crop yields and profitability [4]. The following topics are problematic in basic centre pivot systems:

- over or under irrigation
- human error
- electricity and water utilisation
- hardware failures
- labour management

2.1 Over or under irrigation

To design an effective irrigation control system, the system designers need to have a good understanding of over and under irrigation of soil.

Over or under irrigation has a direct influence on crop growth. Plants mainly absorb water through osmosis at root level. Osmosis is the process where a water solution moves through a partially permeable membrane from a high concentrate to a low concentrate. As the membrane is partially permeable, minerals can be selectively let through while water cannot be prevented from going through.

When soil is severely over watered the salute concentration in the soil is much higher than inside the plant cells. Water is now forced into the plant cell until the plant cell's solute concentration is equal to the solute concentration in the soil or the plant cell ruptures in the plant.

With slight over watering the force of water into the plant causes the membrane to fail in controlling the mineral absorption of the cell. This often leads to slightly over watered plants revealing a nutrient deficiency.

Low levels of oxygen in the soil causes a delay before the plant resumes growth known as plant stress or crop stress. Over watering can also cause minerals to be flushed away from the roots when water drains through the soil.

When under watering occurs the plant enters stress as it uses more energy taking in water than what it can produce. This is known as the wilting point. The plant cells loose so much water that the ectoplasm pulls the cell's sides inward giving the wilted look. Because the plant cells do not rupture from under watering the recovery time is much less than in over watering. It is often good for root growth if the plant is slightly under watered for at least once a season. The roots will grow toward water in the soil, and into areas where new minerals are located.

2.2 Human error

Farm workers require soil and crop knowledge to determine the estimated amount of water to be irrigated. Incorrect settings result in over or under irrigation. Other errors are the lack of water leak detections and routine mechanical maintenance inspections.

2.3 Electrical power and water utilisation

Existing irrigation systems motors are powered through electrical drives operating at very low speeds, consuming more power due to torque decreasing exponentially with motor speed. Water resources are wasted with over watering in the form of runoff and excessive water drainage. Due to extended runtime water is lost due to evapotranspiration and extra electricity is consumed to move the tower over larger distances.

2.4 Hardware failures

Due to the lack of early warning systems and water leak detection hardware failures occur including:

- punctured wheels
- clogged or damaged sprinklers
- defective water valve
- soil shifting above the PVC pipeline
- malfunctioning electrical contactors

2.5 Labour management

The labour act determines that for any additional hours worked, over and above their contractual weekly hours, farm workers should be remunerated overtime or be given time off. Growing very water sensitive crops needing additional irrigation and care will cost on average 1.5 times more in labour during weekends and public holidays.

If substitute labourers lacking skills and experience are used, additional training has to be provided which increases operational risk and cost. It puts management resources under considerable strain [4].

2.6 Control system

Manual systems with some advanced timing features mostly use controlling relay logic and are a proven technology [5]. It however, lacks full automation, intelligence and remote access. A fully automated system will technically increase the complexity of the system, but also make the system simpler from an operator point of view once the relevant experience or training has been acquired [4].

3. SOIL FACTORS AND MOISTURE CONTENT FOR OPTIMUM IRRIGATION

In designing an automated system for optimum irrigation, at least a basic understanding of soil factors to be considered and its moisture contents are required.

Irrigation scheduling means to keep the soil moisture content within an allowable depletion level. The reasons to why irrigation scheduling would be applied are as follows [6]:

- Prevent under & over watering
- Prevent unnecessary crop stress
- Creating the ideal air-water balance in the soil
- Promoting root development
- Improving fertilizer uptake
- Save on energy costs
- Manage soil water buffer effectively
- Facilitate crop manipulation
- Optimize salinity management to assist the farmer in selecting specific fertilizers or next type of crop depending on the estimated salt content of the soil. [6]

Soil factors to consider for optimal irrigation:

- Each soil texture and structure needs to be watered differently due to absorption rates to maintain correct air-water balance for optimal plant growth. Soil types can vary in just one field, thus it would be ideal to be able to apply water to suit the needs of each individual area [6].
- Temperature affects the water absorption of soil and can only be partially influenced by watering cycles, but on the average irrigation field it is unpredictable [6].
- Soils consisting of multiple layers of soil of various types (stratified) influence water movement through the soil therefore it is important to be able to control watering parameters to focus on a specific depth of interest [6].
- During hot days or dry weather conditions, roots make less contact with its soil resulting in the absorption of less water than normal and irrigation time must be increased [6].

- Applied water can take up to 24 hours to reach various depths still being monitored for soil moisture, the soil moisture values cannot be used directly to control an automated system. Thus, additional calculations and processes must be implemented to apply water accurately to the field. These can be established by doing a soil analysis over time to determine the amount of water needed to raise soil moisture at a certain depth by a specific amount. The outcome can then be used to generate a specific formula which will determine the water requirements, so that after a 24 hour delay from application the moisture level at a certain depth should be at the desired limit [5].

4. PROTOTYPE AUTOMATED CENTRE PIVOT FIELD IRRIGATION DESIGN

An operational basic centre pivot irrigation system was selected as a prototype for automation. Information about the current electrical and mechanical systems was gathered to determine which system changes should be made to facilitate automation.

4.1 Wireless soil probe location in irrigation area

Wireless communication is used as it makes probe placement easy in a field from 4 to 40 Hectares. Current probe battery life is one season and solar powered probes are under development.

The system was designed to facilitate up to eight wireless probes with the intention that the irrigation area is divided into eight equal sections. The minimum recommended number of probes to be used would be three. It should be distributed across the irrigation area, as accurately as possible to the control system, indicative of the different soil types or conditions in the field.

4.2 Mechanical design

A special angle control cam was designed to change the existing angle control system from a start stop system to a variable electrical drive system shown in figure 2.

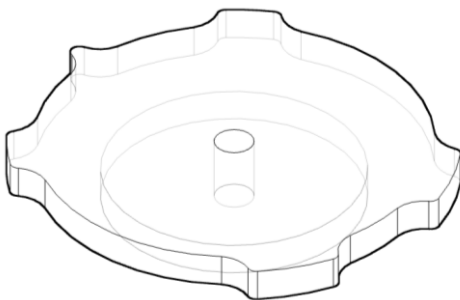


Figure 2: RnB Solutions Control Cam

This was achieved by analysing the existing system to obtain the angular gain on the control cam. The angular gain is obtained by using a double lever system from the

pivot pipeline to the rod which holds the control cam shown in figure 3.

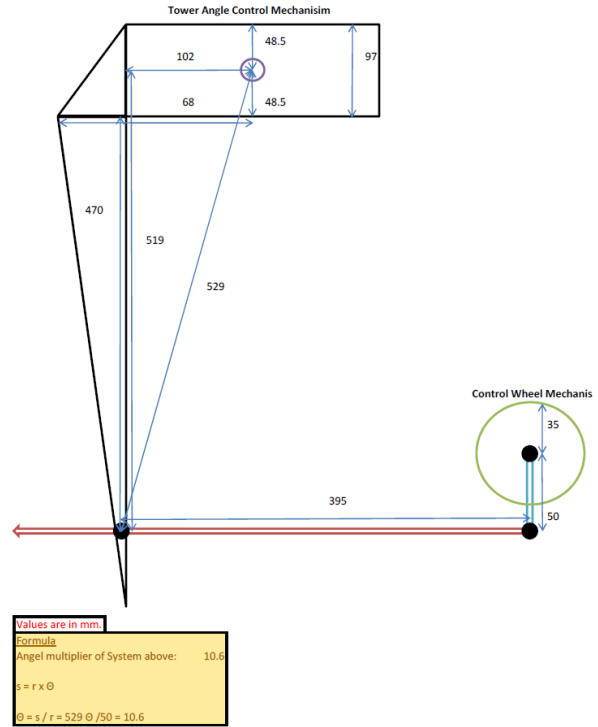


Figure 3: The shown Agrico control cam system was changed to facilitate pivot rotational control with electrical variable drives.

4.3 Network design

Figure 4 show the SCADA system situated in the farm house use an 802.11g wireless network link in bridge mode to connect the controller and HMI onto the LAN. The LAN is reachable via WAN using port forwarding on the router of the house. A VPN server is used to give access to the WAN from the internet.

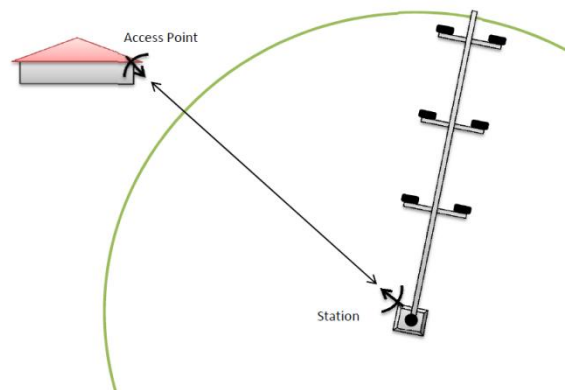


Figure 4: Wireless Link Layout Diagram

4.4 Control system design

The block diagram in figure 5 shows the overall functionality of the automation system.

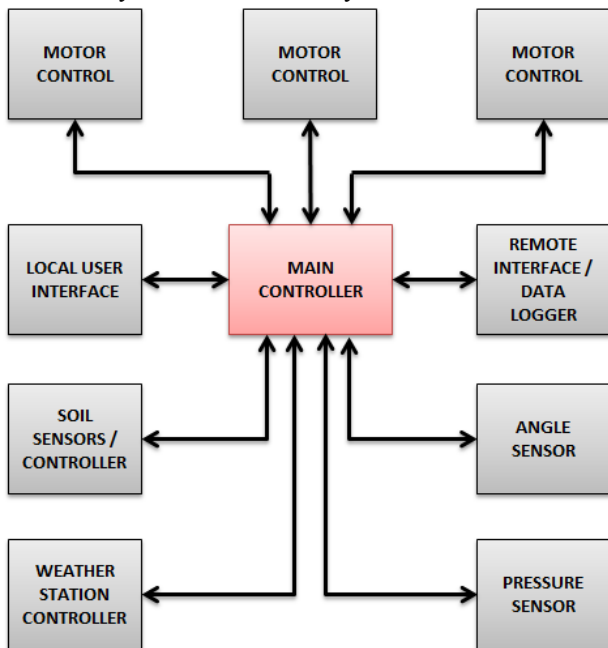


Figure 5: Control System Block Diagram

The function of each sub-system is:

- **Main Controller:** It functions as the core of the system, controlling all processes, calculations and data handling. The P3000 Programmable Automation Controller (PAC) is used due to the 50MB memory capacity that can be used for data as well as providing flexibility with multiple communication protocols.
- **Local User Interface:** An HMI was selected allowing users advanced control and system animation.
- **Motor Control:** It controls the movement of each tower of the pivot using variable speed drives. Motor speeds need to be accurately controlled keeping all the towers of the system in-line and irrigating at specific rates. Modbus gateways were added to the drives allowing Modbus TCP communications between the main controller and motor drives.
- **Intelligent soil probes:** Used to monitor soil moisture levels and report to the main controller. A DFM soil probe package was selected as it incorporated multiple wireless probes that can measure at multiple levels in the soil. A RS-485 Modbus RTU facilitates stable and robust communication between controller and probes.
- **Weather Station Controller:** The weather station controller logs and calculates weather data for 12 to 24 hour weather predictions. The main controller uses the data to determine irrigation time periods. A wireless Davis weather station system was chosen for the application. It is a cost effective solution with advanced weather analysis capabilities. Historical data can be accessed over a RS-232 serial interface with the main controller.

- **Pressure Sensor:** An analogue pressure transmitter was selected providing the main controller with flexible set point adjustability. The pressure is used for safety and process interlocking.
- **Angle Sensor:** It detects the actual position of the pivot tower array in the field. An absolute encoder provides accurate positioning using Gray coded digital inputs. The 1024ppr encoder sensitivity is less 0.5 degrees of pivot rotation.
- **Remote Interface / Data Logger:** The remote SCADA system needs to interface with the main controller for data logging, real-time alarms, HMI and historical data.

4.5 SCADA and HMI design

The SCADA system was designed in consultation with the farmers. A help file was created to guide SCADA users. All system options can be accessed via labelled buttons located on the left hand side of Human Machine Interface shown in figure 6.

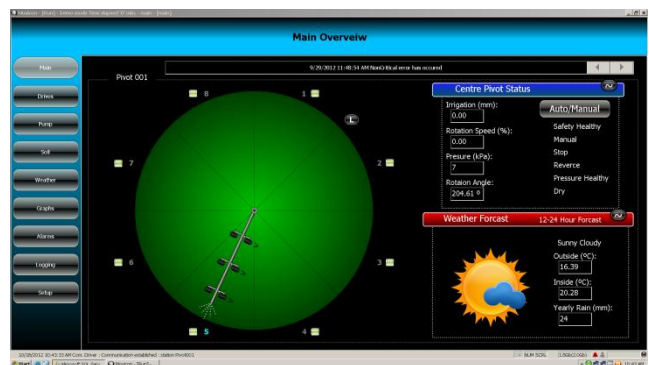


Figure 6: SCADA Graphical User Interface

The screen list diagram in figure 7 gives a partial view of system functionality such as:

- ‘Drives Overview’ where each drive can be selected for status or configuration.
- ‘Pump Overview’ for water pump status.
- ‘Soil Overview’ for soil temperature and moisture.
- ‘Weather Overview’ for current weather details.
- ‘General Graphs’ for rotational angle, irrigation rate, water pressure and more.

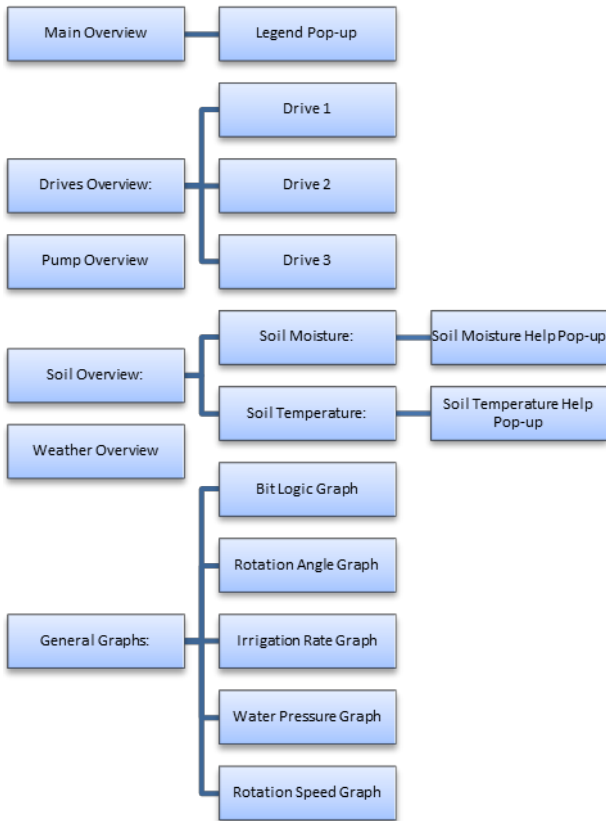


Figure 7: SCADA Screen List Diagram

5. SYSTEM IMPLEMENTATION AND TESTING

All sub systems have been integrated into the existing centre pivot.

- The mechanical system modifications have been tested to comply to design specifications.
- Each sub system was tested individually for functionality, fully integrated and commissioned.
- Soil samples were taken from the field at the designated locations for the wireless probes.
- The probes were placed in the designated locations and irrigated with pre-determined amount of water per time duration.
- The logged data was carefully studied to determine timer values, system constants and recipe settings for each field soil type.
- The SCADA system uses logged data for system functionality verification.

During the initial testing phase the following difficulties were experienced:

- Weather station RS-232 Driver: The 3rd party software driver documentation was still in draft format creating integration problems which were solved by “port sniffing” and communication data analysis.
- Modbus gateway module random failures: Motor drive harmonics caused network failures.

- Harmonic Interference – When the drives were operated at frequencies below 45 Hz harmonic interference was experienced on various devices. High pitch sound emitted from switch mode power supplies on the local farm grid was observed. Installation of line reactors on the power input side of the motor drives reduced harmonics by 60% solving the problem.

6. INITIAL RESULTS

The project is currently in its second testing phase and the initials results are encouraging. The farmer reported the following:

- There is visual evidence of increased growth in crop density which appears to be greener and healthier.
- The weed density has decreased which is good considering that the system has been operational from spring this year, a period when weed growth tend to increase in comparison to winter.
- The overall running time of the pivot is less compared to the same period last year.
- Although the system run time has decreased, it cannot be assumed that power consumption has been reduced as pivot motors run at variable speeds.
- System run time has decreased therefore it can be concluded that water usage has been reduced.

7. CONCLUSION

The automated prototype centre pivot field irrigation system has been designed, installed and commissioned according to the specification and continual feedback of participating farmers, resulting in decreased pivot run time and water utilisation.

Real-time user feedback and automated pivot control have reduced operational, maintenance and labour costs.

Initial results are based on the farmer’s comparison of historical data and visual observation.

8. RECOMMENDATIONS

During the second project phase data should be logged, analysed, interpreted and integrated into the system using scientific methodology. Overall system reliability should be calculated taking sub-system reliability into account.

Neural networks will provide a higher level of system decision making and should be considered. A modular approach to product commercialisation should be evaluated as it will provide three simple to advanced levels of automation to the market.

Government structures for product development assistance and guidance can be consulted towards successful product commercialisation.

9. REFERENCES

- [1] Oxford University Press (Undated) [Online]: “Irrigation”, <http://www.oxforddictionaries.com>, 2012
- [2] AGRICO: “Technical Documentation”, *Agrico documentation*, 2009.
- [3] South African Irrigation Institute (SABI) (Undated). [Online]: “Design norms”, <http://www.sabi.co.za/designNorms.html>, 2012.
- [4] D. Schoeman: “Pivot System Automation and Problems”, *Interview*, February 2012.
- [5] AGRICO [Online]: “AGRICO Centre Pivot”, [AGRICO Centre Pivot.pdf](#), 2012
- [6] D. Mercker: “Effective Root Zone Management with DFM-Probes”, *DFM documentation*, 2012.

MEASUREMENT METHODOLOGY FOR THE INVESTIGATION OF HOME ENTERTAINMENT CONSOLES

A.J. Bredekamp* and Prof G. Atkinson-Hope**

* Cape Peninsula University of Technology, PO Box 652, Cape Town 8000, South Africa E-mail: bredekampa@cput.ac.za

** Cape Peninsula University of Technology, PO Box 652, Cape Town 8000, South Africa E-mail: atkinsonhopeg@cput.ac.za

Abstract: This paper presents a methodology for determining the power consumption of home entertainment equipment as well as the effect that such devices have on harmonic distortion levels. Home entertainment equipment includes television sets, DVD players and home theatre. The methodology presented consists of two parts, performing measurements and generating results. The methodology presented includes steps for mathematically combining the measured voltage and current waveforms of individual devices. The goal is to determine total current and voltage waveforms for a combination of devices. The methodology also describes how to analyze the resultant synthesized waveforms so as to determine the power consumption at each harmonic.

Keywords: harmonic distortion, home entertainment, power consumption, television

1. INTRODUCTION

Modern digital home entertainment equipment demand power of high quality from the grid. The number of home entertainment devices is increasing, yet our understanding of the effect that they have on power quality is incomplete.

Bredekamp et al measured the power consumption of home entertainment equipment in 2004 [1]. The shortcoming with this study was that it did not include LCD, Plasma and LED based TV sets. Also, no study was conducted on combinations of home entertainment equipment to establish, compare, evaluate and analyse their real power consumption under standby and running operating conditions. In a typical household home entertainment device such as DVD players, amplifiers, decoders and TV sets will often be placed in a single storage unit or console which can be evaluated as a unit.

Roth et al [2] studied the power consumption of a variety of consumer electronic devices including home entertainment equipment. This study did not include digital televisions (LCD, LED, Plasma).

Besides their power consumption, one must also consider that home entertainment equipment are non-linear loads [3]. Some work [4] has been recorded to date that investigate the harmonic distortion generated by televisions. The bulk of power studies performed on television sets so far have focused on the standby mode power consumption with little or no attention to the power and harmonics during on-mode. [5][6][7][8][9]

One area of concern is the prevalence of simulation studies as opposed to the analysis and comparison of actual measurements with calculated and/or modelled results.

2. RESEARCH STATEMENT

The main contribution of this research will be the development of a methodology for the measurement and evaluation of the harmonics produced by home entertainment devices as well as the power consumed by such devices at fundamental and harmonic frequencies.

For the purpose of this research home entertainment devices will include televisions, DVD players and hi-fi/surround sound equipment.

The developed methodology will contain procedures for combining the harmonic and power measurements from separate devices mathematically as if the devices are connected to the same power outlet socket, like they would be in a console.

3. THEORETICAL BACKGROUND

3.1 Linear and Non-Linear loads: Most if not all domestic loads are non-linear. A non-linear load is an ac load where the current is not proportional to the voltage. Loads that fall into this category are loads such as Silicon Controlled Rectifier (SCR) controlled light dimmers, computers, laser printers, switch-mode power supplies, refrigerators and televisions. [3]

Figure 1 shows a measured current waveform for a typical non-linear load, in this case a DVD player. The current waveform no longer has a sinusoidal shape and is, instead, severely distorted. The current waveform in figure 1 is a complex waveform which according to Fourier can be represented as the sum of sine and cosine functions of different amplitude and frequency or harmonics [10]. Figure 2 shows a bar graph of these harmonics. Harmonics labelled 1, 5 and 7 indicate the odd harmonics and correspond to 50, 250 and 350 Hertz,

respectively while 3 and 9 correspond to triplen harmonics [10]. The load current harmonics in figure 2 are typical for a non-linear load as they contain odd and triplen harmonics. The reason for this is that waveform of figure 1 is periodic. Even harmonics are usually only found with non-periodic waveforms.

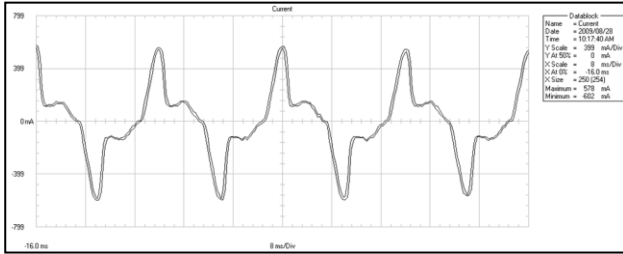


Figure 1: Measured current waveform of a typical non-linear load

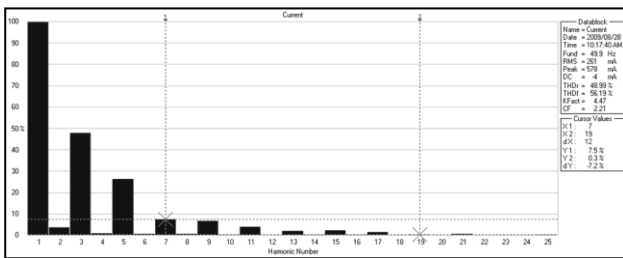


Figure 2: Spectrum view of the waveform in figure 1 showing the harmonic components

3.2 Calculation of power in the presence of harmonics:

To determine the power under non-sinusoidal conditions, it is necessary to first represent the current and voltage waveform in such a way that the separate harmonics can be viewed. Figure 1 represents a complex waveform that can be represented by: [11]

$$y = Y_{1m} \sin(\omega t + \psi_1) + Y_{2m} \sin(2\omega t + \psi_2) + \dots \quad (1)$$

Where:

Y_{nm} = amplitude of the harmonic numbered n

ψ_n = phase angle of harmonic numbered n

m = peak value of harmonic

The process of harmonic analysis is then a case of finding the coefficients $Y_{1m}, Y_{2m} \dots$ etc., and the phase angles $\psi_1, \psi_2 \dots$ etc. Fourier analysis of the waveform in figure 1 will allow us to determine the aforementioned coefficients and phase angles.

Figure 3 demonstrate how a single circuit with non-sinusoidal voltages and currents can be decomposed into three separate circuits each with sinusoidal voltages and currents. Figure 3 (B) will allow us to calculate the power due to the fundamental while figures 3 (C) and (D) will

allow us to calculate the powers due the third and fifth harmonics [12].

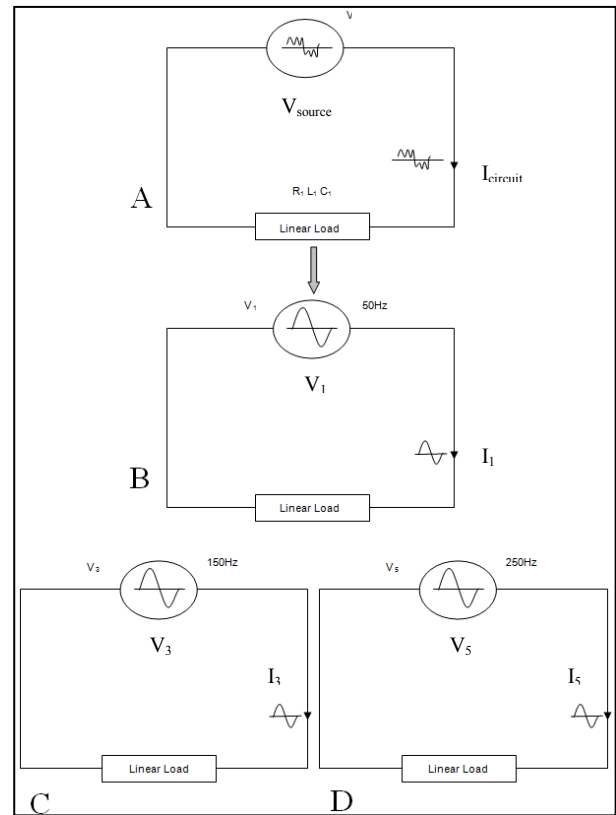


Figure 3: Decomposition for a linear load being fed from a voltage source (background harmonics)

Figure 3(A) shows a linear load being powered from a distorted voltage source, V_{source} (background harmonics). The linear load produces a current, $I_{circuit}$. Performing a Fourier analysis on the waveforms of V_{source} and $I_{circuit}$ will allow us to express both waveforms in terms of their harmonic components using equation (1) [10]:

$$\begin{matrix} V_{source} = V_{1peak} \sin(\omega t + \psi_{V1}) + V_{3peak} \sin(3\omega t + \psi_{V3}) + V_{5peak} \sin(5\omega t + \psi_{V5}) \\ I_{circuit} = I_{1peak} \sin(\omega t + \psi_{I1}) + I_{3peak} \sin(3\omega t + \psi_{I3}) + I_{5peak} \sin(5\omega t + \psi_{I5}) \end{matrix}$$

A
B
C
D

Figure 4: V_{source} and $I_{circuit}$ expressed in terms of their harmonic components

In figure 4 the combinations marked B, C and D correspond to the voltage and current components of harmonics 1, 3 and 5 in figure 3 (B), (C) and (D), respectively. In terms of phasor diagrams V_{source} and $I_{circuit}$ from figure 3 can also be expressed as:

From figure 3, the power due to harmonic n can be expressed as:

$$P_n = V_n I_n \cos(\phi_{I_n}^{V_n}) \quad (2)$$

Where:

P_n = the power due to harmonic number n

V_n = RMS value of the voltage at harmonic n

I_n = RMS value of the current at harmonic n

$\phi_{I_n}^{V_n}$ = the phase difference between voltage harmonic n and current harmonic n

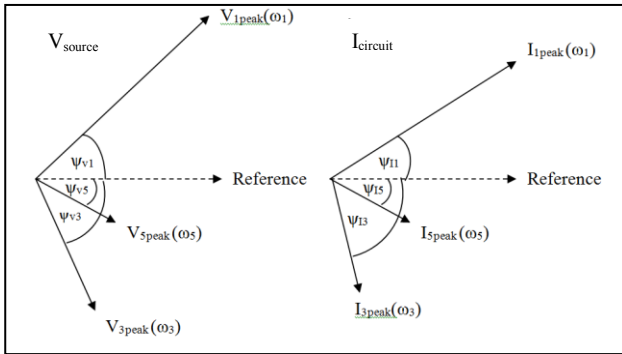


Figure 5: Phasor diagram for V_{source} and $I_{circuit}$

Depending on the values of ψ_{i1} and ψ_{v1} in equation (2) P_n can be negative. This means that P_T in the presence of harmonics can be expressed as [12]:

$$P_T = \sum_{h=1}^n P_h = \pm P_1 \pm P_3 \pm P_5 \pm \dots P_n \quad (3)$$

Where:

P_1, P_3 and P_5 = the power due to harmonics 1, 3 and 5 respectively

P_h = power due to harmonics

P_T = total power

The RMS values of V_{source} and $I_{circuit}$ can be expressed as: [12]

$$V_{source\ RMS} = \sqrt{(V_1)^2 + (V_3)^2 + (V_5)^2} \quad (4)$$

and

$$I_{circuit\ RMS} = \sqrt{(I_1)^2 + (I_3)^2 + (I_5)^2} \quad (5)$$

4. TELEVISION POWER MEASUREMENT

4.1 Average Picture Level: When measuring the power consumption of a television set the APL (Average Picture Level) has to be taken into account. APL is an indication of the brightness of a scene being viewed on a television. The brighter the image being viewed, the higher the APL value and visa versa. The reason APL is important is that

the power consumption of a television set varies with picture brightness. For a CRT set, the brighter the image being displayed, the more intense the electron beam of the CRT has to be with a corresponding increase in current drawn. The same is true for plasma sets except each pixel has its own electron source. The brighter the image being displayed the more electrons are needed per pixel with a corresponding increase in current drawn. LCD based TVs do not produce light. The image is formed by filtering the light (with coloured liquid crystal filters) produced by a back-light. The back-light is often a cold cathode fluorescent tube or LEDs. Back-light modulation (BLM) is a technique introduced with LCD TVs whereby the back-lights' intensity is varied according to the brightness of the scene.

This means that the power consumption of an LCD panel with no back-light modulation remains constant for all APLs while the power consumption of a plasma, CRT and LCD television with BLM will vary with APL [13].

APLs for all countries are very similar varying from 30% in Australia to 35% in Japan. Unfortunately, APLs below 40% is the region where television energy consumption has its greatest variation.

It is vital to consider APL as a factor when measuring television power consumption.

4.2 International Electrotechnical Commission (IEC) 62087: For the purposes of this research we are interested in the power consumption of a television set at a specific and static APL which requires the use of a static test pattern. The IEC 62087 standard uses a three bar black and white pattern for the measurement of On Mode power. This pattern has an APL of 50%. Televisions at this APL level will show a power consumption of 100%.

To more realistically test the power consumption of television sets, the revised IEC test method includes natural moving image test clips that produce more realistic measurements of power consumption.

4.3 JEITA: The other standard relevant to the measurements performed in this research is the Japan Electronics and Information Technology Industries Association (JEITA) standard that uses four patterns, 0% Black (black display), 100% White Raster (brightest display), three bar Black and White (50% APL) and colour bars (50% APL). The results of the measurements are then averaged.

4.4 Conclusion: Jones and Harrison [13], argued that the IEC 62087 and JEITA standards for measuring power consumption in television sets are inadequate and unrealistic. It was shown that in addition to the power consumption of the pictures being displayed the test method should also consider the contribution to power consumption of the following factors:

- Audio – How much amplification is provided for audio and what are the typical listening levels?
- Digital Tuners – These tuners often stay active during standby in order to download updates to television firmware.
- Standby Power – How much power does the set consume during standby mode?
- Energy Saving Features and Settings – What energy saving features are available and are they enabled by default.

5. MEASUREMENT METHODOLOGY FOR HOME ENTERTAINMENT EQUIPMENT PART A

This section introduces the methodologies developed for the measurement, and results generation, of home entertainment equipment. This section also includes the harmonic study methods used to arrive at the data needed for analysis and conclusions.

The methodology can be divided into two parts, A and B. During part A, measurements are performed, followed by part B where the results are generated.

5.1 Part A: Perform Measurements: The first step in the methodology is to develop a measurement setup for conducting the required investigation. Figure 6 shows the general measurement setup used. The setup provides for the measurement of individual, as well as combinations, of devices. Voltage and current transducers are applied between the device(s) and the power socket outlet (LN) to measure current and voltage.

A power quality analyzer is used together with a computer (PC or laptop) to record measurements.

5.2 Step 2: Select Power Quality Analyzer and Transducers: The second step in the methodology is to select a power quality analyzer and appropriate transducers as the investigation involve the measurement of non-sinusoidal quantities. An instrument such as the Fluke 43 Power Quality Analyzer would be a suitable choice. It is, however, vital to choose a current clamp transducer capable of accurately measuring currents of less than 2A such as the Fluke 80i-110s.

5.3 Current Clamp Arrangement: To accurately measure the very small currents in question it was necessary to construct and add a toroidal coil. Current from the load is passed through a 10 turn toroidal coil. The current probe is clamped around the coil during measurements to form a dedicated current clamp arrangement. By transformer action, this multiplies the current in the probe jaws by 10 providing a more substantial current to the transducer as step down transformers step up current.

5.4 Voltage Transducer Arrangement: For power measurements the Fluke 43B also requires a voltage transducer which is provided for the 220VRMS (50Hz)

AC level. The voltage transducer takes the form of two crocodile clips clipped to a stripped portion of the power cable between the device to be measured and the wall socket outlet. See figure 6.

5.5 Power Measurement Arrangement: To measure the power consumption of a device, a piece of 2-core cable is placed between the device to be measured and the power socket outlet as shown in figure 6.

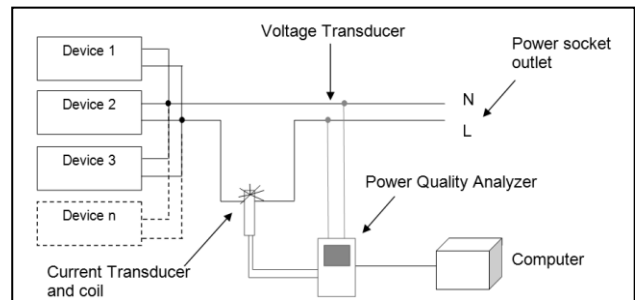


Figure 6: General measurement setup

Inserted into one of the conductors of the 2-core cable is a 10-turn toroidal coil such that the load current passes through the coil. The jaws of the current probe are then clamped over the coil. During measurements the coil was fanned out to minimize inductance. Clipped onto a stripped portion of the 2-core cable is the voltage transducer.

5.6 Step 3: Set up monitoring software on computer: FlukeView is the software that accompanies the Fluke 43B. FlukeView provides a graphical user interface (GUI) that enables a user to view/store the meter screen captures (e.g. the parameters set for measurements, power consumption, THD etc), voltage and current waveforms and spectrums. The generated results are saved as files on the computer.

5.7 Step 4: Select single device to measure: Select the home entertainment device to measure.

5.8 Step 5: Is device a television?:

For this next step, the device to be measured is identified. Section 4 describes APL and the IEC 62087 and JEITA as being essential considerations for television power measurement. Thus the methodology makes specific allowance for TVs and takes APL into account (Step 5, Figure 7).

5.9 Dedicated APL methodology for the measurement of television sets: The importance of this methodology is that power consumption is measured whilst considering APL settings. This is a contribution not found in existing literature. To facilitate field measurements of home entertainment devices where it might not be possible to introduce customized test images, the methodology does not use any special testing video material. The dedicated APL methodology for television sets are:

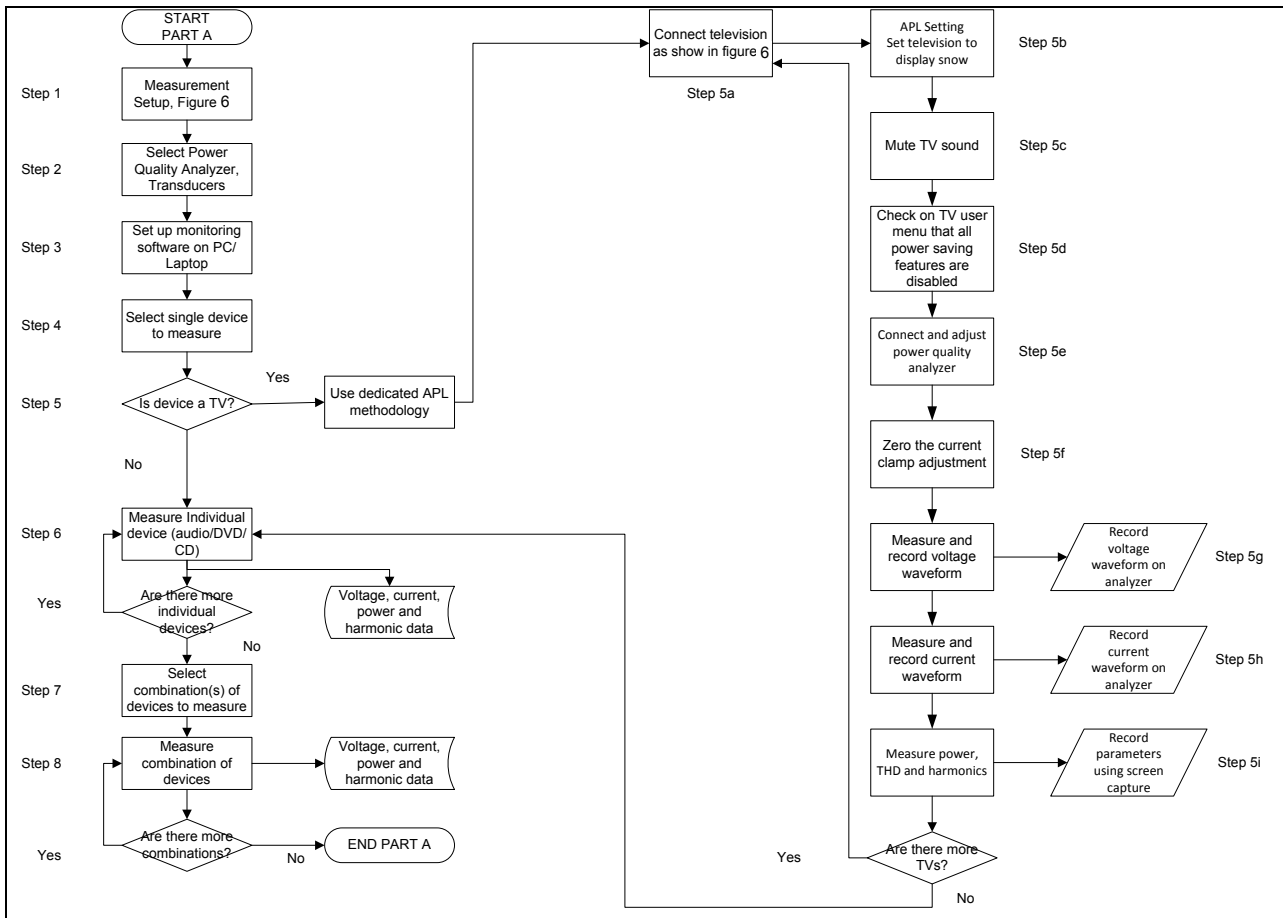


Figure 7: Detail of steps in part A, Perform Measurements

- All power saving features was bypassed. This was done to determine the worst-case scenario power measurement.
- All televisions were set to display a snow pattern. A snow pattern on a television set has a random distribution of peak white and black pixels. Lawrence Berkeley National Laboratory also used a “snow” pattern to perform television power measurements [14]. A snow pattern simply provides a standard “image” that will be the same on all sets measured.
- Controls for brightness, contrast and colour saturation was adjusted to represent actual viewing APLs.
- The sound on all televisions was muted during testing.
- All measurements were captured to a computer running FlukeView

5.10 Measure individual devices (audio/DVD/CD): Single devices are measured using the setup of figure 6. To ensure maximum power drawn, CD/DVD players were measured while actually playing back a disc. Also, the volume controls of home theatre amplifiers were adjusted to the middle of their range.

5.11 Steps 7 and 8: Select and measure combinations of devices: Select a combination of devices as they may be

grouped together in a home entertainment console. The television would be operated under APL setup and CD/DVD devices under disc playing operation. The volume controls of amplifiers are set to their mid-points.

6. PART B, GENERATE RESULTS

Once the measurement stage of the research methodology (Part A) has been completed, the next stage, Part B (Figure 8), is completed. Part B is the methodology to generate the results using the FlukeView and Microsoft Excel software. Figure 8 shows the methodology used to generate visualisation results for the measurements taken during the Part A (steps 1-8) investigation.

6.1 Step 1: Display measured voltage and current waveforms in FlukeView: The measurement results for each device were first displayed in FlukeView as voltage and current waveforms. The discrete time samples that make up these waveforms, in FlukeView, are then exported to Microsoft Excel for further processing.

6.2 Step 2: Export discrete time samples of waveforms to Microsoft Excel as a spreadsheet: Microsoft Excel was used to synthesise the total current waveforms from separate measurements and also to generate the current and voltage harmonic spectra through the use of the Fast Fourier Transform function. Finally, Excel was used to

calculate the power due to each harmonic as well as the total power using equations (2) and (3) respectively.

Voltage and current waveforms captured to FlukeView in Part A, steps 5, 6 and 8, were exported to Excel for further processing by using the “Copy Data” option in FlukeView under the “EDIT” menu with the data values pasted into Notepad. The sampled current and voltage samples are then pasted into Excel with headings indicating which device it is associated with. Each device has a column for current samples and one for voltage samples. The current and voltage samples are aligned in time. The same procedure is used if the data represents voltage and current measurements for a combination of devices.

6.3 Perform calculations in Microsoft Excel: At step 3 the methodology splits into two paths depending on whether one will be analysing the data from devices measured as a combination/individually, or synthesizing voltage and current for a combination of devices using data from individual device measurements. The next section will demonstrate how Microsoft Excel was used to perform calculations specific to portions of the methodology.

6.4 Step 6.b: Synthesize total current waveform from individual current measurements: One of the goals of this research was to combine results from home entertainment devices mathematically and determine the total current that would be drawn by the combination using individual device measurements. By applying equation 6, the total current waveform was synthesised by the addition of two or more sampled current values at the same sampling interval. The instantaneous total current is then given by:

$$i(t)_s = i(t)_1 + i(t)_{1+n} \quad (6)$$

Where:

$i(t)_s$ = the total instantaneous synthesised current

$i(t)_1$ = instantaneous current for device 1

$i(t)_{1+n}$ = instantaneous current for device 1+n

6.5 Steps 4.a and 7.b: Perform FFT on voltage and current waveforms: Once the total current waveform was synthesised in step 6b (section 6.4), the Fast Fourier Transform tool in Excel was applied to the total current waveform data to determine the frequency spectrum.

Using this process, a list of the current harmonics magnitudes and their associated phase angles were produced. The same procedure was followed for the voltage waveform to determine the voltage spectrum.

6.6 Step 8b Plot total current and voltage spectra:

Plotting the data generated in section 6.5 against frequency will produce the current spectrum. Similarly the magnitudes of the voltage frequency components can be plotted against frequency to produce the voltage spectrum.

6.7 Step 8a and 11b: Calculate power at each harmonic and the total power: Apply equation 2 to calculate the power due to each harmonic. Use the magnitudes and phase angles of the currents and voltages at each harmonic to determine the power due to each harmonic as well as the total power using equations 2 and 3.

7. RESULTS

Bredenkamp et al [15] applied the presented methodology to conduct case studies grouping devices together, as they may be found in a console at home, to determine the effect that a combination of home entertainment devices has on harmonic distortion levels.

Levels of current harmonics for case studies including an LCD or Plasma television as part of a group of devices was found to be below the maximum allowed by the EN 61000-3-2 standard. The EN 61000-3-2 standard places limits on the levels of current harmonics produced by home entertainment devices. It was also found that the evaluated LCD and Plasma television sets complied with the maximum limits on current harmonics.

The power consumption of individual home entertainment devices was also measured. The total power consumption of a combination of devices was also calculated from individual device measurements by using the specially developed methodology.

It was found that the power consumption of LCD television sets was below the maximum imposed by the Energy Star standard which governs power consumption. Only in one case was the power consumption of an LCD set slightly above the maximum set by the standard.

The power consumption of Plasma televisions were mostly above the maximum set by the Energy Star standard. It was found that LCD based television sets use less power than Plasma sets of equivalent screen size. It was also found that the typical range of power consumption for a home entertainment “unit” or console was 100 to 200W.

8. CONCLUSION

The research concludes that the current harmonics of new LCD and Plasma based televisions does not pose any concern for power quality.

By applying the methodology and evaluating and comparing the results, Bredenkamp et al also demonstrated the validity of the methodology.

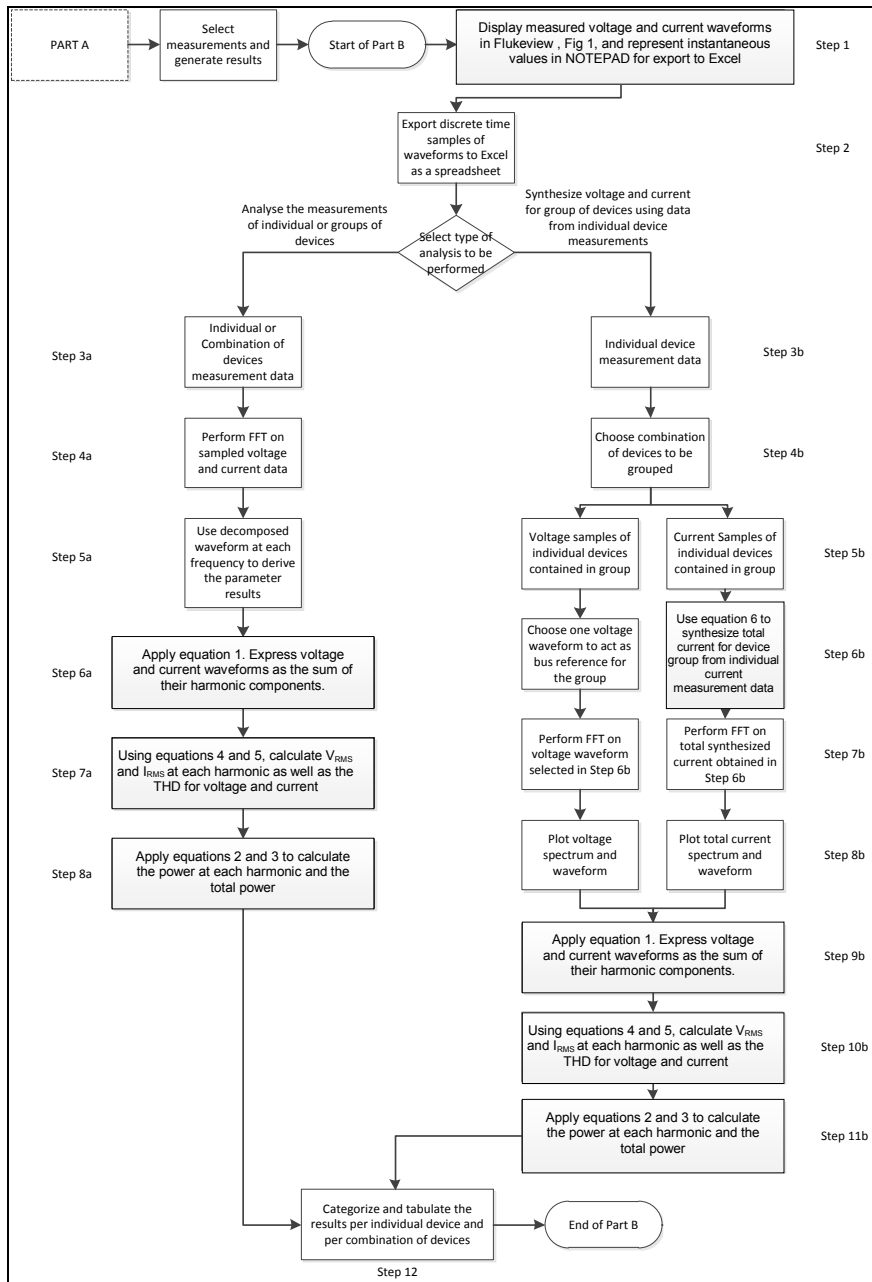


Figure 8: Detail of steps in part B, Generate Results

9. REFERENCES

[1] A.J. Bredekamp, E. Uken, and L. Borrill: "Standby Power Consumption of Domestic Appliances in South Africa", *Proceedings of the Domestic Use of Energy Conference 2006*, Cape Town, pp. 211-216, 2006.

[2] K. Roth and McKenney: "Residential consumer electronics electricity consumption in the United States", *ECEEE 2007 Summer Study*, 2007.

[3] Tricolite, 2010: "Difference between linear loads and non-linear loads", [online] Available at: <www.tricolite.com/News9.pdf> [Accessed 7 September 2010]

[4] W.M Grady, A. Mansoor, E.F. Fuchs, P. Verde and M. Doyle: "Estimating the net harmonic currents produced by selected distributed single-phase loads: computers, televisions, and incandescent light dimmers", *Power Engineering Society Winter Meeting*, vol.2, pp.1090-1094, 2002.

[5] J. Rabaey: "The standby power challenge: Wake-up receivers to the rescue", *International Symposium on VLSI Technology, Systems, and Applications*, p.42, 2009.

- [6] Hang-Seok Choi and D.Y Huh: "Techniques to minimize Power Consumption of SMPS in Standby Mode", *Power Electronics Specialists Conference*, pp. 2817-2822, 2005.
- [7] L. Mcgarry: "Standby power challenge", *Proceedings of 2004 International IEEE Conference on the Asian Green Electronics*, pp. 56-62, 2004.
- [8] I. Wacyk, D. Giannopoulos and S. Mukherjee: "Plugging the global power leak [appliance standby mode power reduction]", *IEE Review*, 46(6), pp.23-27, 2000.
- [9] K. Clement, I. Pardon J. and Driesen: "Standby Power Consumption in Belgium", *International Conference on Electrical Power Quality and Utilisation*, pp.1-4, 2007.
- [10] R.C. Dugan, S. Santoso, M.F. McGranaghan and H.W. Beaty: *Electrical Power Systems Quality*, McGraw-Hill, 2002
- [11] J. Shepherd, A.H Morton and L.F. Spence: *Higher Electrical Engineering*, Longman, second edition, 1998
- [12] G. Atkinson-Hope: *Single Phase and Three-Phase Circuit Analysis, Power Systems Engineering*. Cape Peninsula University of Technology, unpublished, 2000
- [13] K. Jones and B. Harrison: "The impact of changing TV technologies and market trends on the energy consumption on TVs and the need for a better TV energy test method", *ECEEE 2007 Summer Study*, 2007.
- [14] Ecos., 2010: "Assessment of Options for Improving Energy Efficiency Test Procedures for Displays", [online] *EfficientProducts.org* . Available at: <http://www.efficientproducts.org/%5Creports%5Ctvs%5CEcos_Display%20Test%20Procedure%20Report_FINAL.pdf> [Accessed 9 July 2011]
- [15] A.J. Bredekamp and G Atkinson-Hope: "Measurement Methodology Investigating Home Entertainment Consoles and Comparison Against Energy Star and Harmonic Standards", *Masters Thesis*, 2012

MULTI-TERMINAL HVDC VOLTAGE SOURCE CONVERTER OPEN LOOP TRANSFER FUNCTIONS

W.M. Phetha* and L. Chetty**

* School of Engineering, Howard Campus, University of KwaZulu Natal, Durban, 4000, South Africa
E-mail: 209515521@stu.ukzn.ac.za

** HVDC Centre, School of Engineering, Westville Campus, University of KwaZulu Natal, Durban, 4000, South Africa
E-mail: chettyl2@ukzn.ac.za

Abstract: This paper presents the derivation of the open loop transfer functions of a three-terminal MTDC VSC system using inductive modelling methodology intended for stability studies and to design the controllers using vector current control scheme. In using the inductive technique, each transfer function was derived by characterising the step response caused by a step input applied to the MTDC VSC system running at steady state simulated in PSCAD/EMTDC. Each characterized step response plot along with the corresponding error from the measured step response is presented.

Keywords: HVDC, multi-terminal, vector current control, transfer function.

1. INTRODUCTION

The innovation in the field of power electronic devices, dc cable systems and controls technology, resulted in the development of voltage source converter (VSC) based high voltage direct current (HVDC) transmission technology, which has given rise to a lot of interest and investigation by energy developing companies. The major motivation behind such interest and investigation in VSC HVDC transmission system is its ability to form an integration path for renewable resources available from remote locations, often offshore or near the sea. Herterem discussed this methodology of massive integration of renewable resources into Europe as the European super-grid, and discusses its potential and obstacles [4]. One of the major obstacles of the super-grid is balancing of power and hence stability of the VSC HVDC transmission system functioning as multi-terminal VSC HVDC meshed grid. This is due to the unpredictable generation output of the renewable sources of energy from different remote locations. The other issue is transmission of power from remote locations to load centres. Hence, this paper focuses on developing a mathematical model of a multi-terminal VSC HVDC system.

The development of analytical mathematical models of many dynamic systems such as VSC based HVDC transmission systems has been appreciated in the field of electrical power systems engineering [7], [8]. It is essential that the analytical mathematical model predicts the dynamic behaviour of the non-linear system. In general, there are two methodologies that are used in obtaining an analytical mathematical model of a dynamic system. The often used method is the “deductive modelling”, which involves describing the dynamic system using differential equations and established principles in order to obtain a mathematical model. On

the other hand, the least used method is “inductive modelling”, which involves using experimentation input-output data from the original system to obtain the mathematical model in a form of transfer functions [5]. Basically, the inductive model can be described as the ratio of the system’s step response to the step input to the system assuming one is working in frequency domain, which results in the transfer function. Research has revealed that multi-terminal direct current (MTDC) VSC systems involve complex interaction equations between the converters via the DC grid, the interaction of which normally leads to stability problems, and the higher order nature of the system makes it virtually impossible to develop accurate analytical models using deductive modelling [7] – [9].

2. MTDC VSC SYSTEM

The MTDC VSC system presented in this paper has three VSC terminals each connected to a stiff AC grid as shown in Figure 1. The MTDC VSC system contains the phase reactor, dc capacitors, HVDC cable. Normally the transformer and the passive filter are included, but in this paper are omitted for simplicity of the analysis.

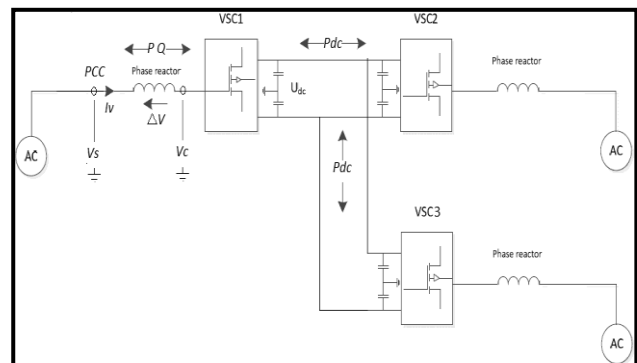


Figure 1: Three-terminal VSC HVDC transmission system

2.1 VSC principle of operation

The operation of the VSC HVDC system can be thought of as a variable voltage source connected to an AC network via a three-phase reactor. This implies that the amplitude, phase angle and the frequency can be controlled independently of each other. The phase voltage of the converter is given by the following equation;

$$V_C = \frac{1}{2} U_{DC} M \sin(\omega t + \mathcal{G}) + \text{harmonics} \quad (2.1.)$$

Where ω is the fundamental frequency, U_{DC} is the dc voltage across the dc link, t is time, \mathcal{G} is the phase shift of the output voltage depending on the position of the modulation wave, and M is the index ratio which is the modulating (sinusoidal) wave signal to the carrier wave signal. According to [1], in order to control reactive and active power, magnitude and phase shift of the modulating (sinusoidal) wave signal can be controlled independently to give any combination of the voltage magnitude and phase shift of the converter voltage in relation to the ac system (grid) voltage. The active power P is given by the equation (2), and the reactive power Q is given by the equation (3) below, where X_L is the reactance of the phase reactor.

$$P = \frac{V_C V_S \sin(\mathcal{G})}{X_L} \quad (2.2.)$$

$$Q = \frac{V_C [V_S - V_C \cos(\mathcal{G})]}{X_L} \quad (2.3.)$$

From equation (2), when the shift angle $\mathcal{G} < 0$ the converter voltage V_C is phase advanced in relation to the ac system voltage V_S , resulting in a voltage drop ΔV across the reactor. In this case, the VSC will deliver active power to the ac system while absorbing it from the dc link, operating as an inverter. On the other hand, when the shift angle $\mathcal{G} > 0$ the ac system voltage V_S is phase advanced in relation to the converter voltage V_C , resulting in a voltage drop ΔV across the reactor. In this case, the VSC will absorb the active power from the ac system and inject it to the dc link, operating as a rectifier. The reactive power on the other hand, according to equation (3) is dependent on the difference in voltage magnitude between the converter and the ac system. When $[V_S - V_C \cos(\mathcal{G})] > 0$, VSC absorbs reactive power from the ac system and when $[V_S - V_C \cos(\mathcal{G})] < 0$, the VSC sends the reactive power to the ac system, as shown in Figure 2.

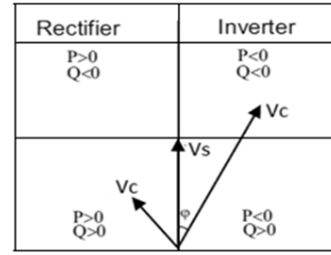


Figure 2: VSC HVDC mode of operation observed from VSC1

Using a consistent rule for defining positive and negative directions for current and power flows makes understanding the overall system operation easier [3]. In this study, AC current and AC power will have positive value if each is going away from the VSC-HVDC at the point of common coupling to the dc link.

2.2 Vector current control

The three-terminal VSC HVDC system to be modelled in this paper has three terminals each having a different control configuration to maintain stability of the whole system. The three terminals are each connected to a stiff grid where the grid voltage is constant. Hence, only the active power or dc voltage and reactive power can be controlled at each station as shown in Figure 3.

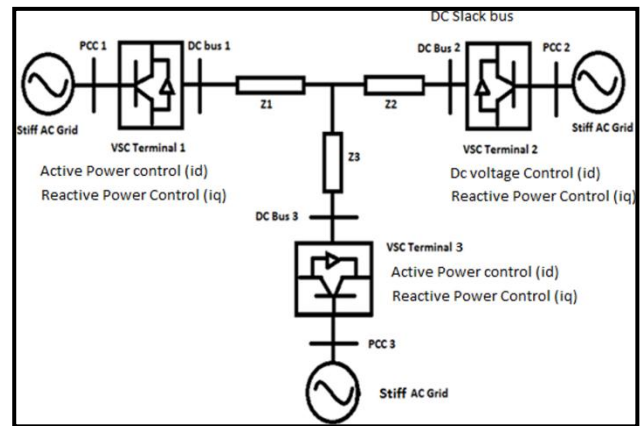


Figure 3: Three terminal HVDC grid

In the case of dc voltage droop control, two or more terminals participate in dc voltage control, thereby sharing the duty of instantaneous power balancing among them [10]. This control scheme offers redundancy in the MTDC VSC system because if one terminal goes out of service, the remaining terminal will carry out the task of regulating the dc voltage to compensate for the unbalances in the MTDC system.

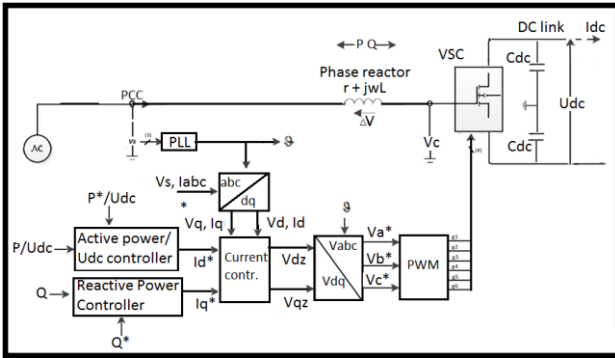


Figure 4: Vector current control Schematic diagram

For each VSC terminal, as shown in Figure 4, a vector current (or inner current) is the chosen strategy. The three-phase voltages and currents are transformed to a d-q synchronous reference frame [1]-[3], where the d-axis is aligned to the voltage of phase A measured at the point of common couple (PCC). A PLL is used in determining the angle θ for the transformation. This implies that the q-axis component of the measured voltage is zero [1]-[3]. The control scheme shown in Figure 4 assumes a balanced condition of the system, as the positive and negative sequences are not shown. However, in practice, the negative and positive sequence components are taken into account. The active power controller calculates the active reference current I_d^* given the measured power P at PCC and the reference power P^* through a feedback loop. The active reference current I_d^* is then sent to the current controller. Similarly, if a dc voltage controller is used in the case of a dc slack bus control scheme, it also calculates the active reference current I_d^* given the measured dc voltage U_{dc} at the dc link and the reference voltage U_{dc}^* through a feedback loop, and is sent to the current controller. On the other hand, the reactive power controller calculates the reactive reference current I_q^* given the measured reactive power Q and the reference reactive power Q^* through a feedback loop, and sends it to the current controller. The current controller then calculates the reference converter voltage, V_{dz}^* and V_{qz}^* , and through d-q to three-phase Park transformation the three-phase signal in p.u are obtained. The three-phase reference voltages are used to generate firing signals for the converter using PWM.

3. MTDC VSC SYSTEM MODELLING

This section defines two different approaches or methodologies used to derive a mathematical analytical model, namely the deductive modelling, and the inductive modelling techniques. In general, there are two methodologies that are used in obtaining a mathematical analytical model of a dynamic system. The often used method is called the “deductive modelling” [5], which involves describing the dynamic system using differential equations and established principles in order to obtain a mathematical model.

On the other hand, the least used method is the “inductive modelling”, which involves using analysis of input-output data from the original system operating at a steady state to obtain the mathematical model in a form of transfer functions [5]. Basically, the inductive model can be described as the ratio of the system’s step response to the step input to the system assuming one is working in frequency domain, which is simply a transfer function.

In ref. [7] Jovcic et al. presented the analytical model for a two terminal VSC HVDC transmission system. The converters used were 2-level VSCs with bipolar configuration using PWM firing signal generation for control of the converters. The model was simulated in MATLAB as a small signal dynamic model linearized around the steady state. The analytical model of the overall VSC transmission system consists of three models for each sub-system namely, the dc system model, AC rectifier model and an ac inverter model presented in state space form. However, the control scheme chosen for the VSC was the magnitude-angle control method unlike the often used vector current control. The system process was described using differential equations, which implies that the methodology used to obtain the analytical VSC model was “deductive modelling”. Haileselassie et al. investigated an MTDC VSC system that has 5 VSC terminals [9]. It is configured to use two VSC terminals as sending converter stations, and the other three converter stations are configured to be receiving converter stations. The aim of the investigation was to compare two control schemes: control scheme 1 using the vector current control approach that uses PI controllers and the control scheme 2 using PID controllers in order to compare the performances and analyse dynamics of the MTDC VSC system. The approach used to develop an analytical model was similar to the methodology presented in [7], [8].

The discontinuous and non-linear nature of transfer functions through the converters also gives rise to difficulties to developing an analytical model. A literature review of the above papers [7]-[9] shows that the most used approach in developing a mathematical analytical model of MTDC VSC Systems is deductive modelling. In fact there was no literature encountered that used the inductive approach for this purpose. However, it is evident that MTDC VSC systems involve complex interaction equations between the converters via the DC grid, the interaction of which normally leads to stability problems, and the higher order nature of the system. Based on this premise, an inductive modelling approach is proposed in developing a mathematical analytical model in a form of plant transfer functions for a MTDC VSC system in this paper.

4. INDUCTIVE MODELLING OF VSC HVDC

In implementing the inductive modelling approach, the VSC HVDC system was linearized around the steady state operating point. Once the system was run to a steady

state at open loop in, the system was perturbed by applying a step input. The output step response was then measured. The plant transfer function was determined by obtaining the ratio of the Laplace transform of the step response to the Laplace transform of the step input. The open loop controlled three-terminal VSC HVDC system, shown Figure 6, was modelled in PSCAD/EMTDC. A step input was applied to the reference voltage V_{dz} or V_{qz} one at a time in each VSC terminal, while all other inputs at other terminals are fixed. Then step responses of the DC voltage, active power and the reactive power in each terminal were measured.

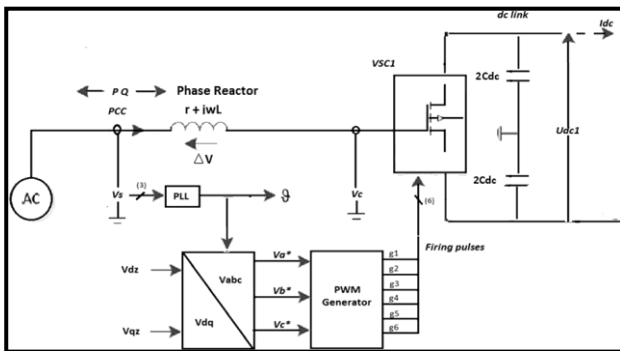


Figure 6: VSC HVDC in open loop connection

The MTDC VSC system has three terminals, hence six inputs. Each step input corresponds to 9 step response outputs. A step input to V_{dz1} will not only affect VSC1 terminal outputs, but also VSC2 and VSC3 outputs. This implies that a change in each VSC terminal will cause a disturbance to other VSC terminals via the dc link. Hence, the number of open loop transfer functions of grid connected three-terminal VSC system is 54. If a deductive model were to be used in deriving the transfer functions, this indeed would require complex interaction equations between the converters as evidently stated in [7]-[9]. However, in using the inductive model, the derivation of complex interaction equations can be avoided.

5. PSCAD/MTDC SIMULATION RESULTS

The three terminal VSC test system shown in Figure 1 was simulated in open loop control in PSCAD/MTDC to operate at steady state. To demonstrate the VSC is operating as expected, measurements at VSC2 terminal were recorded and displayed in Figure 7 and Figure 8.

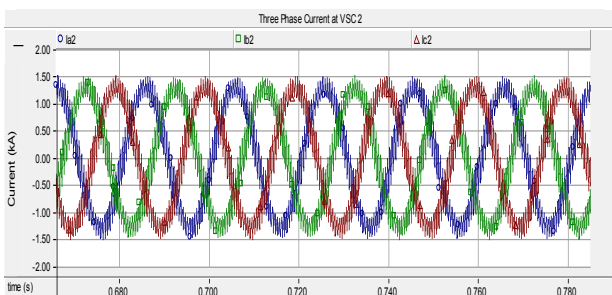


Figure 7: Three phase current at VSC2

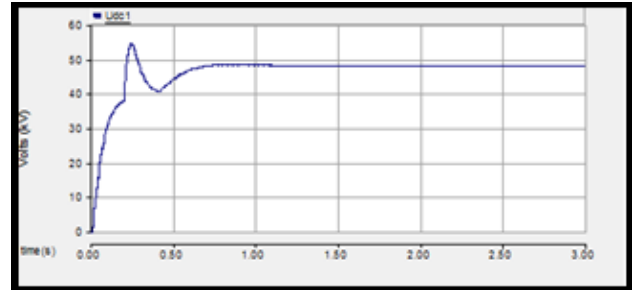


Figure 8: DC Voltage at VSC 2

VSC Terminal	Udc (kV)	Idc (kA)	Active Power (MW) @ PCC	Reactive Power (Mvar) @ PCC	Vdz (pu)	Vqz (pu)	M
1	48.169	-0.83	-38.656	40.462	0.704	0.591	-10 ⁰
2	48.471	0.71	34.339	8.416	0.860	0.314	10 ⁰
3	48.358	0.12	7.08	17.339	0.811	0.431	2 ⁰

Table 1: Summarized results of measured DC voltage, active and reactive power at steady state operation

A summary of the steady-state operating conditions are illustrated in Table 1.

The process used to calculate the dc voltage, active power, and reactive power transfer functions where the inputs at VSC1 terminal are excited is as follows:

1. Simulate the three-terminal VSC HVDC system such that it reaches steady-state.
2. Fix the d-q axis reference voltage inputs in VSC 2 (V_{dz2} , V_{qz2}), VSC3 (V_{dz3} , V_{qz3}), and V_{dz1} in VSC1.
3. Apply a step increase of a small signal 0.05 (small signal model) to the d-component of the reference voltage V_{dz1} at VSC1, and measure the reactive power Q_A (at VSC1), Q_B (at VSC2), and Q_C (at VSC3) step response. Similarly measure the active power P_A (at VSC1), P_B (at VSC2), and P_C (at VSC3) step response. And finally, measure the dc voltage U_{dc1} (at VSC1), U_{dc2} (at VSC2), U_{dc3} (at VSC3).
4. Fix the d-q axis reference voltage inputs in VSC2 (V_{dz2} , V_{qz2}), VSC3 (V_{dz3} , V_{qz3}), and V_{dz1} in VSC1.
5. Apply a step increase of 0.05 to the q-component of the reference voltage V_{qz1} at VSC1, and measure the reactive power Q_A (at VSC1), Q_B (at VSC2), and Q_C (at VSC3) step response. Similarly measure the active power P_A (at VSC1), P_B (at VSC2), and P_C (at VSC3) step response. And finally, measure the dc voltage U_{dc1} (at VSC1), U_{dc2} (at VSC2), U_{dc3} (at VSC3).
6. Capture the input/outputs data obtained in steps 2-5 i.e. the input and the step response of each output, and export it to MATLAB.
7. In MATLAB, use the System Identification Tool Box to approximate or characterize each step response in time domain.
8. Validate each characterized step response with the exact measured step response and Compute the error.

9. If the error is greater than +2, then repeat step 5 and step 7.
10. Use the System Identification Tool Box to calculate each transfer function of which there would be 18 transfer functions for two input signals.

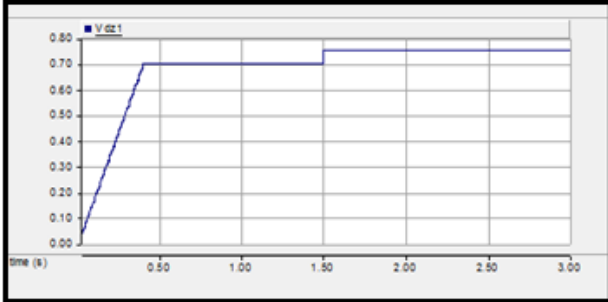


Figure 9: Reference voltage input V_{dz1} at VSC1 terminal

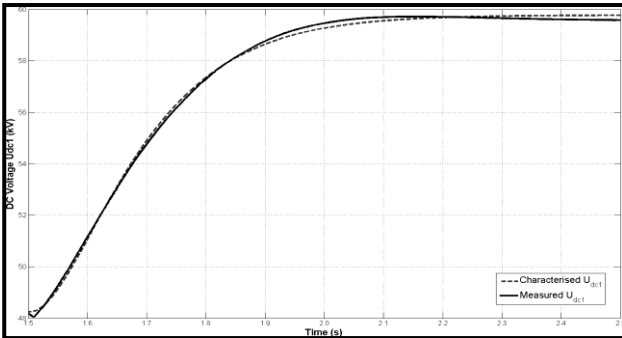


Figure 10: Measured and characterized dc voltage (U_{dc1}) response at VSC1

Using the characterized DC voltage (U_{dc1} at VSC1) Figure 10, the transfer function estimated using SITB in MATLAB is:

$$G1(s) = \frac{\Delta U_{DC1}}{\Delta V_{dz1}} = \frac{79.32}{(1 + 0.3827s)(1 + 0.3827s)} e^{-0.000594s} \quad (5.1.)$$

The error between the measured and the characterized DC voltage step response is shown in Figure 11.

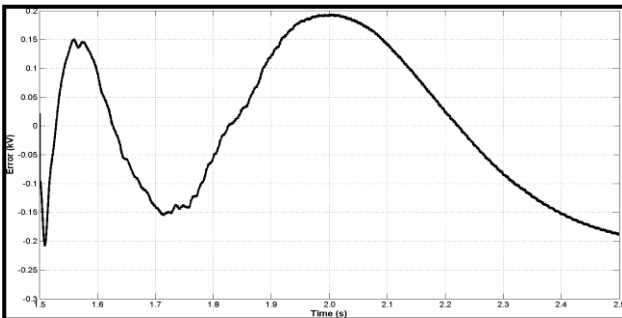


Figure 11: Error between measured and the characterized step response

Figure 11 clearly illustrates that the characterized DC voltage U_{dc1} step response adequately approximates the measured DC voltage U_{dc1} at VSC1 since the error is less than 0.2 kV difference between the measured result and characterised response, which is approximately a 0.34% error. However, the error shows significant dynamics. The rest of the 53 transfer functions derived are included in the file “*Additional results transfer functions*” attached.

6. SENSITIVITY TO INITIAL CONDITIONS

The inductive modelling can be visualized by a block diagram shown in Figure 12.

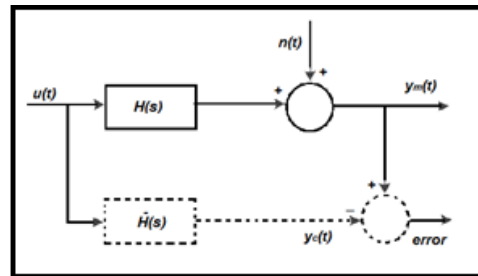


Figure12: Inductive Modeling Block diagram [8]

According to ref. [6] and [11], the measured process output response $y_m(t)$, will consist of the uncorrupted process output and additional process noise and/or measurement noise $n(t)$. The inductive model will therefore have a system response described as,

$$\hat{H}(s) = H(s) + \frac{N(s)}{U(s)} \quad (6.1.)$$

Hence, it was then stated that inductive model technique may contain sensitivity to noise. Based on the premise that the output response is dependent on the initial conditions, this section investigates the sensitivity of the derived step response equations. The investigation presented in this paper is for VSC 2 terminal step response equations.

The process used to investigate the sensitivity of the derived step responses at VSC 2 for the step input V_{dz2} , is as follows:

1. Model the three-terminal VSC HVDC system at open loop, shown in figure 6, in PSCAD/EMTDC.
2. Simulate the three-terminal VSC HVDC system such that it reaches steady-state of the set initial condition (IC), capture a snap-shot at this point.
3. Fix the d-q axis reference voltage inputs in VSC 2 (V_{qz2} , V_{dz3} , V_{qz3}), and in VSC1 (V_{dz1} , V_{dz2}).
4. Apply a step increase of 0.05 to the d component of the reference voltage V_{dz2} at VSC 1 at 1.5 seconds, and measure the reactive power Q_B (at VSC2) step response. Similarly measure P_B (at VSC2) step response. And finally, measure the dc voltage U_{dc2} (at VSC2),

5. Capture the step response data obtained in step 4 and export it to MATLAB.
6. In MATLAB, plot the original characterized step response and plot the measured the step response from PSCAD with a different initial condition and plot the error between them.

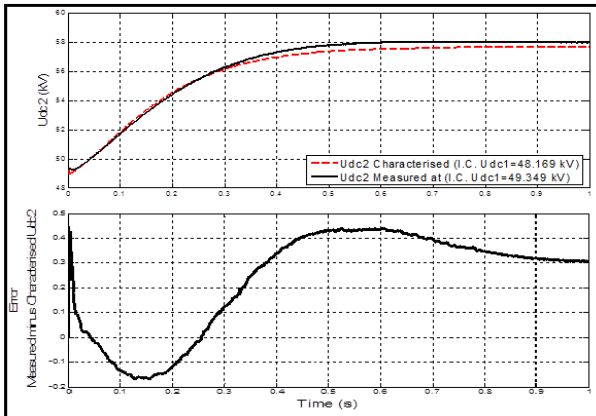


Figure 13: Sensitivity of Udc2 at VSC 2- step input Vdz2

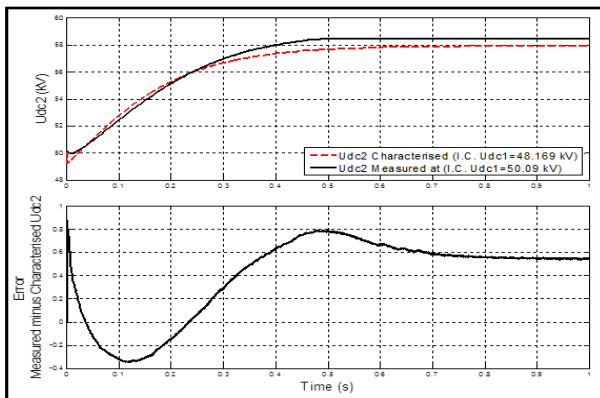


Figure 14: Sensitivity of Udc2 at VSC 2- step input Vdz2

Fig. 13 clearly illustrates that the characterized dc voltage at VSC2 (U_{dc2}) step response is not too sensitive to initial conditions, since the profile of the measured step response is not altered except for the small deviation in magnitude where the error is less than 0.45. However, based on the increased error of 0.8 in Fig. 14, illustrates that the sensitivity of the characterized U_{dc2} step response increases with the increase in the difference between the original initial conditions and varied initial conditions. Hence, the mathematical model derived is dependent on the initial conditions at steady state.

7. CONCLUSION

Presented in this paper is the inductive approach in developing a mathematical model for the MTDC VSC system. The open loop transfer functions were derived using the system identification toolbox in MATLAB. Due to the interaction between the converters via the dc link one input change affects outputs at other terminals. It is essential that a mathematical model takes into account the interaction or coupling effect between the converters,

thus motivating the necessity to derive all transfer functions. For each transfer function, the characterized step response used to obtain the transfer function, was compared to the actual measured system step response. The resulting error was found to be insignificant. In addition, the step responses used to derive the transfer functions proved to be more sensitive to initial conditions when the variation of the initial conditions became large. Hence the mathematical model derived is dependent on the initial conditions of the MTDC VSC system operating at steady state.

8. REFERENCES

- [1] D. Cuiqing: "The control of VSC-HVDC and its use for large industrial power systems", *Chalmers University of Technology*, 2003
- [2] T.M. Haileselassie: "Control of Multi-terminal VSC-HVDC Systems", *Norwegian University of Science and Technology*, 2008
- [3] C. Bajracharya: "Control of VSC-HVDC for wind power", *Norwegian University of Science and Technology*, 2008
- [4] D. van Hertem and M. Ghandhari: "Multi-terminal VSC HVDC for the European supergrid: Obstacles", *Renewable and Sustainable Energy Reviews*, pp.3156–3163, 2010
- [5] A. Groessler: "Inductive and Deductive System Dynamics Modelling", *International Conference of the System Dynamics Society*, pp. 9780-9794, 2007
- [6] L. Chetty: "Design synthesis of LCC HVDC control systems", *University of KwaZulu- Natal*, 2011.
- [7] D. Jovcic, L.A. Lamont, L. Xu.: "VSC Transmission model for analytical studies", *IEEE Power Eng. Soc. Gen. Meet*, pp. 1737–1742, 2003.
- [8] D. Jovcic, L.A. Lamont and K. Abbott: "Control system design for VSC transmission", *Electric Power Systems Research*, pp. 721-729, 2007
- [9] A.M. Alseid, D. Jovcic and A. Starkey: "Small Signal Modelling and Stability Analysis of Multi-terminal VSCHVDC", *University of Aberdeen*, 2011
- [10] T.M. Haileselassie and K. Uhlen: 'Impact of DC Line Voltage Drops on Power Flow of MTDC Using Droop Control'. *IEEE Trans. on Power Delivery*, pp. 8945-8
- [11] RAKE H: 'Step response and frequency methods'. *Automatica*, 16, (1980), pp. 519-526

TABLET BASED WIRELESS MEASUREMENTS FOR POWER APPLICATIONS

H.L. Brummer, C.W.I. McAfee and K.J. Nixon *

* School of Electrical & Information Engineering, University of the Witwatersrand, Private Bag 3, 2050, Johannesburg, South Africa

Abstract: There are a number of benefits to using wireless measurement equipment in power engineering environments. Such a system would separate users from dangerous or complex environments. A further improvement on such a system is the addition of a wireless tablet device (Apple iPad) being used as the user interface to Measurement Device. This system is discussed in terms of its application in a power engineering environment, and the design decisions are presented. The final device is a wireless oscilloscope, that samples a live real time signal at 132.1 kS/s, with 8 bit resolution. The measured signal is continuous, and the recorded data is capable of being saved and resent for later analysis.

Key words: CC3000, Chain of Responsibility, iOS, MSP430, Oscilloscope, Round-Trip Time, Wireless.

1. INTRODUCTION

A wireless measurement system offers many advantages over traditional fixed line instruments, the most important of which is the ability to separate the user from dangerous environments. A further improvement would be the addition of a wireless device that is capable of providing the user interface (UI) to the measurement device. This paper presents the design, testing and analysis of a measurement device that connects wirelessly to a tablet device. This device acts as a wireless oscilloscope used on an educational three-phase test bench, however the concepts and practical application of this measurement device have a broader application in the power industry.

A wireless measurement device could be used inside a machines laboratory, electrical substation or even an entire manufacturing plant. It could be used at multiple points along a transmission line, or even used to control and monitor smart grid configurations. In addition to this, using an tablet as a UI offers improved comfort to managers and test personnel, and due to the wireless capabilities, the user is safe from large moving equipment, and high voltage environments. In summary this device would offer safety, convenience and versatility.

A high level overview of the system components is presented, as well as the major sub-systems. Each subsystem highlights the important design decisions used in terms of the intended power environment where the device will be operated. The complete system test methods and results are discussed, and important findings are elaborated. The final results after optimisation are presented and future work is highlighted.

2. BACKGROUND

The wireless measurement system has been designed for use on an educational three-phase test bench, situated in

a machines laboratory. This bench outputs 9 channels representing the different line voltages and currents, as well as the phase voltages. These benches test variations of three-phase loads, as well as motor configurations. Although these benches operate at 50 Hz, the motor tests introduce signals with higher order harmonics that may be relevant in the testing process. All of these factors are relevant in a variety of power engineering applications, and designing the system to handle these allows reuse of the system in alternative environments.

There are many different variations in how this system could operate, however for this design the system is being used to demonstrate a laboratory to students. Thus the device must be capable of recording a test session, and be able to resend the test data. Therefore it is necessary for the saved data of the measured signal to be continuous. An emphasis must be made on the fact that a live real time signal is continuously being sampled and sent over a wireless network. Given these specifications the following design criteria were defined for the measurement device and the wireless platform:

- Capable of sampling 8-bit data at ≥ 100 kS/s.
- The measured signal should be complete (no missing data).
- iOS based application provides basic scope functionality
- The measured signal should be recorded for later analysis.

Existing solutions of this nature include those offered by National Instruments [1]. This solution is capable of continuously acquiring up to 51.2 kS/s of simultaneous 24-bit data on four channels.

3. SYSTEM ARCHITECTURE

Figure 1 depicts a high level overview of the components of the system developed in this project. A design goal is to achieve as much decoupling as possible, in particular between the tablet device and the measurement device. Therefore each component and device, as a whole, may be developed almost independently of the other.

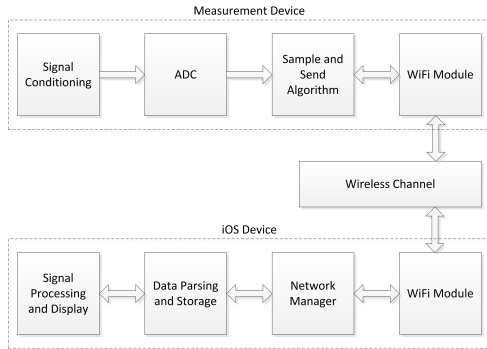


Figure 1: High level overview of functional components of the system.

The Apple iPad was chosen as the tablet device due to its popularity among the academic staff, and the advantages that the iOS development environment offers. The tablet has Bluetooth and WIFI available for wireless connectivity, however WIFI was chosen because it is widely used, and because it offered higher speeds. The TCP/IP protocol was chosen over UDP as the primary communications protocol between the devices. This is primarily because TCP guarantees the data throughput, for a trade-off on faster speeds [2]. Furthermore, TCP allows the load of introducing packet overhead such as Cyclic Redundancy Checks (CRCs) to be removed from the low level microprocessor used for the measurement device. All these factors must be considered for the system to be used in alternative applications.

4. THE COMMUNICATION PROTOCOL

The tablet device and measurement device are configured in a client-server architecture. This allows the measurement device to listen for connections and simply serve requests made to it by clients (tablet device). In order to maintain a decoupled design a custom protocol was defined as seen in the sequence diagram Figure 2. The protocol is kept simple to reduce processing requirements on the microprocessor. The protocol also defines a standard interface between the measurement devices and clients connecting to it. This decouples the microprocessor implementation from the iOS implementation by reducing dependency on implementation details.

To facilitate the protocol a general message structure is defined in Listing 1. The `Command` field in the message defines the type of action being requested or the type of response. The `DataSize` field describes the amount of actual data to expect. The `DataLoss` field is defined for

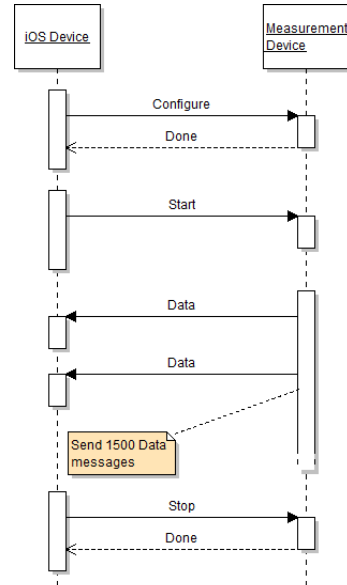


Figure 2: Sequence diagram of protocol messages.

diagnostic and testing purposes. The `Data` field contains the data associated with the request or response. The first three fields are referred to as the message header, and are required in all messages.

Listing 1: General Structure for protocol messages.

```
<Command><DataSize><DataLoss><Data>
```

5. IOS DEVELOPMENT

iOS is an embedded device operating system used by Apple Inc. for their mobile devices. Programming in iOS offers a unique approach to software engineering practices due to their required design patterns. The following sections describe the core functional components of the iOS software implementation, and can be summarised into four main focus areas:

- Network and Thread Management.
- Network Data Storage Mechanism.
- Protocol Parser Design.
- Real Time Software Oscilloscope.

5.1 Network and Thread Management

Given that drawing to the display is slow and runs on the main thread, it potentially blocks incoming data and impedes the performance of the network [3]. Streaming data from the Network Management component and processing and storing it in the Network Data Storage component is process intensive and renders the display unresponsive. Therefore the receiving stream of the Network Management component is run in a separate thread.

It is this threaded behaviour that allows the the iOS device (tablet) to maintain a high data throughput and a responsive user interface. This is verified in the performance testing in Section 7.1. This increase in performance comes at the price of complexity. Since data is received by one thread and displayed by another, accessing data has to be made thread safe through the use of “locks” to ensure that only one thread accesses the data. This is also known as the Readers-Writers Problem [4].

5.2 Network Data Storage Mechanism

The measurement device continually streams new data on request. This data needs to be managed for use in saving and displaying the data. Thus the data needs to be accessed from a central location. Network data is stored centrally and is maintained by the `NetworkDataStore` class. The `NetworkDataStore` class is implemented as a singleton [5]. This allows for the data to exist only once. In addition the `NetworkDataStore` class may only be associated with one network connection at any one time to ensure consistency of the data in the event that unexpected hopping between measurement devices occurs.

The implementation also allows for the management of the amount of data that can be streamed and saved to the iPad. Performance tests revealed that approximately 24 million data points could be stored in RAM before the application is forced to close. The data limit is set to 20 million providing some leeway for conversion and saving to disk. This assumes that the application is the only one running on the iPad.

5.3 Protocol Parser Design

The protocol used for the communications in this system has the message structure in Listing 1. Each part of the message has a unique function and is explained in detail in Section 4.

Using the Chain of Responsibility design pattern allows network messages to be parsed and processed by objects in the parsing chain and hiding the details of this parsing from clients of the parsing chain [5]. Each class in the chain implements the `ProtocolParserInterface` and may or may not contain a reference to another class implementing the interface. Each class defined encapsulates the behaviour required to parse each section of a message for the network and are named accordingly. These relationships are expressed in Figure 3.

The parsing objects here encode data contained in `Message` objects into raw byte data that is of an acceptable form for the communications protocol. `Message` objects are supplied by clients of the parser. `Message` objects are an object oriented representation of protocol messages. Inversely messages received as raw byte data can be parsed into `Message` objects that are useful to clients of the parser.

This method of using `Message` objects is intentionally used to decouple the protocol parsing from the network management.

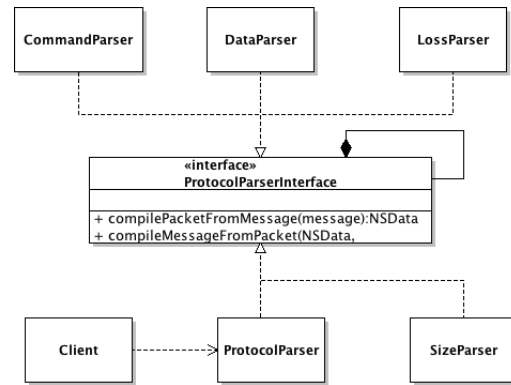


Figure 3: Protocol Parser classes in chain of responsibility.

5.4 Real Time Software Oscilloscope

The main view of interest in the application is the real time oscilloscope. The oscilloscope allows limited time scaling, amplitude scaling and amplitude shifting. The scope uses information provided by a device management class to display meaningful information on the screen. Figure 7 shows the scope in operation.

The drawing functionality of scope is achieved through the use of core-plot, an open source plotting framework for OS X and iOS [6]. The scope reads data from the `NetworkDataStore` class described in Section 5.2 periodically by means of a timer which manages the refresh rate of the scope.

6. EMBEDDED SYSTEMS DEVELOPMENT

6.1 Background

An embedded system based around a Mixed Signal Processor (MSP) from Texas Instruments was chosen as the microprocessor in the Measurement Device (MD) [7]. The specific device chosen is the MSP-EXP430FR5739 & CC3000 experimenter’s kit [8]. The experimenter’s board is capable of operating at 24 MHz, and sampling at a maximum rate of 200 kS/s. This kit was chosen because it has support for a plug in Wi-Fi module, and Application Programming Interfaces (APIs) have been provided to simplify development [8]. In addition to the Wi-Fi support provided by Texas Instruments, and the simplicity of connecting the Wi-Fi module, the MSP device has been designed to operate under low power modes, and supports Direct Memory Access (DMA). DMA is capable of transporting memory from one register to another without the intervention of the main processor, thus allowing two processes to run simultaneously [7].

One of the primary disadvantages with this device is its input voltage range for the ADC, which is 0-3.6 V. This requires further signal conditioning of the measured signal to be transformed to a value within this range, otherwise the device could be damaged. The limited voltage range also requires a high level of accuracy in

the signal conditioning, otherwise the resolution of the measurements will drop. The other limitation of the device is that it only has 16 kB of memory, which limits the amount of buffer space for storing sampled data.

6.2 Design Pattern

The initial design pattern relied on a single buffer being populated, and then being sent. This meant that while the buffer was being sent, samples were missed. This is the traditional approach used in embedded system design before the introduction of DMA [7]. The implemented design pattern used in the MSP is built around the simple principle that for a signal to be continuously sampled and sent, the MSP would have to be able sample and send at the same time. Using DMA allowed for samples to be transferred from the Analogue to Digital Converter (ADC) to a memory buffer, while another memory buffer is sent. This results in data being sampled and sent at the same time. Figure 4 shows the implemented design pattern, and also emphasizes the simplicity of creating a Wi-Fi connection on the MSP. The device waits for a client to connect through the router on the TCP/IP layer, and once a client connects it waits to receive a request message.

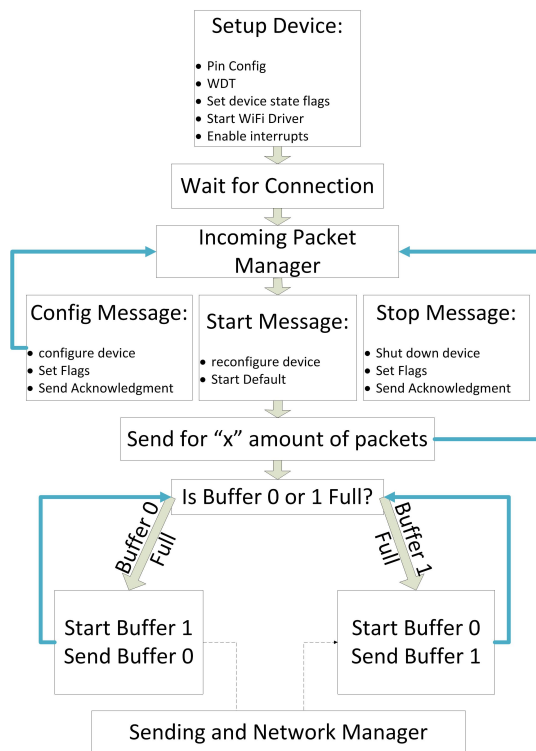


Figure 4: Improved Design Pattern.

This design pattern revolves around the use of DMA, and switching between two buffers. When a “Send Data” request is received the ADC and DMA are started (both run in parallel to the main processor). When an ADC cycle completes the DMA retrieves the sample data, stores it in a buffer, and restarts the ADC. This is raw data, with 8 bit resolution. This process repeats with the DMA incrementing through the buffer until filled, after which the

DMA triggers an interrupt and allows the buffer to be sent. The packet header is then added to the data, and sent by the sending function API. Before the send function is started, the DMA is activated again, and the newly sampled data is passed to the secondary buffer. This process continues for a set amount of packets, and then stops to check for new messages from the client. Note that the sending function is a blocking action in the main code, and only one packet is sent at a time. This limits the speed of the system. There are two variables that effect the performance of the system: sampling rate, and packet size. The effects of these are presented in sections 7.2 and 7.3.

7. TESTS AND FINDINGS

The testing procedures applied to this system all focus on the effective sampling rate and lossless data throughput. Three components of the system are identified as possible sources of throughput throttling and data loss. Namely:

- Speed of data acquisition and processing in software.
- Non-determinant Round-Trip Times (RTT) [9].
- Microprocessor sampling rate and buffer size.

These are tested for performance and lossless throughput. The sections below describe this in detail.

7.1 Data Acquisition Performance

To ensure data is throughput continuously the iOS based software is required to process the data at a rate greater than or equal to what it receives. By setting the measurement device to deliver maximum throughput, the load on the iPad is analysed. Maximum throughput delivered to the iPad is compared to throughput test run on a Unix machine. Table 1 compares performance on the iPad versus performance on the Unix machine. These results indicate that the iPad is capable of handling maximum throughput.

Table 1: Throughput performance.

	Max Throughput
iPad	189.15 kB/s
Unix Machine	184.8 kB/s

7.2 Effect of TCP/IP and Round-Trip Time

The use of TCP/IP introduces secure data transfer at the expense of non-deterministic events that cause the Round Trip Times (RTTs) of messages to be inconsistent [9]. If RTTs are longer than the time it takes to fill ADC buffers, then data loss results from samples not being recorded. Thus throughput does not reflect sample rate. The effect of this can be seen visually on the application as discontinuities in the signal. Throughput only reflects true sampling rate when zero samples are missed in-between packets being sent. Thus an analysis was performed using the ping network utility with a payload of 1472 bytes

(maximum allowed) [10]. The round trip times result in the probability distribution in Figure 5.

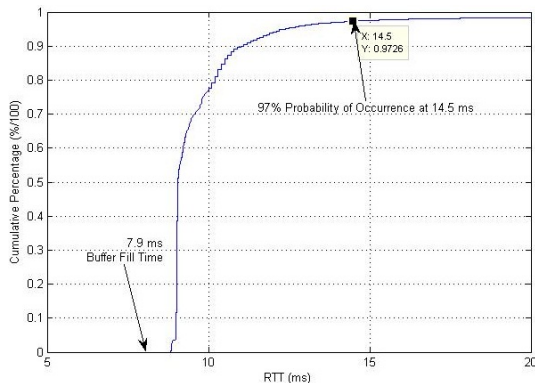


Figure 5: Cumulative distribution indicating percentage chance for RTTs occurring.

Figure 5 indicates the RTT required to send 1472 bytes to a host and back. The implemented protocol in Section 4. sends messages of approximately 1455 bytes in size, to which the response is an acknowledgement. It is thus reasonable to assume that the RTTs indicated by the Ping program are a worst case and serve as a starting point for optimizing sampling rate to match throughput without loss.

Figure 5 shows that the time taken to fill a buffer is 7.9 ms with the MSP sampling at 200 kS/s. This figure also indicates that 97% of the RTTs occur at 14.5 ms or less. Therefore the sampling rate of the MSP must be adjusted downward (slower) until the time taken to fill a buffer matches the time taken to send a buffer. Under this situation almost no samples will be missed in-between packets being sent. Note that due to the probabilistic nature of the RTTs, there is never a 100% probability that no samples will be missed, but the effects can be mitigated.

7.3 Measurement Device Speed Test

Using “Netcat”, and a Linux command line script a connection was established and streamed data was piped into a file for 5 seconds. Using the time and file size, a simple calculation shows the throughput of the device in “kilobytes per second” (kB/s) (see Figure 6).

Figure 6 shows that there is a substantial difference between the two design patterns, and that rate of throughput slows down after 600 bytes in a packet. The maximum throughput achieved is 184.8 kB/s. There is an upper bound for the size of the data in a sent packet (1460 bytes), which is a limitation of the Wi-Fi module, as well as the API of the sending function [11]. The throughput values presented are the true data transmission rates, where the true data consists of the sample data in the packets, and not the packet headers. This throughput consists of purely sample data, but does not guarantee the sample rate.

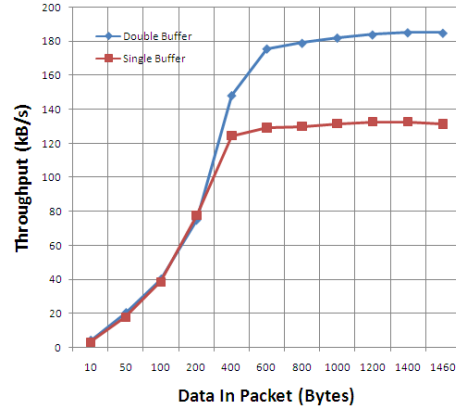


Figure 6: Transmission Rate of MD & Design Patterns.

8. FINAL RESULTS

The process of finding the optimal sampling time indicated that a sample rate of 100 kS/s would provide a 97% (or greater) probability of reliable and continuous data being sent. Using this theory, the MSP code was incrementally adjusted to slow down the sample rate until the average missed ADC cycles were found to be near zero. When the missed ADC cycles are zero, then the throughput is equal to the sampling rate. The final transmission rate (sample rate) for the MD is 132.1 kS/s. At this rate the time to fill the buffer is 11 ms.

In summary the MD is configurable to measure one of 9 input channels. The measured signal is continuous, and the application provides the functionality to save the data and email it. The transmission rate (sampling rate) is above the required 100 kS/s.

9. FUTURE WORK

The implemented iOS solution uses threading to achieve high performance and ensures data integrity by using “locks”. Threading introduces a large amount of complexity, therefore for improved stability further testing must be done to improve thread safety and performance. Lastly a significant performance increase may be achieved if “lazy instantiation” is used to convert raw byte data to objects, as not all the data processed by the Protocol Parser is displayed on the screen.

This project has the capability of being applied in alternative power environments where different system success criteria exist. For example, it may be possible to optimise the packet size for different situations, such as a trade-off in transmission rate for power requirements (using less energy for portable applications) [12]. This may be necessary at points along a rural transmission line.

The protocol is very simple and as such relies heavily on the guarantees provided by TCP. The possibility of using UDP instead of TCP is a serious consideration, and may require further research. By using UDP, the probabilistic RTT concerns would not have been a factor.

UDP would have transmitted at a consistent rate, and combined with its lower overhead of memory, would have improved the transmission rate of the device. There is no guarantee that the data will arrive safely, and CRC may be required. This adds its own memory overhead to each packet sent. Additionally, the main sending loop inside the MSP would become more complex, effectively slowing down the throughput. It is not feasible to implement UDP in this project due to the MSP used, but may be possible on a device with higher specifications.

Apart from system noise, another signal issue that occurred is shown in Figure 7. In-between packets the same inconsistency occurred, where a portion of the samples would be shifted down, and then followed by a negative impulse. These are not samples being lost, as confirmed by a Wireshark capture test. This abnormality cannot be explained, and requires further investigation.

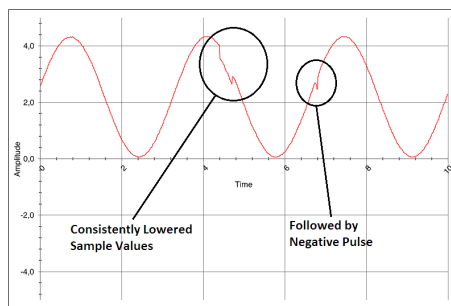


Figure 7: Signal Error.

The method used in determining the RTT is inaccurate, however for this project the theory provided is accurate, and guided the developers to the correct approach of finding a solution. For the system to be optimised even further, the RTT will have to be calculated more accurately.

10. CONCLUSION

Three main designs have been presented: the simple network protocol, the iOS based application and the Measurement Device (MD). The protocol allowed for decoupled design and operation. In the application the use of threading was vital, and on the measurement device DMA and dual buffering ensured reliable and high speed data transmission. Testing revealed that the message RTTs are non-deterministic due to the probabilistic nature of the network. To mitigate this the sampling rate was lowered to compensate for RTT variations. The modular design proposed allows for future work to be carried out in other power engineering applications. The final system is a wireless oscilloscope that is capable of continuously sampling a live real time signal, and transmitting that data over a wireless network. The signal is sampled with an 8 bit resolution at 132.1 kS/s, and is represented visually by a software oscilloscope on a tablet device. All the design criteria for the three-phase test bench have been met, and the device operated correctly in the machines laboratory.

ACKNOWLEDGEMENT

The authors would like to thank Eskom for the support of the High Voltage Engineering Research Group through the TESP programme. They would also like to thank CBI-electric for support, the department of Trade and Industry (DTI) for THRIP funding as well as to the National Research Foundation (NRF) for direct funding.

REFERENCES

- [1] National Instruments. "Wireless Data Acquisition (DAQ).", last accessed 15 July 2012. URL <http://www.ni.com/data-acquisition/wireless/>.
- [2] J. F. Kurose and K. W. Ross. *Computer Networking, A Top-Down Approach*. Pearson, 2010.
- [3] Apple Inc., last accessed 23 October 2012. URL <http://developer.apple.com/library/ios/DOCUMENTATION/General/Conceptual/Devpedia-CocoaApp/DrawingModel.html>.
- [4] A. Silberschatz, G. Gagne, and P. Galvin. *Operating System Concepts*, chap. 6, pp. 206–207. John Wiley and Sons Inc., 2005.
- [5] E. Gamma. *Design Patterns: Elements of Reusable Object-Oriented Software*. Addison-Wesley Professional Computing Series. Addison-Wesley, 1995.
- [6] "core-plot - Cocoa plotting framework for OS X and iOS.", last accessed 24 October 2012. URL <http://code.google.com/p/core-plot/>.
- [7] S. F. Barret and D. J. Pack. *Microcontroller Programming and Interfacing - Texas Instruments MSP430*. Morgan & Claypool, 2011.
- [8] "Texas Instruments Wiki.", 2012. URL http://processors.wiki.ti.com/index.php/CC3000_Wi-Fi_MSP430_FRAM.
- [9] J. Kurose and K. Ross. *Computer Networking: A Top-Down Approach*. Pearson, 2010.
- [10] Fedora Manuals. "Fedora Manpages: PING(8).", last accessed 24 October 2012. URL <http://linuxmanpages.net/manpages/fedora17/man8/ping.8.html>.
- [11] "Texas Instruments: CC3000 Release Notes.", 2012. URL http://processors.wiki.ti.com/index.php/CC3000_Release_Notes.
- [12] P. Lettieri and M. B. Srivastava. "Adaptive Frame Length Control for Improving Wireless Link Throughput, Range, and Energy Efficiency." In *INFOCOM '98. Seventeenth Annual Joint Conference of the IEEE Computer and Communications Societies. Proceedings. IEEE.*, vol. Vol 2., pp. 564 – 571. 1998.

Topic B

Electromagnetics

CALCULATIONS OF GEOMAGNETICALLY INDUCED CURRENTS (GICs) IN THE NAMIBIAN TRANSMISSION NETWORK

M N Simon, D T Oyedokun, C T Gaunt

Dept. of Electrical Engineering, University of Cape Town, Cape Town, South Africa

Abstract: Geomagnetically Induced Currents (GICs) in electrical transmission network creates major problems to power systems including increased non-active power, transformers operating in non-linear regions and generation of harmonics. Over the years, different GIC calculation tools have been developed. In this paper, power system nodal admittance method for GIC calculation is compared with a previous technique applied on the Namibian network. In addition, the Namibian network in 2002 is compared to the existing network in 2012. It is found that the GIC magnitudes in some substations have increased more than in others.

Keywords: GIC, Namibian network, storm, transmission lines, non-active power, harmonics

1. INTRODUCTION

The sun undergoes an 11 year solar cycle of sunspot activities. Near the end of the cycle, the sunspots frequently erupts sending large masses of charged particles towards the Earth's surface. The interaction of the charged particles with the Earth's magnetic field causes the fluctuations of the magnetic field. As the magnetic field fluctuates, a ground quasi-DC current induced also known as Geomagnetic Induced Current (GICs). GICs flow in the electrical transmission networks through the grounded neutral of power transformers [1,2]

Previous solar storms that had significant effects on power system networks are; the 1989 Quebec storm that resulted in a blackout of the entire Quebec region of Canada [2], the Halloween storm that resulted in a blackout in the city of Malmo in southern Sweden [3] and transformer damage in Southern Africa [4].

Previous work done [5] looked at the risk of GICs on the Namibian network. This study looks at GICs in the Namibian network using a different approach called the Nodal Admittance network. Comparisons with the a , b parameter method and the Nodal Admittance method are made and thereafter GIC calculations are performed for the existing Namibian network

1.1 Susceptibility of the Namibian network

Previously, it was believed that areas located in regions of low/mid-latitudes such as Namibia and South Africa were not highly susceptible to GICs. However, since 2002 research done on the Southern African network showed that the network is also susceptible to GICs [5,6]. Magnitudes as high as 108 A were calculated at Alpha substation in the South African network using the 13 March 1989 storm data.

One of the reasons for the susceptibility of the Southern African networks is the high ground conductivity and the

presence of long transmission lines and this situation is evident in the Namibian transmission configuration.

1.2 Effects of GICs on power systems

GICs enter the transmission network via grounded neutral of star-transformer. Thereafter, the current divides equally among the three phases of the transformer. Under normal operations of the transformer, i.e. in the absence of GICs, a linear relationship exists between the magnetic flux and the magnetisation currents. At the same time, the magnetic flux confines itself within the magnetic core. However, sometimes, the presence of GICs biases the magnetic circuit and causes transformers to operate in the non-linear region of the B-H loop, with an increase in the leakage flux. In a non-linear region, the saturated core becomes of much higher reluctance which then forces flux - referred to as leakage flux - to follow other alternative paths in regions of less reluctance (such as air, oil and tank walls). This causes transformers to draw larger excitation currents, which introduce even and odd harmonics [6]. When the amount of GIC is significant or large enough, the transformer goes into half cycle saturation which may lead to increased Var consumption, possibility of voltage collapse, harmonics production, overheating and noise.

2. COMPARISON BETWEEN A AND B PARAMETER METHOD AND THE NODAL ADMITTANCE METHOD

2.1 a and b parameter method

Previously GIC calculations were done using this method developed by [7]. This method is divided into two parts [7] namely:

- Geographical calculation

This includes the use of Faraday's induction law to calculate the electric field strength components E_x and E_y in the whole network at any particular time. It is important to note that this particular method used a

uniform electric field and uniform ground resistivity for the entire network.

- Network calculation

This includes the calculation of network constants, a and b parameters, of each substation using the network data.

Thereafter, the GIC for each substation can be calculated using equation (1)

$$I_{GIC} = aE_x + bE_y \quad (1)$$

Where:

a, b are network parameters

E_x is the electric field component in the x direction

E_y is the electric field component in the y direction

2.2 Network Nodal Admittance method

The network nodal admittance method used in this paper is described by Trichtchenko et al [8] and explained in details by Oyedokun et al [9]. The method is divided into two sub-sections namely:

- Earth Surface Potential (ESP) calculations

The ground conductivity model together with measured magnetic field data from magnetic observatories is used to calculate the electric field given in V/km at each network position. Thereafter, the ESP can be obtained from the electric field. This step accommodates non-uniform plane waves and non-uniform ground conductivity. An approach to ground conductivity in Southern Africa has been formulated [10].

- Network calculations

From the ESP induced in the network, the GIC magnitudes at each point in the network can be calculated at different nodes in the transmission network using Ohm's and Kirchhoff's laws. The network modal admittance method allows the flexibility of using different electric field and different ground conductivity for each substation in the network. This is crucial because at any particular point in time, different regions of the network are exposed to different electric fields.

Based on approximate agreement with measurements, the use of a uniform electric field and ground conductivity may have been an adequate approximation; however, research has shown that the use of an interpolated electric field improves the error between measured and simulated results [11].

3. CORRELATION BETWEEN KOEN'S AND THE NODAL ADMITTANCE RESULTS

The a and b parameter as described above was applied to Namibian network shown in Figure 1 [6]. For that study, only transmission lines of 220 kV and 400 kV were considered. Only long lines (>100 Km) were included for

it is believed that shorter lines do not make significant difference to the results [6].

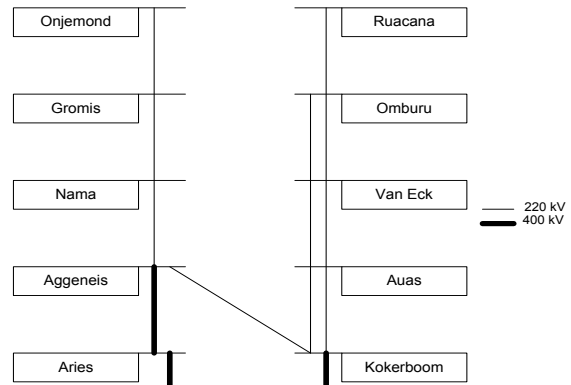


Figure 1: Namibian Network [6]

The network depicted in Figure 1 was used in the network nodal admittance method using the same uniform field and ground conductivity parameters that were used in 2002 and results were compared to previous calculated results obtained using the a, b parameter method [6]. Figures 2 and 3 show the results for the Ruacana and Kokerboom substations using both methods. The electric field data used are from the 13 March 1989 storm.

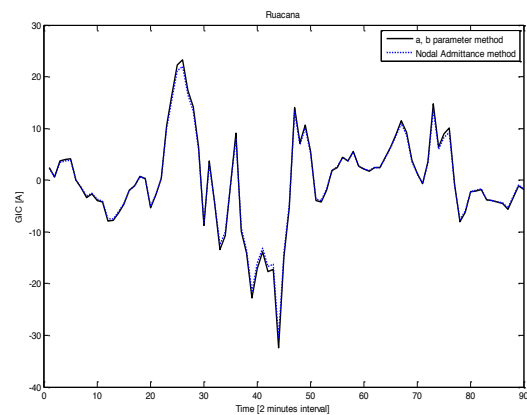


Figure 2: Simulated results for the Nodal Admittance and the a, b parameters Method for Ruacana substation

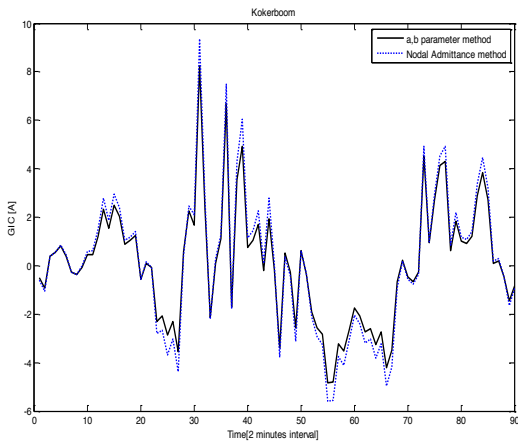


Figure 3: Simulated results for the Nodal Admittance and the *a, b* parameters Method for Kokerboom substation

Despite the different methods used for GIC calculations, the differences between the results obtained using the *a, b* parameters and the network nodal admittance method is small. In both cases, the GIC calculated is shared among all the transformers in a particular substation.

In this paper, only two substation results are shown; Ruacana in the north and Kokerboom in the south of Namibia.

From the result it was found that Ruacana substation had the highest GIC magnitude. Research showed that substations located at the ends of the transmission lines appear to be most susceptible to GICs. This finding is consistent with other studies [12] that indicated substations located at the extremes of the network have the highest GICs.

4. CALCULATION OF GICs ON THE CURRENT NAMIBIAN NETWORK

Having compared the results obtained using the *a* and *b* parameters and the nodal admittance method and found good correlation, we applied the nodal admittance method to the existing 2012 Namibian network. The objective of this study is to see how susceptible the current network is compared to the network as it was in 2002. Since there have been new substations built in the network, we wanted to investigate the effect this had on the GIC magnitudes in the network, using the same 1989 storm data.

Figure 4 illustrates the existing Namibian network. Over the last 10 years, the Namibian network has undergone many modifications in order to be able to supply the increased demand.

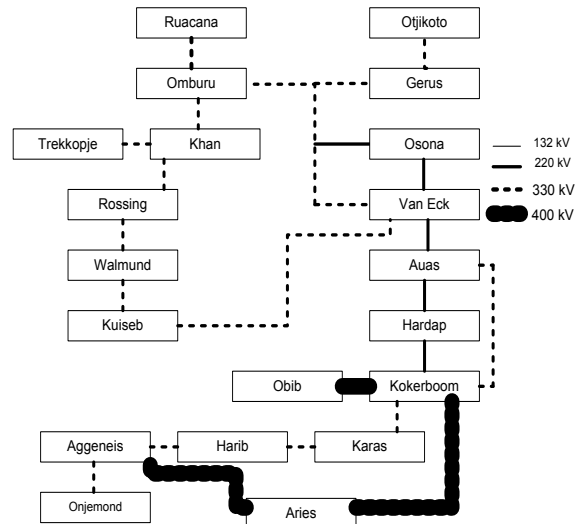


Figure 4: The Namibian existing network

Figures 5 and 6 shows GIC calculation results for the existing Namibian network still using uniform field and ground conductivity.

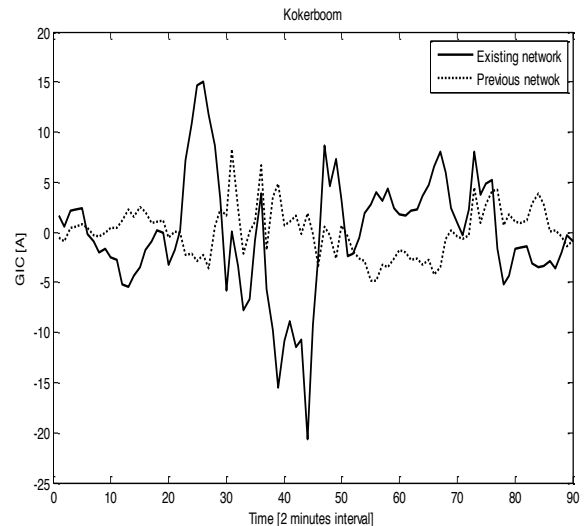


Figure 5: Previous and existing network GIC for Kokerboom substation

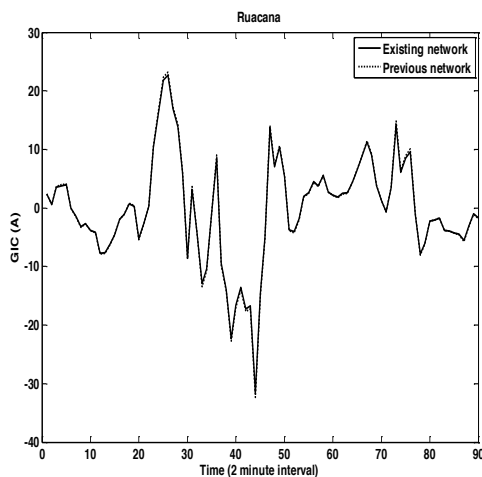


Figure 6: Previous and existing network GIC for Ruacana substation

It can be seen in Figure 5 that the maximum GIC expected for Kokerboom increased from 15 A to 20 A while the maximum GIC magnitude for Ruacana showed no change as can be seen in Figure 6. One of the reasons for the increased magnitude of Kokerboom substation can be associated with the changes in the network particularly in the Southern region. Over the 10 year period, the number of substations has doubled and the number of substation interconnections has increased from 13 transmission lines to 31 transmission lines.

5. CONCLUSION

- a) The Nodal Admittance software gives results similar to Koen's results using the same input assumptions and it can be used to analyse the existing network with GICs constrained assumptions.
- b) Changes in the network configuration resulted in an increased in GIC magnitudes for some substations.
- c) The susceptibility of some of the substations in Namibia to damage from GICs may have increased following the increase in GIC magnitudes.

This is a work in progress for the analysis of the Namibian transmission network. The accuracy of the calculations is being tested by measurements on the system. The exposure of all the substations to a variety of geomagnetic storms will be determined. Possible approaches to mitigation of damage and disruption will be developed.

ACKNOWLEDGEMENT

The technical collaboration and financial support of M.N Simon from NamPower and financial support from THRIP for the broad programme of GIC research are gratefully acknowledged.

REFERENCES

- [1] V.D. Albertson, J.M. Thorson, S.A. Miske: "The Effects of Geomagnetic Storms on Electrical Power Systems", IEEE PAS-93, No. 4, pp 1031-1044, July/August 1974
- [2] J.G. Kappenman, V.D. Albertson: "Bracing for the geomagnetic storms", IEEE Spectrum, pp.27-33, March 1990
- [3] R.J. Pirjola, D.H. Boteler: "Geomagnetically induced currents in European high-voltage power systems", IEEE Ottawa, May 2006
- [4] C.T. Gaunt, G. Coetzee: "Transformer failures in regions incorrectly considered to have low GIC-risk", Paper no. 445, IEEE Power Tech, Lausanne, Switzerland, 1-5 July, 2007
- [5] J. Koen: "Geomagnetically induced currents and their presence in the Southern African electricity transmission network". PhD Thesis, University of Cape Town, 2002
- [6] J. Koen, C.T. Gaunt: "Disturbances in the Southern African Power network due to geomagnetically induced currents", Cigre, Paris, paper 36-206, August 2002
- [7] M. Lehtinen, R. Pirjola: "Currents produced in Earthed conductor networks by Geomagnetically induced electric fields", *Annals Geophysicae*, Vol.3, No. 4, pp. 479-484, 1985.
- [8] A. Trichtchenko, D.H. Boteler, A. Foss: "GIC modelling for an overdetermined system", Canadian Conference on Electrical and Computer Engineering (CCECE), IEEE Canada, Ottawa, Canada, May 7 – 10, 2006
- [9] D.T. Oyedokun, M.N. Simon, C.T. Gaunt: "Introduction of a more detailed calculation of Geomagnetically Induced Currents in transmission networks" Southern Africa Universities' Power Engineering Conference (SAUPEC) 2013, Potchefstroom, South Africa, 31 January to 1 February, 2013
- [10] C.M. Ngwira, L.A. McKinnell, P.J. Cilliers, A. Viljanen, R. Pirjola: "Limitations of the modelling of geomagnetically induced currents in South African power network", *Spaceweather*, Vol. 7, S10002, 2009.
- [11] T.A. Tjimbandi: "Geomagnetically induced currents in South Africa", BSc(Eng) Thesis, University of Cape Town, 2007
- [12] T. Zatzirua: "Investigation of Geomagnetically induced currents in the transmission network of Namibia". BSc(Eng) Thesis, University of Cape Town, 2005
- [13] E.H. Bernhardt, T.A. Tjimbandi, P.J. Cilliers, C.T. Gaunt: "Improved calculation of geomagnetically induced currents in power networks in low-latitude regions", Power Systems Computation Conference, paper 677, Glasgow, July, 2008

SMALL ENCLOSURE SHIELDING EFFECTIVENESS TESTING

J. A. Andriambeloson, H. C. Reader and, G. C. M. Coetzer *

* *University of Stellenbosch, Dept of Electrical and Electronic Engineering, Stellenbosch, South Africa
andyjoely@gmail.com, hcreader@sun.ac.za, gcmcoetzer@gmail.com*

Abstract: A nested-enclosure methodology is presented for small enclosure shielding effectiveness (SE) evaluation. Two excitation positions within the enclosure under test are investigated particularly for the under-moded condition. A battery driven stirrer was built to paddle the fields inside the shielded enclosure. Preliminary measurement shows a SE convergence for both used probe positions at higher frequency. The enclosure corner-position excitation is recommended for under-moded enclosure SE measurement.

Key words: Shielding effectiveness, stirrer, small enclosure, nested-enclosure.

1. INTRODUCTION

To meet the electromagnetic compatibility (EMC) requirements of an electronic system, metallic enclosures are frequently used by engineers for radio-frequency interference (RFI) mitigation. The enclosure plays two major roles. The first consists of minimising the penetration of external RFI inside the sensitive environment. The second is the prevention of the self-generated noise from the electronic equipment within the enclosure coupling to the exterior. A variety of methods are available for enclosure shielding effectiveness (SE) measurement. [1], for instance, presents a standard for the SE measurement of enclosures larger than two metres. In this paper, we are interested in smaller enclosures which might find application in sub-station equipment racks or equivalent environments. A nested-enclosure technique is used for the SE investigation. A portable mechanical stirrer has been built to stir the modes inside the EUT. This work constitutes a preliminary step towards our work on time-domain (TD) enclosure shielding characterisation for the Karoo Array Processor Building (KAPB) of the Karoo Array Telescope (MeerKAT) system.

2. SHIELDING EFFECTIVENESS DEFINITION

In general, the shielding effectiveness (SE) of a material is related to the electromagnetic propagation through that material. [3, 4] define SE as the ratio of the incident and transmitted field (E or H) in equation (1), before and after incorporating the shield under test. In this definition, the incident wave is assumed to be uniform and illuminating an infinitely homogeneous shield.

$$SE = -20\log_{10} \left(\frac{\text{Transmitted Field}}{\text{Incident Field}} \right) \quad (1)$$

3. MEASUREMENT PRINCIPLE

Briefly, the nested-enclosure methodology is based on a reverberating environment principle. The EUT is placed inside a reverberation chamber and the enclosure itself

is stirred [2]. The stirrers change the boundary of both cavities and this allows the receiver and the transmitter to remain in the same positions during the measurement. In contrast, the standard measurement requires different positions to be able to characterise the correct field value to be used in the SE calculation.

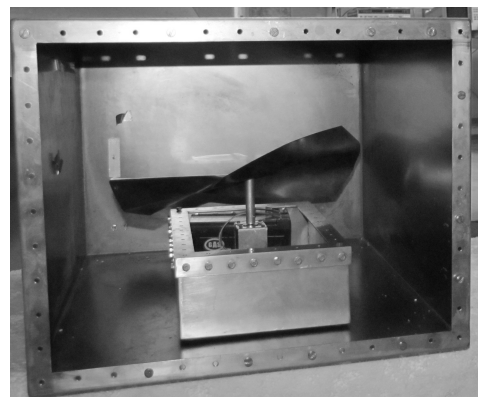


Figure 1: The EUT, opened at the front, with the battery driven paddling system placed in the enclosure

Figure 1 shows a picture of the portable stirrer and the EUT used in this work. The enclosure is made of mild-steel and is 60cm x 50cm x 40cm. Figure 2 presents the overall setup. The vertical and horizontal stirrers of the external reverberation chamber, the EUT and the log periodic dipole array (LPDA) antenna used to measure the fields outside the enclosure are all visible.

We are particularly interested in the shielding variation obtained from 300 MHz up to 1.2 GHz at seven non-harmonically related frequencies. In the first instance, the enclosure's lid was omitted; then it was closed; finally, the lid/enclosure seam was fully covered with conductive tape. The enclosure opening area is pointed towards the wall, on the right side of figure 2, to avoid direct coupling with the LPDA antenna. These measurements examine the best method to seal the enclosure. This investigation also gives some indication of the conductive tape shielding characteristics.

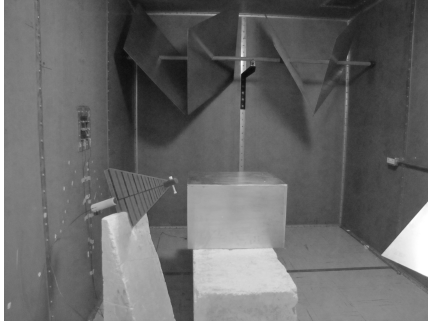


Figure 2: The measurement setup showing the receiving LPDA antenna, the EUT and the horizontal stirrer

3.1 EUT stirrer

The portable stirrer is an autonomous battery-driven stepper motor, activated by a RENESAS R8C27 microcontroller and a stepper-motor controller L297. The motor is connected to an H-bridge formed by NMOS power transistors and Schottky diodes. The H-bridge acts as switches to drive the motor coils while the diodes circulate the current back to the battery to save energy. A significant increase in battery life was seen. This allowed a stirring operation longer than 6 hours. A graphical user interface is available, through an LCD panel, to help the user to configure the stirrer. The following parameters are configured: rotation mode (continuous or stepped), speed, direction, initial delay and runtime. The motors stepping type, half or full step mode, is automatically set according to the speed. The stepper motor was particularly chosen since it has a high torque to speed ratio, allowing for different paddle sizes. The paddle is made of a twisted copper sheet of 1 mm thickness, bent into a spiral-type shape (see figure 1).

3.2 EUT Excitation

From cavity theory, it is known that the field distribution inside the EUT is not uniform due to standing wave patterns. The field pattern inside the enclosure, also called a mode, have resonant frequencies given in equation (2)

$$F = \frac{c}{2} \sqrt{\left(\frac{m}{w}\right)^2 + \left(\frac{n}{h}\right)^2 + \left(\frac{p}{l}\right)^2} \quad (2)$$

In this equation, w, h and l represent the length, the width and the height of the cavity resonator. m, n and p are the modes indices and c is the speed of light in air. Figure 3 shows a longitudinal cut of the H-field pattern inside the EUT, for 4 different modes, computed using MATLAB. We can see from this that the H-field is strong at the corner of the enclosure (marked M) for each mode. A square loop antenna was, therefore, placed at the bottom left corner of the enclosure, named P1, to be able to excite the EUT. A picture of this setup is seen in figure 4.a. The loop antenna is fed from the exterior through a bulkhead sub-miniature version A (SMA) connector located at the back of the

enclosure.

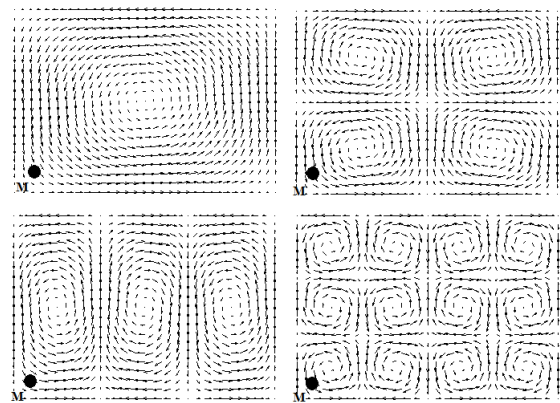


Figure 3: H-field pattern for four different modes over one cross-section of the EUT

The presence of the stirrer inside the small enclosure leads to more a uniform field distribution. This increases the likelihood that similar fields are seen at any probe position within the central region. In reality, this field uniformity is not ideal for all the frequencies of the chosen range. A frequency of at least three times the first cut-off frequency of the EUT is necessary to benefit the stirrer's effect, according to [5]. To check this property, the loop antenna was placed at a second position named P2, close to the centre of the enclosure as seen in figure 4.b. The same measurements as those used for the probe in position P1 were taken.



Figure 4: Enclosure excitation positions: a) Position P1: Loop placed at the bottom left corner. b) Position P2: Loop placed near the enclosure centre

3.3 Measurement routine

Ideally, the stirrers are synchronised for the nested enclosure method to achieve an accurate SE result. The stirrer shown in figure 1, inside the enclosure, is set to rotate continuously at a speed of 30 rpm (mode-stirred) over the measurement. The fields inside the outside RC are recorded on a vector network analyser (VNA), through the LPDA antenna on the right hand side of the EUT. 72 fields values are measured for each frequency of the frequency range per revolution of the small stirrer. During this time, both the vertical and the horizontal stirrers are fixed. They are, subsequently, moved simultaneously by 5 degree, every time a full rotation of the EUT's paddle is

performed. The measurement ends once the RC's stirrers complete one full turn.

4. RESULTS AND DISCUSSIONS

Using the S-parameter data from the measurement, the equation expressed in (1) becomes:

$$SE = -20\log_{10} \left(\frac{S_{21} \text{ with shield}}{S_{21} \text{ reference}} \right) \quad (3)$$

where $S_{21} \text{ reference}$ represents the measured S_{21} when the EUT is not present.

A matrix of $7 \times 72 \times 72$ S-parameters are obtained for each frequency of the range and for each enclosure configuration. The average S_{21} of that matrix is evaluated and used in the calculation of SE in equation (3). In figure 5, the S_{21} obtained at P1 is shown, when the lid is fully taped. The dashed curve represents the average of the overall S_{21} measurement and the other curves correspond to the individual S_{21} at the 72 positions of the vertical and horizontal stirrers.

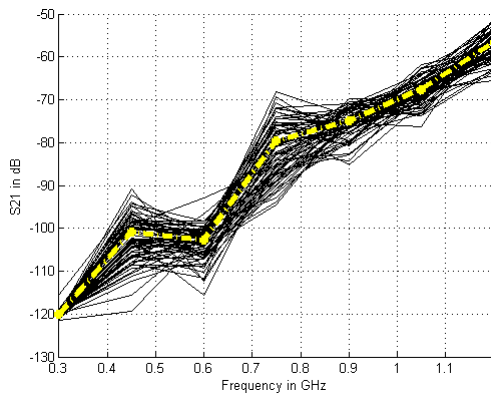


Figure 5: Measured S_{21} when the EUT is closed and the seams are fully taped

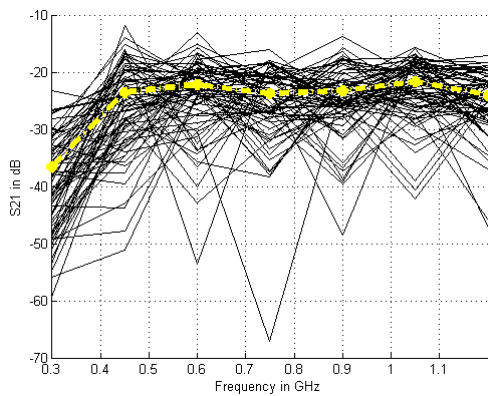


Figure 6: S_{21} average variation outside the enclosure

Thereafter, the ratio of the averaged S_{21} in figure 5 and in figure 6 is calculated to find the SE of the EUT when

the lid is closed and sealed with conductive tape. Similar results as those shown in figure 5 are obtained for the second lid configuration. The same procedure is applied and this gives the SE curves in figure 8. Here, a bigger variation of more than 10 dB is seen between P1 and P2 at low frequencies (less than 900 MHz) for the various lid configurations. The variation is less than 10 dB beyond this frequency. Due to the fact that the low frequency part of the range of interest is around the lowest resonant mode of the EUT (390 MHz), this behaviour is expected. Insufficient modes are produced inside the smaller chamber and the stirrer is not efficient enough to smooth out the generated fields. In this case, the magnitude of the field measured by the probe in P1 will not be the same as the field measured at P2. At higher frequencies, however, the number of modes generated inside the enclosure is higher, as indicated by the total number of modes versus frequency shown in figure 7. The stirrer's effect is more efficient at high frequencies and this reduces the difference between the average field at both probe positions. The total number of modes inside a cavity resonator of length l , width w and height h is given in terms of the frequency f in equation (4).

$$N(f) = \frac{8\pi}{3}wlh \left(\frac{f}{c} \right)^3 - (w+l+h) \frac{f}{c} + \frac{1}{2} \quad (4)$$

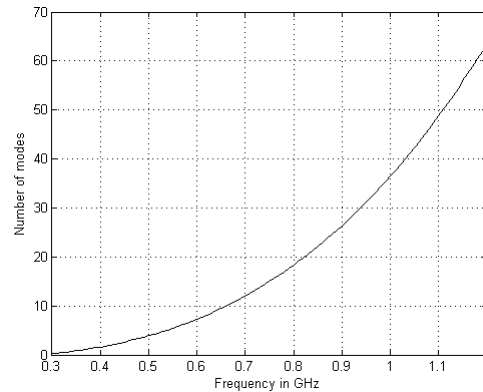


Figure 7: Number of modes of the EUT with frequency

Theoretically, if the lowest usable frequency of a reverberation chamber, in [5], taken as three times the lowest resonant frequency is used, we would expect to measure almost the same average field at P1 and P2 beyond 1.17 GHz. The EUT is not working as a RC before 1.17 GHz. But, the trends of the curves in figure 8, for both positions, show a SE convergence at a frequency closer to 900 MHz. We believe, however, that the SE obtained with the probe at P1 corresponds to the accurate SE estimation because it is placed at a maximum H-field location for all the modes. As a consequence, the probe in position P1 is recommended for a SE measurement with a loop antenna for an under-moded enclosure. The probe in position P2 could be used once the RC conditions are met. However, an extension of the frequency range must be done to check the repeatability of the measurement and the similarity between the SE at P1 and P2 for the over-moded condition.

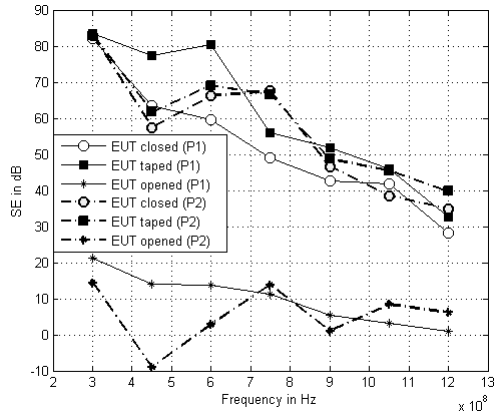


Figure 8: SE of the enclosures in P1 and P2 for all the lid configurations

We can also see from the SE measured at P1, that the enclosure provides a SE of at least 15 dB at its first resonant frequency even if the EUT is left open. This shielding decreases with frequency and becomes 0 at 1.2 GHz, which is around three times the lowest mode. As in the previous discussion, this is caused by the resonant property of the EUT. All signals less than, or close to, the lowest resonant mode could not exist inside the EUT which is now behaving like an electromagnetic waveguide. At present, the SE seems to be decreasing linearly with frequency. We cannot state this with confidence until the frequency resolution is improved

From the SE measurements made at P1, represented by the lines with circles and squares, the conductive tape effect on the enclosure shielding can be evaluated and is shown in figure 9. The SE at 300 MHz is very low because the measurement reaches the noise floor of the VNA at that frequency. This could be also seen in figure 5 and in figure 8 where the same SE is obtained, at P1, for this frequency. The last result in figure 9 shows that the conductive tape improvement on shielding is decreasing with frequency. This could, however, be compromised by other issues such as the apertures used to connect the lid to the enclosure (shown in figure 1).

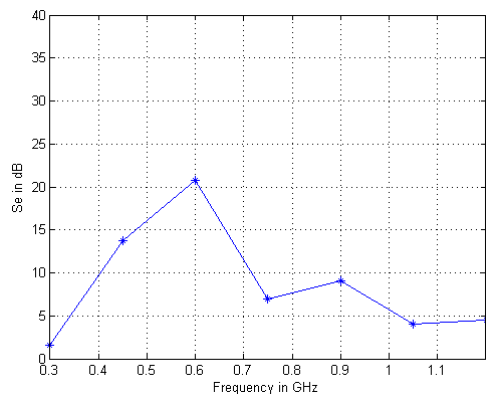


Figure 9: SE of the conductive tape

5. FURTHER WORK

A TD characterisation of the SE will speed-up the measurement time. With the setup and the frequency range used here, the measurement of the S-parameter matrix mentioned in section 4. takes an hour. The overall investigation took around 12 hours. A time improvement of at least 60% is expected, and this will also allow a better SE resolution.

6. CONCLUSION

The investigation of the SE of a metallic enclosure was presented in this paper as the first step on nested-enclosure SE evaluation methodology. A battery-driven stirrer was specially built and used to paddle the modes in the EUT. A loop antenna placed inside the enclosure was used to estimate the SE over a frequency range of 300 MHz up to 1.2 GHz. We found that the probe position at the corner of the enclosure allowed a good estimation of the SE for an under-moded chamber. The enclosure provided a shielding around 15 dB near the lowest mode even when the enclosure was left open. The effect of conductive tape on the shielding was also evaluated in a preliminary fashion.

REFERENCES

- [1] IEEE: "IEEE Std 299: IEEE Standard Method for Measuring the Effectiveness of Electromagnetic Shielding Enclosures", December 1997.
- [2] W. J. Krzysztofik, R. Borowiec, B. Bieda: "Some Consideration on Shielding Effectiveness Testing by Means of the Nested Reverberation Chambers", *RADIOENGINEERING*, Vol. 20 No. 14 pp. 766-774, December 2011.
- [3] C. H. Fang, S. Q. Zheng, H. Tan, D. G. Xie, and Q. Zhang: "Shielding effectiveness measurements on enclosures with various apertures by both mode-tuned reverberation chamber and gtem cell methodologies", *Progress In Electromagnetics Research B*, Vol. 2, pp. 103-114, 2008.
- [4] C. Christopoulos: *Principles and Techniques of Electromagnetic Compatibility*, CRC Press Llc, 1995.
- [5] M. Poci, I. Dotto, G. D'Abreu: "Experimental Definition of the Lowest Usable Frequency (LUF) of an Aluminum Made Reverberation Chamber with Reference to the IEC 61000-4-21 Standard", *International Symposium on EMC*, Vol. 3 pp. 849-852, December 2006.

TESTING THE RESPONSE OF LABORATORY BENCH TRANSFORMERS TO GEOMAGNETICALLY INDUCED LIKE CURRENTS

H K Chisepo, C T Gaunt and D T Oyedokun

University of Cape Town, Department of Electrical Engineering, Private bag X3Rondebosch 7701, South Africa

Abstract. The problems that come with Geomagnetically Induced Currents (GICs) have been in the limelight of power systems research for over two decades, the main component at risk being the power transformer. The effect of severe geomagnetic disturbances has not only caused overwhelming damage in classic auroral regions but also has been seen in regions incorrectly considered to be low GIC-risk, such as Southern Africa. Literature has reported various conclusions concerning the susceptibility of different types of transformers to GIC damage, some of which have been contradictory or solely based on research comments. Laboratory testing of different core types of transformers to GIC-type currents may therefore be of considerable value in order to adequately characterize transformer response. This paper presents a rigorously developed protocol for characterising a transformer based on its magnetization curve and the testing of bench scale transformers to GIC-type currents. The implementation of this protocol using PSCAD/EMTDC and corresponding laboratory setups led to a sound characterization of the transformers' electrical and magnetic response to GICs.

Key Words: Geomagnetically Induced Currents, Magnetization curve, Non-active power, General Power Theory

1. INTRODUCTION

Approximately every 11 years major disturbances occur on the surface of the sun due to its solar cycle. Large amounts of coronal mass ejections (CMEs) are then launched into space and if the earth happens to be within their trajectory collision with its protective magnetosphere occurs [1]. Complex changes then occur in the ionospheric current systems resulting in large magnetic variations that induce electric fields [2]. According to Faraday's law of electromagnetic induction, these induced electric fields then cause Geomagnetically Induced Currents (GICs) to flow in the ground where they enter HV transmission lines through the neutrals of grounded power transformers. Solar storms that lead to high levels of GICs are statistically more likely to occur during periods close to the solar maximum and the descending phase of the solar cycle, but are not limited to those times [3].

GICs typically have a low frequency (<1Hz) compared to the AC frequency and therefore appear as quasi-dc currents. When they enter power transformer neutrals, and the resultant offset to the magnetisation characteristics is high enough, half-cycle saturation occurs. Saturation of power transformers then results in an increased presence of harmonics, overheating of transformer windings, increased reactive power demand, voltage collapse and maloperation of relays and Static Var Compensators (SVCs) [4]. For example, during the 1989 geomagnetic disturbance (GMD), the Hydro Quebec power station caused a major blackout due to maloperation of relays [3-5]. Damage caused by GMDs is therefore extremely costly in terms of replacing power transformers, possible customer interruption costs or loss of revenue due to the time it takes to restore the system.

The effects of GICs in power transmission networks have been observed for over two decades in several parts of the world and with the approach of the Solar Cycle 24 there is increasing concern in the electric

power industry about the possible damage that may occur [6]. Results from a small scale transformer model in [7] concluded that the three limb single phase and five limb three phase transformers were highly and moderately susceptible to the effects of GICs respectively, while three phase three limb transformers were virtually immune to GICs. Later it was then reported [8] that a three phase three limb transformer had reached saturation due to the presence of 2nd, 4th and 6th harmonics during a moderate GMD. It can therefore be seen that there are some contradictions in literature regarding the core type – susceptibility function of transformers to GIC effects.

Laboratory testing may therefore be of considerable value in order to adequately evaluate the electrical and magnetic response of transformers to GICs. It is imperative to carefully test transformers of different core types with GIC-type currents so that important relationships may be established. In this paper, a rigorously developed protocol for testing bench-scale transformers with varying levels of dc is presented.

Also presented in this paper are two approaches to measuring apparent power and non-active power under non-ideal conditions such as those caused by GICs in power systems: (a) the conventional approach [8] and (b) the general power theory [10-12]. These differences are investigated in the context of GICs and transformers.

2. LABORATORY PROTOCOL

2.1 Apparatus

The test equipment and laboratory set up is an updated version of a similar procedure in an early report [15]. Apparatus involved three 120/230V, 300VA three limb single phase transformers, and three 120/230V, 100VA three limb single phase transformers. Voltages and currents were measured by an IEC76-1 (1976) compliant Yokogawa WT1600 Digital Power Meter. The meter is capable of

performing online measurements and also has a facility whereby the instantaneous values of the voltage and current waveforms can be recorded and stored for post processing. Fast Fourier Transforms were done up to the 10th harmonic (500Hz). Samples were taken over two and half cycles with a resolution of 1002 readings (20.04 kHz), thus satisfying the Nyquist Criterion. Other measurements required external circuitry and were monitored using a high resolution Agilent 6000 series oscilloscope. The transformers supplied power to a balanced bank of power resistors in each phase for each loaded experiment. The supply voltage to the transformers was a three phase variac from the laboratory wall supply (See Fig. 1).

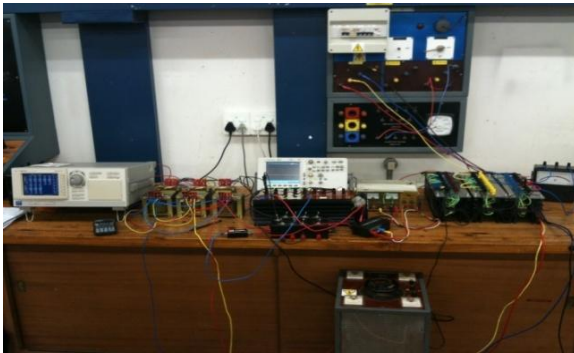


Figure 1: Bench-scale laboratory set up

2.2 Purpose of experiments

In the development of the protocol, the purpose of the laboratory test system was to emulate a GIC event that occurs in typical HV power transmission networks. Such a system normally involves a generator step-up transformer, transmission lines and a load transformer supplying the load. In this protocol it was important for the source transformer to be significantly over-rated in terms of capacity (VA) and voltage so that the dc that would be injected as a function of the much smaller load transformer characteristics would have a negligible effect on its magnetization characteristics. The transformers are arranged into banks of single-phase transformers and the transformer under test (TUT) is the load transformer. Fig. 2 below is a single phase diagrammatic representation of the laboratory set-up.

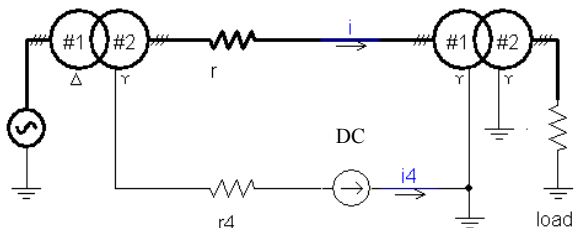


Figure 2: Single phase diagram of the laboratory arrangement of dc injection into the neutral of the load transformer.

2.3 Magnetization curve and parameter characterization

In order to model the system as accurately as possible, more parameters were required and

therefore a brief procedure of basic tests was undertaken. Having ensured a clean or ‘low distortion’ supply [20], preliminary transformer tests were performed. First, the applied voltage at no load was slowly varied from zero to 120% of the name plate rating and the corresponding input current *i* and output voltage *v* values were recorded for each transformer. These *v* and *i* values were then used to plot the magnetization curves of the transformer cores as shown in Fig. 3.

Magnetization curve

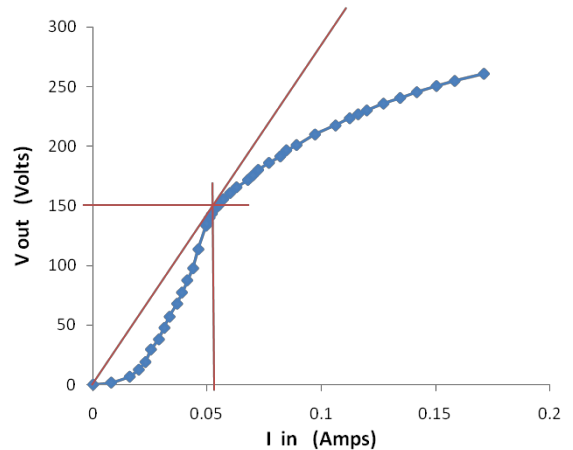


Figure 3: Magnetization curve of the load transformer core

The knee point of the $V_{out}-I_{in}$ curve was selected to be the point where a straight line drawn from the origin is tangent to the curve at its knee, representing maximum permeability, as defined in [13]. This depicts the ‘true’ linear region of the transformer core steel. Possibly for economic reasons these transformers were designed to operate close to and into their saturating region and hence the name plate ratings represented over-excitation. In the rigorous transformer tests that ensued, it was important to distinguish between the region with distortion and the region without distortion with regards to the core’s magnetic characteristics.

The knee point voltage, V_{knee} , of the load transformer was 33.3% below the name plate rating with a magnetizing current I_{mag} of 55mA (See Fig. 3 above). The new transformer ratings are chosen based on the magnetization curve of each transformer as shown in Table 1. The I_{mag} magnitude at the knee point of the magnetization curve of the TUT was then used as a reference for the dc injection experiments.

Table 1: New transformer ratings based on the magnetization curve and operating voltages used.

Transformer	New voltage rating per phase
Source	80/150V operated as 42/80V
Load	80/150V operated as 80/150V

2.4 Open circuit and short circuit tests

Open circuit and short circuit test were performed based on the new transformer ratings in Table 1 in

order to generate parameters for simulations in PSCAD/EMTDC. The open circuit test was used to determine the line impedance elements and the no load losses. The short circuit test was used to determine shunt admittance elements.

Having performed these preliminary transformer tests, a set of experiments was then defined to investigate the response of the TUT with varying dc injection levels in per unit of the I_{mag} .

3. EXPERIMENTAL PROCEDURE 1

3.1 Varying load tests

In order to investigate the effect of the loading condition on the TUT, several varying load tests were performed. These tests involved varying the load from approximately 55% to 100% of the full load at different applied voltage levels. After a series of tests it was shown that an increase in the non-active power absorbed by the transformer was a function of the applied voltage and was independent of the resistive loading condition, as expected.

3.2 Setting up of the DC injection circuit

During the preliminary tests, it was decided that the magnitude of dc injection levels were to be a fraction of the magnetizing current in order to monitor the transformer's behavior before saturation and after saturation. It was therefore sound to use a 1.5V torch cell to facilitate very small dc injection levels in the order of $0 \cdot I_{mag} - 1.4 \cdot I_{mag}$. A voltage divider was used to vary the dc as opposed to using a variable resistor so as to keep the equivalent neutral resistance r_4 less than the 'transmission line' resistance r (see Fig. 2) thus mimicking HV networks. A current LEM module measured the dc in the neutral while the Yokogawa Power Meter measured the dc components in the transmission lines (1/3 of the neutral dc in each phase).

3.3 Voltage, Non-Active Power and varying DC

Findings from a series of tests verified the power curve relationship between applied voltage and non-active power and the injection of dc yields a vertical shift of this curve, as expected.

4. POWER CALCULATIONS

In preparation for experiments in chapter 5 whereby non-ideal conditions were expected, a power calculation comparative analysis was undertaken.

4.1 Comparison of approaches to Non-active power Q

The concept discussed in [15] identifies the difference between the terms reactive power and non-active power and describes them in a general power theory that was developed for m-wire systems. The differences in the conventional measurements [16] and the new approach are contrasted:

a) Conventional Power Theory

Instantaneous power $p(t)$ is given by the following equation:

$$p(t) = e_1 i_1 + e_2 i_2 + e_3 i_3 \quad (1)$$

where e and i are the instantaneous voltages and currents in each phase. The average power P is then given by average of $p(t)$ over a whole cycle. The apparent power S is given by:

$$S = E_1 I_1 + E_2 I_2 + E_3 I_3 \quad (2)$$

where E and I are the RMS values of e and i in each phase. The power factor is P/S ratio as usual.

b) General Theory of Power

Unlike the conventional theory, the derivation of the general theory [11, 12] and its application take into the account the losses in the neutral [15]. It was therefore important for the neutral resistance to be known for each experiment. The neutral current need not be measured as it can be determined using the instantaneously sampled values and applying Kirchoff's Law:

$$i_4 = -(i_1 + i_2 + i_3) \quad (3)$$

The components of S are P and Q (non-active power) as usual and Q is uniquely defined to have two components: Q_a the component that can be compensated without energy storage, and Q_A the component that requires energy for compensation. This definition brings rise to a 3-dimensional power triangle (See Fig. 4 below)

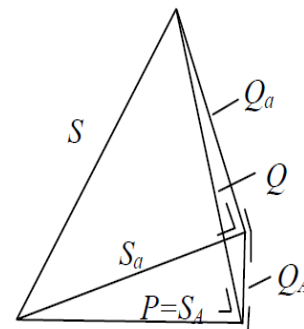


Figure 4: Complete power triangle, in which $Q = Q_a + Q_A$ and S = apparent power without any compensation, S_a the apparent power after compensation without energy storage, and S_A the apparent power after complete compensation so that $S_A = P$ [11].

4.2 Practical measurement

Using the set-up in Fig. 2 and the measurement conditions described in chapter 2, the two power theories were contrasted. The injected dc ranged from $0 \cdot I_{mag} - 1.6 \cdot I_{mag}$. The corresponding absorbed non-active power and levels of dc are represented in per unit in Fig. 5.

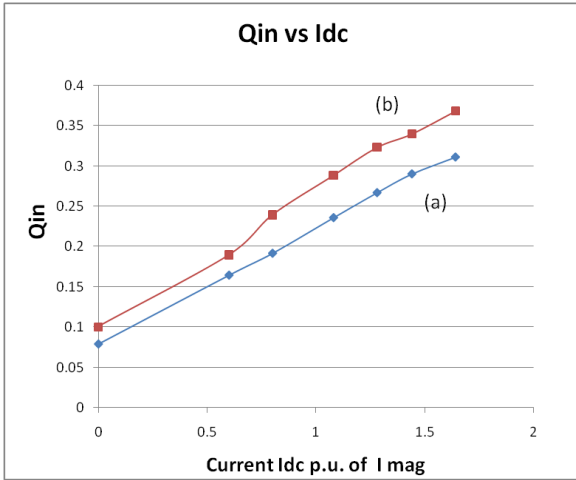


Figure 5: Non-active power associated with varying levels of DC into the load transformer in per unit. (a) Conventional (b) General power theory.

It can be seen from this test that non-active power into the load transformer increases linearly in order to fulfil magnetisation requirements as reported [1, 17] when calculated with the conventional approach. On the other hand, calculations using the general power theory, which includes the effect of the neutral current, show that non-active power at same operating voltage is higher than what is indicated by the conventional method, as also reported in [22]. The rest of the apparent power calculations in the dc injection experiments were therefore done using the general formula so as not to underestimate the conditions in the transformer.

5. EXPERIMENTAL PROCEDURE 2

As previously mentioned, the transformer of interest in all the dc injection experiments was the load transformer. It was important also to verify that the deliberately over-rated source transformer was not driven into saturation and merely acted as a source. Monitoring saturation in the transformers was done by (a) the tracing of BH loops, (b) measuring the harmonics generated, and (c) an analytical determination of saturation.

5.1 BH Loops and the effect of DC injection

The permeability μ of a magnetic material is defined by the ratio of the flux density B to the magnetizing force H . The relationship between B and H is non-linear because the permeability varies as the Weiss Domains align themselves along an external field. This non-linear B - H relationship may be viewed in a hysteresis loop.

When a current $i(t)$ flows through the primary windings of a transformer of N turns and a geometric length l , an auxiliary magnetic field $H(t)$ is generated [18]:

$$H(t) = \frac{N_1}{l} \cdot i(t) \quad (4)$$

Faraday's law stipulates that when there is a changing magnetic field in the secondary windings of a transformer, then the induced voltage $V_2(t)$ is

proportional to the rate of change of flux ϕ and the number of turns N_2 in the windings:

$$V_2(t) = N_2 \frac{d\phi}{dt} \quad (5)$$

where ϕ is the product of the magnetic flux density $B(t)$ and the cross section area A of the core. $B(t)$ can therefore be determined by integrating both sides of equation (5), and practically by tapping off the induced voltage $V_2(t)$ and integrating it with an RC circuit ($R \gg 1/\omega C$). The voltage across the capacitor $V_C(t)$ and $i(t)$ were then recorded using the Agilent oscilloscope and the corresponding hysteresis loop was traced in an XY plot (See Figs. 6 and 7 below).

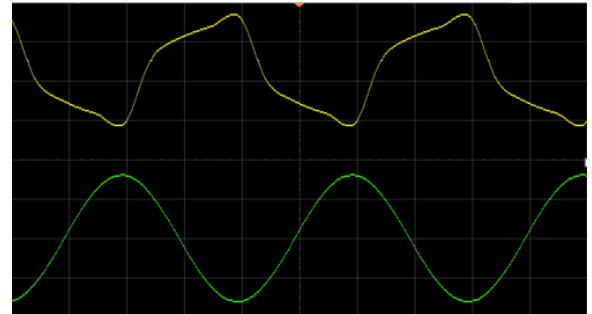


Figure 6: Wave-traces of the magnetizing current $i(t)$ (top) and the integrated voltage $V_C(t)$ of the TUT recorded by the oscilloscope (Voltage = V_{knee} , Current = I_{mag} , Open Circuit)

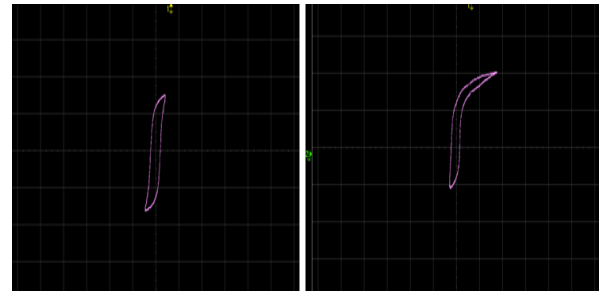


Figure 7: Hysteresis loop of the TUT in the laboratory at the knee voltage without DC (left) and with 70mA DC, 1.3 p.u. of I_{mag} (right). Injection of DC leads to a vertical shift and a distortion of top of the loop.

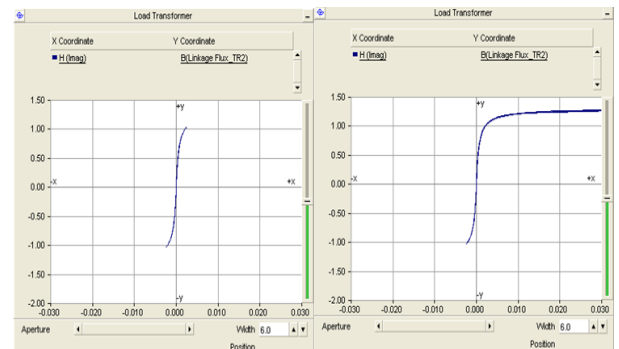


Figure 8: Hysteresis loop of TUT modelled in PSCAD using the magnetic flux versus the magnetising current. No DC (left), and 70mA DC injected (Right).

The diagrams above show the effect of dc injection on the TUT operating at its knee point voltage at no load. The dc injection causes a vertical shift of the loop as well as the flattening of its top. This effect can be further amplified by increasing the level of dc, as also reported in [14], and the transformer will experience 'deep saturation'. Simulations in

PSCAD/EMTDC showed agreement in terms of the shape that results from the distortion of the BH loop to the effect of different levels of dc injection. The hysteresis loops of the source transformer for all values of dc in per unit of I_{mag} showed very little or no change both in the laboratory and in the simulations.

5.2 Harmonics caused by DC injection

According to recommended harmonic limits [20], it is important to distinguish between voltage harmonics and current harmonics. After a series of tests with dc as a fraction of the magnetizing current (\ll maximum load current), it was seen that the voltage waveforms of the TUT were unaffected by this moderate dc. The tests performed on the load transformer were at open circuit. For current waveform analysis at a light loading configuration, total demand distortion (TDD) is preferred to indicate the measure of distortion as opposed to total harmonic distortion (THD). The rationale behind this is TDD is a function of the maximum load current, while THD is a function of the actual fundamental current and could therefore exaggerate the distortion levels when the transformer is lightly loaded [17,20]. Fig. 9 shows the harmonics generated by the TUT at different levels of dc injection.

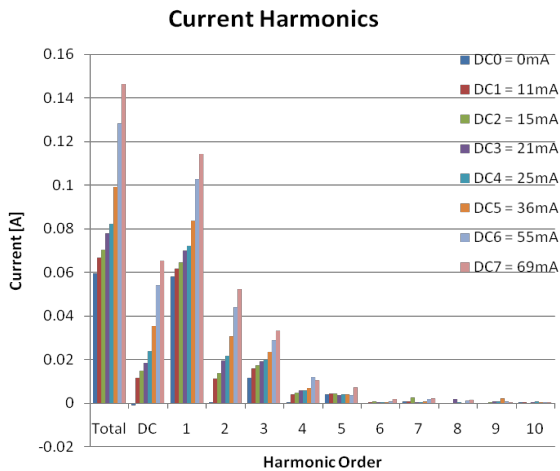


Figure 9: Current harmonics generated at varying levels of dc injection.

Harmonics were recorded up to the 10th order since higher order harmonics were very small. At no dc, the only harmonics present are the 3rd and 5th harmonics. With the injection of just 11mA of dc, there is the sudden appearance of 2nd and 4th harmonics though they are of smaller magnitudes compared with the 3rd harmonic. As dc is increased beyond 36mA, the 2nd harmonic becomes significantly larger than the 3rd harmonic indicating commencement of saturation. The fundamental RMS component increases considerably with increasing dc owing to the significant increase in the asymmetrical exciting current drawn by the TUT which lags the system voltage by 90 degrees, leading to non-active power losses in the system. The same effect is reported in [4, 21]. Fig. 10 shows the measured

linear relationship between the TDD of the transformer and increasing levels of dc injection similar to that in [17].

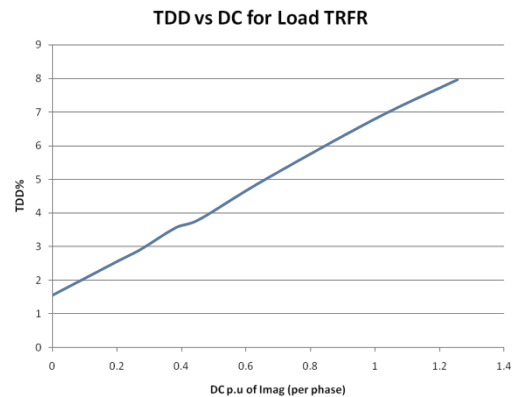


Figure 10: Representation of the total demand distortion (TDD) and increasing levels of dc injection.

5.3 Analytical Determination of Saturation

A series of dc experiments resulted in the significantly larger source transformer exhibiting very little or no distortion in terms of the hysteresis loops and harmonic content. To complete the rigorous approach to testing the effect of dc injection on the TUT while keeping the source transformer immune to dc, an analytical approach was implemented. By using several unique points on the BH loop and deriving a rigorous analytical solution, McLyman [13] defined the saturation of a transformer as the point where the peak exciting current I_{peak} is twice the average exciting current I_{avg} i.e. $I_{peak} = 2I_{avg}$ (See Fig. 11). The exciting current waveform of the source transformer was therefore examined for all the dc injection levels. I_{peak} was determined by selecting the maximum sample point over half a cycle. I_{avg} was determined using the following equation: $(I_0 + I_1 + I_2 + \dots + I_n)/n$, where I represents the value of a sample point and n is the total number of sample points in a half cycle. The source transformer remained unsaturated for all levels of dc injection.

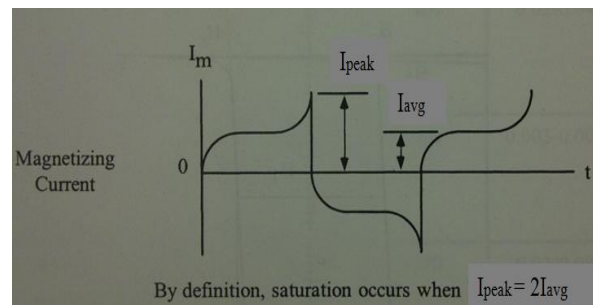


Figure 11: Definition of saturation using the magnetising current waveform [13].

6. CONCLUSIONS

A rigorous laboratory protocol for testing bench scale transformers with different levels of dc injection has been presented. Laboratory and simulation results have been discussed and the conclusions from these results are therefore:

- a) The magnetization curve can be used to characterize the linear region of a transformer core steel. The corresponding magnetizing current at the knee point should be used as a reference for dc injection levels to monitor pre- and post-distortion conditions of the TUT.
- b) The effect of GIC on the magnetization characteristics of a transformer depends on the relative capacity and operating voltage of the transformer.
- c) It was demonstrated that the increase in non-active power demand in a transformer is a function of the applied voltage and the level of dc injected, and is independent of the resistive loading condition.
- d) Under distorted and unbalanced conditions the calculated non-active power and apparent power using conventional approaches differs significantly from those using the general theory of power. This may often result in over-optimistic measurements of the power transfer capacity of the networks.
- e) Hysteresis loops may be used as an indicator of the presence of GICs whereby a vertical shift and a distortion of one half of the loop depends on the magnitude and direction of the GIC.
- f) DC injection resulted in significant harmonic content increase namely the 2nd, 3rd and 4th harmonics. However findings in [8] reported a substantial 6th harmonic in a three phase transmission transformer during a GMD. This dissimilarity may be due to the different core-types under consideration.

Further work involves incorporating the developed laboratory protocol for investigations in the medium voltage range (33kV, 48kVA) in order to test different core-types of transformers with dc currents.

REFERENCES

- [1] TS Molinski, "Why utilities respect geomagnetically induced currents", *Journal of Atmospheric and Solar-Terrestrial Physics*, No. 64, pp.1765-1778, 2002
- [2] DH Boteler and RJ Pirjola, "The complex-image method of calculating the magnetic and electric fields produced at the surface of the earth by the auroral electrojet", *Geophysics Journal International*, pp.31-40, 1998.
- [3] A Thompson, CT Gaunt, P Cilliers, JA Wild, B Opperman, LA McKinnel, P Kotze, CM Ngwira, SI Lotz, "Present day challenges in understanding the geomagnetic hazards to national power grids", *Advances in Space Research*, vol. 45, pp. 1182-1190, 2010
- [4] JG Kappenman and VD Albenn, "Bracing for the Geomagnetic Storms", *IEEE Spectrum Magazine*, pp. 27-33, March 1990.
- [5] DH Boteler, RJ Pirjola, H Nevanlinna, "The effects of Geomagnetic Disturbances on electrical systems at the earth's surface", *Advanced Space Research*, Vol. 22, No. 1, pp 17-27, 1998
- [6] R Girgis, K Vedante and K Gramm, "Effects of Geomagnetically Induced Currents on Power Transformers and Power Systems," *Cigré Session*, 2012
- [7] N Takasu, F Miyawaki, S Saito, Y Fujiwara, "An experimental analysis of DC excitation of transformers to geomagnetically induced currents", *IEEE Transaction on Power Delivery*, Vol. 9, No. 2, 1994.
- [8] J Koen, CT Gaunt, "Disturbances in the Southern African Power Network due to Geomagnetically Induced Currents," *Cigre Session*, Paris, 2002.
- [9] A Emanuel, "Summary of IEEE Standard 1459: Definitions for the Measurement of Electric Power Quantities under Sinusoidal, Non-sinusoidal, Balanced or Unbalanced Conditions," *IEEE Trans. On Industry Applications*, 2004.
- [10] M Malengret and CT Gaunt, "General theory of instantaneous power for multi-phase systems with distortion, unbalance and direct current components", *Electric Power Systems Research*, Vol. 81, pp. 1897-1904, 2011
- [11] M Malengret and CT Gaunt, "General theory of average power for multi-phase systems with distortion unbalance and direct current components," *Electric Power Systems Research*, Vol. 84, pp. 224-230, 2012
- [12] CT Gaunt and M Malengret, "True power factor metering for m-wire systems with distortion, unbalance and direct current components", *Electric Power Systems Research*, Vol. 95, pp. 140-147, 2013
- [13] CWT McLyman, *Transformer and Inductor Design Handbook*, Marcel Dekker Inc., 3rd ed., 2004.
- [14] M Heindl, M Beltle, D Schneider, S. Tenbohlen, DT Oyedokun, CT Gaunt, "Investigation of GIC related effects on power transformers using modern diagnostic methods", *ISH*, Hannover, 2011
- [15] CT Gaunt and M Malengret, "Why we use the term non-active power, and how it can be measured under non-ideal power supply conditions", *IEEE PES PowerAfrica Conference*, Johannesburg, 2012
- [16] IEEE Power and Energy Society, "Standard definitions for the measurement of electric power quantities under sinusoidal, non-sinusoidal, balanced or unbalanced conditions, *IEEE Std 1459-2010*
- [17] J Berge, "Modeling and Mitigation Of Geomagnetically Induced Currents on a Realistic Power System Network", *IEEE Electrical Power and Energy Conference*, pp. 485-490, 2011
- [18] PC Sen, *Principles of Electric Machines and Power Electronics*, John Wiley and Sons, 2nd ed., 1997
- [20] T Blooming and DJ Carnovle, "Application of IEEE Std 519-1992 Harmonic Limits", *IEEE IAS Pulp and Paper Conference*, 2006
- [21] EF Isumbingabo and M Malengret, "Evaluation of the performance of a power transformer under varying dc injection and mitigation of adverse effects," *SAUPEC*, Johannesburg, pp. 248-253, 2010
- [22] P O'Donoghue and CT Gaunt, "Non-active power in a transformer carrying Geomagnetically Induced Currents", *SAUPEC*, Johannesburg, 2010

Topic C

High voltage

A REVIEW OF FACTORS THAT AFFECT CORONA ELECTROPORATION OF IN-VITRO SAMPLES IN A HIGH VOLTAGE POINT-PLANE GAP TEST APPARATUS

N. K. Chetty* and L. Chetty**

* HVDC Centre, School of Engineering, University of KwaZulu-Natal, Private Bag X54001, Durban, 4000, South Africa E-mail: 8422762@stu.ukzn.ac.za

** HVDC Centre, University of KwaZulu-Natal, Private Bag X54001, Durban, 4000, South Africa E-mail: chettyl2@ukzn.ac.za

Abstract: High voltage corona has beneficial applications and is used in various applications. More recently, in the biomedical field, electroporation induced by high voltage corona has also been investigated. There appears to be great potential for the use of corona electroporation in applications like genetic engineering, drug delivery and cancer treatment. Research in this field is in the early stages and in order to successfully implement this technique, an analysis of the corona current is an important exercise in leading to the understanding of the development of high voltage discharge and the breakdown mechanism under varying conditions. There are various factors that affect corona discharge and these factors and their effect on the discharge are reviewed in this paper.

Keywords: High voltage corona, electroporation

1. INTRODUCTION

Corona discharges, which are caused by the electric fields produced by electrodes with sharp edges, are low powered electrical discharges. When a sufficiently high voltage is applied to an electrode, an electric field is created around the conductor which ionizes the air around the conductor. If the gradient of the electric field is not high enough to cause arcing to ground, the discharge is self-contained and is referred to as a corona discharge [1].

Corona has been commonly used in many commercial applications in the past and more uses for this phenomenon are still being found [1]. One important application that has recently been attempted in the biomedical field is the use of corona to facilitate electroporation. Electroporation is a technique that utilizes electricity to assist in the delivery of molecules like drugs and DNA to biological cells [2]. It is a universal cell membrane phenomenon that allows transport of molecular material into cells for various biological applications [3]. The electric fields cause changes to a cell membrane which increases the permeability of the cell membrane [4]. The exact mechanism of electroporation is not known but it is thought that when the cell is exposed to a high enough electric field, aqueous filled pores are created in the bilayer lipid membranes. It is this breakdown that results in the permeability of a cell membrane, thereby making the process of electroporation possible [4]. Cells have a natural trans-membrane voltage of approximately 0.1 V [3]. When pulsed potentials of 150mV to 500 mV and with pulse duration in the region of μ s to ms are applied, rearrangement of the structure of the cell membranes occur, which results in the formation of pores in the

membrane [3], [5]. Cell membranes can withstand a trans-membrane potential of up to 1 V and this relates to an electric field strength of about 2000 kV/cm when short pulses of duration μ s to ms are used [5]. For isolated cells of mammals, electroporation occurs at electric field strengths of around 1 kV/cm when short pulses are used [3].

The traditional method of electroporation requires electrodes to be in direct contact with the skin and involves relatively high currents. This is a major drawback as it inflicts pain and discomfort on the subject being treated [2]. It also causes damage to the cell DNA and to the muscle tissue. Further, the area of treatment is relatively small and localized. It is envisaged that the technique of corona electroporation can be perfected so that this method can be utilised instead of the direct application of electrodes. This results in a minimization of the harmful effects and results in an increase in the area of treatment.

Once the applied voltage is removed, the cell enters the recovery phase where the pores diminish and eventually disappear. Resealing of the membrane occurs within ms to seconds [5].

Very little research has been done in the area of corona electroporation to date and it has not been established as yet exactly how corona facilitates the delivery of molecules to cells. In the only experiment found in previous research for in-vitro testing, it was assumed that corona electroporation could result in one of two ways. First, it is thought that, due to the deposition of ions on the sample, an electric field results in the conductive culture medium which results in pore formation in the

cell membranes. The second theory is that when the ionic current flows through the culture media, the ions exchange charge with the cell membrane, thereby resulting in pore formation in the cell membrane [2].

In our proposed research, no assumptions will be made and all factors that might affect corona electroporation during in-vitro testing of tissue samples will be investigated. For in-vitro testing, the apparatus that will be used is a point-plane gap. In this paper, all factors that affect the generation and characteristics of corona in a high voltage point-plane gap are reviewed and presented.

It is the aim of our research to test the effectiveness of in-vitro corona electroporation by testing all the factors that can have an effect on the process. Actual experiments using tissue samples and fluorescent imaging will be used to investigate each of the factors individually.

2. FACTORS THAT AFFECT ELECTROPORATION

2.1 Apparatus Used to Generate Corona

For corona electroporation, a point-plane-gap appears to be the most likely configuration, especially for in-vitro testing in the early experimentation phase of our research.

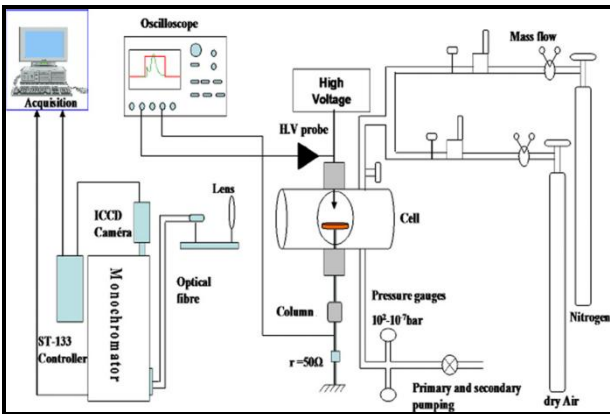


Figure 1: Typical experimental setup that can be adapted and used for corona electroporation [6]

A typical experimental setup that can be adapted and used for in-vitro corona electroporation is illustrated in Figure 1. The generation device is a point-plane gap housed in a cylindrical closed chamber. This experiment is conducted at atmospheric pressure and with artificial air. With some modifications, the system shown in Figure 1 can be modified to include varying pressure, humidity and gas types. A pumping system of dry air and nitrogen is used in this case. A spectrophotometer was used to capture the UV, visible and NIR emission spectra. Images of the discharge were captured with an intensified charge-coupled device (ICCD) camera [6]. For this arrangement, the construction of the point electrode and the gap between the point and plane has a direct effect on the discharge mechanism and the corona current. The shape, size and number of points in the electrode as well as the

type of material it is constructed from are all important considerations. The nature and amplitude of the applied voltage is also important. So too is the pressure, humidity and type of gas used (if any). For corona electroporation, it has also been found that the rise times of the corona pulses can also improve the efficiency of the method [7]. In Figure 2, the dependence on the gap distance of the corona current at different positive voltages is shown. As the gap distance for a particular, pre-determined range increases, the corona current decreases accordingly [6].

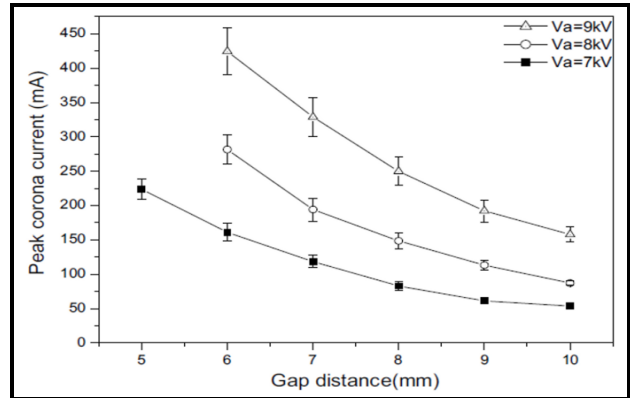


Figure 2: Peak corona current versus gap distance for three applied voltages ($\tau=40\mu s$, $f=100\text{Hz}$, $\rho=25\mu m$) [6]

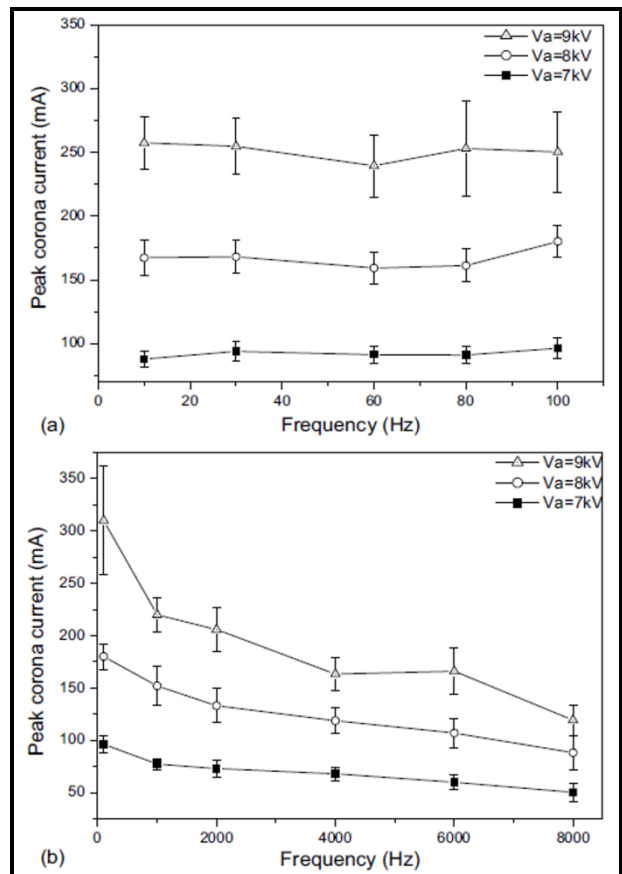


Figure 3: Graphs of peak corona current for different frequencies for three values of positive applied voltage at a chosen gap distance [6]

From Figure 3, it can be seen that for frequencies from 10 Hz to 100 Hz, the peak corona current is fairly constant. For frequencies between 100 Hz and 8 kHz, the peak corona current decreases with increasing frequency. It has also been shown that the number of tips does affect the corona discharge. Firstly, the saturation current for two tips is twice that of the single tip. Secondly, the distance at which saturation is reached is twice the distance of the gap between the anode and cathode electrodes [6].

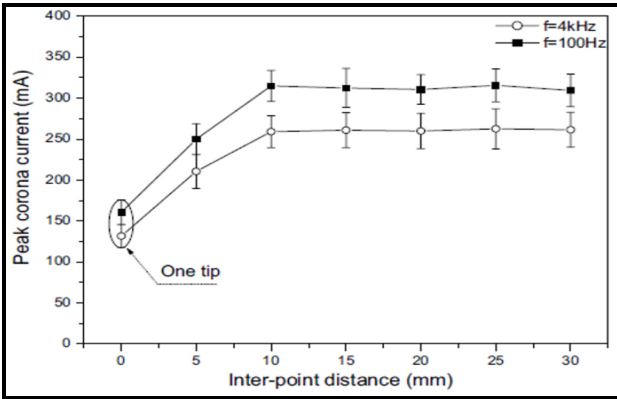


Figure 4: Peak corona current for one and two tips with increasing inter-tip distance for different applied frequencies [6]

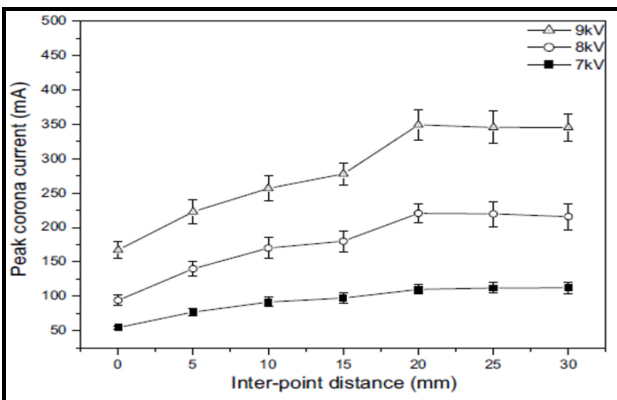


Figure 5: Peak corona current for one and two tips with increasing inter-tip distance for different applied voltages [6]

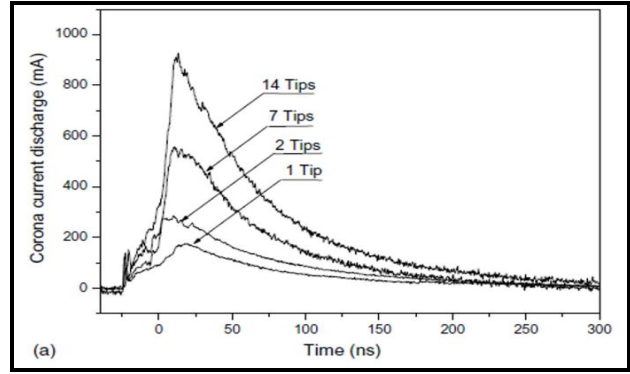


Figure 6: Comparison of the instantaneous corona current for different number of tips [6]

From Figures 4 and Figure 5, it is clear that the peak corona current for a single tip is less than that for two tips and Figure 6 indicates that the instantaneous current is greater for multiple tips. For a generator with multiple tips, the current increases with increasing inter-tip distance only up to a certain distance after which it remains fairly constant [6]. In experiments, the sample can either be placed between the two electrodes or below the ground electrode. In the latter case, the ground electrode would be in the form of a grid or ring. The former is termed direct treatment and the latter, indirect treatment. The indirect treatment method with a grid has shown to be less effective as the electric field, ion species and corona current that the sample is exposed to is reduced by the presence of the grid [8].

2.2 Ionic Species Produced

Corona in air also results in the production of many species that are chemically active. These species include “ions, free radicals, excited atoms and molecules” [8]. Analysis of the emitted spectrum is therefore important in studying corona discharge characteristics. The reason for conducting the spectroscopic analysis is to attempt to identify some of the important excited species that exist in the corona discharge. These species can be of importance in corona electroporation [6].

Different ionic species are produced when a flow of gas like helium is introduced. One experiment measured the optical emission spectrum for a 5 slm flow of helium for various pin densities. The results are plotted in Figure 7. As can be seen from the plot the emission intensity for both helium and oxygen atoms increased for both an increase in the applied voltage as well as an increase in the pin density [9]. The oxygen ions are as a result of the exposure of the experimental apparatus to air.

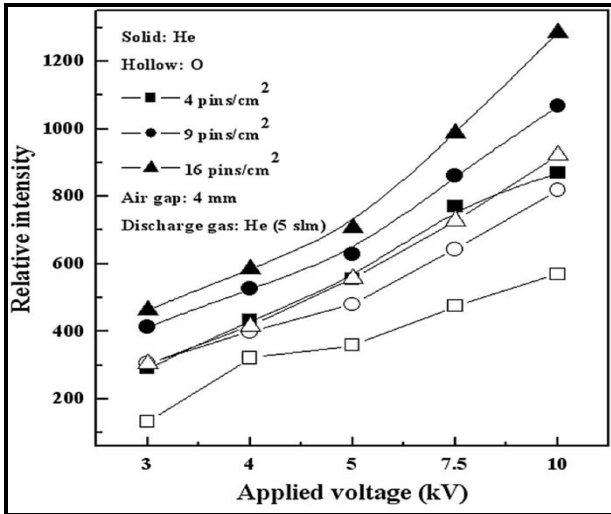


Figure 7: Optical emission intensities from He metastable and oxygen atoms as a function of applied voltage for different pin densities [9]

The action of the ions produced by corona is an important contribution to the success of corona electroploration. These ions settle onto the sample and results in the creation of an electric field [2]. This electric field facilitates electroploration thereby allowing the transfer of molecules like DNA and drugs into the cell. A negative effect is that the reactive oxygen species cause damage to molecules within the cell like DNA and proteins and also affect the lipids. This, in turn, affects the lipid membranes surrounding the cell which can result in death to cells [8].

2.3 Applied Pulsed Voltage and its Effect on the Nature of the Discharge

The nature of the corona discharge and the corona current are different for positive DC, negative DC and AC applied voltages because the ionization process for each is different [10], [8].

Negative DC: The electron emission for negative corona is more stable and easier to control. Therefore, it is more readily used in practical applications [10]. The negative current is greater than the positive current and is typically less than 100 μA [8]. The pulses have fast rise times in the nanosecond range, last for about 100 ns and with repetition rate in the kHz to MHz range [11], [8]. The rise time of the current pulse increases and its duration decreases as the applied voltage increases [12]. When negative voltages are applied in atmospheric air, due to the presence of oxygen, Trichel current pulses result since the space charge formed is negative [8]. The onset of corona occurs at approximately 5 kV and the Trichel pulses appear immediately after corona onset [12]. It should be noted that negative corona discharge is composed of a steady component as well as a pulsed component. The steady component is produced by the applied pulsed voltage as well as the current flowing from the electrode to the ionized region between the electrodes [11]. As the negative voltage is increased, the DC part of

the corona current increases and becomes the greater current component [8]. The continuous current is much smaller than the peak of the pulsed current, however, over time, the continuous current represents a more significant component than the pulsed component [11]. The DC part of the corona current, therefore, is the largest component of the average corona current [8]. The average corona current amplitude increases with increasing voltage, however, the amplitude of the Trichel pulses decreases and the pulse frequency increases. After the average current reaches a value of 120 μA , with an applied voltage of approximately 11.4 kV, the Trichel pulses ceases and the corona became pulseless. The corona then changes to glow after 320 μA . The rise of the corona current in the glow region is much steeper than in the previous regions and, as the voltage increases, the spark gap eventually breaks at about 740 μA [12]. A graph showing Trichel pulses is presented in Figure 8 [11].

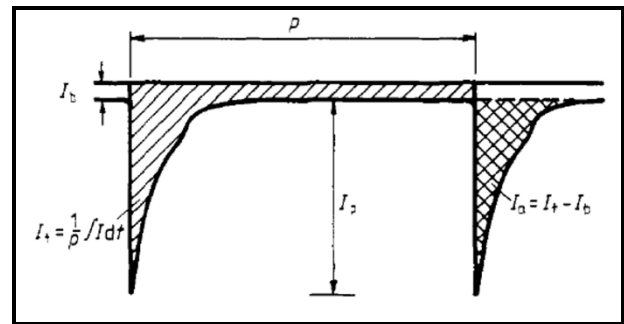


Figure 8: Graph of the Trichel pulse [11]

The important characteristics of the pulse are identified as the repetition period p , the height of the peak I_p , area of the pulse I_a and the steady current I_b as depicted in the Figure 8. Firstly, there is a linear increase in the repetition frequency of the pulses with total current and with no dependence on the voltage. Secondly, after a Trichel pulse, the value of the current reduces to 10% of its peak level in a time of 100 ns – 150 ns. This fall in current continues slowly until a steady value is reached after about 2 μs . After 200 ns, the shape of the pulse does not change much with a change in voltage. When the repetition time of the current pulse is greater than 2 μs , I_b can be measured directly and it was discovered that it is directly proportional to the total current, I_t . For currents where the next pulse starts before the steady state was reached, the steady component of the current can be obtained by subtracting the Trichel pulse from the total waveform. For discharges where the transit time of the charge carriers is longer than the system time constants, the current in the external circuit is not equal to the number of charge carriers reaching the electrodes every second. This is because movement of the charge carriers anywhere in the discharge induces current in the external circuit. The instantaneous current is mainly as a result of the movement of electrons. The movement of ions in the drift region can only be detected when there are no electrons. During the tail end of the Trichel pulses, the movement of ions mainly contributes to the current. The

pulse is caused by the movement of electrons near the point which is an area of high field [11]. When air flow is introduced, the appearance of the corona is different, but the characteristics of the current are similar to that produced in atmospheric air [8].

Positive DC: The positive current is less than the negative current and its value is less than 100 μA . In atmospheric air, steady state corona current is observed. The current pulses that are formed have a magnitude that is much greater than the steady state component. The frequency of the current pulses is in the range up to tens of kHz [8]. The shape of the corona discharge waveform shows three peaks. The first and third peaks are related to the capacitive current during the increasing and decreasing stages of the applied voltage. It is the second peak that represents the discharge current. A plot of this current is shown in Figure 9.

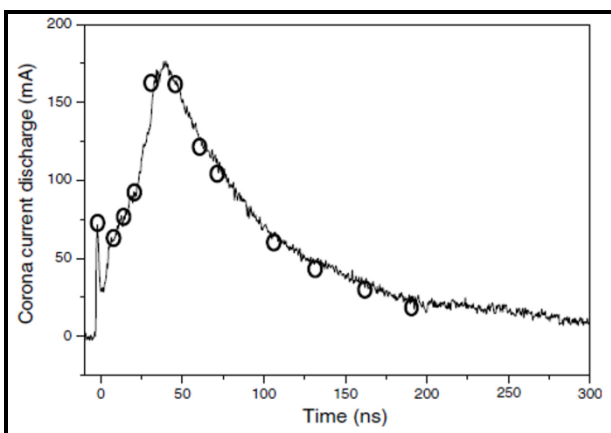


Figure 9: Plot of corona current discharge versus time [6]

There is an initial, brief peak of approximately 70 mA with duration of about 4 ns. At this point, there is intense ionization that is generated by the electric field at the tip. After this initial peak, the electron avalanche reaches a critical size and the space charges that have accumulated at the tip start moving towards the cathode. This is the primary streamer propagation and the corona current increases rapidly to about 175 mA when the streamer reaches the cathode at a time of around 50 ns. Immediately after, there is a change from displacement current to conduction current till up to about 70 ns. This corresponds to the secondary streamer propagation. After this point, the decrease in the corona current is more gradual and lasts for more than 300 ns. In this case, the pulse duration of 40 μs chosen, is lower than the natural frequency of the corona discharge, which is in the region of 20 kHz. Thus, the relaxation time of the discharge current lasts until the next pulse (and therefore next corona discharge) occurs. The peak corona current increases as the applied voltage is increased. The peak corona current remains constant for applied frequencies from 10 Hz to 100 Hz for a particular gap distance. For higher frequencies from 100 Hz to 8 kHz, the peak corona current decreases as the frequency increases.

When the applied frequency is low enough, there is enough time for the gas medium to return to original conditions and so the next pulse is not affected by the previous pulse. This happens when the applied pulse is lower than the natural frequency of the discharge current, which is in the region of 20 kHz for applied DC voltage [6]. It has also been proven that the rise times of the corona current pulses in a point-plane gap can be decreased by the application of overvoltage. Rise times of 50 ns to 60 ns were observed in this manner. Further adjustments of the circuit made rise times of around 30 ns possible [7].

AC: The use of AC voltage is not common and one experiment was conducted on AC in helium. It was found that the discharge characteristics of a pin-to-plate dielectric plasma barrier discharge generator in Helium with applied AC have similar characteristics to the behaviour of corona discharge. An increase in the discharge current occurs as the applied voltage increased. For a given voltage, when the pin density increases so too does the discharge current. There is also an increase in the densities of the metastables and dissociated species. The optical emission intensities increased with an increase in applied voltage as well as an increase in the pin density. For experiments which comprise of units that are open systems, optical intensities of oxygen and nitrogen are also observed due to the small amount of air that leaks into the system. An increase in the applied voltage causes an increase in the power consumed and there is an increase in the plasma density. There is almost a linear increase in power consumed with an increase in gap-size up to a 4 mm gap. Further increases in gap distance causes a decrease in the power consumed. An increase in the pin density results in an increase in the discharge current which results in an increase in the power consumed [9].

2.4 Frequency and Harmonics of the Corona Current

Another factor that needs to be considered to fully establish the characteristics of the corona onset and the corona effect is the frequency components of the corona current. It is important to be able to analyse the harmonic frequencies of the corona current as this provides an indication of the characteristics of the corona current and the onset characteristics of the corona current. To measure all the frequency components of the corona current, it is therefore useful to perform an analysis of the harmonic wave characteristics of the corona current. A harmonic wave is a frequency in the signal that is an integer multiple of the fundamental frequency. Due to frequency fluctuations, it is difficult to obtain a sample of a full period. Major errors can, therefore, arise as a result of the fence effect and spectral leakage. The fence effect can be minimized with a high sampling rate and the wide frequency band. In order to further minimize the effects of the fence effect and spectral leakage, the method of windowed FFT analysis can be used. To solve the problem of long-range leak, a suitable window function

can be used or a greater measurement time can be used. The short-range leak can be solved by using an interpolation FFT algorithm. One experiment was conducted for which the harmonic analysis of the corona current was done for a high voltage conductor. In this case, an advanced windowed interpolation FFT algorithm was used. As many as 11 harmonic and sub-harmonic waves were identified before and after the onset of corona. It was observed that after the onset of corona, the odd-order harmonic in the corona current increases. The even-order harmonic also increases, but not as drastically. The triple- and quintuple- harmonic frequencies increase to a large extent [13]. The harmonic values of the positive DC voltage was the highest followed by negative DC voltage and then by the AC voltage. For values of the same distance between electrodes and the same voltage, the 50 Hz fundamental current for the AC voltage is the highest followed by the negative voltage and thereafter, the positive voltage. However, the current harmonics have the lowest value for the AC voltage [10]. The harmonic analysis of the current before and after the onset of corona is plotted and compared in Figure 10 [13].

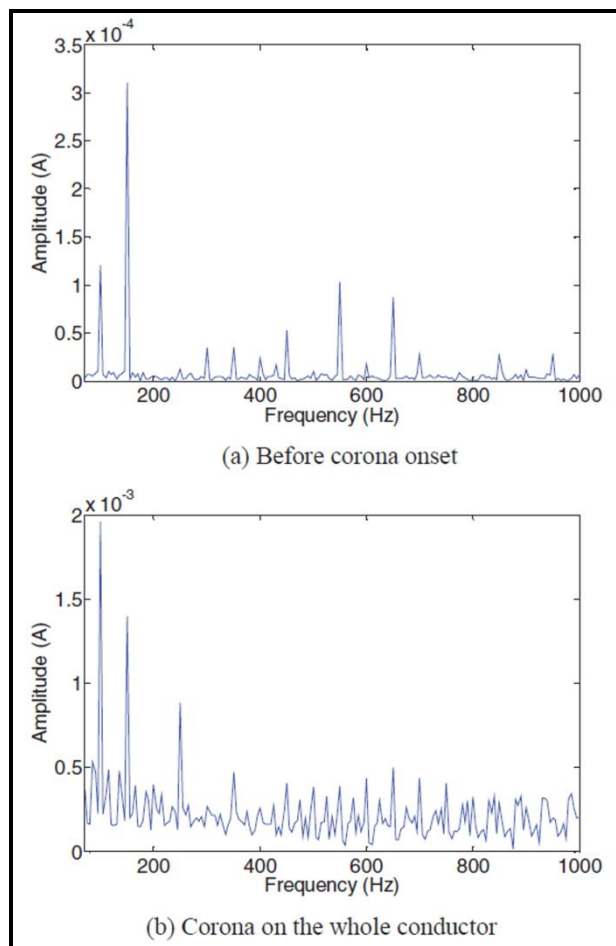


Figure 10: Harmonic wave analysis of the current before and after the onset of corona on the conductor [13]

3. FUTURE WORK

From our review of corona characteristics in a point-plane gap, we have identified the factors that most probably have an effect on the degree of electroporation during in-vitro testing. The effect that these factors have on corona electroporation has not been studied before. It is the aim of our research to build a suitable test apparatus and establish the optimal conditions for in-vitro corona electroporation. Once in-vitro testing has been completed and analysed, it will pave the way for research into the adoption of this technique for in-vivo applications.

It is hoped that the ultimate goal of research into corona electroporation would be its utilization in the treatment of cancer and AIDS.

4. CONCLUSION

As can be gathered from the above discussion, corona electroporation has the potential of being a useful phenomenon in the fields of medicine and biotechnology. It is a non-contact, non-invasive procedure with negligible side effects that can be successfully utilised for procedures like genetic engineering, drug delivery and treatment of cancerous cells. The research in this area is still in the early stages and continued research in this field is important to fully understand the mechanism and the factors that will enable the establishment of an optimal procedure.

5. REFERENCES

- [1] J. Chang, P. A. Lawless and T. Yamamoto: "Corona Discharge Processes", IEEE Transactions on Plasma Science, Vol. 19 Issue 6, pp. 1152-1166, December 1991.
- [2] N. Ramachandran, M. Jaroszeski and A. M. Hoff: "Molecular Delivery to Cells Facilitated by Corona Ion Deposition", IEEE Transactions on Nanobioscience, Vol. 7, Issue 3, pp. 233-239, September 2008.
- [3] J. C. Weaver: "Electroporation: A General Phenomenon for Manipulating Cells and Tissues", Journal of Cellular Biochemistry, Vol. 51 Issue 4, pp. 426-435, 1993.
- [4] F. Appolonio, M. Liberti and P. Marracino: "Electroporation Mechanism: Review of Molecular Models Based on Computer Simulation", 6th European Conference on Antennas and Propagation (EUCAP), Prague, pp. 356-358, 26-30 March 2011.
- [5] T. Y. Tsong: "Electroporation of Cell Membranes", Biophysical Journal, Vol. 60, pp. 297-306, August 1991.

- [6] A. Mraïhi, N. Merbahi, M. Yousfi, A. Abahazem and O. Eicheald: "Electrical and Spectroscopic Analysis of Mono- and Multi-tip Pulsed Corona Discharges in Air at Atmospheric Pressure", *Plasma Sources Science and Technology*, Vol. 20 No. 6, 2011.
- [7] B. R. Natarajan, G. R. Gurumurthy and J. Amarnath: "Corona Pulse Rise Time Measurements between Point Plane Electrodes in Atmospheric Air", 2010 Annual Report Conference on Electrical Insulation and Dielectric Phenomena, West Lafayette, pp. 1-4, 17-20 October 2010.
- [8] I. V. Timoshkin, M. Maclean, S. J. MacGregor, J. G. Anderson, M. P. Wilson, T. Wang and M. J. Given: "Pulsed Periodic Corona Discharges for Biological Decontamination", *IEEE Pulsed Power Conference*, Chicago, pp. 1155-1159, 19-23 June, 2011.
- [9] Y. Lee and Yeom, G: "Characteristics of a Pin-to-plate Dielectric Barrier Discharge in Helium", *Journal of the Korean Physical Society*, Vol. 47, No. 1, pp. 74-78, July 2005.
- [10] G. N. Popa, S. I. Deaconu and I. Popa: "Analysis of the Corona Currents from Pins to Plate Geometry", *Proceedings of the 12th WSEAS International Conference on Systems*, Heraklion, Greece, pp. 143-148, July 22-24, 2008.
- [11] J. A. Cross: "An Analysis of the Current in a Point-to-Plane Corona Discharge and the Effect of a Back-ionising Layer on the Plane", *Journal of Physics D: Applied Physics*, Vol. 18, No. 12, Pp. 2463-2471, 1985.
- [12] K. Shang, X. Xue and X. Wang: "Trichel Pulse Characteristics in Negative DC Corona Discharge", *Power and Energy Engineering Conference (APPEEC)*, Wuhan, Pp. 1-4, 25-28 March 2011.
- [13] F. Lu, S. You, Y. Liu and L. Zhu: "Harmonic Wave Analysis of Conductor Corona Current Based on Wide Frequency Band Measurement", *International Conference on Electrical and Control Engineering (ICECE)*, Yichang, pp. 2258-2261, 16-18 September 2011.

AN INVESTIGATION INTO THE PROBABILITIES OF 66kV and 132kV BUSHING FAILURES AND MITIGATING AGAINST THE ASSOCIATED RISKS.

E. Russell*, R.T. Harris, W. Phipps and A.G. Roberts**

* Eskom Distribution Eastern Cape Operating Unit Plant Department,
Corner of Bonza Road and Quenera Road, East London Beacon Bay 5205,
South Africa, E-mail: elgan.russell@eskom.co.za

** Faculty of Engineering, the Built Environment and Information Technology Nelson Mandela Metropolitan University, Port Elizabeth, South Africa
E-mail: raymond.harris@nmmu.ac.za, william.phipps@nmmu.ac.za, alan.roberts@nmmu.ac.za

Abstract: Eskom Distribution (Dx) Eastern Cape Operating Unit (ECO) has a total of 603 power transformer high voltage (HV) bushings operating within its substations. The oldest bushings in operation are believed to be 44 years old, youngest bushings being 1 year and average age of the entire population being 15 years. With the bushing population ageing, the bushing health deteriorates as well. The status of bushings required a comprehensive maintenance strategy to be developed and executed with the aid of a bushing failure estimation tool (BFET) to lessen unpredictable failures. In order to develop the BFET, inputs had to be derived from critical electrical tests carried out on bushings along with other contributing factors that could negatively affect bushing health in order to determine which year the bushing is likely to fail. The criteria for the BFET was made up of the following critical tests and contributing factors: tan delta tests, infra-red scanning tests, discharge activity tests, HV circuit breaker operations, overloading and environmental contamination.

Keywords: Thermography scanning, tan delta test, discharge activity test, bushing failure estimation tool, circuit breaker operations, overloading, environmental contamination.

1. INTRODUCTION

Resin impregnated paper bushings (RIP) makeup 24% and oil impregnated paper (OIP) bushings makeup 76% of the total HV bushing population. The status of HV bushings required a comprehensive maintenance plan to be developed and executed in the ECO with the aid of a BFET to lessen unpredictable failures. The purpose of the research was to address the following risks: Reducing the probabilities of bushings failing, that can lead to surrounding field personnel getting injured. The surrounding primary plant may become damaged resulting in financial loss to business. Failing to supply customers with electricity will lead to financial loss to business. Start capturing test results of bushings and improve the accuracy of bushing inventory.

In order to carry out the above a risk/condition based maintenance strategy was chosen as the preferred solution to prevent failures before it happens, due to it having knowledge of the condition of the asset. The two solutions not chosen was routine based maintenance strategy using only tan delta tests every four years. The other option was the replacement based maintenance strategy, replacing the bushing after 35 years of service, without carrying out any tests on the bushing during its lifespan.

2. HYPOTHESIS

A Risk/Condition based maintenance strategy was developed to carry out critical tests on HV bushings with the aid of a bushing failure estimation tool (BFET). This

will reduce the probabilities of bushings failing in Eskom Dx ECO.

3. DATA COLLECTION AND STRUCTURE

Figure 1 shows a total of 603 bushings in Dx ECO as well as their age categories. In terms of age as a determining factor, the bushings between 0 and 30 years of age was operating at a lower risk then the 60 bushings in the 31 to 40 age category which was operating at a medium to high risk. The 6 bushings in the 41 to 50 age category were operating at an even greater risk.

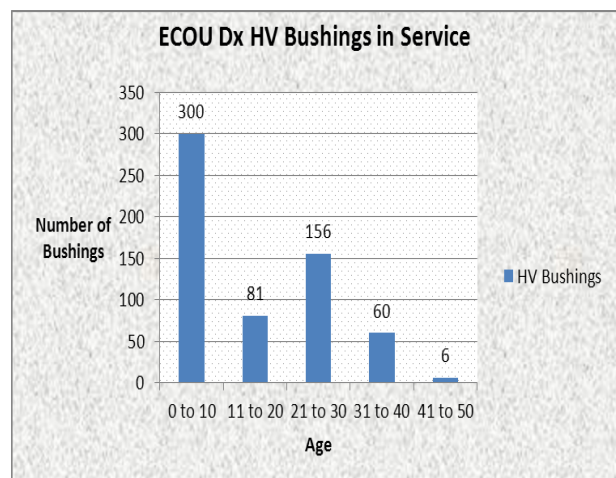


Figure 1: ECO Dx HV Bushing Age Category

3.1 Factors leading to bushing failures

Table 1: Bushing Failure Reasons

Failure	Possible Results	Methods of Detection
Moisture insulation	Moisture enters	Power factor test Hot-collar test
Broken connection between ground sleeve and flange	Sparking in apparatus tank or within bushing. Discoloured oil	Power factor test Uncharacteristic odour Dissolved gas-in-oil Thermo graphic scanning
Corona	Internal breakdown Radio interference Treeing along surface of paper or internal surface	Power factor test Radio-influence voltage test Thermo graphic scanning

Table 1 shows a few failure modes of bushings, as well as the results of the failure modes [1]. Column 3 shows what methods can be applied in order to detect the failure mode. These various failure modes, results and method of detection was used to enhance the authors' understanding with respect to bushing failure modes and detection methods in order to develop the bushing failure estimation tool.

3.2 ECOU Substation HV Circuit Breaker Operations

Figure 2 shows the number of operations which these circuit breakers have performed with respect to transient faults/auto reclose of operations and switching operations from 01 July 2011 to 01 June 2012. Only circuit breakers that performed operations in excess of 24 operations per annum or 2 operations per month were retrieved. The circuit breakers which did not exceed 24 operations per annum or an average of 2 operations per month was not included in the figure 2. The majority of the substation circuit breakers below were located inland. The circuit breaker operations were used as criterion in the development of the bushing failure estimation tool.

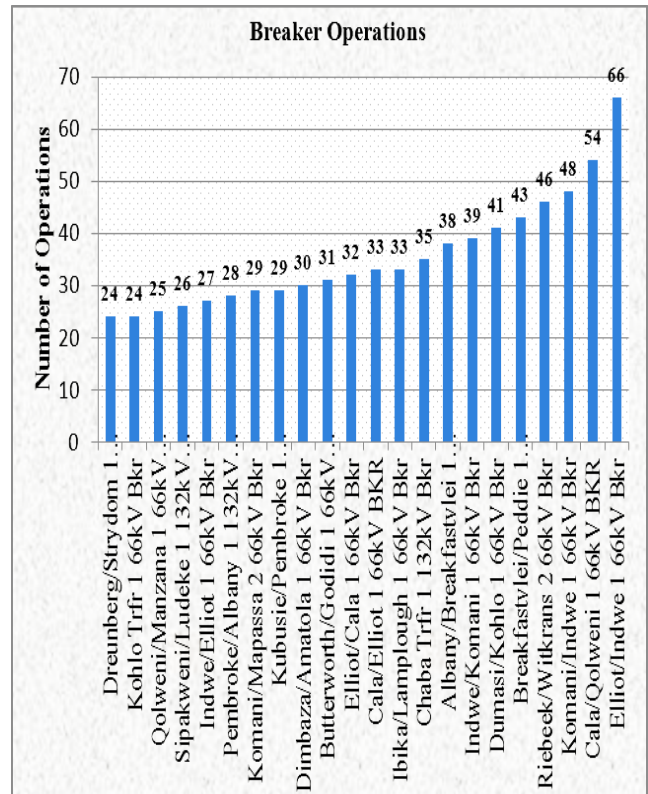


Figure 2: ECOU SS HV Circuit Breaker Operations

3.3 Power Transformer Overloading

Table 2: ECOU Transformer overloaded above 80%

FSA	Transformers	Rating (MVA)	Measured (MVA)	Simulated (MVA)	Load (%)
PORT ELIZABETH	Glenden Trfr1 66/11kV	5	5.8	5.8	124.20
QUEENSTOWN	Kubusie Trfr1 132/22kV	20	11.47	17.63	88.90
PORT ELIZABETH	Fort Beaufort Trfr2 66/11kV	10	7.95	8.03	80.02
MTHATHA	Mafini Trfr1 66/22kV	10	8.52	9.31	93.11
MTHATHA	Mafini Trfr2 66/22kV	10	7.94	8.64	86.41
MTHATHA	Mbashe Trfr1 66/22kV	5	5.00	5.05	101.00
MTHATHA	Paynes Farm Trfr1 66/22kV	5	3.95	4.01	80.02
EAST LONDON	Yellowwoods Trfr1 66/11kV	10	8.57	8.66	85.28
QUEENSTOWN	Skietkop Trfr1 66/22kV	2.5	2.03	2.03	80.37
EAST LONDON	Buffalo Trfr1 11/22kV	7	5.2	5.21	82.24
EAST LONDON	Buffalo Trfr1 11/22kV	7	5.1	5.21	82.24

Table 2 shows the ECOU power transformers which are loaded 80% and above [2]. Overloading was used as a criterion to establish an input in the development of the bushings failure estimation tool. Only transformers overloaded more than 100% was scrutinize to establish if the current flowing in the phases are exceeding the bushings operating capability.

3.4 Environmental Contamination

Light contamination (LC): Industries with low-density emission-producing residential heating systems and areas with some industrial areas or residential density, but with frequent winds and precipitation. Medium contamination (MC): Industries not producing highly polluted smoke

and or with average density of emission-producing residential heating systems, areas with high industrial and/or residential density but subject to frequent winds and or precipitation, and areas exposed to sea winds but not located near the sea coast. Heavy contamination (HC): High industrial density and large city suburbs with high density emission-producing residential heating systems and areas close to the sea or exposed to strong sea winds. Extra-heavy-contamination (EHC): Industrial smoke producing thick, conductive deposits and small coastal areas exposed to very strong and polluting sea winds [3].

3.5 Interpretation of Data

Within the ECOU 66 bushing were at risk of failing in service due to their age. The rest of the bushings were within safe operation due to their younger age category. The challenge was to operate the bushing safely until it becomes a risk to the ECOU, as determined by the critical tests and BFET. Accompanying the critical tests is visual inspection to detect the bushings from failing prematurely. Visual inspections do not require the bushing to be removed from service and is often the first line of ensuring the bushing is physically in healthy state. The results from the failure modes are techniques that can detect the defect in its early stages and even prevent the failure from happening. The majority of the HV circuit breakers were located inland, as oppose to the coastal area. Where the circuit breakers operated excessively, it was expected that a high number of faults e.g. lightning was evident. These bushings can get affected by these faults and therefore the health status may deteriorate. The same circuit breaker operations challenges with respect to lightning were not evident at the coastal areas. The ECOU coastal area experience challenges with environmental contamination, as a fair amount of bushings are located within the coastal area. Medium and high contamination was the extreme case for these bushings located at the coastal area of the ECOU. The probabilities of finding a bushing being operated above its operating capability were low, as the majority of the power transformers was operating within their rated capacity rating. Bushings in the ECOU are usually higher rated then the power transformer capacity rating and therefore no bushings was found to be operated above its capacity.

4. CRITICAL SITE TEST AND CONTRIBUTING FACTORS

4.1 Surface Discharge Test

Discharge surveying can detect decomposing and pollution of the insulation. Bushings failing due to localized discharges are a result of accumulated surface contaminants. Bushing failures is often disastrous, it is therefore difficult to establish the exact point of failure. The contaminants dependence on dielectric properties, location and thickness can be modelled. The results demonstrated that bushings are highly sensitive to

contaminants on the lower porcelain [4]. Partial discharge can decompose and pollute the insulation of bushings, reducing insulation properties resulting in bushing failure. Partial discharge measurement may be used to determine the ageing condition of bushing. The partial discharge surveyor 100 (PDS100) tool was useful in determining the source and severity of the discharge. The dielectric strength of the bushing will therefore be equal to the weakest insulation impurity of the bushing. Table 3 shows the discharge value which the bushing emits which equates to a score given. The higher the discharge intensity value in decibels (dbm) the lower the score. The discharge measurement of bushings is essential and was used as an input criterion in developing the bushing failure estimation tool (BFET) as seen in table 9.

Table 3: Surface Discharge Scoring Guide

3. Discharge Value (dBm)	Score
Below 450MHz - No Change	100
Below 450MHz - Change	80 - 99
450MHz and 800MHz (< 4)	75
450MHz and 800MHz (4)	70
450MHz and 800MHz (5)	65
450MHz and 800MHz (6)	60
450MHz and 800MHz (7)	55
450MHz and 800MHz (8)	50
450MHz and 800MHz (9)	45
450MHz and 800MHz (10)	40
450MHz and 800MHz (> 10)	< 20
Greater than 800MHz (2)	80
Greater than 800MHz (3)	60
Greater than 800MHz (4)	40
Greater than 800MHz (> 4)	< 20

4.2 Infra-Red Scanning (Thermography)

The infra-red thermography plays an important role in determining if the bushing has any anomaly temperature. Bushings can be profitably inspected with thermography. A normal signature is at or close to ambient air temperature. Any unexplained, anomalies thermal signature or rise over ambient/another phase temperatures are considered indicative and warrant further investigation. A bad connection at the bottom of a bushing can be confirmed by comparing infrared scans of the top of the bushing with a sister bushing [5]. Table 4 shows the temperature anomalies (ΔT) measured on the bushing which equates to a score given. The higher the temperature anomaly the more at risk the bushing was, as the severity increases. The higher the temperature anomaly the lower the score equates. Infra-red measurement of bushings was used as an input criterion in developing the bushing failure estimation tool as seen in table 9.

Table 4: Infra-Red Scoring Guide

IR Scan °C (ΔT)	Score
≤ 5	100
10	90
15	80
20	65
25	50
30	35
35	20
≥ 40	5

4.3 Tan Delta Test

High tan delta values are undesirable and indicate that the bushing insulation has been contaminated with moisture. Low tan delta values measured is an important criterion to show a well dried bushing cellulose material which is probably equal in life expectancy to thermally upgraded (65 °C) transformer insulation [6]. Tan delta values for bushings are very dependent on the moisture content of the insulation. The upper limit for OIP bushings are 0.55% and the RIP bushings are 0.85%. Table 5 shows the tan delta measurement on bushing which equates to a score given. The higher the %tan delta measured on the bushing, the more at risk is the bushing becomes. Each tan delta measurement equates to a score given. Tan delta measurement of bushings is essential and was used as an input criterion in developing the bushing failure estimation tool as seen in table 9.

Table 5: Tan Delta Scoring Guide

% TD Value at 10kV	Score
≤ 0.30	100
0.35	90
0.4	80
0.45	70
0.5	60
0.55	50
0.6	40
0.65	30
0.7	20
≥ 0.75	< 10

4.4 Environmental Contamination

Bushings exposed to pollution must have adequate creep distance, measured along the external contour of the insulator, to withstand the detrimental insulating effects of contamination on the insulator surface [3]. Table 6 shows that each level of environmental contamination categorized and equates to a score given. The higher the contamination the more at risk is the bushing becomes as the severity increases. Environmental contamination was used as an input criterion in developing the bushing failure estimation tool as seen in table 9.

Table 6: Environmental Contamination Scoring Guide

Environment Risk	Score
No Contamination (NC)	100
Low Contamination (LC)	75
Medium Contamination (MC)	50
High Contamination (HC)	25
Extra High Contamination (EHC)	0

4.5 High Voltage Circuit Breaker Operations

Transient phenomenon is an aperiodic function of time and does not last longer. The duration for which they last is very insignificant as compared with the operating time of the system. Yet they are very important because depending upon the severity of these transients, the system may result into outages. High voltage bushings can be affected by switching operations, lightning and faults on the power network [7]. Continuous transient faults can deteriorate the bushings health status [8]. These transients' faults causes circuit breakers to operate and there indicates where majority of the transient are present. Table 7 shows that circuit breaker operations have been categorized and score given to the relevant risk category. The circuit breaker scoring guide is used as an input criterion in the development of the bushing failure estimation tool as can be seen table 9.

Table 7: Circuit Breaker Scoring Guide

CB Ops Risk	CB Ops	Score
Low (L)	≤ 20	100
Medium (M)	21 - 60	50
High (H)	≥ 61	10

4.6 Power Transformer Bushing Overloading

Bushings are chosen at higher current rating capacity compared to the transformer phase current capacity in order not to overload the bushing, which will inevitably damage the power transformer. The use of bushings with current ratings greater than the transformer current ratings, reduces the temperature rise inside the bushing at rated transformer current. Overloading a bushing can deteriorate the bushings health which will inevitably result in bushing failure [8]. Therefore, it is good practice to choose bushings with higher-rated currents than that of the transformer; or to use bushings with high temperature paper and sealing materials. Consequently, the bushings will not be overloaded, or not overloaded much, during the transformer overload [9]. Table 8 shows overloaded bushings will have a value scoring 0 and a bushing being operated within its designed capacity will score 100. Bushing overloading is important and will be used as a criterion to develop the bushing failure estimation tool.

Table 8: Overloading Scoring Guide

Overloading	Score
No (N)	100
Yes (Y)	0

4.7 Bushing Failure Estimation Tool

The bushing failure estimation tool in table 9 used values obtained from table 3, 4, 5, 6, 7 and 8 to be inserted in the input column of the BFET as can be seen in table 9. Once these values are inserted, the BFET estimates the year the bushing is likely to fail. The BFET acts as an aid to decide when to put mitigating plans in place before the bushing fail, reducing the probabilities of the bushing failing while in operation. The BFET can also be used to drive the risk/condition based maintenance strategy. Thus plans could be put in place to order bushings when it enters the medium risk category.

Table 9: Bushing Failure Estimation Tool

TEST RESULTS and FACTORS	INPUTS	High Risk	
Tan Delta Value _Start at (Range: 0.3 - 1)	0.66	Medium Risk	
Infra Red Scanning Value (Range: 0 - 75)	25		
Surface Discharge Value (Use Table)	50		
Environmental Contamination	nc		
Overloading	n		
Circuit Breaker Ops	h		
SCORE DESCRIPTION	Weight out of 100	% SCORE	Weighted Score
Tan Delta Value	50	28	14
Infra Red Scanning Value	15	60	9
Surface Discharge Value	20	50	10
Environmental Contamination	5	50	2.5
Overloading	5	100	5
Circuit Breaker Ops	5	10	0.5
		Total Weighted Score	41
YEARS REMAINING	6.5		
CURRENT YEAR	2012		
ESTIMATED FAILURE YEAR OF BUSHING	2019		

5. IMPACT OF CONDITION / RISK BASED MAINTENANCE STRATEGY

The probabilistic risk assessment technology is applied to RCM analysis on power plant equipment. The minimum maintenance risk cost is taken for an optimized objective to solve the optimum maintenance cycle. A method to calculate the maintenance risk cost through probabilistic risk is can be determined to find the optimum maintenance cycle for power plant equipment. The relationship between fault rate and maintenance activities including condition monitoring and preventive maintenance is comprehensively analysed. Then an optimum model of maintenance risk cost is set up, and an overall maintenance strategy with optimum maintenance

cycle can now be obtained [10]. The strategy shows the critical tests which were required, the craft required to carry out these tests, as well as what tests can be done without an outage. The thermography test and discharge activity tests require no outage and the test can therefore be carried out live. Labour cost per craft was allocated for each test as well as the time duration to execute the critical test. An annual cycle was chosen for the thermography test and discharge activity tests. While a 6 yearly cycle was opted for the tan delta test to be carried out on these bushings. Opting to carry out tan delta test on a 6 yearly cycle meant approximately 100 bushings will be tested annually. With a population of 174 power transformers in operation, 26 of those power transformers have three 132 kV bushings on their primary side and three 66kV bushings on their secondary side. The rest of the 149 power transformers either have three 132 kV bushings on their primary side and or 66kV bushings mounted on their primary side only. This resulted in approximately 4 outages per annum for power transformer fitted with bushings on the primary and secondary side of the power transformer. Power transformer fitted with bushings only on the primary side required 25 outages to be arranged per annum to carry out the tan delta tests. The 26 power transformers with HV bushings on their primary and secondary side needed approximately 5 outages per annum. Summating these outages in order to carry out tan delta tests on all the bushings resulted in 31 outages that had to be arranged.

5.1 Required stock level (Spares)

An improved stock level accuracy can only be accomplished once a tan delta tests, surface discharge tests and thermography tests are carried out on all the bushings in ECOU. The test results should then be inserted into the input data section of the bushing failure prediction tool. The BFET indicated the health status of the bushing and estimate which year the bushing was likely to fail. Only once all the bushings have gone through this exercise the stock level accuracy can be improved. Stock level can be improved by stocking up on spares where bushings exceed 35 years of age as can be seen in table 10 below.

Table 10: HV Bushing older than 35 years

1. SS	2. MVA	4. Age	5. Tech.	6. Bushing	7. (kV)
Bosberg	10	37	OIP	3	66/11
Bulhoek	5	44	OIP	3	66/22
GHTextiles	6	42	OIP	3	66/11
GHTextiles	7.5	40	OIP	3	66/11
GHTextiles	7.5	40	OIP	3	66/11
Kudu	10	36	OIP	3	132/11
Kudu	10	36	OIP	3	132/11
Lamplough	10	39	OIP	3	66/22
Lamplough	10	38	OIP	3	66/22
Riebeek	5	37	OIP	3	66/22

Column 6 in the table 10 shows how many bushings were required for spares and column 8 reflects the voltage ratio. It can be seen that the bushing technology was OIP and therefore it was wise to purchase RIP technology due to its longer lifespan, better reliability and its robust texture.

6. CONCLUSION

The references used explained the behaviour of bushings when subjected to various conditions. The value of the critical tests which can be carried out on the bushings cannot be underestimated as explained by the references. To estimate when a bushing is likely to fail without these critical tests being carried out will be impossible. The limits of the critical tests and other visual checks described by the references were ultimately used as a guide in developing the bushing failure estimation tool. It also enhanced the investigators knowledge with respect to the causes of bushing failures and the methods of detection. Knowing which year the bushing was likely to fail, the risk was reduced by replacing the deteriorated bushing with a healthier bushing. Opting to repair the deteriorated bushings or choosing to live with the risk a little longer was dependent on the risk severity. Knowing the entire bushing population estimated years to failure, a required stock level plan can be put in place to purchase bushings in order to have an accurate stock level. In order to improve the accuracy of the BFET one has to follow a comprehensive maintenance plan e.g. tan delta tests, infra-red scanning, discharge activity test at the recommended frequencies, as well as include the factors like overloading, circuit breaker operations and environmental contamination.

7. RECOMMENDATIONS

In order to optimise the risk based maintenance strategy, the infra-red scanning and discharge activity test had to be carried out annually in order to start accumulating the test results data. The tan delta tests had to be carried out on a 6 yearly cycle in order to start accumulating the test results data. The bushing failure estimation tool should be continually refined in order to improve the accuracy towards a minimum of at least 90%. During the accumulation of the tests results one should utilise the BFET to establish which bushings are at risk and either replace, repair and de-commission it. Plans should be put in place to procure the amount of bushings that will be required to replace the bushings at risk, as the lead time for bushing is approximately 6 months. Once the BFET indicate that the bushing is at high risk, it will be wise to first consult the relevant stakeholders and only then choose to replace, repair or even live with the risk a little longer if the risk due to failure is minimal.

8. REFERENCES

[1] Dennis A. Schurman, "Testing and Maintenance of High Voltage Bushings," in Power System Maintenance Manual. Colorado, United States of

America: Western Area Power Administration, 1999, Chapter 6.

- [2] Athini Pantshwa, "Distribution Eastern Cape Operating Unit Load Test Report," Eskom Distribution, East London, Network Optimisation Load Test Report EDNO 0006, 2011.
- [3] James H. Harlow, ELECTRIC POWER TRANSFORMER ENGINEERING SERIES, 9th ed., James H. Harlow, Ed. Florida, United States of America: CRC Press LLC, 2004.
- [4] D.J. Smith, S.G. McMeekin, B.G. Stewart, and P.A. Wallace: "The electric field modelling of a high voltage bushing with contaminants on the lower porcelain surfaces," Electrical Insulation and Dielectric Phenomena (CEIDP), 2011 Annual Report Conference, pp.555-558, 16-19 Oct. 2011
- [5] U.S. Department of the Interior Bureau of Reclamation Reclamation, Transformers: Basics, Maintenance and Diagnostics. Denver Colorado, United States of America, 2005.
- [6] Transformers Committee of IEEE Power Engineering Society, "IEEE Draft Guide for Application of Power Apparatus Bushings," IEEE Standards Activities Department, New York, Standard Std C57.19.00-1991, 2011.
- [7] C.L Wadhwa, High Voltage Engineering, 3rd ed. Delhi, India: New Age International (P) Ltd, 2010.
- [8] Raymond Harris, High Voltage Engineering Lectures, 2012.
- [9] Shibao Zhang, "IEEE TRANSACTIONS ON POWER DELIVERY," Evaluation of Thermal Transient and Overload, vol. 24, no. 3, p. 7, JULY 2009.
- [10] Gu, Yujiong; You, Lianhuan; "Optimization on maintenance cycle for power plant equipment based on probabilistic risk assessment," Technology and Innovation Conference, 2006. ITIC 2006. International , vol., no., pp.80-84, 6-7 Nov. 2006
- [11] R. Snell and Dr. Roderick Thomas, "A guide to infrared thermography for condition monitoring," Energize, pp. 34-38, June 2006.

AN OVERVIEW OF THE ELECTRICAL TREEING PHENOMENA IN SOLID DIELECTRICS

Darryn R. Cornish and Cuthbert Nyamupangedengu

School of Electrical & Information Engineering, University of the Witwatersrand, Johannesburg, Private Bag 3, Wits 2050, Johannesburg South Africa, E-mail: darryn.cornish@students.wits.ac.za

Abstract: Electrical treeing is an insulation degradation phenomenon that is caused by localised enhanced electric field resulting in breakdown of insulation at molecular level. Once initiated, trees quickly progress to complete failure. In high voltage insulation engineering, it is therefore essential to understand and design for insulation endurance to degradation through treeing. A good understanding of treeing mechanisms is required and this has sustained research in the treeing phenomenon for many years. There is now a general agreement on how trees initiate propagate and eventually cause complete insulation failure. Tree detection and classification techniques have also been developed. Research in treeing phenomenon is ongoing worldwide in response to the need for keeping pace with increasing demands of quality in the electric power industry.

Keywords: Electrical trees, insulation, Partial discharges, insulation defects, insulation failure

1. INTRODUCTION

Electrical trees are gas filled micro-tubes that develop in regions of localised high electric field in solid insulation [1]. The micro-tubes are tree shaped and that is the reason they are called electrical trees. An example of an electrical tree is as shown in Figure 1. Once initiated, the trees progressively propagate between the electrode gap and eventually bridge the insulation. Electrical treeing is an insulation degradation phenomenon that characterise the final phase of most failure modes of insulation.

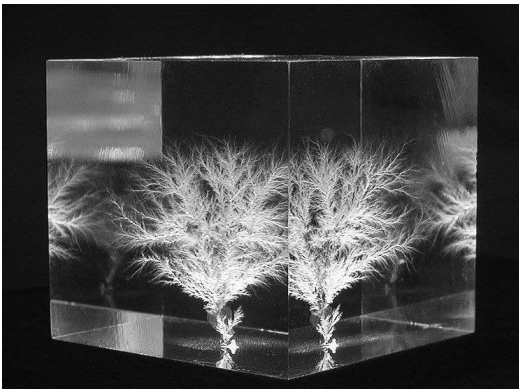


Figure 1: An electrical tree grown in a cube of Polymethyl Methacrylate (PMMA) [2].

Causes of electrical trees include; metallic protrusions into the insulation along the electrical/insulation interface, embedded particles in the insulation and water trees. These defects initiate electrical trees in the insulation under high electric field conditions. Severely aged partial discharge defects also initiate electrical trees in the final phases of progression to complete insulation failure.

In the design and development of high voltage equipment, the knowledge of treeing endurance

capabilities of the insulation is essential. In that regard there has been sustained efforts in research to understand the electrical treeing phenomenon in solid electrical insulation.

This paper presents a review of various key aspects in treeing knowledge accumulated thus far. A significant body of knowledge on electrical treeing has been built up through many years of research and field experience. There is however need to continue research on treeing mechanisms in insulation especially in view of the need to keep up to speed with challenges associated with contemporary power system performance requirements.

2. ELECTRICAL TREEING MECHANISMS

Localised stress enhancement is a precondition for tree inception. Depending on the type of insulation defect causing the stress enhancement, different types of electrical trees occur. Typical insulation defects that initiate electrical trees are as illustrated in Figure 2 [3]. Once initiated electrical trees progressively propagate from the point of initiation until the insulation is completely bridged. The trees will eventually cause a complete short circuit.

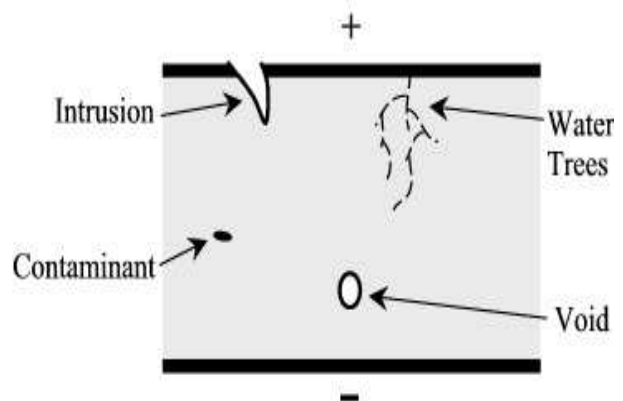


Figure 2: Illustration of the causes of electrical treeing.

2.1 Tree inception mechanism

The electric field strength around a stress enhancement body or feature can be orders of magnitude bigger than that in the host insulation. For a needle-plane electrode configuration (simulating a conductive protrusion into the insulation), the maximum Laplacian electric field strength at the needle tip is given by equation 1 [4].

$$E_{\max} = \frac{2V}{r \ln\left(1 + \frac{4d}{r}\right)} \quad (1)$$

Where;

V is the applied voltage [kV_{rms}],

r is the needle tip radius [μm],

d is the gap between the needle tip and grounded plane electrode [mm].

As an example, for an insulation gap of 3 mm, needle tip of 5 μm and voltage across the electrode of 20 kV, the maximum field strength at the needle tip would be about 1 000 kV/mm compared to the background field strength of 6.7 kV/mm. At such high electric field, electrons that may be present in the insulation gain energy and accelerate towards or away from the needle tip depending on the polarity of the electric field as illustrated in Figure 3. The highly energetic electrons, having extracted energy from the field, bombard the insulation molecules and impart energy. This damages the molecular structure by weakening the links between the molecules [5]. The process may result in molecular bond scission creating microchannels in the insulation. The phenomenon also emits optical energy known as electroluminescence [5].

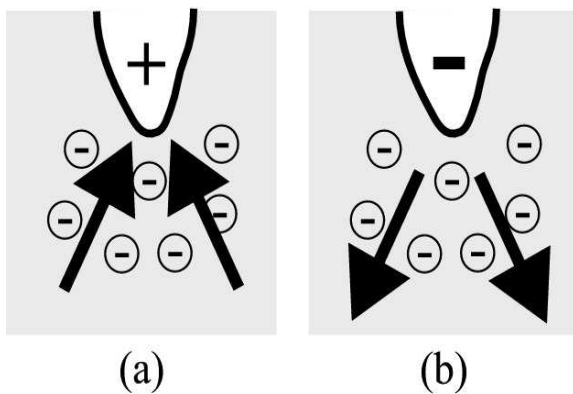


Figure 3: The electron motion for intrusion with overall (a) positive charge and (b) negative charge.

If the voltage across the electrodes is alternating, electric charge is repeatedly injected and extracted increasing the damage susceptibility of the molecular structure. This damage explains why some materials, such as Cross-Linked Polyethylene (XLPE), are especially susceptible to treeing. The dielectric strength of XLPE is in its cross-linked molecular bonds. Damage to these cross-links literally weakens the molecular structure.

2.2 Propagation stage

Once a tree has been initiated, gas molecules migrate into the micro-tubules. Partial discharges (PDs) are initiated in these microtubes. The PDs are micro gas explosions and the energy from this activity further erodes the microchannel surface consequently widening and elongating the tree channels. The wider and longer channels support bigger PDs. The increase in PD activity feeds into further propagation, forming a reinforcement cycle until the final failure stage is reached [1].

The manner in which the tree propagates into the insulation is both deterministic and probabilistic. Consequently researchers have used combinations of deterministic and probabilistic techniques to simulate the propagation of electrical trees in insulation [6-8]. Despite numerous efforts in modelling electrical tree mechanisms, the treeing phenomenon is not yet fully understood. There are therefore opportunities for developing better simulations of treeing propagation mechanisms.

2.3 Failure stage

Once the tree has spread far enough into the insulation, complete breakdown is guaranteed. It is however noted that some researchers have observed the trees completely bridging the insulation but not resulting in immediate complete failure, and this is attributed to the probabilistic behaviour of the treeing mechanisms which still needs to be further understood [9]. Similarly some cases only require the trees to reach a certain threshold length beyond which complete short circuit failure will occur. In any case however, once a tree has started to form, eventual failure is guaranteed and is generally not far into the future and in some cases, as little as 1 hour. The time to failure duration is primarily dependent upon the stress, insulation material and distance between conductors.

3. ELECTRICAL TREE TYPES

Among many ways of classifying electrical trees, the most common classification is by shape. The treeing pattern is a function of the type of defect initiating the trees, the electric field strength, type of the insulation and type of the voltage across the electrodes.

Bush trees: Bush trees are very similar in shape to their namesakes. The micro-tubules form multiple exits from the geometrical stress enhancement body, instead of one focused root. A bush tree is characterised by a multitude of short micro-tubules clustered around the stress enhanced region as illustrated in Figure 4a. Bush trees commonly occur under relatively high electric field strength [1]. The partial discharge signals associated with bush tree types are characterised by dominant relatively small pulse magnitude.

Branched trees: Branched trees are almost the opposite of bush trees. They comprise of both short and long branches extending into the insulation from the point of initiation. The PDs associated with branched electrical

trees comprise of both big and small discharge magnitudes. Conditions conducive to the growth of branched electrical trees include relatively low electric field strength.

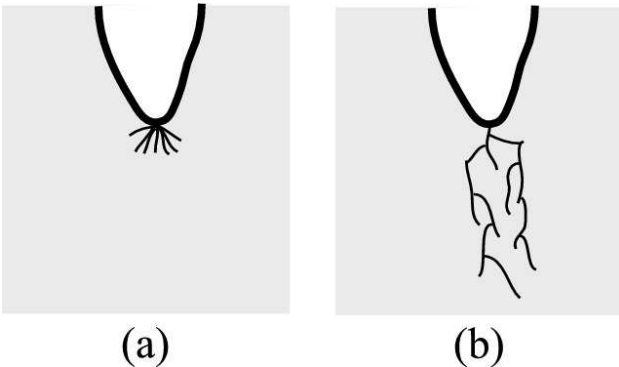


Figure 4: Micro-patterns of (a) bush and (b) branched trees.

Bush-Branch trees: There are cases where the tree growth conditions favour both bush and branched trees such that the resulting tree shape is a combination of bush and branch trees and is therefore named bush-branch tree type as illustrated in Figure 5.



Figure 5: Combination of bush and branched trees.

Bowtie trees: Bowtie trees generally form around a solid contaminant embedded in the insulation. The trees initiate and progress towards both electrodes as illustrated in Figure 6.

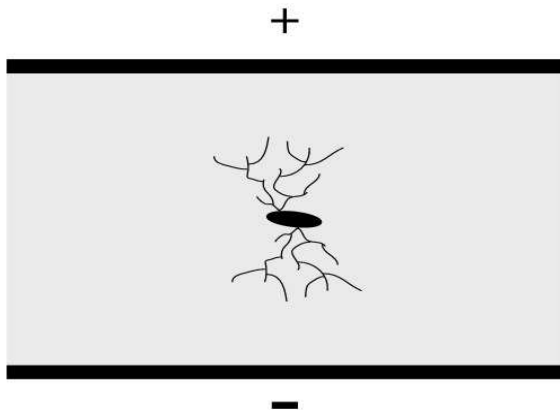


Figure 6: A bowtie tree initiated due to a contaminant.

4. ELECTRICAL TREE DETECTION

Electrical treeing mechanisms emit optical and electromagnetic energy. Detection and analysis of the emitted energy gives information about the treeing process. PD detection techniques are used to detect the electromagnetic energy in electrical trees [1]. Electrical treeing PD signals are however typically small such that detection is currently only feasible under laboratory conditions and mostly impossible in field conditions. An example of tree PD phase-resolved pattern detected by the authors in epoxy resin is shown in Figure 7.

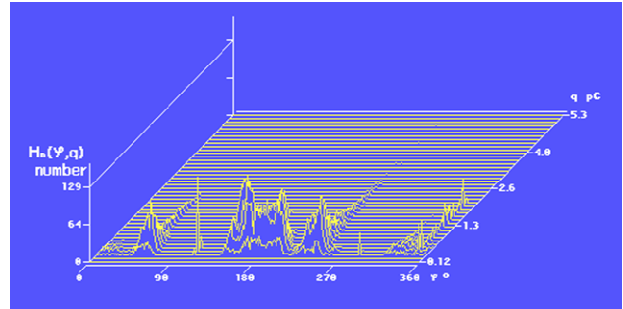


Figure 7: A three dimensional PD phase-resolved pattern of electrical trees in an epoxy resin needle to plane electrode setup.

Partial discharge signals in electrical trees are typically erratic in repetition and magnitude and this is due to physiochemical processes associated with PD mechanisms. In the research work conducted by the authors and published elsewhere [10], the PD activity alternatively extinguished for some period and reignited cyclically as the trees evolved from inception to complete failure. Figure 8 shows an example of tree partial discharge magnitude variations over the tree life from inception to complete failure. In the Figure, it is evident that the PD magnitude initially started at about 20 pC and progressively decreased to complete extinction in 2 hours. It remained extinct for the next 5 hours after which it reignited but with an average magnitude of 2 pC for 7 hours. In the last 6 hours of the tree life the PD magnitude reached a magnitude of 140 pC before complete failure. The insulation in this case was a nanocomposite epoxy (AlO₃/epoxy) [10].

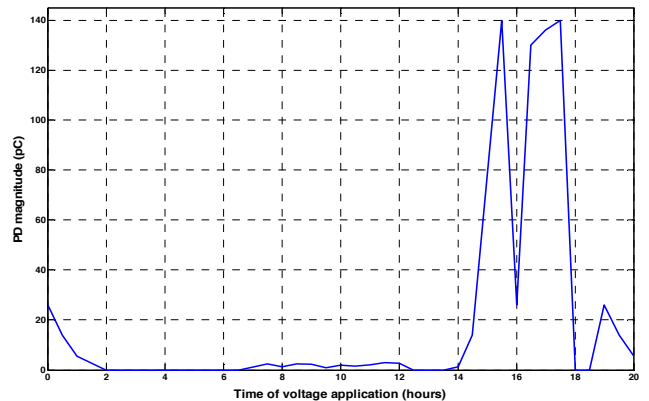


Figure 8: An example of electrical tree PD magnitude variations over the whole tree life [10].

In addition to optical and PD detection, photographic techniques are also widely used to record electrical trees. An example of an electrical tree grown in Perspex by the authors is shown in Figure 9. Various image processing techniques such as fractal dimensions are used to extract useful information from tree images. A major shortfall with photographic imaging techniques of tree detection is in that the insulation has to be transparent. In that regard, recently, some researchers at the University of Manchester have reported promising results on the development of an x-ray based tree imaging technique that can 'see trees' through non-transparent insulation [11]. The technology however is still under initial research.



Figure 9: A microscopic photographic image of an electrical tree grown in Perspex.

5. THE FUTURE IN ELECTRICAL TREE RESEARCH

It is now generally agreed that contemporary and future research trends in the electric power industry are largely dictated by the need to use higher voltages, miniaturisation of equipment, more stringent reliability requirements and cost effectiveness [12]. Since electrical treeing endurance is a key insulation performance parameter, the phenomenon has to be well understood as a prerequisite for designing and developing electrical insulation that meets the increasing performance demand of modern power systems. Consequently electrical tree endurance performance in existing insulation designs are being continuously studied with the aim of devising performance improvement. Furthermore where new insulation is being developed such as nanocomposite electrical insulation, electrical tree studies have become an important tool in the research and development of the insulation [13].

6. CONCLUSION

While significant knowledge on electrical treeing phenomenon has been generated through research worldwide, the ever increasing quality demands in the power industry entail further research in the treeing

phenomenon. In development of new insulation such as nanocomposites, electrical treeing research is further motivated.

7. ACKNOWLEDGMENT

The authors would like to acknowledge with gratitude Eskom for their support of the High Voltage Engineering Research Group through TESP. They would also like to express gratitude to the Department of Trade and Industry (DTI) for THRIP funding and to thank the National Research Foundation (NRF) for direct funding of the research group.

8. REFERENCES

- [1] L. A. Dissado, "Understanding Electrical Trees in Solids: From Experiment to Theory", *IEEE Transactions on Dielectrics and Electrical Insulation*, Vol. 9, No. 4, pp. 483-497, August 2002.
- [2] Bert Hickman, "A 3D Electrical tree image" <http://en.wikipedia.org/wiki/File:ElectricalTree1.jpg> last accessed 4 December 2012
- [3] F. H. Kreuger, *Partial discharge detection in high-voltage equipment*. London: Butterworths, 1989.
- [4] L. Cisse, S.S. Bamji and A.T. Bulinski, "Electric field calculations for needle-plane geometry and space charge in polyethylene", *IEEE Transactions on Dielectrics and Electrical Insulation*, Vol. 10, No. 1, 2003
- [5] T. Tanaka, "Charge Transfer and Tree Initiation in Polyethylene Subjected to ac Voltage Stress", *IEEE Transactions on Electrical Insulation*, Vol. 27, No. 3, pp. 424-431, June 1992.
- [6] K. Wu, Y. Suzuoi and H. Xie, "Model for partial discharges associated with treeing breakdown: I. PDs in tree channels", *Journal of Physics D: Applied Physics*, Vol. 33, No. 10, pp. 1197-1201, 2000.
- [7] K. Wu, Y. Suzuoi and H. Xie, "Model for partial discharges associated with treeing breakdown: II. Tree growth affected by PDs", *Journal of Physics D: Applied Physics*, Vol. 33, No. 10, pp. 1202-1208, 2000.
- [8] K. Wu, Y. Suzuoi and H. Xie, "Model for partial discharges associated with treeing breakdown: III. PD extinction and re-growth of tree", *Journal of Physics D: Applied Physics*, Vol. 33, No. 10, pp. 1209-1218, 2000.
- [9] T. Tanaka, "Comprehensive understanding of treeing V-t characteristics of epoxy nanocomposites", *Proceedings of the 17th International Symposium on High Voltage Engineering (ISH)*, paper No. E-008, Hannover, Germany, 2011.

- [10] C. Nyamupangedengu, R. Kochetov, P. H. F. Morshuis and J. J. Smit: "A Study of Electrical Tree Partial Discharges in Nanocomposite Epoxy", *IEEE Conference On Electrical Insulation and Dielectric Phenomena*, Delta Centre-Ville Montréal, pp. 912-915, October 2012.
- [11] R. Schurch, S. M. Rowland, R. S. Bradley and P. J. Withers: "A Novel Approach for Imaging of Electrical Trees", *IEEE Conference on Electrical Insulation and Dielectric Phenomena*, Delta Centre-Ville Montréal, pp. 593-604, October 2012.
- [12] H Okubo, Enhancement of electrical insulation performance in power equipment based on dielectric material properties", *IEEE Transactions on Dielectrics and Electrical Insulation*, Vol. 19, No. 3. pp733-754, 2012.
- [13] M.G. Danikas and T. Tanaka, "Nanocomposite – A review of electrical treeing and breakdown", *IEEE Electrical Insulation Magazine*, Vol. 25, No. 4, pp. 19-25, 2009.

IN-SERVICE CONDITION MONITORING OF SURGE ARRESTERS WITHIN ETHEKWINI ELECTRICITY

Makhosonke Gumede* and G. Frederick d’Almaine**

Dept of Power Engineering

Durban University Technology,

*E-mail: makhosonke.gumede@yahoo.com

**E-mail: dalmaine@dut.ac.za

Abstract: It is extremely important to measure the condition of the surge arresters while they are in service so that they can be removed from service before they fail. This paper presents systems for the monitoring of polymer housed surge arresters within eThekweni Electricity using various diagnostic methods. The systems measure the resistive leakage current that continuously flows through the ZnO varistor during normal service operation and temperature via infrared thermo vision for fault prediction purposes. The measurements are applied for diagnosis of 120kV/65kA surge arresters of different makes on 132kV and 275kV substations. Leakage current measurement and infrared analysis were valuable in obtaining sufficient information for failure of arresters. The thermal heat was detected inside an arrester and normal leakage current measurements. Tests were performed on surge arresters that are still in the system and test results were compared to the results from the tests performed on failed units. Results obtained from different tests, (tests mentioned above) were compared to the test results from different families or designs.

Keywords: Polymer housed surge arrester, infrared scanning, and leakage current measurements.

1. INTRODUCTION

Overvoltages in an electrical network may occur due to lightning strikes, system faults or switching operations. These overvoltages could reach dangerous amplitudes for electrical network apparatus. To protect the network equipment and to guarantee security and reliable operation, surge arresters are applied to all types of electrical transmission and substation systems.

Generally, surge arresters are constructed using nonlinear resistive elements covered by polymer insulators. Ageing of the polymer insulators is caused by environment factors such as UV, contaminations, moisture ingress and electrical stress including leakage current, local discharge and corona discharge [1]. These phenomena may eventually cause failure on surge arresters in the system. Hence, it is important to monitor the surge arrester while in service so as to increase its life span.

According to IEC standard 60071-2 surge arresters are very important devices placed within an electrical power system to ensure appropriate insulation coordination and to protect valuable equipment such as power transformers, circuit breakers etc. against lightning, transient voltage and switching surges. It has been reported that polymer housing material used for outdoor insulation is subjected to a number of degradation influences during service. These include tracking and erosion due to dry band arcing and possible material degradation from the environment such as ultraviolet rays, hydrolysis, fungi, and chemical attack by alkalis, acids and hydrocarbon liquids and vapors[2],[3],[4].

eThekweni Electricity has experienced a trend where a certain family of surge arresters fails without any anomalies on the electrical system (such as lightning strikes, switching operations or system faults). Fig .1 represents a number of surge arresters that failed on the system from year -2000 to 2004. Since this has happened in the past and continues to happen, a decision was taken to perform an investigation to identify the causes of failure and find optimal solutions.

The main intentions of this paper are to investigate the failure of surge arresters by performing various tests such as leakage current measurements (offline) and infra-red scanning (online) to identify the fault proximity; improve the surge arrester specification to avoid failure in the future and extending the life time of the polymer housing surge arrester.

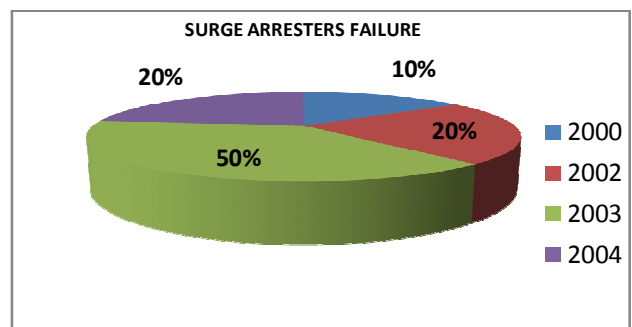


Figure 1: Surge arrester failure at eThekweni Electricity

2. BACKGROUND

The most advanced gapped silicon carbide arrester was the first really effective overvoltage protection for high voltage power networks. Gapped Silicon carbide surge arresters were developed in the 1930's to give good protection against overvoltages. These silicon carbide arresters were used on both transmission and distribution systems.

As the technology advanced rapidly, polymer housed surge arresters were introduced for the first time in the mid-1980s in MV electrical systems and proved to be a solution to the problems which could not be solved, for instance poor performance of several porcelain housed arrester designs which often suffered from sealing deficiencies, extreme sensitivity to pollution and unsatisfying overload performance [4]. Polymer housings (silicon rubber) has been the material of choice for high voltage insulation because of better behavior in polluted areas.

The silicon rubber is the only material offering hydrophobicity compared to other materials [5]. The polymer housed surge arrester has several other advantages including a better short circuit capability, increased personnel safety, flexibility in erection and a less brittle nature compared to porcelain and silicon carbide surge arresters. Over seven years of experience with polymer housed surge arresters have proved that as they are less prone to moisture ingress than porcelain arresters, they therefore minimize one of the most common causes of failure of surge arresters [6].

At the end of 1980s polymer surge arresters were available up to 145kV system voltage and today polymer housed surge arresters have been accepted up to 550 kV system voltages. They appeared on the market around 1990s, being niche products at this time. The actual share of polymer housed HV arresters is now estimated to be 25% to 30% and is rising [10], [4].

3. IN-SERVICE DEGRADATION OF ZNO SURGE ARRESTERS

The electrical stresses, counting leakage current and dry-band discharges, are directly responsible for tracking and erosion. Formation of sparking discharge is closely related to the variation trends of the total leakage current and creates high temperature spots that lead to bond scissions and other chemical changes on the surface insulation [1].

The ZnO varistor degradation is used to describe the electrical condition of a varistor relative to its past or future state when under the influence of external stresses [7], [8].

The amount of degradation is a good quality indication of varistor reliability and is usually used for foreseeing the life span of ZnO varistor [8]. The process of degradation causes the gradual increase of current with time on arrester.

It has been recognized that partial discharge is a dangerous ageing process first noticed in the last century when HV technology was introduced for the generation and transmission of electrical power [9].

It must be appreciated that, besides electrical stress caused by voltage or impulse currents, the following factors can accelerate the degradation process:

- Sealing defects leading to ingress of moisture as show on figure 2



Figure 2: Slip of polymer housing

The Humidity increases up to the level of 40-50%. However, at very high humidity levels, about 95%, there is the possibility of condensation at temperature changes. The moisture layer on the internal wall of the housing or on the varistor column can initiate the internal flashover [7].

- Long term ageing during normal service voltage
- Discharges due to surface contamination

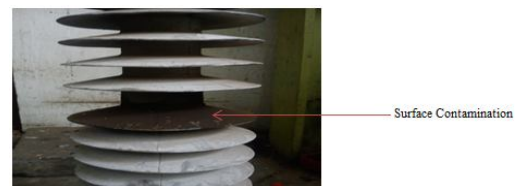


Figure 3: Surface contamination

- Internal partial discharge on the internal components of the surge arrester (varistor), as shown in figure 4 below.



Figure 4: Internal partial discharge [20]

- Design and physical arrangements of ZnO surge arresters.
- Overloading due to temporary and transient overvoltages.

4. FAILURE OF SURGE ARRESTERS

Polymer housed surge arresters are exposed to different types of stresses such TOV, switching overvoltages and lightning overvoltages. Moisture ingress may also cause accelerated ageing at the normal operating voltage. The surface deterioration and contaminant deposition on the specimen surface may cause a reduction in hydrophobicity of insulation material of a surge arrester. These stresses may cause the instantaneous overloading that will result in puncture, cracking or flashover of ZnO block varistors.

Hence, the failure of the surge arrester may appear in different ways:

- The arrester with a polymer housing may burn open the external insulation; such failed arresters are shown in Figure 5.
- The aged or overloaded arresters may show reduced protection against overvoltages, e.g. during transient overvoltage's, for instance due to high energy temporary overvoltages, the arrester can fail before it actually has suppressed the overvoltages.
- An arrester can cause an earth fault due to internal flashover, partial discharge (which can be caused by external pollution or birds, monkeys etc.) and temporal overvoltage (TOV) which can occur in electrical networks etc.

The arrester failures may cause severe damage to the neighboring apparatus and be a safety risk for the maintenance staff.



Figure 5: Metal Oxide surge arresters with polymer housing that failed during normal service operation.

5. TEST SELECTION

There are no simple, practical field tests that will determine the complete protective characteristics of surge arresters

[12], but the condition of the metal oxide surge arresters are measured by performing different tests, such as partial discharge (P.D) [13], radio interference detection [3], leakage current measurement and infrared scanning (I.R). Polymer materials can have more easily show exaggerated ageing due to partial discharge and leakage currents on the surface. However, if these problems are not detected they can cause the strength and frequency of the partial discharge to increase [11] and also leakage currents and may lead to catastrophic failure of the metal oxide arrester on system. These phenomenon are dangerous and can cause a total outage of the metal oxide arrester [14].

These tests can be performed with apparatus usually available, which will give sufficient information to determine whether the arrester can be relied upon to perform under normal conditions. By performing these measurements the information will be obtained and these tests will indicate units whose insulating qualities have deteriorated [12]. The following tests selected on this investigation were chosen after review of appropriate literature studies.

- Leakage current test (offline)
- Infrared scanning

The testing will not only cover the surge arrester condition but it will also cover their major active parts, for instance zinc oxide varistor (ZnO) and insulation of arresters.

5.1 Infrared thermography

A defective surge arrester loses its characteristic as an insulator under power frequency condition. It will allow the leakage currents to flow through it. This can cause the temperature to increase inside the ZnO varistor which might cause the arrester to fail. However, to detect and diagnose a fault, it is vital to select a set of inputs whose information is reliable.

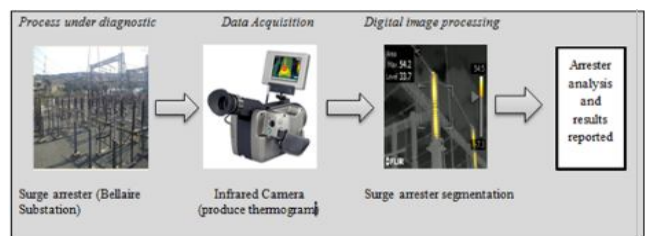


Figure 6: Methodology applies

Consequently, implementing the infrared thermograph as a tool for a data collection on this investigation will be helpful in obtaining the condition of surge arresters. Therefore, the methodology is applied for review on

120kV/65kA surge arresters on transmission substations of eThekweni electricity.

It is recognized that if there is a temperature difference between two points, there will also be heat transfer between those two points. Therefore, heat can be transferred in number different methods such as conduction, convection, evaporation or condensation and radiation. Here the focus is more on moisture condensation.

A Thermogram is a digital photo, taken by a device that is able to capture for example a lightning rod and codify its temperature using colors levels. As soon as all data is collected, it is necessary to apply digital image processing methods. This process enables the extraction of some thermographic variables from the thermogram (e.g. maximum and minimum temperatures). These variables are used by the diagnosis tool developed. The analyses are developed by considering some areas of the surge arrester thermograms by means of temperature gradient criteria.

5.2 Leakage current test

The current flowing from the hot conductor to ground over the outside surface of a device is called leakage current. But in case of the surge arrester insulation, it is the current flowing over the surface of the surge arrester insulation Fig.9 [12]. *“If no ground exists, the current flowing from a conductive portion of a device to a portion that is intended to be non-conductive under normal conditions”* [19].

During normal service the surge arrester carries a continuous small leakage current flowing through the surface, typically in a range of 0.2-3mA [20]. The total current flowing through the arrester is composed of resistive leakage current. The resistive leakage current is produced due to the changes of the schottky barrier which is formed between the zinc oxide (ZnO) grains and increases with arrester deterioration or aging (which is caused by environmental factors such as UV, contaminants and humidity) [15],[16].

However, the increase in the resistive leakage current will cause an increase in the power losses and hence increased temperature in the ZnO-block. The leakage current is directly proportional to hydrophobicity loss, especially for composite insulation.

The more the loss of hydrophobicity or reduction of silicon insulation, the higher the leakage current [21]. These leakages current can cause damage to the stability of the arrester, particularly in the low conduction zone where the V-I characteristic of a ZnO varistor is very sensitive to temperature [8].

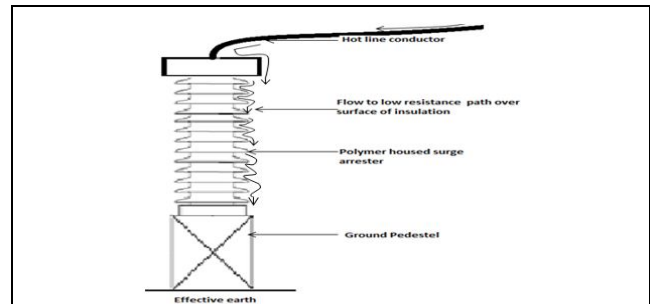


Figure 7: Leakage current flow to low resistance path over surface insulation.

The leakage current flowing through the surge arrester consists of a large capacitive current I_c and a small resistive component I_r . For a complete surge arrester, the capacitive current depends on the number of varistor columns that are in parallel. Fig.8. shows waveform of the leakage current components when a rated operating voltage is applied to a surge arrester.

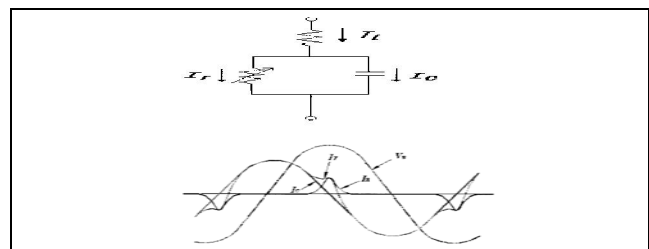


Figure 8: Equivalent circuit of surge arrester and waveform of the leakage current components [15]

Metal oxide surge arresters are known to exhibit an increase in resistive leakage current in relation with the arrester operating time [10]. As is well known, the increase of resistive and capacitive current will cause an increase in power losses (I^2R) and thereby an increase in ambient temperature. So an increase in temperature may bring a surge arrester to a temperature which exhibits an inadequate safety margin of thermal stability. This depends on the overall surge arrester design [16].

Heat dissipation is reduced at the centre of a column, as an arrester here is higher than those at the ends. Many researchers have reported that an increase of resistive current can be considered as an indicator of the arrester condition, and with the continued operation, in time it can cause failures or permanent degradation [10].

The resistive leakage current is the most important factor in arrester diagnostics, but the total leakage current and third harmonic component flowing through an arrester are widely employed as an ageing indicator [13], therefore the goal of leakage current measurements is to find the

insulation performance of the insulator, as it has been reported by other researches, that the leakage current change according to contamination surface [17].

5.2.1 Offline leakage current measurement

Offline leakage current measurement can be performed with a mobile AC or DC test instrument. For safety reasons, the offline leakage current measurement is mainly to be used because it requires the surge arrester to be disconnected from the electrical system. The disadvantages of offline leakage current method are the cost of the required equipment and the need for disconnecting the surge arrester from the power system [13].

Measurements carried out online under normal service voltage are the most common method. For practical and safety reasons, the leakage current is normally accessed only at the earth end of the surge arrester. In order to allow measurements of the leakage current that flows in the earth connection, the arrester must be equipped with a base insulated from the pedestal.

6. SURGE ARRESTER EVALUATION

Recently, eThekweni Electricity uses different types of family brand of surge arresters in substation for protection purpose on the system. The following brands are:

- Surge arresters manufacture A
- Surge arresters manufacture B
- Surge arresters manufacture C

Therefore, the data acquisition process will focus on the above mentioned brands. Hence, the graph below illustrates the failure of different brands from year 2001 to 2004.

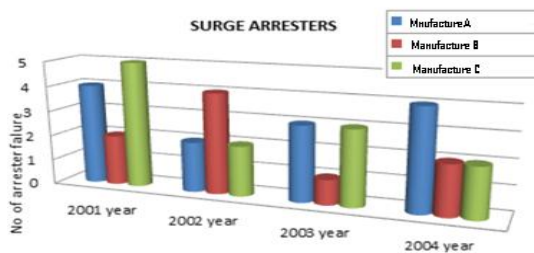


Figure 8: Graph showing failure of arrester from year 2001-2004

7. INFRARED THERMOGRAPHY RESULTS

The infrared (IR) analysis was conducted while the surge arresters were energized and under full load. Through the investigation eThekweni Electricity has discovered that the

polymer housed surge arresters are showing heating inside the metal oxide while in operational service.

The infrared (IR) analysis was conducted while the surge arresters was energized and under full load. Through the investigation eThekweni Electricity have discovered that the polymer housed surge arresters they showing the heating inside the metal oxide while in operation service. (Note that the yellow in center of the image is a hot spot). The measurements were completed on 3 different substations from October 2012 to November 2012.

7.1 Inspection in Substation A

The diagnoses were executed for ZnO surge arresters, station class surge arresters have superior electrical performance because their energy absorption capabilities are greater, and the discharge voltage (protection levels) is lower and the pressure relief is greater. They are polymeric encapsulated, installed at major substation A. This family type of surge arresters has affected the reliability of eThekweni transmission system.



Figure 10: Thermo-grams for substation A, 2 arresters were showing high amount of heat

7.2 Inspection in Substation B

The following result were collected from ZnO surge arresters, polymeric encapsulated, installed at major substation B, located at line 1. The inspections were executed on 132 kV.

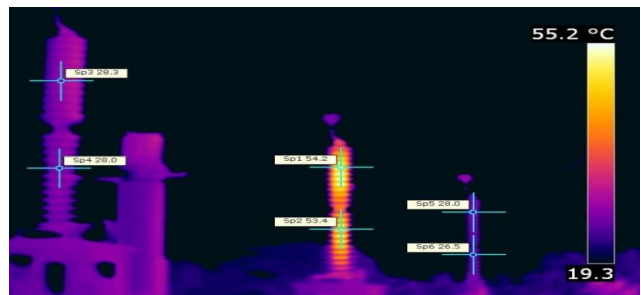


Figure 10: The thermal heating problem with these arresters could have affected the reliability of the substation B line 2

7.3 Inspection in Substation C

The following result were collected from ZnO surge arresters, polymeric encapsulated, installed at major substation C, located at line 2.

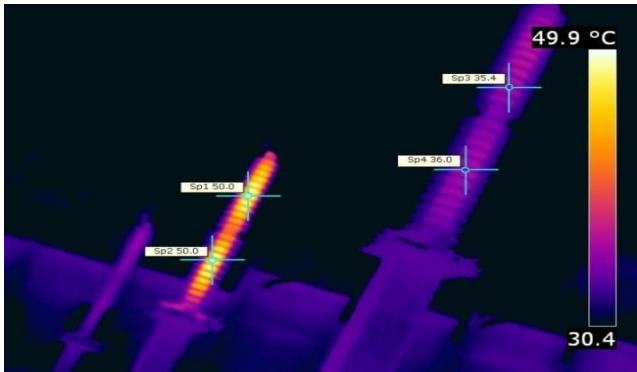


Figure 11: Thermo-grams for substation C was showing the high amount of heating inside arrester

8. FAILURE CRITERIA OF ARRESTER

Since the outcomes of this study are dependent upon the standards used to assess satisfactory surge arrester behavior, the surge arresters were considered “failed” if their measured behavior did not matched the following standards.

- Satisfying the performance levels guaranteed in manufacturers data.
- Meet the required performance measures outlined in the pertinent industry standards.

9. LEAKAGE CURRENT TEST RESULTS

The following results from the tables below represent the offline leakage currents that were measured. The information includes the type and brand, the serial number and location (Red, White and Blue phases).

The rated voltage of arrester is 98kV. The arrows indicate the measurements value of leakage currents in millampere.

Table 1: Resistive currents in milliamper for manufacture A

	Location	Serial Num	Rated kV	Test Modes	Test kV	mA
1	R-Ph	01C2018	98	GND RB	10	0.131
2	W-Ph	97F2822	98	GND RB	10	0.137
3	B-Ph	01C2015	98	GND RB	10	0.131

Table 2: Resistive currents in milliamper for manufacture B

	Location	Serial Num	Rated kV	Test Modes	Test kV	mA
1	R-Ph	W53E550-02	98	GND RB	10	0.131
2	W-Ph	W53E550-03	98	GND RB	10	0.137
3	B-Ph	W53E550-01	98	GND RB	10	0.131

Table 3: Resistive currents in milliamper for manufacture C

	Location	Serial Num	Rated kV	Test Modes	Test kV	mA
1	R-Ph	W53E550-02	98	GND RB	10	0.149
2	W-Ph	W53E550-03	98	GND RB	10	0.146
3	B-Ph	W53E550-01	98	GND RB	10	0.149

10. CONCLUSION

The conclusion of this research was based on leakage current test and infrared scanning analysis of the family of surge arresters that are failing on the system. During the field trail evaluation in eThekweni Electricity substations, furthermore surge arresters that had been measured are proving to be in unsatisfactory condition. They were running abnormally hot inside the zinc oxide (ZnO) varistor. Moreover, surge arrester A were having a light spot in the midpoint of insulation, this demonstrates that the heat starts there because this type of brand on the middle of the surge the sealing collar between the last upper shed and first of lower shed (middle) was defected (figure 2).

Therefore, this gives rise to moisture ingress and this was causing the heating inside varistor blocks to increase. On this issue, the design must improve the joint sealing integrity by construct with a continuous rubber from top to bottom so as to increase life span of arrester. The total leakage current measurement was also performed in arresters in accordance with the recommendation from IEC standard [22] to gain additional information concerning condition of arresters. The increase in the resistive leakage current on the surface insulation does not necessary mean that the arrester will fail. Hence, the evidence we acquired will help us to improve the surge arrester specification so as to avoid failure in the future and will also benefit us with replacing them before they fail on the system.

11. REFERENCE

[1] K.J Lim “The Performance of Tracking Aging and Surface in Polymer Insulator” *International Conference on Electrical Engineering*, pp. 1-4, 2002.

[2] L.S. Nasrat and A. Nosseric, “Evaluation of Polymeric Insulating Materials under Polluted Conditions”, *GIGRE*, 15-402.2002.

- [3] C.A Christodoulou, M.V Avgerinos, L. Ekonomou, I. F Gonos and I.A Stathopoulos “Measurement of the resistive leakage current is surge arresters under artificial rain test and impulse voltage subjection” *IEEE*, Vol. 3, Iss. 3, pp. 256–262, 15th January 2009.
- [4] V. Hinrichsen, Technische Universität Darmstadt “Latest Designs and Service Experience with Station-Class Polymer Housed Surge Arresters” *INMR WORLD CONFERENCE*, pp. 85-96, 19 November 2003.
- [5] M Amin, M Akbar and S Amin “hydrophobicity of silicone rubber used for outdoor insulation (an overview)” *International Conference*, Vol.1, pp. 10-26, 30 April 2007.
- [6] M. G Comber, M.G. Vermilye, S.F. LaCasse, R.M. Reedy “Lightning Protection of Transmission Lines with Polymer-Housed Surge Arresters” *EEI T&D Meeting Palm Beach*, pp. 2-11, 18 May 1994.
- [7] Krystian, Leonard Chrzan “Influence of moisture and partial discharges on the degradation of high-voltage surge arresters” *European Trans. On Electrical Power*, 14 pp. 175-184, 2004.
- [8] A. Haddad and D. Warne “Advance in high voltage engineering” *IET*, pp. 139-283, 2004.
- [9] Eberhard Lemke DE “Guide for Electrical Partial Discharge Measurements” in compliance to *IEC 60270*, No. 241, pp. 1-4, December 2008.
- [10] B. Richter, W. Schmidt, K. Kannus, K. Lahti ABB Switzerland LTD. Tampere University of Technology (Switzerland) , V. Hinrichsen, C. Neumann W. Petrusch, K. Stein Feld, Darmstadt University RWE NET AG FGH Mannheim Siemens “Long Term Performance of Polymer housed MO-surge arresters” *International Conference on Large High Voltage Electric Systems*, Vol.2, CIGRE, pp. 1-8 2004.
- [11] P. Cossoboon, M. Romanowski, Kristen Koether “High Voltage Magnetic Insulation Testing” *CARTS USA*, pp. 2-12, 28-31 March 2011.
- [12] ABB “Surge arrester selection and application guide” *12th International Conference on Electricity Distribution: Contributions (7 v.)*, pp. 2-14, 1993.
- [13] H. R. P. M. de Oliveira, M. L. B. Martinez, I. G. Campos Jr., R. G. de Oliveira Jr., C. de Salles and C. Lefort “New Techniques for Field Inspection of Medium Voltage Surge Arresters” *Power Tech, IEEE Lausanne*, pp. 1-5, August 2007.
- [14] B Ronald. Standler “Protection of Electronic Circuits from Overvoltages” *New York International Conference*, pp. 99- 139, 1989.
- [15] Gyung-Suk, Ju-Seop Han, Jae-Yong Song, and Hwang-Dong Seo “Measurement method of the resistive leakage current for lightning arrester diagnostic”. 18 April 2005
- [16] H.G Cho, U.Y. Lee, S.W. Han, J.U. Cheon, K.J. Lim “The Performance of Tracking Aging and Surface in Polymer Insulator” *International Conference on Electrical Engineering*, pp.1-4, 2002.
- [17] V. Hinrichsen - Siemens AG, “Metal Oxide surge Arrester”, *Fundamentals 1st Edition*, 2001.
- [18] I.A.D. Giriantari and T.R Blackburn “Surface discharge characteristic of silicone rubber surge arrester housings with high humidity and pollution”, *Australasian Universities Power Engineering Conference (AUPEC) Brisbane-Australia*, pp.1-6, September 2000.
- [19] M Amin, S Amin and M Ali “Monitoring of leakage current for composite insulators and electrical devices” 03 December 2007.
- [20] V. Larsen and K. Lien “In-service testing and diagnosis of gapless metal oxide surge arresters” *International Symposium on Lightning Protection*, pp.1-6, 26th - 30th November 2007.
- [21] M Amin, A Mohammad and S Amin “hydrophobicity of silicone rubber used for outdoor insulation (an overview)” 30 April 2007.
- [22] *IEC international standard 60099-5*” surge arresters- Part 5: Selection and application recommendations”, Edition 1.1, March 2000.

MOBILE MULTI-VOLTAGE ARTIFICIAL POLLUTION TESTING CHAMBER FOR HIGH VOLTAGE INSULATORS

J. A. Almeida *, N. D. Smit * and K. J. Nixon *

* School of Electrical & Information Engineering, University of the Witwatersrand, Private Bag 3, 2050, Johannesburg, South Africa.

Abstract: An artificial pollution testing chamber is presented in this paper which is designed in accordance to IEC and IEEE standards. The design of the chamber boasts a 23.12 m³ volume and is mounted on nylon wheels for mobility. To deliver the high voltage into the chamber a through-wall bushing is designed, which can withstand very heavy pollution at 49.5 mm/kV, at 132 kV_{L-L}. A contamination control system provides manual control of 12 micro mist nozzles, responsible for generating salt- and clean-fog within the chamber. A data acquisition system allows for the monitoring of climatic data, while logging the leakage current across the test insulator over a 0-25 mA range with 65 µA resolution. Leakage current results across glass discs and polymer insulators under clean- and salt-fog tests are provided and analysed.

Key words: Artificial Pollution Testing, Salt Fog Test, Clean Fog Test, High Voltage Clearances, Leakage Current, Shunt Resistor, Data Acquisition System.

1. INTRODUCTION

Modern power systems transmit electrical energy at high voltages within complex mesh systems, often over long distances through a variety of environments, requiring special considerations with regard to insulators used [1]. The main practical challenge of maintaining an ideal insulator in any transmission network is that all insulators have an external surface which will become contaminated with pollution at some stage of the insulator's service life [2]. This pollution layer has the potential to carry leakage current, giving rise to heating, electrical discharges and erosion of the insulation material [1, 2].

IEC 60507, IEC 61245 and IEEE Standard 4 describe standard electrical test methods for insulators, such as salt-fog, clean-fog and heavy rain tests [3-5]. A mobile high voltage artificial pollution chamber is presented in this paper, to follow these standard testing procedures. A focus on the physical dimensions of the chamber is presented, along with the design of the through-wall high voltage bushing to deliver AC and DC voltages up to 132 kV_{L-L}. High voltage clearances are specified in the testing standards [3-5]. A contamination control system is developed, which is responsible for generating and controlling the salt- and clean-fog procedures. A data acquisition system based on the Arduino Mega 2560 development board is used to measure and log leakage current, temperature and humidity over extended periods of time [6]. These leakage current measurements on various insulators are achieved through the use of a basic shunt resistor setup.

These subsystems are evaluated, along with leakage current results from preliminary testing on multiple insulators, to determine the viability of this chamber for mobile, multi-voltage testing purposes. A key design aspect is that this is a research chamber and does not necessarily follow the typical standard testing procedures.

2. BACKGROUND

2.1. Relevant Standards

Two standards provide the focus for the procedures outlined in artificial pollution tests; namely IEC 60507 [3] and IEC 61245 [4] for the AC and DC conditions respectively. Further information on these artificial pollution tests can be found within SANS 62217 [7] and IEEE Standard 4 [5], with general high voltage test techniques outlined in SANS 60060-1 [8]. For further classification of pollution conditions and the selection of insulators according to their polluted environment, SANS 60815-1/2/3 provide the required information [9-11].

2.2. Comparison between Indoor and Outdoor Pollution Testing

Extensive tests are required to evaluate different insulator designs and their behaviour under contaminated conditions to accurately predict their performance and lifespan in service [1, 12]. Indoor and outdoor tests are utilised, each with their own advantages and disadvantages. For outdoor tests, whilst the climatic variables are uncontrolled, over extended periods of time exposure levels will be similar to that experienced by insulators in similar environments. However, it is often difficult to relate exposure levels from one site to another, making it difficult to compare the performance of different insulators. Indoor or artificial pollution tests have been developed to normalise insulator exposure conditions, which reproduce these conditions occurring during service operation. These tests are designed to be representative, repeatable, reproducible and cost effective.

2.3. Parameters for Insulator Performance

Experience has shown that temperature, moisture and pollution levels are the most significant environmental conditions affecting the performance of an insulator,

along with the surface properties of the insulator i.e. hydrophobic or hydrophilic [1, 12]. The development of leakage current and dry-band arcing is found to be a slow time-dependent process, where polymer insulators are found to be far more effective at suppressing and preventing the formation of dry-band arcing than conventional porcelain and glass insulators [1, 12]. Dry-band formation and subsequent dry-band arcing is dependent on the evaporation rate of the conductive pollution layer. This is monitored by recording leakage current pulses and waveforms over time. The non-linear characteristics of the leakage current and dry-band arcing current results in significant 3rd and 5th harmonic components, which can be used along with the magnitude of the leakage current to determine the probability of flashover and hence the performance of the insulator [1].

3. CHAMBER DESIGN

3.1. Physical Dimensions

The structural frame of the chamber is a 2.5m×3m×3m cube, with a 0.33 m high pitched roof at 15°. This results in an overall volume of 23.12 m³. Figure 1 provides a basic model of the actual chamber, with the appropriate dimensions. Two sides of the chamber have clear, strong plastic for viewing purposes and a thick wooden plank supports the weight of the bushing. Steel gratings are laid on the floor to carry the weight of any person suspending or replacing the test insulator, while allowing the water to drain via the tiled floor underneath. A plastic door has been made available on the opposite side of the bushing.

A pitched roof allows for any build up of droplets, from the high humidity in the chamber, to roll off to the sides away from the test insulator. This ensures better results as dripping on the insulator affects its degree of wetting. The bushing is fitted 1.45 m above the steel base, with the interior high voltage end sitting 1.6 m into the chamber. If unsupported, the end sags to 1.35 m clearance from the steel gratings and clears a 1.25 m distance from any wall or ground point around it. For 76.21 kV, this satisfies the 1 m per 100 kV requirement [3].

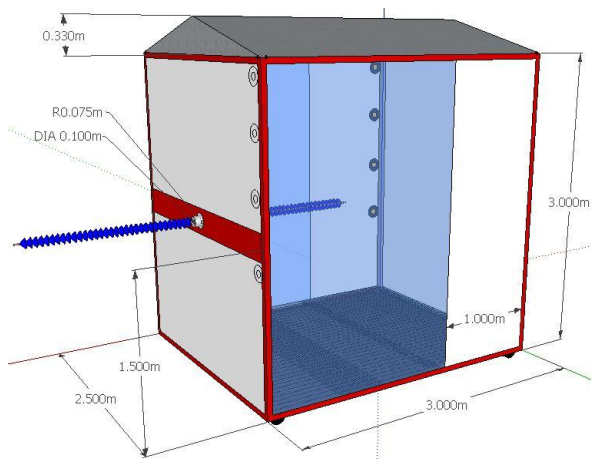


Figure 1: Chamber design model with dimensions.

Protection is provided through visible earth points by the wheels of the chamber, ensuring the structure is properly grounded. Warning labels on the walls of the chamber and warning lights on the control box also provide visible protection.

To provide a better view into the performance of the chamber under energised conditions, a 2-dimensional finite element analysis was performed. Figure 2 provides a wide view of the chamber and bushing and the relevant field lines at 76.21 kV. The largest field experienced is 8.2 kV/cm.

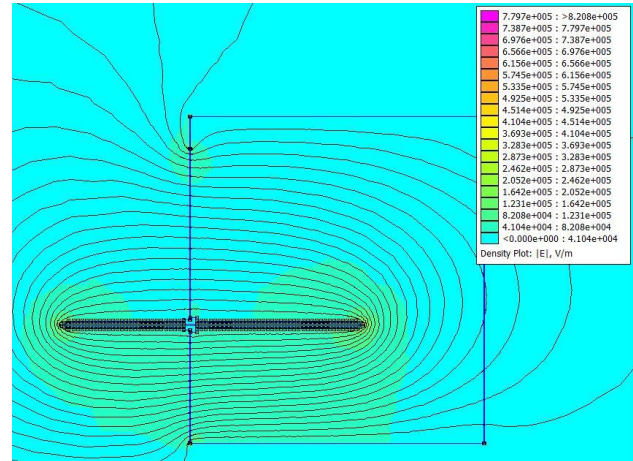


Figure 2: Equipotential plot for the wide view of the chamber at 76.21 kV.

3.2. Bushing Design

For the construction of the bushing, a hollow 15mm copper pipe is used for the high voltage delivery through the wall. To keep it mechanically strong, a mild steel rod is fitted inside the pipe (provides support). Fitting the bushing to the wall and providing separation from the high voltage involves a machined plastic mounting. This allows for hydrophobic weather sheds to be fitted over the copper pipe and sealed with silicone. IEC 60507 states a clearance of 1 m per every 100 kV and with the phase-to-ground voltage for 132 kV_{L-L} being 76.21 kV, a minimum length for the external side of the bushing is 1m [3]. For safety factors, and also taking into account DC conditions, a 1.2 m minimum length is sufficient. The interior side of the bushing requires a rating for very heavy pollution conditions (at 76.21 kV) and this provides a creepage distance of 50 mm/kV minimum.

For the final dimensions, 31 sheds are used on the exterior side of the bushing to cover 1.2 m, and 40 sheds provide a creepage distance of 49.5 mm/kV on the interior side. To reduce excess corona on the end connections of the bushing, round aluminium pieces were machined and fitted [13]. They boast a threaded hole to easily screw in a 6 mm connection. Figure 3 provides the dimensions.

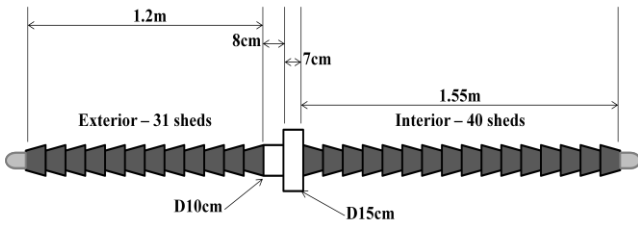


Figure 3: Through-wall 132 kV_{L-L} bushing diagram with relevant dimensions.

3.3. Contamination Control System

This system is responsible for the generation of the clean and salt-fog within the chamber and was designed as per the standards [3-5]. The system utilises 12 micro mist spray nozzles with an average droplet size of 10 μm [14]. The physical dimensions of the chamber limited the placement of the nozzles, where the final layout selected consisted of two fixed vertical columns of 6 nozzles at 0.5 m intervals, on opposite sides of the chamber (1.95 m from the test insulator). The water or salt solution is pumped at a maximum flow rate of 400 ml/min at 7 bar for the entire spray system and is manually controlled via a bypass valve. A reservoir and drip tray are needed to separate clean spray solution from used solution as the untreated steel grating deposit significant amounts of rust into the used solution which has the potential to block the spray nozzles.

4. DATA ACQUISITION SYSTEM

4.1. Measurement Unit

The measurement circuitry is housed within an IP65 plastic enclosure directly above the test insulator and contains transducers used to measure temperature, humidity and leakage current. An LM35 linear temperature sensor having a 0.5 °C accuracy and Relative Humidity (RH) measurements are achieved with the HMZ-435CHS1 linear output humidity module, which has a ±5% RH accuracy over the range of 10-90% RH [15, 16]. The temperature and humidity transducers are mounted on the underside of the enclosure to accurately determine environmental conditions surrounding the test insulator while ensuring no direct contact with spray droplets.

Measurements of surface arcing on insulators for HVAC and HVDC testing have previously been achieved by low sensitivity monitoring of current within the 25-100 mA range; however, they do not show how changes in leakage current and dry band formation on insulators propagate over time [12]. This system is designed to measure leakage current until dry band arcing occurs, requiring leakage current measurements of between 0-20 mA. Leakage current measurements are obtained through the typical shunt resistor circuit shown in Figure 4, where 1-100 Ω shunt resistors were tested, giving the relation $V_{out} = R \times I_{in}$. A 100 Ω shunt resistor was installed in the final design giving the relation $V_{shunt} = 100 \times I_{in}$,

ensuring a significantly higher signal to interference ratio and sensitivity [17].

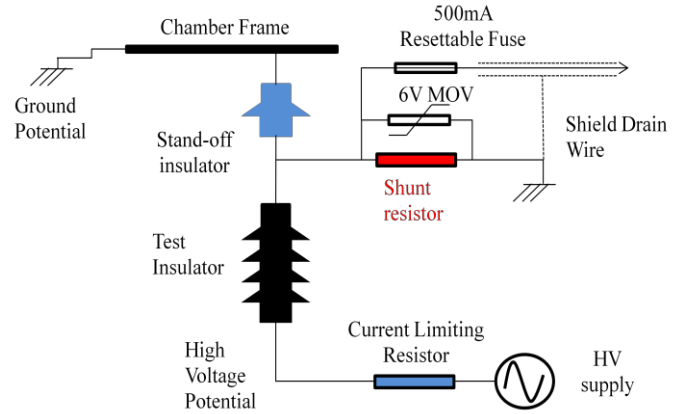


Figure 4: Leakage Current Measurement Circuit.

A cable comprising of six pairs of individually screened, twisted pair conductors is used for the transmission of voltages from the measurement unit to control box. This cable is selected due to its screening properties to provide shielding from electromagnetic interference and electrostatic interference from corona discharges, pump motor and radio-frequency transmitters [17]. The screen is connected directly to earth only at the measurement unit to ensure effective bonding to earth and to prevent loops for electromagnetic coupling [17].

4.2. Signal Conditioning

Signal conditioning circuitry, comprising of filters and ultra-low offset voltage operational amplifiers, eliminates the need for external nulling and providing high accuracy [18]. The output voltage from the shunt resistor is passed through an inverting amplifier with adjustable gain, achieved through a multi-turn potentiometer, to allow easy calibration. A final gain of 0.75 is selected for the 100 Ω shunt resistor. An inverting summing amplifier provides a 2.5 V_{DC} offset to the amplified voltage signal in order for the ADC module to record the negative half cycles of the waveform. From the Nyquist sampling theorem, a continuous signal can only be reconstructed if the frequency components of the signal are less than half the sampling rate. Since the highest harmonic of interest, is the 5th harmonic (250 Hz), an active second order 500 Hz low pass filter is introduced to the system to remove interference from higher frequencies [17].

4.3. Software Routines

The Arduino Mega 2560 development board (Mega) has a 10 bit Analogue to Digital Converter (ADC) which uses successive approximation to convert analogue voltage signals between 0-5 V into a digital representation within a minimum of 100 μs [6]. An Arduino Ethernet Shield [19] and DS1302 Real Time Clock (RTC) are attached to the Mega in order to facilitate logging of recorded data within a structured directory system according to the start time and date of any test within the

chamber (i.e. 19-10-12/M14-36.txt).

Software routines are developed to avoid clashes between conversions, calculations, data storage and communications through the use of accurate timing, provided by software interrupt routines and two buffers. Each buffer contains 256 ADC samples (512 bytes) and is chosen to allow continuous storage and serial transmission of data without large delays during analogue sampling and exhausting the memory limitations of the Mega [6].

Leakage current is sampled at 2 kHz by the Mega, which stores the first 256 samples within `buffer1` before storing the next 256 in `buffer2`. Once `buffer1` is full, samples are written to `buffer2` and the data contained within `buffer1` is written to a microSD card present on the Ethernet Shield and sent serially at a baud rate of 115200 as the integer value recorded (between 0 and 1023). This process then switches once `buffer2` is full of sampled data. Temperature and humidity inputs are sampled at approximately 8 Hz and converted to their corresponding temperature and relative humidity values based on the output characteristics of the transducers. Environmental conditions and the run time of the active tests are displayed on an LCD display mounted on the front of the control box, along with a basic user interface comprising of push buttons.

5. PRELIMINARY TESTING

The voltage across the 100 Ω shunt resistor is monitored and logged through an Arduino-based measurement control box. A 1 Ω shunt resistor does not provide a measurable leakage current in comparison to that of the 100 Ω. An oscilloscope and multimeter monitor the values and waveforms recorded across the resistor during the test. This is to ensure the logged data corresponds to the actual measurements.

Two glass disc insulators were cleaned and a salt fog test performed at rated voltage of 30 kV, with a solution of 50 g/l. Figures 5 and 6 provide the leakage current results and the FFT of these to view the significance of the third harmonic [20]. The same discs were then sprayed with a salt solution of 224 g/l, allowed to dry and a clean-fog procedure was performed. Figures 7 and 8 provide the necessary resultant waveforms.

A 33 kV polymer insulator was coated with kaolin and a salt fog test performed with a 50 g/l solution. No measurable leakage current was recorded in the preliminary stages of the test, but the waveform progressed to a sinusoidal shape with a peak voltage of 0.03 V. The relevant waveforms are provided in Figures 9 and 10, for the magnitude and FFT of the leakage current respectively.

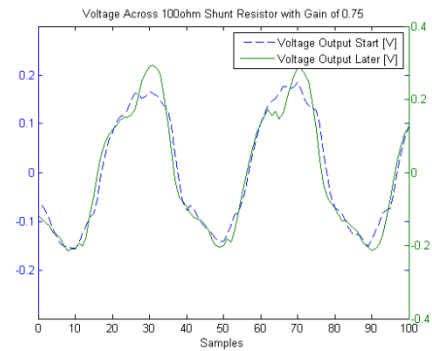


Figure 5: Leakage current across the 'clean' discs.

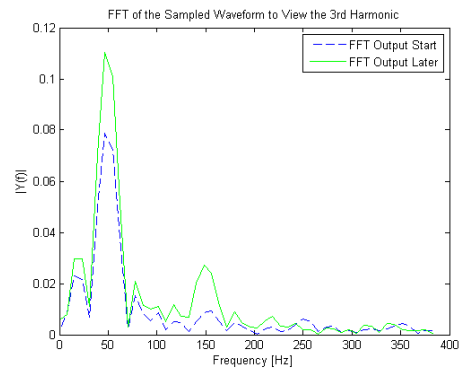


Figure 6: FFT of the leakage current results across the 'clean' discs.

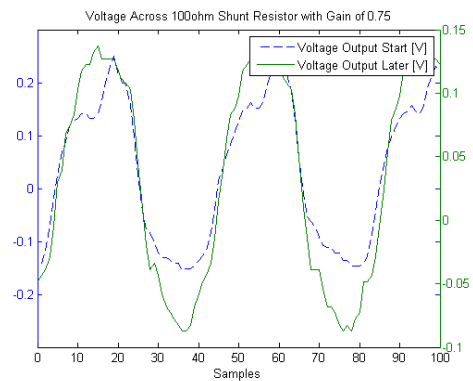


Figure 7: Leakage current across the 'dirty' discs.

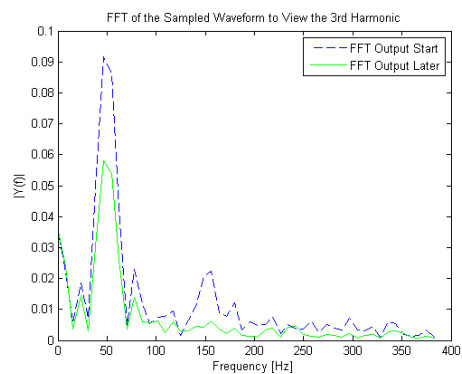


Figure 8: FFT of the leakage current results across the 'dirty' discs.

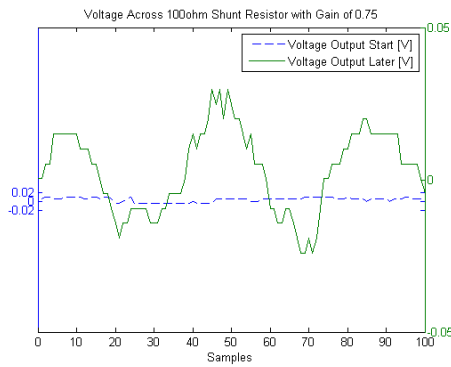


Figure 9: Leakage current across the polymer insulator.

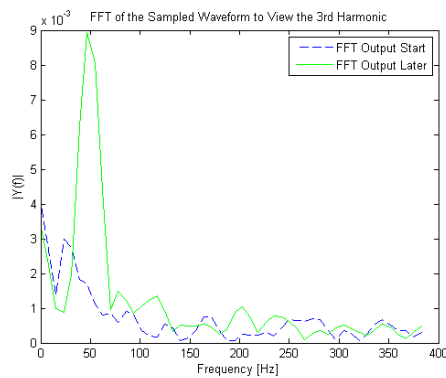


Figure 10: FFT of the leakage current results across the polymer insulator.

An interesting observation occurred on the oscilloscope when performing a very heavy pollution test on a 24 kV polymeric insulator. Large discharges were viewed in correlation to the peaks of the supply voltage which corresponds to corona discharges discussed by Bologna, et al [21].

6. OBSERVATIONS

6.1. Bushing Performance

A key observation relates to the performance of the bushing as the testing progresses and the chamber becomes more heavily polluted. This resulted in tracking at the plastic junction. In the first instance, this occurred at ~30 kV. The weather shed was then sealed to the junction and the bushing was cleaned. Further tests then resulted in the discharges occurring above ~40 kV. Unfortunately this is not acceptable for testing conditions as the bushing is rated up to 76.21 kV. A possible solution requires the elimination of the conductive layer on the plastic junction before each test commences. Once the elimination of this conductive layer is achieved, the electrical field stress on the interior copper conductor is reduced and tracking is eliminated or at least very much reduced [13].

6.2. Contamination Control System Performance

The contamination system ideally requires atomising

spray nozzles to deliver clean water or a salt solution at a rate of 500 ml/min/nozzle with an average droplet size between 5-10 μm [3-5]. The number of nozzles required is dependent on the length of the test insulator and they are placed on opposite sides of the chamber, a minimum of 3 m away at 0.6 m intervals [3-5]. The maximum flow rate of the contamination system was found to be 400 ml/min when the bypass valve was fully closed, resulting in a pressure of 7 bar. As discussed previously, the droplet size produced is 10 μm ; however the flow rate of the solution is significantly lower. Extra nozzles were installed to compensate, but these do not meet the minimum distance requirements. Overall, a relative uniform spray distribution is achieved within the chamber as required, with a slightly higher distribution on the lower sheds of the test insulator and chamber bushing. The relative humidity of the chamber is found to increase to 85% during a 20 minute test, with a steep increase during the first 7 minutes of a test, and a slow decrease in humidity when the sprays are inactive after a test. One of the predominant disadvantages of the system involves the use of a drip tray limiting the maximum test time to 40 minutes.

6.3. Data Acquisition System Performance

The limited leakage current measurement range (approximately 35 mA_{peak}) and low sampling speeds are the main disadvantages of the implemented data acquisition system. However, the increased accuracy allows the measurement of leakage current up to 65 μA . Additionally the system only records the leakage current waveform, but cumulative charge and pulse recording can provide more meaningful information during extended periods of testing [12, 22]. Measurement of environmental conditions within the chamber satisfies the standard requirements [8], where temperature and humidity measurements are within an expanded uncertainty of 1 $^{\circ}\text{C}$ and 1 g/m³ respectively. The gain of the signal conditioning circuitry was found to be highly stable, however the DC offset varied from test to test by a maximum of 3 mV.

6.4. Evaluation of Results

The first test involves the ‘clean’ discs, which initially displays a low leakage current that gradually increases as the test progresses. The FFT of these waveforms displays the significance of the third harmonic, which increases as the test progresses and this falls in line with findings discussed by Suda [20].

For the initially ‘dirty’ glass discs, a large leakage current and high 3rd harmonic contribution is noted. This is due to the heavy pollution on the discs. As the test progresses, the contribution from the 3rd harmonic and even the 1st harmonic reduces. This is because the clean fog gradually cleans the glass discs, reducing the pollution layer.

Low leakage current results are expected for the polymer insulator due to its hydrophobic surface. This prevents the pollution on the surface from forming continuous paths

for the leakage current to easily flow and consequentially result in dry-band arcing. The pre-conditioning should provide higher leakage current results as the pollution can accumulate on the new hydrophilic layer provided by the kaolin on the insulator surface [23]. A clear increase in the leakage current is noted as the test progresses, with the sinusoidal 50 Hz waveform clearly seen. Further, more intense pre-conditioning may be required. A limitation of the existing supply is the current rating, at 330 mA for over load conditions. The standards state that the minimum supply current required for a specific creepage distance of 25 mm/kV is at least 1.35 A [3]. These insulators can be subjected to much higher pollution conditions, which would require an even higher supply current.

7. CONCLUSION

The mobile artificial pollution research chamber is designed in accordance to IEC and IEEE standards, adhering to clearance specifications and following the salt- and clean-fog generating systems and testing procedures. Final dimensions for the chamber stand at 23.12 m³, with a minimum clearance of 1.25 m. The high voltage bushing is rated at very heavy pollution up to 49.5 mm/kV, at an overall length of 2.9 m. Both ceramic and polymer insulators could be tested in the chamber up to 132 kV_{L-L}. The bushing is currently limited to ~40 kV until further treatment or cleaning is applied to the junction. A contamination control system provides manual control of 12 micro mist nozzles responsible for controlling the salt- and clean-fog within the chamber. Additionally a data acquisition system allows monitoring of temperature and humidity within the chamber, along with the leakage current over the 0-25 mA range with a 65 µA resolution. Higher leakage current results were obtained across the glass disc insulators in comparison to that of the polymer insulators.

ACKNOWLEDGEMENT

The authors would like to thank Eskom for the support of the High Voltage Engineering Research Group through the TESP programme. They would also like to thank CBI-electric for support, the department of Trade and Industry (DTI) for THRIP funding as well as to the National Research Foundation (NRF) for direct funding.

REFERENCES

- [1] Farzaneh M, Chisholm W M. *Insulators for Icing and Polluted Environments*. John Wiley & Sons, Inc., Hoboken, New Jersey, 2009.
- [2] Looms J S T. *Insulators for High Voltages*. Peter Peregrinus, England, 1988.
- [3] IEC, *IEC 60507: Artificial Pollution Tests on High Voltage Insulators to be used in a.c. Systems, 2nd Ed, 1992*.
- [4] IEC, *IEC 61245: Artificial Pollution Tests on High Voltage Insulators to be used in d.c. Systems, 1st Ed, 1993*.
- [5] IEEE, *IEEE Standard Techniques for High-Voltage Testing (Revision of IEEE Std 4-1 978)*, 1995.
- [6] Arduino, <http://arduino.cc/en/Main/ArduinoBoardMega2560>, accessed on 24/10/2012.
- [7] SANS/IEC 62217:2006: *Polymeric insulators for indoor and outdoor use with a nominal voltage > 1000V, Edition 1*, 2006.
- [8] SANS/IEC 60060-1:2011: *High Voltage test techniques, Part 1, Edition 2*, 2011.
- [9] SANS/IEC 60815-1:2009: *Selection and dimensioning of high-voltage insulators intended for use in polluted conditions; Part 1: Definitions, information and general principles, Edition 1*, 2009.
- [10] SANS/IEC 60815-2:2009: *Selection and dimensioning of high-voltage insulators intended for use in polluted conditions; Part 2: Ceramic and glass insulators for a.c. systems, Edition 1*, 2009.
- [11] SANS/IEC 60815-3:2009: *Selection and dimensioning of high-voltage insulators intended for use in polluted conditions; Part 3: Polymer insulators for a.c. systems, Edition 1*, 2009.
- [12] Kawa D.F, Chavez M.J, *Practical PCA-DA System for measurements of leakage current pulses on polymer insulators under wet contaminated conditions*, IEEE magazine, 1992.
- [13] Kuffel E, Zaengl W S, Kuffel J. *High Voltage Engineering: Fundamentals*. Second Edition, Elsevier Ltd., 2008.
- [14] Nube F, Magic Mist Solutions, http://www.magicmist.co.za/Misting_systems_Information.html, accessed on 24/10/2012.
- [15] National Semiconductor, *LM35 Precision Centigrade Temperature Sensors*, America, November 2000.
- [16] Ghitrone, *HMZ-435CHS1 Humidity module specifications*.
- [17] Bentley, JP. *Principles of Measurement systems*, 4th Edition, Pearson Education Limited, 2005.
- [18] Analog Devices, *Ultralow Offset Voltage Operational Amplifiers: OP07*, U.S.A, 2002.
- [19] Arduino, <http://arduino.cc/en/Main/ArduinoEthernetShield>, accessed on 24/10/2012.
- [20] Suda T. *Frequency Characteristics of Leakage Current Waveforms of a String of Suspension Insulators*. IEEE Transactions on Power Delivery, Vol. 20, No. 1, January 2005.
- [21] Bologna F F, Reynders J P, Britten A C. *Corona Discharge Activity on a String of Glass Cap-and-Pin Insulators under Conditions of Light Wetting, Light Non-Uniform Contamination*. IEEE Bologna Power Tech Conference, Bologna, Italy, June 23-26, 2003.
- [22] Elombo A I. *An Evaluation of HTV-SR Insulators with Different Creepage Lengths under AC and Bipolar DC in Marine Polluted Service Conditions*. MSc. Thesis, University of Stellenbosch, 2012.
- [23] Gutman I, Dornfalk A. *Pollution Tests for Polymeric Insulators made of Hydrophobicity Transfer Materials*. IEEE Transactions on Dielectrics and Electrical Insulation, Vol. 17, No. 2, Pg. 384-393, April 2010.

PROPOSED OPTIMISATION OF HVDC LINES

R.G. Stephen* and C.T. Gaunt**

* Eskom Technology Division, 1 Maxwell Drive, Sunninghill, Sandton, South Africa
E-mail: rob.stephen@eskom.co.za

** Department of Electrical Engineering, University of Cape Town, South Africa
E-mail: ct.gaunt@uct.ac.za

Abstract: The cost of HVDC terminal equipment is reducing making the benefits of HVDC, especially point-to-point transmission, more attractive. This paper explores the characteristics of HVDC lines and proposes steps for the optimisation of the line with regard to the selection of tower and conductor types. HVDC lines differ from HVAC lines in that there are many more options available to the designer. Each pole, for example, need not be on the same tower or follow the same route. Impedance is not a function of bundle size or phase spacing and capacitance to ground can be neglected. In addition the voltage can vary per scheme and is not dependent on the surrounding network. The paper proposes determining the voltage of the line up front as this is a function of power and length. Once this is determined the line configuration and conductor and tower family can be optimised.

Keywords: HVDC, Line optimisation.

1. INTRODUCTION

HVDC lines are different from HVAC lines in that they have more tower configuration options possible. The poles need not be on the same structure and may follow different routes. There may also be a ground or metallic return.

Thus in optimising HVDC lines one needs to understand the key parameters of the line and what tower, pole spacing or height above ground and what bundle configuration needs to be in place to realise the optimum line design.

It is also necessary to understand the meaning of optimisation [9]. In this case it implies meeting the design and power flow constraints (such as resistance and corona) for the lowest cost. It also implies producing a design which allows the lowest Life Cycle cost (LCC) or a balance between LCC and the design and power flow constraints.

2. CHARACTERISTICS OF HVDC LINES

HVDC lines are normally point-to-point connections and as such can have a voltage and power flow tailor made to the requirements of the grid. In addition, that the conductor poles need not be on the same structure imposes fewer constraints for optimisation.

2.1 Load Flow Characteristics

The load flow on DC lines is determined merely based on the $V=IR$; Ohm's law. The maximum power flow is a function of the permissible volt drop and the line length [1]. Thus, with a higher sending end voltage, lower resistance and shorter distance the power flow can be increased. As there are limited means to adjust the

distance the designer has the option of sending end voltage, allowable voltage drop, and resistance.

2.2 Calculation of DC resistance

The DC resistance of a conductor is determined by calculating the resistance of each stranding layer and adding the combined resistance of each layer as per the parallel resistance equation [2]. The resistance of each layer is a function of the resistivity of the material, the lay ratio and the diameter of the strand wire. The ferrous and non-ferrous components of the conductor can be calculated separately and added as per two parallel resistors [2].

2.3 Different conductor types

The conductor type and selection for HVDC is similar in process and options to HVAC lines [7]. However, due to the normally higher load factor of HVDC lines which do not depend on network impedance to determine load flow down the line, it may be prudent to use conductors with higher aluminium to diameter ratio. These conductors will have trapezoidal or z shaped strands to ensure there are minimal air gaps between the strands and layers. This allows for lower resistance than round stranded conductors for the same diameter. It is therefore possible to increase the power flow for the same wind loading on the towers.

High temperature conductors [8], (conductors that sag far less than conventional conductors and operate up to 250°C) may be an option if the peak power flow requirement is uncertain and the link may be required to transmit higher power levels for short periods of time. This may be the case for connection to wind generators.

2.4 Corona inception gradient

The inception gradient of corona in DC (negative corona has a lower inception voltage than positive) is a function of the conductor roughness, the radius and the air density [3,4]. The smaller the conductor diameter, the rougher the conductor, the lower the air density, the lower will be the inception voltage. This means that the conductor will have corona present at a relatively low voltage. The maximum voltage stress present on the conductor is dependent on the bundle diameter, height above ground of the conductor bundle, the diameter of the conductors in the bundle and the spacing between the poles. It is important to ensure the maximum voltage present is below the inception gradient.

Therefore, as with AC parameters, the gradient is dependent on the size of the bundle and the pole spacing as well as height above the ground. The larger the conductor diameter and the more subconductors in the bundle the more resistant the bundle is to corona. The voltage to ground can therefore be increased and the power capability improved.

The corona power loss is a function of the extent to which the line exhibits corona at a certain voltage. This parameter should be as low as possible to avoid increased losses in the HVDC transmission.

2.5 Mechanical considerations

These are similar in DC and AC lines. However, a choice of monopole HVDC lines may force the conductor bundle to reside on one side of the tower inducing forces around the base and resulting in a higher cost than a bipolar line.

Wind loading and conductor selection based on the percentage steel in the conductor and diameter are important considerations for mechanical optimisation.

2.5 Thermal considerations

The thermal rating of the conductor is a function of conductor temperature relating to sag and height of the conductor above the ground.

In the case of DC current there is no magnetic heating as found in AC steel-cored conductors [10,11]. This means the resistance does not increase with current in the case of DC which is an advantage.

With HVDC transmission the load factor is likely to be higher than with HVAC lines and as such the cost of losses is a major consideration. Thus in long point-to-point lines the conductors with larger aluminium areas resulting in lower overall losses are likely to provide for optimal design. In the case of peaky loads such as in the case of wind generators, high temperature conductors may be used. These will result in a high transfer

capability without incurring large I^2R losses. This assumes the voltage drop will not be excessive under maximum power flow.

2.6 Conclusion on parameters

The table below summarises the options relating to conductor and bundle selection for HVDC lines. Where:

- “Bad” implies that the option chosen will require that parameter to be studied in depth and mitigation action taken.
- “Good” means that the parameter will be favourably influenced by action (e.g. the voltage drop will be lower with large Al area conductors).
- “Neutral” means that the parameter chosen will not be affected by the choice of action.

Action	Parameter	Voltage drop	Corona	Mechanical loading	Thermal rating
+ and - pole spacing decrease		Neutral	Bad	Good	Neutral
Large Al area/cond (less conductors)		Good	Bad	Good	Bad
Diameter bundle increase		Neutral	Bad	Bad	Neutral
High steel content		Neutral	Neutral	Bad	Good

Table 1 Relationship between actions taken in line design and effect on voltage drop, corona, mechanical loading and thermal rating

It is apparent that for low corona and corona loss, the requirement is for a high number of sub conductors in the bundle. This needs to be coupled with low overall bundle diameters and high pole spacing.

3. OPTIMISATION PROCESS

For HVDC lines the optimal voltage selection for a given power flow and distance is possible. This combination of parameters has been investigated [5] using a very comprehensive analysis of costs of a range of line configurations, voltages, and terminal stations. Fig. 1 allows a designer to rapidly determine the voltage level for a particular load and line length.

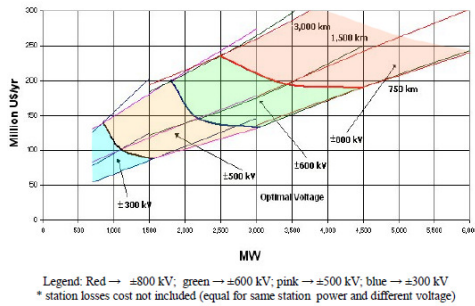


Figure 1: Optimal voltage as a function of converter station power and line length [5]. The yearly cost (y axis) is the line investment and losses as well as station cost.

In Fig. 1, three sets of line length are indicated namely 750 km, 1500 km and 3000 km and sets of curves of the costs for the alternative voltages are indicated. From this the boundaries of changing optimal voltage is identified. For example, for 1500 km with power transfer below 3500 MW the voltage ± 600 kV is the most economic whereas above this level ± 800 kV is preferred. [5].

This work provides a good indication of the required system voltage and can be used as the first step in the optimisation process.

3.1 Steps for optimisation

Based on the above the following steps are proposed for optimisation of HVDC lines.

Decide On Optimal Voltage: From the curves of Nolasco [5], the voltage level can be decided. There is therefore no need to initially design lines for different voltage levels.

Decide On The Conductor/Bundle Configurations: The bundle configuration and pole spacing can determine the corona inception voltage. This can be optimised to reduce the overall line losses.

The following figure from [5] indicates the percentage of costs for different voltages for a given power transfer.

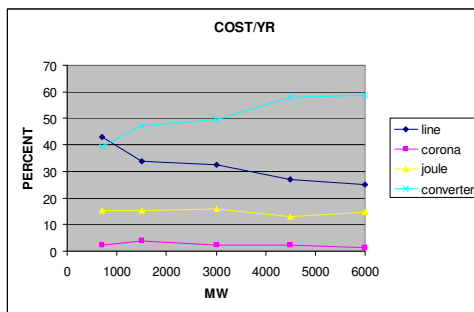


Figure 2: Cost parcels in % of total for each case (1500 km line) [5]

Of note in Figure. 2 is that the corona power losses are relatively low in cost. This is due to the line designs ensuring that the E_{max} (maximum voltage gradient present on the conductor) is below the E_c (voltage at which the conductor will exhibit corona) values so the conductors will not be running in corona. The converter losses are higher than the line costs and losses combined which indicate that the voltage selection needs to be carefully chosen. This is especially true where the case being considered is in the border of two voltage levels. It should be noted that for HVDC voltage levels, the discrete voltage levels are based on standard equipment presently in use at those levels. The actual operating level of the line can be varied below the highest rated level.

Optimise The Line Design: With the voltage known and the number of conductor bundle options determined, it is possible to determine the tower and conductor foundation combination that is optimal for the power transfer and line length considered.

The tower configurations are more varied in the case of HVDC than in HVAC. Monopole, bi-pole, and tri-pole are possible, as well as bi-pole with a metallic return. [12]

In addition to these options there are also the options of guyed vs. self-supporting, cross rope, mono-pole or H-pole, etc. The foundation and total line cost will depend on these options chosen.

From this design process, it is suggested to use an indicator (referred to in the next section. Note development of the indicator is beyond the scope of this paper but is described elsewhere [6]) which will objectively determine the best set of options from a group of design options.

Re-check the voltage line design converter combination: From the initial determination of the voltage and the converter design relating to the voltage choice, it is necessary to recheck the final design to determine whether the original assumptions are valid or not. If valid, the line design can be finalised based on detailed analysis of the final group, as indicated by the objective determination process [6].

4. HVDC INDICATOR FOR OBJECTIVE DETERMINATION OF LINE DESIGN.

Based on the analysis [6], the following can be used as an Appropriate Technology Indicator for HVDC. Note that an indicator for optimisation was introduced by the author for HVAC previously. The HVDC indicator is novel and has not been in use before.

$$ATI_{dc} = w_1 LCC + w_2 P_{losscorona} IC + w_3 \frac{MVA_{thermal}}{IC} \quad (1)$$

where

ATI_{dc}-Appropriate Technology Index for DC lines
 LCC-is the life cycle cost expressed in terms of a score from 1 to 10 and IC is the initial cost.
 $P_{losscorona}$ -is the power loss due to corona.
 IC-is the initial cost.
 $MVA_{thermal}$ is the thermal rating of the line and depends, on the templating temperature of the line.

The terms in the ATI_{dc} equation are normalised into a score out of 10 to ensure these terms can be added.

The weightings are determined by system operators, but the analysis should vary the weightings and take the option with the highest ranking across all variations of weightings. This will represent the most robust design.

5. CASE STUDY.

Singh [1] provides 3 examples for 500 kV lines with the parameters shown in Table 2.

In the process described the first step in the design process is to determine the optimum voltage to use. This is done using the figure 1 [5]. In using this 800 kV should have been chosen. Thus the examples in the 500 kV range, discussed below, are for example only and would suit a power transfer of 1500 MW for 3000 km.

CASE	LCC (Rbn)	LOSSES (Rbn)	CORONA LOSS kW//km	THERMAL (AMPS)
5 IEC 800	20.45	1.45	17.45	4650
5 BERSFORT	18.91	1.61	17.45	4375
4 IEC 800	17.86	1.76	19.95	3720

Table 2 Data For Three Cases At 500 kV

Where 5 IEC 800 means 5 conductors of type IEC 800 [6]

In deriving the above table, the following assumptions were made [1]

Aluminium costs as follows: R360/mm² (500kV), R380/mm² (600kV), R420/mm² (800kV)
 R20/MWh was used to calculate the cost of losses

The losses include the corona loss which was calculated as an average of the fair and foul weather conditions. The life cycle of the asset was assumed to be 25 years

From the above the following ratios and scores are calculated for Table 3. It is assumed for the scores that the 5 IEC 800 conductor case is the base case with a score of 3.

CASE	LCC	CORONA*IC	THERMAL
5 IEC 800	3	3	3
5 BERSFORT	4.03	4.3	3.52
4 IEC 800	4.73	3.78	2.94

Table 3 Scores For Ratios

In determining that the IEC 800 is the “normal or present” practice with a score of 3/10. One point on the curve is then determined. It is necessary to determine the other point in order for the line equation to be determined.

For LCC the score of 10 was assumed for a LCC of R10bn (negative slope as the lower the better). For the corona loss ratio a value of 100 (kW/ kmR) (negative slope) was taken as a score of 10 and for the thermal rating a value of 500 (Amps/Rand) was assumed to obtain a score of 10. Note that although the assumptions for the score of 10 are fairly random the overall comparison of the scores of the different options is still valid as the same scoring curves are applied to all cases.

Using the above scores, the weighting factors were varied, giving the results shown in Table 4.

CASE	0.8,0.1,0.1	0.4,0.4,0.2	0.2,0.4,0.4	0.1,0.1,0.8	0.1,0.8,0.1	0.4,0.2,0.4
5 IEC 800	3.00	3.00	2.99	2.99	3.00	3.00
5 BERS	4.01(2)	4.05(1)	3.94(1)	3.65(1)	4.21(1)	3.88 (1)
4 IEC 800	4.46(1)	4.00(2)	3.64(2)	3.21(2)	3.79	3.82(2)

Table 4 Varying Weighting Factors And Ranking (Brackets)

Table 4 indicates that the option 2 of 5 Bersfort conductors ranks as the best option for the wide range of weighting factors and it can be concluded that this is the best option. In this case the life cycle cost option gives the option 3 as the best option. Thus, if LCC is the main criteria for the utility this option may be chosen. However, the best result as a function of the initial cost is the option 2.

6. CONCLUSION.

In summary the process for optimisation of HVDC lines is as follows:

The optimisation process for a line design given a power transfer and line length requirement is proposed as follows:

- Determine the voltage level from the methods proposed by Nolasco [5].
- Determine the conductor/bundle configurations that will meet the corona level limits for the selected voltage level
- Determine the range of tower, conductor and foundation combinations using an objective indicator.
- Once the final group of line design options have been finalised, revisit the voltage, converter, line design options to check if the options chosen are indeed valid. If not the process needs to be restarted.
- Finalise the system design.

The process of optimisation of HVDC is similar to that of HVAC lines [6]. HVDC applies different parameters which can vary. HVDC voltage options are wider than HVAC. A wide variety of different tower types with single pole, bipole or bipole with metallic return or tri pole structures can be considered. Despite the wide variety of alternatives, an objective indicator has been developed [6] together with an optimisation process.

7. REFERENCES

- [1] A. Singh, A. Britten, R. Stephen, D. Muftic “Optimised conductor and conductor bundle solutions for long distance HVDC transmission”, *Inaugural IEEE PES 2005 conference and exposition in Africa Durban, South Africa, 11-15 July 2005*:
- [2] R.G. Stephen: “The thermal behaviour of overhead conductors sections 1 and 2”, *Cigré SC:22 Overhead lines.: Electra.. No: 144 pp. 107-125 1992.*
- [3] P.S. Maruvada: *Corona performance of high voltage transmission lines*, Baldoch, Hertfordshire, Research Studies Press Ltd. 2000.
- [4] EPRI: *HVDC transmission line reference book* EPRI TR-102764, Project 2472-03. September 2003
- [5] J. Nolasco: “Impacts of HVDC lines on the economics of HVDC projects” *Cigré TB 388 Joint working group B2/B4/C1.17*
- [6] .R.G. Stephen “Objective determination of overhead line design” *PhD thesis, University of Cape Town, 2011.*
- [7] D. Douglass, “Economic measures of bare overhead conductor characteristics” *IEEE Vol 3 No2 April 1988*
- [8] D. Douglass, “Conductors for the uprating of overhead lines” *Cigré Brochure 244 2004 SC B2 Overhead lines WG B2.12*
- [9] EPRI, “Transmission line design optimization – TLOP Manuals” *EPRI Research project 2151-1, January 1986*
- [10] D. Douglass, “Alternating Current (AC) resistance of helically stranded conductors” *Cigré Brochure 345 2008 SC B2 Overhead lines WG B2 12*
- [11] J.S. Barrett, O. Nigol, C.J. Fehervari, R.D. Findlay, “A new model of AC resistance in ACSR conductors”. *IEEE Trans on Power Delivery, vol 1, no 2, Apr 1986, pp198-208.*
- [12] EPRI, “HVDC Transmission line reference book” *EPRI TR-102764, Project 2472-03. September 2003*

SENSITIVITY ANALYSIS OF Z-SOURCE BREAKER

Y. Singh * and L. Chetty**

* School of Engineering, Howard Campus, University of KwaZulu Natal, Durban, 4000, South Africa
E-mail: yeshivsingh@yahoo.com

** HVDC Centre, School of Engineering, Westville Campus, University of KwaZulu Natal, Durban, 4000, South Africa
E-mail: chettyl2@ukzn.ac.za

Abstract: A new solid state DC breaker called the Z-Source breaker has shown promise for application in HVDC. The sensitivity of this breaker has not yet been investigated. This paper presents a sensitivity analysis performed on a 24V practically constructed Z-Source breaker. The operation of the Z-Source breaker is verified using comparisons to simulations. The sensitivity analysis focuses on time taken to dissipate fault energy and time taken for the breaker to commutate off. The curve generated for turn off time measured at different fault currents is likened to preset IDMT curves used by some protection relays for the purpose of protection coordination.

Keywords: Z-Source breaker, sensitivity analysis, IDMT curve

1 INTRODUCTION

With the increasing number of people becoming interested in decreasing their carbon footprint, the demand for renewable energy has gone up considerably. For some, sources of renewable energy are long distances away. To transfer energy efficiently over these long distances HVDC links are the most efficient mode. Using an HVDC network to connect many renewable sources to consumers would reduce costs and would come with benefits such as load sharing. The protection system of such a network is a very important component. One of the key components of an electrical protection system is the circuit breaker.

One of the main technologies which have to be properly developed for multi-terminal HVDC networks to be possible is HVDC circuit breakers. DC circuit breakers which can act at voltages in the 100kV to 500kV range during high short circuit currents do not exist as yet. There have been many proposed designs for high voltage DC circuit breakers from as early as the 1980's. These breaker designs had shortfalls in either the time of operation or the energy handling capability. The common schemes involving mechanical breakers and the principle of electrical resonance were always too slow for application to short circuit conditions due to the limitations of the opening time of mechanical breakers [1]. The reliability of mechanical breakers which use the principle of electrical resonance for energy dissipation is low since an arc is required to trigger the resonant circuit. Solid state breakers using semiconductor devices in place of mechanical breakers are more promising in terms of time of operation. One of the main considerations when using semiconductor switches is still the dissipation of the fault energy once the breaker has acted. Some circuitry (often complex) is needed to handle the dissipation [1].

A new type of solid state breaker called the Z-Source breaker [2] shows promise for use in HVDC. This breaker was originally developed to be used in the protection system for the electrical network on a ship. It features fast turn off, automatic commutation, efficient dissipation of fault energy and simple circuitry. The reaction of the Z-Source breaker to different fault conditions has not been tested as yet. The aim of this paper is to present results of testing a 24V Z-Source breaker under different fault conditions.

2 EXISTING DC BREAKER DESIGNS

The concept of DC breakers has been around since 1964. The earlier designs such as the parallel path breaker and the DC air breaker relied on an electrical arc created by opening a classical air breaker to commutate off [3]. The later introduced triggered fault current limiters solved the problem of fuse conduction losses by only introducing the fuse into the main conduction path during a fault condition. It did this by using explosives to destroy a section of conductor so that fault current flows through the fuse in parallel with the destroyed section [4]. With the introduction of semiconductor switches, hybrid switching was developed. This was a combination of semiconductor switches and classical AC breakers which attempted to create a current zero for the AC breaker to open on [3]. Superconducting Fault current limiters, a very recent technology, hold a section of conductor at a temperature which makes the conductor superconductive. During a fault, the temperature of the conductor would increase making it lose its superconducting nature and therefore experience an increase in resistance. The extra resistance limits the fault current [5]. Solid state breakers use semiconductors to provide dielectric isolation to a fault. The Z-Source breaker is the most recent solid state breaker technology (June 2012). It used a resonant circuit to create a current zero which would commutate a thyristor in the main current path off [2].

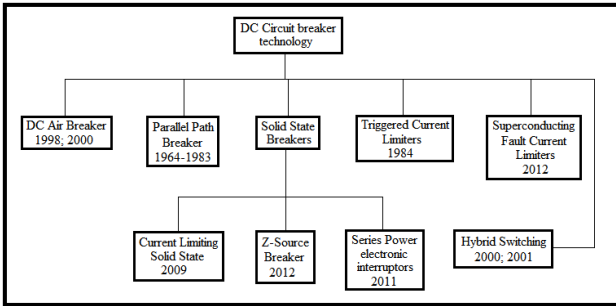


Figure 1: DC Breaker Technologies

3 THE 24V Z-SOURCE BREAKER

The test circuit consists of a 24V DC power supply connected to a resistive load via a Z-Source breaker (Figure 2). A fault would be applied across the load. Due to the availability of transformers for the DC power supply and SCR's for use in the breaker, a 24V system was decided upon with a variable fault level from approximately 1Ω to 20Ω . The available SCR had a holding current of 5mA. The normal load was therefore chosen as a 200Ω resistor in order to ensure an operating current of approximately 120mA, well above the holding current. The reverse recovery time of the SCR being used is $100\mu s$. The capacitor and inductor values therefore had to be specified so that once resonance occurs, the time taken for the thyristor to become forward biased would be longer than $100\mu s$ giving the SCR enough time to complete reverse recovery. 0.1Ω resistors were used in series with the breaker capacitors and inductors current measurement purposes (Figure 3). A 0.5Ω resistor in series with the SCR was used to measure the current through the SCR (Figure 3).

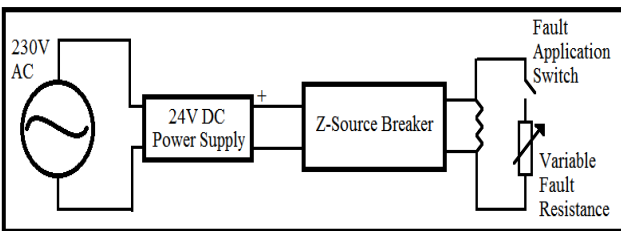


Figure 2: Experimental setup

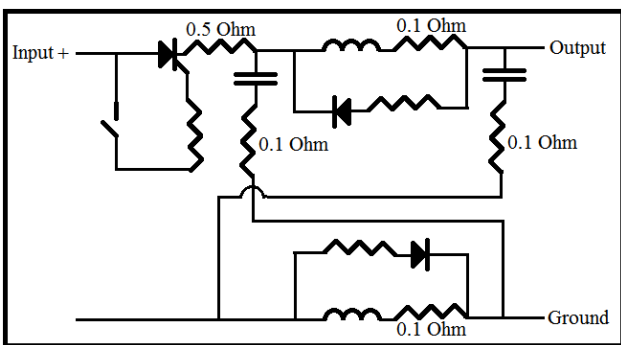


Figure 3: Z-Source breaker measurement resistors

Before building the 24V circuit, the breaker performance was simulated using the Electronics Workbench Multisim software. These simulations were used to check whether the practical breaker was functioning correctly. The value of the measured result is approximately the same as the simulated result for the transient inductor, capacitor and fault currents (Figures 4, 5, 6). The transient waveforms are also very similar. Notice the oscillations in the transient waveforms (Figures 4, 5, 6). These oscillations begin to appear as fault resistance increases. They occur as a result of the charging and discharging of the capacitor and inductor. For very low fault resistances there is higher current which takes a longer time to discharge. Before the end of one oscillation the energy will have been dissipated by resistance in the breaker making the waveform seem without oscillations. The amplitude of the oscillations in the measured result is lower because of parasitic resistances in the practical circuit. The small bump at the start of the measured transient waveforms is caused by a small flashover inside the fault application switch. The current spike caused by the flashover can be clearly seen in Figure 6.

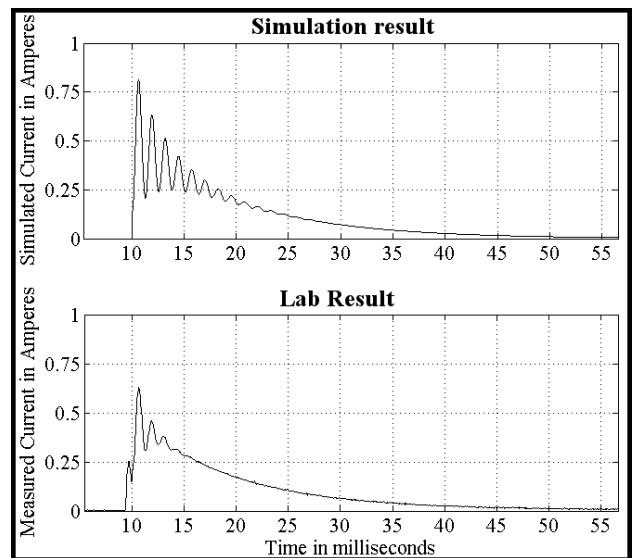


Figure 4: Transient Capacitor Currents

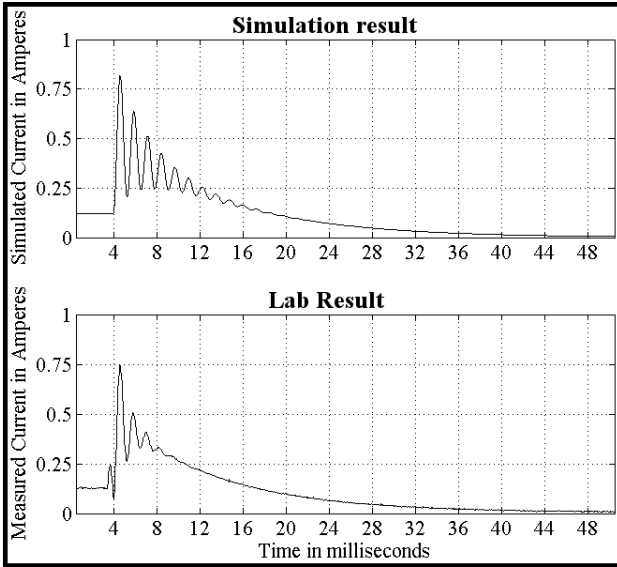


Figure 5: Transient Inductor currents

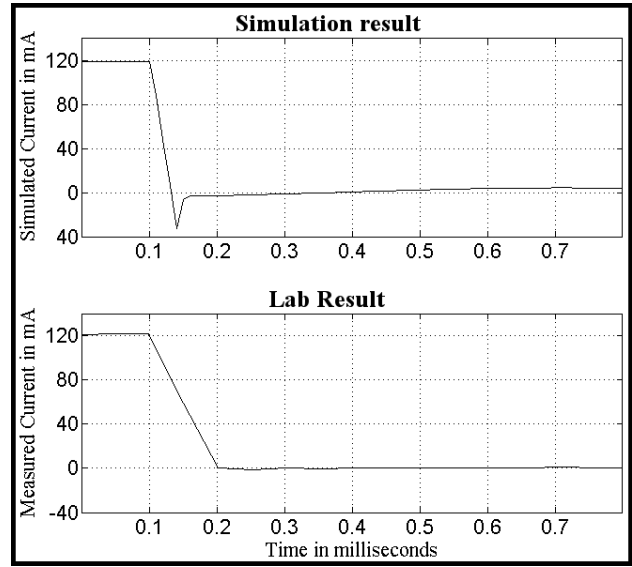


Figure 7: Transient SCR currents

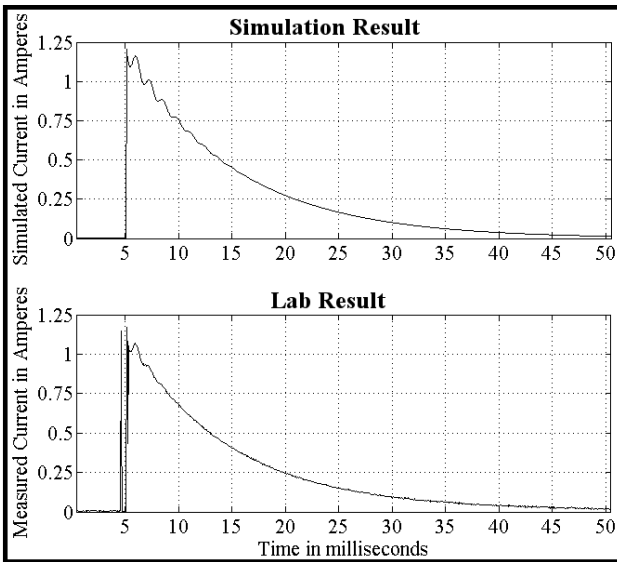


Figure 6: Transient Fault Currents

With reference to Figure 7, the SCR current waveform in simulation shows a dip below zero and then a rise above zero for a short time. This is caused by the reverse recovery of the SCR which initiates as soon as the SCR current reaches zero. This dip is not seen in the measured result due to the fact that the SCR used had a holding current of 5mA and possibly underwent reverse recovery before the SCR current reached zero.

4 SENSITIVITY ANALYSIS

The Z-source breaker was tested under different fault resistances from 0.2Ω to 19.7Ω . Each reading shown in the plots to follow is an average of the readings from five tests performed under the same conditions. The values measured for each test were the maximum fault current, the time taken to dissipate the fault current and the time taken from the application of the fault to the end of the reverse recovery of the thyristor. The plot of time to dissipation of fault current against fault resistance (Figure 8) could be approximated to a linear relationship. It shows that as fault resistance is increased, the time needed for fault energy dissipation increases. The one point on the plot which does not conform to the trend occurs at 0.2Ω fault resistance and is due to the inductor becoming saturated, therefore increasing the time needed for dissipation of the fault energy. The plot of peak fault current against fault resistance (Figure 9) revealed that fault current increases as fault resistance is decreased. The curve can be approximated to be a power curve. Since the plot in Figure 8 approximated to a straight line and the plot in Figure 9 approximated to a power curve, the plot of time taken to dissipate fault energy against fault current should be a power curve. The plot does approximate to a power curve as can be seen in Figure 10.

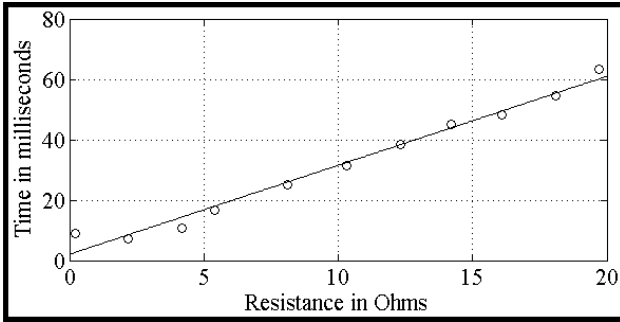


Figure 8: Dependence of fault dissipation time on fault resistance

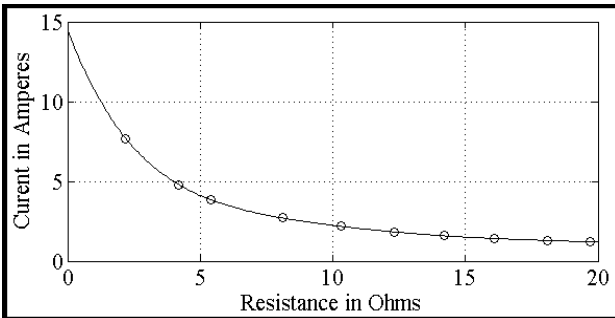


Figure 9: Dependence of peak fault current on fault resistance

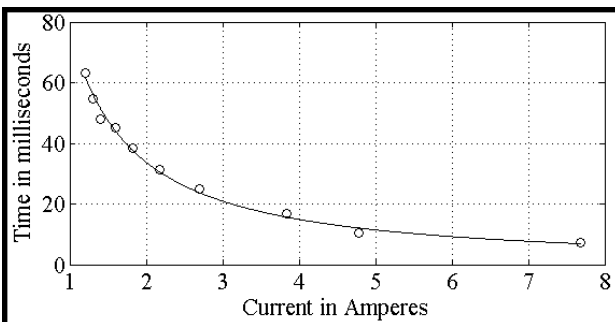


Figure 10: Plot of dissipation time against peak fault current

The plot of thyristor turn off against fault resistance (Figure 11) approximated to a 6th order polynomial when the point where the fault resistance was 0.2Ω was omitted. That point demonstrated a turn off time of more than 200μs which is much greater than all the other readings. The thyristor turn off time decreases with fault resistance until the fault resistance is dropped below 4Ω. From Figure 9 it can be seen that near 4Ω the peak fault current is between 4 and 5 Amperes. From simulations it was found that inductor current is almost half the value of the fault current. The inductors used in the building of the Z-Source breaker have a saturation current of 2A. The inductors were therefore heavily saturated during the application of faults below 4Ω in resistance. It is possible that this increased the time taken for the thyristor current to drop below the holding current of the thyristor, therefore increasing the time taken from the application

of the fault to the end of the reverse recovery of the thyristor. In the inverse definite minimum time (IDMT) curve (Figure 12), results from testing below 4Ω fault resistance were omitted. The curve plots thyristor turn off against peak fault current and shows that the breaker reacts faster as fault current increases. The curve approximates to a 4th order polynomial and has a knee point around 2A.

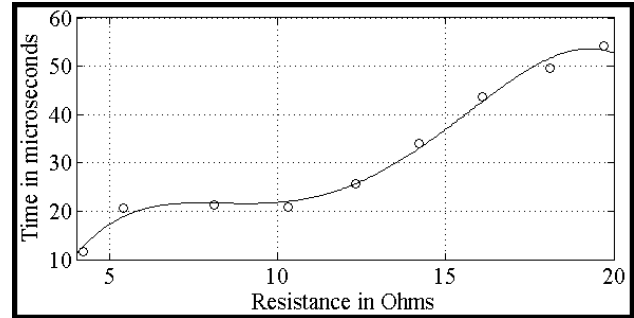


Figure 11: Dependence of breaker reaction time on fault resistance

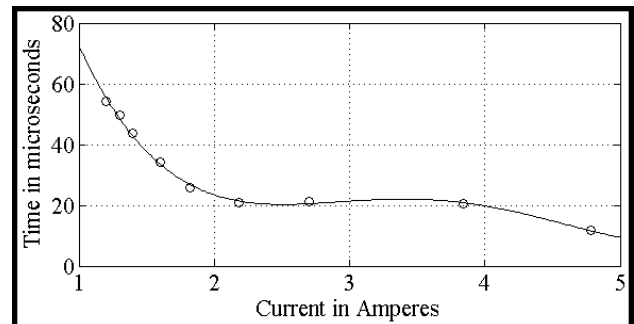


Figure 12: IDMT curve

5 CONCLUSION

A practical 24V Z-Source breaker was built and verified by comparison to simulations. The performance was as expected. A sensitivity analysis was performed on the Z-Source breaker by changing fault resistance (and hence fault current) for each test. The sensitivity analysis showed that the Z-Source breaker possesses a standard IDMT curve. This result is significant since most protection relays in AC systems use built in IDMT curves to work out when to open each of the breakers it controls (protection coordination). The Z-Source breaker already follows an IDMT curve and has automatic commutation therefore protection coordination in an HVDC network should not be a problem. The Dissipation time curve obtained from sensitivity analysis showed that breaker response becomes slower as the peak fault current magnitude decreases. This is significant because it shows

that the Z-Source breaker should be designed with the minimum possible harmful fault current in mind since the breaker will not commutate off if the peak fault current is too low. Further work which may be done includes investigating how the IDMT curve of the Z-Source breaker may be manipulated by varying the energy component values of the Z-Source breaker. This is important since different parts of a network may require different protection coordination times. Simulation of the Z-Source breaker applied to a multi terminal HVDC system also needs to be done. This will allow testing of the protection coordination ability of the Z-Source breaker and of how well it can work around faults as part of a protection scheme.

6. REFERENCES

- [1] Franck C. M: "HVDC Circuit breakers: A review identifying future research needs", *IEEE Transactions on Power Delivery*, pp. 1-8, April 2010
- [2] Corzine K. A. and Ashton R. W: "A new Z-source DC circuit breaker", *IEEE transactions on power electronics Vol. 27 No. 6*, pp. 2796-2803, June 2012
- [3] Atmadji Ali M. S: "Direct current hybrid breakers: A design and its realization", pp. 1-14, 2000
- [4] Meng L. W: "The use of triggered current limiters to reduce prospective fault currents in high voltage systems", *The Singapore Engineer*, pp. 28-30, October 2008
- [5] Manohar P. and Wajid A: "Superconducting fault current limiter to mitigate the effect of DC line fault in VSC-HVDC System", *IEEE*, 201

Topic D

Machines

A Review of Condition Monitoring Techniques and Typical Failure Modes with Regards to Large Rotating Electrical Machines

W. Doorsamy* and W. Cronje**

* School of Electrical and Information Engineering, University of the Witwatersrand, Johannesburg, South Africa E-mail: Wesley.Doorsamy@students.wits.ac.za

** School of Electrical and Information Engineering, University of the Witwatersrand, Johannesburg, South Africa E-mail: Willie.Cronje@wits.ac.za

Abstract: In the last few decades condition monitoring techniques have significantly advanced due to emphasis on preventive maintenance. This is particularly evident with larger machines within the area of electricity generation. An investigation into common failure mechanisms in rotating electrical machines, employed in industry, is presented. Additionally, a review of condition monitoring methodologies developed to address these issues is presented. The purpose of this document is to consolidate the past work and current practices in order to gain perspective of future requirements and trends in the condition monitoring domain.

Keywords: Condition monitoring, preventive maintenance, failure mechanisms, rotating electrical machines.

1. INTRODUCTION

Electrical rotating machines have become commonplace in modern living and feature in various facets, both domestically and industrially. Smaller machines are usually sufficiently robust to endure use within various devices and usually outlive most components of the parent device. It is therefore not necessary to monitor the health of these machines as failure thereof is minor and unlikely.

Machines utilised in core processes in power generation can feature capacities exceeding 1 GW, whilst machines utilised in support processes in other industries can exceed 100 MW. Furthermore, the advancement of machines has come about through an increase in demand for process optimisation and specialised requirements specific to the application. Due to the sensitive nature of these applications, invested interest and complexity, it is essential to have dedicated systems to monitor these machines. The area of condition monitoring has inherently followed this advancement with new and progressive techniques being made available.

This paper presents a review of condition monitoring techniques and technologies that are available. Additionally, the need for monitoring is also established through a deliberation of typical failure mechanisms experienced with machines in practice.

2. BACKGROUND

There are different types of methods that are used to prevent equipment failure/damage and unintended process shutdown. These methods correspond to different levels/margins of security. For example protection relays provide the interception of overcurrent faults and may

initiate a sequence which results in the machine being disconnected.

Although protection is essential in preventing catastrophic failure in many cases, it only provides action once the fault has reached an advanced stage. Condition monitoring differs as it is established to provide preventive maintenance and therefore exhibits proactive characteristics. This originates from the need to prevent unplanned shutdowns which requires methods that anticipate faults, failure and damage.

The anticipation of incipient faults and replacement of components prior to failure would eliminate the consequences of unexpected equipment failure. This capability has long been desired by industry with failure prediction tracing back over 50 years, yet it still remains relatively elusive [1]. Although literature on the topic of condition monitoring techniques continues to grow rapidly, it is not necessarily in the direction that is most beneficial to industry. This is due to many factors such as the specialised nature of the newly developed technology i.e. covers a limited fault scope, complexity of the condition monitoring tool i.e. requires specialised training to implement, and cost considerations.

The foremost motivations for developing predictive maintenance and increasing implementation of condition monitoring equipment in industry are:

- Progression of modern plants towards automation and hence lower level staffing and supervision.
- Economic consequences with unplanned shutdowns and undetected damage/deterioration of equipment.

- Increased availability of cost-effective, cheap and reliable condition monitoring equipment that is fast becoming a norm [2].

The advantages of condition monitoring depend however on factors such as the cost of the monitoring equipment relative to the machine or system which is being monitored, ability of the monitoring system to detect early faults as well as amount of warning time before failure or major damage is incurred.

The purpose of this review is to provide a basic description of the advancement of monitoring equipment with respect to rotating electrical machines. This advancement is not only related to the need for preventive maintenance, but also to growth in knowledge of root failure mechanisms. Diagnosis of root failure mechanisms is essential in preventive maintenance and is therefore examined. Similar literature reviews place emphasis on the available technologies, however a more fundamental approach is taken here through providing a basic overview of failure modes and associated technologies together with a contemporary index of relevant literature.

3. ELECTRICAL MACHINE FAILURE MODES

Most typical failures in machines result from a process of successive faults. These incipient faults tend to develop from abnormalities and may therefore be considered to be ‘symptoms’ of a root cause or as a result of multiple factors. The failure is therefore believed to be a result of progression of faults through a cascading effect.

For example, a synchronous generator can operate at high speed and the rotor windings experience high centrifugal forces. This can result in insulation degradation and may eventually lead to inter-turn short circuit faults. Furthermore, localised heating may lead to thermal bending in the rotor and thus rotor eccentricity. Eccentricity can lead to vibration and eventually bearing failure. This cascading effect is illustrated in Figure 1.

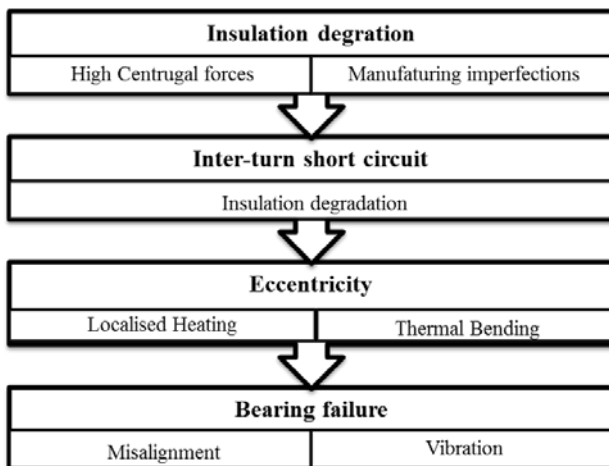


Figure 1: Example of progression of faults towards failure mode in a synchronous generator with root causes

Some of the major faults with electrical rotating machines, experienced in industry, which can lead to serious damage, can be broadly listed as follows [3, 4]:

- Stator winding faults
- Rotor winding faults
- Air gap faults (static and dynamic eccentricity)
- Broken rotor bars and cracked end-rings
- Slip ring or brush failure
- Core or lamination damage
- Circulating currents and earth faults
- Failure of peripheral equipment such as bearings, gearbox, cooling system, bushings and electrical connections

Mapping of the areas where these failure modes occur on a rotating electrical machine is illustrated in Figure 2 [3].

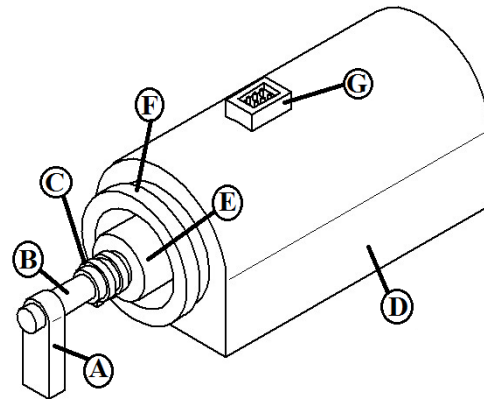


Figure 2: Generalised electrical rotating machine with mapping of failure mode areas (index given in Table 1)

Table 1: Index of various areas given in Figure 1 mapped to corresponding faults

Area	Failure Mode
A	Bearing Failure
B	Shaft Eccentricity
C	Slip ring or brush failure
D	Cooling system failure, circulating currents
E	Rotor winding damage, core damage
F	Stator winding, end winding damage, core damage
G	External electrical faults

Insulation faults are a major contributor to failure in rotating machines as stator and rotor windings are affected. In application, insulation is exposed to adverse environmental conditions, electrical stresses and mechanical stresses. The stresses cause degradation of insulation over time in different forms. Mechanically, abrasive effects occur while electrically partial discharge activity degrades the material. An example of environmental effects is thermal ageing due to operation under high temperatures. Insulation faults usually result

in inter-turn winding faults on the stator and rotor [5 - 7]. Rotor winding inter-turn faults is a common occurrence in generators and can cause vibration, increased shaft voltages, winding burn-out, loss of excitation and more [8]. Additionally, end-winding faults and stator winding coolant system faults can also occur.

Connection faults are more common in machines at higher voltages where there is increased dielectric stress on bushings and larger forces on conductors. Bushing failure may occur due to mechanical stresses such as vibration or electrical tracking enabled through debris deposited on exposed surfaces. Partial discharge activity is an indicator of this condition [3, 9 and 10].

A core fault is usually limited to large turbine-driven machines where large laminated cores bear excessive magnetic and electrical loads. Insulation failure and foreign bodies between core plates causes electrical connection that initiates circulating currents in core. The circulating current, coupling with the main flux, can lead to additional weakening of the plates through heating. Eventually, a number of issues arise such as buckling, melting, cavity formation and eventually an earth fault through stator conductor damage [11 - 13].

Induction motors are exceptional rugged, however larger machines are exposed to intense thermal stresses and starting duty. This results in high rotor temperatures and high centrifugal loading on end-rings. Defects also occur during the manufacturing process such as casting defects in die cast rotors and poor joints in brazed or welded end-rings. These factors are found to be the primary causes of broken rotor bars and cracked end-rings. Furthermore, current migration due to skin effect can also result in uneven heating of rotor bars (expansion) and cause separation from end rings [14 - 16].

Defects in brazed joints and slip rings can also cause severe damage in machines. Current imbalances in external resistors and circuits connecting to slip rings can result in overheating of rotor. Threading and grooving of rings also occur over time, while arcing can occur on rings due to loss of brush contact. This can result in brush gear failure and damage to the rotor and rotor windings as well as earth faults [3, 17 and 18].

An air-gap eccentricity fault can occur due to an unequal positioning of the rotor relative to the stator. Static and dynamic eccentricity occurs for a number of different reasons such as bearing wear, shaft deflection, thermal bending etc. Eccentricity can also result in critical damage through mechanical rubbing between stator and rotor, bearing failure, vibration and asymmetric magnetic fields [19 - 21].

Bearing failure is a common in application and occurs gradually but can result in devastating effects on the machine. The previously mentioned eccentricity is one of the causes for bearing failure, however there are many

normal operating conditions and other fault conditions that affect the life of a bearing. Normal operating stresses may occur from vibration, inherent eccentricity and bearing currents due to solid state drives. Other sources of failure include corrosion due to contaminants (abrasive particles), heating due to incorrect lubrication and indentation and brinelling due to improper misalignment or installation [23, 24].

Other faults can occur in larger machines with heat exchangers. The coolant may leak due to machine resonance or debris blockage causing pipe failure. This leads to discharge activity or insulation pyrolysis.

4. CONDITION MONITORING TECHNIQUES

A variety of methods are available for the purpose of addressing the issues described in the previous section. Selection of the appropriate technique is dependent on many factors such as the actual machine, application and economic feasibility.

4.1 Chemical monitoring

Insulation and lubrication oils are compound organic materials that can release a number of products upon degradation. As previously described, insulation degradation plays a vital role in different failure modes and therefore many early warning techniques are available to detect such products. Thermal degradation of insulation material may occur after it exceeds its maximum allowable operational temperature and give off certain vapours/gases of the chemicals used during manufacture. Such a thermochemical decomposition of organic material is termed pyrolysis.

Therefore, chemical techniques employ detection of matter or gases such as carbon monoxide and other hydrocarbons to determine early signs of insulation wear and excessive heating. Techniques utilising specialised instruments to collect decomposition products in generator coolants are available. An example of instrument is the ion chamber detector or 'core monitor' [25, 26].

As mentioned previously, bearing fatigue is a common failure mechanism and detection of this fault is therefore essential. An example of a method used to diagnose such a fault is detection of debris in oil produced during bearing wear [27].

4.2 Thermal monitoring

Temperature monitoring of a machine consists of techniques such as localised temperature monitoring using detectors and distributed temperature monitoring.

Localised monitoring uses thermocouples, resistance or embedded temperature detectors. These are usually embedded in the stator winding, stator core and even with

the bearings. A drawback of this is that metal type detectors require electrical isolation and therefore a secure distance from windings must be selected. However, heat flow equations can then be used to determine the actual winding temperatures. Bulk monitoring is a method which utilises internal and external coolant temperatures to determine thermal state of the machine. Advancements in this area have seen development of non-contact methods that utilise infrared-sensors or -cameras to measure rotor temperatures [28, 29].

4.3 Vibration monitoring

Vibration faults can originate broadly from two types of sources i.e. mechanical and electromagnetic sources. Typical root causes of this failure mode are bearing failure, mechanical failure, waveform distortion, structural resonance, winding damage and magnetic asymmetries.

Vibration monitoring is a widely used technique largely due to versatility and success achieved in practice. Although vibration analysis comprises of monitoring vibration levels according to specific standards and fault detection, vibration signal processing techniques can be used for fault diagnostics i.e. fault severity and origins.

Various instruments are available for vibration measurement e.g. non-conductive fibre optic accelerometers used on end-windings, and allows for signals/data to be collected. Through analysing frequency spectra of these signals it is possible to diagnose specific faults such as eccentricity, bearing damage and broken rotor bars [30, 31].

4.4. Electrical monitoring

Faults on a machine usually results in perturbations of electrical quantities of a machine such as the current voltage and power. Machine faults and disturbances in these electrical quantities also cause variations in the magnetic fields that may be detected. There are many techniques for detecting faults however these electrical techniques are similar in many ways. An overview of the more comprehensive methods is addressed here.

Stator faults are usually associated with insulation failure e.g. inter-turn faults, which are due to the causes described in Section 3. On-line partial discharge monitoring has been found to be a reliable method of diagnosing most high voltage stator winding insulation failure processes. Numerous methods are available for the early detection of partial discharge activity in this context. Some examples are earth-loop transient, capacitive coupling and RF coupling methods [8, 9, 32].

Another method which has also given reliable results in diagnosing winding stator winding, rotor bar and even end ring faults is transient analysis of the stator current.

The method allows for diagnosis through measurement and analysis of current imbalances. An extension of this method this method is also used with a power decomposition technique (PDT) to derive positive and negative sequence voltages and currents for use in a fault detection algorithm.

Due to the construction asymmetry of a rotating electrical machine, a net shaft or axial leakage flux is inevitable. Axial flux techniques utilise externally mounted search coils or Hall probes as sensors to detect leakage/stray flux. Pre-populated tables are used to identify variations in the flux harmonics with various faults such as inter-turn, broken rotor bar and eccentricity faults [33, 34].

A similar technique to the axial flux method uses shaft voltages to detect faults. Early measures to ground shaft currents which cause bearing damage, primarily used in large turbo-generators, has evolved into a method of diagnosing various faults on a machine through analysis of these induced signals. The technique utilises specialised brushes on either side of the rotor shaft to measure induced voltages along length of the machine [20, 35].

The use of artificial intelligence (AI) techniques has extended from control purposes into the area of condition monitoring. Techniques include expert systems, artificial neural networks (ANNs), fuzzy logic, fuzzy - neural networks (NNs) and genetic algorithms (GAs). These systems have been developed to automate the interpretative stage and indicate fault conditions precisely by tracing the relevant possibilities of root causes [36, 37].

5. FUTURE CONSIDERATIONS

The more comprehensive techniques tend to be implemented and used in industry. Due to the techniques covering specific areas of preventive maintenance e.g. certain chemical methods used only for diagnosing insulation wear, a combination of the various techniques are used to cover the entire machine. Additionally, many techniques, although effective, are quite complex in terms of implementation e.g. certain invasive monitoring techniques, and require specialised training of operators/technicians.

These factors contribute to the need for a simple, reliable, cost effective and comprehensive condition monitoring tool that can provide supervision over a wide area of fault mechanisms. In recent years there has been a growth in the development of electrical methods which utilise AI techniques. This is due to the ability of these systems to not only provide sensitive diagnostics, but to do so automatically as detecting minor inconsistencies and perturbations in a machine is imperative to incipient fault diagnosis.

6. CONCLUSION

A literature review of various condition monitoring techniques for electrical rotating machines was presented. The failure modes experienced in application and corresponding origins/root causes were also described. It is implausible to conceive a detailed account of all condition monitoring techniques, however an adequate overview of the more comprehensive techniques and associated failure modes has been presented.

Emphasis was placed on progression towards preventive maintenance and mitigation of root failure mechanisms. Complete automation of the condition monitoring process from measurement to interpretation, with the objective of accurate incipient fault diagnosis, is ultimately the future ambition.

15. REFERENCES

- [1] J.L. Kohler, J. Sottile and F.C. Trutt: "Condition-based maintenance of electrical machines", *IEEE Industry Applications Conference, Thirty-Fourth IAS Annual Meeting*, Vol. 1, pp. 205 - 211, 1999.
- [2] P.J Tavner: "Condition monitoring-the way ahead for large electrical machines", *IEEE Fourth International Conference on Electrical Machines and Drives*, pp. 159 - 162, September 1989.
- [3] P.J. Tavner, B.G. Gaydon and D.M. Ward: "Monitoring generators and large motors", *IEE Proceedings, Part B, Electric Power Applications*, Vol. 133, No. 3, pp. 169 - 180, May 1986.
- [4] L.K. Agrawal and S.B.L. Tripathi: "Study of fault detecting techniques in electrical Machines", *VSRD-IJEECE*, Vol. 1, No. 8, pp. 478 - 489, 2011.
- [5] X. Dang, N. Tai, J. Liu: "Stator winding's inter-turn fault intelligent diagnosis in large turbo-generator by Elman neural network", *IEEE International Conference on Advanced Power System Automation and Protection (APAP)*, Vol. 3, pp. 1672 - 1677, October 2011.
- [6] L. Yonggang, L. Jianwen, S. Wei: "On-line fault detection of inter-turn short circuits in turbo-generator rotor windings", *IEEE International Conference on Electrical Machines and Systems*, pp. 763 - 768, October 2008.
- [7] R. Fisser, D. Makuc, H. Lavric, D. Miljavec and M. Bugeza: "Modelling, analysis and detection of rotor field winding faults in synchronous generators", *IEEE XIX International Conference on Electrical Machines (ICEM)*, pp. 1 - 6, September 2010.
- [8] S. Wang, L. Heming, L. Yonggang, Y. Wang: "The diagnosis method of generator rotor winding inter-turn short circuit fault based on excitation current harmonics", *IEEE 5th International Conference on Power Electronics and Drives Systems*, Vol. 2, pp. 1669 - 1673, November 2003.
- [9] G.C. Stone, B.A. Lloyd, S.R. Campbell and H.G. Sedding: "Development of automatic, continuous partial discharge monitoring systems to detect motor and generator partial discharges", *IEEE International Conference on Electrical Machines and Drives*, pp. MA2/3.1 - MA2/3.3, May 1997.
- [10] W. Wei, L. Wufeng, C.R. Li, D. Lijian, Q. Su and C. Chang: "The estimation of insulation condition of generators by on-line monitoring of partial discharges using a new detector", *IEEE International Symposium on Electrical Insulation*, pp. 40 - 43, April 2002.
- [11] A.C. Smith, D. Bertenshaw, C.W. Ho, T. Chan and M. Sasic: "Detection of stator core faults in large turbo-generators", *IEEE International Conference on Electrical Machines and Drives*, Vol. 3, pp. 763 - 770, May 2009.
- [12] P.J. Tavner and A.F. Anderson: "Core faults in large generators", *IEE Proceedings - Electric Power Applications*, Vol. 152, No. 6, pp. 1427 - 1439, November 2005.
- [13] R. Romary, C. Demian, P. Schlupp and J. Roger: "Off-line and On-line Methods for Stator Core Fault Detection in Large Generators", *IEEE Transactions on Power Electronics*, Vol. PP, No. 99, pp. 1, 2011.
- [14] B. Mirafzal, and N.A.O. Demerdash: "On innovative methods of induction motor inter-turn and broken-bar fault diagnostics", *IEEE Transactions on Industry Applications*, Vol. 42, No. 2, pp. 405 - 414, March/April 2006.
- [15] Y. Wei, B. Shi, G. Cui and J. Yi: "Broken rotor bar detection in induction motors via wavelet ridge", *IEEE International Conference on Measuring Technology and Mechatronics Automation*, Vol. 2, pp. 625 - 628, April 2009.
- [16] R. Supangat, N. Ertugrul, W.L. Soong, D.A. Gray, C. Hansen and J. Grieger: "Detection of broken rotor bars in induction motor using starting-current analysis and effects of loading", *IEE Proceedings - Electric Power Applications*, Vol. 153, No. 6, pp. 848 - 855, November 2006.
- [17] R.D. Hall and R.P. Roberge: "Carbon brush performance on slip rings", *IEEE Paper and Pulp Industry Technical Conference*, pp. 1 - 6, June 2010.
- [18] Y. Michiguchi, S. Tanisaka and S. Izumi: "Development of a collector ring monitor for

- sparkling detection on generators”, *IEEE Transactions on Power Apparatus and Systems*, Vol. PAS-102, No. 4, pp. 928 - 933, April 1983.
- [19] D.R. Rankin and I. Wilson: “The use of shaft voltage to detect air gap eccentricity and shorted turns in salient pole alternators”, *IEEE 7th International conference on Electrical machines and Drives*, pp. 194 - 197, September 1995.
- [20] C. Bruzzese, G. Joksimovic and E. Santini: “Static eccentricity detection in synchronous generators by field current and stator voltage signature analysis - part I: theory”, *IEEE XIX International Conference on Electrical Machines (ICEM)*, pp. 1 - 6, September 2010.
- [21] J. Faiz, B. M. Ebrahimi, H. A. Toliyat and M. Valavi: “Mixed eccentricity fault diagnosis on salient pole synchronous generator using modified winding function”, *IEEE Progress In Electromagnetics Research B*, Vol. 11, pp. 155 - 172, November 2006.
- [22] B. M. Ebrahimi, J. Faiz, M. Javan-Roshtkhari and A.Z. Nejhad: “Static Eccentricity Fault Diagnosis in Permanent Magnet Synchronous Motor Using Time Stepping Finite Element Method”, *IEEE Transactions on Magnetics*, Vol. 44, No. 11, pp. 4297 - 4300, November 2008.
- [23] S. Chen and T.A. Lipo: “Bearing currents and shaft voltages of an induction motor under hard and soft switching inverter excitation”, *IEEE Industrial Applications Conference (IAC)*, Vol. 1, pp. 167 - 173, October 1997.
- [24] W. Saadoui and K. Jelassi: “Induction motor bearing damage detection using stator current analysis”, *IEEE International Conference on Power Engineering, Energy and Electrical Drives*, pp. 1 - 6, May 2011.
- [25] T. Sorita, S. Minami, H. Adachi, M. Takashima and S. Numata: “The detection of degraded materials in turbine generators by chemical analysis”, *IEEE International Symposium on Electrical Insulating Materials*, pp. 751 - 754, September 1998.
- [26] C.C. Carson, S.C. Barton and F.S. Echeverria: “Immediate warning of local overheating in electric machines by the detection of pyrolysis products”, *IEEE Transactions on Power Apparatus and Systems*, Vol. PAS-2, No. 2, pp. 532 - 542, March 1973.
- [27] R. Dupius: “Application of oil debris monitoring for wind turbine gearbox prognostic and health management”, *IJPHM Annual Conference on Prognostics and Health Management*, No. 044 pp. 1 - 15, September 2010.
- [28] J.R. Ramussen and C.B. Tuttle: “Early detection of internal stator winding faults using rotor-mounted infrared sensors”, *IEEE International Conference on Electrical Machines and Drives*, pp. 800 - 802, May 1999.
- [29] M. Ganchev, B. Kubicek and H. Kappeler: “Rotor temperature monitoring system”, *IEEE XIX International Conference on Electrical Machines (ICEM)*, pp. 1 - 5, September 2010.
- [30] M. Tsytkin: “Induction motor condition monitoring: Vibration analysis technique - A practical implementation”, *IEEE International Conference on Electrical Machines and Drives*, pp. 406 - 411, May 2011.
- [31] M.R. Bissonette: “End-winding vibration monitoring and interpretation”, *IEEE International Symposium on Electrical Insulating Materials*, pp. 285 - 290, June 2012.
- [32] F.T. Emery, B.N. Lenderking and R.D. Crouch: “Turbine-generator on-line diagnostics using RF monitoring”, *IEEE Transactions on Power Apparatus and Systems*, Vol. PAS-100, pp. 4974 - 4982, December 1981.
- [33] H.A. Toliyat and T.A. Lipo: “Transient analysis of cage induction machines under stator, rotor bar and end ring faults,” *IEEE Trans. Energy Conversion*, Vol. 10, No. 2, pp. 241–247, June 1995.
- [34] H. Henao, C. Demian and G.A. Capolino: “A frequency-domain detection of stator winding faults in induction machines using an external flux sensor,” *IEEE Transactions on Industrial Applications*, Vol. 39, No. 5, pp. 1272–1279, September/October 2003.
- [35] P.I. Nippes: “Early warning of developing problems in rotating machinery as provided by monitoring shaft voltages and grounding currents,” *IEEE Transactions on Energy Conversion*, Vol. 19, No. 2, pp. 340 - 345, June 2004.
- [36] F. Filippetti, G. Franceschini, C. Tassoni and P. Vas: “Recent developments of induction motor drives fault diagnosis using AI techniques,” *IEEE Transactions on Industrial Electronics*, Vol. 47, No. 5, pp. 994 - 1004, October 2000.
- [37] R.M. Bharadwaj, A.J. Parlos, A.H. Toliyat and S.K. Menon: “A neural network-based speed filter for induction motors: Adapting to motor load changes,” *IEEE International Joint Conference on Artificial Neural Networks*, Vol. 5, pp. 3447 - 3450, July 1999.

DESIGN OF A NON-INTRUSIVE CABLE CONDITION MONITORING TECHNIQUE BY MEANS OF PARTIAL DISCHARGE

H. van Jaarsveldt* and R. Gouws**

*School of Electrical, Electronic and Computer Engineering, North-West University, Potchefstroom, South-Africa. E-mail: * 20569408@nwu.ac.za ** Rupert.Gouws@nwu.ac.za*

Abstract: The purpose of this paper is to discuss the design of a non-intrusive condition monitoring technique for medium- and high-voltage power cables. Partial discharge (PD) was used to design the non-intrusive condition monitoring technique, with specific focus on XLPE power cables. A simple A-B-C model was used to derive an equivalent circuit for partial discharge, due to a void in the insulation material of a power cable. The condition monitoring technique is based on the classification of PD activity according to 5 distinct levels of PD. The design of the condition monitoring technique is of such a nature that it can easily be adapted to be used for different input voltages as well as different types of electrical cables. This technique can thus be seen as an effective and useful technique of cable condition monitoring. Future work will include the use of the results discussed in this paper to aid the construction as well as calibration of a practical model. This model will be used to perform non-intrusive condition monitoring of power cables by means of PD measurements.

Keywords: Condition monitoring, non-intrusive, partial discharge (PD), XLPE power cables, void size, apparent charge

1. INTRODUCTION

Electrical cables are an essential part of an electrical network and also play a vital role in the safety of such a network. Often high voltage cables are used for underground transmission of electricity. For this reason, the conductor must be completely isolated, other than with overhead lines where air forms part of the insulation. Due to the fact that the conductor must be completely isolated, the cables are much more expensive than normal overhead lines [1]. Due to environmental as well as operational stressors, electrical cables will degrade over a period of time. This degradation is caused by electrical, chemical and mechanical stress. Insulation degradation can lead to the failing of electrical cables, which will have a direct economic impact and will also compromise the safety of the system in which the failing cables are used. The degradation of the insulation materials, used within electrical cables, will ultimately cause the cable to fail [2]. It is therefore important to constantly monitor the condition of electrical cables, to be able to estimate their remaining operational life.

Different factors must be considered when choosing a condition monitoring technique. These factors include: the cable being tested, physical environment, affordability, ease of use, as well as required results obtained from tests. Certain elements must be considered in order for the chosen condition monitoring technique to be effective. The most important elements are: [3]

- Selection of cables to be monitored
- Database development for monitored cables
- The monitoring of the service environment
- Identifying expected factors leading to aging and degradation

- Selection of suitable condition monitoring techniques
- Regular test and inspection activities
- Periodic review and assessment of the monitored cables.

The ideal condition monitoring technique can be described as a technique which adheres to a list of nine desired attributes listed in [3]. It is however not possible for a single technique to adhere to all of the desired attributes. The most important attribute for a condition monitoring technique is to be non-intrusive as well as non-destructive. The advantage of a non-intrusive technique is that measurements can be taken without the cable being taken out of operation. Another advantage is that measurements of the cables being tested can be taken under operating conditions. The major disadvantage of non-intrusive techniques is that it has significantly less sensitivity than that of intrusive techniques. Condition monitoring techniques can be divided into two main groups, in-situ techniques and laboratory techniques [3]. Although laboratory techniques can yield important data, the focus of the research will be on in-situ techniques, as this is more useful in the industry, as it can be used to perform measurements in the field.

Research has shown that partial discharge (PD) in electrical cables is one of the main reasons for insulation degradation. Partial discharges (PD) can be described as localised electric discharges that do not bridge the complete distance between electrodes, indicating the presence of cavities as well as defects within the insulation material of electrical cables [4]. Once PD has

occurred in a cable, it will continue to degrade the insulation of that cable to the point of failure. PD usually occurs due to cavities or voids within the insulation material of the electrical cable [5].

2. MATERIALS AND METHOD

2.1 Materials

A number of different types of cables, each with its unique set of advantages and disadvantages, are available for the transmission of electrical energy. Cross-linked Polyethylene (XLPE) cables are the preferred choice for secondary reticulation, among the mining industry in South-Africa. Cross-linked polyethylene insulation was developed to improve the maximum operating temperature of the cable. XLPE also has the advantages that it improves impact strength, dimensional stability, tensile strength and the resistance to aging. The construction process of an XLPE cable is very important, as poor construction can lead to impurities within the cable and will ultimately cause PD activity within the cable [6].

The different layers of a typical medium voltage XLPE cable can be seen in Figure 1. Secondary reticulation within the industrial sector is between 6.6 kV and 11 kV . From this it can be determined that the thickness of the XLPE layer of a cable, used for secondary reticulation, will range from 3 mm to 6 mm [6].

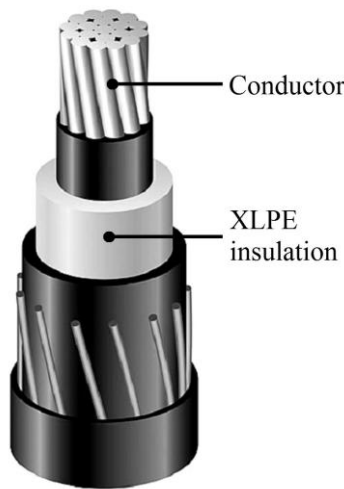


Figure 1: Layers of a XLPE cable [6]

The thickness of the insulation layer as well as the relative permittivity (ϵ_r) of XLPE was used to construct a test object, from which a simple A-B-C model [7] can be derived. Typical voids within the insulation of XLPE cables have a volume of 10 mm^3 with a height of 2–3 mm and a radius of 1–2 mm [8]. The test object, which will be used for the simulations, is shown in Figure 2. The dimensions of the object are 30 mm x 30 mm x 6 mm. The volume of the void will vary for some of the simulations.

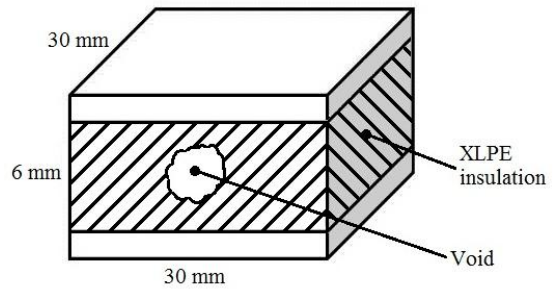


Figure 2: Test object with a centred cylindrical void

The values for C_a , C_b and C_c , shown in the A-B-C model, are calculated by means of the following three equations [4]:

$$C_a = \frac{\epsilon_0 \times \epsilon_r \times (a - 2r) \times b}{c} \dots\dots\dots(1)$$

$$C_b = \frac{\epsilon_0 \times \epsilon_r \times r^2 \times \pi}{c - h} \dots\dots\dots(2)$$

$$C_c = \frac{\epsilon_0 \times r^2 \times \pi}{h} \dots\dots\dots(3)$$

ϵ_0 = permittivity of free space

ϵ_r = relative permittivity of XLPE

r = radius of void (mm)

h = height of void (mm)

The three determined capacitance values were used to construct the A-B-C model. The A-B-C model is based on the circuit shown in Figure 3. This model was designed to investigate the effect of PD due to voids within the insulation material of electrical cables. The A-B-C model makes use of three capacitors to represent PD activity. The first capacitor is the capacitance caused by the void and the second represents the capacitance close to the void. The rest of the healthy insulation is represented by the third and final capacitor.

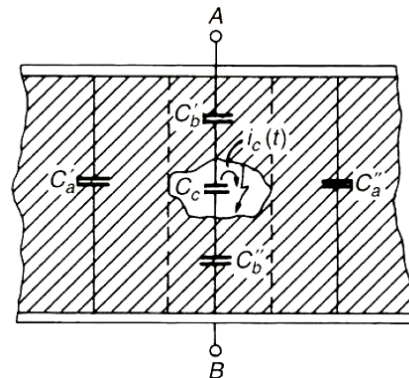


Figure 3: A-B-C model for PD due to voids [7]

2.2 Monitoring Technique

Calculated parameters as well as a number of constant values are used to simulate PD activity within the insulation of XLPE cables. A SIMULINK® model was created to simulate PD activity due to the void in the XLPE insulation material. Figure 4 illustrates the SIMULINK® model. The model consists of a filter component (r), a measuring capacitor (C_m) and a coupling capacitor (C_k). The test object with the void is represented by the A-B-C model, which house the three capacitance values C_a , C_b and C_c . The measuring component of the model is connected to the circuit by means of a parallel $R L C$ circuit. Parameters from this model were exported to the MATLAB® environment where further calculations were performed.

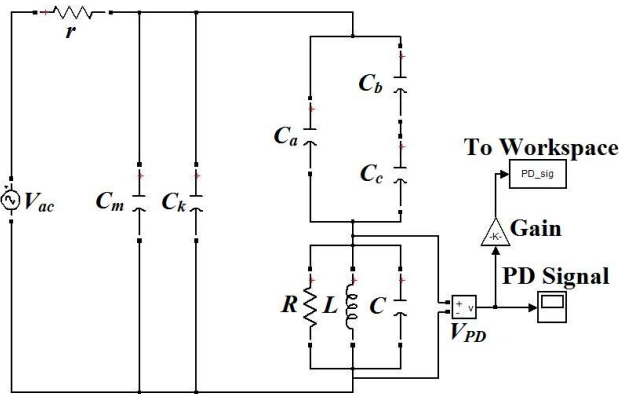


Figure 4: PD simulation model in SIMULINK®

The main purpose of the simulations is to aid the design process of an effective non-intrusive condition monitoring technique for power cables. The operational flow of the non-intrusive condition monitoring technique is shown in Figure 5. The first step of the condition monitoring technique is to measure the PD activity within the cable. The script files created in the MATLAB® environment is then used to analyse the collected data and also to compute a number of specific parameters. The “ q ” illustrated in Figure 5 is the apparent charge of the measured PD signal, measured in pC. The apparent charge of the PD signal will be used to classify the PD activity according to 5 predetermined levels of PD. The specific requirements [9] of each PD level are illustrated in Figure 5. As can be seen from the figure, level 1 is the least significant level of PD with level 5 being the most destructive. The level of PD activity can directly be linked to the remaining operational life of the specific cable [5]. Once the level of PD is determined a specific preventive action can be taken. The preventive action can be determined by considering the approximate remaining life of the cable. Continuous monitoring is required in order for this technique to be successful. The most important part of the non-intrusive condition monitoring technique is the process of classifying the PD activity according to the 5 levels.

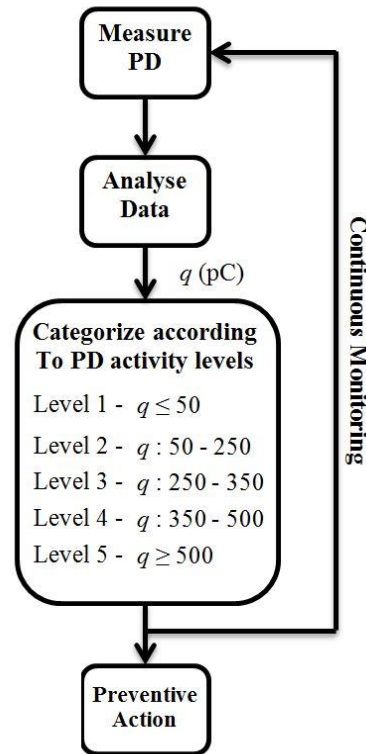


Figure 5: Operational flow of the condition monitoring technique

Once the PD signal is measured, it will be used to classify the PD according to 5 different levels. The different levels will be determined by means of the maximum amplitude of the calculated apparent charge of the PD signal, as well as the number of PD pulses [5]. Level 5 will have the highest probability of cable failure. Cables with no PD activity will be classified as level 1 PD. Level 1 will include PD activity below 50 pC and generally will have no degrading effect on the insulation of a cable [9]. This means that cables classified as level 1 PD will be safe for operational purposes. When the PD is caused by stressors such as thermal, mechanical and environmental, but does not degrade the insulation, it will be classified as level 2 [5]. On-going degradation by means of these stressors will eventually cause the cable to fail. The degradation however will be at a slow rate. Level 3 PD will cause degradation of the insulation material. This is also the most unpredictable level of PD activity and therefore it is important to re-test these cables regularly. Usually level 3 PD cables have a lifespan of more than 5 years, with some even more than 10 years [5]. Level 4 PD will result in serious degradation of the cable’s insulation material and will cause definite cable failure. The general lifespan of cables classified as level 4 is 5 years or less. Some cases of level 4 PD activity can cause the cable to fail within 2 years [5]. The most severe cases of PD activity will be classified as level 5 PD. It is necessary to investigate the PD in this level by means of other measuring techniques. Level 5 PD activity can cause an

electrical cable to fail within the first year of detection. It is therefore necessary to take immediate action once this level of PD is detected in cables [9]. This classification system will form the basis of the condition monitoring technique. The measured PD signals will be classified according to the various levels and from there decisions can be made as to the severity of the PD activity and also the preventive actions to be taken.

2.3 Simulations

A constant void size of 12.57 mm³ was used for the first set of simulations. The initial input voltage of 6 kV was incremented with 0.5 kV values until the final input voltage of 11 kV was reached. The values for the parameters used in the first simulations are given in Table 1. The correlation between input voltage and maximum amplitude of the measured PD signal can be studied from these simulations. An important parameter for the classification of the PD activity according to the 5 levels is the number of PD pulses per cycle. The number of PD pulses was also obtained from this set of simulations.

Table 1: Standard parameter values for simulations

Parameter	Value
Dimensions of test object	30 x 30 x 6 (mm)
Input voltage	6 kV – 11 kV
Permittivity (free space) (ϵ_0)	8.854×10^{-12}
Relative permittivity (ϵ_r)	2.3
Radius of void (r)	1 mm
Height of void (h)	4 mm
C_a	2.8510×10^{-12} F
C_b	3.1988×10^{-14} F
C_c	6.9539×10^{-15} F

The most important part of the condition monitoring technique is to obtain the apparent charge (q) of the measured PD signal. It is also important to study the correlation between the void size, within the insulation, and the apparent charge of the measured PD signal. To be able to study this correlation the second set of simulations was done with a constant input voltage of 6 kV and a void size varying between 12 mm³ and 315 mm³. The apparent charge of the measured PD signal is determined by means of the following equation [4]:

$$q = C_b \times V_c \dots\dots\dots(4)$$

q = Apparent charge of measured PD (pC)

C_b = Capacitance value of area closest to void (F)

V_c = Voltage across void capacitor (V)

The apparent charge of the measured PD signal is used, due to the fact that an accurate measurement of the actual PD signal is not possible.

3. RESULTS

The various sets of simulations were used to investigate PD at different values of the input voltage as well as for different sizes of a single cylindrical void in the insulation. The measured PD signal at an input voltage of 6 kV and with a void size of 12.57 mm³ is shown in Figure 6. The measured signal for each specific simulation was exported to MATLAB® in order to perform the necessary calculations. The signal represented in Figure 6 is without noise and thus only gives data of the simulated PD activity within the cable.

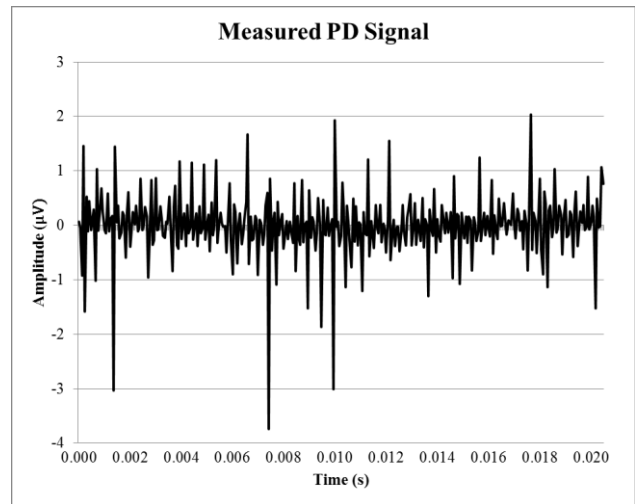


Figure 6: Measured PD signal at 6 kV

For the second set of simulations the volume of the void (V) must vary between 12 mm³ and 315 mm³. This was done by using a constant height (h) of 4 mm and increasing the radius (r) from 1 mm to 5 mm. The calculated volume values are shown in Table 2.

Table 2: Calculated void volume values

r (mm)	h (mm)	V (mm ³)
1	4	12.566
2	4	50.265
3	4	113.09
4	4	201.06
5	4	314.15

The three capacitance values used within the A-B-C model will vary, due to the fact that the void size for the second set of simulations will not be kept constant. Equations (1-3), were used to calculate the values for C_a , C_b and C_c . The calculated capacitance values for the void sizes are shown in Table 3.

Table 3: Calculated capacitance values

C_a (pF)	C_b (pF)	C_c (pF)
2.851	0.03199	0.00695
2.647	0.12780	0.02782
2.444	0.28790	0.06259
2.240	0.51180	0.11130
2.036	0.79970	0.17390

The calculated results from Table 2 and 3 were used to perform the PD simulation by means of the SIMULINK® model. Data obtained from the SIMULINK® was analysed by means of a script file created in the MATLAB® environment and yielded the results shown in Table 4. These results are used to investigate specific parameters which are used to classify the PD activity within the cable according to the 5 levels. The two most important data sets shown in Table 4 include the PD pulses as well as the apparent charge (q) of the measured PD signal.

Table 4: Calculated results

V_{in} (kV)	PD Pulses	Size (mm ³)	C_b (pF)	V_a (V)	q (pC)
6	120	12.566	0.0319	381.1940	10.01
7	126	50.265	0.128	381.1949	40.06
8	123	113.09	0.288	381.1960	90.14
9	123	201.06	0.512	381.1995	160.2
10	124	314.15	0.799	381.1910	250.4

As mentioned, the number of PD pulses per cycle (0.02 s) is an important parameter used for the classification of the measured PD activity. The number of pulses, for an input voltage of 6 – 11 kV ranged between 120 and 128 pulses. A graph illustrating the number of pulses per cycle is shown in Figure 7. Due to the random nature of PD activity it is difficult to predict the number of pulses for a specific input voltage.

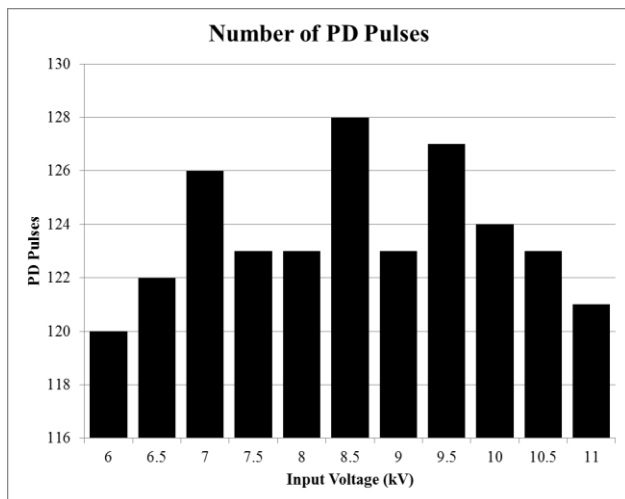


Figure 7: Graph depicting number of PD pulses per cycle

It is important to obtain accurate measurements for the number of PD pulses per cycle, in order to successfully classify the PD activity according to the 5 levels. The best way to obtain accurate values for the number of PD pulses is to obtain a base value of the operational environment of the cable. This can then be used to eliminate external noise from the actual measurements. The elimination of noise can significantly improve the accuracy of the condition monitoring technique.

The most important parameter obtained from the simulation results is the apparent charge (q) of the measured PD signal. The apparent charge will eventually be used to classify the PD activity within a specific cable according to the 5 predetermined levels of PD activity. The correlation between void size and apparent charge of the measured PD signal was also studied by means of the graph illustrated in Figure 8.

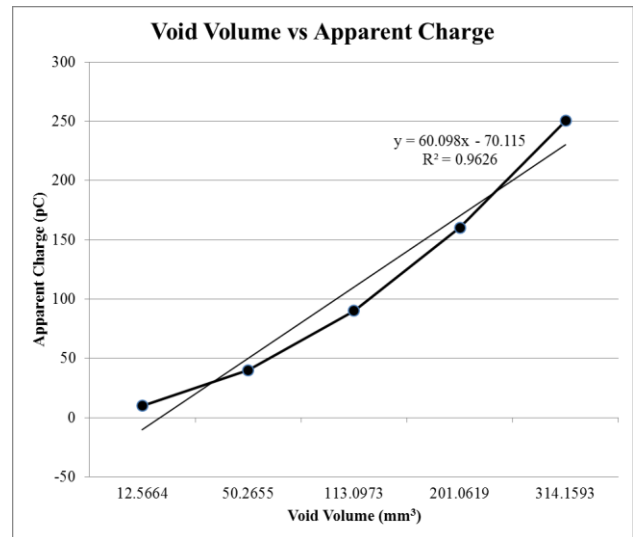


Figure 8: Graph of void volume vs apparent charge

From the above graph it can be seen that the correlation between void volume and the apparent charge of the measured PD signal is almost linear. In Figure 8 it can be seen that the R^2 value is 0.9626. Due to the fact that this value is close to 1 it can be said that the assumed trendline or the fitted trendline is a very close approximation to the actual values. By studying the correlation between the volume of the void and the apparent charge the conclusion can be made that a void with a bigger volume will cause more severe PD activity within the XLPE cable. Measured values for the apparent charge of the PD signal as well as the formula of the trendline $y = 60.098x - 70.115$ can be used to determine an approximate value for the volume of the void within the cable's insulation material.

From the results discussed in this section the PD activity within a specific cable can be classified according to the 5 PD levels. The 5 levels of PD activity can directly be linked to the remaining life of a cable. This information can be used to determine a preventive action for each level of PD. Once a void with significant size appears within the insulation material of a cable, it will grow to the point where the PD activity, due to the void will cause degradation to the point of cable failure. Premature cable failure can thus be prevented by means of successful analysis of the results discussed within this section of the paper.

4. CONCLUSION

Various conditions will contribute to the degradation of the insulation material of electrical cables. PD is the main cause for degradation of insulation materials used within electrical cables. The degradation will continue until the point of cable failure. Due to the disadvantages accompanied with premature failing of cables it is important to continuously monitor the condition of electrical cables.

The simulation results discussed in this paper were used as the first steps in developing a non-intrusive condition monitoring technique. The development of this technique is still in the design phase and therefore various aspects of PD activity still needs to be investigated and then incorporated in the final design of the cable condition monitoring technique. The condition monitoring technique will be based on the measuring and classification of PD activity according to 5 predetermined levels. An approximate remaining operational life is determined for each level of PD activity and then used to identify the appropriate preventive action for the specific level of PD activity. The condition monitoring technique makes use of both the number of PD pulses per cycle, as well as the apparent charge of the measured PD signal to classify the PD activity according to one of the 5 levels. The classification criteria of the monitoring technique can be updated to comply with one of the IEEE standards. The best suited for the project is IEEE std 400TM-2001, the IEEE Guide for Field Testing and Evaluation of the Insulation of Shielded Power Cable Systems [10]. The main purpose of this guide is to provide an overview of the various tests available for evaluating the insulation of cable systems in the field. The guide also has a specific section on PD testing, with the main focus on PD fundamentals, partial discharge characterization and also the measurement of PD activity. It is important to adapt the current classification criteria to this IEEE standard in order for the final product to be accurate and to be able to obtain relevant data.

At the moment the simulation model shown in Figure 4 does not incorporate the high frequency model of a power cable. This has a direct and significant influence on PD magnitude. It is therefore critical that future work will include the incorporation of the high frequency model of the power cable in the simulation model. This will lead to the simulation results being more accurate when compared to actual measured results. Future work will also include an in depth study of the statistical nature of PD activity. The project research and results obtained from simulations will be used for the design, construction and implementation of a practical model. This model will be used for non-intrusive condition monitoring of power cables by means of PD measurements. The results obtained from measurements taken by the practical model can be compared to that of simulation results. This then can be used to validate the accuracy of the constructed model.

5. REFERENCES

- [1] J.R. Lucas: *High Voltage Engineering, Department of Electrical Engineering*, University of Moratuwa, Sri Lanka, revised edition, 2001.
- [2] G. Chen and F. Baharudin: "Partial Discharge Modelling Based on a Cylindrical Model in Solid Dielectrics", *International Conference on Condition Monitoring and Diagnosis*, Beijing, China, April 2008.
- [3] L.R. Villaran M: *Essential Elements of an Electric Cable Condition Monitoring Program*, Brookhaven National Laboratory, NY, pp 62-96, 2010.
- [4] A. Sabat and S. Karmakar: "Simulation of Partial Discharge in High Voltage Power Equipment", *International Journal on Electrical Engineering and Informatics*, Volume 3, pp 234-247, 2011.
- [5] N. Ahmed and N. Srinivas: "Partial Discharge Severity Assessment in Cable System", *Transmission and Distribution Conference and Exposition*, Volume 2, pp 849-852, 2001.
- [6] I.A. Metwally: "High-voltage power cables plug into the future", *IEEE Potentials*, volume 27, issue 1, pp 18-25, Jan-Feb 2008.
- [7] M.F. Badillo, L.N. Navarrete, A.G. Parada and A.C. Miranda: "Simulation and analysis of underground power cable faults", *International Meeting of Electrical Engineering Research*, pp 50-57, April 2012.
- [8] C.Y. Ren, Y.H. Cheng, P. Yan, Y.H. Sun and T. Shao: "Simulation of Partial Discharge in Single and Double Voids Using SIMULINK[®]", *Twenty-Seventh International Conference Record of the Power Modulator Symposium*, pp 120-123, May 2006.
- [9] Emerson: "Partial Discharge Testing for Cables", *Electrical Reliability Services*, Columbus, Ohio, December 2008.
- [10] IEEE Power Engineering Society: *IEEE std 400TM-2001 IEEE Guide for Field Testing and Evaluation of the Insulation of Shielded Power Cable Systems*, The Institute of Electrical and Electronics Engineers Inc., NY, pp 13-15, January 2002.

DESIGN CONSIDERATIONS IN THE IMPLEMENTATION OF AN ELECTROMAGNETIC BRAKE FOR A 15 KW PM WIND GENERATOR

J.H.J. Potgieter and M.J. Kamper*

* *Department of Electrical and Electronic Engineering, Banghoek Road, University of Stellenbosch, Stellenbosch 7600, South Africa E-mail: kamper@sun.ac.za*

Abstract: In this study a basic overview is done on the different braking mechanisms for wind turbine systems. For utility scale wind turbines, most standards specify that two independent braking mechanisms should be used. Aerodynamic and mechanical braking are mostly utilised. For small scale systems electrical braking configurations seems to be the most favourable option. The main focus in this paper is, thus, on the operation and implementation of an electromagnetic brake for small scale wind turbine systems. Several aspects are identified which influences the braking capabilities of permanent magnet generators of which the most important are the end-winding inductance and the end-effects of the permanent magnets. Calculation techniques to obtain the braking resistance value which can also be implemented in the design optimisation of PM wind generators are also shown. A 15 kW PM wind generator is used as a case study to evaluate the effectiveness and performance of the electromagnetic brake, with some practical measurements also shown.

Key words: PM generators, wind turbine, electromagnetic braking

1. INTRODUCTION

All wind turbines require a braking system, as torque is constantly being exerted on the turbine if there is air-flow over the blades. The three main braking methods currently being used are aerodynamic, mechanical and dynamic electrical braking or electromagnetic braking. For utility scale wind turbines most design standards require at least two independent braking systems. At least one brake needs to be on the low speed shaft if a geared drive train is used. It is also common practice to have at least one aerodynamic brake, which is a requirement specified by some standards. As with the other components in the wind turbine system the braking mechanism should be adequately designed to be able to keep the turbine from rotating during a 50 year high gust. Ideally the braking mechanism should also be designed for a lifetime of at least 20 years [1–6].

Aerodynamic systems make use of tip air brakes or by pitching the blades to reduce the torque exerted on the turbine. Small scale systems are mostly less complex and they generally make use of a passive furling technique to turn the wind turbine out of the wind if the wind speed exceeds the maximum operating speed. Mechanical brakes make use of conventional disk brakes as in motor vehicles, with a metal disk fixed to the shaft to be braked. During braking hydraulic callipers pushes the brake pads against the disk. Clutch brakes are also used to some extent. Actuation of clutch type brakes are normally done via springs applying the needed pressure and are released by compressed air or hydraulic fluid [4]. The mechanical brake can either be applied to the low speed or high speed shaft in geared wind generator systems. The brake on the low speed side needs to be able to handle the large amount of torque exerted directly by the turbine. However, although the torque is much less on the high speed side,

the brake system will be subjected to large centrifugal forces due to the high speed. Also in this case the brake needs to act through the gearbox which could increase gearbox loading and decrease the reliability of the system. Furthermore during a gearbox failure the brake might not be able to stop the turbine. Mechanical brakes also make use of hydraulic systems which could lead to failures if it comes into contact with salt, sand or other abrasive substances. Brake pads and in some cases bearings needs to be replaced several times during the lifetime of the turbine if braking occurs frequently.

With electrical dynamic braking, currents are induced in the stator windings and power is diverted and dissipated in most cases through a resistive dump load. For wind turbines using an induction generator (IG) electrodynamic braking is done through a resistive load and a capacitor bank for excitation of the IG. Examples of such systems are given in [1, 2, 5]. It is also mentioned that the electrodynamic brake can be applied in stages, to obtain a more dynamic and smoother braking curve to reduce the loading on the rest of the turbine structure and tower, but this increases the complexity of the system. Thyristor switched capacitors and chopper controlled resistors can also be used as mentioned in [2] to vary the braking torque during braking, but again this increases the complexity and reduces the robustness of the system. In many cases the mechanical brake is still applied after the initial speed is low enough and to keep the system from rotating once it is brought to standstill. This is generally referred to as “parking” of the wind turbine. Although a mechanical brake is still used the wear and tear and, thus, maintenance of the mechanical brake is significantly reduced.

For PM wind generators, as no excitation is needed, electromagnetic braking is employed by connecting the

stator terminals only to a resistive dumping load as in [6–9]. Electronic schemes are also used as for the small wind generator in [10] where braking is done by shorting the generator through an active MOSFET switch. The dumping load can also be connected to the active-rectifier side of the power electronic converter similar as in [2] where electrical braking is performed through a rectifier and chopper circuit. This will allow for more control over the braking torque to reduce the loading on the turbine structure, but again the reliability and robustness of the system is reduced due to more components being added in the main power flow path.

From the reviewed literature it is found that most large utility scale wind generators make use of a mechanical brake and an aerodynamic brake. In [5] an in depth study is done on the feasibility of an electrodynamic brake (EDB) for large wind turbines. It is found to reduce the wear on brake pads and increase the reliability of the braking system. However, especially if a parking brake is still needed the EDB was not found to be economically comparable to other braking systems currently in use. It was mentioned that this system could be feasible in regions where grid failures occur often and braking is frequently required.

For small scale PM wind generators electromagnetic braking offers a much better solution. The drive trains of these systems are very simple in nature, mostly without a gearbox. In many instances the pitch of the blades are fixed and passive stalling techniques are used. With the torque much more manageable in this case it makes sense to employ electromagnetic braking instead of maintenance intensive mechanical brakes. The focus of this study is, thus, to implement a simple and robust electromagnetic braking mechanism for a 15 kW PM wind turbine system.

2. PROTOTYPE PM WIND GENERATOR

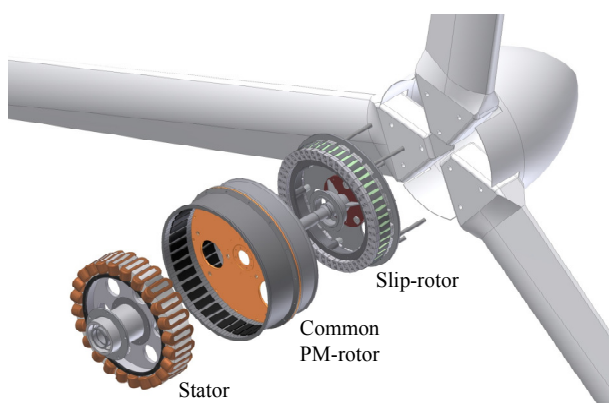


Figure 1: Example of a new concept SS-PMG [11].

The case study PM wind generator forms part of a new novel concept known as a slip-synchronous permanent magnet generator (SS-PMG) as explained in [11]. This is a direct drive, directly grid-connected PM wind generator, thus, without gearbox or power electronic converter. The generator consists of two integrated generating



Figure 2: Case study 15 kW PM wind generator being field tested.

Table 1: Parameters of wind turbine system evaluated.

Parameter	Value
Turbine diameter	7.2 m
Rated power	15 kW
Rated torque	1000 Nm
Rated rotational speed	150 r/min
Cut-in wind speed	4 m/s
Rated wind speed	11 m/s
Pitch	Fixed
Yaw	Passive with tail vane.
Protection	Passive auto-furling above rated wind speed.

units, a conventional PM synchronous generator (PMSG) connected directly to the grid and a turbine connected smaller slip permanent magnet generator (slip-PMG) with short-circuited solid-bar windings similar as in conventional induction machines. The direct grid connection is made possible due to the damping provided by the slip of the second turbine connected generator.

In Table 1 the specifications of the wind turbine system evaluated is shown. For safety reasons the generator should be able to at least brake up to a wind speed of 12.0 m/s with the turbine facing full into the wind. The generator is synchronised to the grid by means of a grid synchronisation controller as explained in [12]. It is also possible to remove the slip-PMG from the system and to operate the PMSG in conjunction with a solid-state converter (SSC) as explained in [13]. The evaluation of the braking mechanism discussed in this study can, thus, be done as for a conventional PM wind generator. The whole aim in the design of this small wind turbine is to have an extremely robust, simple and reliable generating system with very few moving parts. This means that maintenance throughout the lifetime of this generator needs to be at an absolute minimum.

3. PROPOSED BRAKING SYSTEM

From the reviewed literature it can be concluded that although mechanical and aerodynamic braking systems are predominantly used for utility scale wind turbines, electromagnetic braking seems to be the best option for small scale systems.

It would be possible to implement a controlled electrical

braking mechanism as discussed in [10] by utilising the active switch of the synchronising controller or the active rectifier part of the SSC system. This will, however, decrease the reliability of the system especially if there is a loss of grid power. A passive braking circuit which is activated by a normally closed contactor, is a better solution in this case. If the grid fails the contactor will move to its normally closed position and the braking circuit will be activated. If the wind turbine is not operating the braking circuit will be in the brake position by default. In this position the turbine will slowly coast at a very low rotational speed on the resistance load. However, if it needs to be brought to a complete standstill or so called park position, another switch can be used to short-circuit the generator terminals. In this position the movement of the turbine will be almost negligible. The braking diagram is shown in Fig. 3.

As will be shown in Section 5, a capacitor bank can be installed adjacent to the resistance load to increase the maximum torque, by slightly advancing the current angle of the PMSG. Very basic heating elements which are readily available and cheap are used for the braking resistors. Wire wound resistors which are much smaller can also be used but are much more expensive. In any case the dumping load can be placed at the base of the tower where space is not so much of a constraint. Also readily available and cost effective general power system capacitors are used. The resistance dump load used to brake the wind turbine is shown in Fig. 4 with the capacitor bank mounted on the side. As mentioned in [5] the operating time of the braking mechanism compared to the rest of the turbine system will be significantly less. This means that with the known low failure rates of resistors and capacitors, chances of these components failing are very low. To have some redundancy in the system three to four resistors are placed in parallel depending on the ohm value. If one fails enough torque should still be developed by the generator to bring the turbine to a standstill. The contactor responsible for activating the braking circuit can also be replaced by two parallel contactors for more redundancy. Procedures can also be implemented during the start-up of the wind turbine to test the braking system after a certain duration in operating time. These procedures could help detect failures before they become too severe. The weakest link in the system is the cabling in the tower and the slip-rings which connects the generator in the nacelle to the rest of the system. It is still a question for this small-scale system if additional braking and protection mechanisms are required.

4. BRAKE TORQUE MODELLING

The electromagnetic braking characteristics of the generator can easily be calculated with a per phase equivalent approach. This is especially useful if a quick evaluation is needed of the braking characteristics for an existing PM generator. As discussed in [11] the modelling and design optimisation of the SS-PMG is done in the dq -reference frame. A modification of this modelling by including the

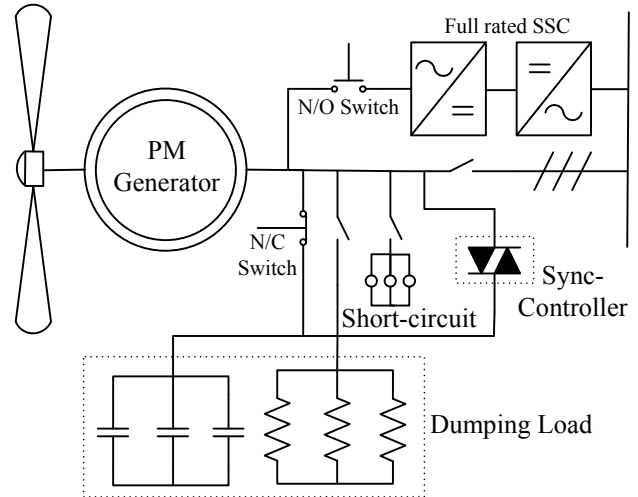


Figure 3: Electrical braking diagram of the SSC-PMSG and SS-PMG systems.



Figure 4: Resistance dump load with a capacitor bank used for electrical braking of the wind generator.

braking resistance can also be implemented in the design optimisation.

4.1 Per-phase equivalent Modelling

Fig. 5 shows the per phase equivalent circuit of the PMSG during braking with R_b , the braking resistance and R_s and X_s the per phase resistance and synchronous reactance of the PMSG. The induced voltage per phase is indicated by E_s . From Fig. 5 the amplitude of the per phase current I_s

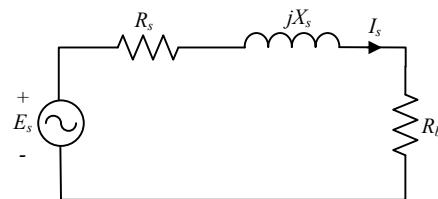


Figure 5: Per phase equivalent circuit of the PMSG during braking.

is given as

$$|I_s| = \frac{E_s}{\sqrt{X_s^2 + (R_s + R_b)^2}}. \quad (1)$$

With the braking power given as

$$P_s = 3|I_s|^2(R_s + R_b) \quad (2)$$

and $E_s = K\omega_s$ and $X_s = \omega_s L_s$, which includes the end-winding inductance component, L_e , the generator torque can be expressed as

$$T_s = \frac{2 P_s}{p \omega_s} = \frac{3p}{2} \frac{K^2 \omega_s (R_s + R_b)}{\omega_s L_s^2 + (R_s + R_b)^2}. \quad (3)$$

The maximum torque is obtained where

$$\frac{dT_b}{d\omega_s} = 0 \quad (4)$$

with

$$\omega_b = \frac{R_s + R_b}{L_s} \quad (5)$$

and

$$T_b = \frac{3}{4} p \frac{K^2}{L_s} \left(K = \frac{\sqrt{2} p \lambda_m}{4} \right). \quad (6)$$

It is clear from (6) that the maximum torque is dominated by the per phase inductance. In [14] calculation techniques are proposed to more accurately calculate the inductance by taking the end-winding effects into account which is generally ignored in the design of non-overlap winding PM generators. However, if a quick brake resistance calculation is needed for an existing PM generator a short-circuit and open circuit test can be conducted. From the open circuit voltage and short-circuit current the per phase inductance can be calculated. This value can then be used in (5) to calculate the value of R_b at the required speed which can be obtained from the turbine curves. With the short circuit test the value of T_b can be verified as the value of T_b is independent of the resistance. This will be shown in Section 5.

4.2 DQ-equivalent Modelling

The dq -reference frame static modelling procedures discussed in [11] can also be modified to take the electromagnetic braking calculations of the generator into account during optimisation.

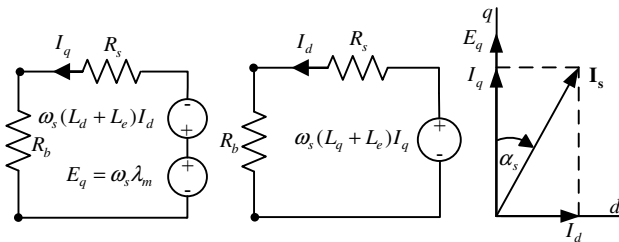


Figure 6: DQ-equivalent circuits and vector diagram of the PMSG during braking.

From the dq -equivalent circuits the steady-state dq -equivalent equations are given by

$$0 = -(R_s + R_b)I_q - \omega_s(L_d + L_e)I_d + \omega_s \lambda_m \quad (7)$$

and

$$0 = -(R_s + R_b)I_d + \omega_s(L_q + L_e)I_q. \quad (8)$$

The dq -inductances L_d and L_q are given as

$$L_q = \frac{\lambda_q}{-I_q}; \quad L_d = \frac{\lambda_d - \lambda_m}{-I_d}. \quad (9)$$

The developed torque can be expressed as

$$T_s = \frac{3}{4} p [(L_q - L_d)I_d I_q + \lambda_m I_q]. \quad (10)$$

By rewriting (7) and (8) the dq -currents can be expressed as

$$I_d = \frac{\omega_s^2 \lambda_m (L_q + L_e)}{(R_s + R_b)^2 + \omega_s^2 (L_d + L_e)(L_q + L_e)} \quad (11)$$

and

$$I_q = \frac{\omega_s \lambda_m (R_s + R_b)}{(R_s + R_b)^2 + \omega_s^2 (L_d + L_e)(L_q + L_e)}. \quad (12)$$

However, finding the derivative of (10) in terms of ω_s by substituting (11) and (12) in (10) is a complex mathematical exercise. Observing (10) and knowing that $L_d \approx L_q$ for the surface mounted PM machines considered, it can be concluded that the maximum torque is dominated by the term $\lambda_m I_q$. It would be much easier to find the breakdown speed (ω_b) where I_q is at a maximum. With I_q as given in (12)

$$0 = \frac{dI_q}{d\omega_s} = (R_s + R_b)^2 - \omega_s^2 (L_d + L_e)(L_q + L_e) \quad (13)$$

and finally

$$\omega_b \approx \frac{(R_s + R_b)}{\sqrt{(L_d + L_e)(L_q + L_e)}}. \quad (14)$$

The value for the breakdown slip speed, ω_b , calculated in (14) can now be used in (11), (12) and (10) to calculate T_b .

5. RESULTS

Fig. 7 shows the open circuit voltage and short circuit current of the PMSG and the calculated per phase inductance is shown in Fig. 8. With a SL winding used for the prototype PM generator, it is found that this generator has a very high per phase inductance. With the maximum torque value inversely proportional to the per phase inductance, this generator will have a low breakdown torque value. This can be seen in Fig. 9 with a breakdown torque value of only 1.23 pu.

Also in Fig. 9 the different braking torque curves calculated by means of FE, where the braking resistance is varied from 0 to 4.5 ohm is shown. The change in resistance only influences the electrical time constant of

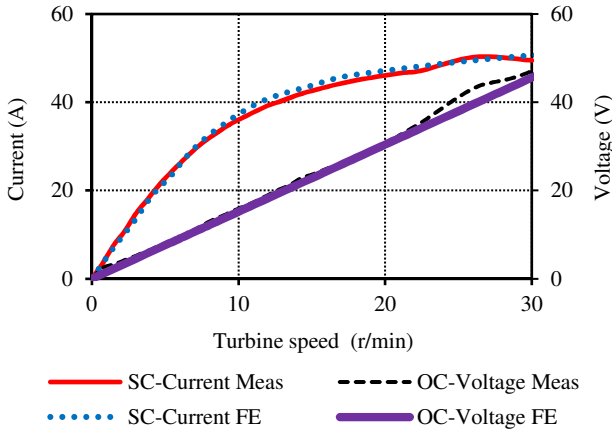


Figure 7: Measurement of the short-circuit current and open circuit voltage for the PMSG versus rotational speed.

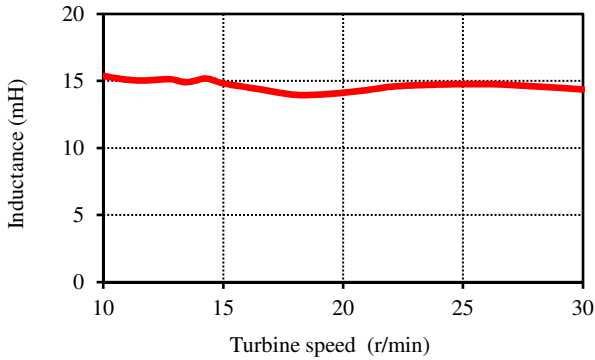


Figure 8: Per phase inductance of the PMSG calculated with the short-circuit and open-circuit tests.

the braking system and has no effect on the maximum torque value. For the SS-PMG system it is important that the maximum torque of the slip-PMG unit is always higher than that of the PMSG to ensure that the slip-speed does not increase too much. If the slip-speed becomes too large the PM-rotor will come to an abrupt stop, because of the much lower inertia of the PM-rotor as compared to the cage-rotor and turbine. The turbine and cage rotor will then continue to rotate at a very high speed, which can not only cause damage to the turbine, but also to the slip-PMG unit due to the heat generated by the losses at such a high slip frequency.

In Fig. 10 the consequence of ignoring the end-winding effects is clearly seen. If the end-winding effects are ignored the generator seems to provide enough torque to be able to brake if the wind speed exceeds 12 m/s. However, in reality this is not the case as the actual torque is much less due to the significant increase in inductance if the end-winding inductance is taken into account. It is also found that the fringing effects on the PM ends influence the value of the inductance and PM flux linkage. This problem was overcome by adding a capacitor bank in parallel with the resistance load to increase the torque just enough to adequately brake the turbine in a wind speed of 12 m/s. This new braking torque curve can also be seen in Fig. 10.

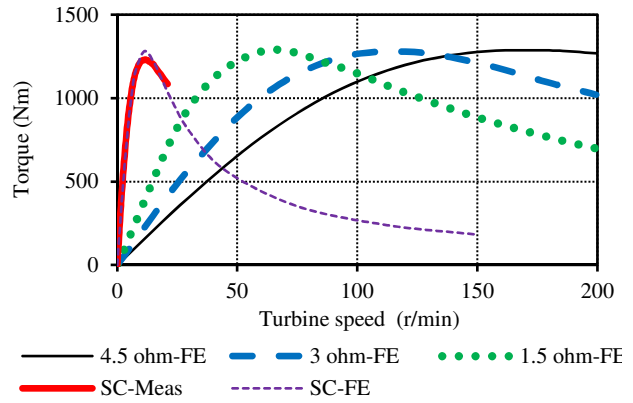


Figure 9: Generator electromagnetic braking torque curves versus rotor speed calculated by means of FE simulation with different values for R_b .

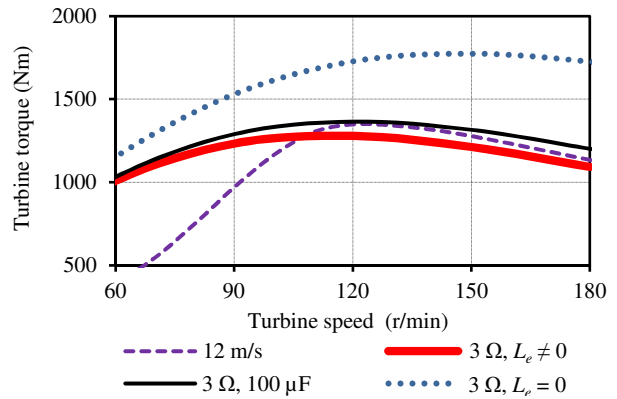


Figure 10: Turbine curve at 12 m/s shown with the generator electromagnetic braking torque curves with only a resistive load, with the end-winding effects ignored and with the end winding effects taken into account, and with a capacitor bank added.

As the speed is reduced the effects of the capacitors starts to diminish, because of the drop in frequency. Most large PM wind generators have a very low electrical frequency so very large capacitors will be needed if this technique is applied. However, for smaller systems and due to the SS-PMG being directly grid-connected in this case the electrical frequency is much higher. Fig. 11 shows the time it takes the generator to stop if the electromagnetic brake is applied at a wind speed of 12 m/s. The stop time is just above 4.5 seconds.

6. CONCLUSIONS

In this paper several of the braking mechanisms used for wind turbine systems are studied. Although electrical braking has been proposed for utility scale wind generators, it seems that for large systems aerodynamic and mechanical braking are still the most economically. For smaller systems, however, it seems more favourable to make use of electrical braking. Electrical braking systems are more robust and require much less maintenance than mechanical braking systems and it also seems more cost effective at the smaller power levels. A basic per phase

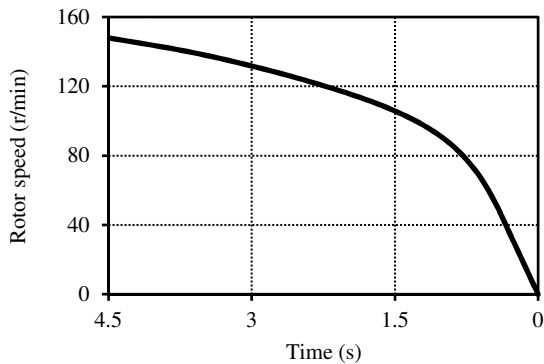


Figure 11: The turbine speed versus braking time.

equivalent approach making use of the open circuit and short circuit tests to calculate the per phase inductance is followed in this study to calculate the braking resistance and to get an indication of whether the maximum torque induced by the generator is sufficient. This approach is more useful if a brake needs to be specified for an already existing PM wind generator. For better accuracy the electrical braking calculations can be incorporated in the FE modelling procedures in the dq -reference frame. This ensures that the braking capabilities of the generator can be sufficiently taken into account during optimisation. If possible the final design should be verified by transient FE analysis. A very important aspect which should be taken into account within all the modelling and simulation procedures are the end-effects in the generator. It is found that especially for large diameter wind generators with low aspect ratios the end-winding inductance and the end-effects of the PMs can influence the maximum torque value significantly. The maximum achievable breakdown torque is inversely proportional to the per phase inductance of the generator. It should also be taken into account that the inductances varies with load and that the dq -inductance values for surface mounted PM machines are not necessarily the same although it is assumed as such in some calculations. For the prototype generator studied it is found that the maximum torque of the final design is too low to brake the generator at the required wind speed. To rectify this problem a capacitor bank is installed in conjunction with the braking resistors to slightly increase the maximum torque value. Depending on the maximum torque requirements other generator topologies, for instance double-layer non-overlap windings or also conventional 3-phase overlap windings might be better suited if electromagnetic braking with high maximum torque requirements are needed. These generator types normally have a lower per phase inductance.

REFERENCES

- [1] L. M. Craig, Z. Saad-Saoud, and N. Jenkins, "Electrodynamics braking of wind turbines," *IEE Proc.-Electr. Power Appl.*, vol. 145, no. 2, pp. 140–146, 1998.
- [2] K. Rajambal, B. Umamaheswari, and C. Chellamuthu, "Electrical braking of large wind turbines," *Renewable Energy*, vol. 30, no. 15, pp. 2235–2245, 2005.
- [3] Det Norske Veritas and Riso National Laboratory, *Guidelines for Design of Wind Turbines*, 2nd ed. Jydsk Centraltrykkeri, Denmark, 2002.
- [4] "Wind power plants," ABB, Technical Application Papers 13, 2011.
- [5] "Electrodynamics braking of large wind turbines," Garrad Hassan and Partners Ltd., ETSU W/45/00519/REP, 1999.
- [6] P. V. Yankov, A. Van den Bossche, and V. C. Valchev, "Successive resistive braking circuit for permanent magnet wind turbine generators," in *14th International Power Electronics and Motion Control Conference, (EPE-PEMC 2010)*, Ohrid, Republic of Macedonia, 2010.
- [7] C. Koch-Ciobotaru, R. Boraci, I. Filip, and C. Vasar, "Study of brake transient regimes for a small wind generator," in *3rd IEEE International Symposium on Exploitation of Renewable Energy Sources, (EXPRESS 2011)*, Subotica, Serbia, 2011.
- [8] A. Sugawara, K. Yamamoto, T. Yoshimi, and S. Sato, "Research for electric brake using ntc thermistors on micro wind turbine," in *10th International Power Electronics and Motion Control Conference, (EPE-PEMC 2006)*, Portoroz, Slovenia, 2006.
- [9] S. Eriksson, H. Bernhoff, and M. Leijon, "A 225 kW direct driven PM generator adapted to a vertical axis wind turbine," in *Advances in Power Electronics*, J. Pomilio, Ed. Hindawi Publishing Corporation, 2011.
- [10] A. F. Fredericks and I. D. deVries, "Design of an auto-braking regulator for a small wind generator," in *AFRICON 2007*, Windhoek, Namibia, 2007.
- [11] J. H. J. Potgieter and M. J. Kamper, "Design of new concept gearless direct-grid connected slip-synchronous permanent magnet wind generator," *IEEE Trans. on Industrial Applications*, vol. 48, no. 3, pp. 913–922, 2012.
- [12] U. Hoffmann, P. Bouwer, and M. J. Kamper, "Direct grid connection of a slip-permanent magnet wind turbine generator," in *Energy Conversion Congress and Expo (ECCE2011)*, Phoenix (AZ), USA, 2011.
- [13] J. H. J. Potgieter and M. J. Kamper, "Torque and voltage quality in design optimisation of low cost non-overlap single layer winding permanent magnet wind generator," *IEEE Trans. on Industrial Electronics*, vol. 59, no. 5, pp. 2147–2156, 2012.
- [14] —, "Evaluation of calculation methods and the effects of end-winding inductances on the performance of non-overlap winding PM machines," in *Proc. Int. Conf. on Electrical Machines*, Marseille, France, 2012.

DESIGN OF A PROTOTYPE POWER LINE INSPECTION ROBOT

N. du Plessis and R. Gouws

North-West University, Faculty of Engineering, Private Bag X6001, Post-point 288, Potchefstroom, 2531, South Africa, E-mail: 21195676@nwu.ac.za

Abstract: The purpose of this paper is to provide the design of a prototype power line inspection robot for the monitoring of Eskom transmission lines. It should also determine if an inspection robot would be a feasible solution to aid Eskom in monitoring their lines for potential problems and should also determine if it would be a viable financial choice to implement an inspection robot as to their current inspection methods. The designed prototype robot must be capable of balancing on a transmission line wire, should be capable of driving on it and to manoeuvre past certain obstacles that are found on a transmission line. Tests were done to ensure that the robot is capable of performing these tasks and other relevant tasks. The main reason for the prototype is to ensure a future development platform for an inspection robot. In return it would result in a cost effective, easy to maintain and a safer environment for the inspection staff.

Keywords: Transmission lines, manoeuvrability, centre of gravity, inspection robot, balancing.

1. INTRODUCTION

Eskom is the biggest distributor of power in South Africa and therefore has thousands of kilometres of transmission lines running across the country, as shown in figure 1 [1, 2]. These lines must consistently be patrolled and maintained to ensure optimal use of the lines. A detailed helicopter inspection is done every two years. To prevent the occurrence of catastrophic failures, every transmission line needs to be inspected regularly. Key components need to be checked for potential problems, for example a line connector has the potential to fail very quickly if damaged [1]. Eskom currently uses foot patrols and helicopters to do annual checks on the lines at a cost of about R36 million per year [2]. Elements that make these inspections so costly and time consuming are the fact that not all of the transmission line towers are so easily accessible, due to rural developments, cities and mountain areas. Mountains pose a problem for the foot patrols as there are not always roads available. Cities and rural areas pose a problem for the helicopters as there are lots of buildings and other elements that could potentially put the helicopter and its team at risk [1, 3].

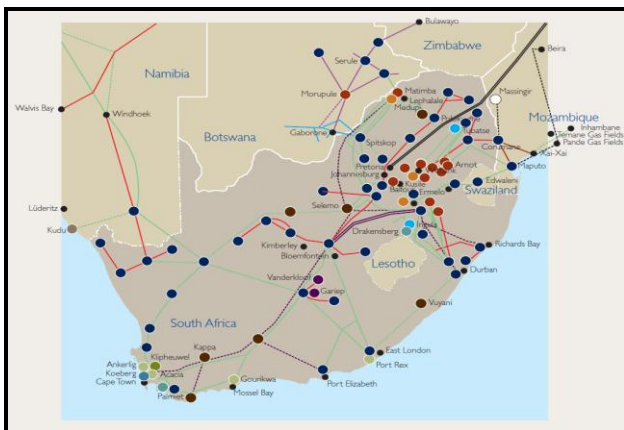


Figure 1: Transmission line grid map of Southern Africa

A prototype robot needs to be conceptualized and designed, so that it would be capable of running on a wire and manoeuvre past normal transmission line obstacles that might block its path. It must also ensure that it does not damage any components on the transmission line or the robot itself, whilst manoeuvring past these obstacles [1]. The robot should also be able to incorporate a monitoring system that could monitor the transmission line as the robot drives along it. The robot needs to function in such a manner that the fast helicopter inspection and foot patrols can be replaced by it [1-3].

The robot must be able to manoeuvre past obstacles on the transmission lines whilst monitoring the line for signs of defects, deterioration, bird nests and other related problems. The robot should not cost more to construct and maintain than what Eskom is already paying for inspection. The robot should be a feasible solution that would be easy to use and maintain.

Because transmission line inspections are very expensive, the robot with its monitoring system must be inexpensive to ensure the projects feasibility. The initial capital outlay for the building of this robot will be costly. However, by taking the current inspection costs into consideration, the construction as well as the maintenance of this robot is well in reach.

Still to be discussed in this paper is the methodology of how the robot should be tested to ensure that it would be a feasible solution. The results of these tests will then be discussed after the methodology. From these results a conclusion can be drawn. Areas that could use improvement or upgrading, thus sections for future work and recommendations will be added before the final conclusion is reached.

2. MATERIAL AND METHOD

Through researching previous projects with similar scopes, a basic idea was formed on what the robot needs

to do, what needs to be avoided, what the elements are that need improving, how to base the design of the robot and what tests should be done. Figure 2 represents the conceptual design of the robot. This was done by comparing previous projects with similar scopes, projects such as the Cable Crawler [4], the CAS robot [5-6], the Expliner [6] and the LineScout robot [6-7].

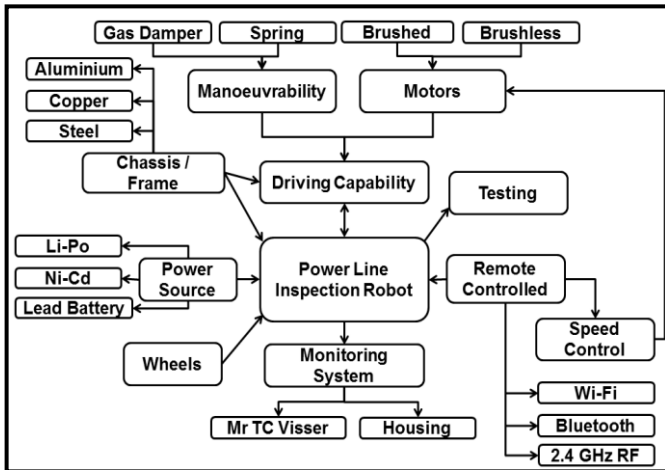


Figure 2: Conceptual design for the transmission line inspection robot

From these projects and the conceptual design, a basic concept was created for the robot. The robot will consist out of six wheels, four are vertical and two horizontal, it will have casings to hold the electronics and the batteries, the vertical wheels will be attached to arms that can open when passing obstacles and the motors will be mounted on the bottom of these wheels. To determine if the robot would be feasible, certain elements need to be tested. These elements are stated below:

2.1 Virtual Test

By using SolidWorks®, a virtual concept can be created. This concept can then be tested as the real robot would have been tested. If the virtual robot is capable of passing the tests, the chances will be higher that the real robot would also succeed. This will also decrease the building time of the robot, as all the dimensions are available to the manufacturer.

2.2 Balancing Test

An important aspect of the robot is that it should be capable of balancing itself on a transmission line cable. Thus a testing rig will be constructed to simulate a transmission line. The robot will be placed on the line and see if it is capable of keeping its balance. If the robot keeps its balance different angles will be tested to see if the robot can keep its balance at these angles.

2.3 Communication Test

As this is just a prototype, the robot will need commands from a user on the ground. The user must be able to communicate these commands to the robot with little to no interference. The distance at which the robot will still be capable of receiving commands, how well the communication is on an open field in comparison with a crowded city area and how the robot will react if the communication link is broken should be determined.

2.4 Manoeuvrability Test

The robot must be capable of manoeuvring past certain obstacles found on a transmission line, as seen in figure 3. These obstacles were replicated and installed on the test rig’s transmission line to determine if the prototype is capable of driving past these components without damaging the components, the line or the robot.

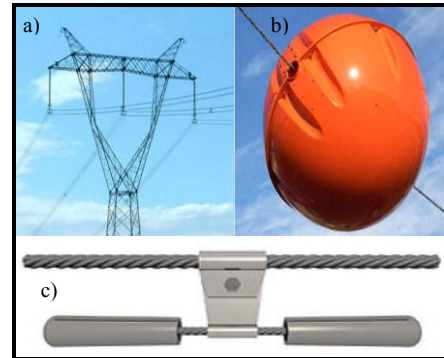


Figure 3: Obstacles found on a transmission line: a) tower structure, b) visibility marker and c) damper

2.5 Power Consumption Test

The battery of the robot should also be monitored. This will give the user a rough estimate of how far the robot will be capable of traveling on the line at certain speeds. The battery should also be tested to see what the amount of power is that the robot requires.

3. RESULTS

Test results demonstrate the feasibility of a project. The results obtained from the tests mentioned above, as well as some additional test results, are stated below:

3.1 Motor Results

The motors used on the robot were tested with and without a load. Their revolutions per minute (RPM) were determined to define what speed would be ideal to travel along the transmission line.

Revolutions per Minute Test: One can determine the amount of RPM of the motor by determining the amount of volts applied to the motor. The motor has a “kv” rating and this rating is used to indicate the amount of RPM that can be delivered for each volt sent to the motor. The results that could be acquired from a 4 cell Li-Po battery can be seen in table 1.

Table 1: Revolutions per minute per volt

Volts (V)	RPM
1	620
3	1860
5	3100
7	4340
9	5580
11	6820
13	8060

No Load Test: Tests were done on the motor whilst there was no load acting in on to the motor. The current was measured to determine the amount of power that will be delivered to the motor. The results were taken before

start-up, during start-up and during the running phase, after the current stabilized. The results can be seen in table 2. The tests were done whilst only the ESC (Electronic Speed Controller), receiver and the motor was connected to the battery.

Table 2: No load testing results on motor

Motor Status	Current (A)
Not Active	0.13
Start-up	4.14
Running	0.68

From these results one can see that the starting phase takes a lot of current, as does any motor at start-up. The main result is the current during the running phase. The motor was operated at quarter throttle, this means at a voltage value of 3.7 V. Taking this voltage value, it can be used to determine the RPM at which the motor was turning and the results of the RPM was 2294 RPM. The total power being dissipated, through the motor and ESC, during the running phase can be calculated using the volts needed to drive the motor and the current being dissipated to make the motor turn. To get the total power, the voltage and current, mentioned above needs to be multiplied with one another. The result for the no load running phase was 2.516 W.

Load Test: Tests were done on the motor whilst a load was acting in on to the motor. The current was measured to determine the amount of power that the motor was dissipating due to the increased load. The load placed on the motor was more than the load it would face on the transmission line. The results were taken before start-up, during start-up and during the running phase, after the current stabilized. The results can be seen in table 3. The tests were done as only the ESC, receiver and the motor was connected, whilst experiencing a load.

Table 3: Load testing results on motor

Motor Status	Current (A)
Not Active	0.13
Start-up	6.69
Running	3.13

From these results one can see that the starting phase takes a lot of current. The main result is the current during the running phase. The motor was operated at quarter throttle, this meaning at a voltage value of 3.7 V.

Taking this voltage value, it can be used to determine the RPM at which the motor was turning and the results of the RPM was 2294 RPM. The total maximum power being dissipated, through the motor and ESC, during the running phase can be calculated by using the volts needed to drive the motor and the current being dissipated to make the motor turn. To get the total power, the voltage and current, mentioned above needs to be multiplied with one another. The result for the full load running phase was 11.581 W.

3.2 Battery Results

The battery can be seen as the heart of the project, as it is the power source to all the crucial elements inside the robot. If the battery is dead, nothing could work, thus knowing how long the battery would last could ensure

that the project would stay running as long as possible. Important factors would be the life span of the battery with the components connected to it as well as the time it will take to recharge the battery.

Battery Discharge Test: An important factor to keep in mind is that with a Li-Po battery, the voltage value should never drop below 2.5 V or else one risks the chance of damaging a cell, causing an unbalanced effect inside the battery and in the end damaging the whole battery. ESC cuts of the power to the motors as soon as the voltages are too low for further operation, ensuring that the user does not discharge the battery past the 2.5 V level.

To determine how long it will take before the battery is fully discharged. The amount of power needs to be determined. The power needed to run the motors have been calculated in the motor test section. By using the results obtained for the running phase of both no load and full load, the following results can be obtained, as displayed in table 4.

Table 4: Discharge rate for the Nano-tech 4 cell 4000 mAh Li-Po battery

Load Type	Operating Time (min)
No Load	176.47
Load	38.34

From this result, it can be seen that at full load, the system can be operated longer than half an hour, but as this is at the maximum load the motors would endure, the life cycle of the battery would increase. From this statement, the result would be anything between 38.34 min and 176.47 minutes.

Battery Charge Test: Due to the fact that the battery has a rated capacity of 4000 mAh, the battery can be recharged at a minimum rate of 4 amperes and a maximum of 10 amperes. It is important to use a Li-Po compatible charger with balancing capabilities to ensure even and balanced charging or else one runs the risk of damaging the battery.

The power capability of the charger will determine the time it would take to recharge the batteries, as will the amount of current used to charge the batteries. If a 50 W charger is used at a capacity of 4 ampere's, the batteries would take an hour to charge to full strength. As the batteries have a capacity rating of 25 A to 50 A, one could charge the batteries at a higher capacity. Thus by charging the batteries at a capacity of 10 A would state that the batteries will be recharged in 20 – 30 minutes.

3.3 Chassis Results

The chassis is the key element for the project, without it working properly, the components such as the monitoring system would be of no use. Thus the chassis should be stable, balanced and importantly not be too heavy. If the chassis pass all these criteria, the robot will be capable of functioning as required.

Balancing Test: The first test will be to see whether the robot could balance itself on the test rig transmission line. This determined whether the robot had a lower centre of gravity than the transmission line as well as how balanced

the electronic layout was inside the chassis. Figure 4 shows the result for the balancing test.

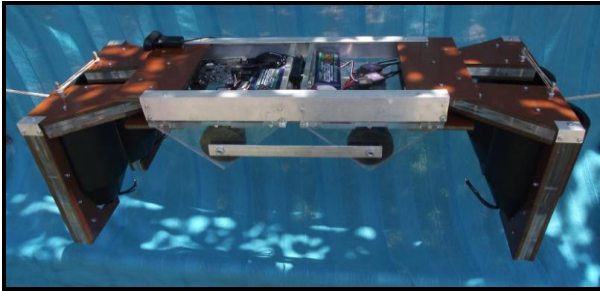


Figure 4: Robot balancing on transmission line

The results are clear to see that the robot is capable of balancing itself on the transmission line without any problems. The wheels have enough weight to ensure that the robot has a lower centre of gravity than the centre of gravity of the transmission line. Thus the robot is balancing itself without any problem.

robot needs to be as light as possible, nothing more than the average weight of an adult male [1]. People are used to inspect the transmission lines inside an isolated structure. The structure helps the person to crawl along the wire to inspect for any problems that could occur on the transmission line.

The robot was placed on a scale to determine its weight. The robot weighed in at 24 kg with all the components inside the chassis. This states that the robot is indeed lighter than the average male adult and should not pose any risk of causing a short circuit on the transmission line.

Manoeuvrability Test: As the robot will be traveling along a transmission line, it will encounter certain obstacles found on the line. These obstacles need to be crossed without the robot losing its balance. Firstly the robot needs to be able to cross the tower structure, as this is the obstacle that it will have to cross the most on its journey. Figure 5 shows how the robot crosses the



Figure 5: Robot balancing on transmission line

Tilting Test: To be sure that the robot would stay balanced through the tests, a tilting test was conducted to see whether the robot could rectify itself if it should get tilted via the wind or an obstacle on the line. A test was done with and without the components to see at what angle it stopped rectifying itself. The results from the test can be seen in table 5.

Table 5: Tilting angle rectifying test results

Angle (degree)	Without components	With components
10	Balanced	Balanced
20	Balanced	Balanced
30	Balanced	Balanced
40	Balanced	Balanced
45	Balanced	Unbalanced
50	Unbalanced	Unbalanced

With the results shown in the table above, one can clearly see that the components do have an impact on the stability of the robot. The layout of components is near optimal as the difference in angle between the chassis with components and the chassis without is only in the region of 5 degrees. This states that if the wind should tilt the robot, it can be tilted up to ± 40 degrees without it losing its balance.

Weight Test: The weight of the robot is crucial, as it cannot make the wire droop by more than two meters whilst it is running on it. If the earth wire on the transmission line should droop more than two meters, it could cause an arc between the phase lines and the earth wire and thus causing a short on the line [1]. Thus the

transmission line tower.

From this figure it can be seen that the robot has no trouble crossing the tower and continuing its journey along the transmission line. The long vertical wheels aid the crossing phase as it keeps gripping onto the wire and thus keep the robot stabilized through the whole process.

The dampers found on the transmission line the robot poses no threat to damaging it, as the robot has a big surface that will pass over it. The high visibility markers were not tested due to the fact that the robot still had some balancing issues while driving on the test rig transmission line, but in theory it would be capable of manoeuvring past it as the markers are round. The wheels have been designed to accommodate for the markers shape, it will aid the robot in maintaining its stability over the obstacle.

3.3 Communication Results

To ensure that the robot can be in communication with the user in certain areas where the user can not follow the robot, such as in mountain or certain rural areas, it would be ideal that the robot can be controlled over a certain distance and how it will react to the interference caused by the transmission line itself. This would aid the user and lower the risk of harming the environment or to have the risk of an injury during the monitoring process.

Communication Distance Test: The robot's communication distance was tested, as well as what happens if the communication was not possible. First the distance test was performed. The results from this test can be seen in table 6, where indoor represents a building

crowded environment and outdoor represents open spaces. The test was done to see if the receiver registered the command at that specific distance. From the results one can see that the remote control is much more efficient in open areas than in crowded areas with large buildings that can block the signal.

Table 6: Communication distance test

Distance (m)	Indoor	Outdoor
500	Received	Received
700	Received	Received
900	Received	Received
1000	Fail	Received
1200	Fail	Received
1500	Fail	Received
1800	Fail	Fail

The next test was to see what would happen if the robot did not receive any form of communication from the user. This was tested by running the motors at quarter throttle for a few minutes and then switching of the controller. This simulated the loss of signal between the robot and the user. As soon as the signal was broken, the motors stopped spinning. This is caused due to a fail-safe programmed into the receiver. The receiver registers the input commands from the user. These commands are sent to the ESC via an analogue format.

The ESC processes these commands and controls the motor to these values given. As soon as the signal gets lost, the receiver will stop receiving commands, thus causing it to send a zero value to the speed controllers, causing the motors to stop.

Communication Interference Test: The robot’s communication module was tested near a transmission line to determine if the line would distort or interfere with the communication signal between the robot and the user. To test this possibility a quad-copter was used to fly above a transmission line for a while. The quad-copter used to test this theory is shown in figure 6a. The result of the test can be seen in figure 6b where the quad-copter is flying over the transmission line and still responding to the commands of the user.

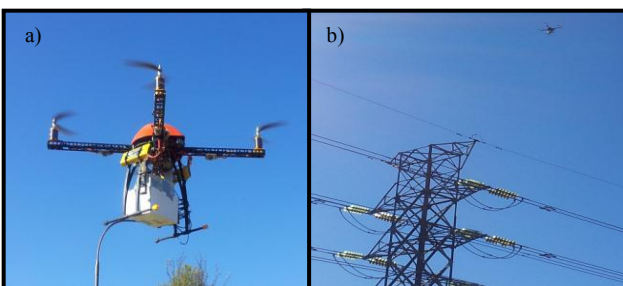


Figure 6: a) Quad-copter used for communication test.

b) Quad-copter flying over transmission line

4. RECOMMENDATION & FUTURE WORK

The materials used to build the robot is sufficient for a prototype, but for the real project aluminium or carbon-fibre should be used to ensure that the robot has a lightweight, very strong structure and can serve as an

isolator between the electronics and the magnetic fields created by the transmission lines. By automating the whole system, the project could be benefited as it would reduce even more costs in the future, due to the fact that human control will be vastly limited.

An electronic speed controller with the ability to reverse would also be a good addition to the electronics, thus the robot would be able to reverse if the operator would want to inspect an area that the robot already passed. By adding geared motors will ensure better propulsion capability for the robot on the transmission line as well as better balancing capability. A means to recharge the batteries can also be found to keep the batteries charged and ensuring a longer production time.

A mechanism can be designed to aid the robot in certain areas where the robot has to go around a bend due to the nature of the transmission line. This mechanism can also be used to ease the process of manoeuvring past obstacles on the transmission line. A control system can be installed to ensure that the robot will always keep its balance, no matter the circumstances. It is also recommended that the chassis is built more streamlined to ensure that the robot does not get destabilized due to the weather. The chassis should also be made weatherproof to withstand all the elements that occur in South Africa and any country that would use this project to monitor their transmission lines. In future the robot’s size can be increased to house other types of monitoring systems, such as the LiDar system that Eskom uses with their helicopter inspections.

The robot can be replaced by an unmanned aerial vehicle (UAV) that can be flown over the transmission line to inspect the lines, thus replacing the need for the aerial inspections and the ground inspections. The UAV would be capable of checking the entire transmission line at any point. The UAV can either be a small electronic quad-copter, as they are more stable than normal radio controlled helicopters, or a drone type of plane. These UAV’s should also be automated or a dedicated controller should be appointed to inspect the transmission lines with it.

5. CONCLUSION

Inspecting the transmission lines are a costly affair, thus by building a robot to run on the transmission lines would greatly reduce these costs. The robot will need to be designed in such a manner that it would satisfy all the criteria’s stated to certify that the robot could do what is expected from it. It should be capable of overcoming all the obstacles that it would encounter on the transmission line. These elements are the transmission line towers, high visibility markers and dampers.

By researching possible solutions or methods already applied to solve the problem, aids one in discovering an alternative method to solve the problem. Also by knowing different solutions helps one to choose one and focus on improving it. By knowing the problem and the solution, one can start implementing the solution by determining what elements would suite the solution and why would they be a fitting choice.

After the prototype robot was constructed, it was tested to determine whether it would work or not. The first and most important test was to see whether the robot was able to balance itself on a wire. The robot had no difficulty balancing itself on the wire, and so that test was passed.

The next test was to see how far the robot could be tilted without losing its balance. The robot was tested with and without its components to see how it would react. The difference in angle between the two tests was ± 5 degrees, as the chassis with components could be tilted up to ± 40 degrees without any problem. The robot passed the tilting test better than expected.

The weight of the robot also plays an important role in the balancing characteristics of the robot. By making the robot heavier at the bottom ensures that the robot has a lower centre of gravity than the wire it will be traveling along. By making the robot heavy also poses the risk of creating a short circuiting arc between the earth wire and the phases. Due to the fact that the robot weighs only 24 kg, it would not hold any risk of damaging any element found on the transmission line.

The robot also had to be tested to see whether it was capable of manoeuvring past obstacles found on a transmission line. First the robot was tested to see if it was capable of crossing over a transmission line tower, the robot did so successfully. Next it had to cross over a simulated damper mechanism, the robot crossed over it without damaging the unit. Next the robot had to cross over a suspended high visibility marker on the transmission line. The robot had some difficulty in passing this obstacle but was still able to pass it successfully. The difficulty in passing the visibility marker is the fact that the robot has to open its wheels to pass it, causing a slight disturbance in the balance of the robot.

The communication tests were done to see how far the robot would be able to be operated, by the user, and what would happen if it would go out of the communication range. So the first test was done to determine the distance that the robot can still receive commands from the user in dense building areas and in wide open areas, as these are the two areas that transmission lines are normally located. The communication distance was a lot farther for the open area than for the crowded area, this is due to the fact that buildings tend to block or reduce the signal power that is being transmitted from the user to the robot. By having the robot travel such a vast distance would surely reduce the chances of the user getting injured or not being able to complete the inspection process of the power lines in mountain, rural, municipal or city areas. Also the robot does not stand a chance to continue running if the communication is lost between the robot and the user, due to the fact that the robot has a fail-safe programmed into the receiver that would ensure that the robot would stop as soon as it loses communication with the user. The communication was also tested near a transmission line to determine if it would cause any interference with the communication. The result was that the line did not interfere or distort the communication signal.

To conclude this paper, the robot passed all the tests and could be a feasible solution, with some further improvements, for the monitoring problem faced by Eskom. The prototype robot is a lot cheaper to construct and to maintain than it would cost Eskom to fly their helicopter for an hour [2, 3]. The prototype robot is not the final solution but it can be seen as a solution and future work is definitely required to ensure that it would be the solution Eskom needs to reduce transmission line inspection costs.

6. REFERENCES

- [1] T. Pillay and S. Bisnath: *Fundamentals and practice of overhead line maintenance*, Eskom Holdings Ltd and Endangered Wildlife Trust, Johannesburg, 2004.
- [2] Eskom. (2012, Mar.): *Eskom's integrated report 2010. Financial results*. [Online]. http://financial.results.co.za/2010/eskom_abridged-ar2010/index.html
- [3] Eskom: *Routine inspection and maintenance of transmission lines*, Eskom, Johannesburg, TST41-637, 2008.
- [4] J. Berchtold, M. Buchel, C. Dold, W. Fischer, C. Bermes, R. Siegwart and M. Buhlinger: *Inspection of high voltage power lines – a new approach*, Autonomous System Lab, Zürich, 2006.
- [5] F. Zhang, Y. Jiang, G. Liu and X Peng and H. Wang: *Development of an inspection robot for 500 kV EHV Power*, IEEE Report, Taipei, 2010.
- [6] K. Toussaint, N. Pouliot, and S. Montambault: *Transmission Line Maintenance Robots Capable of Crossing Obstacles: State-of-the-Art Review and Challenges Ahead*, Journal of Field Robotics, Vol. 26, No. 5, pp. 480-482, 2009.
- [7] N. Pouliot and S. Montambault: *Geometric design of the LineScout, a teleoperated robot for power line inspection and maintenance*, Hydro-Québec, Pasadena, CA, 2008.

EVALUATION OF RELUCTANCE SYNCHRONOUS MACHINE ROTOR TOPOLOGIES FOR POSITION SENSORLESS CONTROL

W.T. Villet * and M.J. Kamper *

* Electric machines laboratory, Department of Electrical and Electronic Engineering, University of Stellenbosch, Stellenbosch 7600, South Africa E-mail: 15053830@sun.ac.za, kamper@sun.ac.za

Abstract: Certain aspects regarding the geometry of the reluctance synchronous machine (RSM) limits the position sensorless control capability of the RSM drive. Two RSMs, which are designed for improved position sensorless control capability at zero reference current, are evaluated and compared to a standard RSM. The efficiency of these three RSM drives are evaluated and compared. The efficiency of the position sensorless controlled drives are also evaluated and compared to the efficiency of the drives when controlled with an encoder. The speed bandwidth of these three drives are investigated when controlled with an encoder and position sensorless. Thermal and efficiency evaluations are done on all three RSM drives to determine if the position sensorless control methods cause excess losses and i.e. heat transfer. Finally, the harmonics of the position estimation error are evaluated to investigate and compare the position sensorless capabilities of the three RSM drives.

Key words: Reluctance synchronous machine drives, Position sensorless control

NOMENCLATURE AND DEFINITIONS

Symbols:

u, i, ψ	Voltage, current and flux linkage
R, L	Resistance and inductance
T_m	Mechanical torque
θ_r, ω_r	Rotor- angle and speed
θ_e, ω_e	Electrical- rotor angle and speed
Δ, Σ	Difference and sum

Indices:

s, r	Stator and rotor
a, b, c	Stator phase axes
α, β	Stator fixed cartesian axis
d, q	Rotor fixed direct and quadrature axes

Scalar values are written in normal letters, e.g. R or τ , vector values are written in small bold letters, e.g. \mathbf{i} or $\boldsymbol{\psi}$ and tensor matrices are written in bold capital letters, e.g. \mathbf{L} or \mathbf{T} . Subscripts describe the location of the physical quantity, e.g. R_s is the stator resistance. Superscripts specify the reference frame of the quantity, e.g. $\mathbf{i}_s^{(r)}$ is the stator current vector in the rotor reference frame. Superscript T is used to transpose a vector and superscript -1 for the inverse. The matrix \mathbf{J} is used for orthogonal rotation.

$$\mathbf{J} = \mathbf{T}\left(\frac{\pi}{2}\right) = \begin{bmatrix} 0 & -1 \\ 1 & 0 \end{bmatrix}$$

\mathbf{J} is the vector equivalent to the complex operator j . Estimate quantities are indicated with a hat, e.g. $\hat{\theta}_e$.

1. INTRODUCTION

An increased percentage of generated electric power is converted to mechanical power by means of electric machines. This has developed a need for energy efficient variable speed drives. Lately the reluctance synchronous machine (RSM) has been identified as a possible alternative to induction- and permanent magnet (PM) machines. This machine has no rotor windings or permanent magnets, making manufacturing easy and affordable. Investigations made by Vagati [1] [2] and Kamper [3] showed that the RSM is comparably efficient when compared to an induction machine (IM) under closed loop control.

A position sensor is necessary to implement proper closed loop control by means of field oriented control (vector control). Position sensors are expensive, fragile and increases the complexity of the control unit. Two methods of position sensorless control for RSM drives are proposed in [4] and [5]. A hybrid position sensorless control method which combines the methods described in [4] and [5] is proposed in [6]. It is shown in [4] that a lack of inductance saliency at small reference current vectors limits the position sensorless capability of the drive. Without a sufficiently large enough inductance saliency it is not possible to track the electrical rotor angle with the position sensorless control method proposed in [4].

Two RSM rotor configurations are presented as an alternative to the RSM rotor used in the investigations of [4], [5] and [6]. The two alternative RSM rotors have a larger inductance saliency at small current vectors.

One lingering question that still exists regarding position sensorless control is the performance of the position sensorless controlled drive. Can the position sensorless controlled drive be compared to normal field oriented

control with an encoder? The aim of this work is to evaluate and compare different aspects of these three drives with regards to the position sensorless control method proposed in [6].

2. RELUCTANCE SYNCHRONOUS MACHINE

The three evaluated RSMs have two pole pair rotors with distributed stator windings. The q-axis of the RSM is aligned with the flux barriers and the d-axis, at an angle of 45° , is aligned with the maximum permeance of the steel. The maximum torque per ampere current angle of the RSM is at 60° . The RSM can be described by the stator voltage equation of (1). The vector product of the flux and the current produce the torque of the machine as given in (2).

$$\mathbf{u}_s^{(s)} = R_s \mathbf{i}_s^{(s)} + \frac{d\psi_s^{(s)}}{dt} \quad (1)$$

$$T_m = \frac{3p}{2} \mathbf{i}_s^{(r)T} \mathbf{J} \psi_s^{(r)} = \frac{3p}{2} (\psi_d i_q - \psi_q i_d) \quad (2)$$

The rotor configuration of RSM used in [4–6] is as shown in Figure 1(a). To adhere to convention as chosen by [7], this will be referred to as the lateral rib configuration. As stated above, it was found in [4] that this machine has a very small inductance saliency at zero reference current. The inductance saliency of the machine is defined as:

$$\Delta L = \frac{L_d - L_q}{2} \quad (3)$$

where

$$L_d = \left. \frac{\partial \psi_d}{\partial i_d} \right|_{i_q=0}, \quad L_q = \left. \frac{\partial \psi_q}{\partial i_q} \right|_{i_d=0} \quad (4)$$

The high frequency injection (HF) position sensorless control method tracks the inductance saliency of the machine at standstill and low speeds [6]. It is not possible to control the drive with the HF injection position sensorless control method if the inductance saliency is too small [4].

Figure 1(b) shows the proposed alternative RSM rotor design for high inductance saliency at small current magnitudes. To adhere to convention this will be referred to as the ideal rotor configuration. To reduce the torque ripple of the RSM, a third RSM rotor is built with a skewed ideal rotor configuration. All three rotor configurations start out with identical rotor lamination geometries. Two stacked rotors (skewed and unskewed) are filled with an epoxy-resin where after the ribs are removed with a CNC machine to form the geometry of Figure 1(b). The unskewed ideal rotor is shown in Figure 2 with its ribs removed.

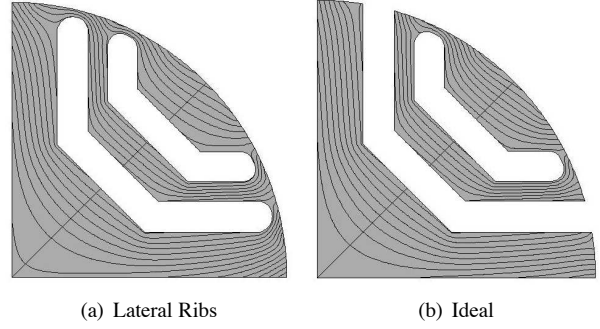


Figure 1: (a) Lateral rib (machine 1)- (b) and ideal rotor (machines 2 and 3)



Figure 2: Ideal rotor (machine 2) filled with epoxy.

All three machines have identical stators with distributed winding configurations. The rated current for all three machines are 3.5 A rms. The rated speed for all three machines are 1500 RPM. The position sensorless control method used is the one proposed in [6]. The details of this method are not discussed in this work.

The three RSM topologies will be referred to in the rest of this work as follows:

- Machine 1 Lateral rib rotor RSM drive
- Machine 2 Unskewed ideal rib rotor RSM dirve
- Machine 3 Skewed ideal rib rotor RSM drive

3. EFFICIENCY EVALUATION

The three RSM drives are compared in terms of their input- and output power as well as their shaft power in Tables 1-3. Measurements are made with an encoder and without (position sensorless). The tests are performed on a test bench where the RSM is connected via a torque sensor to an induction machine (IM). A digital torque sensor is used to measure the shaft power. The test setup is shown in Figure 3.

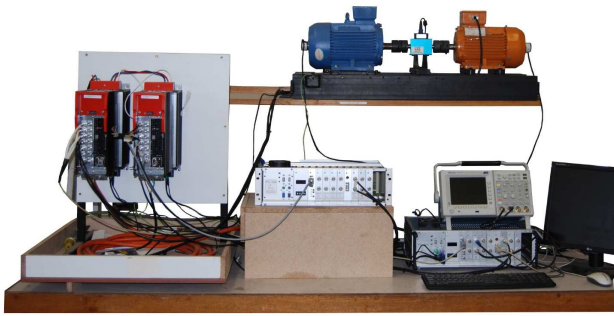


Figure 3: Test bench with IM on the left and RSM on the right [6].

The rating of the two DC link connected drives are 7.5 kW and 5.5 kW respectively. The input and output power of the RSMs are measured with a Norma power measurement device. The performance of the drives are evaluated at rated speed. The shaft power developed by machine 1 when controlled with an encoder is taken as the “base” value to compare all three drives. The induced current of machines 2 and 3 are varied during evaluation to obtain a power rating of ± 1.147 kW.

The results in Tables 1-3 show that the losses obtained, in each drive respectively, when controlled with a sensor are almost identical to the losses obtained when controlled position sensorless. These results then indicate that the position sensorless control of RSM drives does not result in additional losses. The importance of these result should not be underestimated. Misalignment can occur between the actual d-axis- and the estimated d-axis of the RSM if the position sensorless control method is inaccurate. This will result in the drive not operating at its maximum torque per ampere angle. Furthermore these results show that machines 2 and 3 have a higher torque per ampere rating than that of machine 1.

The efficiency comparison of the three drives are shown in Table 4. These results show the efficiency of each individual drive is almost identical when controlled position sensorless and with an encoder. These results also show that machines 2 and 3 are slightly more efficient than machine 1.

4. BANDWIDTH EVALUATION

The dynamic behaviour of the RSM drive is determined by it’s maximum speed bandwidth. To investigate the

Table 1: Measurements of lateral rib rotor RSM (machine 1) drive.

	Current [p.u]	Input/ Output Power	Shaft Power	Losses
Encoder	1.0	1.357 kW	1.147 kW	0.21 kW
Sensorless	1.0	1.355 kW	1.142 kW	0.21 kW

Table 2: Measurements of lateral rib rotor RSM (machine 2) drive.

	Current [p.u]	Input/ Output Power	Shaft Power	Losses
Encoder	0.91	1.348 kW	1.156 kW	0.19 kW
Sensorless	0.91	1.36 kW	1.159 kW	0.20 kW

Table 3: Measurements of lateral rib rotor RSM (machine 3) drive.

	Current [p.u]	Input/ Output Power	Shaft Power	Losses
Encoder	0.93	1.355 kW	1.153 kW	0.20 kW
Sensorless	0.93	1.361 kW	1.158 kW	0.20 kW

Table 4: Efficiency comparison of the three RSM drives

Machine	1	2	3
Encoder	84.52%	85.76%	85.09%
Sensorless	84.28%	85.22%	85.08%

speed bandwidth of the three RSM drives, sinusoidal speed reference signals are applied to the drive at no load while in speed control. The sinusoidal speed reference signal has an amplitude of ± 1500 RPM. The frequency of the speed reference signal is increased until the drive is unable to track the reference speed. This is followed by a decrease in the sinusoidal speed reference amplitude until the drive is able to completely track the reference speed. This process continues until it is impossible for the RSM drive to track the reference speed.

Figure 4 compares the bandwidth of the three RSM drives when controlled with an encoder and Figure 5 with position sensorless operation. Figure 4 shows that the bandwidth of all three RSM drives are very similar. Figure 5 shows that although machines 2 and 3 have a limited bandwidth at high frequencies, it can deliver unity response at higher speed reference frequencies than that of machine 1.

The bandwidth of the unskewed ideal rib rotor RSM with position sensorless control is more or less the same as when controlled with an encoder, up until 1.8 Hz. Figure 5 shows that the skewed ideal rib rotor RSM has a smaller bandwidth when controlled position sensorless than its unskewed counterpart. It can thus be concluded that some of the position sensorless controlled drive’s bandwidth is sacrificed when the rotor is skewed.

5. THERMAL EVALUATION

The three RSM drives are subjected to thermal tests while controlled with a position sensor and position sensorless. All three machines are subjected to rated conditions for an hour. The main objective of these tests are to determine if there is a noticeable difference in temperature when

the drive is operated position sensorless, compared to operation with an encoder. The secondary objective is to determine if the epoxy-resin and removal of the ribs causes a noticeable difference in rotor heat. It might be that the removal of the ribs influence the way heat is transferred within the machine.

The casing of the machine is enclosed, thus the closest point to measure the rotor temperature is at the drive end of the shaft. The temperature difference of the measured results of the shaft are shown in Figure 6. The abbreviations in Figure 6 are: "SC" = Sensored control and "SLC" = sensorless control. Figure 7 shows the temperature difference of the measured results of the temperature increase over time on the casing of the RSMs.

Figure 6 indicate that the shaft of the position sensorless controlled drives are slightly hotter than when controlled with an encoder. The difference in temperature however

is very small. The results in Figure 6 also show that the shaft of machine 2 is slightly cooler. Again the difference in temperature when compared to the other two machines is very small. Figure 7 show that the temperature rise on the casings are almost identical during all 6 cases.

6. HARMONIC EVALUATION OF THE POSITION ESTIMATION ERROR

During position sensorless control the position sensorless control method makes position estimation errors. This can be defined as:

$$\theta_{error} = \theta_e - \hat{\theta}_e \quad (5)$$

where θ_e is the electrical rotor position and $\hat{\theta}_e$ the estimate electrical rotor position. All three position sensorless

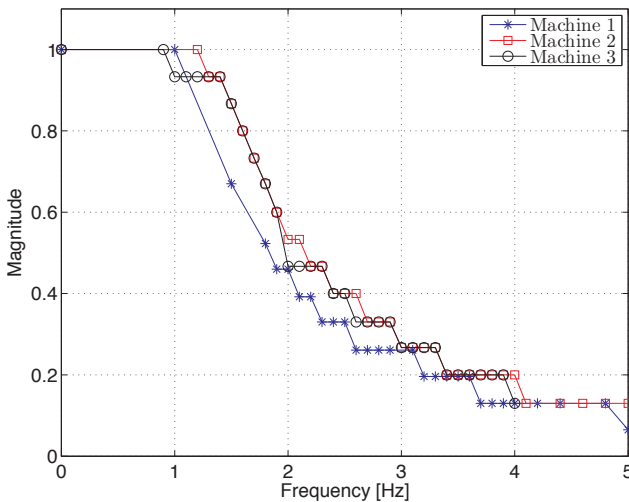


Figure 4: Measured bandwidth of RSM drives with an encoder.

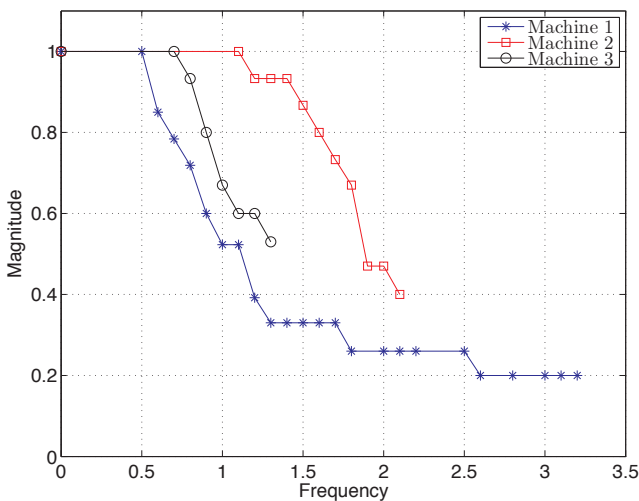


Figure 5: Measured bandwidth of RSM drives with position sensorless control.

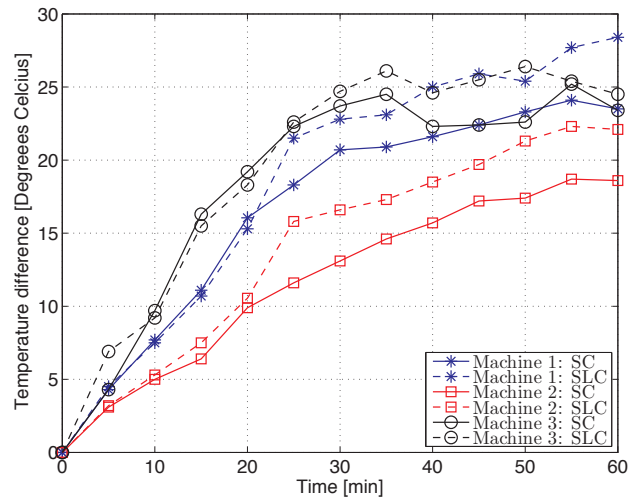


Figure 6: Measured temperature at the drive side shaft of the RSM rotor.

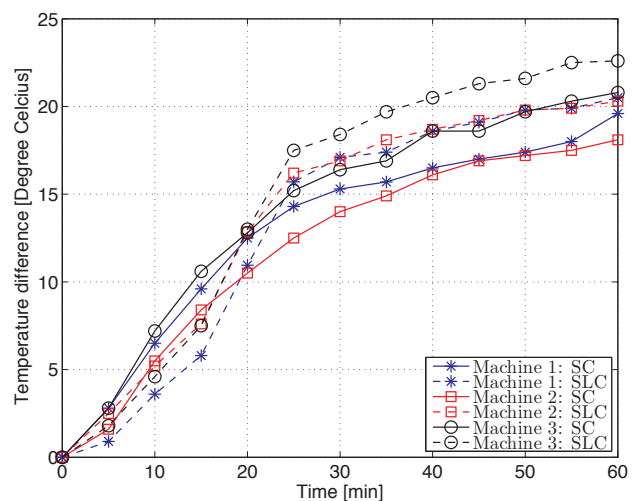


Figure 7: Measured temperature on the outside casing of the RSM.

controlled drives are evaluated with speed control at rated speed under full load. The FFT of θ_{error} under these conditions are displayed in Figure 8. As shown in [6], the fundamental saliency position sensorless control method is in control at rated speed. In [5] it is shown that the fundamental saliency position sensorless control method is dependent on a sufficiently large enough rotor speed to function properly. It is also shown in [5] that the position estimation error is related to the rotor frequency. The effect of this phenomena can be seen in Figure 8. It is clear that there are large 50 Hz harmonics present in the position estimation error of all three machines at rated conditions.

In effect the phase locked loop (PLL) of the fundamental saliency position sensorless control method proposed in [5] is fed θ_{error} , which is speed dependant. Figure 8 shows that the skewed ideal rib rotor RSM has the largest harmonic at 50 Hz and the smallest one at 25 Hz. This is due to the skewing of the rotor which reduces harmonics in the machine. This graph suggests that it is easier for the fundamental saliency position sensorless control method to track the electrical angle of machine 3 due to the reduction in harmonics in θ_{error} which is fed through the PLL. This statement is also confirmed during practical measurements of the three machines.

In a second test the position sensorless controlled RSM drives are given a speed step from 0-1500 RPM under full load. The FFT of θ_{error} of these results are displayed in Figure 9. It is shown in [6] that the high frequency (HF) position sensorless control method is in control of the drive at standstill and low speeds. As shown in [8], a HF voltage is superimposed onto the fundamental control voltage to demodulate the electrical rotor angle. The position estimation error is scaled by the magnitude of the saliency as well as the magnitude of the propagation of the injected high frequency voltage.

Figure 9 shows that θ_{error} of machines 2 and 3 have harmonics at the injection frequency of 478 Hz. The results of Figure 9 show that the injected HF signal propagates well in machine 2 due to the magnitude of the HF harmonic. It seems that the position sensorless control capability of machine 3 is less than that of machine 2, but if considered that the harmonic in the position estimation error of machine 1 is so small that it can not be displayed it is safe to conclude that machines 2 and 3 are well suited for HF injection position sensorless control.

7. CONCLUSION

Performance evaluation of the three RSM drives in Section 2 show that the two ideal rotor RSM drives produce more torque per ampere than the lateral rib rotor RSM. It is also found that the position sensorless control method does not add additional losses to the drive. The efficiency of the two ideal rib rotor RSMs are more than that of the lateral rib rotor RSM.

It is found that the speed bandwidth of the position sensorless controlled drive is sacrificed when the rotor

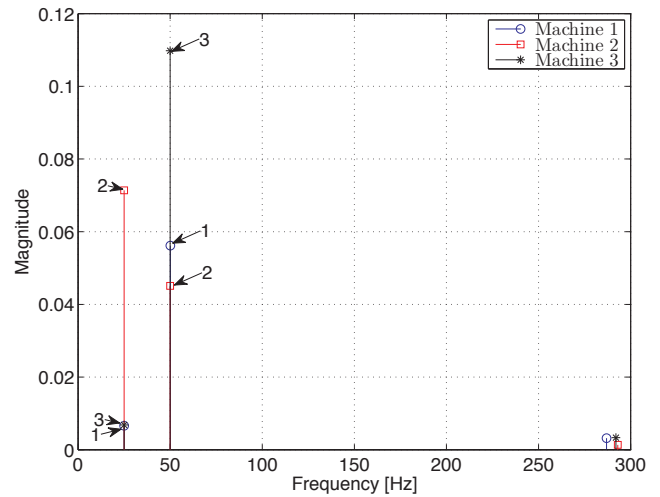


Figure 8: FFT of position estimation error signal at rated speed under full load conditions.

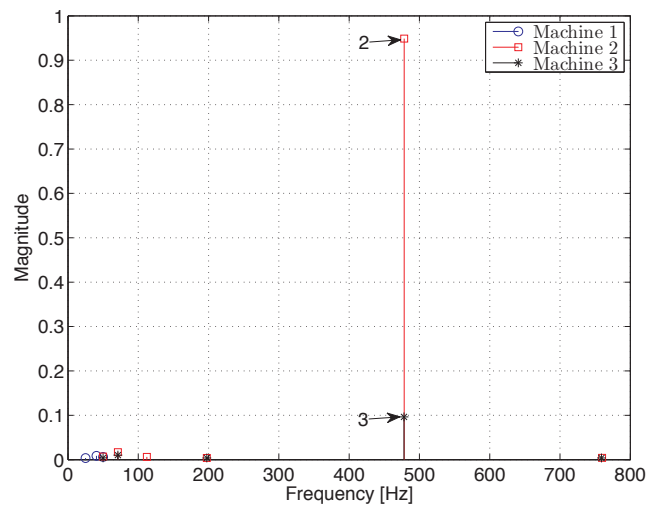


Figure 9: FFT of position estimation error signal at during a speed step of 0-1500 RPM at full load.

is skewed. Measured results show that even though the bandwidth of the position sensorless controlled skewed ideal rib rotor RSM is lower than that of its unskewed counterpart, its bandwidth is still larger than that of the position sensorless controlled lateral rib rotor RSM.

Thermal evaluation of the three RSM drives shows that there is a small temperature difference in rotor shaft temperature when the drive is controlled position sensorless when compared to temperature increase while controlled with an encoder. The temperature difference however, is not significant enough to conclude that position sensorless control causes additional heat losses. Results obtained from the thermal evaluation also indicate that the removal of the rotor ribs does not affect the temperature rise of the rotor.

Finally the harmonic evaluation of the position estimation error show that the reduction in harmonics, due to the skewing of the rotor, coupled with the removal of the ribs to create the ideal rotor RSM configuration, increases the position sensorless control capability of the drive.

sensorless control”, *Applied Power Electronics Conference and Exposition, 2008. APEC 2008. Twenty- Third Annual IEEE*, pages 879-885, Feb. 2008.

ACKNOWLEDGMENT

The electric machines laboratory (EMLab) from Stellenbosch University would like to thank the Lehrstuhl für Elektrische Antriebssysteme und Leistungselektronik from the Technical University of Munich for their participation in this project. The EMLab would also like to thank them for opening up their laboratory facilities towards us.

REFERENCES

- [1] A. Fratta and A. Vagati: “Synchronous reluctance vs induction motor: a comparison”, *Proceedings Intelligent Motion*, pp.179-186, April 1992.
- [2] A. Vagati: “The synchronous reluctance solution: a new alternative in AC drives”, *20th International Conference on Industrial Electronics, Control and Instrumentation, 1994. IECON '94*, pp.179-186, Sep 1994.
- [3] M.J. Kamper, F.S. Van der Merwe and S. Williamson: “Direct finite element design optimisation of the cageless reluctance synchronous machine”, *Energy Conversion, IEEE Transactions on*, pp.547-555, Sep 1996.
- [4] W.T. Villet, M.J. Kamper, P. Landsmann and R. Kennel: “Evaluation of a simplified high frequency injection position sensorless control method for reluctance synchronous machine drives”, *6th IET International Conference on Power Electronics, Machines and Drives (PEMD 2012)*, March 2012
- [5] P. Landsmann, R. Kennel H.W. de Kock and M.J. Kamper: “Fundamental saliency based encoderless control for reluctance synchronous machines”, *Electrical Machines (ICEM), 2010 XIX International Conference on*, Sept. 2010
- [6] W.T. Villet, M.J. Kamper, P. Landsmann and R. Kennel: “Hybrid Position Sensorless Vector Control of a Reluctance Synchronous Machine through the Entire Speed Range”, *15th International Power Electronics and Motion Control Conference, EPE-PEMC 2012 ECCE Europe, Novi Sad, Serbia*, September 2012
- [7] N. Bianchi and S. Bolognani: “Influence of rotor geometry of an interior PM motor on sensorless control feasibility”, *Industry Applications Conference, 2005. Fourtieth IAS Annual Meeting. Conference Record of the 2005*, October 2005
- [8] D. Raca, P. Garcia, D. Reigosa, F. Briz, and R. Lorenz: “A comparative analysis of pulsating vs. rotating vector carrier signal injection-based

PERFORMANCE EVALUATION OF A CENTRIFUGAL PUMP SYSTEM UNDER VARIABLE SPEED OPERATION

C. Kühn* and P.J. Randewijk**

*Electrical Engineer at Langeberg Municipality, Ashton, South Africa Email: curren.kuhn@live.com

**Department of Electrical and Electronic Engineering, Stellenbosch University Email: pjrandew@sun.ac.za

Abstract: The aim of this research project investigates the performance of a centrifugal pump system under variable speed operation. Operating a pump under variable speed operation brings the affinity laws into play. These equations were firstly investigated before it was applied to the overall investigation of pump performance. Distinction is made between three types of systems, a system with high static head (lift system), the second system is a high loss system with no- or little static head and the third is a mixed type system. The “correct” affinity laws were then used to apply to a system with a minimum pressure requirement. The theory proved accurate and was confirmed by practical findings. It has been found that both the pump and the VSD experience a slight drop in efficiency for small changes in speed. A maximum of 5% drop occurred in the efficiency of the pump for a 30% reduction in speed. Further reductions in speed resulted in a more rapid drop in efficiency.

Keywords: Variable speed drive (VSD), pump efficiency, system curve, static head, power consumption.

1. INTRODUCTION

Many aspects of irrigation pumping systems consist of compromises or trade offs between first costs of the system and the running costs. Purchasing cheaper systems without considering the higher running cost is a tendency among users resulting in a widespread use of, inefficient and non cost-effective systems. In terms of running costs a significant portion of the operational cost in water distribution systems can be related to pumping [1]. Therefore, variable speed pumping has been a recent consideration with the aim of varying the duty point of the pump to match delivery rate to demand. Depending on the system characteristics, this approach can lead to considerable savings in operational costs. In particular cost reductions, where advantage can be taken of the demand variability leading to a significant decrease in energy consumption.

Pumping systems are usually designed to meet maximum design discharge which might occur just for a limited time [2]. In on-demand systems such communal water supply, there is a variation in flow and pressure as a result of seasonal changes in water requirements and human behaviour. The energy consumption of the system depends on the systems flow rate, operating pressure and the period of time the system operates. Savings can be realized by reducing these variables, either by changing the system’s characteristics or the pump’s characteristics.

2. PIPELINE SYSTEMS

The relationship between the flow in a pipeline and the head loss produced is described by the system curve of the pipeline. The essential elements to include in a system design, is the static head and the friction head.

Adding the static head to the friction head losses as the flow increases gives the total head (H) and is essentially a parabola with its origin at the value of the static head.

$$H = K_1 Q^{1.85} + K_2 Q^2 + H_s \quad (1)$$

with:

K_1 = some constant indicating the system’s resistance

Q = delivery rate in m³/h

K_2 = some constant indicating the losses due various pipe fittings

H_s = static head in m

Distinction is made between three types of systems, a system with high static head (lift system), the second system is a high loss system with no- or little static head and the third is a mixed type system [3]. These are illustrated in Figure 1. The head-capacity curve of the pipeline to which the pump is installed is called a system curve and determines the performance of the pump. In order for the pump to achieve flow the pump must overcome the opposing head represented by the system curve. The opposing head consists of static head, frictional head losses in the pipeline and the type of liquid being pumped. Static head is the difference in height of the supply and the discharge which is independent of the flow rate. Friction head refers to friction loss on the liquid being moved in the pipeline and the various pipe fittings.

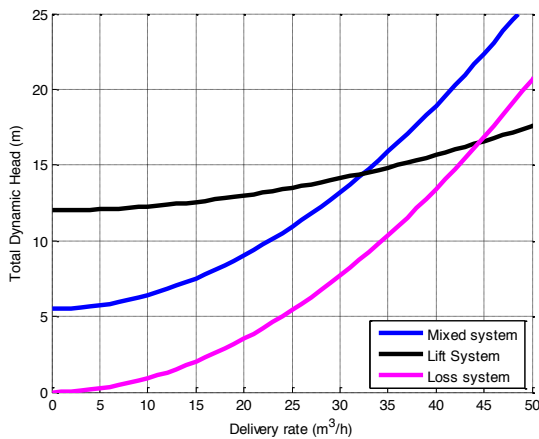


Figure 1: The three types of systems identified

The system was initially designed for a static head of 12 meters, but after applying the affinity laws for speed relating to pressure and flow rate, it was noticed that the operating region for variable speed pumping was greatly reduced. Not allowing the speed to be varied less than about 70% of the nominal speed. For the purpose of this study it was necessary to vary the speed to at least 50% of the nominal speed. To achieve this, the static head was lowered to 5.5 meters and allowed the speed reduction to reach 55%.

3. SYSTEM DUTY POINT

Pump performance curves are usually determined at a constant impeller rotational speed by varying the flow (Q) by means of throttling. These characteristic curves are plotted as head (H) against flow where the head or pump pressure is measured in meters (m) and the flow is measured in cubic meters per hour (m^3/h). The head-capacity curve of the pump and the system curve are plotted on one graph and the operating point of the pump is found at the intersection of these plots, Figure 2.

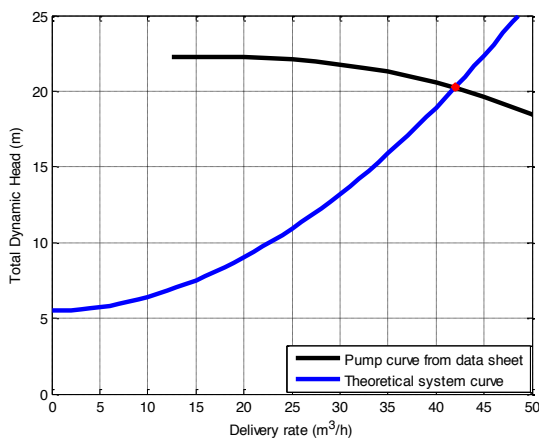


Figure 2: Pump operating point in a given system

The intersection is the head and capacity at which the pump would operate at a certain shaft speed in a given piping system. Distinction is made between three kinds of power, supplied power from an external source to the motor and controller denoted P_{in} , shaft power from the motor to the shaft denoted P_{shaft} , and hydraulic power imparted from the impeller to the fluid denoted P_{hyd} . The hydraulic power can be calculated at the pump's operating point by,

$$P_{hyd} = \frac{Hg\rho Q}{3600} \tag{2}$$

with:

H = head in m

Q = delivery rate in m^3/h

ρ = fluid density (998.2 kg/m^3 at 20°C for water)

g = gravitational constant 9.81 m/s^2

The power required to drive the pump shaft at the operating point can be expressed as

$$P_{shaft} = \frac{P_{hyd}}{\eta} \tag{3}$$

with η being the efficiency of the pump at the duty point.

3.1 Changing the System Duty Point

When varying the speed of a pump the basic system characterisation stays unaffected with only the pump characteristics changing. Changing the impeller rotational speed is accomplished by changing the drive motor's shaft speed, usually by means of a Variable Speed Drive (VSD) and brings the affinity laws into play. This is a set of equations that can be applied to estimate the performance of the pump under variable speed operation. During variable speed operation, both system head and flow rate reduces for a lower drive speed which results into lower power consumption. These laws states as follows:

- Flow is proportional to speed ($Q \propto N$),
- Head is proportional to the square of the speed ($H \propto N^2$),
- Required shaft power is proportional to the cube of the speed ($P \propto N^3$).

It has become somewhat of a “fashion” to install VSD's into pumping systems, due to the third affinity law;

power is proportional to the cube of the speed. A common first impression is that centrifugal pumps are more efficient at lower speeds, which is not necessarily true. These laws do not make any statement of the efficiency of the pump. Understanding these laws and why they work is key in applying them correctly.

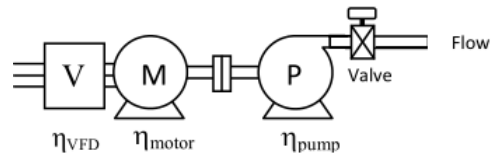


Figure 3: Pump system block diagram [1]

4. AFFINITY LAWS

In order to use the “correct” affinity laws to estimate the power using the flow rate, some adjustments needed to be made to the power equation for systems with static head [4].

$$\frac{P_2}{P_1} = \left[\left(1 - \sqrt{\frac{H_{min}}{H_N}} \right) \frac{Q_2}{Q_1} + \sqrt{\frac{H_{min}}{H_N}} \right]^3 \quad (4)$$

Where:

P = required power in W

H_{min} = minimum system head (static head) in m

H_N = duty point total head in m

Equation (4) incorporates the minimum pressure requirement in a given piping system for estimating the power requirements at a given duty point. It can be seen that as H_{min} decreases towards 0, equation (4) becomes that of the original affinity laws stated earlier.

5. SYSTEM MODEL

Discussing the efficiency of centrifugal pumps revolves around four efficiencies [1],

- Hydraulic efficiency,
- Mechanical efficiency,
- Drive efficiency,
- The overall system efficiency which is the product of the above.

Mechanical efficiency is a measure of the losses between the drive shaft and shaft input at the impeller and relative to other losses mechanical losses are small and are usually ignored [5]. Drive efficiency refers to the effectiveness of the pump driver which includes the motor and the VSD. Thus, the total drive efficiency will be the product of the motor efficiency and the VSD’s efficiency, Figure 3.

6. THEORETICAL ESTIMATES OF COMPONENT EFFICIENCY

6.1 VSD

The efficiency of the VSD is based on the research done by the Irrigation Training and Research Center [6]. The study concluded an efficiency of 95% for a VSD manufactured by Danfoss.

6.2 Three-phase induction motor

Determining the motor’s efficiency was done using the method of constant volts-per-hertz (V/f). The input voltage to the motor is adjusted proportionally with the input frequency, keeping the flux constant in the machine. The model of Figure 4 was used with the accompanied equations. The motor parameters were obtained using the Automatic Motor Adaption (AMA) feature of the Danfoss VLT® FC302 Automation Drive. The parameters are shown in Table 1.

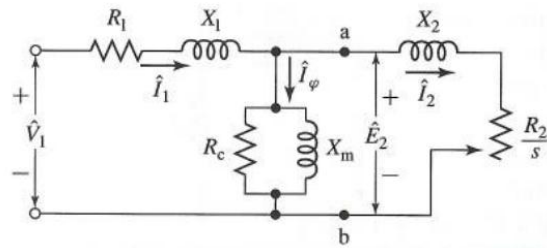


Figure 4: Per phase induction motor equivalent circuit [7]

Table 1: Induction motor parameters

R_1 [Ω]	X_1 [Ω]	R_2 [Ω]	X_2 [Ω]	R_c [Ω]	X_m [Ω]
2.05	3.04	1.85	3.04	1466	60

Using Table 1’s values the model was simulated to obtain the efficiency of the induction motor under variable speed operation.

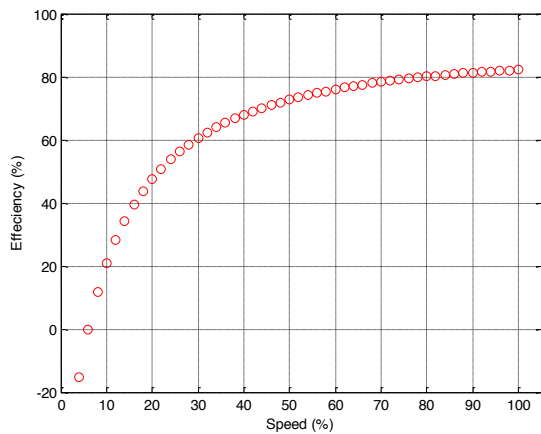


Figure 5: Induction motor efficiency for constant V/f control

It can be seen that the motor efficiency is about 82.25% at nominal speed and decreases slightly towards a 74.8% efficiency at 55% speed. The motor nameplate rating indicates an efficiency of 83% at full speed which compares well with the result obtained. It is noted that the drop in motor efficiency becomes more rapid for speeds lower than 60%.

6.3 Pump

Using the affinity laws, Figure 6 was obtained. Table 2 contains the data obtained from Figure 6. The hydraulic power is calculated at each duty point using equation (2) and will further be used to determine the pump's efficiency.

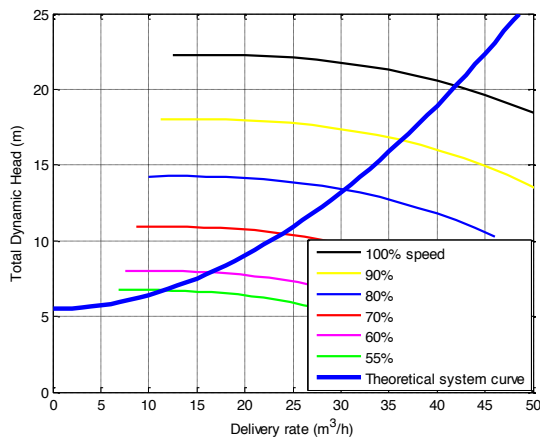


Figure 6: Estimate duty points for various speeds

Table 2: Theoretical estimates at various duty points

Speed <i>N</i> (%)	Duty point		
	Flow <i>Q</i> (m ³ /h)	Total Head <i>H</i> (m)	Output Power <i>P_{hvd}</i> (W)
100	42	20.26	2314.58
90	36	16.67	1632.38
80	30	13.41	1094.29
70	24	10.5	685.46
60	16	7.88	342.95
55	11	6.61	197.78

A complete table of the theoretical system estimates is given in Table 3.

Table 3: Complete system analysis

Speed <i>N</i> (%)	VSD	Efficiency		Power (W)	
		Motor	Pump	Shaft power	Total input
100	95	82	70	3307	4232
90	95	81	61	2673	3462
80	95	80	53	2083	2740
70	95	78	45	1540	2069
60	95	76	38	914	1266
55	95	75	35	562	791

The above table indicates a change in the pump's efficiency under variable speed operation, with a maximum drop of 9% for each 10% decrease in speed. Theoretical values indicate a drop in pump efficiency but needs to be confirmed by practical data obtained from testing the designed system.

7. PRACTICAL FINDINGS

7.1 Test Setup

Tests were conducted in a sequential manner. Starting at nominal operating speed the speed was reduced in steps of 10% of the nominal speed down to 55% speed. The total input power to the system, e.g. to the drive, was measured using a three-phase power measuring device. The drive provided a function to view the input power to the motor making it possible to determine the efficiency of the drive itself. Further readings were the flow rate, digitally displayed on the flow rate measuring device, and the pressure displayed in volts on a voltmeter. After the test readings were recorded at the duty points, the system was throttled to determine the pump curve at that specific speed. Five throttling stages were deemed sufficient for

determining the pump curve. This process was repeated at all reduced speeds. The constructed system and measurement setup are shown in Figure 7 and Figure 8 respectively. The vertical elevation (static head) between pump suction and the discharge in the top tank is 5.5 meters.



Figure 7: Constructed pump system

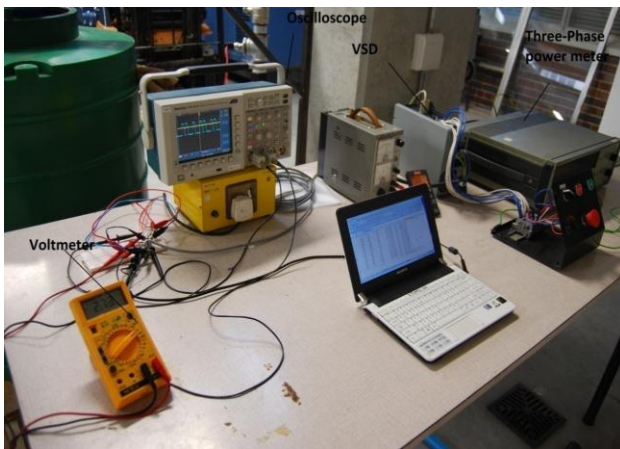


Figure 8: Test setup

7.2 Results

In Figure 9 the true pump curves are plotted with the theoretical system curve. The system was designed for the pump to operate close to its best efficiency point. It can be seen that true resistance of the system is a bit lower than the theoretical. This also explains the lower head measured at nominal speed.

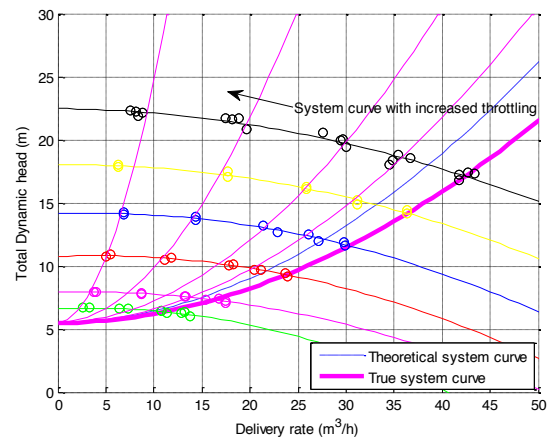


Figure 9: True measured pump curves

Also using Figure 9, a comparison of the average energy consumption between the throttled system and variable speed operation is shown in Table 4. The throttling occurs at 100% speed. The valve is first fully open and then it gets partially closed for the five different throttling stages. It can be seen that the savings on energy consumption increases for lower speed operation compared to the increased throttling. From 17.9% to as much as 64.45% energy savings occurred at reduced speeds for variable speed operation.

Table 4: Comparison of energy consumption between a throttled system and variable speed operation

Variable Speed			Throttled System		Savings (%)
Speed N (%)	Input Power (W)	Flow Q (m³/h)	Input Power (W)	Flow (m³/h)	
55	743	11.82	2090	8.34	64.45
60	960	17.54	-	-	-
70	1485	23.64	3440	19.62	56.83
80	2213	29.33	3630	30.06	39.04
90	3128	35.87	3810	34.56	17.90
100	4442	43.08	4442	43.08	0.00

7.3 Efficiency

The efficiency of both the VSD and the pump are plotted in Figure 10. It is evident that both the component's efficiencies decrease with the speed being varied. Working with the extreme values it can be seen that an efficiency drop of no more than 7% occurred for a total of three consecutive 10% reductions in speed. Below 70% speed the drop in efficiency becomes more rapid with a maximum drop of 19% occurring for the speed being reduced a further 15%. For the VSD a drop of 6% occurred for the entire speed range.

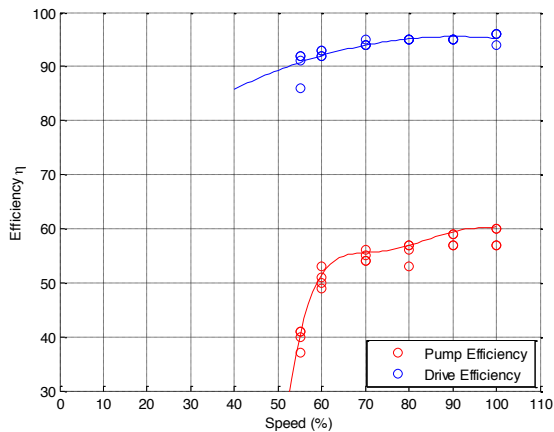


Figure 10: Efficiency plot of the VSD and pump

The average values are plotted in Figure 11 with constant efficiency lines. It is noted at nominal conditions, that the pump efficiency is about 58% instead of 70% as indicated by the pump data sheet. This can be ascribed to the drop in head measured. From Figure 11 it can be seen that as the speed is reduced the pump duty point moves from 58% constant efficiency line towards the 40% constant efficiency line. The drop in efficiency can be seen to be more rapid for speeds lower than 70%.

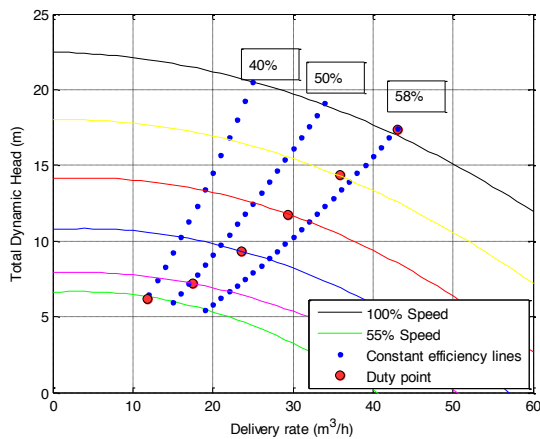


Figure 11: Pump operation with constant efficiency lines

8. CONCLUSION

Having considered the theoretical calculations and the practical findings on the pump and VSD efficiency, it can be concluded that a definite change in efficiency occurs under variable speed operation. The change in pump efficiency is mainly because of the system duty point movement, with VSD losses and motor duty point movement also having an effect. Practical findings in

pointed out that over small variations in speed, a slight reduction in the pump's efficiency occurred. An approximate 5% drop in pump efficiency takes place for a 30% decrease in speed. However, at a speed lower than 70% a more rapid drop in efficiency occurred. At 70% speed a considerable amount of power can be saved. This being the case, variable speed pumping can be highly beneficial for on demand systems where demand varies with time and behaviour.

The system's efficiency increases as the speed is reduced accompanied by a reduction in flow. For systems with low- or no static head, benefits from VSD's thus seem promising. But for systems with high static head the benefits of VSD's is greatly limited. A proper analysis on the system should be done to determine the viability of a VSD controlled pumping system. Also, if energy efficiency is a major concern, then a throttling system would be out of the question.

The authors would like to thank Eskom for the financial support for this research via their TESP program.

9. REFERENCES

- [1] A. Marchi, A. Simpson and N. Ertugrum, "Assessing variable speed pump efficiency in water distribution systems", *Drink. Water Eng. Sci.*, Vol. 5, pp.15-21, 2012
- [2] F. Barutcu, N. Lamaddalen and U. Fratino, "Energy Saving For A Pumping Station Serving An On-Demand Irrigation System", *Irrigation Science*, Vol. 30, Issue 2, pp.157-166, 2012
- [3] Wallbom-Carlson, "Energy Comparison, VFD vs. On-Off Controlled Pumping Stations", *Scientific Impeller*, pp. 29-32, 1998
- [4] Vaillencourt, R.R, "The Correct Formula for Using the Affinity Laws When There Is a Minimum Pressure Requirement", *Energy Engineering*, Vol. 102, No. 4, pp. 32-46, 2005
- [5] W. Randall and P. Whitesides, "Basic Pump Parameters and the Affinity Laws," 2012. [Online]. Available: <http://www.pdhonline.org/courses/m125/m125content.pdf> [Accessed 7 September 2012].
- [6] C. M. Burt, X. Piao, F. Gaudi, B. Busch and N. Taufik, "Electric Motor Efficiency under Variable Frequencies and Loads", *ASCE Journal Irrig. Drain. Engr* 134(2), pp. 129-136, 2008
- [7] A. Fitzgerald, C. Kingsley and S. Umans, "Induction Motor Model and Analysis," in *Electric Machinery*, New York, McGraw-Hill, 2003, pp. 313-320.

PERFORMANCE COMPARISON OF INDUCTION MOTOR AND LINE START PM MOTOR FOR COOLING FAN APPLICATIONS

C. Mutize and R.-J. Wang*

* Department of Electrical and Electronic Engineering, Stellenbosch University, Private Bag XI, Matieland 7602, South Africa E-mail: mutizec@gmail.com; rwang@sun.ac.za

Abstract: This paper presents the design of a line-start permanent magnet (LSPM) motor by modifying a commercial premium efficiency cage induction motor (IM) for cooling fan applications. Two-dimensional transient finite element (FE) analysis is applied to both IM and LSPM motor to compare their starting and synchronization performance for fan-type load. It clearly shows that the LSPM motor has better efficiency and power factor than that of IM at steady-state. However, the transient starting performance of the LSPM compares less favorably with that of the IM.

Key words: Line-start motor, permanent magnet, induction motor, design optimisation, finite element method, transient performance, cage winding.

1. INTRODUCTION

Line-start motors are usually squirrel-cage induction motors, which are of relatively poor efficiency, power factor and power density. Global environmental concerns raise the need for improving energy efficiency in industry. There has been significant research effort into developing alternative energy efficient motors. Amongst others, the line-start permanent magnet (LSPM) synchronous motor has been regarded as a promising candidate to replace traditional line-start induction motor. The difference between LSPM synchronous motor and adjustable speed PM synchronous motor is that the former has cage winding in the rotor to assist with starting. The concept of LSPM synchronous motor was first described by Binns in 1971 [1]. Comparing with induction motor, the LSPM synchronous motor is of the following merits:

- High power factor (consume no reactive power);
- Under steady-state, there is no winding loss in rotor so that the efficiency can be high;
- Considering relatively low thermal loading, it is even possible to remove fan for small power machines;
- The air-gap in a LSPM motor is usually larger than that of induction motor, which can effectively reduce stray loss.

Although LSPM motors possess many advantages over induction motors, the design of this type of motor still has many challenges. This is mainly attributed to that LSPM motor has to fulfil both asynchronous starting and synchronous operations. With both magnets and cage winding in the same rotor, there is an inherent competition of space between them, which often unavoidably leads to a quite complicated rotor structure. Furthermore, the localized magnetic saturation in various parts of the machine also makes it very difficult to accurately predict some key performance parameters especially during the transient process. In short, the rotor design of LSPM motor is not an easy task.

Although a lot of research has been done on the LSPM motor topics [1–8], the challenge remains the limited synchronisation capability with inertia. This paper compares the steady-state and transient starting and synchronisation behaviour of an induction motor with that of a LSPM motor for cooling fan applications.

1.1 Characteristics of fan-type load

The load torque is proportional to the square of the fan rotation speed. This type of loads exhibit variable load torque characteristics requiring much lower torque at low speeds than at high speeds, which implies that the load torque is relatively low when starting up.

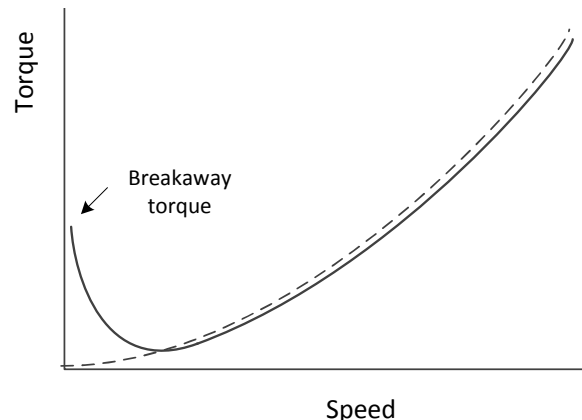


Figure 1: Torque-speed characteristics for fan-type load.

The steady-state torque-speed characteristics of fans may be represented by the shape shown in Fig. 1 (dotted line). These characteristics are often approximately represented by assuming that the torque T required is proportional to the square of the speed n :

$$T = T_{rated} \times \left(\frac{n}{n_{rated}}\right)^2 \quad (1)$$

where T_{rated} and n_{rated} are rated torque and speed of a fan load respectively. Note that this approximation is generally

invalid at low speeds because most practical fans have to overcome a significant breakaway torque (as shown in Fig. 1) when starting. A more practical fan torque-speed curve is thus implemented in the transient analysis.

2. INDUCTION MOTOR CONFIGURATION

A WEG 2.2kW 525V 4-pole three-phase premium efficiency cage induction motor has been selected as a reference motor for the study. The winding layout of the induction motor under study is given in Fig. 2. From a production perspective, it would be cost-effective if standard IMs can be easily modified to a LSPM motor. In this study, the stator and rotor cage winding is kept unchanged.

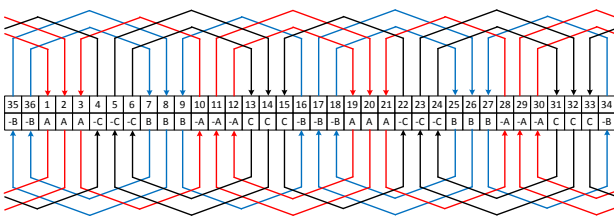


Figure 2: The winding layout of the induction motor stator.

3. DESIGN OF LINE-START PM MOTOR

The design of a LSPM motor can be a complicated multi-variable and multi-criteria optimization problem [6]. Since the same stator and cage winding are used, the only variables are those that change the magnet position, size of magnets and the width of the rib as shown in Fig. 3.

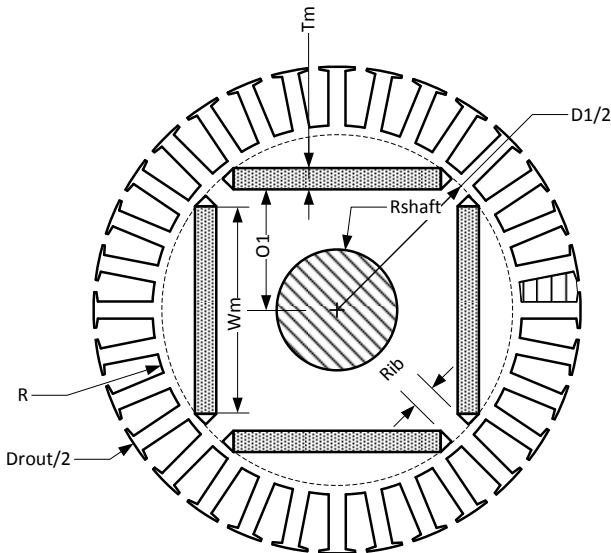


Figure 3: The selected LSPM topology.

3.1 Design optimization

The basic design method employed here is to use a combination of both analytical and FEM performance calculations. Considering the less demanding starting torque

Table 1: Main design dimensions of LSPM.

Description	Stator	Rotor
Outer diameter (mm)	160	97.9
Inner diameter (mm)	99.9	26.8
Axial length (mm)	121	121
Wire diameter (mm)	0.643	-
Winding type	lap	cage
Coil pitch	23/3	-
Phase connection	Delta	-
Number of slots	36	28
Number of conductors per slot	82	-
Number of strands per conductor	2	-
Magnet width (mm)	-	32.96
Magnet thickness (mm)	-	5.68
Air-gap length (mm)	1	-

requirement of fan-type loads, the design optimisation is performed for steady-state and full-load condition by using analytical method. The objective is to optimise for maximum efficiency while subjected to the constraints such as output power and power factor.

The generated optimum design is then verified by using 2D transient FE analysis to check the starting and synchronization performance. In the case that the motor fails to start, new design iterations need to be carried out until a satisfactory design is found. The flow chart of the LSPM motor design procedure is given in Fig. 4. The main dimensions of the optimum design of LSPM motor are summarised in Table 1.

4. PERFORMANCE COMPARISON

To compare the performance of LSPM motor with that of IM for cooling fan applications, both steady-state and transient performances of both type motors are simulated and presented in the following subsections.

4.1 Steady state

As shown in Fig. 5, it can be observed that the LSPM draws lower current than that of induction motor at steady-state. The induced voltages (EMF) (Fig. 6) for both motors are practically the same, which implies that the amount of magnet material used is appropriate. The comparison of the steady-state performance of IM and LSPM motors is given in Table 2. It is evident that LSPM motor has better efficiency and power factor than that of IM.

4.2 Transient performance

The transient performance of LSPM motor is of particular interest as this type motor is known for its relatively poor transient performance. Transient 2D FE analysis has been applied to calculate the starting and synchronization performances. For both motors the stator is powered from 3-phase 525V supply at 50Hz frequency. The system inertia and fan-load characteristic have also been

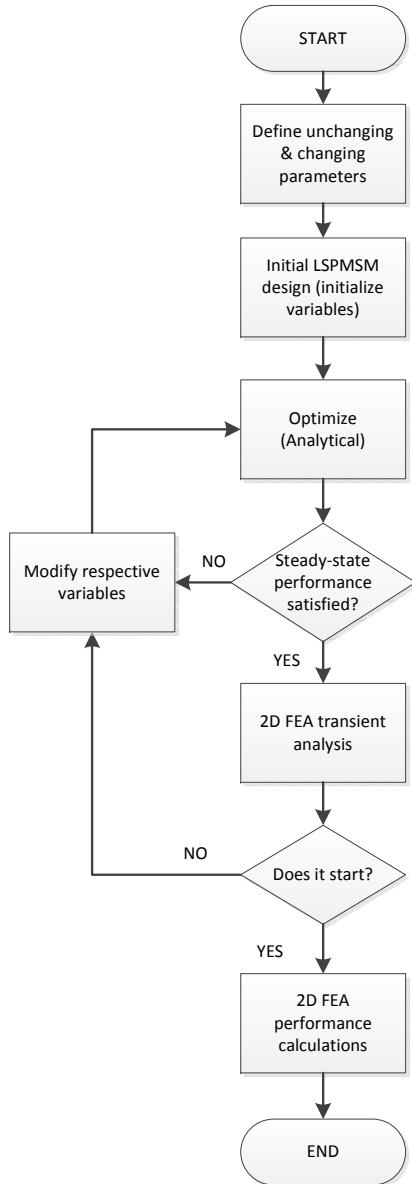


Figure 4: Flow chart of LSPM motor design procedure.

implemented in the FE analysis. For a load torque of T_L , the instantaneous rotor acceleration is governed by the following equation:

$$\frac{d\omega_r}{dt} = \frac{P}{J}(T_e - T_L) \quad (2)$$

where T_e is the electromagnetic torque, J is the inertia, P is the number of pole pairs, ω_r is the angular speed of the rotor. Fig. 8 is the flux plot of the LSPM motor under full load at a certain time step.

Figs 8-9 show the current waveforms of both motors during load starting process. It can be seen that LSPM motor draws slightly higher starting current than that of IM.

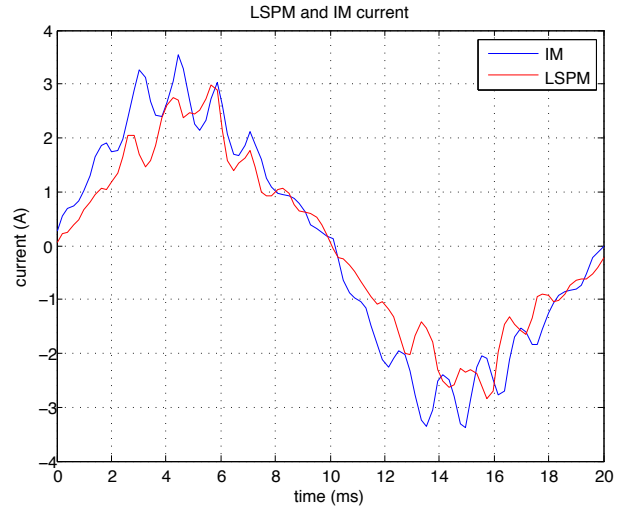


Figure 5: Steady-state currents of IM and LSPM.

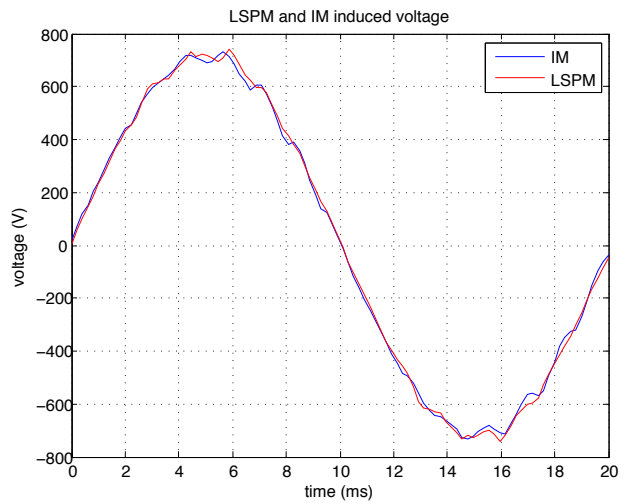


Figure 6: Induced voltages of IM and LSPM.

The speed-time responses for both LSPM motor and induction motor under load are plotted on the same graph as shown in Fig. 10. The IM is pulled into synchronism about 80 ms faster than that of LSPM motor. Figs 11-12 show the torque-time characteristics for both motors at the same condition.

As shown in Figs 13-14, for fan-type loads with relatively low inertia, the instantaneous speed-torque trajectory for both LSPM motor and induction motor show no sign of repetitive pole-slips profiles at starting. The synchronization process for both motors are satisfactory, though the IM demonstrates a slightly better performance with a smaller locus surrounding rated speed.

5. CONCLUSION

This paper presents the design of a LSPM motor by simply modifying a commercial premium efficiency IM for cooling fan applications. The steady-state and transient

Table 2: Steady state performance of IM and LSPM.

Description	LSPM	IM
Power (kW)	2.28	2.22
Current (A)	2.5	3.47
Voltage (V)	525	525
Rated speed (rpm)	1500	1435
Efficiency (%)	93.6	87
Power factor	0.99	0.8
Rated torque (Nm)	14	14.6
Frame size	100L	100L

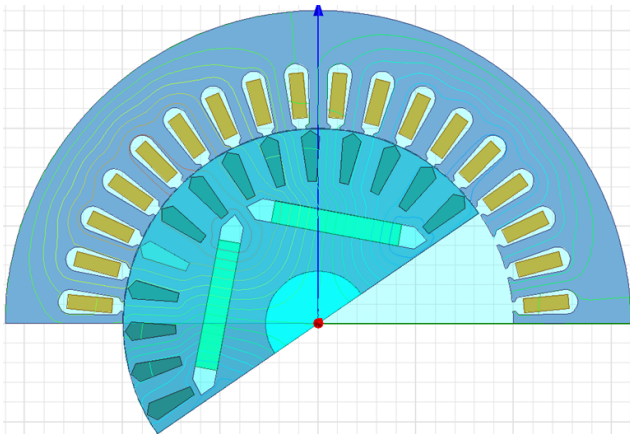


Figure 7: Flux plot of the LSPM under full load.

performances of both motors are computed and compared by applying extensive 2-D transient FE analysis. It clearly shows that the LSPM motor has better efficiency and power factor than that of IM at steady-state. Although the excellent transient starting performance of the LSPM is evident, the IM exhibits a slightly better overall transient performance for fan-type loads.

ACKNOWLEDGMENT

This work was supported in part by Eskom Tertiary Education Support Program (TESP), Sasol Technology Research and Development, and the National Research Foundation (NRF).

REFERENCES

[1] T.J.E. Miller: "Synchronization of line-start permanent magnet ac motors", *IEEE Trans. PAS* 103:1822-1828, 1984.

[2] W. Fei, P. Luk, J. Ma, J. Shen and G. Yang: "A high performance line-start permanent magnet synchronous motor amended from a small industrial three-phase induction motor", *IEEE Trans Magnetics*, vol.45, no.10, pp.4724-4727, October 2009.

[3] J. Li, J. Song and Y. Cho: "High performance line start permanent magnet synchronous motor for

pumping system", *2010 IEEE International Symposium on Industrial Electronics (ISIE)*, pp.1308-1313, 4-7 July 2010.

[4] T. Ding, N. Takorabet, F. Sargos, X. Wang: "Design and analysis of different line-start PM synchronous motor for oil-pump applications", *IEEE Trans Magnetics*, vol.45, no.3, pp.1816-1819, March 2009.

[5] A. Isfahani, S. Vaez-Zadeh, A. Raham: "Evaluation of synchronization capability in line start permanent magnet synchronous motors", *IEEE International Electric Machines and Drives Conference (IEMDC)*, pp.1346-1350, 2011.

[6] W. Jazdzynski, M. Bajek: "Modeling and bi-criterial optimization of a line start permanent magnet synchronous machine to find an IE4 class high efficiency motor", *International Conference on Electrical Machines (ICEM)*, 6p, September 2010.

[7] A. Aliabad, M. Mirsalim, N. Ershad: "Line-start permanent magnet motors: significant improvements in starting torque, synchronization, and steady-state performance", *IEEE Trans Magnetics*, vol.46, no.12, pp.4066-4072, December 2010.

[8] W. Kim, K. Kim, S. Kim, D. Kang, S. Go, H. Lee, Y. Chun, J. Lee: "A study on the optimal rotor design of LSPM considering the starting torque and efficiency", *IEEE Trans Magnetics*, vol.45, no.3, March 2009.

APPENDIX

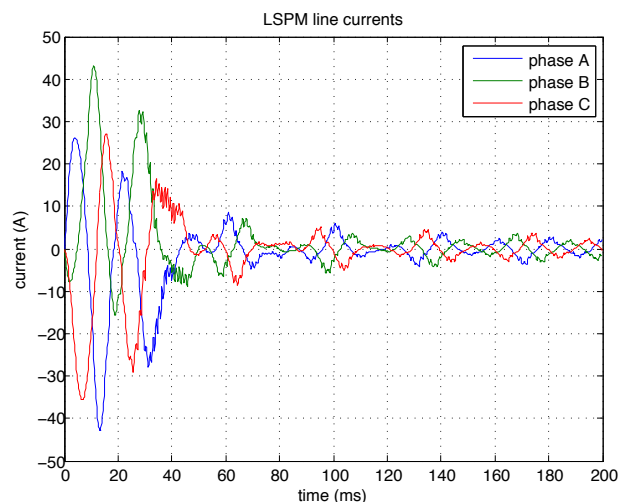


Figure 8: LSPM line currents versus time (under load).

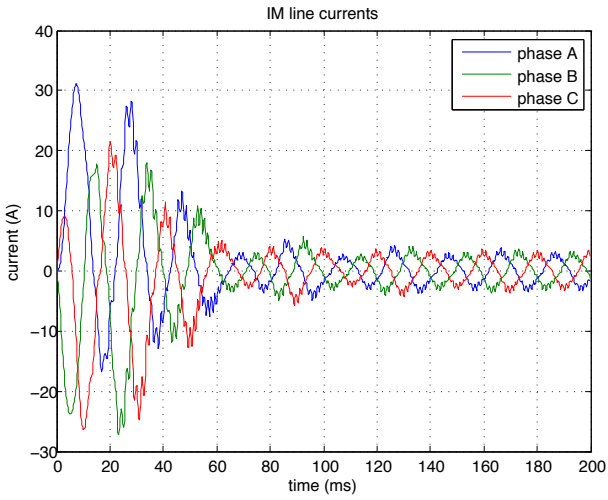


Figure 9: IM line currents versus time (under load).

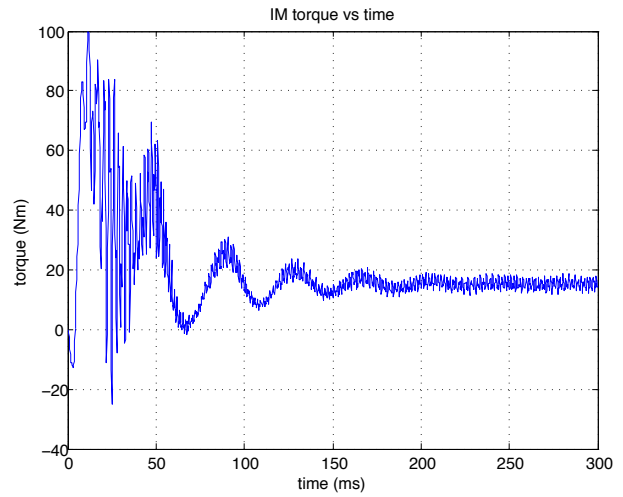


Figure 12: IM torque versus time (under load).

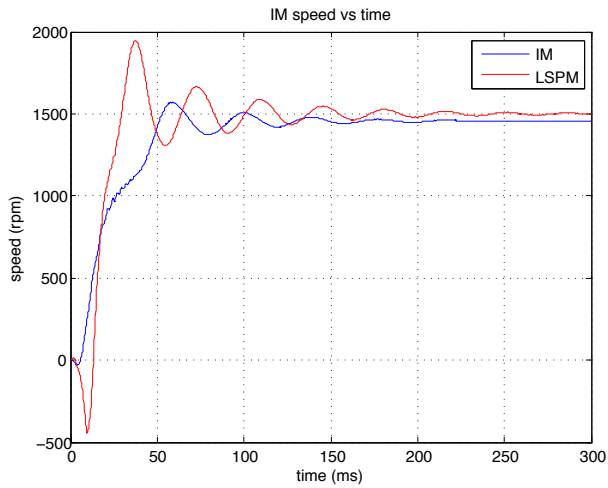


Figure 10: Speed versus time curves of LSPM and IM

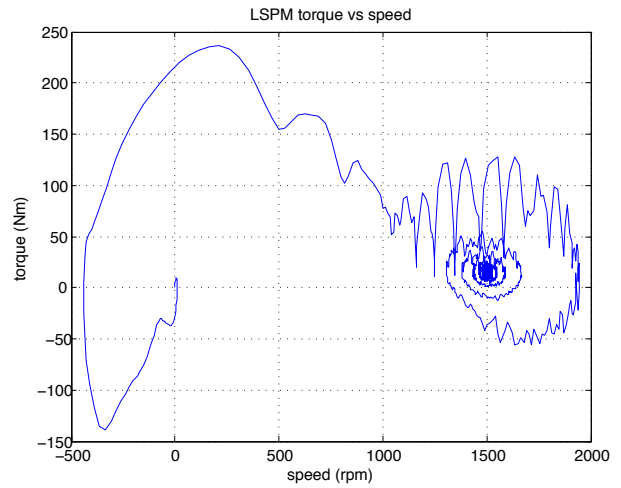


Figure 13: LSPM transient torque-speed trajectories.

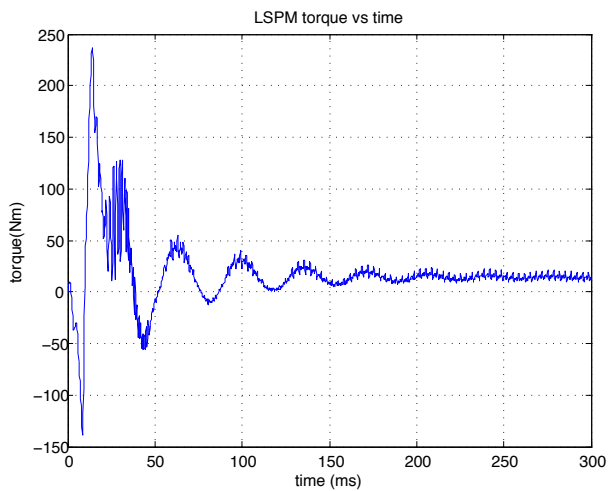


Figure 11: LSPM torque versus time (under load).

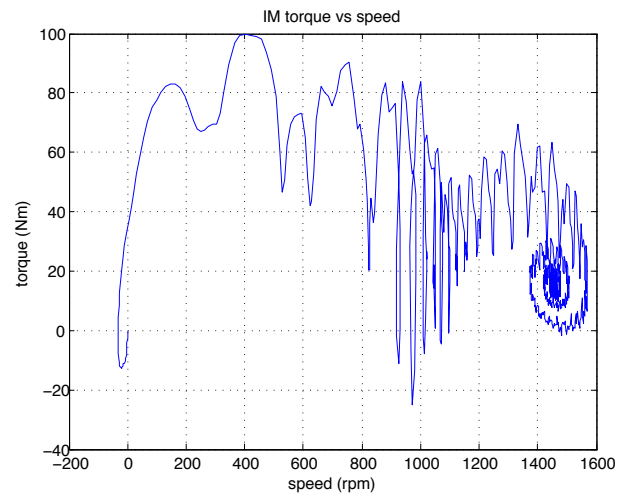


Figure 14: IM transient torque-speed trajectories.

TRANSMISSION LINE MONITORING SYSTEM FOR A POWER LINE INSPECTION ROBOT

T.C. Visser and R. Gouws

North-West University, Faculty of Engineering, Private Bag X6001, Postpoint 288, Potchefstroom, 2531. South Africa, E-mail: tjaart.c.visser@gmail.com

Abstract: Eskom has thousands-of-kilometres of transmission lines running across South Africa. The current methods of overhead power line inspection (foot patrols and air inspections) have been implemented for a long time now and are expensive and infrequent. The aim was to develop a prototype monitoring system, which had to fit into a transmission line robot to collect information from the power line and will allow a person to remotely (wirelessly) inspect the power line. The hardware consists of a PandaBoard[®] (SBC) together with a 5 MP camera and GPS receiver to collect information. High detail (resolution) photos of the power line covered the biggest problem faced on the lines, namely: hardware fatigue. The evidence was then accessible on a website hosted by the PandaBoard[®] via Wi-Fi. The solution is light weight, compact and has a low power consumption. The monitoring system makes collecting evidence easy and fast. The results obtained by this prototype are satisfactory as a concept for further development and can provide a feasible and improved solution for monitoring of transmission lines for Eskom.

Keywords: Monitoring system, transmission line inspection, inspection robot, PandaBoard

1. INTRODUCTION

Eskom has thousands-of-kilometres of transmission lines running across South Africa [1]. All of these lines have to be patrolled and maintained. Eskom is currently doing a foot patrol and a fast helicopter inspection annually together with a detail/slow helicopter inspection every two years on each of these lines.

These methods of overhead power line inspection has been implemented for a long time now and it is expensive and infrequent [2]. When a key component on a tower starts failing, like a wire connector, it has the tendency to fail completely over a short period of time. Almost like the snow ball effect. Although multiple departments inspect the lines, some lines are routed in remote areas (across mountains, over rivers, etc.) which means inspection is more difficult and more time consuming [3].

Eskom mostly collects detailed photos [4] during these inspections coupled with an occasional infrared photo (usually during slow helicopter inspection). Using a helicopter to collect these photos results in high costs to Eskom. Hijacking has also become a big issue during foot patrols. The robot will also contribute to safety around live lines by not requiring a person to climb onto the live wire for close inspection, but only for maintenance [5].

This project is the first step towards an implementable inspection robot in the future, therefore this attempted monitoring system is a baseline to further expand and improve towards the complete monitoring solution intended by this project. Some key features have been identified to aim for in this first attempt as indicated in the list shown below.

- The monitoring system must incorporate sensors to collect evidence from the line.
- The sensors must collect information at a high rate to ensure that data from each part of the line are collected to prevent blind spots which may overlook key components that can cause line failure.
- The monitoring system will make use of a wireless communication device to transmit the newly collected information to a remote device.
- The wireless broadcasting range at this stage doesn't need to be very far as it is only essential to have wireless connectivity to form a base communication system. Range boosters can easily be inserted in the future to increase the range.
- The monitoring system must be integrated with the inspection robot and use its battery source without disrupting the robot's operation [6].

The aim of the project was to successfully complete an integrated hardware system which will allow the collection of detailed evidence (HD photos) together with sensors that provide location (time and GPS coordinates). The system also has to incorporate software which will utilize the hardware to a point where the intervals of data collection cover the complete line and then host the evidence, wirelessly, over a network [4, 6].

2. MATERIALS AND METHOD

2.1 Technical survey and recommendations

After spending time at Eskom during vacation training in their central transmission division located in Simmerpan,

the following problems have been identified as problems which Eskom face on their overhead transmission lines:

- Hardware problems (visible components) - This include all the physical fatigue noticeable by the human eye. Ground patrols use HD cameras to take pictures of each overhead power line tower and then take it to their office to process and look for suspicious components.
- Hardware problems (non visible occurrences) - The two invisible killers are weak connections and corona. Both are detectable by an infrared camera. Corona is also detectable with an ultraviolet camera. These two camera technologies are very expensive.
- Wire problems - Overhead power lines have to comply with clearance standards. Breaching these limits results in flashovers. To measure these distances, Eskom uses a Lidar scanner to create a 3D model which shows all the distances. But just like the infrared and ultraviolet cameras, Lidar systems are very expensive.
- High inspection costs - The estimated budget in Eskom for aerial inspections is about R 36 million per year. The helicopter is capable of a 100 km of fast inspection per hour, but costs R 14 000 an hour (excluding pilot and staff salary).

After understanding what problems Eskom face, one cannot help but wonder if the alternative solutions do not really provide the solution that Eskom needs. Eskom is currently spending a lot of money just to patrol the transmission lines. By buying a robot which specializes in temporary close inspection and small repairs (like the LineScout® and Expliner), Eskom is only shifting towards better safety for humans and not towards saving money during foot patrols whilst improving safety. Thus the LineScout® and Expliner do not meet the solution Eskom require.

The Cable crawler, just like the LineScout® and Expliner, is a very big and heavy robot. Its monitoring system isn't close to being finished, so it's too early to tell whether the developers are heading in the right direction. The High-Wire acrobat is showing potential for future use by Eskom, but the high cost and the fact that field testing will only start in 2014, eliminates the High-Wire Acrobat as a current competitor.

If a monitoring system, which only looks for visible damage (not expensive), can be placed in robots which can run autonomously on a live lines doing close inspections, then the slow helicopter inspections will decrease greatly. To complete the monitoring solution, an infrared camera and a Lidar scanner can be combined with the fast helicopter inspections to search for the invisible problems (corona and weak links). The monitoring system has to provide GPS positioning and HD photo data from very great distances to provide the live line crew with enough evidence to minimize ground patrolling. This way Eskom still has a complete monitoring system, but with fewer ground patrols and

slow helicopter inspections which then results in a more cost efficient solution.

2.2 Concept draft

From the technical survey and the budget for this project, it was decided that the monitoring system should consist of the following hardware: a HD camera, a GPS receiver, voltage regulator with protection and a PandaBoard® with onboard Wi-Fi. This will provide the required hardware functionality which the software can use to form the monitoring system. The concept breakdown is shown in figure 1.

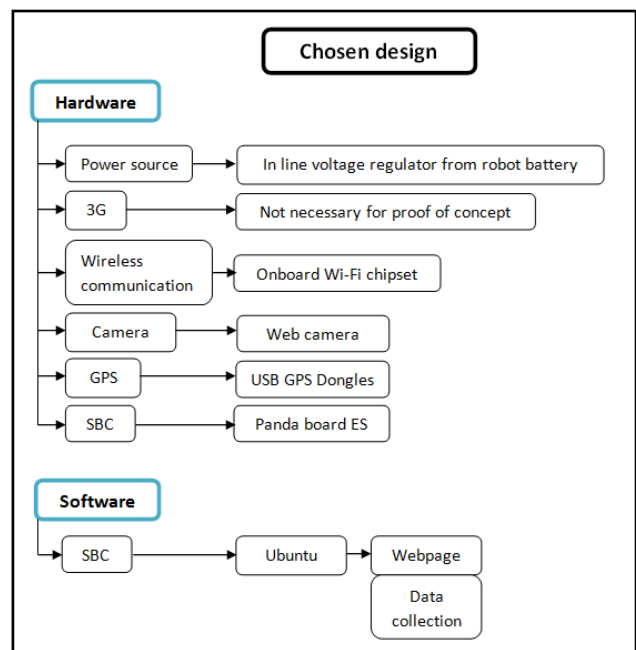


Figure 1: The hardware and software concept breakdown

For the software side there are two main requirements, namely: the data collection and the wireless hosting of the data. Below is the concept discussion of each of the requirements.

Data collection

The program which will record the evidence every few seconds must be able to do the following:

- take a picture
- get time stamp
- get coordinates
- combine the evidence into one file (rename the picture with the time and coordinates)
- save the file in a common location so that the web page can also access it
- wait a preset delay and start the process all over again
- allow for controllable parameters so that the user can change the parameters through the website

The program will basically be one big loop running over and over just collecting data. If all the taken data is placed in one common file location, the website just has to be written to display all the data in that file location.

Wireless data hosting (website)

The web page will be password protected to prevent security breaches. The following functionality must be provided:

- password protection
- display taken data
- allow user to download data
- allow user to delete already downloaded data
- allow user to control the data collection program

2.3 Materials

The chosen hardware for the concept is: a HD camera, a GPS receiver, a voltage regulator with protection and a PandaBoard® with onboard Wi-Fi. The PandaBoard® is a single board computer which will be programmed to use the sensors to collect information, process the info and then host the data. Figure 2 displays the assembled system.



Figure 2: The assembled monitoring system with sensors

The hardware specifications are:

- 1.2 GHz dual core processor
- 1 GB RAM and 16 GB SD card
- Onboard Wi-Fi and Ethernet port
- Ubuntu 11.10 OS
- 720p webcam
- USB GPS receiver with <10 m accuracy
- 5 V regulator with inline fuse. (2-6 cell Li-Poly)
- a total weight of 280 grams

2.4 Software implementation

Each one of the programs are individually discussed below regarding how they implement the requirements.

Data collection

The program is written in BASH since it is basic, fast and has direct access to the IO communications. The basic concept of the program is shown in figure 3.

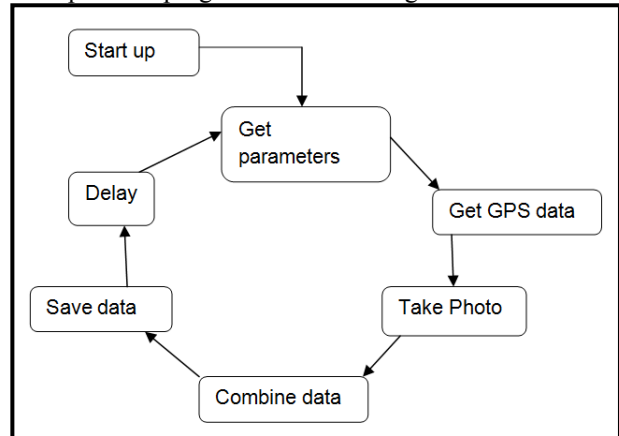


Figure 3: Overhead flow diagram for data collection

Each of the phases shown in figure 3 are discussed below:

- Start-up phase: This phase is responsible for the initialization of the program. During this time the program sleeps for one minute to give the GPS receiver time to allocate satellite reception (the datasheet states it requires 48 seconds for a cold start), sets the start up parameters, navigates the terminal to the relevant directory and sets the GPS com port with the correct settings, namely: 4800 bps, n, 8, 1 for NMEA.
- Parameter phase: The program reads the values of the parameters from a text file (which the website can change) and sets the relevant variables, namely: run, delay and colour. The run determines whether the program should sleep or collect data, the delay states the length of the intervals between data collections and the colour determines if the photos taken by the program must be colour or greyscale. Greyscale photos use less space. The program stays inside the parameter loop unless or until the run parameter changes to true.
- GPS phase: During this phase the program extracts the required location and time from the GPS receiver. The detailed flow diagram is shown in figure 4.

To retrieve the GPS data, the program runs two separate commands simultaneously. One runs in the background to stop the other program from continuing to write the GPS data to a text file. Then the program searches for the relevant data in the text file and starts string manipulation to retrieve the coordinates and time.

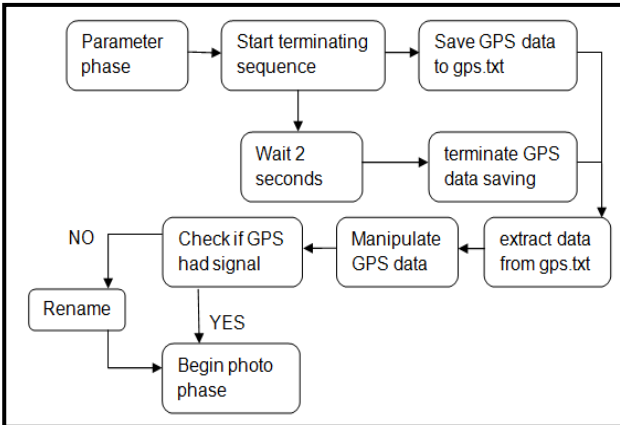


Figure 4: Flow diagram of the GPS phase

A fail-safe is included to rename the location if the GPS receiver has stopped working. How and what the string manipulation does is shown in figure 5.

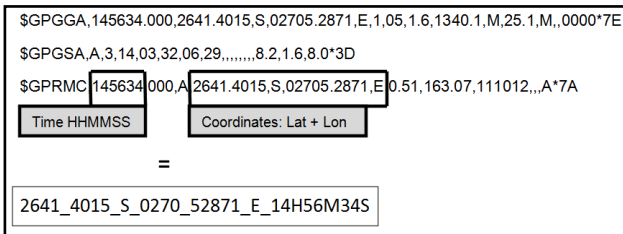


Figure 5: How the GPS data is string manipulated

- Photo phase: The program takes a colour or greyscale photo (depending on the colour parameter) with a program called Fsw webcam and then saves the photo to a folder called phpimages with the name acquired from the string manipulation in the GPS phase. The program can only take 1280x720 pictures with the webcam since it does not have the ability to software optimize the picture.
- Delay phase: The last part of the program is a sleep function which lets the program sleep for the time value specified by the delay parameter. When the delay is over, the program loop starts over.

Website

The website was created by using LAMP® (Linux Apache MySQL PHP) as it provides all the requirements for the website. Apache provides the ability to host the website over the network of the PandaBoard® and MySQL adds a database which will be used by the PHP written website. A database was created with a table to keep track of all the user accounts and to give the website user and password protection. The table creating code is shown in figure 6.

```
users | CREATE TABLE `users` (
  `id` int(11) unsigned NOT NULL AUTO_INCREMENT,
  `user_name` varchar(45) DEFAULT NULL,
  `user_password` varchar(45) DEFAULT NULL,
  `user_status` varchar(45) DEFAULT NULL,
  PRIMARY KEY (`id`)
) ENGINE=InnoDB AUTO_INCREMENT=4 DEFAULT CHARSET=latin1 |
```

Figure 6: Code to create the "users" table in the database

The "user_status" from figure 6 splits the users into two divisions, namely: normal - and super user. Only a super user can create more user accounts and set data collection parameters. The website is made up from multiple pages and the interlinking is shown in figure 7.

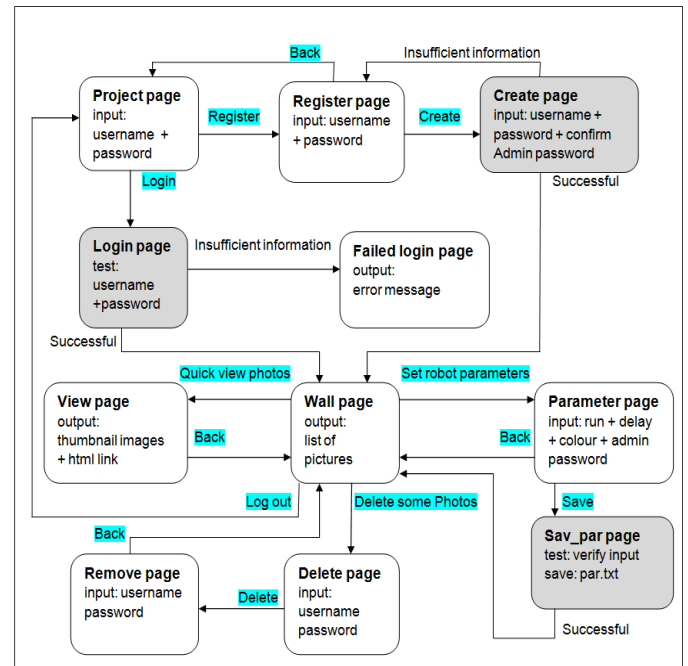


Figure 7: Flow diagram of the PHP WebPages

Some of the blocks in figure 7 are coloured in to symbolize the pages where the webpage will be making use of the MySQL database. The words that are highlighted represent buttons which the user must click in order to move to the next page. The words that are not highlighted are automated responses of the webpage. To simplify the explanation of the methods and ideas of the website, the individual pages are divided in to the following groups:

- Log in phase - Project, Register, Create, Login and Failed login. These pages allow a user to register an account with the permission of a super user and/or login in with the registered account in order to gain access to the data collected by the monitoring system.
- Wall phase - Wall. The wall page is the main page of the website which displays a table of hyperlinks of all the collected data with the created date-time and size. This keeps the page size low and allows for quick browsing.

- Parameter phase - Parameter and Sav_par. These pages allow the super users to set parameter of the data collection program by saving the values to the text file that the data collection program uses.
- Quick view phase - View. This page shows small thumbnail pictures with hyperlinks to allow the user to quickly search for specific pictures to download.
- Removal phase - Delete and remove. The remove page also displays small thumbnail pictures, but with an added delete button to allow the user to delete the unnecessary data.

3. RESULTS

To test the monitoring system before integration with the robot, the system first had to pass a test under full operation. At this stage of the robot prototype, live wire testing was ambitious for the little time and funds available for the project, but electromagnetic interference (EMI) is one of the biggest problems which the monitoring system will face on a power line. So to test the monitoring system in a realistic simulation, the system was strapped into a box and fitted to a quad-copter. The quad-copter then flew over a transmission line whilst the monitoring system was running. Figure 8 shows the quad-copter with the fitted monitoring system.

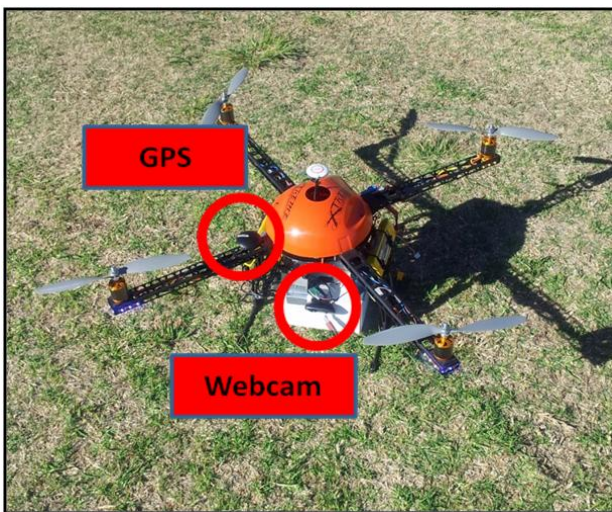


Figure 8: The system installed on a quad-copter

The quad-copter flew right above the power line, far enough to avoid risks, but close enough for the system to experience the EMI. The system was set up to take data at 9 second intervals. Figures 9 to 11 shows a sequence of three pictures that was taken with their names.

The last three digits from each photo name confirm that each picture was taken nine seconds apart. The latitude and longitude was tested by comparing the known location of the test and the results from typing the data into a GPS. The test showed that the GPS receiver remained accurate to less than 10 m whilst being exposed

to the EMI. For comparison of the images, figure 12 is an image taken by Eskom during a Helicopter inspection.

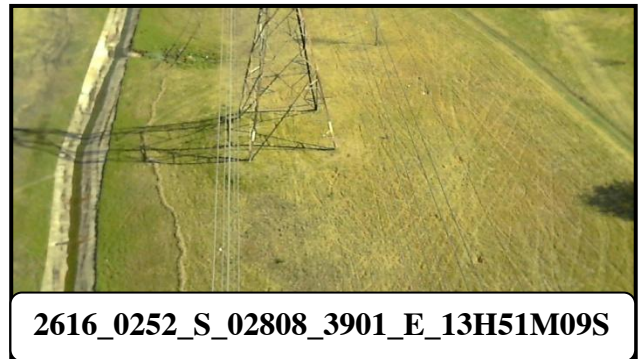


Figure 9: The first photo of a sequence

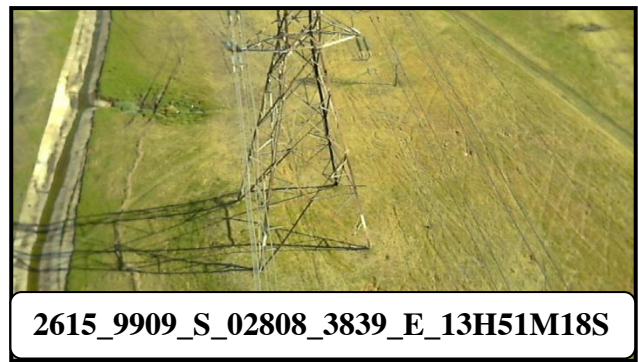


Figure 10: The second photo of a sequence

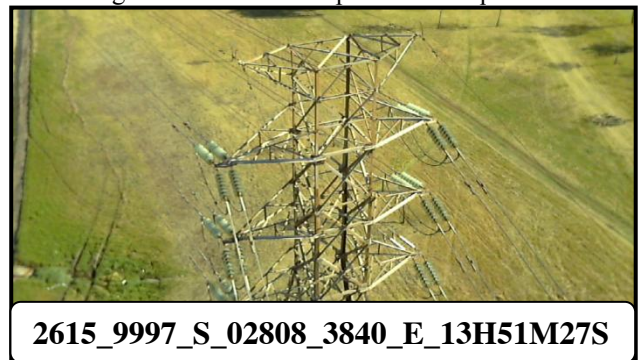


Figure 11: The third photo of a sequence

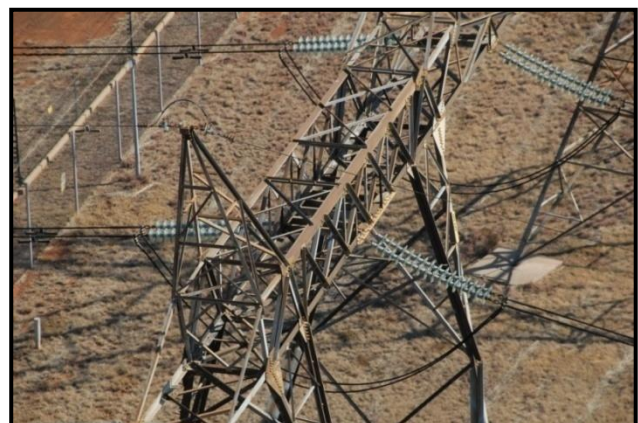


Figure 12: An aerial inspection photo taken by Eskom

The monitoring system's photos lack the quality of photos taken by Eskom, but that is due to the fact that Eskom uses higher resolution cameras. Once the monitoring system has an upgraded camera and hangs directly on the power line, the monitoring system will be more effective. The website was not the main focus during the test, but still operated without fault during testing. A detailed test was done to evaluate all the corners of the website and revealed only small issues which were fixed.

The system's current consumption was tested before integration to ensure that the robot could provide the necessary power. Figure 13 displays a graph of the load under different phases of operation. The system peaks at 1 A and uses 800 mA rms during data collection. The monitoring system was then integrated into the inspection robot for further testing [6]. Figure 14 shows the integrated systems which forms a prototype inspection robot.

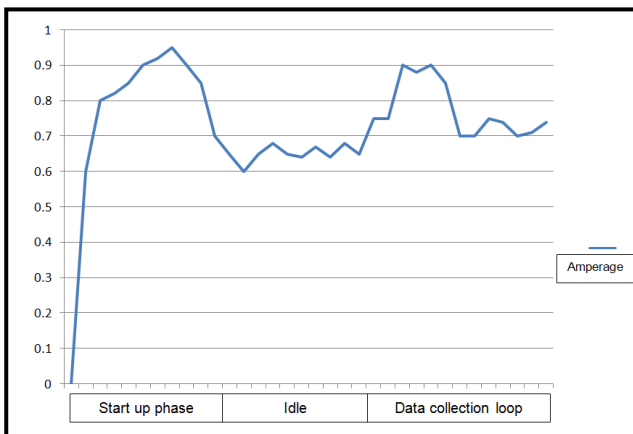


Figure 14: The amperage consumption of the system



Figure 15: The completed prototype inspection robot

4. CONCLUSION

The project required the development of a monitoring system which would fit into an inspection robot and

through wireless communication allowed for remote inspections. As required, two sensors were used, GPS and camera, and were it not for budget constraints, more sensors to complete the monitoring system could have been added. The 3G, infrared and Lidar systems can later be added to the system and make the system effective enough to replace the foot patrols and most of the aerial inspections. For each hour the helicopter is not used, Eskom saves money.

The monitoring system provided very good results. The data collected by the system are for the most part the same as what Eskom would typically collect during one of their inspections, which makes it a direct substitute with lower running costs than the current method.

To conclude, the monitoring system which weighs 280 g can take 60 000 photos with very accurate GPS coordinates at a minimal time interval of 5 seconds and successfully hosts the data over the onboard Wi-Fi chip. This allows a person to remotely inspect the power line. The project objectives are met and some features are additionally included, like the parameter page which allows the user to control the data collection program through the website, to increase the performance and effectiveness of the system.

5. REFERENCES

- [1] Financial results, Eskom's "Integrated Report 2010", [online] available: http://financialresults.co.za/2010/eskom_ar2010/eskom_abridged-ar2010/index.html, [Accessed: 22/11/2012], pp. 9.
- [2] P.C. Pelsler, "Routine Inspection and Maintenance of Transmission Lines", August 2008, Available at Eskom with unique identifier: TST41-637, Revision 1, pp. 6.
- [3] S. Montambault and N. Pouliot, "Design and Validation of a Mobile Robot for Power Line Inspection and Maintenance", published in "6th International Conference on Field and Service Robotics-FSR 2007, Chamonix: France (2007)".
- [4] T. Pillay and S. Bisnath, "Fundamentals and practice of overhead line maintenance," Eskom Holdings Ltd and Endangered Wildlife Trust, Johannesburg, 2004. pp. 3-239.
- [5] S.A. Corley, "Robotic Tightrope Walkers for High-Voltage Lines", Spectrum IEEE, Nov 2009, [online] Available:<http://spectrum.ieee.org/robotics/industrial-robots/robotic-tightrope-walkers-for-highvoltage-lines>, [Accessed: 22/11/2012].
- [6] N. du Plessis, "Line inspection robot", Final year project document, North-West University, 2012.

UPGRADE OF THE ANTIQUATED 3TM2500 TRANSFORMER SCHEME TO PROVIDE IMPROVED TRANSFORMER PROTECTION

M. Sandt* and R. Harris**

* Marvin Sandt, Eskom EDFS – Protection, Eskom EDFS – Eastern Cape Operating Unit East London, South Africa, South Africa E-mail: S211228931@nmmu.ac.za

** Dr Raymond Harris (Mentor), Faculty of Engineering, the Built Environment and Information Technology Nelson Mandela Metropolitan University, Port Elizabeth, South Africa E-mail: Harris.Raymond@nmmu.ac.za

Abstract: The failure of the 7UT512 and 7SJ50 relays on the 3TM2500 transformer scheme minimizes efficient protection on the Ncora substation power transformer. Damage to the 20 MVA transformer as a result of uncleared faults could lead to long customer outages, negative impact on performance indicators and compromise the safety of operating personnel. Restoration of the transformer protection under an emergency outage is done by retro fitting an SEL 387A current differential relay into the 3TM2500 scheme. This is achieved by modifying the transformer protection scheme and remote access drawings to accommodate the change and by utilizing a specially developed Omicron relay testing template to test the new relay settings efficiently. The new settings are generated from a setting spreadsheet developed for this purpose using the old Siemens relay settings. They are also calculated and verified in the DigSilent Powerfactory Software to prove correct grading.

Keywords: Relay failure, replacement SEL 387A relay, unprotected power transformer

1. INTRODUCTION

Ncora Substation is a 66/22 kV substation in the Eastern Cape Operating Unit. It has one 20 MVA power transformer that supplies approximately 8 MVA of customer load. Recently, the 3TM2500 Siemens protection scheme relays have failed, which has resulted in the most expensive equipment of a substation to be without sufficient protection. These failed relays have a problem in their power supply circuit that fail after years in service [1]. To avoid any damage to equipment, injury to operators and negative impact on key performance indicators, transformer protection has to be restored in minimal time. This scheme is also found at three other Eskom Distribution Substations in the region and therefore this same method can be utilized if the problem arises at these sites. The failed phase two relays do not have any remote access functionality and therefore this function will also be implemented for future fault investigations and settings changes.

2. PROBLEM STATEMENT

The failure of the 3TM2500 transformer scheme relays have resulted in the Ncora 66/22 kV transformer to be without sufficient protection against system and internal faults.

2.1 Sub-Problems

- Customers can experience long outage times, which will reflect badly on key performance indicators.

- Uncleared faults can damage equipment, which can also endanger the lives of operating personnel in the substation yard.
- No remote access functionality inhibits any off-site fault interrogation and setting changes.

3. HYPOTHESIS

The solution is to retrofit a Schweitzer Engineering Laboratories 387A current differential relay into the 3TM2500 scheme and perform all the necessary tests. It is a phase four numerical relay, which will replace the functions of all the failed phase two Siemens relays. It will provide all the protection required by a 20 MVA power transformer including the remote communications functionality.

The relay can be fitted into the swing frame panel and connected to the back plate wiring via a pre-wired loom developed for this application. Refer to figure 1.



Figure 1: SEL 387A Relay mounted in the panel

4. LITERATURE REVIEW

In order for the successful commissioning of the new protection, various literatures had to be reviewed. The project consists of relay testing and commissioning, design drawing modifications, calculation and conversion of relay settings and verification thereof using the Powerfactory DigSilent Software. The Eskom transformer protection philosophy document [2], SEL 387A relay manual [3] and Network Protection Automation Guide book [7] were the main resources utilized.

4.1 Transformer Protection Philosophy

Transformers are used in various applications and range from a few kVA to several hundred MVA. The size depicts the actual protection package applied to it and the following package is regarded as essential protection for distribution power transformers of ratings above 10 MVA [2].

- Biased Differential Protection.
- High Voltage (HV) Inverse Definite Minimum Time Lag (IDMT) and Instantaneous Phase Overcurrent (O/C) Protection.
- High Voltage Earth Fault (E/F) Protection.
- High Voltage High Impedance Restricted Earth Fault (HV RE/F) Protection.
- Low Voltage High Impedance Restricted Earth Fault (LV RE/F) Protection.
- Low Voltage IDMT Phase O/C Protection.
- Low Voltage DTL/IDMT E/F Protection.
- Surge devices, pressure devices, oil and winding temperatures.

Ncora 66/22 kV transformer 1 has failed differential protection, high voltage inverse definite minimum time and instantaneous overcurrent protection, high voltage earth fault and low voltage inverse definite minimum time earth fault protection. It is only equipped with HV RE/F and LV RE/F protection and the on board surge devices, pressure devices, oil and winding temperature protection. It is important for the transformer to be equipped with essential protection in order for the protection logic to operate correctly.

The differential protection is the unit protection and will trip both high voltage and low voltage circuit breakers. HV Instantaneous overcurrent protection trips both circuit breakers for very close up HV bushing faults and acts as back-up protection for the differential protection. HV IDMT overcurrent protection trips the LV circuit breaker for uncleared LV feeder faults. HV earth fault protection trips the HV circuit breaker for upstream HV earth faults and acts as a back-up to the upstream 66 kV feeder. LV earth fault protection trips the LV circuit breaker for uncleared LV feeder earth faults [2].

4.2 Schweitzer Engineering Laboratories (SEL) 387A Relay

The relay is generally used to protect two winding power transformers, reactors, generators and large motors. The settings allow you to connect current transformers in wye or delta to use with any transformer winding connection. It's an advanced phase four numerical relay and provides the following functions [3]:

- Current Differential Protection
- Low Impedance Restricted Earth Fault Protection
- Overcurrent Protection
- Through Fault Event Monitoring
- Programmable Optoisolated Input and Output Contacts
- Serial Communications
- Clock Synchronization

This modern multifunctional relay provides short circuit protection for both primary and back-up zones. This makes the relay quite flexible and complicated to test [4].

The relay will be configured for Ncora Substation 66/22 kV transformer 1. The differential functions will be used and these settings will be used as per the relay manufacturer recommendations. The winding 1 O/C, residual and neutral elements will be utilized and these settings will be generated from the setting spreadsheet.

The relay will be configured as per the SEL 387A relay in the 3TM5110 protection scheme, but only the used functions will be enabled. Therefore, if future changes are required it can be done while the relay is in service. The relay will be configured with the following output logic.

- OUT 101 – TRIP 1 (Master trip condition, differential and instantaneous overcurrent trip for the main trip circuit)
- OUT 102 – TRIP1 + TRIP 2 (Master trip and HV E/F trip for the back-up trip circuit)
- OUT 103 – TRIP3 (To start the sustained fault timer for uncleared LV system faults)
- OUT 104 – TRIP 1 + TRIP 3 (Master trip and LV breaker main trip circuits)
- OUT 105 – 50NN3T + 51NN3T + 51P1T (LV breaker back up trip circuits)
- OUT 205 – S1LT1 + S2LT1 (LV E/F and SE/F alarm for indication to SCADA)
- OUT 207 – S1LT2 (Differential trip to SCADA for indication)

The relay dimensions allow for easy installation into the transformer panel. It is 502 (mm) × 124.5 (mm) × 223.5 (mm) in size and therefore no extra cutting or drilling is required as seen in figure 1 [3]. The blanking plate needs to be removed and the relay installed using four cage nuts.

4.3 Relay Testing and Commissioning

Protection relays form part of a very important task in an electrical system. If faults are detected the relevant protection relay needs to operate the relevant breakers to isolate the fault. This will maintain electrical supply to the healthy part of the system. It is therefore important that these relays are properly tested and checked to perform its functions correctly before it is put into service [5]. Commissioning tests prove the design and installation as to avoid any nuisance tripping. The aim is to ensure correct functioning of the scheme as a whole. The logic must be tested to confirm all inputs, outputs, logic gates, controls and alarms [6]. The following tests are considered as common checks during site commissioning [7].

- Wiring diagram check as per the design drawings
- General inspection of equipment
- Relay self-check and communications checks
- CT circuit checks
- Relay setting checks
- Tripping and alarming circuit function checks
- Secondary injection check at different values
- Primary injection of the relay to prove stability
- Testing the scheme logic

The project requires that all these tasks be performed because several CT and tripping circuit wiring will be done. Most of the injections are done using the Omicron primary and secondary injection test sets. The primary stability injections are done using a three-phase supply and all the secondary injections are done with the Omicron Test Universe Software using the relay template developed for this project.



Figure 2: Omicron CPC 100 Primary Injection Set

Figure 2 shows the test set used to perform the primary injections and the polarity checks of the CT's [8]. This is important to ensure correct ratio and polarity of the CT circuits used for the differential protection.



Figure 3: CMC 256 Secondary Injection test set

The secondary injection test set, CMC 256, in figure 3 was used to perform all secondary injections. The test template was developed in the Omicron Test Universe software. The test template consists of differential characteristic, overcurrent and earth fault pick up and multiple test point testing. When testing multifunction relays certain settings must be disabled to accommodate testing. When performing the differential tests the instantaneous overcurrent functions must be disabled [6].

5. RELAY AND SITE TEST RESULTS

Testing forms an important part of the project and the results must be correct to permit the commissioning of the new transformer protection. The following focuses on the differential and overcurrent test results.

5.1 Relay Test Results

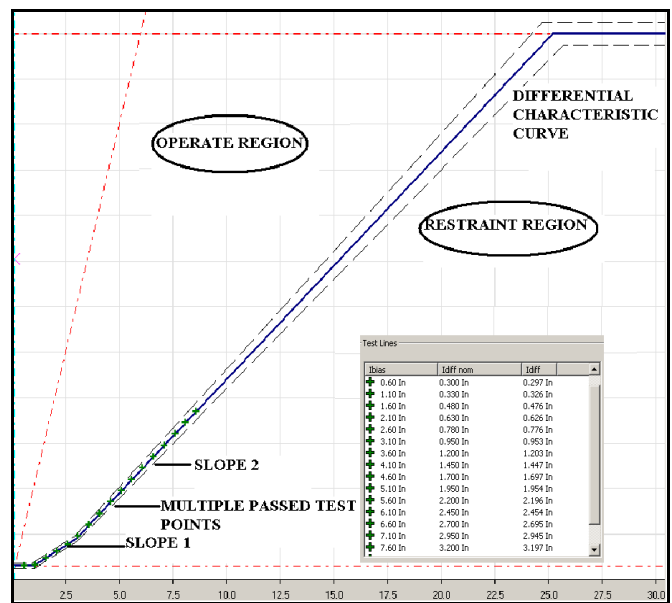


Figure 4: Differential Curve Test Result

Figure 4 shows the results for the phase-to-phase fault. The test searches along the characteristic curve and distinguishes the operating and restraint regions. The operating region is above the curve and the restraining region below the curve. Various test points for different fault levels were tested. Maximum deviation from the curve ranged between -1.23% and 0.08%. These settings tested accurately. The differential trip time for differential protection is instantaneous. Several fault types with multiple test points were tested and found to be accurate. The maximum tripping time for this relay was 46.1 ms, which is considered to be instantaneous.

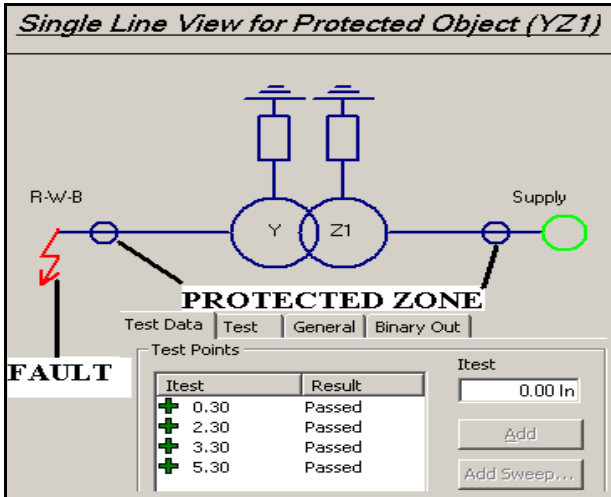


Figure 5: Differential Through Fault Result

Figure 5 shows the through fault module. This module checks the relay for stability during external faults. This is an important check as it will prove relay stability for external faults. If these through faults are not cleared by the relevant protection then the transformer back up protection will operate. Faults were simulated on both sides of the transformer for various fault types and multiple test points. The test was run for several seconds to wait for a differential trip. No tripping was recorded, which proves the stability function to work correctly. Restraining values and operating values were recorded to ensure that no operating current was recorded by the relay.

The harmonic restraint module was used to check the 2nd and 5th Harmonic restraint function of the relay. Different fault types at multiple test points were used to check the percentage setting of the fundamental. The module searches along the percentage setting and decides whether to operate or restraint for inrush or overfluxing conditions during energizing. This function is important because you do not want your transformer to trip during energizing if there is no fault. Transient magnetizing current can be as high as 8-12 times the transformer rating and this current is only seen by the HV CT-s [4]. This should trigger the differential element, but if the harmonic component is above the percentage setting it will block a trip condition. However, if there is a severe fault during inrush conditions the highset function of the relay will be triggered. This is known as the unrestrained element [9].

Figure 6 shows the overcurrent module in the relay test template. It was used to check the overcurrent and earth functions of the relay. Again, various fault types with multiple test points were tested and proved to be correct. The actual effective setting of the function was also checked and when it was picked up, the corresponding element LED asserted in the target menu of the relay. All the overcurrent and earth fault settings tested accurately.

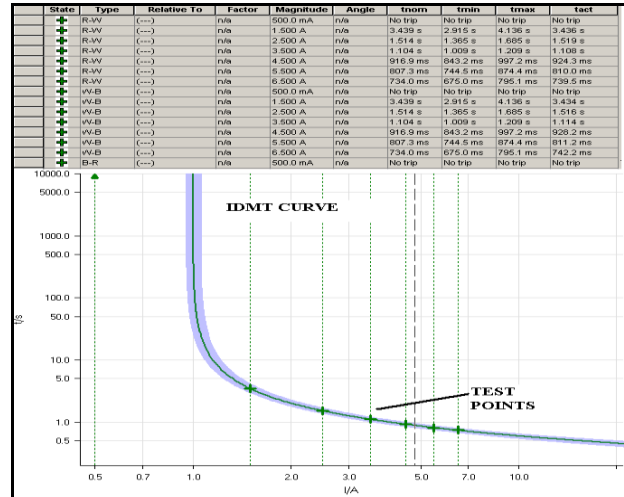


Figure 6: Overcurrent Test Result

In addition to the relay testing, all the corresponding output alarm circuits were also confirmed to be correct. The LCD display on the relay also displayed the correct flagging which will assist the operators when identifying faults.

5.2 DigSilent Setting Verification Results

The settings for the SEL 387A relay were generated from the setting spreadsheet. The spreadsheet uses the existing Siemens relay settings and converts it into SEL 387A settings template. Once the conversion was done it was transferred to the relay using the SEL 5010 Relay Assistant software. In addition, the settings were also calculated and verified on the DigSilent software. The IDMT curves for the transformer protection was plotted against the 22 kV feeders and various faults were simulated to verify correct tripping of circuit breakers as per the protection tripping philosophy.

Figure 7 illustrates the tripping time of the various protection functions for a fault on the 22 kV busbar. The plot shows the overcurrent and earth fault protection curves for the transformer and the 22 kV feeders. The philosophy requires the transformer LV breaker to trip for the 22 kV busbar fault and none of the 22 kV feeder breakers. The transformer HV IDMT protection tripped the LV circuit breaker and no tripping was issued by the feeders. No tripping is shown by the infinite tripping time of the respective relays. Only the HV IDMT overcurrent relay issued a trip in 757 ms for this particular fault. Multiple fault scenarios were simulated to prove correct tripping of the circuit breakers at different locations of the substation. Figure 8 shows the substation overview in the DigSilent software. Faults were simulated on the 22 kV and 66 kV lines and busbars.

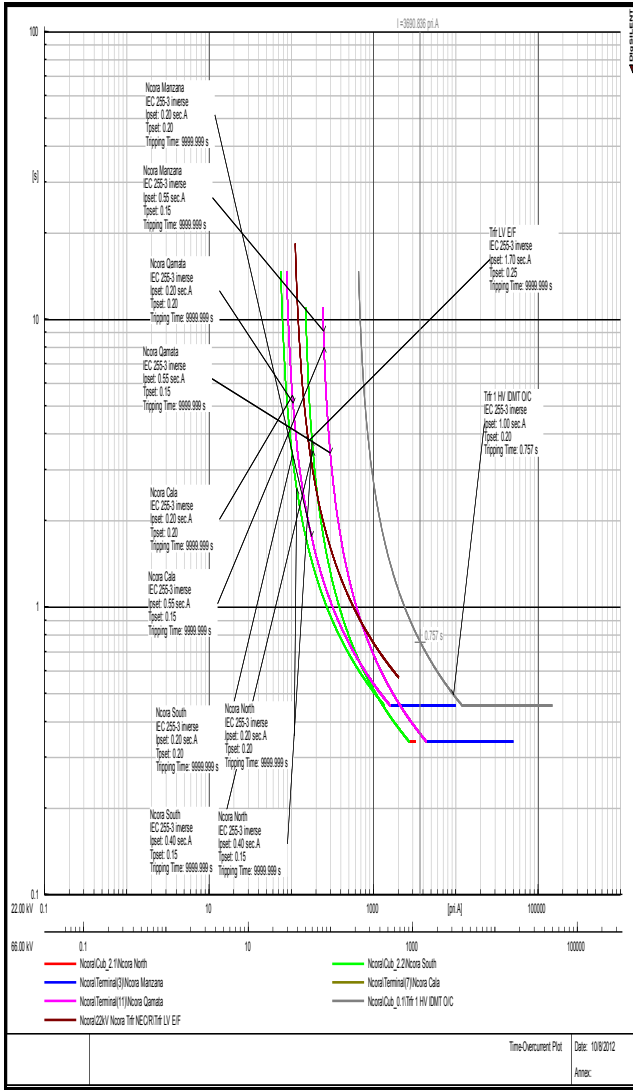


Figure 7: DigSilent plot of a 22kV Busbar O/C fault

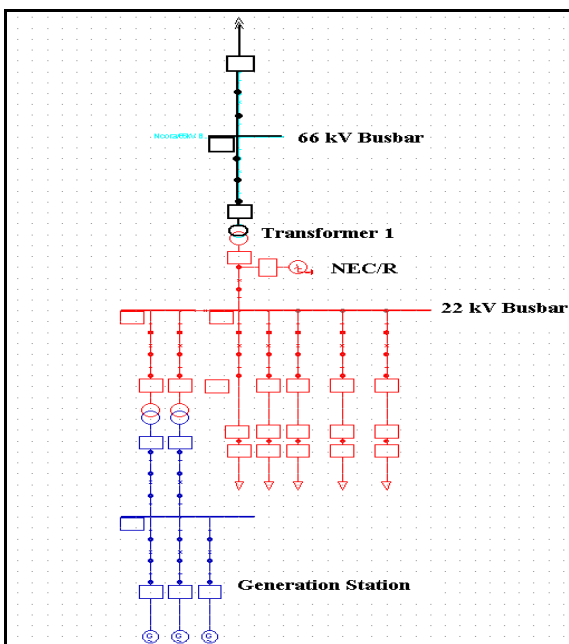


Figure 8: Ncora Substation Overview

5.3 Site Test Results

Primary injection and function testing with the primary plant forms part of the site tests because the HV and LV CT-s circuits were disconnected and therefore required re injection. All the ratio and polarity results were proven to be correct.

Table 1: HV CT's Primary Injection

Secondary Current					
Phase Injected	Primary Amps	A111	A131	A151	A172
R	60 A	312.2 mA	0.4 mA	0.3 mA	312.3 mA
R-W	60 A	306.9 mA	303.3 mA	0.3 mA	0.2 mA
R-B	60 A	292 mA	0.4 mA	297 mA	0.2 mA
Polarity test on red phase: ok					

Table 2: LV CT's Primary Injection

Secondary Current					
Phase Injected	Primary Amps	A311	A331	A351	A372
R	60 A	101.8 mA	0.3 mA	0.2 mA	102.4 mA
R-W	60 A	103.1 mA	103.4 mA	0.2 mA	0.2 mA
R-B	60 A	102.3 mA	0.3 mA	102.7 mA	0.2 mA
Polarity test on red phase: ok					

Table 1 and Table 2 show the primary injection results. A primary current of 60 A was injected and the expected ratio was obtained. On the 200/1 ratio the secondary current is approximately 300 mA and on the 600/1 ratio approximately 100 mA. The polarity was also checked with an Omicron Cpol polarity checker to be correct.

The primary differential stability check was done to prove the differential function. The results were checked in the relay terminal view with a laptop connected to the relay. The function was monitored using the "meter diff" command in level 1 of the relay. Table 3 illustrates the results.

Table 3: Differential Stability Injection Results

Restraint Condition:			
Restraint Current	0.1	0.1	0.1
Operate Current	0	0	0
Operate Condition:			
Restraint Current	0	0	0
Operate Current	0.1	0.1	0.1
Primary Current:			
HV CT's	10 A	10 A	9 A
LV CT's	29 A	30 A	30 A

A three-phase voltage was applied to the HV CT-s and a three-phase short was applied after the LV CT-s. This setup simulates the current entering the system to be equal to the current leaving the system. Table 3 shows

that there are more restraining currents than operating currents for a restraint condition and therefore stability is achieved. Next, a three-phase voltage was applied to the HV CT-s and a three-phase short was applied before the LV CT-s. This setup simulates current entering the system unequal to current leaving the system. This will calculate differential current to operate the differential protection. Table 3 shows more operating current than restraining current.

The primary plant was also function checked with the secondary plant. The tripping philosophy was checked to trip correctly for the different protection. This is to ensure that the correct circuit breaker trips. The table below illustrates the correct tripping philosophy applied to this transformer.

Table 4: Tripping Philosophy

	HV Breaker	LV Breaker	SFT Start
Diff Trip	√	√	
HV Inst. O/C	√	√	
HV E/F	√		
HV IDMT O/C		√	√
LV E/F		√	√
LV SE/F		√	√

Once all the site pre-commissioning checks were done the transformer protection was commissioned and the load readings were measured on all the used CT circuits. All load readings results were correct as expected.

The remote access function to the relay was also commissioned. The existing system only catered for the ABB DPU relays via a Moxa Nport and a Moxa switch setup. The OPGW on the 66 kV feeder shield wire allows the use of a fibre core for remote access. The fibre is routed into the Moxa switch, which is linked via Ethernet cable to the Moxa Nport switch. An additional Nport device was installed to cater for the new SEL 387A. The Nport device was configured using the Nport Administrator software and port1 was setup for the RS422 connection to the relay [10].

6. CONCLUSION AND RECOMMENDATIONS

The restoration of the transformer protection at Ncora substation by means of retrofitting a SEL 387A relay into the 3TM2500 scheme has proven to be useful. By wiring up the relay and performing all the pre-commissioning tasks before the emergency outage, site work can be achieved in minimal time. By use of the settings spreadsheet to generate the new SEL 387A settings and transfer thereof, one can set the relay in very little time without consulting the settings department. The specially developed relay testing template allows technician to easily and effectively test the relay. The DigSilent software proved the tripping philosophy of the substation breakers to be correct. All site test results and checks passed correctly and the new transformer protection was

commissioned within the allowable outage time. By using this approach to restore the transformer protection, all tasks as per the procedure drawn up can give positive results. Long customer outages, damage to expensive plant and injury to personnel can be avoided. This method easily satisfies the objective set out and is recommended at all the other 3TM2500 scheme sites where similar problems can occur. However, the ultimate solution will be to replace the entire 3TM2500 scheme with a 3TM5110 protection scheme, which will provide a more reliable transformer protection scheme as a whole. This approach would however take longer to implement, but would definitely provide the required functions for many years.

7. REFERENCES

- [1] Eskom Distribution, *Distribution Technical Bulletin 00TB-07*, May2000
- [2] P Gerber, *Transformer Protection Philosophy*, Eskom, Standard, SCSAGAAG0 Rev 3, February 2011.
- [3] *Current Differential Relay Instruction Manual*, Schweitzer Engineering Laboratories, SEL 387A Pullman, WA USA 99163-5603, 2002
- [4] Charles J. Mozina, "Protection and Commissioning of Multifunctional Digital Transformer Relays at Medium Voltage Industrial Facilities", *IEEE Transactions on Industry Applications*, Vol 41, No 6, pp. 63-73, November 2005
- [5] M. Achterkamp, *Power System Protection Relay Testing Moving From Certification Testing to Application Testing*, KEMA T&D, The Netherlands, 2004
- [6] James R. Cloosen, Mike Young, "Commissioning Numerical Relays", *IEEE Transactions on Industry Applications*, Vol 38, No.3, pp. 81-91 May 2002
- [7] R. Grabovickic, C. Labuschagne, N. Fischer and O. Glynn, "Protection of Transformer-ended Feeders using Multifunctional Relays", *IEEE Transmission and Distribution Conference*, pp. 1-7, May 2012
- [8] *Omicron Reference Manual*, Omicron electronics GmbH, 2002 Omicron, CPC 100, 2004
- [9] *IEEE Guide for the Application of Current Transformer Used for Protective Relaying Purposes*, IEEE Std C37.110-1996, Chapter 7, Differential Protection, October 1996
- [10] Moxa Inc. *Moxa Nport IA5150/5250 Series User's Manual*, 4th Edition, September 2009

Topic E

Power electronics

MINIATURE INTEGRATED CO-AXIAL CURRENT SHUNT FOR HIGH FREQUENCY SWITCHING POWER ELECTRONICS

A.L.J. Joannou* D.C. Pentz*

* *Group on Electronic Energy Processing (GEEP), Dept. of Electrical and Electronic Engineering Science, Corner of University Road and Kingsway Road, University of Johannesburg, Johannesburg 2006, South Africa E-mail: aljoannou@gmail.com*

Abstract: Power electronic converters are now able to operate at very high frequencies due to the development in GaN and SiC power semi-conductor technologies. Measuring such high frequencies with rise and fall times of a few nanoseconds requires specialised instruments and a good knowledge of measurement techniques. This paper introduces a current shunt designed to be integrated into these high frequency power electronic converters. The shunt is required to have a high bandwidth in order to reduce the measurement error.

Keywords: Current measurement, high frequency, co-axial shunt.

1. INTRODUCTION

The drive towards smaller power electronic converters has forced the operating frequencies of converters to increase, such that the normally large energy storage elements of these converters can be reduced in physical size. Although size limitations still exist due to the magnetic elements, the overall reduction is still considerable. Previously, the limitation of the maximum switching frequency of these converters was the transistors.

Developments in power semi-conductor technology introduced Silicon carbide (SiC) power switching transistors which are able to switch in the RF range, and even newer semi-conductors have been introduced for power switching, the GaN transistors, which are said to be able to achieve even better characteristics than the SiC devices as discussed in [1] and [2]. These recent developments in semi-conductor switches have now left other technologies to trail. One such technology has been identified as accurate current measurement. Although actual measurement probes are well developed, especially for voltage measurement, the high frequency switching operation of the circuit can cause stray flux to couple onto the measurement leads causing considerable measurement error.

Current probes also often require that a loop be added to accommodate a current probe. This loop adds inductance to the circuit which will change the operating characteristics of the circuit. Ideally HF and RF switching power electronic circuits should have as little parasitic inductance and capacitance as possible. This implies that current and voltage sensors should be carefully designed and characterised to ensure that the parasitic impedance they add is negligible, or at least will not drastically affect the circuit operation. This is especially important for new switching devices such as eGaN FETs [3].

2. CURRENT MEASUREMENT IN POWER ELECTRONIC CONVERTERS

Measuring current in power electronic circuits is important for several reasons, such as protection and control. Measuring current in RF devices in the past was not a concern, since the devices were either low power, or operated under sinusoidal conditions. Measuring the pulsed current waveforms in power electronic circuits requires current sensors with high bandwidth capability.

The bandwidth of any device corresponds to the 3dB knee frequency which also correlates to a 45 degree phase shift at that 3dB point. This large phase shift can cause inaccurate measurement and possibly failure in the circuit. For instance, if a phase arm is switching out of phase, a phase shift (which correlates to a time shift) in either of the drive signals can cause a short circuit current through the switches which would be detrimental to the circuit and/or the power switches. This is why it is important to realise that measurement specifications for hard switching power electronic circuits must be strict and that the 3dB rated frequency is not a true or sufficient figure of merit.

Current sensors, specifically in power electronic circuits, aim to achieve the following characteristics as listed in [4]:

- Compact size with a very low profile
- Ease of manufacture and low cost
- High bandwidth for high frequency operation
- Fast response with low parasitic elements introduced
- Reliable with good noise immunity
- High stability with varying temperature

The criteria listed above are used as guidelines while designing the integratable shunt discussed in this paper. The accuracy of a current sensor relies heavily on the impedance matching of the input and outputs of the device under test [5]. Several different shunt technologies are discussed next.

3. INTEGRATED CURRENT MEASUREMENT TECHNIQUES

3.1 Integrated current transformer

Current transformers still require a magnetically permeable core, even at high frequencies. This core can do no less but add to the layout inductance of the power circuit as well as the inherent inductance of the current sensor which limits its rise time response [6]. Another problem with current transformer sensing methods is that only AC waveforms can be measured.

3.2 Current sensing on chip

Some designers have even tested the idea of integrating the sensing technology on the chip for applications as in [5] and [7]. The advantage of current sensing on chip is that the inherent inductance of the sensor is small. Even so, physically measuring this current can still introduce measurement error. This is costly and is not available for all power switches since it is part of the chip manufacturing.

The on state resistance can also be used to measure the current. As more current passes through the power switch, the on state resistance varies as a function of temperature, thus varying the measured quantities. The true limitation of current sensing on chip is the temperature distribution in the chip.

3.3 Integrated Rogowski coil

Rogowski coils can be integrated into a circuit. The limitation of the Rogowski current sensor is the integrator, since the coil itself can be designed to have a high bandwidth [6]. In order to achieve a high bandwidth device, the cost of the integrator exponentially increases making this an unfeasible option.

3.4 GMI and GMR current sensing

Giant Magneto Impedance (GMI) sensors and Giant Magneto Resistive (GMR) sensors [6] are sensor technologies which can also be integrated into the power electronic circuit. This is because their method of operation allows for these devices to reduce in size significantly as discussed in [8]. Although these GMI and GMR devices can be made relatively small, they are costly and complex to be designed into a common power electronic circuit, as well as susceptible to the EMI generated by the power electronics.

3.5 Integrated planar shunt

This shunt resistor is constructed using thick film metallisation technology [6]. The advantage of this shunt design is its ultra-low profile and low cost. The resistance may vary due to the contact resistance [4].

3.6 Co-axial shunt resistor

A typical co-axial shunt resistor is shown in Figure 1. The idea behind the co-axial shunt resistor is to create a shunt with low inherent parasitic elements, high bandwidth and also to be able to measure with low measurement noise. This is achieved by physically placing the measurement lead wire within the field free region of the shunt resistor. The region is field free because it is inside the current carrying tube conductor as indicated in Figure 1, and can be explained with Amperes circuital law. This law states that the magnetic field enclosed by any enclosed path is equal to the current enclosed by that path [9]. Hence the enclosed area inside the shunt will have no magnetic field. The common type of co-axial shunt resistors as indicated in Figure 1 is bulky and is physically large so that it can thermally dissipate the losses. The disadvantage of shunt resistors is they do not offer isolation and they are temperature dependent.

Simply miniaturising the shunt will reduce the area from which it can dissipate the thermal energy losses, hence lowering the power capability of the shunt. The shunt needs to be miniaturised so that it can be integrated into the PCB of the power electronic converter and still be able to dissipate the thermal energy.

The shunts that are discussed in this paper are for low or high voltage, but low current applications, namely below 20 amperes. This low current will correspond to the voltage drop across the shunt resistor being comparable with the leakage flux that could induce measurement noise. Thus the shunt needs to be designed such that the desired signal can be differentiated from the measurement error.

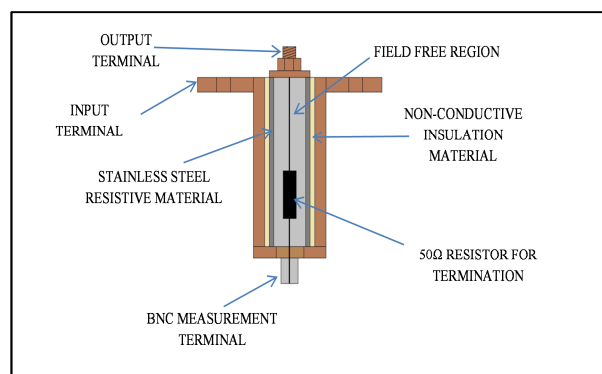


Figure 1: Co-axial shunt resistor

4. MINIATURE INTEGRATED CO-AXIAL SHUNT

Shunt resistors are known to be one of the most accurate and simplest methods of sensing current as discussed in [10]. They are also cost effective. The current is simply determined by the voltage drop across the resistor using Ohm's Law. Therefore it is imperative that the shunts are designed to reduce the effects of parasitic elements. These reasons thus lead to the proposed shunt design

which resembles a co-axial shunt resistor. To reduce the parasitic elements, an integrated design is implemented.

Inspired by the more common co-axial shunt, this shunt resistor mimics the operation to achieve similar characteristics but physically at a much smaller scale. The resistance of the shunt should be small (normally in the order of a few milli-ohm) so that the losses due to the shunt are negligible (1.286 W at 10A). The shunt should also be designed so that the stray flux that could possibly couple onto the measurement is negligible compared to the actual current measurement, hence low measurement error.

The performance of the shunt is dependent on its size as well as placing the measurement leads in a low field region as discussed earlier as well as in [4]. Therefore by miniaturising the design, the shunt resistor should have better high frequency performance. The next issue is the thermal dissipation of the shunt.

In order to keep the cost low, the design should be simple and easy to implement, no exotic metals are used in this miniature shunt design. Instead surface mount (SMD) resistors are used as the resistive material. A cross section of the miniature or even micro shunt design is shown in Figure 2 and Figure 4. The current paths through this shunt are indicated in Figure 4. The current flow in adjacent current carrying paths is in opposite directions, the field around the paths will be weak fields because of the field cancellation. This electromagnetic effect will also cause a high current concentration on the edges of the conductors facing each other on the adjacent paths.

Skin depth and proximity effects are critical phenomena which can affect the resistance and inductance of the shunt. The current distribution of the shunt must be balanced to ensure even current flow throughout the shunt. The arrangement of the SMD resistors is indicated in Figure 3. This concentric arrangement of the SMD resistors of equal resistance will ensure a relatively even current distribution at high frequencies. This also allows for even heat dissipation of the SMD resistors. In Figure 3, eight resistors (the shunt design can include more resistors to design as discussed later) are shown connected in parallel. Connecting the resistors in parallel will increase the electrical power capability of the shunt. Although from a thermal perspective, this implies that the heat dissipating surfaces are closer together. Also, the resistors power dissipation specifications are tested in free air and not when packed closely together.

This shunt design is cost effective and easy to implement and integrate into any high frequency circuit design. This type of shunt can be used for feedback control in the converter, but it is suggested measurement terminals are reconsidered. The components used for this shunt are also chosen as common components which are often used in high frequency power electronic converters. The

constructed integrated co-axial shunt resistor is shown in Figure 5.

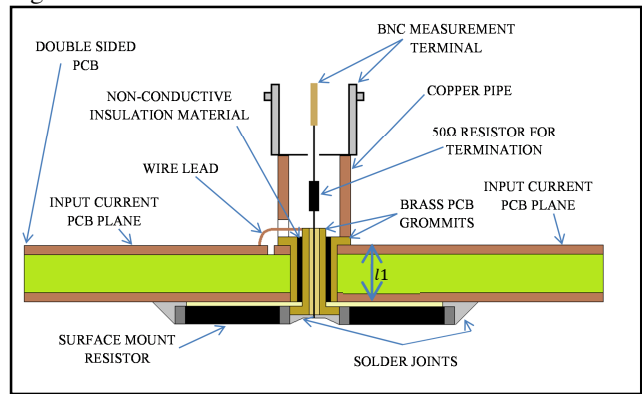


Figure 2: Cross section of miniature integrated co-axial shunt resistor

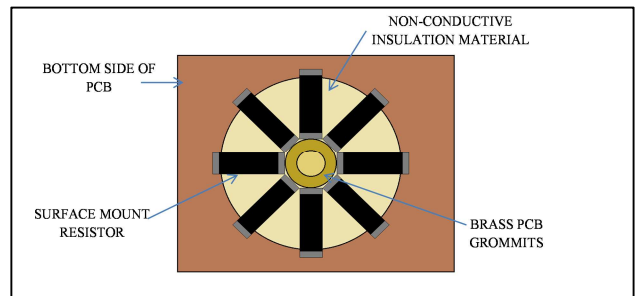


Figure 3: Bottom view of miniature shunt indicating concentric arrangement of SMD resistors

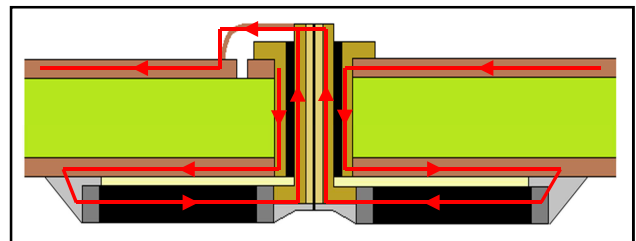


Figure 4: Current path of shunt resistor indicating currents in adjacent paths flowing in opposite directions

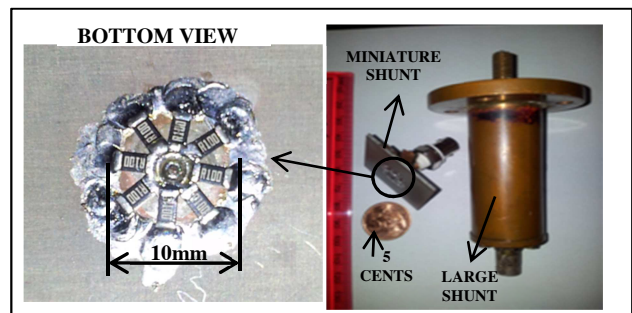


Figure 5: Photo of actual shunt resistor

5. MINIATURE INTEGRATED CO-AXIAL SHUNT DESIGN PROCEDURE

The general approach to design such a shunt is explained below. This is the procedure that was followed during the design of the shunt discussed in this paper.

1. Choose maximum current to flow through the shunt, I [A].
2. Choose the maximum power dissipation of the shunt, P [W].
3. Determine the resistance of the shunt, $R = \frac{P}{I^2}$
4. Determine if the voltage drop measured across the shunt will be sufficient $V = IR$. If not, then revisit steps 1 to 3.
5. Using both the resistance of the shunt as well as the power rating, choose the number of resistors to be placed in parallel. Note that all resistors should be the same value to ensure even current and power distribution. Also, the size of the shunt should be realised. Using too many resistors in parallel becomes impractical. In this step one should also consider the size of the grommet/via that will be used. Ideally the resistors should all be spaced equally around the shunt.

Specifically for the shunt discussed in this paper, the maximum current to be measured is $I=12A$. The maximum power dissipation is chosen as $2W$. Thus the resistance is initially chosen as $R=0.0125\Omega$. Therefore at $12A$, the voltage drop across the shunt will be $150mV$ which is sufficient. Next the resistors were chosen to be $0.25W$ per 1206 SMD package. This means that the number of required resistors would be

$$No. resistors = \frac{Total\ power}{Power\ per\ package} = \frac{2}{0.25} = 8 \quad (1)$$

The most readily available resistance value is 0.1Ω for which a parallel combination of 8 resistors result in a resistance of 0.0125Ω as required. SMD resistors are chosen because of their size advantage but also because they are flat and can be placed relatively close to the PCB, which will result in a lower inherent inductance. Obviously the more resistors, the better, since the surface covered would be larger with closer resemblance to a solid disc. A solid disc will have better current distribution than the discrete resistors. A solid resistive disc can be made using embedded resistor printed circuit board as found in [11]. Such PCB is not readily available and the resistive material used may vary in resistance.

6. CHARACTERISATION

Characterising the shunt resistor so that the results are in fact meaningful is possibly the most important aspect. The impedance measurement guidelines can be followed in [12], [13] and [14].

6.1 DC characterization

Two tests were performed under DC conditions. One test is to determine the DC resistance, and the other to determine the rated thermal capacity versus the experimental thermal capacity at the specified current of $12A$. A four point wire measurement using a FLUKE 5520A Calibrator was used to measure the DC resistance

of the miniature co-axial shunt resistor. The resistance was measured to be $12.86m\Omega$. The theoretical resistance is effectively eight 0.1Ω resistors in parallel which is equal to $12.5m\Omega$. Thus the measured resistance is slightly higher which is acceptable and highly likely due to the tolerance ratings of the resistors, solder as well as contact resistance which is added.

Each resistor used is characterised to have a thermal power dissipation of $0.25W$ in free air. The resistors are placed in close proximity to each other. This yields a problem since the thermal dissipating areas are now close to each other. This will de-rate power specification of each resistor package. Although it is assumed that the maximum possible rating is the listed rating for free air. Since eight 0.25 watt resistors were used, the total thermal dissipation is 2 watts. The DC resistance is $12.86m\Omega$, thus the theoretical power loss at $12A$ is

$$P = I^2R = (12)^2(12.86 \times 10^{-3}) = 1.85 W \quad (2)$$

Theoretically, the shunt should be able to dissipate the thermal losses. A continuous supply of $12A$ DC was passed through the miniature shunt to test its thermal capability. The shunt was tested for one hour without any sign of failure of the shunt, but a slight increase in resistance because of the rise in temperature, which is as expected.

6.2 Frequency characterisation

The shunts' frequency characteristics were measured using two different methods.

Impedance analyser results:

An Agilent 4294A impedance analyser was first used to characterise the shunt resistor. The miniature shunt was measured against a regular large size co-axial shunt, both with the same measurement procedure and setup. The leads of the shunts were initially calibrated out of the measurement, so that only the shunt impedance could be measured.

At low impedances, the Agilent 4294A loses much of its accuracy. Therefore these results are not much of an indication of the characteristics of the shunt. These results are shown in Figure 6 and Figure 7. Figure 6 indicates that the miniature shunt resistor has a 45 degree phase shift at $1.2MHz$, which is questionable. To obtain a reference to this result, a regular large size co-axial shunt resistor was also measured using the same device and the results are indicated in Figure 7. The regular co-axial shunt resistor measures a 45 degree phase shift at just over 300 kHz. This is highly unlikely which leads one to believe that these results are questionable. This could be due to the fact that the impedance analyser used is incapable of measuring accurately at such low impedances. Another experimental characterisation setup is required to justify these results.

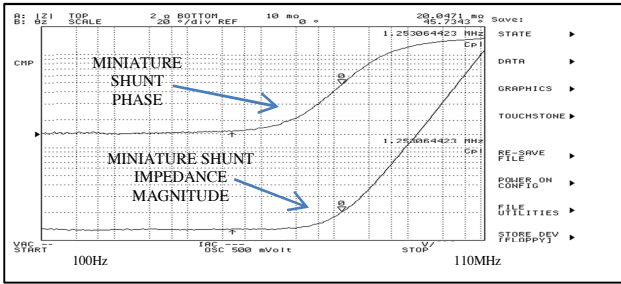


Figure 6: Impedance and phase bode plots captures for miniature shunt resistor

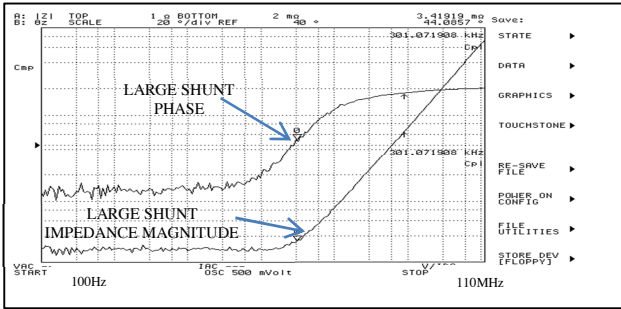


Figure 7: Impedance and phase bode plots captures for regular large co-axial shunt resistor

Vector network analyser results:

An Agilent 8712B Vector network analyser was used to obtain a through-transfer function of the mini shunt. The same procedure was used for the common shunt. Again it should be noted that this instrument also loses accuracy at such low impedances. These results indicate a dominant resonant point at 807MHz, which can be seen in Figure 8. This plot indicates that the miniature shunt is in fact inductive before 807MHz. This needs to be verified with an alternative measurement technique.

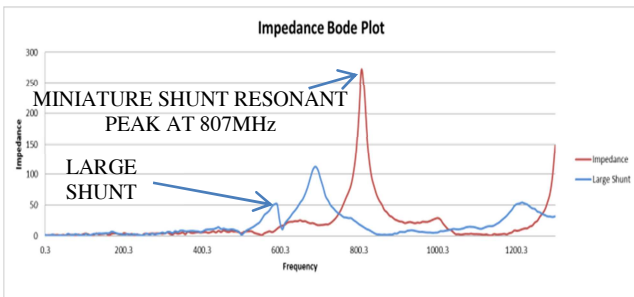


Figure 8: Impedance bode plot for miniature and large co-axial shunt resistor

6.3 Step- response results

An EPC 9001 development board was used which implements eGaN FETs as the power switching semiconductors. These eGaN FETs are able to switch within a few nanoseconds. The shunt resistor was then placed in series with a constructed low inductance resistive load. This load was constructed such that there is uniform current distribution through the load while still maintaining a low inductance. The experimental setup, including the low inductance load is indicated in Figure

9. The experiment was performed at 10 watts, (10V @ 1A).

The power circuit was then setup to induce a 1A current step of a few nanoseconds rise time. The current through the resistor load and shunt was then measured using the shunt resistor and a Tektronix TCP0030 120MHz current probe. The voltage across the resistor load was measured using a Tektronix P5050 voltage probe and a DPO7254 Tektronix oscilloscope was used. These results are indicated in Figure 10.

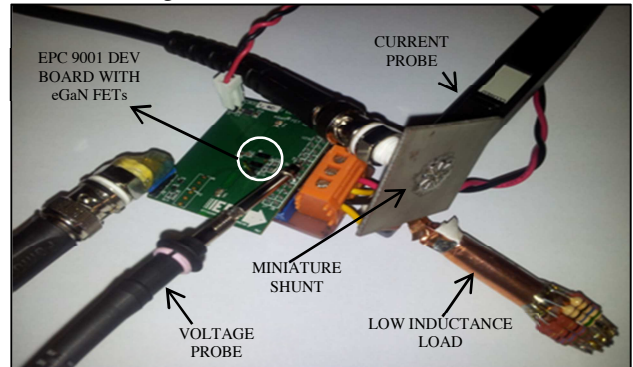


Figure 9: Experimental setup

Figure 10 indicates that there are oscillations in the voltage waveform. This could be due to the complex nature of the load (inherent inductance and capacitance) as well as the inductive loop of the ground return path of the voltage probe, even though the ground loop wire of the voltage probe was removed and short connection loops were soldered in an effort to reduce the voltage probe return loop.

There is also a noticeable delay in the response time of the current probe to the voltage. This could be due to the delay of the hall sensor, long co-axial cable length and amplifier setup of the current probe. The oscillations in the response waveform of the shunt resistor indicated in Figure 10 could be due to reflections and unbalanced source impedance matching and inherent inductance and capacitance resonance of the shunt. This can cause the shunt response to rise faster than the actual measurement. It was also observed that there was no noticeable difference in the shunt measurement with the current probe in the circuit or not.

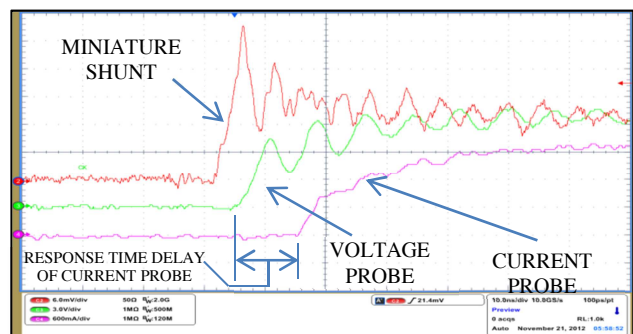


Figure 10: Step response of miniature shunt resistor and current probe

Using the rise time response of the miniature shunt, the bandwidth of the shunt can be estimated using the following equation from [15].

$$t_r = \frac{0.338}{f_{3dB}} \quad (3)$$

The rise time of the shunt to the step response is measured using the oscilloscope to be 2.35ns. This corresponds to a bandwidth of $f_{3dB} = 143\text{MHz}$.

7. FUTURE WORK

The results are not yet satisfactory due to the uncertainty of the results and therefore require more work. Alternative methods of characterising the miniature shunt resistor are being investigated to verify the results presented in this paper. The large shunt still needs to be placed in the same experimental setup to observe its response under the same conditions and compared to the results of the miniature shunt.

The miniature integrated shunt has also been simulated in COMSOL 4.3a. The electromagnetic simulation results are being analysed. The simulated thermal aspects are still to be investigated. The equivalent circuit and theoretical inherent parasitic elements of the miniature co-axial shunt are also being addressed. The equivalent-circuit impedance can also be used to verify the measured characteristics. Implementing the miniature integrated shunt into a HF and possibly RF hard switching power electronic converter circuit using GaN power transistors is also being looked into. The possibility of using embedded thin film resistor PCB and integrating the shunt into such PCB material will allow for better electromagnetic characteristics. This will be investigated and implemented in the near future.

8. CONCLUSION

A current sensor for integrated HF current measurements has been discussed in this paper. The shunt design is low cost and easy to integrate into HF power electronic circuits. The estimated bandwidth of the shunt is 143MHz matches expensive current sensor technologies, such as current probes. The bandwidth also indicates that this type of integrated shunt is capable of measuring rise and fall times of a few nanoseconds. This is suitable for the rated switching times of GaN power transistors. Although this shunt design is intended for integration for GaN based power electronic circuits, it can be integrated into any circuit in which a non-isolated current sensor is required.

9. ACKNOWLEDGEMENTS

I would like to thank Prof. J Daan van Wyk for the original idea on the shunt and suggested experiments. I would also like to thank Dr. Arnold de Beer from the University of Johannesburg and Prof. Ivan Hofsafer from

the University of Witwatersrand for their assistance in measurement with the network and impedance analysers.

10. REFERENCES

- [1] A Lidow, "Is it the end of the road for silicon in power conversion?," in *CIPS*, Nuremburg, 2010.
- [2] N Kaminski and O Hilt, "SiC and GaN devices-competition or coexistence?," in *CIPS*, Nuremburg, 2012.
- [3] A Lidow. (2011) EPC Efficient Power Conversion. [Online]. <http://www.epc-co.com>
- [4] J A Ferreira, W A Cronje, and W A Relihan, "Integration of high frequency current shunts in power electronic circuits," in *IEEE Power electronics specialists conference (PESC)*, Toledo, Spain, 1992, pp. 1284-1290.
- [5] YC Huang, HH Hsieh, and LH Lu, "A low noise amplifier with integrated current and power sensors for RF and BIST applications," in *IEEE-VLSI Test Symposium*, 2007, pp. 401-408.
- [6] C Xiao, L Zhao, T Asada, W G Odendaal, and J D van Wyk, "An overview of integratable current sensor technologies," *IEEE-IAS*, 2003.
- [7] KH Cheng, CW Su, and HH Ko, "A high-accuracy and high-efficiency on-chip current sensing for current mode control CMOS DC-DC buck converter," in *IEEE-Electronics circuits and systems (ICECS)*, 2008, pp. 458-461.
- [8] E R Olson and R D Lorenz, "Integrating giant magnetoresistive current and thermal sensors in power electronic modules," in *IEEE-Applied power electronics conference and exposition (APEC)*, 2003, pp. 773-777.
- [9] W H Hayt and J A Buck, *Engineering electromagnetics*, 7th ed. New York, United States: McGraw Hill Publishers, 2006.
- [10] W Pfeiffer, "Ultra-high speed methods of measurement for the investigation of breakdown development in gasses," *IEEE transactions on instrumentation and emasurement*, vol. IM-26, no. 4, pp. 367-372, December 1977.
- [11] J Wang and S Clouser. Gould Electronics. [Online]. http://www.gould.com/e4/e139/e197/tpyea_r203/tpdownload227/01_ThinFilm_eng.pdf
- [12] Agilent Technologies, 8 Hints for succesful impedance measurements, Application Note 346-4.
- [13] Agilent Technologies, Impedance and network analysis application list, 2012, Revision-2.00.
- [14] Agilent Technologies, Advanced impedance measurement capability of the RF I-V method compared to the network analysis method, Application Note 1369-2.
- [15] H Johnson and M Graham, *High-speed digital design a handbook of black magic*. New Jersey, United states of america: Prentice Hall, 1993.

POWER LOSS ANALYSIS OF TWO-LEVEL AND NPC THREE-LEVEL VOLTAGE SOURCE INVERTERS

*A. Khan, M.A. Khan and P. Barandse.

Department of Electrical Engineering, University of Cape Town. Cape Town 7701, South Africa.
 Email: *akrama.khan@uct.ac.za, azeem.khan@uct.ac.za, paul.barendse@uct.ac.za.

Abstract: The aim of this paper is to compare the power losses in two-level and Neutral Point Clamped three-level PWM voltage source inverters. The DC link capacitor, conduction and switching losses are calculated for low and medium voltage applications. A three-level inverter gives a smoother output voltage because of the intermediate voltage levels in its output waveform. Moreover, it has lower power and Dc link capacitor losses.

Keywords: PWM, NPC, DC-link.

1. INTRODUCTION

A voltage source inverter (VSI) is used to convert a fixed DC voltage to a three phase AC voltage with flexible magnitude and frequency. As the cost of energy is rising with growing industrial concerns the topology and components' selection of the inverter plays an important role in these critical applications. The conventional two-level inverter completely satisfies the low-voltage (L.V) power applications where the nominal line-to-line 690 Vrms (IEC) 575 Vrms (ANSI). Furthermore, the output voltage is synthesised by means of two voltage levels [3].

In contrast, the multilevel inverters offer significant advantages on the medium and high voltage applications. It produces a smoother output voltage with three voltage levels on each terminal and five on line-to-line. This voltage results in a lower THD. Switching losses are also reduced due to faster switching. However, conduction losses are slightly higher because of high forward drop and with static and dynamic voltage sharing and it appears that multilevel topology gives extra benefits. In this paper comparison is made between two-level H-Bridge and three-level Neutral Point Clamped (NPC) inverters.

In two-level inverters increasing the switching frequency can give a smoother voltage but in high power applications it brings more switching losses. In three-level inverters voltage rating of switches can be lower than in the two-level. Lower voltage switches which are used in multilevel inverters are generally faster, smaller and cheaper. A lower voltage variation (dv/dt) in the three level inverter decreases the stress in cables thereby reducing the risk of motor failure due to bearing fault [2].

In this paper the topology of both two and three-level inverters are compared. In particular DC link capacitor losses, switching and conduction losses are compared. The conduction losses of both inverters are based on the V-I characteristics of IGBT-diode modules. On the other hand, switching losses are also estimated on IGBT-diode characteristics.

2. TOPOLOGIES OF TWO LEVEL & THREE LEVEL INVERTERS

In this section both inverter topologies are discussed briefly.

2.1. Two level Inverters

A conventional two-level inverter circuit is shown below in the figure 1.

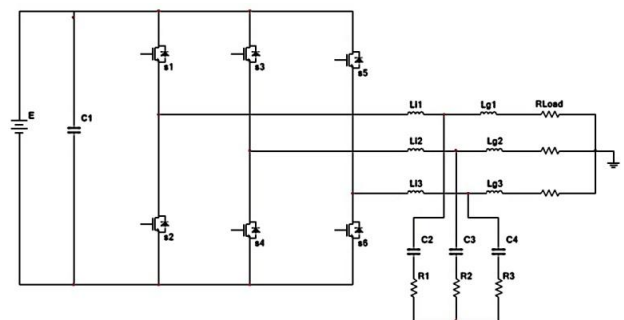


Figure 1: H-Bridge two-level inverter topology

This configuration comprises six switches (IGBT/diode). Diode actually provides a free-wheeling path for current. Pulse Width Modulation (PWM) will be applied for high power configuration. If the maximum potential impact on each switch can be equal to the DC link voltage, i.e E. Then the total voltage variation (dv/dt) at the terminal is also equal to E. The line-to-line voltage has three voltage levels (+E, 0, -E), as shown in figure 2.

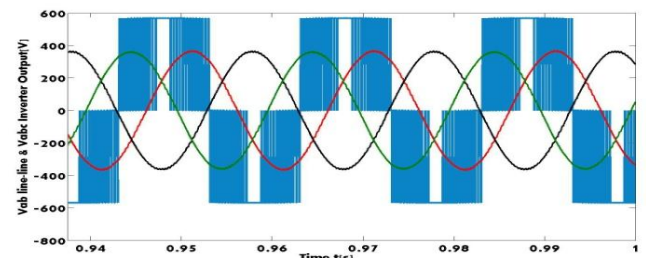


Figure 2: V_{ab} line-line and output voltages for two-level inverter

To obtain a sinusoidal signal, a filter with high component values is required to suppress high frequency harmonics [5].

2.2. Three level Inverters

The three-level inverter circuit configuration is shown below in figure 3.

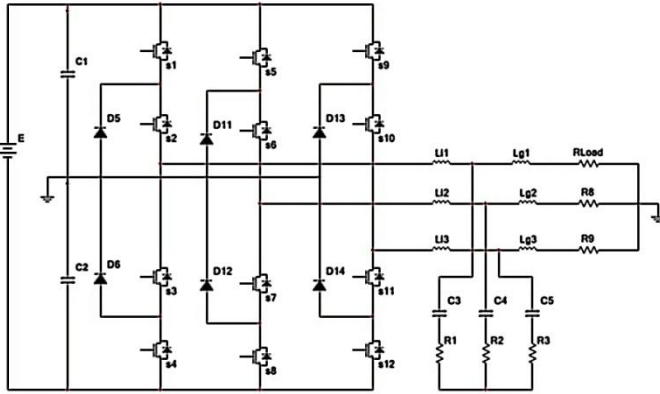


Figure.3: Neutral-Point-Clamped three-level inverter topology

This inverter gives lower potential impact on power semiconductor components. It has extensive diminution of all sorts of electric noises, and also features higher reliability and lower losses. The output terminal voltage has three levels +E/2, 0, -E/2. It can be seen that voltage impact on switches is half of those in a two-level inverter. Therefore each terminal has voltage variation (dv/dt) equal to E/2. The line-to-line voltage has five voltage levels (+E, +E/2, 0, -E/2, -E) as shown in figure 4.

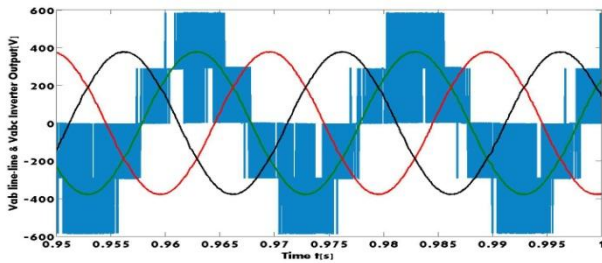


Figure 4 : V_{ab} line-line and output voltages of three-level inverter

The resulting output waveform is more sinusoidal than in the case of two-level topology [5].

3. CALCULATION OF POWER LOSSES

In this section expressions for switching and conduction losses for the two topologies are reviewed thoroughly. DC link capacitor losses are estimated on the basis of rms value of capacitor current. The total power losses can be calculated from the following equation [4].

$$P_{loss} = 3P_{con} + 3P_{sw} + P_{cap} \tag{1}$$

Where P_{con} is the conduction loss, P_{sw} is the switching loss and P_{cap} is the DC link capacitor loss. These values can be calculated from the charge and discharge times of the capacitor [12].

Consider a 30kW system with DC link voltage of 580V, nominal output current of 30A and output voltage of 380V. Switching frequency of 25kHz and inverter output frequency of 50 Hz. The IGBT selection is made for the specifications mentioned above. The switching voltage for three-level inverters is half of that used in two-level inverters. The difference in these voltage ratings has a significant impact on the power loss calculations. The modules used in this study are Semikron SKM 145GB123D and SK75MLI066T.

For example, 600V-IGBT class gives 10% lower ON-state voltage as compared to 1200V-IGBT. Moreover, 600V-IGBT has less switching losses while conduction losses increase by twice that of 1200V-IGBT, shown in the table below:

TABLE I
Parameters Values From The Data Sheet

	IGBT	Conditions (T _j =25°C)	E _{on} [mJ]	E _{off} [mJ]	V _{CE}
600V	SK75MLI066T Trench IGBT	V _{CE} =300V I _O =100A	2.5	3.4	1.1
1200V	SKM145GB123D MOS input	V _{CE} =600V I _O =100A	17	12	1.6

3.1. DC link Capacitor losses:

The DC link capacitor losses can be determined by considering the rms value of current through the capacitor. The capacitor current has a charging and discharging component which can be expressed as [4].

$$I_{C,rms} = \sqrt{I_{d,rms}^2 - I_{d,DC}^2} \tag{2}$$

Where,

I_{crms} is rms value of charge current.

I_{drms} is rms value of discharge current.

$$i_{d,DC}(\phi) = \frac{1}{T_s} (\sum_j T_j \cdot i_{d,j}) = \sum_j \delta_j \cdot i_{d,j} \tag{3}$$

$$i_{d,rms}^2(\phi) = \frac{1}{T_s} (\sum_j T_j \cdot i_{d,j}^2) = \sum_j \delta_j \cdot i_{d,j}^2 \tag{4}$$

I_{d,DC} and I_{d,rms} can be calculated as follows:

$$I_{d,DC} = \frac{1}{2\pi} \int_0^{2\pi} i_{d,DC}(\phi) d\phi \quad (5)$$

$$I_{d,rms} = \sqrt{\frac{1}{2\pi} \int_0^{2\pi} i_{d,rms}^2(\phi) d\phi} \quad (6)$$

If the values of the charging and discharging currents are known, they can be multiplied by the estimated Equivalent Series Resistance (ESR) values of the capacitor. Typical ESR values are given in the table below.

TABLE II
Typical Values of Equivalent Series Resistance

Type	22μF	100μF	470μF	1000μF	4700μF
Standard Aluminum and Ceramic	1 to 5.4Ω	0.3 to 1.2Ω	0.1 to 0.24Ω	0.02 to 0.12Ω	0.01 to 0.23Ω

The loss calculations are given in the following table: [4]

TABLE III
DC Link Loss Calculation

Topology	$I_{C,rms}$	$I_{d,DC}$	$I_{d,rms}$	ESR Ω	Loss/Ca pacitor	Total Loss(W)
Two-Level	31.6	26.9	41.5	0.04	68.89	68.8×3=206.67
Three-Level	73.2	62.3	96.1	0.01	92.31	92.31×2=184.62

Capacitors used for DC link were three for two-level and two for three-level inverter. However, in the case of three-level configuration only one capacitor is used for a single commutation so the total loss can be divided by 2. This can give almost exact results although it still needs further research.

3.2. Switching losses:

The switching losses contribute significantly to the total losses of the system. Switching losses are independent of inverter Modulation Index (M) and Power factor but increase with switching frequency (fs). In order to build an accurate model switching-on and switching-off of IGBTs and diodes need to be considered carefully. In this paper hard switching has been applied on both inverter topologies. Even though the two-level inverter has higher switching losses, soft-switching (ZVS turn-on) could be easily performed reducing its losses. But modeling soft switching events in detail for three-level inverter is extremely complex to deal with. Here, only the on and off times power loss of the switches are discussed. The current dependency of switching losses for the transistor diode module is investigated from the datasheets for both two and three level configurations [12].

3.2.1. Two-Level Inverter switching losses:

IGBT switching behaviour is characterised by the turn-on time delay $t_{d(on)}$, the rise time (t_r) and turn-on energy (E_{on}). The turn-on gate pulse is applied at t_0 and due to the input capacitance of the IGBT the gate voltage V_{GE} rises gradually [12]. After the time $t_{d(on)}$, V_{GE} reaches a threshold voltage V_{CE} during which time the collector current I_c starts to increase almost linearly. Similarly, in a turn-off situation, its behaviour again is dependent on turn-off delay time $t_{d(off)}$, fall time t_f and turn-off energy E_{off} . By discharging the input capacitance of the IGBT, the gate emitter voltage V_{GE} is reduced but V_{CE} remain unchanged until V_{GE} is drained out completely to bring IGBT out of saturation [2].

Estimating the switching losses for the IGBT and diode switching. The turn-on and turn-off energy can be used from the device data sheet as shown in figure 5.

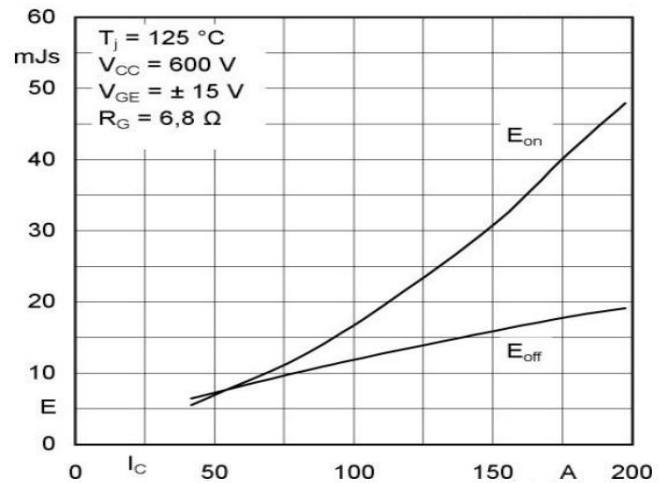


Figure. 5: turn-on /-off energy = f(Ic)

Switching loss can be calculated as:

$$P_{on} + P_{off} = \frac{1}{\Pi} \cdot f_s \cdot [E_{on}(i) + E_{off}(i)] \quad (11)$$

Where E_{on} is the on-energy, E_{off} is off-energy and f_s is switching frequency. The module data sheet gives $E_{on} = 17mJ$ and $E_{off} = 12mJ$ when the rated current is 100A, and using switching frequency $f_s = 25 KHz$. The total switching loss can be calculated from the equation and the power loss per switch is **230W**.

3.2.2. Three-Level Inverter switching losses:

As there are only two commutations per period for IGBTs as shown in the fig.7 the switching losses for the other two switches can be excluded for each cycle.

Equation(11) can be used to estimate the switching losses for the IGBT and diode on the basis of the turn-on and turn-off energy from the data sheet as shown in figure 6 :[12]

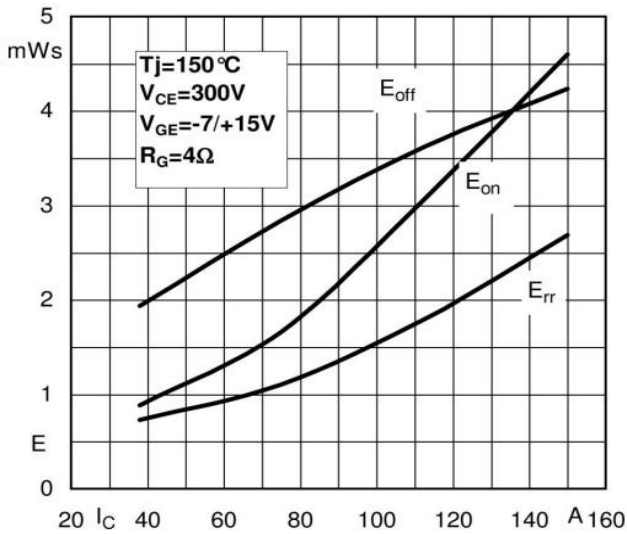


Figure. 6: turn-on /-off energy = f (Ic)

Module data sheet gives $E_{on} = 2.5mJ$ and $E_{off} = 3.4mJ$ when the rated current is 100A and taking switching frequency f_s 25KHz. The switching loss per switch is **46.97W**.

3.3. Conduction losses:

Conduction losses do not depend on switching frequency f_s , but are directly affected by modulation index and Power Factor. Conduction losses are function of currents in semiconductor devices and their saturation voltage values; therefore it can be computed by multiplying voltage and current in an ON state. Conduction losses in IGBTs and diodes for both two and three-level configurations are analysed in this section with the help of the following equations.

3.3.1. Two-level Inverter conduction losses:

The conduction period for semiconductor devices in a single leg of the inverter during half of the switching period is defined as [7]:

$$\alpha_R(\tau) = \frac{1}{2}[1 + M \cos \omega_N \tau] \quad (7)$$

Positive current for the half period can be calculated as:

$$i_{T2}(\tau) = i_{N,R}(\tau) = I_c \cos(\omega_N \tau + \phi) \quad (8)$$

The half cycle current can be integrated to give the conduction losses.

The conduction losses for the IGBT are given as:

$$P_{con_2L_T} = \left[\frac{V_{CEO} \times I_c}{2\pi} + \frac{r_{CE} \times I_c^2}{8} \right] + M \cos \phi \left[\frac{V_{CEO} \times I_c}{8} + \frac{r_{CE} \times I_c^2}{3\pi} \right] \quad (9)$$

Where V_{CEO} and r_{CE} are collector-emitter on state voltage and resistance, V_{FO} is forward voltage drop and r_F is the forward resistance of the diode.

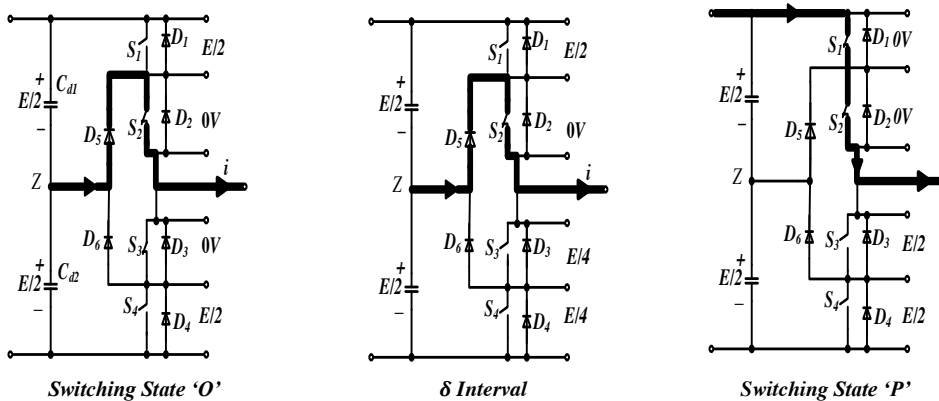
The conduction losses for diode are given as:

$$P_{con_2L_D} = \left[\frac{V_{FO} \times I_c}{2\pi} + \frac{r_F \times I_c^2}{8} \right] - \frac{M}{4} \cos \phi \left[\frac{V_{FO} \times I_c}{8} + \frac{r_F \times I_c^2}{3\pi} \right] \quad (10)$$

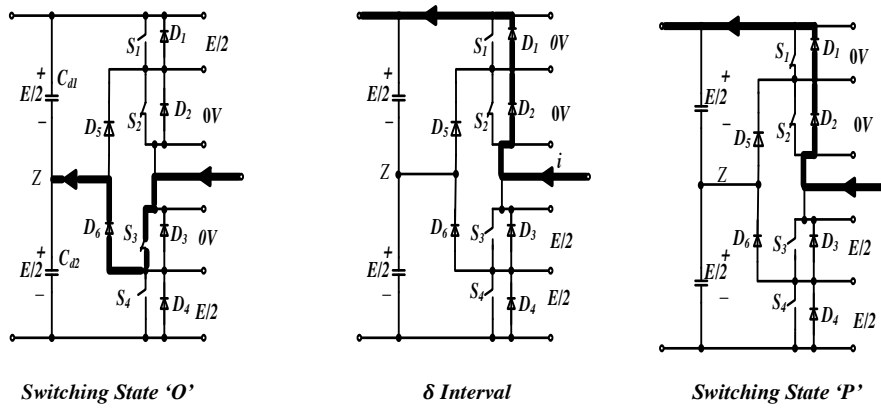
Setting the values as $M=1$, $\phi=1$, $i=100A$ and from data sheet $V_{CEO} = 1.6V$, $r_{CE} = 14m\Omega$, $V_{FO} = 1.4V$, $r_F = 11m\Omega$, $P_{con_2L_T} = 61.8W$, $P_{con_2L_D} = 20.2W$. So total conduction loss per leg of a two-level inverter is $2 \cdot (61.8+20.2) = 164W$.

3.3.2. Three-level Inverter conduction losses:

For three-level configuration the same equations are repeated to calculate loss at each IGBT and diode including the clamping diodes. However, a detailed analysis of the commutation of the inverter is necessary to calculate the specific semiconductor device losses during conduction. The commutation process is illustrated in figure 7 (a & b)



(a) Commutation with $i > 0$



(b) Commutation with $i < 0$

Figure.7: Commutation during switching state ‘O’ to ‘P’

Switching states ‘O’ defines switches S2 and S3 are ON, ‘P’ shows S1 and S2 are ON and ‘N’ denotes S3 and S4 are conducting. Taking the DC input voltage as “E” whereas C_{d1} and C_{d2} are the DC bus capacitors.

Considering a state change from ‘O’ to ‘P’: in the case of $i > 0$, the switching state ‘O’ has switches S2 and S3 switched on while S1 and S4 are off. Positive load current $i > 0$ puts the clamping diode D5 in an on-state. Therefore voltages across switches S2 and S3 are seen as zero and the voltage on each switches S1 and S4 is equal to $E/2$.

S3 is being switched off during the δ interval. The current path remains same. Now S3 is fully gated off, the voltage across S3 and S4 equals to $E/4$. The top switch S1 is turned on in the switching state ‘P’ [10].

The same procedure repeats for negative current cycle as shown in Fig7(b). It can be deduced that only half of the DC bus voltage is experienced by all the switches in the NPC inverter during excursion from state ‘O’ to ‘P’, similarly from ‘P’ to ‘O’ and vice versa. So in a single phase current for a positive cycle two switches and a diode are involved and for a negative cycle two diodes and a switch are involved. Eventually for a whole phase change three stages are involved, e.g ‘PON’.

Setting the values as $M=1$, $\phi=1$, $i=100A$ and from the data sheet $V_{CEO} = 1.1V$, $r_{CE} = 10m\Omega$, $V_{FO} = 1.1V$, $r_F = 8m\Omega$,

$$P_{con_3L_T} = 43.15W \quad P_{con_3L_D} = 15.5W$$

Total losses on the inverter leg are:

$$\text{For (O-P)} : 43.15+43.15+15.5 = 101.8W$$

$$\text{For (P-O)} : 15.5+15.5+43.15 = 74.15W$$

Similarly,

$$\text{For (O-N)} : 43.15+43.15+15.5 = 101.8W$$

$$\text{For (N-O)} : 15.5+15.5+43.15 = 74.15W$$

$$\text{Total Loss} = 2x(101.876+74.15) = \mathbf{352W}$$

3.4. Total Loss Calculation for two and three level inverters:

The total loss can be calculated from equation (1):

It gives conduction loss for single phase and on a single switch. The proper loss equation per phase of either topology is given as: $P_{loss} = 3(P_{con} + 2.P_{sw}) + P_{cap}$ (12)

Following table compares the total losses for the two inverter topologies.

TABLE IV
Total loss calculated for two- and three-level inverters

Configuration	DC link capacitor losses P_{cap} (W)	Switching losses P_{sw} (W)/switch	Conduction losses P_{con} (W)/phase	Total losses per phase (W)
Two level	206.67	230	164	2079
Three level	184.62	46.9	352	1522

From the table above it can be concluded that total losses for two-level inverter is slightly higher as compared to three-level inverter.

4. CONCLUSION

This paper evaluated power loss comparison for two inverter topologies. It was found out that the conduction losses for the two-level inverter are lower than the three-level configuration. However, overall power losses for the three-level configuration are lower for selected semiconductor devices. Three capacitors were used for the two-level inverter DC-link loss analysis. Even if DC-link capacitor losses of the two-level inverter are reduced it cannot compensate for their increased semiconductor losses. Analytical results were

shown with the help of mathematical equations. It was discovered that the three-level configuration has 36% less losses than the two-level. Thus the three-level topology achieves an overall improvement of power conversion efficiency.

5. REFERENCES

- [1] G.I.Orfanoudakis, SM. Sharkh M.A Yuratich and M.A Abusara “Loss Comparison Of Two And Three-Level Inverter Topologies” , International Conference on Power Electronics, Machines and Drives (PEMD),2010.
- [2] P. Alemi and Dong-Choon Lee.”Power Loss Comparison in Two and Three-Level PWM Converters” , International Conference on Power Electronics and ECCE Asia (ICPE & ECCE) , 2011.
- [3] Ralph Teichmann and Stefan Bernet “A Comparison of Three-Level Converters Versus Two-Level Converters for Low-Voltage Drives, Traction and Utility Applications” IEEE Transactions on Industry Applications , Vol.41, No.3 May/June 2005.
- [4] M. Ikonen, O. Laakkonen, M. Kettunen “Two-Level and Three-Level Converter Comparison In Wind Power Application” , <http://www.elkraft.ntnu.no/smola2005/Topics/15.pdf>
- [5] TOSHIBA G9000 UPS, “Multilevel PWM IGBT Technology” White Paper.2008.
- [6] Uwe Drogenik and Johann W. Kolar “A General Scheme for Calculating Switching and Conduction-Losses of Power Semiconductors in Numerical Circuit Simulations of Power Electronic Systems” IPEC, Niigata, Japan, 2005.
- [7] J.W.Kolar, H. ERTL and F.C. Zach “Influence Of The Modulation Method On The Conduction And Switching Losses Of A PWM Converter System” International Conference on Industry Applications Society, Annual Meeting, conference record on the 1990 IEEE.
- [8] R. Krummer, T. Reinmann, G.Berger, “On-Line Calculation of The Chip Temperature of Power Modules in Voltage Source Converters Using The Microcontroller” Proc. Of the 8th European Conference on Power Electronics and Applications, Lausanne, Switzerland. 1999.
- [9] J.W.Kolar, T.M. Wolbank and M. Schrod. “Analytical Calculation of the RMS Current Stress on the DC Link Capacitor of Voltage DC Link PWM Converter System” , IEE 9th International Conference on Electrical Machines and Drives, No.468.1999.
- [10] B. Wu “High Power Converters and AC Drives” IEEE press.2006.
- [11] F.Renken “Analytic Calculation of the DC Link Capacitor Current for Pulsed Three Phase Inverters” , EPE-PEMC, 2004.
- [12] SKM 145GB123D & SK75MLI066T datasheets. Available at http://www.semikron.com/skcompub/en/igbt_modules-81.html

THE IMPACT OF THE CONVERTER MODES ON THE DISTRIBUTION OF ACTIVE HARMONIC POWERS

N P Bokoro* and J H C Pretorius**

*University of Johannesburg, Department of Electrical and Electronic Engineering Technology, Doornfontein Campus.

**University of Johannesburg, Electrical and Electronic Engineering Science, Auckland Park Campus.

Abstract. The identification or localisation of distortion sources in power systems should consist of an important milestone towards the achievement of quality electricity supply. However, one of the major impediments to this task remains the non-existence of a unifying technique or method due among others to the versatile characteristics of most harmonic-polluting loads. In this paper, the distribution of active harmonic powers for the fifth, the seventh, the eleventh and the thirteenth harmonic frequency, between two controlled converters connected to the same bus system, is analysed on the basis of the converter's modes of operation (Rectification or Inversion). The power network under investigation is simulated on the digsilent 14.1 computer program which favourably supports harmonic load flow studies. The harmonic active power trends produced, when converters are either switched in similar or different modes of operation, indicate that the distribution of harmonic active powers is randomly based and therefore independent of the converter operating modes.

Key Words. Controlled converter; firing angle; operating modes; harmonic active power; load flow.

1. INTRODUCTION

Controlled converters are reputed to be traditional sources of harmonics in power systems [1]. When found to be more than one in the network, they tend to exchange distortion [2], while of course polluting other components connected to the system point of common coupling (PCC). In most applications, converters are required to operate either as rectifier or inverter at the expense of the control parameter, which for controlled converters, happens to be the firing angle [3]. Therefore, this change of operating mode is associated to specific regions of the firing angle: $0 < \alpha < 90^\circ$ for rectification and $90^\circ < \alpha < 180^\circ$ for inversion [4]. The effectiveness of controlled converters in power conversion justifies their popularity and dependence in power systems despite the level of distortion they are able to generate in the network [5]. It would therefore be interesting to investigate whether or not the distribution or exchange of active harmonic powers between converters could be influenced by their respective operating modes. To conduct this analysis, a power network consisting of two controlled converters operating either in similar or different states and connected to the same PCC with a linear load is analysed. The supply to the network is from two identical power transformers connected to the external grid. This network is built and simulated on the digsilent 14.1 computer software which performs harmonic load flow at the following designated harmonic frequencies: 5th, 7th, 11th and 13th. Harmonic load flow analysis is therefore based on the following operating case studies:

- (i) Both controlled converters operate in the rectification mode with changing firing angles;
- (ii) Both controlled converters operate in the inversion mode with changing firing angles;
- (iii) Converter 1 operates as a rectifier whereas converter 2 as an inverter, and both with changing firing angles.

In each of these cases, the firing angle is adjusted in every step of ten. Harmonic load flow analysis from the digsilent software under the above conditions suggests that harmonic active power is randomly exchanged or distributed, and is therefore independent of the converter operating modes.

2. SYSTEM TECHNICAL DATA

The supply system is made up of two 5 MVA, 11/0.4 kV transformers connected in parallel and being fed from a 10 MVA external grid. Both harmonic loads in use consist of ac/dc thyristor converters externally controlled, and with the following power and dc voltage ratings: 3 MW, 0.5 kV for converter 1 and 6 MW, 0.5 kV for converter 2. The rectifier converter supplies two 1.5 MW dc loads whereas the inverter is connected to a 600 V dc generator, having an armature resistance of 2.5 Ω and field inductance of 200 mH, through a 1 km dc line with resistance of 0.034 Ω /km and inductance of 35.1 Ω /km. On the other end, the linear load consists of the following: a 1 MW, 0.4 kV at power factor of 0.85 lagging. The system technical data thus described is derived from the software library. Figure 1 shows the power network under investigation.

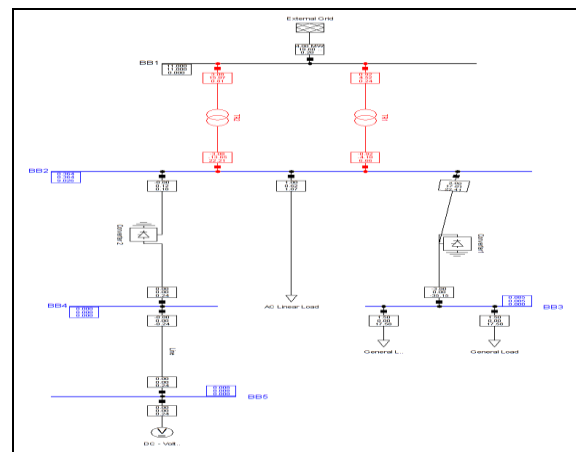


Fig. 1: Digilent model of the power network.

3. HARMONIC LOAD FLOW

One of the methods used to identify the distortion sources in power systems, is the analysis of the direction of active power harmonics [6]. Harmonic load flow such as supported by the digsilent provides both the magnitude and direction of active harmonic powers [7]. It is worth noting that the direction of harmonic active power is revealed in terms of the positive or negative sign preceding the magnitude. Accordingly, the positive sign implies that power is consumed and such a load is a victim of harmonics, whereas the negative sign implies that power is released and such a load is obviously a harmonic source [8]. However, it is a requirement for the software in use that harmonic loads should be defined either as phase correct balanced or unbalanced current sources by the end user. For the purposes of this study, the balanced approach is adopted. Therefore, harmonic loads are defined to be injecting respective characteristic harmonic currents at the proportion indicated in table 1.

Table 1: Proportion of Injected Harmonics

Harmonic Order (n)	Percentage Harmonic Distortion (%)
h_5	20
h_7	14.286
h_{11}	9.091
h_{13}	2.703

4. HARMONIC ACTIVE POWER DISTRIBUTION

The dynamic behaviour of harmonic active powers, between the system components connected to bus 2 (BB2) of the power network under scrutiny, is analysed on the basis of the firing angle variations. For the three operating conditions to be studied the firing angle adjustment for the converters is either incrementally (from 10° to 90° or 90° to 180°) or decrementally (from 90° to 10° or 180° to 90°) varied, and the obtained harmonic active powers expressed in kilowatts are plotted in terms of both direction and magnitude.

4.1 Case 1: Both Converters Operate as Rectifiers

In this case, both converters are switched to be operating on the rectification mode where the firing angle of converter 1 (α_1) is incrementally adjusted while that of converter 2 (α_2) is decrementally controlled. The parameters of the system components are applicable just as defined above. However, it is worth noting that since in this case all converters are treated as rectifiers, converter 2 is consequently defined to be driving a 3 MW dc load. The percentage harmonic injections, as expected for each of the harmonic-polluting loads (converters), are in

accordance to the proportion set in Table 1. Figure 2 depicts the case study network.

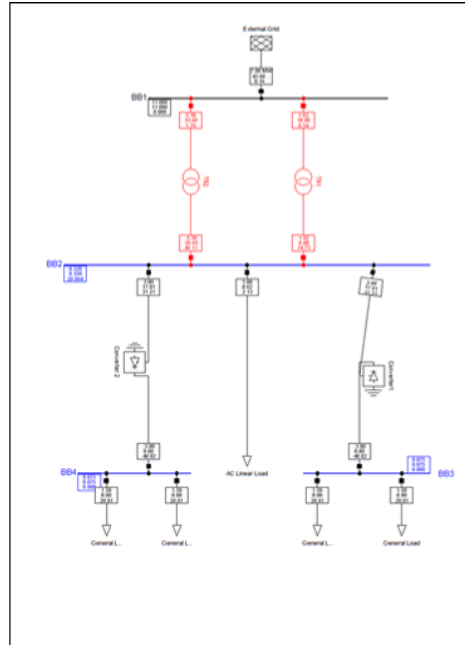


Fig. 2: Power network of case1.

4.2 Case 2: Both Converters operate as Inverters

In this application, both converters are set to operate as inverters where α_1 is incrementally controlled while α_2 is decrementally adjusted. Each of the converter loads is connected to a 600 V dc generator. The harmonic spectrum of the converters as well as the rest of the system components are defined in the similar manner to the first case of analysis. The power system such as described in this case is given in Figure 3.

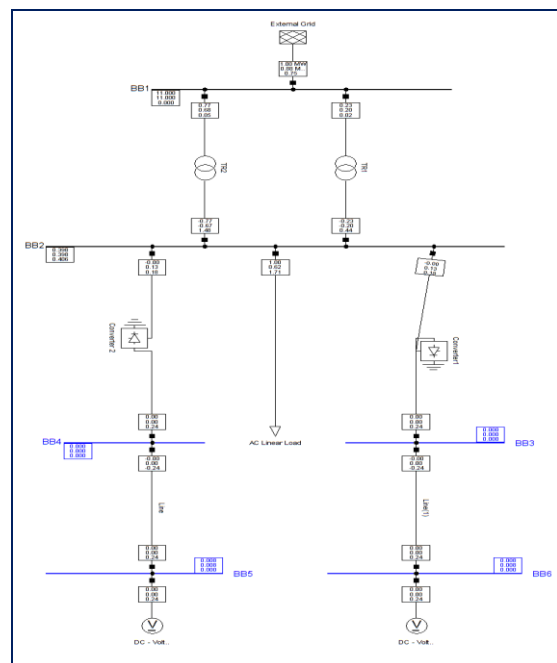


Fig.3: Power network of case 2.

4.3 Case 3: Rectifier versus Inverter

In this case, converter 1 is set to operate as a rectifier while converter 2 is switched in inversion mode. Both α_1 and α_2 are incrementally adjusted within respective operating regions. This study case is shown in figure 1 above.

5. RESULTS AND DISCUSSION

The results obtained subsequent to harmonic load flow analysis based on each study case are presented on Fig. 4, 5 and 6 respectively.

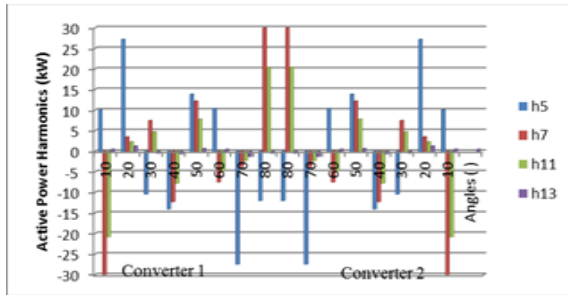


Fig.4: Harmonic active powers versus firing angle (case 1).

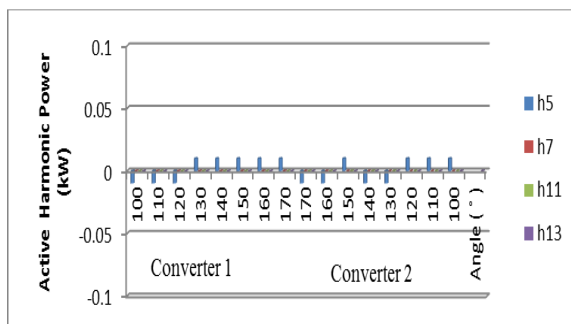


Fig.5: Harmonic active powers versus firing angle (case 2).

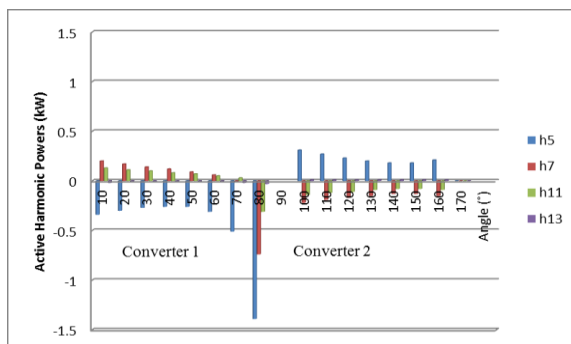


Fig.6: Harmonic active powers versus firing angle (case 3).

The results obtained in Fig. 4 show a non-uniform distribution of harmonic active powers neither in terms of magnitude nor direction. This applies in either direction of the firing angle adjustment. Converter 1 seems to be inheriting 10.09 kW, 27.20 kW, 13.87 kW and 10.41 kW of the fifth harmonic active power at firing angles of 10, 20, 50 and 60 degrees respectively. Yet, for the same harmonic component, the same converter appears to be generating 10.45 kW, 14.09 kW, 27.47 kW and 12.04 kW at 30, 40, 70 and 80 degrees respectively. This trend is also observed right across all harmonic components associated with converter 1. However, at the firing angle of 20 and 50 degrees, converter 1

imports all characteristic harmonics whereas at 40 and 70 degrees, it rather behaves as a generator of all harmonic components. On the other end, converter 2 is no exception to the versatile behaviour of its counterpart, as it generates 12.04 kW, 27.47 kW, 14.09 kW and 10.45 kW of the fifth harmonic active power at 80, 70, 40 and 30 degrees respectively. For the same harmonic component, converter 2 consumes 10.41 kW, 13.87 kW, 27.20 kW and 10.09 kW at 60, 50, 20 and 10 degrees. Similarly, it generates the full spectrum of harmonics at 70 and 40 degrees, while importing all harmonic components at 20 degrees of the firing angle.

Although it is expected that the linear load and the supply transformer receive some proportion of distortion produced, a larger share of harmonics generated is rather interchanged between the two converters, whereby one is acting as a source and the other as the largest consumer. Interestingly, when the firing angle is the same both converters act as sources of harmonics. This could be clearly observed right across the entire rectification region by cross checking the results produced. For instance, when converter 1 is fired at 50 degrees, 13.87 kW, 12.20 kW, 7.78 kW and 0.66 kW are generated, which is exactly the same when converter 2 is operated at the same angle. It could also be shown that out of the total fifth harmonic active power generated by converter 2, given as 12.04 kW, 10.09 kW which represents 83.80 % is consumed by converter 1 while only 16.20 % is shared between the linear load and the supply transformer.

The magnitudes of harmonic components presented in Fig. 5 are proven to be generally low if not inexistent. Harmonic load flow applicable to this case relies completely on the trend produced by the fifth harmonic. Therefore, converter 1 happens to be a fifth harmonic generator between the firing interval of 100 and 120 degrees, while importing the same type of distortion during the larger interval (130 to 170 degrees). On the other end, Converter 2 exports the fifth harmonic at the following firing angles: 170; 160; 140 degrees and 130 degrees. Fifth harmonic consumption for this particular converter occurs at the following angles: 150; 120; 110 and 100 degrees. It could also be noticed that the magnitude of the fifth harmonic active power is constant in any direction and symmetrical when both converters are operating at similar firing angle. This suggests that the distribution of active fifth harmonic power only takes place between the converters.

The results presented in Fig. 6 indicate a generally decay pattern of the magnitude of harmonic active powers over the regional firing angle involved. In terms of the direction, there seems to be a fairly consistent distribution of characteristic harmonics over the range of the firing angle. Thus, converter 1 is consistently generating the fifth and the thirteenth harmonic while consuming the seventh and the eleventh distortion components. However, at 70 and 80 degrees, it does act as a seventh harmonic generator and from 60 to 80 degrees, as a thirteenth

harmonic producer. Converter 2 consistently consumes the fifth and the thirteenth while producing the seventh and the eleventh all along its operation. This therefore suggests that at firing angles of 70 and 160 degrees for the rectifier and the inverter respectively, both converters behave as sources of the seventh harmonic active power. Subsequently, at 80 degrees, the rectifier is seen to be injecting the full harmonic spectrum. It should also be noted that the linear load as well as the supply system happen to inherit harmonic powers at lower quantities compared to that interchanged between the distortion sources. For instance, converter 2 receives 0.20 kW of the fifth harmonic active power out of 0.26 kW generated by converter 1 which is representative of 76.92 % while the rest of the system shares 23.08 % of the distortion produced.

The results produced based on the digilent 14.1 software simulation seem to confirm that the distribution of harmonic active powers, in a power network involving controlled converters, is random both in terms of direction and magnitude, and it is therefore independent of the operating modes of the converters. Furthermore, controlled converters are able to interchange larger share of the distortion generated in the power system, and could therefore behave either as source of harmonics or as harmonic consuming load. However, it is observed in some cases that converters could both be acting as distortion sources, thus able to generate the full spectrum of harmonics. This versatile behavior of converters adds in as an impediment to accurate identification or localisation of distortion sources in power networks.

6. CONCLUSION

This study makes use of the digilent 14.1 computer software in a bid to analyse the impact of the converter's operating states on the distribution of harmonic active power components. Three case studies, which consider possible converter applications, are therefore investigated. The harmonic spectrum used in each of the converters is defined in accordance with the software requirements before simulation attempts. For every case study undertaken, simulation runs conducted produce the harmonic active spectrum variations on the basis of firing angle adjustments. The results obtained suggest that harmonic active powers are randomly distributed across the firing angle and consequently cannot be influenced by the operating modes of controlled converters.

REFERENCES

- [1] G. Chang and Task Force, "Characteristics and Modeling of Harmonic sources-Power Electronic Devices," IEEE Trans.on Power Engineering, vol. 21, pp.62-63, 2001.
- [2] D.Serfontein and A.Rens, "The validation of Single Point Measurements for the Localisation of Multiple Harmonic Sources," 14th Int. Conf. Harmonics and Quality of Power, Italy, 2010.

- [3] M.Rashid, Power Electronics-Circuits Devices and Applications, 3rd ed., Prentice Hall India, 2004, pp.304-640.
- [4] B.K. Bose, Power Electronics and Motor Drives: Advances and Trends, Elsevier Acad. Press, 2006, pp. 328-329.
- [5] K.Zdrosis, "Mathematical Model of 4-quadrant dc Electric Drive with 6-pulse Dual Converter," American Journal of sciences, Science pub., 2005, pp. 1025-1027.
- [6] R. Herrera, P. Salmeron and S. Litran, "Assessment of harmonic distortion sources in power networks with capacitor banks," 11th Int. Conf. on Renewable Energies and Power Quality, Spain, April 2011.
- [7] The Digilent power factory version 14.1 User's Manual. Available on www.digilent.de.
- [8] M. Balci and M. Hocaoglu, "On the validity of harmonic source detection methods and indices," 14th Int. Conf. Harmonics and Quality of Power, Italy, 2010.

Topic F

Power systems

A STEADY-STATE LONG TRANSMISSION LINE PERFORMANCE ANALYSIS OF UHVDC POWER SYSTEMS

F. Kasangala* and G. Atkinson – Hope**

* Cape Peninsula University of Technology, Department of Electrical Engineering Cape Town Campus, Centre for Power Systems Research, Keizersgracht and Tennant Street, Zonnebloem, PO Box 652, Cape Town 8000, South Africa E-mail: franckkas@yahoo.com

** Cape Peninsula University of Technology, Department of Electrical Engineering Cape Town Campus, Centre for Power Systems Research, Keizersgracht and Tennant Street, Zonnebloem, PO Box 652, Cape Town 8000, Technology Transfer and Industrial Linkages Bellville Campus, Symphony Way (off Modderdam Road), PO Box 1906, Bellville 7535, South Africa E-mail: atkinsonhopeg@cpu.ac.za

Abstract: UHVDC technology is the most techno-economically attractive transmission solution to transfer bulk power over long distances of up to 3000 km and even more from remote hydro generating units to load centers with, depending on the transmission capacity, reasonable transmission line losses. In China, the longest UHVDC link, the Xiangjiaba-Shanghai ± 800 kV, 6400 MW, 1935 km link, has been in operation since 2010. For bulk power HVDC transmission projects of transmission distances in excess of 3000 km at specified transmission capacity questions may arise concerning transmission line performance of UHVDC power systems. In this paper, definite impacts of increased transmission distances, of up to 4500 km, and conductor type variations on power loss, voltage drop and efficiency of transmission lines of a well-designed ± 800 kV, 4000 MW, 1500 km bipolar UHVDC power system are determined.

Keywords: Power loss, voltage drop and efficiency of long transmission lines, UHVDC power systems.

1. INTRODUCTION

Power shortage is a major concern in fast growing economies due to the ever-increasing electric energy demand. This imposes an increase in the generation and transmission capacity. Application of High Voltage Direct Current (HVDC) technology has become a common practice to transfer bulk power over long distances from remote hydro generating units to load centers [1]. This satisfies the ever-increasing demand of clean, renewable energy; hence reduced carbon dioxide emissions [1,2]. HVDC offers many advantages over High Voltage Alternating Current (HVAC), such that HVAC experiences stability and transmission efficiency challenges which introduce transmission distance and power control limitations [3]. However, for power transfer requirement of more than 3500 MW a single bipolar HVDC system operating at ± 500 kV or 600 kV might not be sufficient to ensure a minimal cost of transmission lines and losses [2,4]. To overcome this shortcoming the operating voltage was determined to be increased to a new adequate level [2]. This led to an introduction of an Ultra High Voltage Direct Current (UHVDC) technology with an established voltage level of 800 kV. UHVDC is state of the art and has been proven to be the most techno-economically attractive transmission solution to transfer bulk power over long distances of up to 3000 km and even more with, depending

on the transmission capacity, reasonable transmission line losses [1,5,6]. At transmission capacity of 5000 MW losses are approximately 2% per 1000 km [8].

In China, the longest UHVDC link, the Xiangjiaba-Shanghai ± 800 kV, 6400 MW, 1935 km link, has been in operation since 2010 [5]. To reach the potential of Grand Inga dam, to provide sufficient electricity for the African continent primarily to reduce the population's lack of access to electricity services, African interconnection projects would be required. Therefore, three major projects have been identified to transfer bulk power over long distances of up to 5300 km [7]. With such planned UHVDC transmission projects of transmission distances above 3000 km at specified transmission capacity, questions may arise concerning the transmission line performance of UHVDC power systems. It is thus indispensable for power engineers to investigate very long transmission line performance of UHVDC power systems.

This paper investigates the transmission line performance criteria of a well-designed 800 kV, 4000 MW, 1500 km bipolar UHVDC power system, and at increased transmission distances of 1500 km, 2500 km, 3500 km and 4500 km respectively using several conductor types. The approach aimed to evaluate and determine the likelihood of efficient and reliable power transfer capability of UHVDC power systems at increased transmission distances through DiGSILENT steady-state modelling and analysis.

2. THEORETICAL BACKGROUND

2.1 Configurations

HVDC systems can be classified into either monopolar or bipolar links. A monopolar link consists of one conductor of a positive or a negative polarity and a ground or water return path, while a bipolar link consists of two conductors, one positive and the other negative in polarity, as shown in figure 1 [8]. The independent operation capability of poles makes a bipolar link advantageous over a monopolar link such that when one pole is out of service the remaining healthy pole of the bipolar link can operate with a return path in a monopolar mode and transfer half the rated load or more provided that converter equipment and transmission lines are designed with overload capabilities [3,8]. These HVDC system configurations usually have cascaded groups of several converters, each having a transformer bank and a group of valves [8]. To give the desired level of dc voltage from pole to ground the converters are connected in series on the dc side and in parallel on the ac side [8].

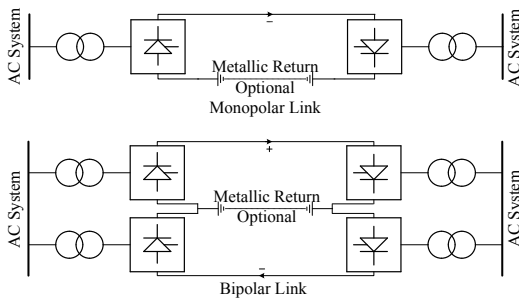


Figure 1: Monopolar and bipolar HVDC links

2.2 Components

The main components of a HVDC system are converters, converter transformers, dc reactors, ac and dc filters, reactive power sources and dc lines. A converter operates either as a rectifier or an inverter thus performs ac/dc or dc/ac conversion of power, while a converter transformer is used to provide a desirable voltage and control ability through its tap changing action [8]. A dc reactor reduces harmonic voltages and currents in the dc line and prevents intermittent current at light load [8]. The ac and dc filters are used to mitigate harmonic voltages and currents generated by converters on both ac and dc sides to prevent overheating of system components and interference with telecommunication systems. The converters used consume reactive power, and under steady-state conditions it is said to be 50% the active power transferred; therefore shunt capacitors, synchronous condensers and or static var compensators (SVCs) are installed to provide the required reactive power [8]. The purpose of a dc line is to efficiently transmit the dc power from the sending-end, rectifier side, to the receiving-end, inverter side. Figure 2 below shows a

bipolar HVDC system with the above described components.

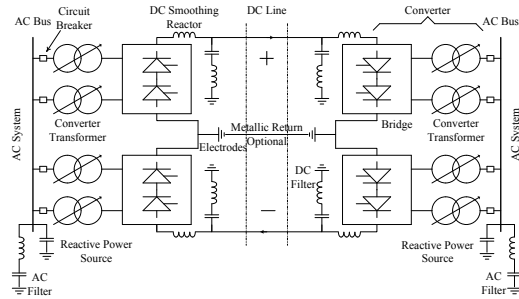


Figure 2: Bipolar HVDC system components

2.3 Circuit analysis

An HVDC converter is a common three-phase, full-wave bridge circuit which provides an instantaneous direct voltage composed of 60° segments of line-to-line ac voltages [8]. By analysing the dynamic operation of the bridge circuit under rectification and inversion mode the average rectifier side and the inverter side direct voltages can be found by integrating the instantaneous direct voltage across the bridge over any period of 60° as shown in equation (1) below [8]. Thus taking into account the effect of the ac source inductance, simplified algebraic equations (2) to (6) are used for calculations:

$$V_{do} = \frac{3}{\pi} \int_{\alpha-\frac{\pi}{3}}^{\alpha} e_{ac} d\omega t \quad (1)$$

$$V_{dr} = V_{do} \cos \alpha - BR_c I_d \quad (2)$$

$$V_{di} = V_{do} \cos \gamma - BR_c I_d \quad (3)$$

$$V_{di} = V_{do} \cos \beta + BR_c I_d \quad (4)$$

Where:

$$V_{do} = \frac{3\sqrt{2}}{\pi} BTV_{LL} \quad (5)$$

$$R_c = \frac{3}{\pi} X_c \quad (6)$$

V_{do} = rectifier or inverter side ideal no-load direct voltage

α = ignition delay angle

e_{ac} = line-to-line ac voltage

ωt = period in radians

V_{dr} = rectifier side direct voltage

V_{di} = inverter side direct voltage

I_d = direct current

R_c = equivalent commutation resistance

X_c = ac leakage commutation reactance

γ = extinction advance angle

β = ignition advance angle

B = number of full wave bridges in series

T = converter transformer ratio

In the rectifier mode of operation the value of the delay angle is 15° to 20° [8]. The equivalent commutation resistance R_c is responsible for the voltage drop, $I_d R_c$ depicted in (2) to (4), due to commutation overlap angle μ . The angle μ depends on the current I_d , the ac leakage reactance X_c and the firing angle α , and its typical full-load value ranges between 15° and 25° [8]. During inverter mode of operation the extinction advance angle γ of a value, with acceptable margin, of 15° is maintained to avoid commutation failure [8]. The sum of γ and μ is the ignition advance angle β ; likewise the sum of α and μ is the extinction delay angle δ . The ignition delay angle of the inverter can be calculated using the following equation.

$$\alpha = 180^\circ - \beta \quad (7)$$

The dc powers at the rectifier and inverter terminals, and the power loss across the dc line are respectively calculated as follows:

$$P_{dr} = V_{dr} I_d \quad (8)$$

$$P_{di} = V_{di} I_d \quad (9)$$

$$P_{dL} = R_L I_d^2 = P_{dr} - P_{di} \quad (10)$$

Where:

R_L = total dc transmission line resistance

Therefore;

$$I_d = \frac{V_{dr} - V_{di}}{R_L} \quad (11)$$

The reactive power consumed by converters is a function of the ac power and the power factor. Assuming zero losses in the converters the reactive power required at the rectifier and inverter sides can be calculated at a specified power factor respectively as follows:

$$Q_{acr} = P_{dr} \tan \theta_r \quad (12)$$

$$Q_{aci} = P_{di} \tan \theta_i \quad (13)$$

Where the rectifier and inverter sides power factors are calculated respectively as follows:

$$\cos \theta_r = \frac{V_{dr}}{V_{do}} = \frac{\cos \alpha + \cos \delta}{2} \quad (14)$$

$$\cos \theta_i = \frac{V_{di}}{V_{do}} = \frac{\cos \gamma + \cos \beta}{2} \quad (15)$$

Equations 14 and 15 imply that to achieve a high power factor for minimal reactive power consumption μ for rectifier and inverter, α for rectifier and γ for inverter should be kept as low as possible. According to equations 12 and 13 it can be seen that the larger the dc power transferred the larger the reactive power required for converters.

2.4 Transmission line performance

The performance of power systems mainly depends on the performance of transmission lines. The transmission line performance is governed by its four line constants, the series resistance and inductance, and the shunt capacitance and conductance [8]. The series resistance accounts for the resistive loss due to joule effect, the primary source of losses accumulated as heat in transmission systems, and additional voltage drops across the line [8]. Thus this affects the ability of a transmission line to perform its function to transfer power efficiently and directly influences the constraint of HVDC transmission by thermal and voltage drop limits. The efficiency of a dc line can be calculated using the following well known equation:

$$\eta = \frac{P_{di}}{P_{dr}} \times 100\% \quad (16)$$

The voltage drop across the dc line is defined as:

$$V_{dL} = I_d R_L = V_{dr} - V_{di} \quad (17)$$

2.5 Design considerations

Pole converter: The voltage and current ratings of a single 6 pulse converter of a HVDC power system reaches up to 400 kV and 4 kA respectively. A ± 800 kV bipolar HVDC power system of a 12 pulse converter configuration per pole is capable of transmitting 3000 MW up to 6400 MW of power. The transport limitation and insulation withstand capability of converter transformers may affect the converter configuration; thus only two 12 pulse converter configurations per pole would be satisfactory [2,4,9].

Transformer selection: Power and voltage ranges influence the transformer size which in-turn introduces transport limitations [9]. For larger size transformers single phase three windings or single phase single winding can be direct solutions [4,9]. HVDC converter transformers of up to 621 MVA with voltage stresses of 50-600 kV have been manufactured by ABB [10]. The three-phase converter transformer rating is equal to the product of the RMS value of the transformer secondary complex current $I_{T_{rms}}$, the integral of an alternating line current wave consisting of rectangular pulses of amplitude I_d , and line-to-line voltage TV_{LL} and is defined by:

$$S_T = \sqrt{3} TV_{LL} I_{T_{rms}} \quad (18)$$

Where $I_{T_{rms}}$ in terms of I_d is:

$$I_{T_{rms}} = \sqrt{\frac{2}{3}} I_d \quad (19)$$

Interconnection of power systems: For ac/dc system interactions, the ac system strength must be considered to prevent problems associated with the operation of a dc system when connected to a weak ac system [8]. The short circuit ratio (SCR) determines relative strengths of ac systems and must be greater than 2, and is defined as

$$SCR = \frac{SC_MVA_of_ac_system}{dc_converter_MW_rating} \quad (20)$$

Overhead conductor selection: Overhead conductor selection for transmission is affected by many factors which includes current carrying capacity, voltage drop and losses. In addition, as shown in figure 3 below, the voltage level of a transmission system need be considered to determine the exact conductor bundle application for reducing corona discharges based on acceptable audible noise (AN) [8].

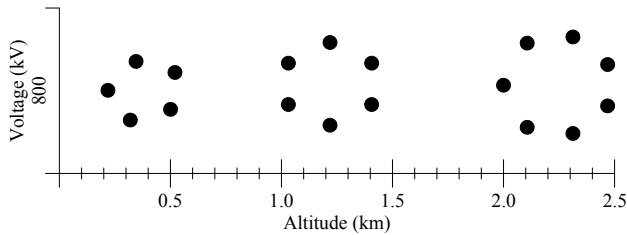


Figure 3: UHVDC conductor bundles for 45 dB maximum

Overhead line construction: The overhead line construction involves the mechanical design of towers that takes into consideration the electrical behaviour for determining adequate horizontal and vertical clearances between lines and to ground. The following diagram shows a typical 800 kV UHVDC tower structure.

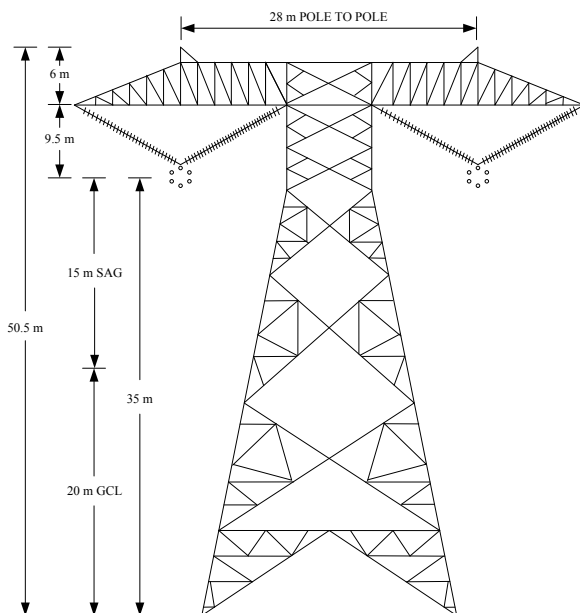


Figure 4: ±800 kV UHVDC type tower structure

2.6 DigSILENT PowerFactory modelling and analysis

To analyse UHVDC power systems under steady-state conditions DigSILENT PowerFactory, a frequency domain software tool, provides a load flow function which is used to calculate the active and reactive powers of all the branches and voltage magnitudes and the phase angles of all the buses. DigSILENT PowerFactory does not facilitate dc tower modelling neither the distributed modelling of lines, only a π - model is possible. User-defined models for HVDC controls are only essential when analysing the dynamic behaviour of HVDC power systems through electromagnetic transient (EMT) and steady-state (RMS) simulation functions.

3. UHVDC POWER SYSTEM NETWORK

The UHVDC network of figure 5 below was modelled and analysed in DigSILENT under steady-state conditions. Thus the ac and dc side harmonic filters were neglected. Network parameters are depicted in tables 1 to 4 below.

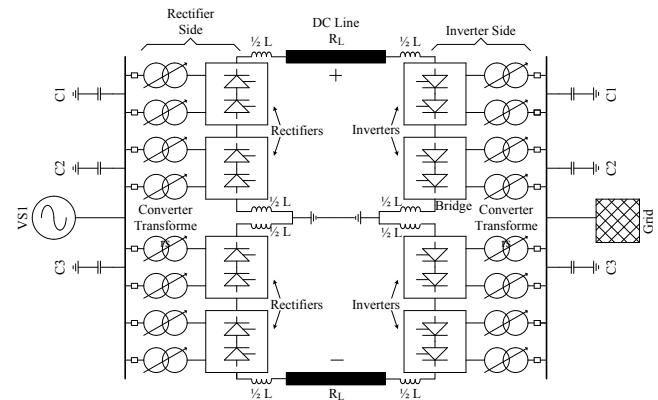


Figure 5: ±800 kV UHVDC power system network

Table I: Voltage sources

Parameters	Rectifier side ideal AC source (VS1)	Inverter side grid supply (Grid)
Voltage (kV)	400	400
V	1	1
ϕ (°)	-	86.186
SC MVA	-	12000
X/R ratio	-	15

Table II: Electrical characteristics of conductors

Conductor name	overall diameter (mm)	DC resistance (Ω /km) at 20°C	Current rating (A)	Number of conductors per bundle
Zebra	28.62	0.0674	635	6
Moose	31.8	0.0547	763	6
Martin	36.17	0.04259	835	6

Table III: Converter reactive power sources

Shunt capacitor	Rectifier side	Inverter side
C1 - C3	722 MVars	-

Table IV: Pole converter specifications

Parameters	Per single pole	
	Rectifier	Inverter
DC power (P_d)	2000 MW	-
Converter reactive power (Q)	1082.167 Mvars	-
DC current (I_d)	2500 A	2500 A
DC voltage (V_d)	± 800 kV	-
No of 12 pulse per pole	2	2
Firing angle (α)	15°	-
extinction angle (γ)	-	15°
Overlap angle (μ)	22.525°	-
Transformer rating (S_T)	595.331 MVA	-
Transformer pu impedance (X_{pu})	0.17 pu	-
Transformer Primary voltage (V_{T1})	400 kV	400 kV
Transformer secondary voltage (V_{T2})	168.385 kV	-
DC reactor (L)	300 mH	300 mH

4. SIMULATION CASE STUDIES

4.1 Case study 1 (CS1)

The existing ± 800 kV UHVDC network in figure 5 was used. The Zebra conductor was selected for a transmission distance of 1500 km and the ac/dc load flow was conducted. Three other ac/dc load flows were conducted at increased transmission distances of 2500 km, 3500 km and 4500 km respectively using the same conductor type. New inverter side modelling data were calculated and altered, while those of the rectifier side were kept constant.

4.2 Case study 2 (CS2)

The Zebra conductor of CS1 was replaced with the Moose conductor. ac/dc load flows were conducted at respective distances as in CS1.

4.3 Case study 3 (CS3)

The Moose conductor of CS2 was replaced with the Martin conductor. Ac/dc load flows were conducted at respective distances as in CS1.

5. RESULTS

Tables V to VII and figures 6 to 8 below depict the steady-state ac/dc load flow results obtained during each case study for analysing the transmission line performance of the ± 800 kV UHVDC power system network shown in figure 5 found on page 4 above.

Table V: CS1 AC/DC load flow results

Parameters	1500 km	2500 km	3500 km	4500 km
P_{dr} (MW)	1999.94	1999.991	2000.043	2000.058
Q_{acr} (MVars)	1052.892	1052.932	1052.972	1052.984
V_{dr} (kV)	800.002	800	799.998	799.997
I_d (kA)	2.5	2.5	2.5	2.5
P_{di} (MW)	1894.635	1824.472	1754.301	1684.1
Q_{aci} (Mvars)	973.432	921.956	871.676	822.592
V_{di} (kV)	757.879	729.792	701.704	673.618

Table VI: CS2 AC/DC load flow results

Parameters	1500 km	2500 km	3500 km	4500 km
P_{dr} (MW)	1999.998	1999.997	1999.998	2000
Q_{acr} (MVars)	1052.94	1052.936	1052.94	1052.94
V_{dr} (kV)	800	800	800	800
I_d (kA)	2.5	2.5	2.5	2.5
P_{di} (MW)	1914.53	1857.55	1800.571	1743.594
Q_{aci} (Mvars)	988.204	946.056	904.7	864.136
V_{di} (kV)	765.812	743.021	720.229	697.437

Table VII: CS3 AC/DC load flow results

Parameters	1500 km	2500 km	3500 km	4500 km
P_{dr} (MW)	1999.998	1999.998	1999.999	1999.997
Q_{acr} (MVars)	1052.94	1052.94	1052.94	1052.936
V_{dr} (kV)	800	800	800	800
I_d (kA)	2.5	2.5	2.5	2.5
P_{di} (MW)	1933.451	1889.087	1844.723	1800.357
Q_{aci} (Mvars)	1002.38	969.284	936.676	904.548
V_{di} (kV)	773.381	755.635	737.89	720.144

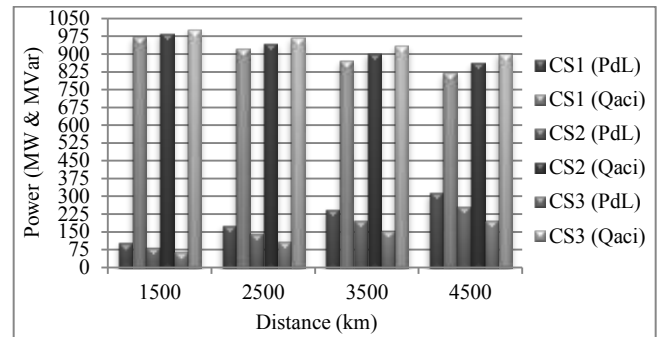


Figure 6: DC line power loss (P_{dL}) & reactive power (Q_{aci})

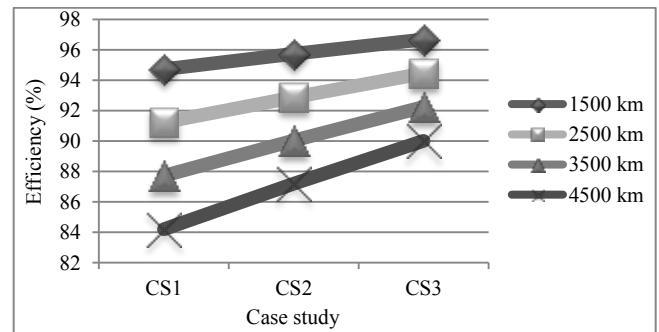


Figure 7: Transmission line efficiency (η)

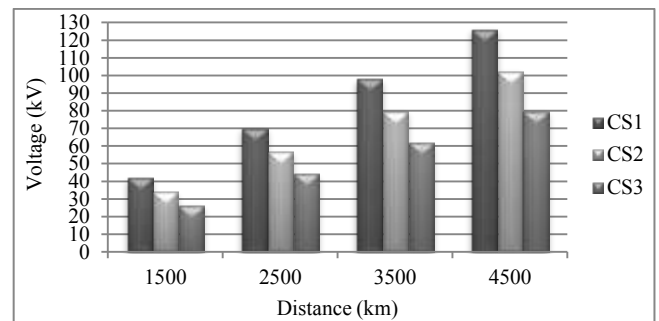


Figure 8: DC line voltage drop (V_{dL})

6. ANALYSIS OF RESULTS

Initially, power loss of 105.365 MW across the line for a transfer capacity of 2000 MW per pole was found in CS1 as shown in figure 6. This increased by 70.2 MW for every 1000 km increase in transmission distance due to the proportional increase in the total resistance of the line, while in CS2 the initial power loss was found to be 85.47 MW and increased by 56.977 MW. The reduced power loss in CS2 in comparison to CS1 resulted from the lower resistance of the conductor used in CS2, while the lowest power loss was depicted in CS3 with an initial value of 66.549 MW and increased gradually by 44.364 MW for every 1000 km increase in transmission distance. However, as shown in figure 6, it was also found that the required inverter reactive power increased from CS1 to CS3 as the conductor resistance decreased, and decreased in each case study with an increase in transmission distance. This is due to the fact that low line losses causes high inverter dc power which results in low power factor i.e. increased P_{di} , and angles β and μ at a constant γ , and vice versa. As a result of line losses, the power transfer efficiencies in CS1 were 94.735%, 91.224%, 87.713% and 84.203% for respective transmission distances of 1500 km, 2500 km, 3500 km and 4500 km as shown in figure 7. In CS2 the power transfer efficiencies were 95.727%, 92.878%, 90.029% and 87.18%, while those of CS3 were 96.673%, 94.454%, 92.236% and 90.018% for respective distances. The voltage drop across the line for CS1 was initially calculated to be 42.123 kV and increased by 28.086 kV for every 1000 km increase in transmission distance as shown in figure 8, while in CS2 it was initially calculated to be 34.188 kV and increased by 22.792 kV and in CS3 it was initially calculated to be 26.619 kV and increased by 17.746 kV. It was found that an increase in the voltage drop caused a decrease in the secondary ac voltage of converter transformers due to a drastic decrease in the inverter dc terminal voltage.

7. CONCLUSIONS

Investigation into transmission line performance of UHVDC power systems can determine definite impacts of increased transmission distances and conductor variations on power loss, voltage drop and efficiency of transmission lines. The effect of conductor variations is much more pronounced at longer distances. For a bipolar UHVDC power system at transmission capacity of 4000 MW, power is transferred with reasonable line losses and voltage drops of approximately 2.219% to 3.512% per 1000 km. For transmission distance of greater than 3000 km, 3500 km up to 4500 km, the efficiency varies from 87.713% - 92.236% down to 84.203% - 90.018% with the optimum efficiency reached when the conductor with the lowest resistance is used. More reactive power is needed by inverters to satisfy minimum line losses and voltage drops; this implies more installation cost of inverter side capacitor banks for less

energy loss cost of transmission lines, and vice versa. In case of very high dynamic overvoltages on a 400 kV ac system, drastic decrease in inverter terminal voltage may cause a restraint on the tap changing voltage control capability of converter transformers thus less reliable. The line losses and voltage drops can be significantly minimised with a subsequent increase in efficiency at longer distances if a conductor with minimum resistance is selected and the bundle sub-conductors are increased such that its current margin corresponds only to its required overload capability to avoid unused thermal capacity. General steady-state and dynamic performance studies of very long transmission line UHVDC power systems are required for extensive implementation.

8. REFERENCES

- [1] U. Astrom & V. Lescale. (2006). "Converter Stations for 800 kV HVDC." *International Conference on Power System Technology*, 2006, pp. 1-7.
- [2] C. Shang, D. Zhang, H. Rao, M. Haeusler and T. Shang. "Converter Station Design of the ± 800 kV UHVDC Project Yunnan-Guangdong." Internet: http://www.ptd.siemens.de/converter_stations_design_YG_zhang.pdf, [Oct. 26, 2012].
- [3] P. Tuson. "HVDC Strengthening in Southern Africa." *IEEE PES Power Africa 2007 Conference and Exposition*, 2007, pp. 1-6.
- [4] H. Huang, R. Velpanur and D. Kumar. "Design Considerations of Ultra High Voltage DC System." Internet: http://www.ptd.siemens.de/050714_Design_Considerations_UHVDC.pdf, [Oct. 1, 2012].
- [5] C. Humpert. "Long Distance Transmission Systems for the Future Electricity Supply – Possibilities and Restrictions." *pEnergy*, vol. 48, pp.278-283, Dec. 2012.
- [6] "First 800 kV high-voltage direct-current link in China now fully operational." Internet: http://www.siemens.com/press/en/pressrelease/?press=/en/pressrelease/2010/power_transmission/ept2010060_90.htm, Jun. 21, 2010 [Oct. 26, 2012].
- [7] V. di Panzu. "The grand inga power plant project." Internet: <http://www.sapp.co.zw/documents/The%20Grand%20Inga%20Project.pdf>, [Nov. 21, 2012].
- [8] P. Kundur. *Power System Stability and Control*. USA: McGraw-Hill, 1993, pp. 463-530.
- [9] B. Bisewski & R. Atmuri. "Considerations for application of ± 800 kV HVDC transmission from a system perspective." Internet: <https://www.teshmont.com/pdf/papers/800%20kV%20Paper.pdf>, [Oct. 1, 2012]
- [10] "ABB power transformers." Internet: <http://www.lgesales.com/pdf/PowerTransformers/PowerTransformers.pdf>, [Nov. 5, 2012].

AN OVERVIEW OF APPLIANCE MONITORING USING POWER SIGNATURE

M.B. Shabalala* and M.V. Shuma-Iwisi**

* *Electronics Research Group, School of Electrical and Information Engineering, Faculty of Engineering and the Built Environment, Private Bag 3, Wits 2050, South Africa E-mail: meshack.shabalala@students.wits.ac.za*

** *Electronics Research Group, School of Electrical and Information Engineering, Faculty of Engineering and the Built Environment, Private Bag 3, Wits 2050, South Africa E-mail: mercy.shuma-iwisi@ee.wits.ac.za*

Abstract: Conventional utility meters do not provide any information about the usage of the individual appliances, they only provide the aggregate energy usage of a home or business premises. Individual appliance load signature identification would provide essential information in load monitoring for energy saving and greenhouse effect reduction initiatives. Load and signal features that are crucial and may be used for load signature identification in a viable and cost effective manner are also highlighted. In this paper various methods of load signature identification are reviewed. Also the challenges and unanswered questions that lie ahead are discussed. Advantages and disadvantages are discussed and a way forward is proposed.

Keywords: Disaggregated data, Load classification, Load identification, Load monitoring, Load signature.

1. INTRODUCTION

The installed utility power meters are primarily intended to serve the utilities billing function. These meters measure the aggregate energy consumed by the customer. Some meters also measure the power factor of the customer's load for additional fees that may be imposed on the customer. However the information provided by these meters is not sufficient. The conventional energy meters make it difficult for consumers to ascertain which devices or appliances are responsible for their energy usage. Energy consumption can vary widely from home to home simply based on differences in individual behaviour. It has been consistently found that energy usage can differ by two to three times among identical homes with similar appliances occupied by people with similar demographics [1-3].

The answers in resolving these problems are in load signature monitoring, in which the power consumption of the individual appliances is monitored. This involves the use of traditional intrusive methods with distributed meters or Non-intrusive Appliance Load Monitoring (NIALM) method which is more practical and is the focus of this paper. Non-intrusive Appliance Load Monitoring uses a single sensor at the main feeder of a house hold thus lowering costs of installation.

The need for load signature analysis is further discussed in Section 2. The technology available for load signature is looked at in Section 3 whereas the design criteria for creating a load signature analysis system are discussed in Section 4. The discussion of the different techniques that have been employed for Non-intrusive Appliance Load Monitoring is presented in Section 5. The problem statement is presented in Section 6 and thereafter the

paper is concluded in Section 7. The references follow in Section 8 immediately after the conclusion.

2. THE NEED FOR LOAD SIGNATURE ANALYSIS

The knowledge of how the individual appliances use the energy would empower the utilities, consumers, regulators, appliance manufacturers and others, to better understand the energy characteristics of the individual appliances and their overall effect on the electric system. Furthermore, accurate and reliable information about the nature and state of the electric system will be helpful in energy saving and reducing greenhouse effects [4].

Knowledge of the appliance/electrical load signatures is the foundation of practical technologies for load identification, load monitoring, diagnostics, power quality control, power circuit design, appliance design and deployment [5]. This knowledge would also strengthen the link between the electric utilities and their customers [5]. It can reveal how homes with similar and different demographics use electrical energy, thus assisting in creating new and evidence based user behaviour models.

Studies in environmental psychology conducted by [6-8] and reviewed by [9] independently show that there are profound misconceptions about energy usage in homes. Consumers vastly underestimate the energy used for heating and overestimate the energy used for appliances, lighting and cooking. Also consumers often estimate appliance energy usage by its perceptual salience (e.g. television and lighting are often overestimated) and also overestimate energy used by machines that replace manual labour tasks (e.g. dishwasher, washing machine) [9]. Furthermore, these misconceptions are reflected in

the steps consumers take to conserve energy. Residents tend to overestimate the effectiveness of conservation measures that depend on short term behaviour changes such as turning the lights off when leaving a room and underestimate technical or building innovation solutions such as replacing an inefficient appliance or upgrading a home's insulation [7]. These misconceptions point to a need for more accurate and specific information about how actions in the home affect energy consumption.

Load signature analysis/disaggregated data could be used by energy eco-feedback systems to both provide pertinent information about energy usage as well as to provide tailored feedback at opportune times [10, 11]. Load signature analysis also has the potential to inform residents about malfunctioning equipment or inefficient settings. The evaluation of gathered data from load signature analysis has the potential of showing ineffective operating practises, and these practices can be identified and the necessary corrective actions can be taken to minimise or eliminate these practises.

The knowledge of how much energy is consumed by each class of appliances is critical to the development and evaluation of evidence-based energy efficiency policies and conservation programs aimed at reducing capital expenditure on additional capacity [9]. Load signature analysis systems can allow utilities to accurately assess and prioritize energy-saving potentials of retrofit or upgrade programs.

The equipment manufacturers and government could compare energy measurements made under controlled test conditions to measurements under actual home usage conditions. This would result in more realistic test procedures and ultimately more energy efficient designs as end-use cases are better understood. This analysis also presents opportunity for power systems planning, load forecasting and new types of billing procedures. Utilities would be able to improve the quality of demand forecasting by having better models of usage. Utilities could suggest specific appliances to turn off or recommend other actions in order to conserve energy during peak load times. Currently, utilities employ different pricing schemes depending on usage, future pricing models could take into account the type of usage and charge accordingly (heating, ventilations or air conditioning, refrigeration and lighting could have different pricing models) [9]. In order to achieve all this, an understanding of load signatures is required.

3. LOAD SIGNATURE ACQUISITION TECHNOLOGY

Some understanding of load signatures has emerged from work in Non-Intrusive Appliance Load Monitoring (NIALM) [12-17], and other methods such as distributed sensing.

The distributed sensing load signature instrumentation

system is a traditional intrusive method which employs meters for each load to be monitored [18]. These meters may incur significant time and cost to install and maintain. The other obstacle is the number of appliances that can be monitored as the meters increase; reliability of the measuring system may decrease [18]. This method of load monitoring is only useful when there are only a few appliances to be monitored, as the number of appliances increase, the use of this method becomes impractical.

The Non-intrusive Appliance Load Monitoring (NIALM) is a modern approach which uses a single sensor that is mounted at the metering panel/main feeder of a household. At this level an observer who switches an electrical appliance on or off, witnesses variations in current and voltage signals on the aggregate signal [15]. An illustration of the sensor placement is shown in Figure 1. NIALM has several advantages compared to traditional methods. This method has lower cost because of the single sensor approach, the energy consumption is lower and it is also easier to install [19].

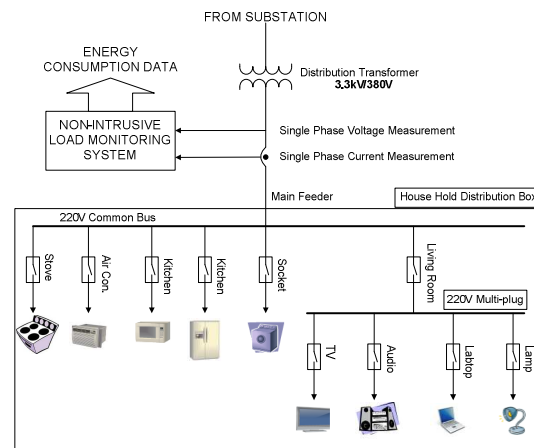


Figure 1: The Non-Intrusive Appliance Load Monitoring Sensor Location adapted from [20] and [28]

However, this method has a number of challenges. One of the challenges is the identification of loads in residential areas where a large number of appliances are connected to the power system at any one time and the diversity of appliances connected [15]. Another challenge is that an appliance is generally switched on while other appliances are already in use/operation. This presents the difficulty of isolating the characteristic parameters of the appliance from the aggregate signal [15].

4. TYPICAL DESIGN CRITERIA OF LOAD SIGNATURE MEASUREMENT SYSTEMS

There are a few factors that need to be considered before NIALM can be implemented. These are: the acquisition of the data necessary for load signature analysis (in terms of the sensitivity of the sensors and the sampling period), the techniques that will be used to identify the individual

appliances and the classifications that will be used for the identified appliances.

4.1 Data Acquisition

The identification of an appliance requires that its power must be clearly higher than the minimum resolution of the measurement device. The author of [15] suggested a minimum resolution of 12 bits. This resolution gives an accuracy of measurement of approximately 0.05% which results in 1 Watt for an appliance that is rated at 2 kW maximum [15]. The appropriate resolution for the work proposed is still to be determined. However, it is envisaged that the sensitivity of the sensing element will be determined by conducting measurement of the minimum current that will need to be measured. The sensitivity level to be used will have to be sufficient to capture the transient behaviour of the appliances.

There are two measurement procedures that may be made [15]. These are:

Asynchronous measurement: Asynchronous measurement consists of measuring voltage and current cyclically at regular intervals (a few seconds). However, events can occur with time differences of the order of one second. The probability of such events increases when the number of appliances increases, and/or when a short-cycle appliance such as a washing machine is in operation. In these conditions, several scenarios can make the interpretation of the measurement very difficult, in particular, if several events occur between successive sampling intervals. Also if a measurement includes the moment at which the event occurs, and finally if a measurement comprises a major transient.

To prevent this, the interval between measurements must be shortened, which leads finally to the continuous measurement method described below.

Continuous measurement: Continuous measurement consists of performing on-going measurements of the current signal by integrating it over a small number of periods and comparing each measurement with the former. If a variation is detected, it can then be analyzed and the identification parameters computed locally.

The continuous method of measurement has several advantages. The detection of events can be accurate since it can involve complex numerical tests, and a certain number of earlier measurements can be stored in memory, which allows the event to be identified locally (the signal before, during and after the event is available). This ability to identify an event locally allows for the transients to be analyzed. This method of measurement will be the focus of the research that will be conducted.

4.2 Signature Identification/Event Detection Techniques

The major research topics on Non-Intrusive Appliance Load Monitoring (NIALM) were focused on the usage of two analysis methods, steady-state and transient analysis.

The steady-state analysis in a NIALM system was developed by the Electric Power Research Institute (EPRI) [17].

The operating schedule of an individual load or a group of loads are determined by identifying times at which the electrical power measurements change from one nearly constant (steady-state) value to another as shown in Figure 2.

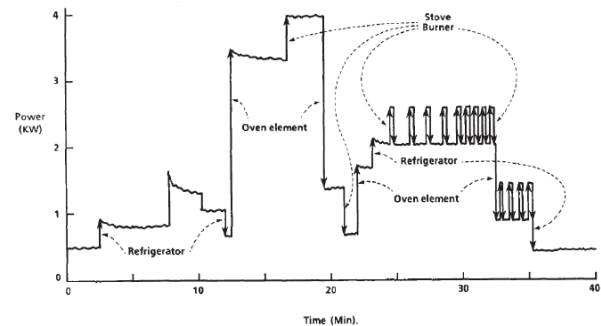


Figure 2: The step changes in a household power consumption due to individual appliances [21]

The operating schedule of an individual load contains the signature of that particular load.

4.3 Load Classification

There are two directions usually taken with appliance load classifications, one is based on the use of the appliance, whereas the other is based on the electrical characteristics of the load. The author of [15] suggested a classification of the appliance loads and has classified the appliance loads into the following six appliance categories based on the characteristics of the load and not on their use.

Resistive appliances: Characterised by zero reactive power, no transient when switching on, or a very short transient (lower than 50 Hz period), and absence of harmonic components of current. Active power is therefore the principal measured value used for their identification.

Pump-operated appliances: This category is characterised by substantial reactive power, long and characteristic transients when turned on and odd numbered harmonic current.

Motor driven appliances: These appliances differ from the pump-operated appliances by their generally less substantial switching on transients.

Electronically-fed appliances: These are the entertainment appliances which are generally characterised by short but very high amplitude switching on transient and a current spectrum rich in harmonic components.

Electronic power control appliances: This category includes appliances, such as halogen lights, some convectors, some vacuum cleaners and some cookers. However this category is difficult to identify since they are characterised by generally varying power levels at which they operate.

Fluorescent lighting: This type of lighting is characterised by a long two-step switching on transient, very high generation of the third harmonic of current and substantial current-voltage phase shift.

These groupings of load characteristics correspond to the underlying power circuitry of the individual appliances [5].

5. DISCUSSION

There have been different techniques used for NIALM; these techniques can be divided into two major categories, namely non-intelligent methods which are more traditional NIALM methods and modern intelligent methods that use Artificial Neural Networks (ANN) and Genetic Algorithms (GA).

5.1 Non-Intelligent Methods

The traditional NIALM methods used real power, reactive power, harmonic content of power signatures and transient energy to determine the status of appliances [15].

The nonlinear loads getting power from the electric system not only consumes real and reactive power, they also introduce harmonics to the power lines [17, 22]. These harmonics can be used as features to detect different loads. Aside from the usage of steady-state analysis, the research team led by Steve Leeb pointed out that the transient waveforms are different for different loads due to the differences of physical characteristics [16, 23-25].

The method developed by Electric Power Research Institute (EPRI) using the steady-state analysis is based on the variations of real and reactive power to detect the status of loads. With this method, the Real power versus Reactive power diagram is plotted (P-Q plane), and by comparing the reactive and real power of the detected appliances with the diagram, different appliances can be identified. An illustration of the P-Q plane is shown in Figure 3. Although this method had been applied to some regular houses with acceptable performance, several problems were pointed out by [18, 25, 26]. This method of detecting appliances is good for appliances with different real and reactive power. From the experiments conducted by [18], it was revealed that analysing the turn on transient energy signatures can enhance the efficiency of load recognition, particularly for different loads with the same real power and reactive power in a NIALM system, and improve the ability of computational speed.

Therefore the analysis of both the steady-state and transient behaviour is necessary for accurate detection and classification of appliance loads.

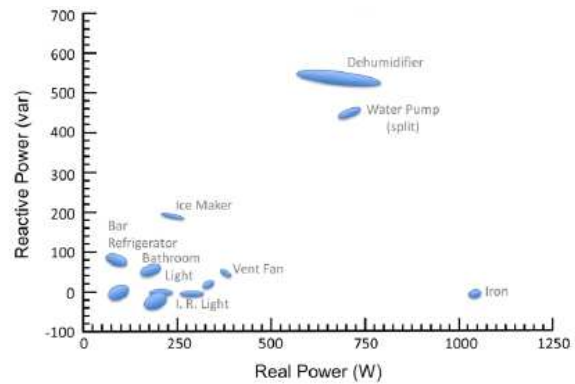


Figure 3: Typical P-Q plane representation [9]

The authors of [4] adapted a technique developed for audio signals from the authors of [27]. This technique is based on the temporal and spectral parsimony of the elementary signals. One measurement is taken compared to taking three measurements of current and voltages at higher sampling frequencies. This saves on memory for the sampled signal, however, taking only one measurement may save on memory but the detection, classification and monitoring of particular appliances may be comprised thus making the analysis inaccurate, and prone to misclassifications. The method proposed by the authors of [4] is dedicated to periodically locally stationary signals embedded in a non-stationary observation. These signals are produced by convectors thus limiting the capabilities of the method to a set of appliances and restricting the use to detecting only convector and/or appliances that produce a similar signal as that of a convector.

The method presented by [5] uses the input current and voltage waveforms in 2-dimensional voltage-current trajectories. A framework of over 120 electrical loads (Single phase office and domestic electric appliances) is proposed. With this method the current and voltage waveforms are turned into more meaningful information. These trajectories reveal the kind of load that is being dealt with, for instance the steady-state V-I trajectory of passive resistive load is a straight line, whilst that of an active resistive load is a “zig-zag” curve along a straight line [5].

This information may be used to classify the loads initially. However, in the effort to meeting the power quality standards, various types of power factor correction circuits have been developed to improve the input current of electric loads. Such development has made great impact on load signatures. When a power factor correction circuit achieves near-unity power factor, the entire load behaves almost like an equivalent resistance thus masking the nature of the load; it becomes

a challenge to differentiate a pure resistive load (e.g., an electric heater) from an air-conditioner with a front-end power factor correction circuit.

5.2 Intelligent Methods

The research undertaken by Chang in [20] aimed at improving the recognition accuracy of NIALM by combining neural network, genetic programming and the turn-on transient energy. This work showed that the inclusion of the turn-on transient energy increases the classification accuracy. The genetic program is used in feature extraction whereas the back propagation neural network is used for the load identification. The author records training and test recognition accuracy of 51.28% and 39.47% respectively for features with real and reactive power, whereas with the turn-on transient energy the accuracy is 100% for both training and testing.

There are other researchers that have undertaken implementation of NIALM with neural networks [9, 19, 22, 28] and generally the identification accuracy is high compared to that of non-intelligent methods, however, the use of neural networks is generally implemented for only a few appliances. The limitation with ANN is with the training where it is unrealistic that sufficient training data will be gathered for a comprehensive list of appliances.

6. PROBLEM STATEMENT

The problem with the current methods of load signature detection, identification and monitoring is that the methods are based on mathematical, statistical or neural approaches. Using statistical methods, the energy of the individual appliances that are detected is estimated. This does not accurately represent the influence that each of these appliances have on the aggregate energy consumption. Neural networks show high identification accuracy however this method requires a large collection of data initially to train the algorithms and also requires vast computational capabilities. This is the reason why neural networks are limited to a manageable number of appliances since it is not realistic to collect individual signatures when there are a large number of appliances for training purposes. One other issue is portability, as these systems are not portable. In neural networks, when moving from one home to another, signatures of new appliances have to be manually recorded and used to train and test the neural network.

This proposal challenges the field of Non-intrusive Appliance Load Monitoring techniques. A novel approach that combines the use of non-intelligent and intelligent algorithms, using the V-I trajectory, P-Q plane, transient analysis and neural networks is proposed. The system to be implemented will be an unsupervised plug-in system that can extract individual signatures from the aggregate reading, train a neural network, detect, identify, classify and monitor the energy consumption of the individual appliances. This system will eliminate the need to manually collect the signatures and train the neural

network since it is entirely unsupervised and can collect signatures to train and test the neural network autonomously.

Success in this research has a potential influence on the design of NIALM devices that are able to detect, identify, classify and monitoring all the known appliances plugged into a home's ac main without even putting manual effort towards training the algorithm, thus a larger number of appliances can be monitored without the worry of the extensive training data collection.

7. CONCLUSION

It is clear how the knowledge of load signature analysis can lead to new models of user behaviour patterns, evidence based energy saving initiatives and eventually a reduction in greenhouse effect. Although some understanding has been achieved from the work in Non-intrusive Appliance Load Monitoring much work still remains to be done. It has been shown that there are misconceptions about the energy consumption of residents thus showing the need for accurate and reliable information about the usage of household appliances.

The research that has been proposed aims at adding to the vast field of load signature analysis by looking at merging a number of non-intelligent methods and intelligent methods in improving the efficiency of NIALM systems, and making the implementation of a NIALM easy. The success of this research will lead to the creation of a device that can collect signatures, train a neural network, detect, identify, classify and monitor the energy consumption of the individual appliances, while it is unsupervised. This device should also have the intelligence to learn load signatures without requiring manual collection of training data.

8. REFERENCES

- [1] J. Seryak and K. Kissock: "Occupancy and behavioural effects on residential energy use", *Proceedings of the annual conference on American Solar Energy Society, Solar Conference*, Austin Texas, pp. 717-722, 21-26 June 2003.
- [2] R.H. Socolow: *The Twin Rivers program on energy conservation in housing: Highlights and conclusions. In Socolow, R. H. (Ed.). Saving Energy in the Home: Princeton's Experiments at Twin Rivers*, Ballinger Publishing Company, Cambridge, MA, pp. 2-62, 1978.
- [3] R.A. Winett, M.S. Neale and H.C. Grier: "The effects of self-monitoring and feedback on residential electricity consumption: Winter", *Journal of Applied Behavior Analysis*, Vol. 12, pp. 173-184, 1979.
- [4] M. El Guedri, G. D'Urso, C. Lajaunie and G. Fleury: "Time-Frequency Characterisation for Electric Load Monitoring", *17th European Signal Processing Conference (EUSIPCO'09)*, Glasgow:United Scotland, pp. 2278-2282, 24-28 August 2009.

- [5] K.H. Ting, M. Lucente, G.S.K. Fung, W.K.. Lee and S.Y.R. Hui: "A Taxonomy of Load Signature for Single-Phase Electric Appliances", *IEEE Power Electronics Specialist Conference (PESC)*, Brazil, pp. 12-18, Jun 2005.
- [6] M. Costanzo, D. Archer, E. Aronson, and T. Pettigrew: "Energy conservation behavior: The difficult path from information to action", *American Psychologist*, Vol. 41 No. 5, pp. 521-528, May 1986.
- [7] W. Kempton and L. Montgomery: "Folk quantification of energy", *Energy*, Vol. 7 Issue 10, pp. 817-827, October 1982.
- [8] E.S. Geller, R.A. Winett and P.B. Everett: "Preserving the Environment: New Strategies for Behavior Change", *Behavior Analyst*, Vol. 5 No. 2, pp. 191 – 197, Fall 1982.
- [9] J. Froehlich, E. Larson, S. Gupta, G. Cohn, M.S. Reynolds and S.N. Patel: "Disaggregated End-Use Energy Sensing for the Smart Grid", *IEEE Pervasive Computing*, Vol. 10 Issue 1, pp. 28-39, Jan-Mar 2011.
- [10] J. Froehlich, "Promoting Energy Efficient Behaviors in the Home through Feedback: The Role of Human-Computer Interaction", *Proceedings of the SGCHI Conference on Human Factors in Computing Systems*, New York, pp. 1994–1998, 2010.
- [11] J. Froehlich, L. Findlater and J. Landay: "The Design of Eco-Feedback Technology", *Proceedings of the SGCHI Conference on Human Factors in Computing Systems*, Atlanta Georgia, pp. 1999-2008, April 2010.
- [12] C. Laughman, K. Lee, R. Cox, S. Shaw, S. Leeb, L. Norford and P. Armstrong: "Power Signature Analysis", *IEEE Power and Energy Magazine*, Vol. 1, pp. 56-63, 2003.
- [13] G.W. Hart: "Nonintrusive appliance load monitoring", *Proceedings of the IEEE*, Vol. 80 Issue 12, pp. 1870-1891, December 1992.
- [14] L.K. Norford and S. B. Leeb: "Non-intrusive electrical load monitoring in commercial buildings based on steady-state and transient load-detection algorithms", *Energy and Buildings*, Vol. 24 Issue 1, pp. 51-64, 1996.
- [15] F. Sultanem: "Using appliance signatures for monitoring residential loads at meter panel level", *IEEE Transactions on Power Delivery*, Vol. 6 Issue 4, pp. 1380-1385, October 1991.
- [16] S. Drenker and A. Kader: "Nonintrusive Monitoring of Electric loads", *IEEE Computer Applications in Power*, Vol. 12 Issue 4, pp. 47-51, October 1999.
- [17] A.I. Cole and A. Albicki: "Nonintrusive Identification of Electrical Loads in a Three-Phase Environment Based on Harmonic Content", *Proceedings of the 17th IEEE Instrumentation and Measurement Technology Conference*, Vol. 1, pp. 24–29, 1- 4 May 2000.
- [18] H.H. Chang, C.L. Lin and H.T. Yang: "Load Recognition for Different Loads with the Same Real Power and Reactive Power in a Nonintrusive Load-monitoring System", *12th International Conference on Computer Supported Cooperative Work in Design*, pp. 1122-1127, 16-18 April 2008.
- [19] Y. Lin and M. Tsai: "A Novel Feature Extraction Method for the Development of Nonintrusive Load Monitoring System based on BP-ANN", *IEEE International Symposium on Computer Communication Control and Automation*, Vol. 2, pp. 215–218, May 2010.
- [20] H.H. Chang: "Load Identification of Non-intrusive Load-monitoring System in Smart Home", *World Scientific and Engineering Academy Society Transactions on systems*, Vol. 9 Issue 5, pp. 498-510, May 2010.
- [21] M. Zeifman and K. Roth: "Nonintrusive Appliance Load Monitoring: Review and Outlook", *IEEE Transactions on Consumer Electronics*, Vol. 57 No. 1, pp. 76–84, February 2011.
- [22] Y. Nakano, H. Murata1, K. Yoshimoto1, S. Hidaka, M. Tadokoro, and K. Nagasaka: "Non-Intrusive Electric Appliances Load Monitoring System Using Harmonic Pattern Recognition - Performance Test Results at Real Households", *4th International Conference on Energy Efficiency in Domestic Appliances and Lighting*, pp. 477- 488, June 2006.
- [23] S.B. Leeb, S.R. Shaw, and J.L. Kirtley Jr.: "Transient Event Detection in Spectral Envelope Estimates For Nonintrusive Load Monitoring," *IEEE Transactions on Power Delivery*, Vol. 10 No. 3, pp. 1200-1210, July 1995.
- [24] S.R. Shaw, S.B. Leeb, L.K. Norford and R.W. Cox: "Nonintrusive Load Monitoring and Diagnostics in Power Systems" *IEEE Transactions on Instrumentation and Measurement*, Vol. 57 Issue 7, pp. 1445-1454, July 2008.
- [25] C. Laughman, K. Lee, R. Cox, S. Shaw, S.B. Leeb, L. Norford, and P. Armstrong: "Power Signature Analysis", *IEEE Power & Energy Magazine*, Vol. 1 Issue 2, pp. 56-63, March/April 2003.
- [26] A. Shrestha, E.L. Foulks and R.W. Cox: "Dynamic load shedding for shipboard power systems using the non-intrusive load monitor", *IEEE Electric Ship Technologies Symposium*, pp. 412-419, 20-22 April 2009.
- [27] L. Benaroya and F. Bimbot: "Wiener based source separation with HMM/GMM using a single sensor", *Proceedings of the 4th International Symposium on Independent Component Analysis and Blind Signal Separation*, Nara Japan, pp. 957-96, 2003.
- [28] J.G. Roos, I.E. Lane, E.C. Botha and G.P. Hancke: "Using Neural Networks for Non-intrusive Monitoring of Industrial Electrical Loads", *IEEE Information and Measurement Technology Conference (IMTC1994)*, Hamamatsu Japan, pp. 1115-1118, 1994.

Component model and network model validation in power system studies

S. Mvuyana^[1, 2], J.M. Van Coller^[1] and T. Modisane^[2]

1 School of Electrical and Information Engineering, University of the Witwatersrand, Private Bag 3, Wits 2050, South Africa.

2 Eskom Holdings SOC Limited, Group Technology Engineering, Megawatt Park Maxwell drive, Sunninghill, South Africa.

Abstract: Power system simulation models form the backbone of most power system studies and thus it is vital to ensure that the models are an accurate representation of the actual power system. Power system component model and integrated network model validation techniques are presented and present utility practices discussed, along with current challenges and short-comings. Software tools used by Eskom for component model and network model validation are presented.

Keywords: Power systems, component model validation, integrated network model validation, testing, simulation.

1. INTRODUCTION

Power system simulation studies form the backbone of most power systems studies and hence it is essential that simulation models used in such studies are proven to be accurate.

Power system components that must be accurately modelled include [1]:

- a. Generation: Turbine governors, Turbine plant, Power System Stabilisers (PSSs), Automatic Voltage Regulators (AVRs)
- b. Transmission: Transmission lines, Power transformers, mechanically switched reactive power devices (capacitors, reactors etc.), Flexible AC Transmission Systems (FACTS) devices (Phase shifting transformers, Static VAR Compensators (SVCs) etc.).
- c. Load representation: Industrial load (e.g. Aluminium smelters, mines, etc.), Residential loads (large towns or cities, etc.), Special load model development [2].

The aim of this paper is to present current model validation techniques and strategies used by various utilities worldwide as documented in the literature and to compare these with Eskom¹ practices so as to improve model validation processes in Eskom. Section 2 presents component validation techniques for elements which influence power system behaviour; Section 3 presents integrated network power system model validation processes; Section 4 presents software tools currently used by utilities (specifically Eskom) and Section 5 presents a discussion and conclusion of the work.

2. COMPONENT MODEL VALIDATION

2.1 Generation:

Most utilities throughout the world treat power stations/plants using a black-box approach. This approach does not consider boiler or detailed turbine process plant

dynamics, with detailed turbine plant dynamics only considered for specialised studies such as Subsynchronous Resonance (SSR) studies or generator end winding vibration studies. The main power plant components considered in power systems studies are:

- a. Generator
- b. AVR
- c. PSS
- d. Generator excitation.

Generator testing: Table 1.1 shows a list of the important parameters for generator modelling [3]:

Table 1.1: Synchronous Machine Model Parameters [3]

X_d, X_q	D and Q axis steady – state reactances (p.u)
X'_d, X'_q	D and Q axis transient reactances (p.u)
X''_d, X''_q	D and Q axis subtransient reactances (p.u)
X_l	Leakage reactance (p.u)
T'_{do}, T'_{qo}	D and Q axis transient open-circuit time constants (seconds)
T''_{do}, T''_{qo}	D and Q axis subtransient open-circuit time constants (seconds)
R_A	Armature resistance
$S_{1.0}, S_{1.2}$	Generator saturation constant at 1.0 p.u. and 1.2 p.u. terminal voltage
H	Inertia constant (MWs/MVA)

Generator Reactances and Time Constant determination ($X_d, X_q, X'_d, X'_q, X''_d, X''_q - T'_{do}, T'_{qo}, T''_{do}, T''_{qo}$): [3] suggests that a general 5 – 10% margin between Original Equipment Manufacturer (OEM) reactance parameters and those obtained during onsite testing is acceptable. There are a host of variables which affect the results obtained during testing. [3] gives a detailed discussion of each of these variables (Current Transformers, Potential Transformers, measuring equipment tolerances etc.).

In general most utilities (including Eskom) find OEM Factory Acceptance Test (FAT) parameters acceptable for use in power system simulation models. Figure 1 adapted from [4,5] shows how the individual inductances (subtransient, transient and steady-state) are obtained from a measured generator stator voltage decay profile.

¹ Model validation carried out by Eskom Operations System Planning in Simmerpan.

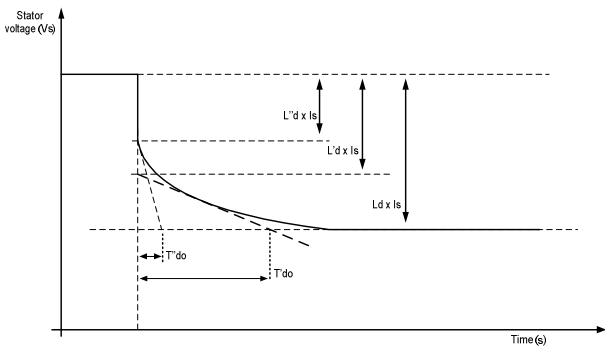


Figure 1 – Estimation of generator reactance and time constants from a stator voltage decay profile. [4,5]

Similarly the individual generator time constants (subtransient and transient) are obtained from the same profile as that of the reactances shown in Figure 1. T'_{do} (field time constant) varies significantly based on when the test is performed (with the unit coming from an outage or going into an outage), this is due to the rotor winding resistance being a strong function of the rotor temperature [3] which, in turn, is a strong function of the generator load cycling.

Inertia constant (H) determination: The generator inertia constant is determined from the various turbine stage rotor inertias, generator rotor inertia, in some cases the exciter rotor inertia and the generator MVA rating. The general trend within industry is to accept OEM values as correct but, with recent competitive trends within the industry, it is common for one manufacturer to supply the turbine rotor(s) and another manufacturer the generator. Hence the combination cannot be tested as a single unit during FATs, implying that H will be an approximated value. Figure 2 shows a measured generator frequency response for a MW rejection test conducted on an Eskom gas turbine unit [6].

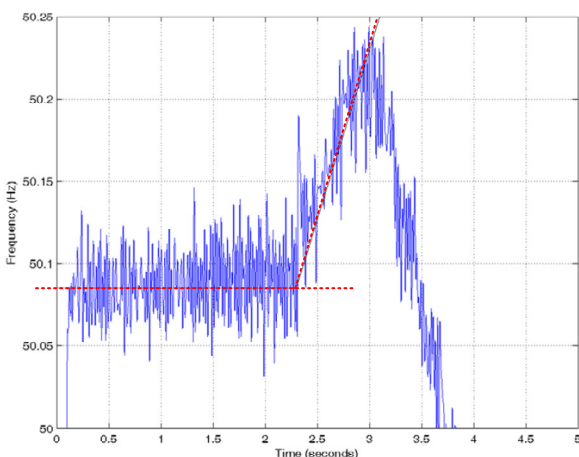


Figure 2 – Gas turbine generator frequency response during a MW rejection test. [6]

H was calculated using equation (1)

$$H = \frac{MVA \left(\frac{d\omega}{dt} \right)}{2P_o} \quad (1)$$

Where:

MVA – Apparent power rating of the generator

$\left(\frac{d\omega}{dt} \right)$ - Rate of change of generator frequency/speed with respect to time

P_o – Active power output of generator during the test.

Based on a survey conducted by utilities worldwide [3] an acceptance margin of $\pm 5 - 10\%$ on the value of H between OEM values and tests conducted onsite is appropriate.

Armature Resistance (R_A): Armature resistance does not influence power systems stability studies significantly, but it helps in providing a small amount of positive damping [7]. In most cases this parameter is usually set to zero (0) in simulation studies.

Generator saturation constants ($S_{1,0}, S_{1,2}$): There is general consensus in industry that OEM saturation curves will differ from site test values. [3] offers a detailed discussion on the factors influencing these parameters [3,5]:

- a. Hysteresis: Voltage level operation prior to the generator being tested and how residual flux is accounted for in the calculation of the saturation parameters
- b. Shorted rotor turns: Shorted turns have a significant impact on open circuit characteristics of the generator and hence saturation parameters [3].

Hence based on this it is crucial that utilities develop stringent FAT criteria and these are adhered to during each of the FAT stages so as to ensure that values obtained from such tests are an accurate representation of the actual generator saturation values.

Automatic Voltage Regulator testing: AVR tests are among the most important tests carried out on power plants with regards to power systems dynamic studies [3]. From Eskom experience, OEMs tend to develop very specific AVRs utilizing special software control functions and algorithms and, through performance testing, choose the closest generic IEEE [8] or IEC [9] standard models.

The challenge presented by this OEM approach is that AVRs in practice tend to perform very differently during system disturbances compared with that predicted by the standard generic models presented in [8] and [9] as noted by [3]. Hence there has been very strong interaction between OEMs and utilities (through IEEE, IEC and Cigre working groups) so as to build detailed AVR simulation models. The ultimate responsibility still lies with the utility in ensuring that the OEM supplies detailed AVR models.

Most utilities tend to perform online AVR parameter validation or commissioning tests and in most instances AVR parameter values such as gain and phase lead are altered so as to improve the AVR performance during

commissioning. The simulation models are however not updated with the commissioned values [3]. Figure 3 shows the generator response for a VAR rejection test performed so as to determine the AVR parameters for an Eskom Gas driven turbine generator unit [6].

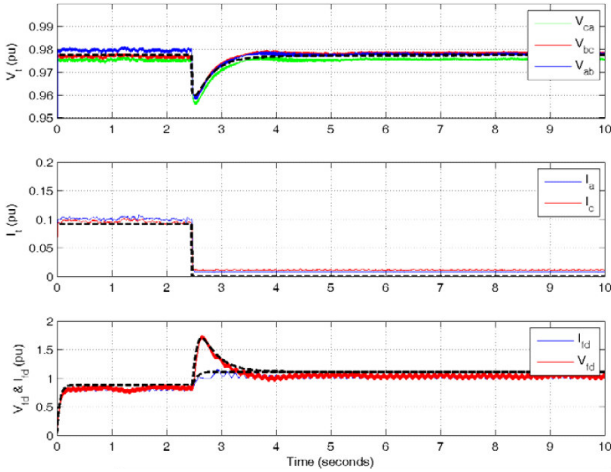


Figure 3 – VAR rejection test. [6]

The generator breaker is opened with the unit AVR set to control the terminal voltage. The generator is previously importing a relatively small amount of reactive power and zero MW of active power so as to observe the dynamic response of the AVR and hence determine its parameters.

Figure 4 shows the open circuit generator response for a step input increase and decrease of 4% into the AVR setpoint, with the terminal voltage response shown on the top half of the Figure.

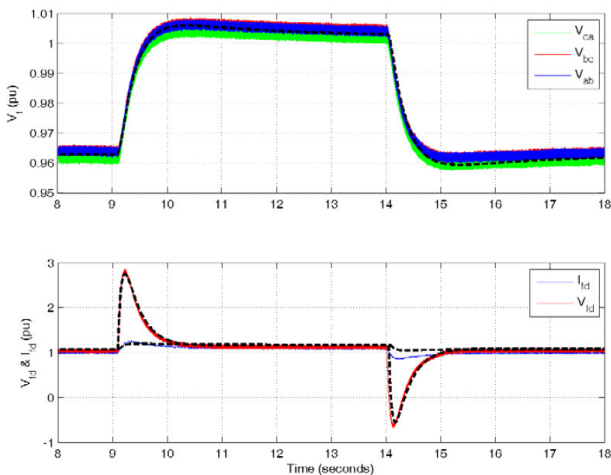


Figure 4 – Step-change-in-setpoint test [6]

The main challenge in performing online AVR parameter validation studies is choosing a suitable generator operating point so as to ensure that the generator is always operating within its capability curve. This is crucial for older excitation systems as some of the designs have been noted to have per unit voltages as high as 47p.u [3].

Generator excitation methodology: [1,10] attribute excitation system representation as one of the key factors behind the 1996 Western Interconnection Power Outages. In some instances software excitation models used were inconsistent with actual plant excitation components (e.g. Static exciters represented by DC exciters). Figure 5 adapted from [1] shows the actual network response (instability) through a crucial transmission line versus the simulated network response (stable) through the same transmission line.

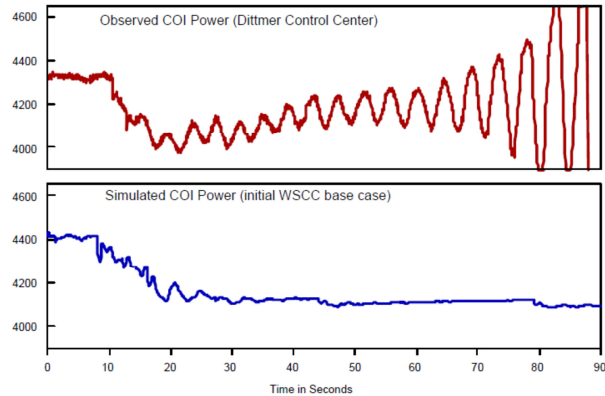


Figure 5 – Actual network response (unstable) versus simulated network response (stable). [1,10]

Hence, based on the information from Figure 5, other detailed studies were conducted by the Western Electric Coordinating Council (WECC) [1]. As a result, a number of transmission lines were de-rated from their original design capacity as the WECC found that power transfer in the region was stability constrained [1].

Power System stabilizer testing: PSSs are by far the most cost effective method currently available to damp power oscillations [11]. PSSs create a damping torque which is applied to the generator rotor in phase with the rotor speed [7,11], through the excitation system. The stabilizing signal used (either speed ($\Delta\omega$), or integral of accelerating power ($\int P_E$) or rate of change of power (ΔP)) creates the required damping torque applied to the rotor. The stabilizing signal is put through a phase-lead block so as to eliminate the phase lag between the AVR setpoint and the generator [11]. [11] suggests that offline PSS tuning is the best practice to be applied by utilities, as this helps to eliminate any de-stabilizing affect which may be introduced by the PSS due to generator interaction and participation in any inter-area mode of oscillation.

PSSs are tested in a similar manner to AVR's (input step response tests) whereby the damping introduced by the PSS is observed by viewing the system response with the PSS out of service and in service [3,6]. Figure 6 shows the measured active and reactive power response of a Gas driven turbine generator unit with the PSS out of service. As can be seen, the active power oscillations are large (± 7.0 MW) and the natural damping of the generator is poor as the oscillations last for a long time (± 6 seconds)

before being completely damped by the generator and network natural damping.

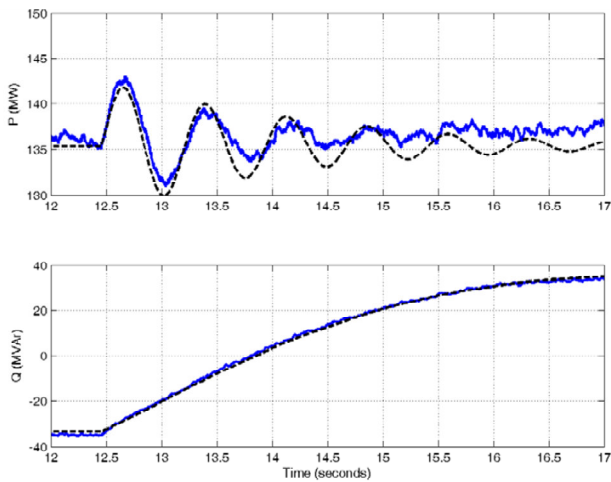


Figure 6 – AVR 4% input step response test (PSS out of service). [6]

The test (4% input step response) is repeated with the PSS in service, and the maximum power oscillation measured is ± 3.0 MW compared to the previous ± 7.0 MW (with the PSS out of service). The results are shown in Figure 7. The PSS introduces a large amount of damping as the oscillations now decay within ± 1.0 seconds.

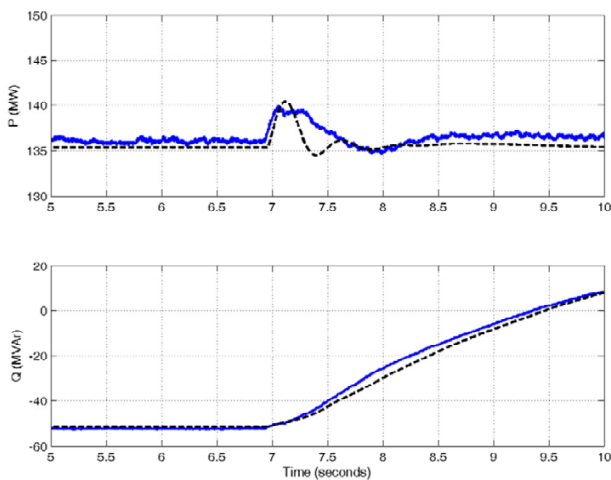


Figure 7 - AVR 4% input step response test (PSS in service). [6]

Tuning of PSSs using offline tools can be a challenging task due to the size of most power systems. Utilities worldwide tend to accept PSS operation mostly for the use of local mode damping due to complexities which may be introduced by improperly tuned PSSs [12].

2.2 Transmission:

Transmission system model verification is also important as incorrect modelling could result in inconsistencies between actual power system behaviour and software models as seen in Figure 5. Transmission system components of interest with regard to system modelling are:

- a. Transmission lines

- b. Power transformers
- c. Mechanically switched reactive power devices (capacitors and reactors)
- d. FACTS devices (phase shifting transformers, SVCs, etc.)
- e. HVDC systems.

Transmission components a – c: Components a – c are modelled using standard models which are widely available in the literature. [13] serves as a good reference for such models and their general treatment in power systems studies. OEM FAT parameter values are generally accepted as adequate for such components. Most utilities, including Eskom, validate software models and parameters by comparing active and reactive power flows in the software models with actual network variables from SCADA and Network State Estimator tools.

FACTS devices: Validation of FACTS device performance (excluding phase shifting transformers) is a complex task and is generally carried out during the commissioning stages. SVCs are the most commonly used power electronics based FACTS device in utility networks; hence there is a great need for model and controller validation of these devices, including the development of acceptable generic models [14]. The challenge with SVC model validation is dynamic operation validation, specifically that of the controller [14] and the control settings chosen for a particular mode of operation.

During the initial SVC commissioning stages it is not always economical or viable to simulate network dynamic stability conditions as these could result in extreme network challenges if there are any unforeseen risks. [15] presents a strategy for using readily available disturbance information and SVC parameters which are recorded so as to validate the performance of SVCs. A case study of the proposed strategy conducted in the WECC network is presented for a particular SVC.

High Voltage Direct Current Systems: In order to reduce network complexities and modelling challenges, utilities tend to model HVDC systems as negative loads. This approach is only valid for steady – state power flow analysis. In order to model HVDC system accurately; the dynamic controller model performance is required. This presents a challenge for older generation HVDC systems as controller model dynamic parameters are not always readily available. [14] presents generic models which can be used in instances whereby there is not sufficient data to create detailed software models.

2.3 Load modelling:

Load modelling is a complex field and one which not all utilities tend to appreciate [1]. Many research efforts have focused on developing accurate power system models which mimic power system behaviour over a wide range of conditions. [2,10] present strategies which were used in the WECC so as to improve load modelling as it was also noted in [1,2] that inappropriate load modelling played a large factor in the discrepancies seen in Figure 5.

Within Eskom Transmission, loads are generally modelled as constant current (active power) and constant impedance (reactive power) loads, and values based on substation busbar load and voltage measurements. For dynamic stability studies, loads are at times represented as composites (mixture of dynamic and static loads) so as to improve the performance of software model dynamics and mimic actual measured power systems behaviour.

3. INTEGRATED POWER SYSTEM MODEL VALIDATION

Integrated power system model validation is the next logical step after component model validation [1]. [1] states that most utilities worldwide do not perform complete power system model validation and cites complexities related to verification as the main deterrent. Utilities according to [1] tend to be confident in creating complete system models with validated component model behaviour but without validating the integrated network model with actual measured data from the network.

Figure 8 adapted from [16] shows proposed dynamic security assessment (DSA) components which are used in model verification processes.

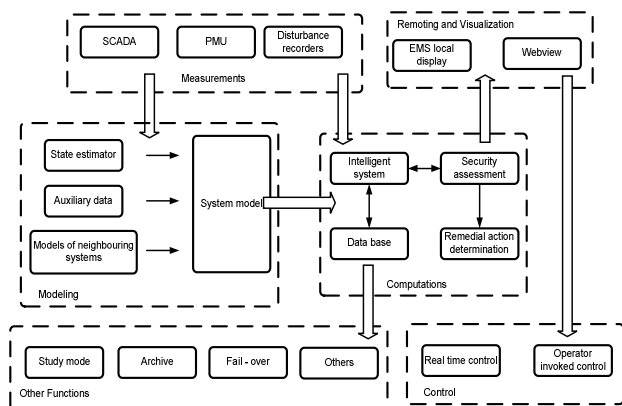


Figure 8 – Proposed DSA structure according to Cigre. [16]

The high level structure used within Eskom for model dynamic security assessment is similar to that shown in Figure 8. Figure 9 adapted from [1] shows a detailed proposal for a model validation process which is similar to that currently used in Eskom.

The general approach followed in dynamic stability model assessment is based on comparison and analysis of the following network parameters and conditions [1,3]:

- a. Network topology
- b. Nodal/Bus voltages
- c. Network power flow
- d. Generation dispatch
- e. Transformer tap positions
- f. Status of switched reactive power devices
- g. Load profile
- h. Load dynamics and load composition
- i. Power plant dynamics

Each of these parameters and conditions are analysed at each of these stages:

- a. Pre – disturbance condition
- b. Disturbance condition
- c. Post – disturbance condition

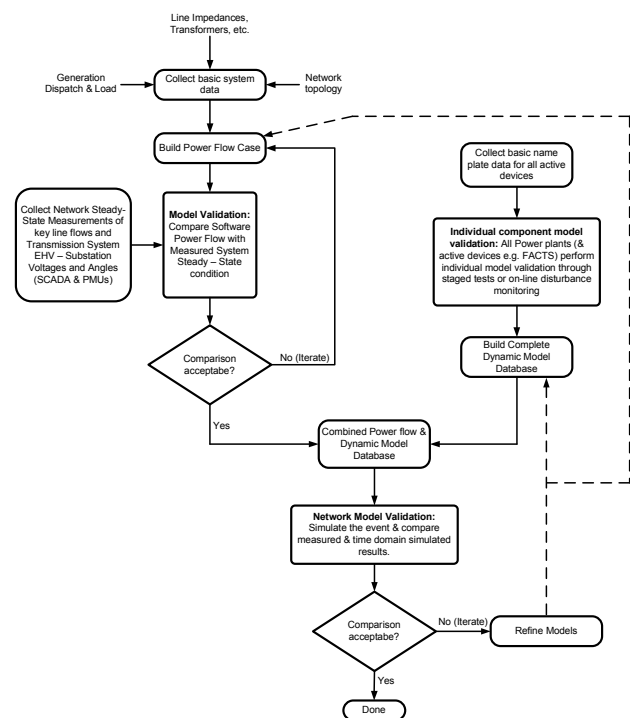


Figure 9 – Proposed integrated network model validation process. [1]

Hence the model validation process shown in Figure 9 is applied during each of these stages (pre-disturbance to post-disturbance) and the network conditions, including parameters, (topology to power plant dynamics) are compared with data from the SCADA system and with the Network State Estimator to ensure an accurate and optimized software network model which is able to mimic both steady-state and dynamic behaviour of the power system.

The main aim of such an exercise is to ensure that the software network model is able to accurately mimic parameter profiles for dynamic and steady-state conditions (not just snapshots of a single moment) to an acceptable level so as to ensure that the operation of the network is both economical and secure. Inappropriate network models can lead to unnecessary over investment in the network which inadvertently increases the operating cost of the network and the price of electricity.

Under investment on the other hand can lead to compromised network security and unnecessary power outages [1].

4. SOFTWARE TOOLS USED FOR MODEL VALIDATION

Software tools currently used for component model validation offer the ability to accept measured parameters and optimize component model parameters, but this should not be used as a substitute for appropriate component models being used. Figure 10 adapted from [17] shows the optimization principle used in DigSILENT® for model parameter optimization based on actual measured parameters.

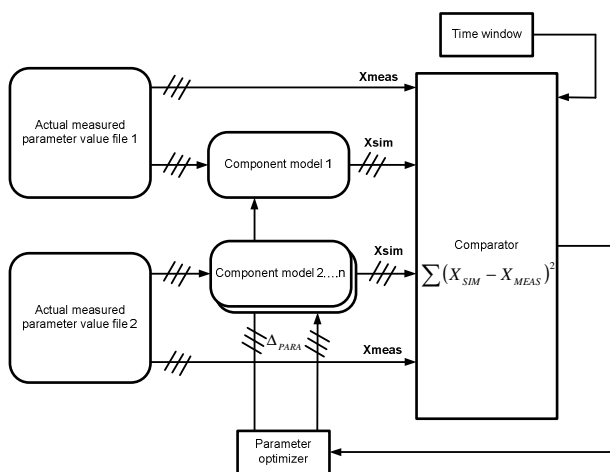


Figure 10 – Model parameter optimization principle used in DigSILENT®. [17]

The optimization principle shown in Figure 10 is similar to that currently used by Eskom. Various software component models are verified using this approach. Figure 11 adapted from [3], shows a simplified representation of the main control loops in a power plant.

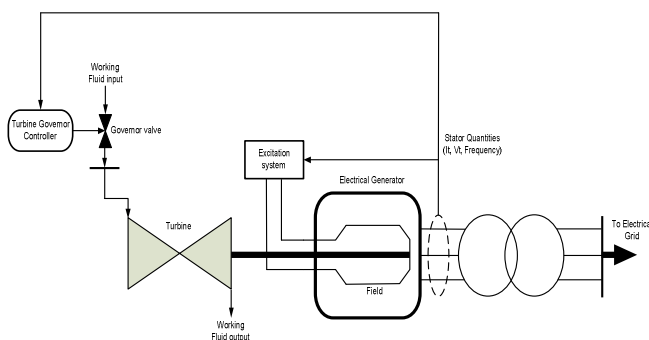


Figure 11 –Simplified model of main power plant control loops. [3]

Verification of a generator software model for a large coal-fired power plant was carried out in [18]. The software model single-line diagram used was similar to that presented in Figure 11. Figure 12 shows the measured parameter response (active power of two units

(a and b)) which was measured on the power system using Phasor Measurement Units (PMUs).

The measured active power response of each unit was used as an input into the software and the generator parameters optimized so as to mimic the measured output (software simulated response (c and d)) using DigSILENT®, the simulated response shown in Figure 12 is not the final parameter response, further iterations were performed, these are not shown in this paper.

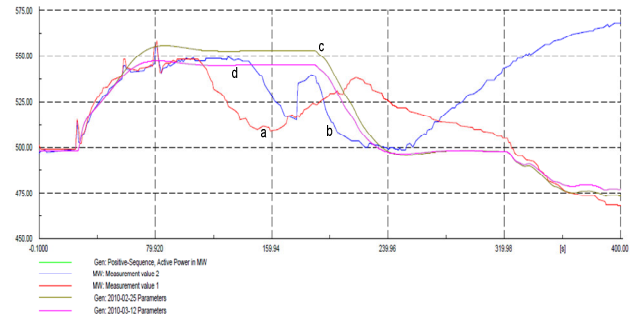


Figure 12 – Measured active power response versus simulated active power response. [18]

Other software tools which are used within Eskom for model validation purposes are:

- a. SCADA
- b. Network State Estimator
- c. DigSILENT®
- d. PSSE®

Other utilities worldwide use various other software platforms which are available and each software package has its own advantages and disadvantages. Hence a detailed needs analysis must be performed prior to choosing any software package

5. CONCLUSIONS

This paper presented a detailed review of power system component model and network model validation techniques which are currently used by utilities worldwide and current model validation practices used within Eskom. Various component validation test results are presented throughout the paper. This work is being carried out as part of a larger research study on the performance of the Eskom network and the full network model response based on measured network parameters.

6. Bibliography

- [1] D. Kosterev, P. Pourbeik E. Allen, "Power system model validation: A White Paper by NERC model validation task force of the Transmission subcommittee," New Jersey Princeton, 2010.
- [2] A. Meklin, J. Undrill, B Lesieutre, W Price, D Chassin, R Bravo, S Yang D Kosterev, "Load Modelling in Power Systems Studies: WECC Progress Update," in *Power Engineering General Meeting*, Pittsburg, PA, July 2008.
- [3] EPRI, Palo Alto, CA, FirstEnergy, Akron, OH, Tennessee Valley Authority, Chattanooga, TN:2007. 1015241, "Power Plant Modeling and Parameter Derivation for Power System Studies: Present Practice and Recommended Approach for Future Procedures.," Electric Power Research Institute, Knoxville, TN 37932, 2007.
- [4] WSCC Control Work Group and Modeling Validation Work Group, "WECC Testing Guidelines for Synchronous Unit Dynamic Testing and Model Validation," Western Electric Coordinating Council (WSCC), WECC Unit Testing Guideline 14 May 2010.
- [5] Ion Boldea, "The Electric Generators Handbook," in *The Electric Generators Handbook*, Leo L. Grigsby, Ed. 6000 Broken Sound Parkway NW, Suite 300: CRC Press, Taylor & Francis Group , 2006, ch. 8.
- [6] Electric Power Research Institute, 3420 Hillview Avenue, Palo Alto, California, 94304, "Dynamic Model Parameter Derivation for Gas Turbine Power Plant Based on Field Tests," Electric Power Research Institute and ESKOM SOC Ltd, Field Test Report 2007.
- [7] F.P de Mello C. Concordia, "Concepts of synchronous machine stability as affected by Excitation control," *IEEE Transactions*, vol. PAS - 88, April 1969.
- [8] IEEE Excitation Model System Model Task Force, "IEEE Recommended Practice for Excitation System Models for PowerSystem Stability Studies," New York, NY 10017-2394, USA, IEEE Std 421.5-1992, 1992.
- [9] Rotating machinery IEC Technical Committee 2, "Part 16: Excitation systems for synchronous machines Chapter 2: Models for power system studies," IEC - 34:16:2, 1991.
- [10] Electric Power Institute Research Institute, 3412 Hillview Avenue, Palo Alto, California 94304, "System Disturbance Stability Studies for Western Systems Coordinating Council (WSCC)," Electric Power Research Institute, California, April 1997.
- [11] G.Rogers - Cherry Tree Scientific Software, "Demystifying Power Oscillations," vol. IEEE Computer Applications in Power Systems, July 1996.
- [12] N. Martins, N. Zeni Jr, J. Soares, G. Taranto J. Ferraz, "Adverse Increase in Generator Terminal Voltage and Reactive Power Transients Caused by Power System Stabilizers," in *IEEE Power and Energy Conference*, 2002.
- [13] Electric Power Research Institute, 3412 Hillview Avenue, Palo Alto, California 94304, *EPRI Power Systems Dynamics Tutorial without Q/A Section*, Electric Power Research Institute, Ed. California: Electric Power Research Institute, 2009.
- [14] Electric Power Research Institute, 3412 Hillview Avenue, Palo Alto, California 94304, "Models and Model Validation for Planning Studies: Technical Update," Electric Power Research Institute, California, EPRI Power Delivery & Utilization 2011.
- [15] P Pourbeik, A Bostrom, P John, and M Basu, "Operational Experience with SVCs for Local and Remote Disturbances," in *Proceedings of the IEEE Power Systems Conference and Exposition*, Atlanta, GA, 29th - November 2006.
- [16] Cigre System Operation and Control Study Committee, "Review of on-line dynamic security assessment tools and techniques," Cigre , Paris, Technical Brochure 325,.
- [17] DIgSILENT PowerFactory, "PowerFactory User's Manual: Version 14.0," DIgSILENT GmbH, Gomaringen, Germany, Software User 's Manual 2008.
- [18] A. Edwards, A. Kopa B. Berry, "A Method for Tuning Model in DIgSilent PowerFactory with Reference to a TGOV5 Governor Tuning Example," Eskom: System Planning and Operations, Johannesburg, South Africa, Instruction Manual - Public document SOPRP0220, 2010.

CONVERTING CONVENTIONAL HIGH VOLTAGE ALTERNATING CURRENT TRANSMISSION LINES INTO A DIRECT CURRENT TRANSMISSION SYSTEM

M.J. Matabaro* and G. Atkinson-Hope**

* Centre of Power System Research, Dept. of Electrical Engineering, Cape Peninsula University of Technology, P.O. Box 682 Cape Town 8000

E-mail: 208002936@mycput.ac.za

**Technology Transfer and Industrial Linkages, Centre of Power System Research, Dept. of Electrical Engineering, Cape Peninsula University of Technology, P.O. Box 682 Cape Town 8000

E-mail: atkinsonhopeg@cput.ac.za

Abstract: Over the last few decades economic growth and industrialization have led to a rapidly rising demand for electric power in many countries. One effect of this increase in demand is that the power transmission systems are nearing a point where they will be unable to meet supply needs. Therefore a need thus arises to consider transmission line alternatives that could substantially increase the power transfer capability of existing high voltage alternating current (HVAC) transmission lines. One alternative is to use high voltage direct current (HVDC) transmission systems as a direct replacement, thus eliminating the need for any major new tower constructions. The existing conductors and tower structures will be used. This paper will demonstrate how the power transfer capability of an existing HVAC transmission line could be maximized by feeding this line with HVDC. The power transfer capability of HVAC lines is limited by the reactive power needed by the line. However, when HVDC is applied, the only loss on the line is due to the resistance of the conductors, thus it is expected that more power will be transferred across the line compared to a HVAC system. In this investigation a methodology will be developed showing how to convert a HVAC line to a HVDC line. To prove the effectiveness of this methodology, a number of scenarios will be investigated as case studies. The research will conclude with findings as to the suitability of converting an existing HVAC line into a HVDC fed system from which increased HVAC can be drawn and supplied at the load end.

Keywords: HVDC, Power Transfer Capability, Creepage Distance, Thermal Capacity, Static Var Compensator, Synchronous Condensers, Short Circuit Ratio.

1. INTRODUCTION

Industrial countries are experiencing increasing difficulty in finding suitable corridors for new overhead transmission lines. This can mainly be ascribed to the dense population. Furthermore, the power industry is under pressure to reduce the impact on the environment. As a result utilities could be forced to utilize the existing right of way (ROW) and make maximum use of the existing infrastructure. The transmission capacity of an existing HVAC line could be increased by the following methods:

- a) Substantial increase in transmitted power by replacement of an HVAC transmission line to a new compact HVAC line or a new HVDC line. Both will require new investment.
- b) Conversion of the existing HVAC line to HVDC with substantial increase in power.

The latter point mentioned is where this research will be pursued. Research by Naidoo et al. [1] indicates that the existing assets could be used for greater power transfer efficiency.

To prove the effectiveness of this methodology, a number of scenarios will be investigated as case studies.

2. RESEARCH AIMS AND OBJECTIVES

The aim of this paper is to investigate and analyse a conventional HVAC transmission line when fed by HVDC while still supplying HVAC at the load end of the line.

Also, the design levels of voltage, current, and power of the converted DC transmission line will be determined according to certain design constraints. The efficiency of the converted transmission line will be evaluated, as well as determining the ratings of the power electronic converters to be used. This paper does not cover environmental and economical considerations. It covers technical considerations that should be taken into account in the conversion of an existing practical HVAC transmission system to HVDC in order to increase the power transfer capability. The main advantage of this approach is that a new line does not have to be built. However, power electronic converters for conversion of the alternating current (AC) to direct current (DC) and vice versa will be needed. The investigation will however be limited only to line commutated HVDC system as bulk power transfer will be considered.

3. LITERATURE REVIEW

The first electric generator was a DC generator, and hence, the first electric power transmission line built by Thomas A. Edison was constructed using DC. It began operation in 1882 and supplied DC to an area of 1.6 km. Despite the initial supremacy of DC, AC superseded DC due to greater advantages [2]. This was mainly because transformers were invented which could easily change voltage levels of transmission, stepping them up or down. However, HVAC transmission lines have an inherent design inefficiency whereby the skin effect results in parts of the conductor not carrying current. With increasing system voltages and the subsequent increase in conductor bundles; this design inefficiency worsens [1]. The power handling capability of AC transmission lines is limited by the thermal loading limit in the case of short lines, the voltage drop limit in the case of medium lines and the stability (angle) limit in the case of long lines. Due to stability constraints, HVAC lines longer than 450 km can only transfer power less than its surge impedance loading (SIL), while power transfer capability of it based on thermal limit is more than its SIL. With voltage magnitudes fixed at both ends of a line, the active power transfer between two active sources is only controlled by the transmission angle (δ). Equation (1) shows that there is a limit to the power that can be transmitted to the receiving end of the line. An increase in power delivered means that $\theta_z - \delta$ has to be zero, which means maximum power will be delivered when $\theta_z = \delta$. Further increase in δ result in less power received.

$$P_R = \frac{V_R V_S}{Z'} \cos(\theta_z - \delta) - \frac{AV^2_R}{Z'} \cos(\theta_z - \alpha) \quad (1)$$

Where:

P_R = active power obtains at receiving end

V_R = receiving end voltage

V_S = sending end voltage

Z' = magnitude of impedance of the line

θ_z = angle of impedance of the line

δ = angle of sending end voltage

A = dimensionless value of parameters depend on the transmission line constants.

α = angle of receiving end voltage

This practical operating transmission angle (δ) is usually limited to 30° [1,3-5].

At these conditions the line conductors carry current much less than their safe current carrying capacity. For optimal use of the lines there is a need to load long HVAC lines close to their thermal limits. One possible way to achieve this is by using Flexible AC Transmission System (FACTS) components [7-8]. Another possibility is that the HVAC transmission line is converted to carry DC; the full conductor current carrying capability can then be fully employed.

Since the DC line requires only two conductors when converting a single horizontal three phase circuit, one extra conductor could be left out or could be used for metallic return [2]. This configuration can eliminate ground electrodes. This is an advantage where it is restricted to use earth as the earth electrode (for environmental reasons, i.e. due to corrosion or interference with buried metal).

There are two reasons for increasing the power transfer capacity by the conversion to DC:

- The line design can stand a higher DC voltage to ground, and
- The conductors can be operated at higher current, limited only by thermal limit and loss considerations in contrast to stability limitations applicable to the AC lines.

However, there are some limiting factors affecting line loadability and insulation levels for both AC and DC transmission. For AC transmission, there are three considerations that affect loadability; thermal factors, voltage drop and stability. For DC, only thermal factors and voltage drop limitations apply [2,7]. These three technical limiting factors should be considered when a HVAC transmission line is to be converted to HVDC operation:

Thermal limitation: Stability limits usually restrict the maximum power that can be transmitted by an AC line to some fraction of its thermal capacity [5]. A DC line can be loaded up to its thermal limit although a margin is usually maintained for emergency capacity. A HVDC transmission line does not have the skin effect, hysteresis, eddy current and proximity effect associated with the AC current, and therefore would lower DC resistance, and as a consequence carry increased current for the same temperature [2]. The current carrying capacity and temperature limit of the existing conductors should not be exceeded when the same conductors would be used to carry the uprated level of power obtained by the conversion to DC transmission [2].

Voltage drop limitation: Since a converted DC line will carry as high DC current as possible, evaluation of DC power losses and voltage drops would be considered. The voltage drop limitation sets a limit on how much current could be carried over the converted dc line [2].

Insulation level limitation: Insulation level set a limitation on how much voltage can be applied to the converted DC line. It is an important factor. Considering that the DC for the breakdown of an insulator is equal to the peak value of the alternating voltage to cause breakdown. The insulation level of the existing HVAC line is determined by the expression

$$AC_{line} = K_1 \times \sqrt{2} \times \frac{V_L}{\sqrt{3}} \quad (2)$$

Thus, the insulation level of the converted bipolar line is

$$\text{Bipolar line} = K_2 \times V_d \quad (3)$$

Where:

AC_{line} = Alternating Current

K_1 = alternating current switching surge factor in per unit

V_L = alternating current line to line voltage in kV

K_2 = direct current switching surge factor in per unit

V_d = direct voltage per pole to ground in kV

The DC voltage which can be applied would at least be equal to the peak AC voltage to ground [3]. However, another aspect to the voltage capability for DC, which is the switching overvoltages on a DC line, are much lower than on the AC line [7]. On long AC lines the switching surge factor (SSF) is between 2.0 and 2.4, for a DC lines, the SSF is 1.7. It is very likely that in the AC to DC transmission conversion more insulators in a string than previously used will be required. AC insulators have much lower

pollution flashover strength under DC voltage than they do under AC voltage, and are therefore unsuitable for DC service [6]. Their change out to DC units is a requisite of AC to DC conversion. AC insulator's poor performance under DC is due to the electrostatic precipitator effect of a steady DC field which attracts dirt particles from the surrounding air and deposits them on the insulator surface [6].

4. CONVERSION CRITERIA

Conversion of AC transmission line structures and conductor systems to DC operation is principally a question of determining the DC voltage which the circuit will sustain. That voltage may be limited by one or more of the following factors:

1. Midspan clearance to ground, buildings and other objects, as governed by codes and individual utility practices.
2. Insulation at the tower, either as found or modified to provide additional creep distance.
3. Electrical gradient on the conductor surface; a concern both for radio and audible noise, but also for risk of anomalous flashovers.
4. Electrical gradient on the earth's surface; an issue relevant to human safety.

5. DESIGN CONSTRAINTS

When existing AC transmission system has to be converted to DC, the following DC/AC ratio is defined:

$$\text{Power ratio } (\beta) = \frac{\text{power of the converted dc system}}{\text{power of the existing ac system}} = \frac{P_{dc}}{P_{ac}} \quad (4)$$

$$\text{Insulation level ratio } (\gamma) = \frac{\text{dc insulation level}}{\text{ac insulation level}} = \frac{K_2 \times V_d}{K_1 \sqrt{2} \times \frac{V_L}{\sqrt{3}}} \quad (5)$$

Based on the above mentioned technical considerations, the following design constraints should be satisfied in the analytical procedure for the AC to DC transmission conversion:

- a. According to voltage drop limitation:

$$I_d \times R_{dc} \leq K_q \times l \times V_d \quad [2] \quad (6)$$

Where:

$$K_q = \text{constant} = (0.625 \rightarrow 1.25). 10^{-4}$$

V_d = direct voltage per pole to ground in kV

l = length of the line in km

R_{dc} = dc resistance in ohms

I_d = direct current in kA.

- b. According to thermal limitation:

$$I_{dc} \leq \text{Existing conductor's current carrying capacity (CCC)} \quad (7)$$

$$c. \quad P_{dc \text{ bipole}} \text{ is equal to } 2 \times V_{dc} \times I_{dc} \quad (8)$$

- d. Power ratio β should be > 1

6. ANALYTICAL PROCEDURE

The following data are known for an existing AC transmission line:

Line's parameters (l, θ, R_{ac}), V_L , alternating current power transfer capability (PTC_{ac}), P_{ac} , I_{ac} and P_{Lac} at the normal operating condition, C.C.C of line's conductors, and $\cos(\Phi)$ is usually kept at 0.866. For the conversion to DC transmission the following analytical steps should be followed:

- i. $V_{dc \text{ pole to ground}}$ is calculated from equation (5) with value of $\gamma = 1.1$ in accordance with the discussion of the limiting factors stated above, $K_1 = 2.0$, and $K_2 = 1.7$.
- ii. Calculate I_d by using equation (6) and check its value according to (7).
- iii. Using the calculated values of $V_{dc \text{ pole to ground}}$ and I_d to find equation (8).

Having determined V_{dc} , I_d , and P_{dc} , proceed to calculate the ratings and basic characteristics of the proposed rectifier and inverter stations for the bipole circuit.

7. NETWORK MODEL

To demonstrate the feasibility of converting HVAC to HVDC two case scenarios will be performed. The first one will be to model an existing HVAC network, while the second one will be to convert an existing HVAC line into HVDC. For the purpose of modeling and load flow analysis, the simulation has been conducted using DigSilent Powerfactory.

7.1 Case study1: HVAC transmission network

The 400kV AC transmission system shown in figure 1 has the following data:

Two bundles dinosaurs conductors per phase.

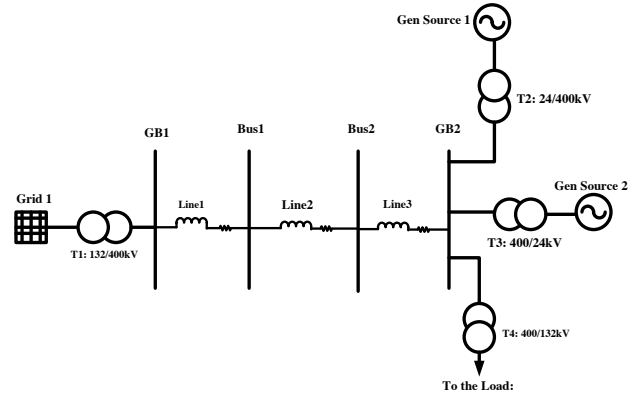


Figure 1: 400kV AC circuit transmission system.

The line has horizontal spacing with 9.4 m between adjacent phases. The line has three sections: GB1 – Bus 1 (350 km), Bus 1 – Bus 2 (400 km), Bus 2 – GB2 (450 km). The generator is modelled using Koeberg power station's rating. Koeberg's machine has the following ratings: nominal apparent power is 1072 MVA, nominal voltage is 24 kV, and power factor is 0.9. The synchronous reactances X_d is 2.46 p.u and X_q is 2.28 p.u.

Table 1: Line Parameters and phase coordinations

Line parameters							
Nominal Voltage	400kv	Minimum operating temperature			20°C		
Nominal Current	1.704 kA	Maximum operating temperature			80°C		
Number of Sub conductors	2	DC resistance @ 80°C			0.0437 Ω/km		
Bundles spacing	0.38 m	Max sag. Phase conductors			11.4 m		
DC resistance @ 20°C	0.0437 Ω/km	Max sag. Ground wires			10.3 m		
GMR (equivalent radius)	14.54312	Earth resistivity			700 Ω		
Outer diameter	35.94 mm						
Tower Coordinates - phase circuit (m)							
Number of phase		X1	X2	X3	Y1	Y2	Y3
Circuit	3	-9.4	0	9.4	21.03	20.724	21.03

Table 2: Earth wire parameters and coordinates earth wires

Earth wire parameters				
Number of Earth wires	2	Nominal voltage		1kV
Number of subconductors	1	Nominal current		0.109kA
DC- Resistance @ 20°C	1.88Ω/km	Earth wire coordinate		X Y
GMR(equivalent radius)	0.0001198mm	Earth wire 1		- 8.3m 25.15m
Outer diameter	13.5mm	Earth wire 2		8.3m 25.15m

7.1.2 HVAC transmission line load flow result

This case study was performed to monitor the performance of all transmission lines (line1, line2, line3). The results obtained identify a potential problem, which is the presence of reactive power into this transmission line. Therefore, HVDC as opposed to HVAC can be a way of eliminating or avoiding the presence of reactive power into this line after being converted to HVDC. Unlike the HVAC transmission line, the HVDC transmission line does not have a reactance.

Table 3: Load flow result of HVAC transmission lines

Elements	P(MW)	Q(MVA _r)	SIL(MW)	I(kA)	Θ(°)
Line 1	450	-328.87	551.4136	0.699	110.449
Line 2	438.605	-83.244	551.4136	0.498	68.978
Line 3	431.321	196.018	551.4136	0.555	21.436

7.2 Case study 2: Procedure for conversion HVAC to HVDC

The conversion of HVAC transmission line is carried with no change made to the conductors and the total rated current remains the same, which in turn means the transmitted power increases proportionally to the adopted new DC line to ground voltage.

7.2.1 Design criteria for line to be converted

This paper emphasises converting HVAC transmissions lines to HVDC. To maintain or keep adequate clearance between energized conductors and the ground, as well as by determining a proper leakage or creepage distance for the insulator.

Clearance to ground

In order to keep at least the same safety value of clearance, conductor to ground clearances are calculated, i.e. the same difference between the minimum conductor height and the electrical clearance according to local standards must be considered while dimensioning clearances. Equation (9) for clearance to ground for an HVDC line can be used [6]:

$$D_{min} = 6 + 0.006 \times (U_{dc\text{poleto}\text{ground}} - 45) \quad (9)$$

Where:

D_{min} = minimum conductor to ground clearance in meters.

Creepage distance

For the HVDC transmission lines a special proven type of insulator must be used with a creepage distance or leakage path to spacing ratio of 3.2:1. In a moderately polluted area, a creepage distance of 30 mm/kV is sufficient whereas, for a heavily polluted area 50 mm/kV may be necessary. The insulator string length can be decided from equation (10) for moderately polluted area, and determined from equation (11) for heavy polluted area [6].

$$L = \frac{0.03 \times U_{dc\text{poleto}\text{ground}}}{3.2} \quad (10)$$

$$L = \frac{0.05 \times U_{dc\text{poleto}\text{ground}}}{3.2} \quad (11)$$

Where:

L = insulator string length in meters

Clearance to the tower structure

Clearance must be chosen to withstand adequate operating voltages and switching surges, also during windy conditions [9]. With switching overvoltage factors in HVDC lines in the range of 1.5 to 1.8 p.u , they are far lower than those for HVAC lines. For the clearance to tower equation (12) is established according to NESC formula based on switching surge strength [6].

$$d = \left(\frac{V_{d\text{poleto}\text{ground}} \times PU \times a}{K \times 500} \right)^{1.667} \quad (12)$$

where:

- $V_{d\text{poleto}\text{ground}}$ = nominal DC voltage per pole to ground in kV
- PU = value of overvoltage peak 1.75 p.u
- K = 1.15 for monopolar lines (conductor window)
- K = 1.25 for bipolar lines (conductor structure)
- a = 1.25

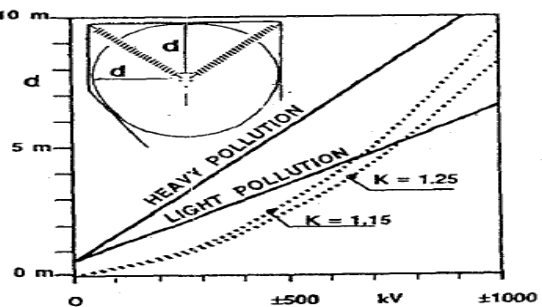


Figure 2: Conductor- tower distance d resulting from switching surge insulation requirements (dotted line) and surface insulation requirements (continuous line) [6].

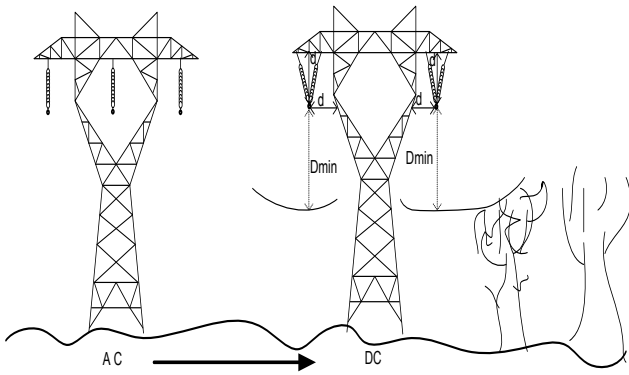


Figure 3: Conversion of HVAC tower to HVDC bipolar line respectively

Corona inception gradient on conductors

When the voltage gradient at surface of a conductor exceeds the dielectric breakdown strength of air, corona and ionization of the air surrounding the conductor result. The conductor gradient voltage should not exceed 26 kV/cm when a DC voltage is applied to a conductor previously operating at AC [7].

7.2.2 Specification for converted HVDC link.

Accurate modelling of the converter at both ends of link is essential to ensure correct operation of the link. The rated DC voltage between the link is calculated using equation (5). The current and power in each leg of the bipole is calculated using equation (6) and (8), these results are display in table (4). Both converter transformers at the end of the link have a rating of 160 MVA, with Z of 0.16 p.u. The rectifier’s firing angle is 15°, and for the inverter it is 146.90835°. The commutation reactances on both transformers at both ends of link are calculated, with rectifier $X_{comp} = 7.799895\Omega$ and for inverter $X_{comp} = 7.1681\Omega$. The overlap angle (μ) is calculated and is 18.09165°.

Table 4: calculated result for converters

Rectifier calculated results			Inverter calculated results		
Pbi-pole (MW)	Vdbi-pole (kV)	Id (kA)	Pbi-pole (MW)	Vdbi-pole (kV)	Id(kA)
1226.3546	845.31411	1.4508	1005.6108	693.1576	1.4508

7.2.3 HVDC transmission network load flow result

The following load flow results were recorded, with eight converters at both end of the links, the total amount of power measured at rectifier side for both links are 1151.9048 MW and 1004.8072 MW on inverter side.

Table 5: HVDC transmission link converted result

Elements	P (MW)	Ptotal (MW)	Q (MVAr)	Qtotal (MVAr)	I (kA)
Pole 1 = Pole 2	609.1934	1218.3864	0	0	1.4272
Single Rectifier/converter	152.2983	1218.3864	67.3152	538.5216	0.2465
Single Inverter/converter	125.5964	1004.7712	72.7636	582.1088	0.6662

7.2.4 HVDC transmission network modelling

The converted link is a bipole, with current control for rectifier set at 1.45076 kA. The DC link is modelled with 12 pulse converter bridges which are made up of two six-pulse bridges. Each of the six pulse converter bridges has four series converters with two in star-to-star transformers, and two in star-to-delta transformers for harmonic cancellation. Figure 4 is a one line diagram of the converted network.

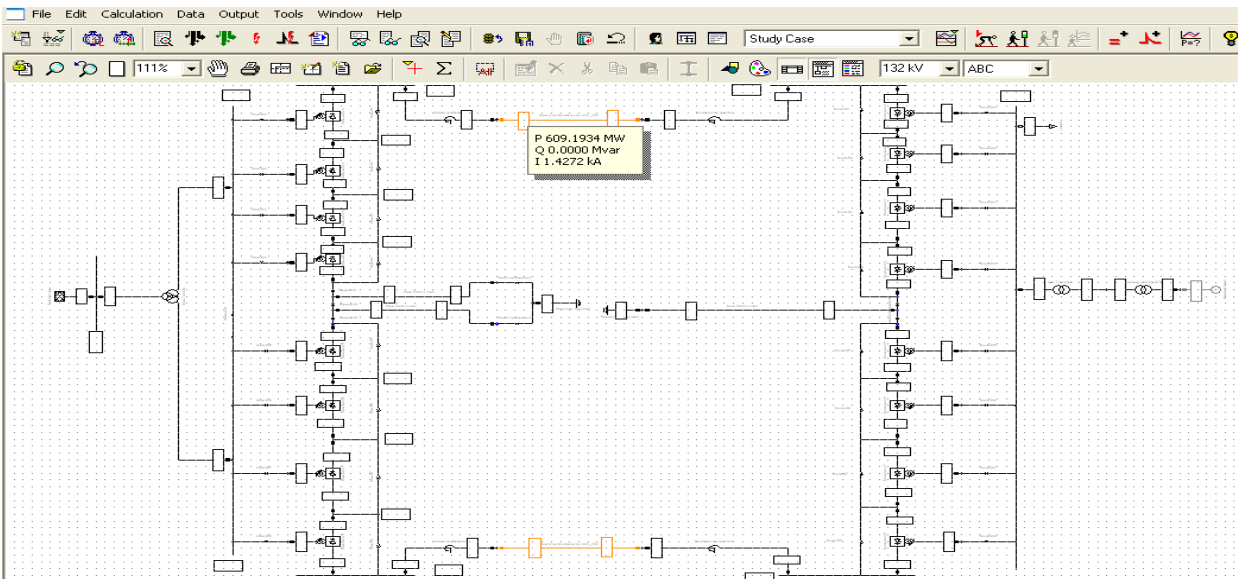


Figure 4: HVDC bipolar transmission system

8. TRANSMISSION CAPACITY

When comparing the transmission capacity for HVAC transmission lines to HVDC, the HVAC depends on the reactive power requirement and security of operation (stability limit for long transmission lines). However, HVDC depends on thermal constraints of the line. The stability of the HVDC system will be influenced by the strength of the AC system at the busbar where the HVDC is connected, known as short circuit to power ratio (SCR). To ensure a proper operation of the DC link, a proper investigation on the effect of the link connected to the AC network was carried out. A preliminary required reactive power by the converter from the AC network was determined from the load flow, and compare with the existing AC network reactive capacity. Final reactive power compensation can only be designed after extensive harmonic studies have been performed. The reactive power was supplied from the AC network at either side of the link. For this network the two generators were modelled using Koeberg power station's rated data and this link was connected to 132 kV, which has a preliminary fault of 17.36 KA, and with SCMVA of 3698.4135MVA. Therefore, the SCR is 3.015778. When taking future load growth in consideration, this could lower the SCR for this network. When the SCR is found to be less than two (< 2), static VAR compensator (SVC) and synchronous condensers (SCOs) may be required on AC systems to compensate for varying reactive power. Existing reactive compensators could be recycled and used as harmonic filters, and can also serve to deliver reactive power when converters are switched on. As DigSilent cannot model a DC tower at moment, for minimum to ground clearance, and clearance to the tower structure, equation (9) and (12) were used to determine adequate clearance between energized conductors and the ground to prevent dangerous contact with the line. The calculated minimum conductor to ground clearance is 8.2659423 m, and 6.60996 m for clearance to the tower structure.

9. CONCLUSIONS

Conversion to HVDC of the existing HVAC transmission lines is an advantage as it allows full utilization of the thermal capacity of the converted line, and enables more power to be transferred through the converted line. The HVAC line proves to have lower power transfer due to the needed reactive power by the line. This paper has demonstrated (when referring to table 3 for HVAC and table 5 for HVDC) that it is technically feasible to achieve more power transfer when converting existing HVAC line to HVDC by using the same conductors, tower bodies and foundations, with changes in insulations. The data presented in this paper may, facilitate preliminary evaluation and stimulate interest for deeper investigations of many actual long transmission lines, which are operating below their surge impedance loading. Furthermore, it is encouraging for power system planners to look at this opportunity when designing transmission lines, such as higher power capacities could be transferred in the existing systems.

10. ACKNOWLEDGEMENT

The authors wish to acknowledge the financial support of Eskom grant and many thanks to Dr Francois Koeslag for doing language checking.

11. REFERENCES

- [1] P. Naidoo, D. Muftic and N. Ijumba: "Investigations into the Upgrading of Existing HVAC Power Transmission Circuits for Higher Power Transfers using HVDC Technology", *Inaugural IEEE PES 2005 Conference and Exposition in Africa Durban, South Africa, 11-15 July 2005*, pp: 139-142.
- [2] M. El-Marsafawy: "On the conversation of an existing practical ac transmission system to dc". *JKAU;Eng.sci*,vol.7.pp41-57,1995.
- [3] P. Kundur P: "Power System Stability and Control", McGraw Hill, New York; 1994.pp:211
- [4] P.S. Maruvada : "Corona Performance of High Voltage Transmission Lines", *Research Studies Press Ltd.* 2000. Baldock, Hertfordshire, England ISBN 0 863 80 254 0.pp:5-6
- [5] J. Smith, W.C. "Stemmet and G. Atkinson-Hope: HVAC/HVDC strategy for solving power delivery shortages to localized area of a national grid". *AC and DC Power Transmission, 2010.ACDC.9th IET International Conference*, 19-21 Oct-2010, pp;1-5
- [6] A. Clerici, L. Paris and P. Danfors : "HVDC conversion of HVAC Line to Provide Substantial Power Upgrading", *IEEE transactions on Power Delivery*, vol.1,1991, pp:324-333
- [7] L.O. Barthold, D.A. Douglas, W.H. Litzenberger and D.A. Woodford: "Upgrading AC transmission to dc for maximum power transfer capacity". *EPRI, Palo Alto,CA, and power system conference,2008. MEPCON2008. 12th international Middle Est.*, March,pp.44-49
- [8] S. Bisnath, A.C. Britten and D. Muftic : "The Planning, Design and Construction of Overhead Power Lines", the Eskom Power Series, Volume1, Crown Publications, 2005

DESIGN AND DEVELOPMENT OF MEDIUM VOLTAGE OPEN RACK HARMONIC FILTERS FOR DISTRIBUTION NETWORKS

A M Meru* and G Atkinson-Hope**

*Department of Electrical & Electronics Engineering, Cape Peninsula University of Technology, P.O. Box 652, Cape Town, 8000, South Africa. E-mail: MeruA@cput.ac.za

** Centre for Power Systems Research, Cape Peninsula University of Technology P.O. Box 1906, Bellville, 7539, South Africa. E-mail: AtkinsonHopeg@cput.ac.za

Abstract. Harmonic filters are the most common means used for harmonic mitigation. Design features of harmonic filters and their use and operation are known theoretically. However, the topic is complex and very little is known on the industrial process of the design stage and what is factored into the design of medium voltage harmonic filters. There is thus a shortage of public domain documentation on this process which is in the know-how of very few specialists. The medium voltage open rack harmonic filter is the most common filter found in industry as well as in mines and is an outdoor installation – it consists of air core reactors, capacitor banks and in some instances resistors. During the design certain assumptions are made. To overcome this limitation, information was gathered by conducting interviews with specialists in the harmonic industry. A network is investigated and two types of harmonic filters are designed to mitigate distortion. Three-Dimensional diagrams were developed to illustrate typically how the final products would appear.

Keywords: Harmonic filter, design.

1. INTRODUCTION

Harmonic filters have been used for mitigation of harmonic currents for a number of decades. Open rack harmonic filters are outdoor installations and are commonly used in the medium voltage industries and mines for industrial installations.

The shortcoming is that knowledge on industrial design of medium voltage open rack type harmonic filters is not well documented and the process is only known to a few specialists. The objective of this work is to make the process more explicit and prove its effectiveness through appropriate case studies.

2. RESEACH STATEMENT

The aim of this paper is to develop an industrial design process for medium voltage open rack harmonic filters which uses actual component values rather than theoretical parameters.

3. INDUSTRIAL DESIGN OF FILTERS

The design of filters for industrial application needs to take into account certain additional factors not traditionally considered. In general, when evaluating if a harmonic filter is required or not, there are two scenarios that need to be considered. The first scenario evaluation is based on the theoretical model of equipment data to be used noted (e.g. cable sizes, transformers, motors). The first process is applied when a new installation is to be implemented and is soft ware based modelling process. The second scenario evaluation is used when a plant already exists and real values of equipment are known and the values used are taken from measurements using power analyzers. Both scenarios however are evaluated

against IEEE 519 standard to make effective mitigation decisions. If limits are not exceeded then new plants is implemented. If existing limits are exceeded the filter will be needed. The process of deciding necessity of designing the filter is shown in Figure 1.

3.1 New Plants

When designing a filter for a new plant, the parameters for the equipment need to be firstly determined. In this method some assumptions are needed. Two common assumptions made are that the loads usually operate at 80% of the full load rating as experience has proven this to be the most successful value. The second assumption is that most loads in the new plant are inductive, such as induction motors, etc. With induction motors operating at 80% full load, the Displacement Power Factor (PF_{DPF}) is usually 0.8 lagging. Both assumptions are factored in when calculating the reactive compensation to be added into the plant.

3.1.1 New plants Data collection

- a) Draw a one line diagram of the plant
- b) Develop a fundamental frequency software model of the plant network based on full load specifications of all equipment to be used. Where applicable use 0.8 PF_{DPF} .
- c) Run at f_1 a load flow and see if the model gives acceptable results, that is, the loads receive their powers, volt drops and PF_{DPF} , are correctly modelled. Improve PF_{DPF} to 0.96 by adding capacitor bank and generate results.
- d) Set the variable loads (e.g. VSDs) to 80% of full load, 0.96 PF_{DPF} . Run at f_1 load flow and record the data require in Table 1.

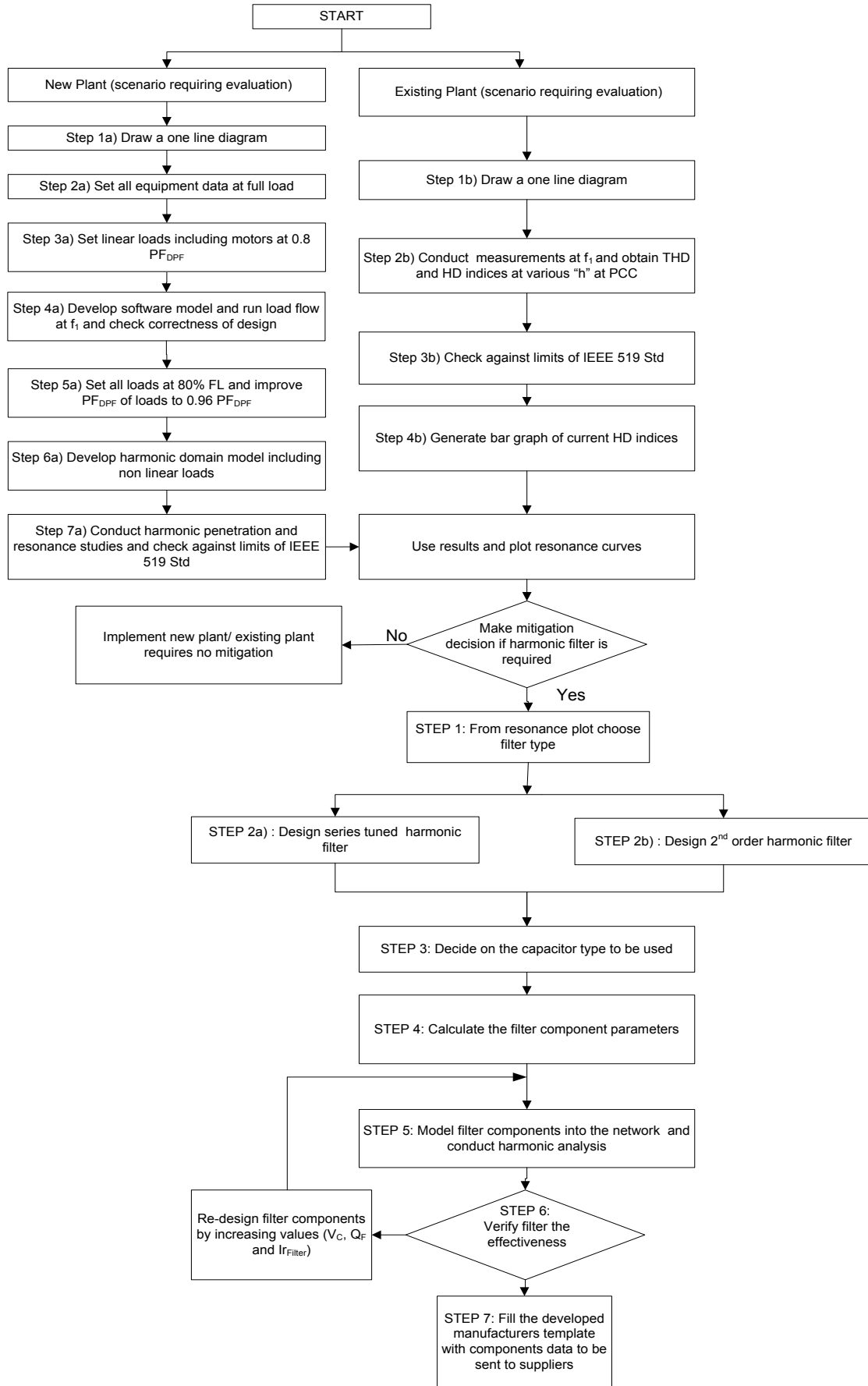


Figure 1: Decision and design of harmonic filter flow chart (A)

- e) Model the VSD(s) as harmonic current sources and develop harmonic domain model and then conduct a harmonic penetration and resonance studies. Check THD and HD indices against limits on the IEEE standard. If exceeded then filter is needed to mitigate the unacceptable distortion level.
- f) If the filter is needed then Table 1 data is needed to commence the filter design. Then obtain data results from the study needed to complete Table 1 for the point in the network where filter is to be added.

Table 1: Plant data at 80% load at 0.96 PF_{DPF} (PF_{DPF} to 0.96 recommended)

Value	Symbol
Voltage	V
Real Power	W
Reactive Power	Var
PF _{DPF}	CosΦ

The above table data is used in the design of both the new plants and existing plants (sect 3.2).

3.2 Existing plants Data collection

A power quality analyser is typically used for measurements such as power, voltage, power factor, current and voltage THD%. A power quality analyser takes readings over a period of time. The analyser has leads that can measure line or phase voltage values depending on connections. For current, each phase is measured by a current transformer (CT). An

3.2.1 Existing plants Data collection

- Check THD and HD readings against IEEE standard limits at PCC and if exceeded, proceed as follows.
- Check loading level for data at point in network where a new filter is to be installed using a power analyser.
- Use the power data, work out PF_{DPF} of 0.8 (cos⁻¹ 36.87°) and adjust S (up or down) to 80% loading assuming linear load.
- Then calculate new P and Q for this 80% loading.
- Complete table 1 for 80% loading and 0.96 PF_{DPF}
- Use this data to start the design process for the industrial filter.

4. FILTER TYPES

The most common harmonic filters used are the series (notch) and 2nd order [1, 2, 3, 4, 5, 6, 7]. The series filter is used to mitigate a specific harmonic while the second order is used to mitigate a wide range of harmonics of the higher order, using:

$$THD_M = \frac{\sqrt{\sum_{h=2} M_h^2}}{M_1} \times 100\% \quad (1)$$

Where M = voltage or current

The series filter consists of a capacitor in series with a reactor while the 2nd order consists of a capacitor in series with a parallel branch having a resistor and reactor.

4.1 Series (notch) filters

The value of the capacitor in the filter is used for power factor correction and the values of the capacitor and reactor for the filter are found in [5]:

The resistance of the reactor is found as:

$$R = \frac{X_C}{Q} \quad (2)$$

Where, Q is defined as the quality factor, which ranges between (30 < Q < 100). With X_L and X_C found at fundamental frequency, the effective rating in VARs of the capacitor is shown as:

$$Q_{filter} = \frac{kV^2}{X_C - X_L} \quad (3)$$

As the impedance of the filter is:

$$Z(h) = R + j \left[hX_L - \frac{X_C}{h} \right] \quad (4)$$

$$h = 6k \pm 1 \quad (5)$$

where $k=1, 2, 3$ up to n

Then the filter current is:

$$I_{f1} = \frac{V_p}{(X_C - X_L)} \quad (6)$$

4.2 Second order filters

In this type of filter, the steps 2,3,4 and 5 found in series filters used except for the effective reactance X_n (characteristic impedance) which is found by equation below:

$$X_n = \sqrt{(X_L \cdot X_C)} \quad (7)$$

Since the resistor is in parallel with the reactor, the value of resistance is found using:

$$R = Q \cdot X_n \quad (8)$$

The Q factor (Q) value of such filters ranges between (0.5 < Q < 5)

In both series and 2nd order harmonic filter capacitor voltage when not considering harmonics is:

$$V_{C1} = I_{f1} X_C V \tag{9}$$

The value is derived from the current found in [8] which merely considers the fundamental current. When harmonics are considered the capacitor voltage becomes:

$$V_C(h) = \sum_{h=5}^{49} I_f(h) \left(\frac{X_c}{h} \right) \tag{10}$$

$$V_C(h) = (I_{f5} \times \frac{X_c}{5} + I_{f7} \times \frac{X_c}{7} + I_{f11} \times \frac{X_c}{11} + I_{f13} \times \frac{X_c}{13}) \tag{11}$$

The actual capacitor used for the harmonic filter has to consider the complex current (I_{rms}):

$$I_{rms} = \sqrt{(I_{f1}^2 + I_{f5}^2 + I_{f7}^2 + I_{f11}^2 + I_{f13}^2)} \tag{12}$$

Thus, the rated capacitor voltage (V_C) for an actual capacitor is the addition of (9) and (10).

$$V_C = [V_C(1) + V_C(h)] \tag{13}$$

The actual value of the capacitor (Q_F) in Vars is:

$$Q_F = \frac{(\sqrt{3V_C})^2}{X_c} \tag{14}$$

Using the Vars, the actual filter current (I_{filter}) of the capacitor will be:

$$I_{filter} = \frac{Q_C}{\sqrt{3V_C}} \tag{15}$$

5. CASE STUDIES

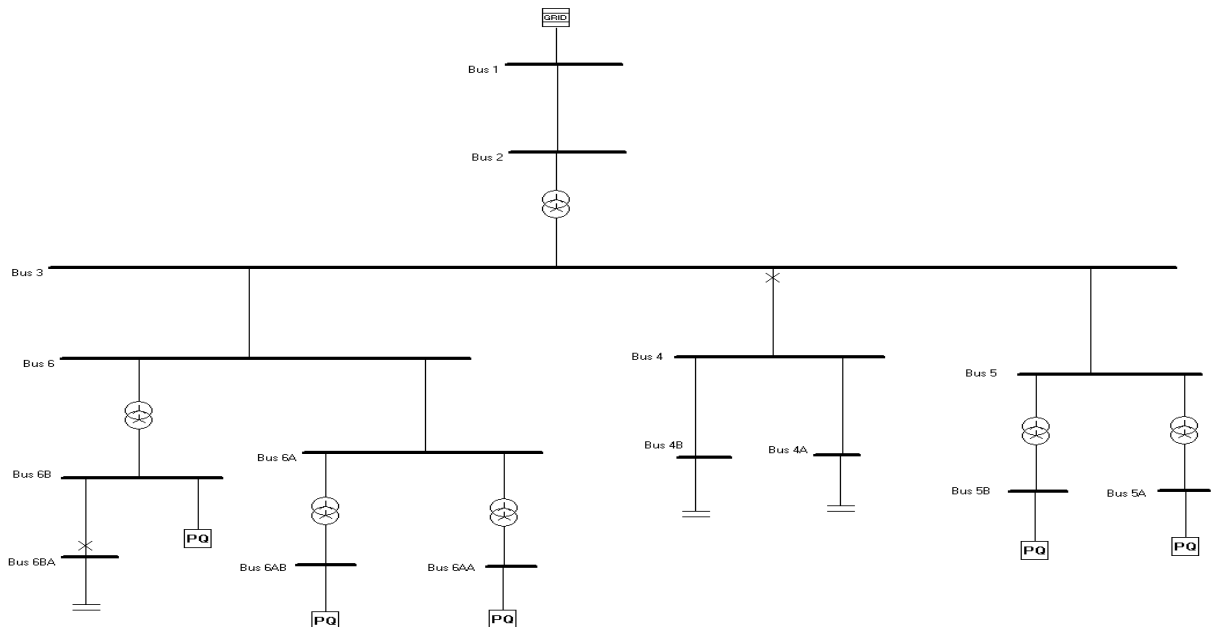


Fig.2: Case study network

Similar formulæ are used in determining the ratings of the actual reactors and resistors. When ordering filter components, the actual values are used as they take harmonic currents into account unlike theoretically designed values. From these equations it is shown that the rated values are higher than theoretical designs.

A reactors manufacturer template has been developed and is shown table 1. The capacitors and resistors will also have similar templates depending on information needed.

Once the actual values are known, the data is put in a template and sent to the manufacturers.

Table 1: Reactor data for manufacturer

Client Name	Alan Meru
Phone	021-4603085
Fax	021-4603705
Email	merua@cput.ac.za
Due Date	Jan - 13
Quote requested by	Alan Meru
System voltage	V
Power frequency (f)	Hz
Tuning Frequency	Hz
Current (1.2 × system I)	A
Reactance (X _L)	Ω
Reactor Rating	H
Q factor of Reactor	
Resistance	Ω
Mounting	Vertical/horizontal
Dimensional limitations	m ²
No of units	

The network used has 3 loads Figure 2 [9]. Two different filters are designed and built for the network for different instances. In the case studies the letters and words mean:

Cap for Capacitor, React for Reactor, Res for Resistor, N for Network, DF for Designed filter, AF for actual Filter. ERACS software [10] was used for the simulations.

5.1 Filter 1

At the main bus (bus 3), the utility supplier can mitigate the harmonics of the whole network by designing a 2nd order harmonic filter using the power factor correction capacitor banks on bus 4. The filter designed (h being 10.8) is a second order harmonic filter due to the harmonics present at that bus-bar. The currents flowing in each of the capacitors initially are seen in Table 2 below.

Table 2: Current in each capacitor banks at buses 4A and 4B

Harmonic	Cap (A)
1	96
5	49.047
7	17.68
11	9.518
13	5.879
17	2.717
19	1.327

When the filter is designed using theoretical values, the currents in each component are shown in Table 3.

Table 3: Designed filter current across Cap, React and Res

Harmonic	C (A)	React (A)	Res (A)
1	97	193	18
5	45.323	82.26	38.082
7	18.047	30.288	19.631
11	7.692	10.778	10.978
13	5.079	6.491	7.813
17	2.473	2.652	4.175
19	1.225	1.221	2.13

Simulations are repeated using actual values as per the manufacturer's template and the currents in each component is calculated and the results are shown in Table 4.

Table 4: Actual filter current across Cap, React and Res

Harmonic	C (A)	React (A)	Res (A)
1	128	255	24
5	35.576	64.569	29.892
7	16.948	28.444	19.435
11	7.41	10.383	10.575
13	4.927	6.927	7.579
17	2.432	2.608	4.105
19	1.21	1.195	2.103

Figure 3 shows the THD_v% and THD_i% values reduced when actual filter component are used.

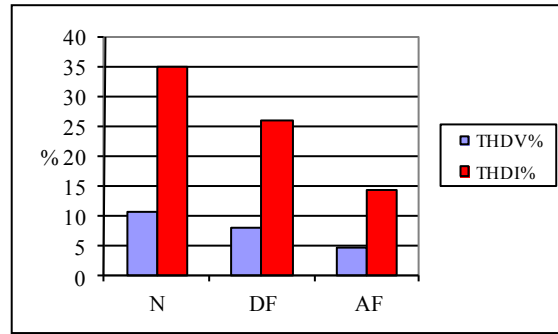


Fig.3: THDV% and THDI% on N, DF and AF

5.2 Filter 2

A second filter was designed for the network for bus 5 where PF correction was done and a 5th harmonic series tuned filter is installed.

Table 5: Harmonic currents across the load at bus 5A

Harmonic	Network current (A)
1	202
5	4.653
7	0.858
11	0.188
13	0.083
17	0.022
19	0.009

Current across the capacitor, designed filter and actual filter are shown below.

Table 6: Rated filter current in C, DF and AF at bus 5A

Harmonic	C (A)	DF (A)	AF (A)
1	139	144	214
5	77.529	83.404	76.953
7	64.385	10.051	9.164
11	4.459	1.482	1.436
13	1.79	0.652	0.638
17	0.426	0.169	0.167
19	0.161	0.065	0.065

Table 6 shows that the fundamental current in the filter increased due to the increase in capacitor rating. The other currents in the filter decreased with the rated filter in network.

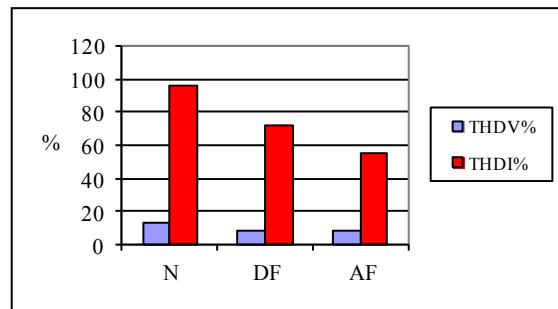


Fig.4: THDV% and THDI% on N, DF and AF installed at bus 5

The $THD_V\%$ and $THD_I\%$ values at the supply bus 3 increased with the filter installed in bus 5 (Figure 4).

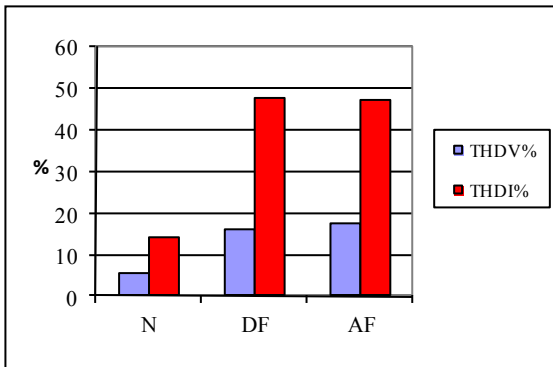


Fig.5: $THD_V\%$ and $THD_I\%$ on N, DF and AF at bus 3

6. CONCLUSION

The process for designing of medium voltage pen rack harmonic filters is a highly specialized field. Design of filters can be done by calculations and component values found. Notwithstanding, theoretical values are not suited for the working world and the process needs to take into consideration actual values which do not neglect the effects of harmonics in the voltages and currents of a filter.

Simulations are needed to verify the importance of actual values as comparative studies can be conducted between theory and world working situations to evaluate the differences. The need for manufacturer templates for capacitors, reactors and resistors are an essential part of the process.

The developed process is shown to be effective. It is anticipated that this work contributes and brings to the public domain the factors that need to be taken into account when applying open rack filters in the working world.

In conclusion, an important contribution of this work is the development of 3-Dimensional drawings (Figures 6 and 7) of two commonly used filters in industry.

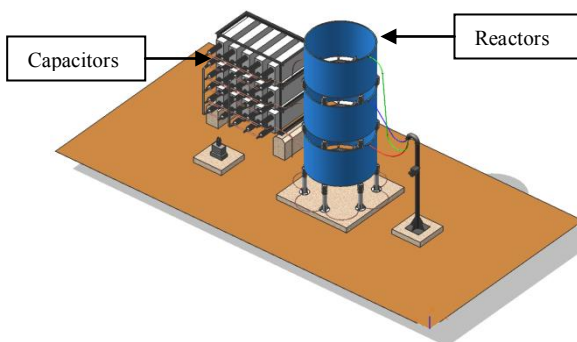


Fig.6: 3-D figure of series (notch) filter

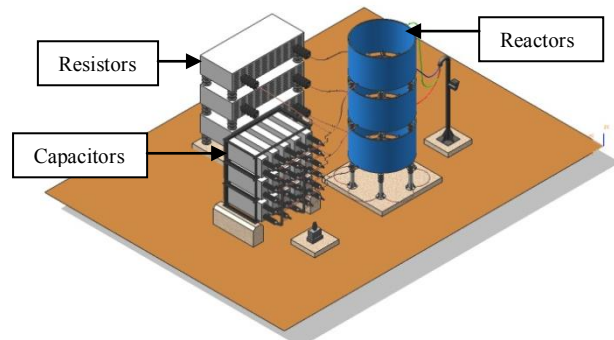


Fig.7: 3-D figure of 2nd order filter

REFERENCES

- [1] E.B. Makram ,E.V. Subramaniam, A.A. Girgis & R. Catoe, "Harmonic Filter Design using Actual Recorded Data". *IEEE Transactions on Industry Applications*, vol. 29, no 6, pp. 1176-1183, November/December 1993.
- [2] S.M. Peeran & C.W.P Cascadden, " Application, Design, and Specification of Harmonic Filters for Variable Frequency Drives". *IEEE Transactions on Industry Applications*, vol. 31, no 4, pp. 841-847, July/August 1995.
- [3] M.F. Mc Granaghan & D. Mueller, "Designing harmonic filters for adjustable speed drives to comply with IEEE-519 Harmonic limits". *IEEE Transactions on Industry Applications*, vol. 35, no 2, pp. 312-318, March/April 1999.
- [4] G. Lemieux, "Power System Harmonic Resonance - A Documented Case", *IEEE Transactions on Industry Applications*, vol. 26, no 3, pp. 483-488, May/June 1990.
- [5] Badrzadeh, B., Smith, K.S. & Wilson, R.C. 2011. Designing Passive Harmonic filters for an aluminium smelting plant, *IEEE Transactions on Industry Applications*, vol. 47(2), March/April.
- [6] Nassif, A.B, Xu, W. & Freitas, W. 2009. An investigation on the selection of filter topologies for passive filter applications. *IEEE Transactions on Power Delivery*, vol 24(3):1710-1718, July
- [7] Pragale Ritchie, Dionise J. Thomas and Shipp, D. David, 2011. *Harmonic Analysis and Multistage Filter Design for a Large Bleach Production Facility*, *IEEE Transactions on Industry Applications*, vol. 47(3), May/June
- [8] IEEE Power Engineering Society. Guide for Application and Specification of Harmonic Filters, New York, pp. 1-53, 24 November 2003.
- [9] E, Thunberg & L, Soder, "Norton Approach to distribution network modelling for harmonic studies". *IEEE Transactions on Power Delivery*, vol. 14, no. 1, January 1999.
- [10] ERA Technology Ltd, ERACS Technical Manual, 8th edition, Chapter 4, pp 4.3, 4.37 & 4.56, April 2005, Ref No 66/4957/9024/008

EFFICIENCY PLAN FOR A DISTRIBUTION NETWORK UNDER CONTINGENCY CONDITIONS

N Ntshamba* and K. Awodele**

University of Cape Town, Department of Electrical Engineering, Rondebosch, South Africa, 7700
 *NTSNWA001@myuct.ac.za, **kehinde.awodele@uct.ac.za

Abstract. This paper focuses on finding an efficiency plan that can be used in a distribution network under contingency conditions to maintain the continuity of supply to the customers at minimum power losses. An algorithm that ensures that there is a maximum number of customers that are receiving electric supply during the contingency condition and the power losses are as minimal as possible was established. The algorithm that is developed was applied to the Malmesbury Farmers1 feeder under contingency conditions. This network is a rural network with radial topology and overhead lines. DigSILENT power factory and ReticMaster softwares were used for the simulation of the network. Different routes of restoring the power supply back to the customers were established by using the algorithm with two different switching methods: truth table switching method and Petri Net switching method. The results obtained from the two simulation tools were compared according to their voltage profiles, source current and power losses. The route with the minimum power losses, voltage and source currents within the limit was chosen to be the route to restore the supply back to the customers. The two switching methods were also compared to see which one is more effective in terms of the time it takes to get to the right interconnection. The Petri Net switching method was chosen to be the most effective switching method to be applied in the algorithm for switching purposes.

Key Words. Distribution networks; contingency conditions; efficiency plan; power losses and continuity of supply

1. INTRODUCTION

The main function of a distribution network is to meet the electricity demand of the customers within operating constraints, economically, reliably and safely [1]. This is achieved by making optimized decisions on distribution network voltage levels, load reliability levels, route of the network, loads and building schedules of the sub-transmission lines and feeders, types and location of switching devices etc [1].

A distribution network is exposed to lightning, short circuit, accidents, etc. When these occur in a distribution network, one or more of the major components of the distribution network may be lost. A loss of one or more major components is called a contingency condition. When a contingency condition occurs in a distribution network, discontinuity of supply occurs to some of the customers and the power losses increase in the network. Most electric utilities do not concentrate on power losses during contingency conditions; they concentrate on keeping the continuity of supply to the customers. Therefore the importance of this paper is to ensure that the power losses are also considered during contingency conditions. Reducing power losses will help the electric utility to generate less electricity and this would help prevent future problems such as global warming that occur due to the gasses that are emitted during the generation of electricity.

Therefore an efficiency plan that will ensure a continuity of supply to the customers at minimum power losses needs to be found. Optimal reconfiguration of the network is done to keep the continuity of supply to the customers at minimum power losses. This is achieved by opening or closing the normally closed and normally opened switches respectively. The opening and closing of switches is done using two switching methods which are truth table switching and the Petri Net switching method. The truth table switching methods helps find all the

possible switching combinations that can be established for the restoration of the supply. From the different combinations, the combination with minimum power losses and with voltage and current within the limits is chosen for the restoration of supply back to the customers. Petri Net switching method works by choosing the normally opened switch that is closer to the place where the component is lost and check if the voltage and current are within the limits. If they are not, the next closer normally opened switch is chosen and so on [1].

Different papers have been published on the reconfiguration of distribution network for power loss reduction using different technique other than Petri Net and truth table switching methods. These techniques are dynamic programming (DP) approach, immune algorithm method, application of automated mapping (AM) and facility management (FM) systems, rapid evaluation method for N-1 contingency condition and others [2-5]

2. MALMESBURY FARMERS 1 FEEDER

Malmesbury Farmers 1 feeder is supplied by 2x20MVA 132/11kV Malmesbury substation. When looking from the resent loading data of Malmesbury Farmer1 feeder which is from August 2011 to March 2012, the feeder peaked on the 15 August 2011 with 99.42A. The overcurrent setting of Malmesbury Farmers1 feeder is 200A, therefore during the peak in August the feeder was not overloaded. There are ±102 customers connected on the feeder and 8 of them are large power user customers and the remaining customers are small power users. The feeder's backbone consists of Rabbit conductor and is 41km in length. There are two shunt capacitors, Kanonkop 450kVar and Weltevrede 300kVar which are used to boost up the voltage and also to decrease power losses. There are also two 200A voltage regulators, Kleinhoop and Weldie installed on the network and

these are used to increase the voltage in the feeder. Weltevrede Shunt Capacitor is currently out of service. Below in fig. 1 is the overview drawing of Malmesbury Farmers1. As can be seen from the feeder overview, if this feeder loses supply, the load connected to it can be transferred to Malmesbury Farmer2 feeder or/and Kalbaskraal Farmers1 or/and Moorreesburg Farmers1 and/or Darling Farmers2 and/or Malmesbury Farmers3 through N/O switches. For this paper the concentration will only be on Kalbaskraal Farmers1, Malmesbury Farmers1 and Moorreesburg Farmers1 [6].

Malmesbury Farmers1 is the feeder that is going to be made to lose a component in order to cause a contingency. The feeder can lose any of the components such as a conductor, circuit breaker, a link, a transformer and a voltage regulator. A loss of a transformer in the feeder would result in customers being without supply and these customers cannot be restored by interconnection since the transformers are on the adjacent laterals. In that case, supply can only be restored back to the customers by replacing or repairing the transformer.

The efficiency plan will be applied for the loss of a circuit breaker and also for the case where a conductor breaks since this is common to overhead lines due to weather conditions and/or human interference. The part of a conductor that will break is shown in fig.1.

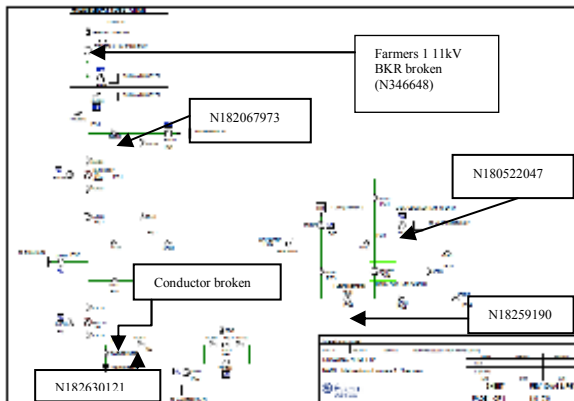


Fig. 1. Malmesbury Farmers1 Overview

2.1 Load Profile

Fig. 2 below shows the load profile of Malmesbury Farmers1 feeder for the month of August when it peaked. It shows how the load changed for this month in 10 minutes intervals.

The peak load of this feeder and the date and time that it occurred are found. From this date and time, the loads of the other feeders that can accept the load of Malmesbury Feeder1 if a contingency occurs on the feeder are also found.

The reason why the peak load is the one that is considered is for a worst case scenario. If the whole load of the feeder can be supplied by other feeders during the case of a contingency in Malmesbury

Farmers1, this would mean that the load of this feeder can be supplied in any other case such as the contingency occurring on the feeder while it is experiencing a normal load. Table 1 below shows the load that was connected to each feeder on the 16th of August, 2012. It also shows the current limits for each feeder and the spare capacity available.

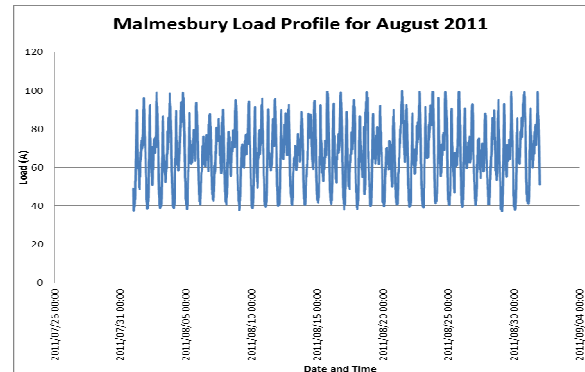


Fig. 2. Loading profile for Malmesbury Farmers1 feeders

Table 1: Loads for Different Feeders on 16/08/2012

	Feeder rating (A)	Load (A)	Available capacity (A)
Malmesbury F1	200	111.35	88.65
Malmesbury F2	280	77.55	202.45
Moorreesburg F1	200	48.43	151.57
Kalbaskraal F1	280	100.19	179.81

Looking at table 1 above, if Malmesbury Farmers1 feeder is lost, the remaining feeders can supply the load of this feeder without any thermal limit problems except Kalbaskraal Farmers1 feeder since the load of Malmesbury Farmers1 is higher than the available capacity of Kalbaskraal Farmers1 feeder. The Fox conductor will experience an overcurrent problem.

3. EFFICIENCY PLAN ALGORITHM

In order to restore the supply back to the customers at minimum power losses, the following steps are followed.

Step 1: Check the load profile of the feeders to be interconnected for the past full year when they were operating under normal condition. It is important to use the recent load data because the load of the feeders increases every year.

Step 2: Select the peak load for Malmesbury Farmers1 feeder. Also find the load for the other feeders for the same date and time that the peak occurred at Malmesbury farmers1.

This sets the worst case scenario of the feeder, therefore if a contingency occurs on the network during Malmesbury Farmers1 peak and the efficiency plan is able to keep the continuity of supply to the customers, the voltage and the current within the limits and keep the power losses at minimum, then the efficiency plan established will be able to work for any case of the loading in Malmesbury Farmers1.

Step 3: After finding the loads for the feeders, adjust the loading for each feeder to the load found.

Step 4: Simulate all the feeders and record the source current, voltage, voltage profile of the feeder and power losses. This shows the operation of the feeders during the normal conditions.

Step 5: Select the N/O points to be interconnected before disconnecting the component to be disconnected.

Step 6: Select the component to be disconnected and disconnect it. After the disconnection of the component, interconnect the interconnection points.

Step 7: Perform simulation and record the source current, voltage, voltage profile of the feeder, load transferred by the feeder and power losses of the reconfigured network for the route established.

Step 8: Check if the voltage and current are within the limits and if one of them is not within the limits, repeat step5, step6 and step7. The voltage limit according to the South African regulations (Gov Limits) has to be within $\pm 10\%$ of the nominal voltage but since the distribution network that is used is an Eskom network, the voltage limits for Eskom distribution network has to be within $\pm 5\%$ of the nominal voltage.

Step 9: Check if there are any other possible interconnections that can be established for the restoration of supply and if there are any, repeat step5 to step8.

Step 10: Compare the power losses, voltage profile of the feeder, the source current and the source voltage for the different routes and choose the route with minimum losses, voltage and current within the limits.

The algorithm is applied on a Malmesbury Farmers1 feeder with contingency conditions. This is applied using a truth table and Petri Net switching methods in order to find the suitable route for the restoration of supply and minimization of power losses.

Fig. 3 illustrates the proposed algorithm of the overall solution

4. COMPUTER SIMULATION

To demonstrate the effectiveness of the proposed algorithm to solve the contingencies, a Malmesbury Farmers1 feeder is chosen for computer simulation. The algorithm is applied while using DigSILENT power factory and ReticMaster as simulation tools. The overview of the feeder is shown in fig.1. The

algorithm is applied using both of the switching

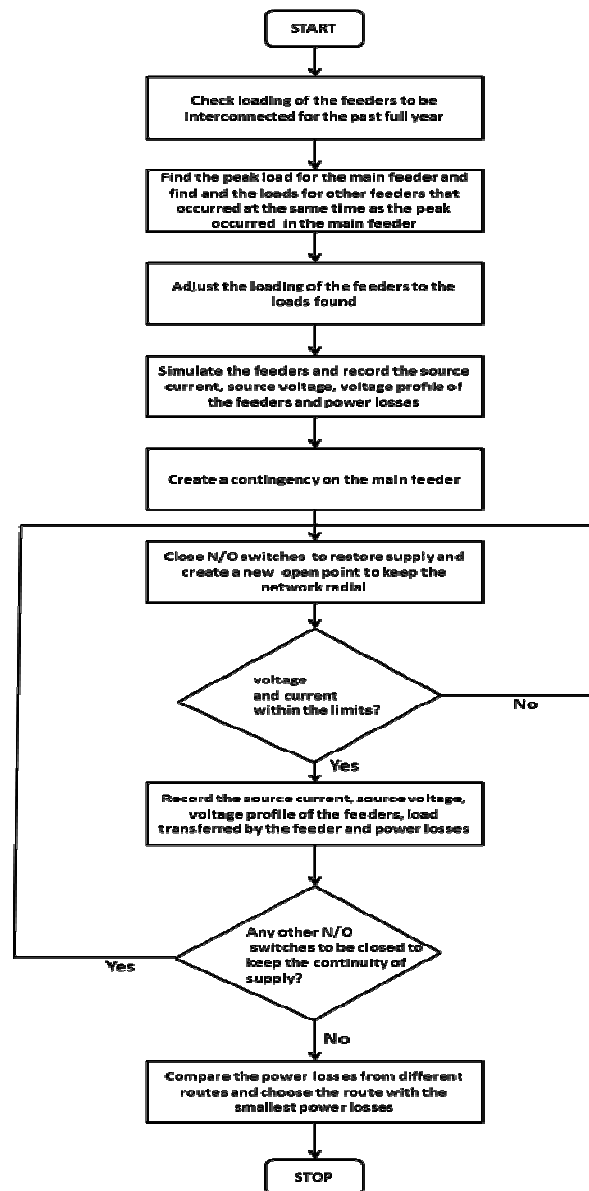


Fig. 3. Overall solution process

methods. Both these switching methods end up getting the same interconnection to be used for the restoration of supply at minimum power losses.

The results that are shown in this paper are for when the feeder loses Farmers 1 11kV BKR and also when the conductor is broken.

4.1 Results obtained before the contingency condition occurred

Table 2: Results obtained from the feeders before the contingency occurred

Feeder Name	ReticMaster		DigSILENT	
	Feeder Load (A)	Power Losses (kW)	Feeder Load (A)	Power Losses (kW)
Malmesbury F1	99.72	252.46	101.75	283.024
Malmesbury F2	79.78	96.292	80.65	104.8814
Moorreesburg F1	52.52	56.718	52.57	60.7248
Kalbskraal F1	102.95	101.649	103.12	107.983

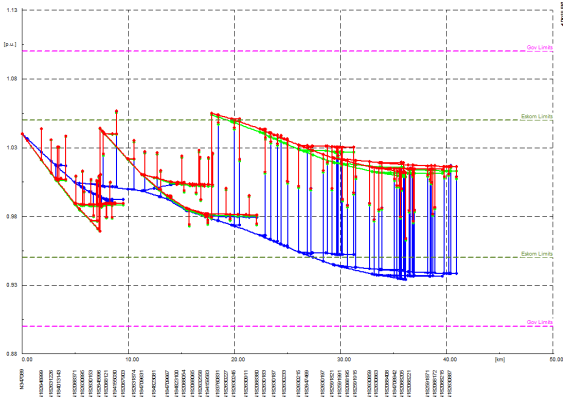


Fig. 4. Malmesbury Farmers 1 voltage profile from DigSILENT

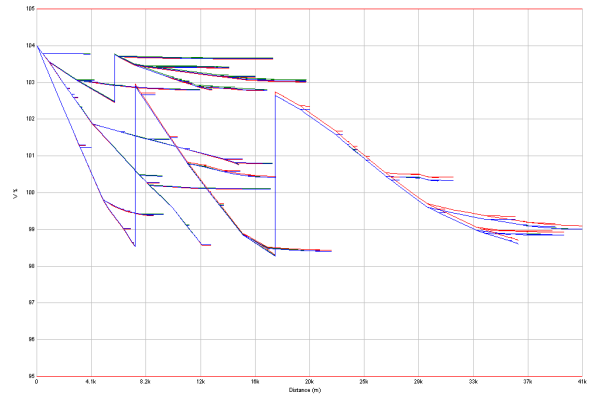


Fig. 7. Malmesbury Farmers 2 voltage profile from ReticMaster

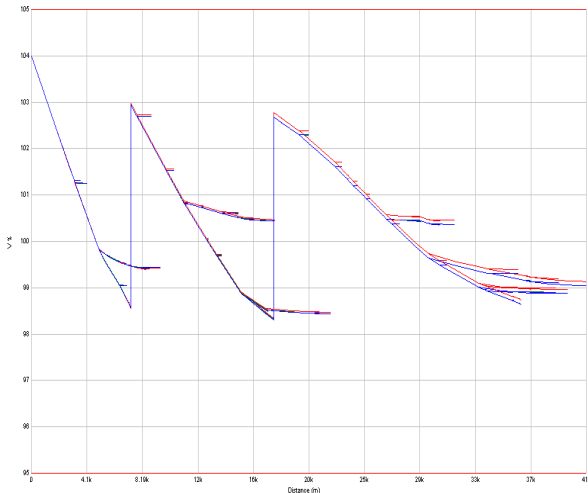


Fig. 5. Malmesbury Farmers 1 voltage profile from ReticMaster

4.2 Results obtained after the loss of Farmers 1 11kV BKR

Table 3: Results obtained from the feeders after the interconnection of feeders

Feeder Name	Switch(es) opened and closed	ReticMaster			DigSILENT		
		Feeder Load (A)	Power Losses (kW)	Load transferred to Malmesbury F1 Feeder (A)	Feeder Load (A)	Power Losses (kW)	Load transferred to Malmesbury F1 Feeder (A)
Malmesbury F2	Opened: N346648 Closed: N182057973	81.3	349.9	00.64	80.64	388.4818	101.77

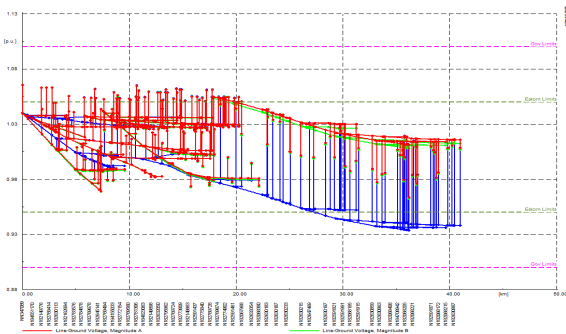


Fig. 6. Malmesbury Farmers 2 voltage profile from DigSILENT

4.3 Results obtained after the loss of a conductor

Table 4: Results obtained from the feeders after the interconnection of feeders

Feeder Name	Switch(es) opened and closed	ReticMaster			DigSILENT		
		Feeder Load (A)	Power Losses (kW)	Load transferred to Malmesbury F1 Feeder (A)	Feeder Load (A)	Power Losses (kW)	Load transferred to Malmesbury F1 Feeder (A)
Mooremeburg F1	Opened: N182690121 Closed: N 180522047	90.3	138.646	46.5	90.33	144.5489	46.81

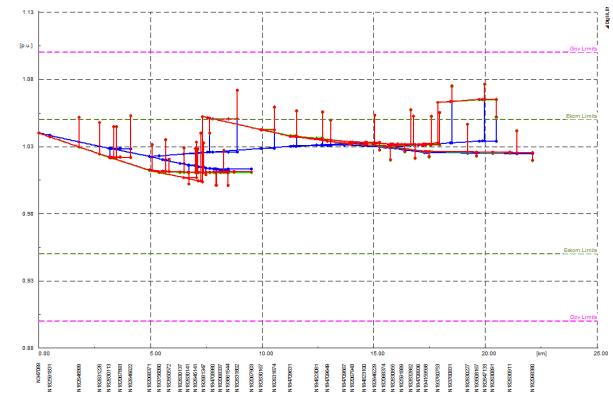


Fig. 8. Malmesbury Farmers 1 voltage profile from DigSILENT

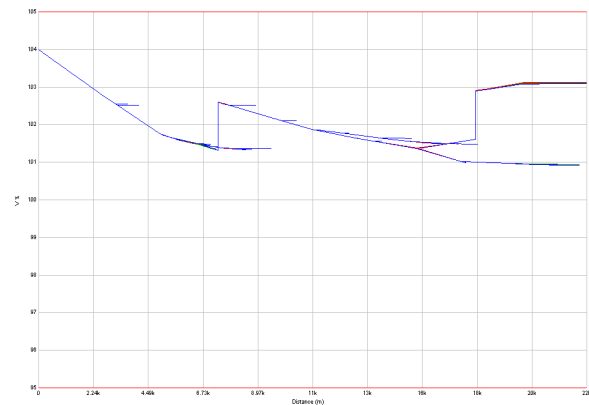


Fig. 9. Malmesbury Farmers 1 voltage profile from ReticMaster

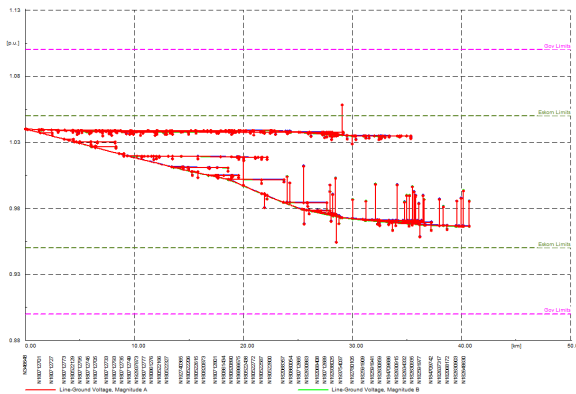


Fig. 10. Moorreesburg Farmers 1 voltage profile from DigSILENT

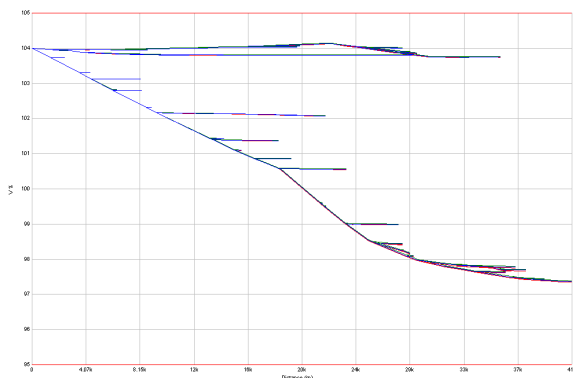


Fig.11. Moorreesburg Farmers1 voltage profile from ReticMaster

5. DISCUSSION OF RESULTS

Comparing the current values from the two simulation tools, the current from DigSILENT power factory is a little bit higher than the current from ReticMaster. This is caused by the AC load flow, unbalanced, 3 phase that is selected when doing a load flow simulation in DigSILENT power factory. The reason for AC load flow, unbalanced, 3 phase to be selected is because of the unequal single phase loads that are present in the feeder. The unequal single phase loads results in the unbalanced loads in the feeder and when the loads are unbalanced, they result in one of phases having a high current and this causes the current to flow in the neutral wire and in turn increases the current in the feeder [7]; whereas in ReticMaster there is no option for simulating an unbalanced load to be selected. The only option that ReticMaster has is an option to make the LPU loads to be balanced since they are three phase loads.

The power losses obtained from DigSILENT power factory are higher than the power losses that are obtained from ReticMaster. This is due to high current that flow in the feeders after a simulation of the feeder in DigSILENT power factory is done.

Looking at the voltage profiles of the feeders from ReticMaster and the voltage profiles of the feeders from DigSILENT power factory, both of the simulation tools give voltage profiles that are within the government voltage limits which state that the voltage in the distribution lines should be within $\pm 10\%$ of the nominal voltage. This is good since all South African distribution networks have to satisfy the

government regulations. The feeders also need to satisfy the Eskom limit which states that the voltage in the distribution lines should be within $\pm 5\%$ of the nominal voltage.

The voltage profiles from ReticMaster are all within the Eskom voltage limits but the voltage profiles from DigSILENT power factory have one or more of the phases being outside the Eskom voltage limits. This is because of unbalanced loads in the phases, as the phase with low load (current) results in high voltage problems and likewise the phase with high load results in low voltage problems. This happens to keep the apparent power constant.

The other reason that caused the voltage profiles from DigSILENT power factory not to be within the limits and the currents and the power losses from the two simulation tools not being the same is because of the different load flow methods that are used by the two simulation tools.

DigSILENT power factory uses AC Newton-Raphson method for load flows performance. Newton-Raphson method is simple, has high iterations and have no mathematic approximations. This method is used to solve non square and nonlinear problems. For this paper, this method is applied in a radial distribution network and radial distribution networks have a high ratio of R/X. A high R/X ratio results to an unreliability in the first order Newton-Raphson and also results in current and power mismatch. This method was mostly established for transmission networks since they have low R/X ratio.

ReticMaster is mainly established for radial electrical networks with voltage level within the range from 132kV to 11kV down to 400V or 230V/120V. This means that this simulation tool is suitable for the feeders in this paper since all of them have a voltage of 11kV and are radial feeders. This simulation tool uses automatic and continuous calculations for load flow calculations [8].

6. CONCLUSION

The objective of this paper was to come up with in efficiency plan for the restoration of supply back to the customers at minimum power losses. The efficiency plan algorithm was used with the application of two switch methods to achieve this objective. The use of truth table switching method helps find the most efficient feeders to be interconnected in case of a contingency. However, this method takes longer to find the suitable interconnection while Petri Net switching method takes shorter time to get to the same results as the truth table method. Therefore, the Petri Net switching method should be used for the algorithm to accomplish minimum power losses, voltage and current within the limits at a shorter time, thus also minimizing the time that the customers are without a supply.

DigSILENT power factory is a good simulation tool for the non-square and nonlinear problems as

discussed in the discussions above. However, it is evident from the results that this tool is not suitable to be used in radial distribution networks since it uses a load flow method that was designed for load flow calculations in transmission networks. It is also evident from the results and discussions that the use of ReticMaster for radial distribution network load flow simulations gives better results than those given by the use of DigSILENT power factory. Therefore in conclusion, ReticMaster should be used for radial distribution network simulations.

functional-overview/. [Accessed 28 September 2012].

ACKNOWLEDGEMENTS

The authors gratefully acknowledge the contributions of Mr M. Van Harte, Mrs N Lukhele and her employees for their support during this research project. and would also like to acknowledge Eskom Western Region for their financial support.

REFERENCES

- [1] T. Yifan: "Power distribution system planning with reliability modeling and optimization," *IEEE Transactions on Power Systems*, Vol. 11, no. 1, pp. 181 – 189, 1996.
- [2] P. M. S. Carvalho, F. J. D. Carvalho and L. A. F. Ferreira: "Dynamic restoration of large-scale distribution network contingencies: crew dispatch assessment," *Proceedings: IEEE Power Tech*, Lausanne, ., pp. 1453 – 1457, 2007.
- [3] L. Fengzhang, W. Chengshan and X. S. G. Jun: "Rapid evaluation method for power supply capability of urban distribution system based on N -1 contingency analysis of main-transformers," *International Journal of Electrical Power and Energy Systems*, Vol. 32, no. 10, p. 1063–1068, 2010.
- [4] L. Chia-Hung, C. Chao-Shun and W. Chia-Jea:n: "Feeder reconfiguration for distribution system contingencies with immune algorithm," *Proceedings: IEEE Power Tech*, Porto, Portugal, September, 2001 .
- [5] T. E. Lee, C. S. Chen, Y. M. Tzeng, M. S. Kang, C. C. Lee, J. S. Wu, T. S. Liu and Y. M. Chen: "The application of am/fm system to distribution contingency load transfer:" *IEEE Transactions on Power Delivery*, , Vol. 10, no. 2, pp. 1126 - 1135, 1995.
- [6] R. Buske and S. Coetzee: "Eskom Distribution - Network Planning," Cape Town, 2012.
- [7] [Online].Available:
<http://www.powersystemsloss.com/2011/07/effects-of-phase-load-balancing-to.html>. [Accessed 11 October 2012].
- [8] [Online].Available:
<http://reticmaster.com/products/reticmaster/reticmaster->

GRID PARAMETER ESTIMATION AT THE POINT OF COMMON COUPLING: IMPLEMENTATION AND EVALUATION OF A METHOD IN LITERATURE

M. I. Naudé *, W.A. Cronjé * and M.V. Shuma-Iwisi *

* School of Electrical and Information Engineering, University of the Witwatersrand, Private Bag 3, 2050, Johannesburg, South Africa.
E-mail: Marlize.Naude@ieee.org, Willie.Cronje@wits.ac.za, Mercy.Shuma-Iwisi@wits.ac.za

Abstract: A complete model of an unknown circuit may be useful in many instances. A number of methods to find the parameters (source voltage, source resistance and source inductance) of an unknown circuit using only measurements made at the point of common coupling, are found in literature. One such method was studied and implemented. The success of the method is tested by analytical, simulated and laboratory experiments. It was found that the method works well for cases with little or no noise, but not when noise is present in the measurements. Experiments are deemed successful if the average error of the three parameters is less than 10%.

Key words: Grid parameters, point of common coupling, Gauss-Newton least squares, source voltage, resistance, inductance

1. INTRODUCTION

In order to do corrective actions, such as power factor correction, harmonic filtering, or to calculate short circuit currents, it is useful to have a model of the entire circuit, including the source side that is usually uncontrollable and unknown [1–6]. A model of such a circuit is shown in Figure 1. It shows the *source* side to the left of the point of common coupling (PCC), and the *load* side to the right. In [1–5], the authors have used a similar model to Figure 1, with the exception being a capacitor in parallel with the load in some cases [2,3].

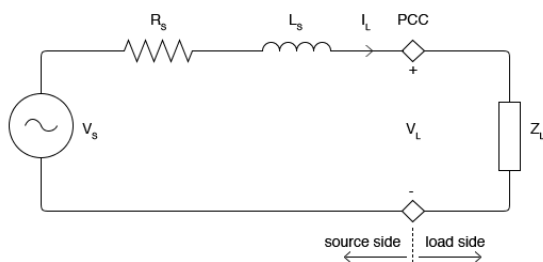


Figure 1: General circuit model showing source side to the left of the point of common coupling

The circuit model in Figure 1 shows a source voltage V_S , a source resistance R_S , a source inductance L_S , and a load impedance Z_L . None of these parameters are known. The source side parameters are, however, of more interest than the load in this case.

In order to find values for the source side parameters, measurements may be made at the PCC only, since both the source and the load sides are accessible only from the PCC (both the source and load sides are treated as black boxes). The measurements that are made are load current I_L and load voltage V_L , as seen in Figure 1. These

measurements are either root mean square (RMS) values with phase information, or waveforms, depending on the grid parameter estimation method employed.

A literature review was done in order to find methods to estimate grid parameters. One method was chosen to implement. This method was tested analytically, in simulation, and in laboratory experiments.

2. LITERATURE REVIEW

Various methods were reviewed [1–5], and based on certain criteria, one method was chosen to implement. Methods that were developed specifically for photo-voltaic (PV) inverters were deemed unsuitable since PV inverters generally have current controllers which are then essential to the grid parameter estimation method [2, 3]. Methods that do not estimate the source voltage V_S in addition to the source resistance and inductance were deemed unsuitable, since the source voltage cannot always be assumed to be known.

The method that was chosen is that which is described by Arefifar and Xu [1]. This method uses equipment that is readily available in the University’s Electrical Laboratory, and seemed likely to give good results.

2.1 Grid parameter estimation method as described by Arefifar and Xu

The paper entitled *Online Tracking of Power System Impedance Parameters and Field Experiences* [1] describes a grid parameter estimation method that uses current and voltage measurements in the form of RMS values and the phase difference between them. At least three measurements should be taken in order to estimate the three grid parameters (source voltage, resistance and inductance). It is assumed that the load side fluctuates, but

that the source side is constant. The grid parameters may change with time, but the assumption is made that they do not change during the course of an experiment. However, the load does change during the course of an experiment, and is in fact necessary for the success of the method, since the method relies on measurements of the same source being made with different loads connected in order to have enough equations to solve for all the unknowns (see later).

Equation 1 (below) describes the circuit illustrated in Figure 1.

$$V_S \angle \vartheta = (R_S + jX_S)I_L \angle 0 + V_L \angle \phi \quad (1)$$

Where:

V_S = source voltage, an RMS value with magnitude V_S and phase angle ϑ ,
 R_S = source resistance,
 $X_S = \omega L_S$, source reactance,
 L_S = source inductance,
 $j = \sqrt{-1}$,
 $\omega = 2\pi f$,
 f = frequency of the source, V_S ,
 I_L = load current, an RMS value with magnitude I_L and phase angle 0 ,
 V_L = load voltage, an RMS value, with magnitude $|V_L|$ and phase angle ϕ .

If three measurements are taken at three different instants in time (t_1 , t_2 and t_3), Equation set 2 may be written.

$$\begin{aligned} V_S \angle \vartheta_1 &= (R_S + jX_S)I_{L1} \angle 0 + V_{L1} \angle \phi_1, \\ V_S \angle \vartheta_2 &= (R_S + jX_S)I_{L2} \angle 0 + V_{L2} \angle \phi_2, \\ V_S \angle \vartheta_3 &= (R_S + jX_S)I_{L3} \angle 0 + V_{L3} \angle \phi_3. \end{aligned} \quad (2)$$

Writing Equation set 2 in real and imaginary parts, then taking the magnitude and squaring each side gives Equation set 3, where the subscript x denotes the real part, and the subscript y denotes the imaginary part of the load voltage. Equation set 3 contains three unknowns and three Equations, and can thus be solved. (Unlike Equation 1, which contains more unknowns than equations, even when written as two equations in real and imaginary form.)

$$\begin{aligned} V_S^2 &= (R_S I_{L1} + V_{Lx1})^2 + (X_S I_{L1} + V_{Ly1})^2, \\ V_S^2 &= (R_S I_{L2} + V_{Lx2})^2 + (X_S I_{L2} + V_{Ly2})^2, \\ V_S^2 &= (R_S I_{L3} + V_{Lx3})^2 + (X_S I_{L3} + V_{Ly3})^2. \end{aligned} \quad (3)$$

From these three sets of measurements at times t_1 , t_2 and t_3 , initial values (known as initial guesses) for the three parameters V_S , R_S and X_S may be calculated. The Gauss-Newton least squares estimation method is then used to estimate the three parameters more accurately

using more sets of measurements (if available). The Gauss-Newton method is an iterative method to solve non-linear least squares problems [7]. The unknown parameters are expressed as a vector. Since there will be noise present in the system and/or measurements, an error or residual term is added. The task is then to find the vector of parameters such that the sum of residuals squared is minimised. An iterative process is followed to minimise the sum of residuals squared until the change in parameters becomes negligible. When the change becomes negligible, it implies that the best possible solution has been found for the given set of measurements.

3. IMPLEMENTATION OF GRID PARAMETER ESTIMATION METHOD AS DESCRIBED BY AREFIFAR AND XU

The method described above was studied and implemented. The exact methodology used by Arefifar and Xu was not included in their published work, so many of the details of implementation had to be rediscovered by the author. Analytical experiments, simulated experiments and laboratory experiments were set up to test the success of the method after implementation. Eight different combinations of known grid parameters were used to test the method using each of the three types of experiments (analytical, simulation, laboratory), with and without added noise (for the analytical and simulated experiments), resulting in 40 experiments in total. Noise is added to calculated or simulated values in order to mimic noise that would be present in practical applications, thus testing the method's ability to handle noisy measurements. $s\%$ noise is added to a calculated or simulated value by multiplying $s\%$ of the actual calculated or simulated value (*actual*) with a random number between -1 and 1 (*rand*). In other words, a value between $-s.rand.actual/100$ and $+s.rand.actual/100$ is added to each calculated or simulated value. Noise is added in this manner to both current and voltage values.

3.1 Analytical Experiments

For each experiment, a known source voltage, resistance and inductance is chosen. Twelve different loads are chosen to provide the necessary variation on the load side, then the complex load voltage and current for each load is calculated using MATLAB. The twelve loads have either an inductive or a capacitive element in series with a resistive element. The calculated load current's phase is shifted to be at 0 radians, and then the calculated load voltage's phase is shifted with the same phase angle. An example of one of these experiments is shown in Figure 2. The initial guess is at iteration 0 on the x-axis, and two successive iterations are calculated before the change becomes negligible. The three calculated parameters are normalised using their known values on the y-axis. Some of the results of the analytical experiments using the grid parameter estimation method described by Arefifar and Xu, with and without added noise are shown in Table 1. An experiment is deemed *successful* if the *average* error is

less than or equal to 10 %. An example of one of these experiments with added noise is shown in Figure 3.

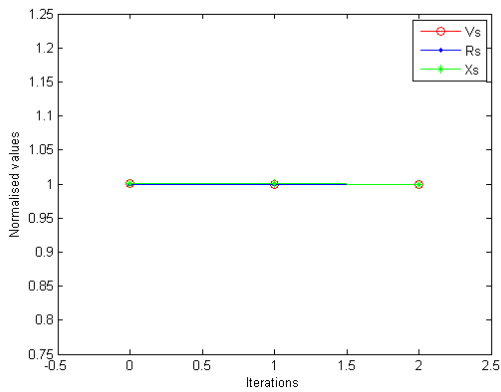


Figure 2: Analytic experiment using the grid parameter estimation method as described by Arefifar and Xu

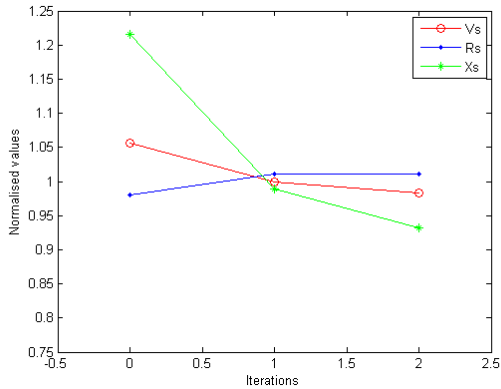


Figure 3: Analytic experiment using the grid parameter estimation method as described by Arefifar and Xu, with 1% noise added

In Table 1 it may be seen that only 1% noise was added to the calculated values. If 2% or more noise is added, more than half of the experiments are unsuccessful, in other words, their average errors are more than 10%. This shows that the method would be very sensitive to noise on the measured RMS and phase angle values. If there is no noise present (such as in Figure 2), then the method works extremely well. The initial guesses of parameter values are almost exactly correct, and the two successive iterations refine the parameter values to within 0.01% average error on all three parameters. However, when only 1% noise is added to the calculated values, the average errors range from 2% to 8%. Figure 3 shows initial guesses at iteration 0, and two further iterations. The first iteration shows all three parameters converging to their correct values. The second iteration however shows two of the three parameters diverging from their correct values again, and the third parameter showing no change. This suggests that the method does not handle noise very well. It is expected that laboratory experiments could be unsuccessful due to the method's sensitivity to noise.

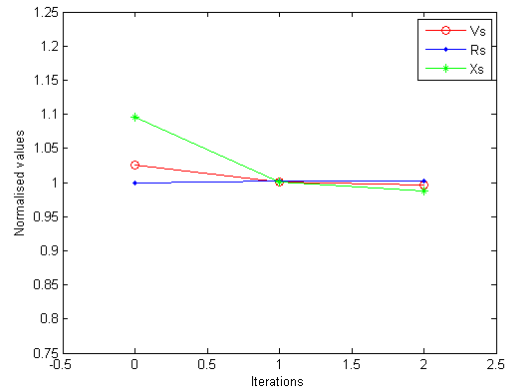


Figure 4: Simulated experiment using the grid parameter estimation method as described by Arefifar and Xu

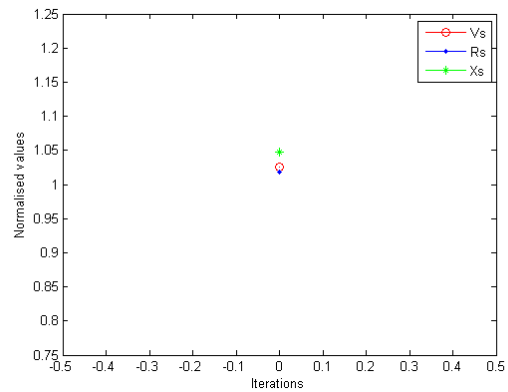


Figure 5: Simulated experiment using the grid parameter estimation method as described by Arefifar and Xu, with 20% noise added

3.2 Simulated Experiments

For each experiment, the same known source voltages, resistances and inductances are chosen that were used for the analytical experiments. Once again, twelve different loads are used to provide the necessary variation on the load side. These circuits were built and simulated in the circuit simulation package OrCAD. The results of the simulations are sampled waveforms that are read using MATLAB, and used to calculate RMS values of the load voltages and currents as well as the phase difference. Noise is added to the waveforms in order to test the method's ability to handle noisy measurements. An example of one of these experiments is shown in Figure 4. Another example of one of these experiments, with noise added, is shown in Figure 5. Figure 5 shows that only the initial guesses of the three parameters could be made. After the initial guesses, no further improvement in the sum of residuals squared could be made. These initial guesses are close to correct, but cannot be improved upon by the Gauss-Newton method. Thus in effect, the result is simply the solution of Equation set 3. Some of the results of the simulated experiments using the grid parameter estimation

Table 1: Some analytic experiments using the grid parameter estimation method as described by Arefifar and Xu

Added noise (%)	Actual parameters			Calculated parameters			Error (%)				Successful
	V_S (V)	R_S (Ω)	X_S ($j\Omega$)	V_S (V)	R_S (Ω)	X_S ($j\Omega$)	V_S	R_S	X_S	average	
0	50.00	29.70	30.47	50.00	29.70	30.47	0.00	0.00	0.01	0.01	Yes
0	50.00	30.11	38.76	50.00	30.11	38.76	0.00	0.01	0.01	0.01	Yes
0	200.00	29.70	30.47	200.00	29.70	30.47	0.00	0.00	0.00	0.00	Yes
0	200.00	30.11	38.76	200.00	30.11	38.76	0.00	0.01	0.00	0.00	Yes
1	50.00	29.70	30.47	49.31	28.99	29.25	1.37	2.40	3.99	2.59	Yes
1	50.00	30.11	38.76	47.14	27.08	35.42	5.73	10.08	8.62	8.14	Yes
1	200.00	29.70	30.47	198.25	28.08	31.03	0.88	5.45	1.84	2.72	Yes
1	200.00	30.11	38.76	202.41	31.76	39.25	1.20	5.47	1.25	2.64	Yes

Table 2: Some simulated experiments using the grid parameter estimation method as described by Arefifar and Xu

Added noise (%)	Actual parameters			Calculated parameters			Error (%)				Successful
	V_S (V)	R_S (Ω)	X_S ($j\Omega$)	V_S (V)	R_S (Ω)	X_S ($j\Omega$)	V_S	R_S	X_S	average	
0	50.00	29.70	30.47	49.83	29.75	30.09	0.35	0.15	1.25	0.58	Yes
0	50.00	30.11	38.76	49.89	30.12	38.53	0.23	0.02	0.61	0.29	Yes
0	200.00	29.70	30.47	199.31	29.75	30.09	0.35	0.15	1.25	0.58	Yes
0	200.00	30.11	38.76	199.55	30.12	38.53	0.23	0.02	0.61	0.29	Yes
20	50.00	29.70	30.47	50.46	30.20	30.48	0.92	1.68	0.02	0.87	Yes
20	50.00	30.11	38.76	49.86	29.59	38.22	0.29	1.74	1.39	1.14	Yes
20	200.00	29.70	30.47	199.82	28.40	30.68	0.09	4.39	0.68	1.72	Yes
20	200.00	30.11	38.76	204.71	30.90	40.40	2.35	2.62	4.21	3.06	Yes

method described by Arefifar and Xu, with and without added noise, are shown in Table 2.

In Table 2 it may be seen that when 20% noise was added, all the experiments were still successful. In this case, the noise was added to the sampled waveform values, and then only the RMS values and phase differences were calculated. If 25% or more noise is added, some of the experiments are unsuccessful, in other words average error > 10%. However, this improvement in noise handling capability compared to the analytical experiments means that the laboratory experiments may not be unsuccessful as often as was initially expected, since the noise on the real measurements will be on the sampled waveform values, and not on the final RMS values (as was the case for the analytical experiments). This means that the RMS values over a few waveforms could still be close to accurate.

This theory was tested by first calculating the RMS values of the simulated, sampled waveforms, and then adding noise to the RMS values. If this is done, only 1% noise can be added, if 2% or more noise is added, some of the circuits are unsuccessful.

3.3 Laboratory Experiments

The grid parameter values that were used for the analytical and simulated experiments were chosen based on the available equipment in the laboratory. The source resistance and source inductance were measured using different measurement instruments and an average value for each was calculated. The source voltage is also

measured during each experiment and recorded. The source voltage is measured at the output of a variac which is connected to the utility. The variac ensures at least some degree of isolation from the possible variations of the utility's grid parameters. However, it is still possible, and very likely, that small changes in the grid parameters will occur. These small changes will invalidate the assumption that the source side parameters are constant. However, assuming that these changes are small enough, it will not affect results significantly. A schematic diagram of the experimental set up is shown in Figure 6.

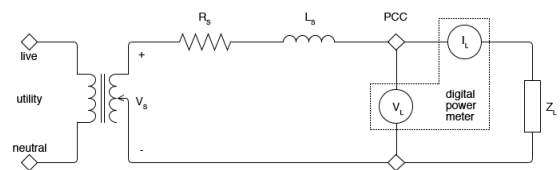


Figure 6: Experimental set up for laboratory experiment

Since the same grid parameter values were used for the analytical, simulation and laboratory experiments, they are directly comparable. A Yokogawa WT1600 digital power meter was used to record RMS values of the load voltage and current as well as phase difference. An example of one of these experiments is shown in Figure 7. Some of the results of the laboratory experiments using the grid parameter estimation method described by Arefifar and Xu are shown in Table 3.

Once again, Figure 7 shows that only initial guesses of

Table 3: Some laboratory experiments using the grid parameter estimation method as described by Arefifar and Xu

Actual parameters			Calculated parameters			Error (%)				Successful
V_S (V)	R_S (Ω)	X_S ($j\Omega$)	V_S (V)	R_S (Ω)	X_S ($j\Omega$)	V_S	R_S	X_S	average	
50.50	29.70	30.47	49.03	26.63	31.42	2.91	10.35	3.12	5.46	Yes
49.92	30.11	38.76	50.64	30.66	41.06	1.44	1.83	5.92	3.06	Yes
200.10	29.70	30.47	196.77	26.28	32.48	1.66	11.52	6.60	6.60	Yes
199.90	30.11	38.76	221.33	49.86	36.28	10.72	65.58	6.42	27.57	No

Table 4: Some laboratory experiments using the grid parameter estimation method as described by Arefifar and Xu, with inductive loads only

Actual parameters			Calculated parameters			Error (%)				Successful
V_S (V)	R_S (Ω)	X_S ($j\Omega$)	V_S (V)	R_S (Ω)	X_S ($j\Omega$)	V_S	R_S	X_S	average	
50.50	29.70	30.47	51.90	29.88	34.98	2.78	0.62	14.79	6.06	Yes
49.92	30.11	38.76	49.87	27.48	41.90	0.10	8.73	8.10	5.64	Yes
200.10	29.70	30.47	206.30	27.53	36.43	3.10	7.31	19.56	9.99	Yes
199.90	30.11	38.76	159.30	12.12	31.03	20.31	59.75	19.96	33.34	No

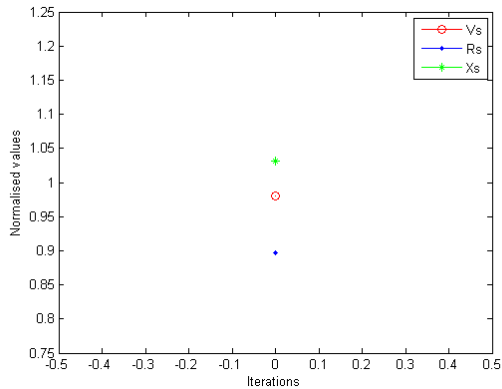


Figure 7: Laboratory experiment using the grid parameter estimation method as described by Arefifar and Xu

the three parameters could be made. The loads that were used for analytical, simulated and laboratory experiments were a mixture of inductive and capacitive loads. If only inductive or only capacitive loads are used, the results are somewhat different. Figure 8 shows the same experiment as Figure 7, but using only inductive loads. It may be seen that roughly the same initial guesses are made in Figure 7 using capacitive and inductive loads, and in Figure 8 using inductive loads only, but that two further iterations were possible when using inductive loads only that were not possible when using inductive as well as capacitive loads. However, these two iterations are of little value, since the parameter values do not converge closer to their correct values. In fact, after the two iterations, the parameters' average error is greater than before (6.06% average error when using inductive loads only, compared to 5.46% average error when using inductive as well as capacitive loads). One possible reason for this may be that the measured values are more closely correlated, and therefore give more possible iterations, but since there are fewer measured values (six loads compared to twelve),

the measured values are less accurate. Table 4 shows the results of the same four experiments that were performed as in Table 3, but with inductive loads only. It may be seen that the average errors of all experiments increased when only inductive loads were used.

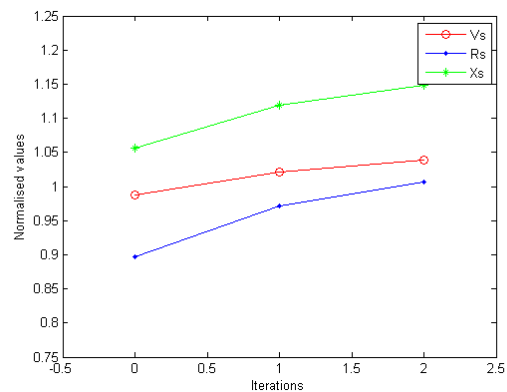


Figure 8: Laboratory experiment using the grid parameter estimation method as described by Arefifar and Xu, with inductive loads only

For the sake of completeness, the same experiments were performed using only capacitive loads as well. Figure 9 shows the same experiment as Figure 7 and Figure 8 but using only capacitive loads. Figure 9 shows that better initial guesses are made when only capacitive loads are used, compared to using inductive as well as capacitive loads or using inductive loads only. After the initial guesses however, all three parameters diverge away from their correct values. Table 5 shows the results of the same four experiments that were performed as in Table 3, but with capacitive loads only. Although there is a significant improvement in the average error for each experiment, it is due to better initial guesses in the case of using capacitive loads only compared to using inductive loads only.

Table 5: Some laboratory experiments using the grid parameter estimation method as described by Arefifar and Xu, with capacitive loads only

Actual parameters			Calculated parameters			Error (%)				Successful
V_S (V)	R_S (Ω)	X_S ($j\Omega$)	V_S (V)	R_S (Ω)	X_S ($j\Omega$)	V_S	R_S	X_S	average	
50.50	29.70	30.47	49.41	27.98	32.24	2.15	5.78	5.80	4.57	Yes
49.92	30.11	38.76	50.55	28.90	42.06	1.27	4.03	8.50	4.60	Yes
200.10	29.70	30.47	201.81	28.99	32.81	0.86	2.39	7.68	3.64	Yes
199.90	30.11	38.76	209.20	31.20	44.61	4.65	3.62	15.08	7.78	Yes

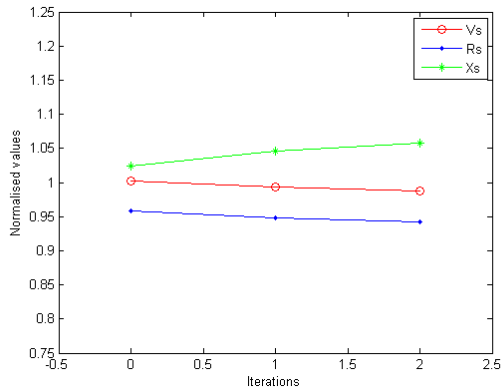


Figure 9: Laboratory experiment using the grid parameter estimation method as described by Arefifar and Xu, with capacitive loads only

4. CONCLUSION

The grid parameter estimation method described by Arefifar and Xu is an extremely good method to use in cases of very low noise. The initial guesses are improved upon and the end result is that all three parameters (V_S , R_S and X_S) converge to their correct values. However, when noise is present in the form of measurement noise or process noise, then the method is not as successful. The initial guesses are less accurate, and the parameters diverge further away from their correct values. Even so, if a first approximation to the grid parameters are sought, this method will give acceptable results.

Another method that shows a lot of potential is the method described by Fusco, Losi and Russo in their paper entitled *Constrained least squares methods for parameter tracking of power system steady-state equivalent circuits* [4]. This method makes use of a Kalman filter to filter out the noise on the sampled waveforms before any further calculations are done. The Kalman filter is designed in such a way that the sampled waveforms are separated into harmonics using a Fourier series. This means that the method is likely to be suitable for non-linear as well as linear loads. The study and implementation of this method is the next step in this research.

REFERENCES

- [1] S. A. Arefifar and W. Xu, "Online tracking of power system impedance parameters and field experiences," *Power Delivery, IEEE Transactions on*, vol. 24, no. 4, pp. 1781 – 1788, 2009.
- [2] L. Asiminoaei, R. Teodorescu, F. Blaabjerg, and U. Borup, "A digital controlled PV-inverter with grid impedance estimation for ENS detection," *Power Electronics, IEEE Transactions on*, vol. 20, no. 6, pp. 1480 – 1490, November 2005.
- [3] L. Asiminoaei, R. Teodorescu, F. Blaabjerg, and U. Borup, "A new method of on-line grid impedance estimation for PV inverter," in *Applied Power Electronics Conference and Exposition, Nineteenth Annual IEEE (APEC)*, vol. 3, 2004, pp. 1527 – 1533.
- [4] G. Fusco, A. Losi, and M. Russo, "Constrained least squares methods for parameter tracking of power system steady-state equivalent circuits," *Power Delivery, IEEE Transactions on*, vol. 15, no. 3, pp. 1073 – 1080, July 2000.
- [5] T. D. Thanh, S. Schostan, K.-D. Dettmann, and D. Schulz, "Non sinusoidal power caused by measurements of grid impedances at unbalanced grid voltages," in *Non sinusoidal Currents and Compensation, (ISNCC), International School on*, June 2008, pp. 1 – 7.
- [6] A. Robert, T. Deflandre, E. Gunther, R. Bergeron, A. Emanuel, A. Ferrante, G. Finlay, R. Gretsche, A. Guarini, J. Gutierrez Iglesias, D. Hartmann, M. Lahtinen, R. Marshall, K. Oonishi, C. Pincella, S. Poulsen, P. Ribeiro, M. Samotyj, K. Sand, J. Smid, P. Wright, and Y. Zhelesko, "Guide for assessing the network harmonic impedance," in *Electricity Distribution. Part 1: Contributions. CIRED. 14th International Conference and Exhibition on (IEE Conf. Publ. No. 438)*, vol. 1, June 1997, pp. 301 – 310.
- [7] Å. Björck, *Numerical methods for least squares problems*. Philadelphia: SIAM, 1996.

IMPACT OF A NETWORK'S COMPONENT FAILURE MODEL ON THE PERCEPTION OF ITS RELIABILITY

M Edimu*, R Herman* and C T Gaunt*

* University of Cape Town, Department Electrical Engineering, Cape Town, 7701

Abstract. The planning procedures of a power network rely on the perception of its reliability. Network components are however affected by a range of factors. The models used to capture vulnerability of network components to failure could be critical to the evaluation of its reliability and the decisions made thereafter. This paper investigates the effect of using either deterministic or probabilistic component failure models in a planning reliability study. Unlike most published work that only considers the magnitude of the reliability indices, this paper also analyzes the impact on the probability distributions of the computed indices.

Key Words. Network planning, Reliability analysis, Risk modelling, Probability density functions

1. INTRODUCTION

Reliability is a key aspect of network planning. Planners aim at achieving optimum levels of reliability with minimum investment in the network. The perceived level of reliability that a given investment scenario yields is thus significant for subsequent planning decisions. Several factors influencing reliability as a whole have been identified in the literature. The network's configuration, loading and component outages are some of the generally known factors [1]-[3]. While the configuration may be stagnant for a given reliability study, a network's loading and component outages are quite variable. A stochastic external environment, attributed mainly to weather elements, is the main cause of variability in network component failure parameters [4]. Component's failure models applied are thus quite important in the assessment of a network's reliability.

Conventionally, reliability parameters are modelled deterministically. It is common to use constant values, typically the average, to model component failure rates. Discrete states have also been applied to capture the variability in failure rates. The failure rate takes on a distinct value in each state and for the whole duration of the state [5]. In [6]-[10], stochastic state modelling approaches were applied to component failure rates. Stochastic adverse state models are based on a random parameter of the adverse weather element influencing the component. The random parameter could be an integral part of the external factor(s) e.g. wind speed for wind related component outages. The parameter could also be as a result of the occurrence of the external factor(s) such as the electric field on the surface of an insulator due to deposited pollutants [11]. While stochastic state modelling varies failure rates, it ignores the seasonal and time-dependency of weather parameters and of the corresponding failure rates.

A time-dependent probabilistic model for stochastic network parameters, including failure rates, was proposed in [12] and extended in [13]. The approach develops Beta probability density function (PDF) models for a given parameter in time windows that characterize different seasons and times-of-day [14]. Network operational time windows have lengths that vary from a day to a couple of months. Planning time windows have a minimum length of one year.

This paper analyses the impact of different component failure models on network reliability. Deterministic and probabilistic models are considered in a planning reliability analysis. The reliability analysis is performed on a network that mimics real South African conditions. The underlying distributions of the indices computed are analyzed to derive a more comprehensive description of the network's reliability.

2. SEQUENTIAL MONTE CARLO SIMULATION (MCS)

MCS techniques have been applied extensively in reliability studies. MCS algorithms are applied when chronological events are involved so that the up and down states cycles of all components are simulated and a system operating cycle is obtained by combining all the component cycles [5]. Sequential MCS algorithms are more powerful when complex systems have to be analyzed, but the computation effort required is significantly higher than non-sequential MCS [5], [15].

A new reliability evaluation approach that incorporates time-dependent probabilistic modeling has been proposed [16]. Unlike the conventional sequential MCS, the time-dependent probabilistic approach (TDPA) only simulates the down states of component lifecycles. This significantly reduces the computation time compared with the conventional sequential MCS. The results of the TDPA-based reliability study are also more dependent on the input component failure models than on the number of simulation runs. The key differences between the

conventional sequential MCS and TDPA are summarized in Table 1.

Table 1: Differences between conventional sequential MCS [16]

Conventional sequential	TDPA
<ul style="list-style-type: none"> • Considers constant component failure rates for a given period, such as for the useful life section of a bath-tub curve. Applies an exponential distribution for component time-to-failure 	<ul style="list-style-type: none"> • Uses PDFs of failure rates to simulate the number of failures in a period as well as randomness in the time of failure, but does not calculate the time-to-failure
<ul style="list-style-type: none"> • Builds the chronological cycle of a component by simulating the time-to-failure and time-to-repair 	<ul style="list-style-type: none"> • Builds the same chronology by simulating how many down states will appear, when each down state begins and how long each down state lasts. System is in up-states at all other times
<ul style="list-style-type: none"> • Conventional sequential MCS is usually applied in planning studies to compute average annual or annualized indices 	<ul style="list-style-type: none"> • Recognizes chronology based on seasonal and time-of-day variability over short periods and can therefore be applied consistently to both planning and operation studies

The key simulation steps applied by the TDPA include [16]:

- 1) Perform a failure mode and effect analysis (FMEA) to determine the failure states and contributing components
- 2) Assume all components are in service i.e. up state.
- 3) Select a component and time window (T_{pt}).
- 4) Select the adverse conditions that affect the component
- 5) Aggregate the component frequency-of-failure data corresponding to each identified failure cause
- 6) Derive the frequency failure PDF from the appropriate data set.
- 7) Generate the number of component failures within T_{pt}
- 8) Randomly assign each failure event to a specific day and time within the analysis period using a uniform random number generator
- 9) Generate the duration-of-failure per event by randomly selecting from the component's duration of failure Beta PDF
- 10) Develop the component's chronological (up-down) state cycle for the analysis period
- 11) Repeat steps 2 to 8 for all components and combine the components' cycles to develop the system lifecycle and provide the failure state cycles for different load points based on the FMEA analysis
- 12) Analyze the lifecycles to compute the load point and system indices

3. ILLUSTRATION EXAMPLE

This section will describe the test network considered and the component failure models derived.

3.1 Test bulk network

The simplified (pseudo) network shown in Fig. 1 was used as the test system. It is similar to a portion of the real South African transmission network and is used because real and relevant data is available, allowing realistic conditions to be modelled. The network is composed of 36 buses with a total load of 6.3 GW. The maximum generating capacity is 2.2 GW with make-up infeed (slack-bus) from Terminal 01. The base voltage and power for the network is 400 kV and 100 MW respectively. Only 1st order contingencies were considered i.e. only system states composed of single component outages were analyzed. Loads were fixed at their maximum values.

An extensive analysis of fault records has been performed to identify the major causes of faults on the South African transmission network and their characteristics [17]. Failure events occurring between 1993 and 2009 were considered and the failure data analyzed. South Africa can be divided geographically into two areas indicating the dominant nature of rainfall activity that is present i.e. frontal and thunderstorm rainfall activity regions. More rainfall falls in the thunderstorm region. The two geographical regions are depicted in Fig. 1. Components in each region are influenced by pollution, birds, bush fires, lightning flashes or a combination of such risk. According to [17], external factors such as wind, animals and human influence corresponded to very low probability events and were thus not included in this analysis. Each network risk significantly influences component outages in the sub-regions shown in Fig. 1.

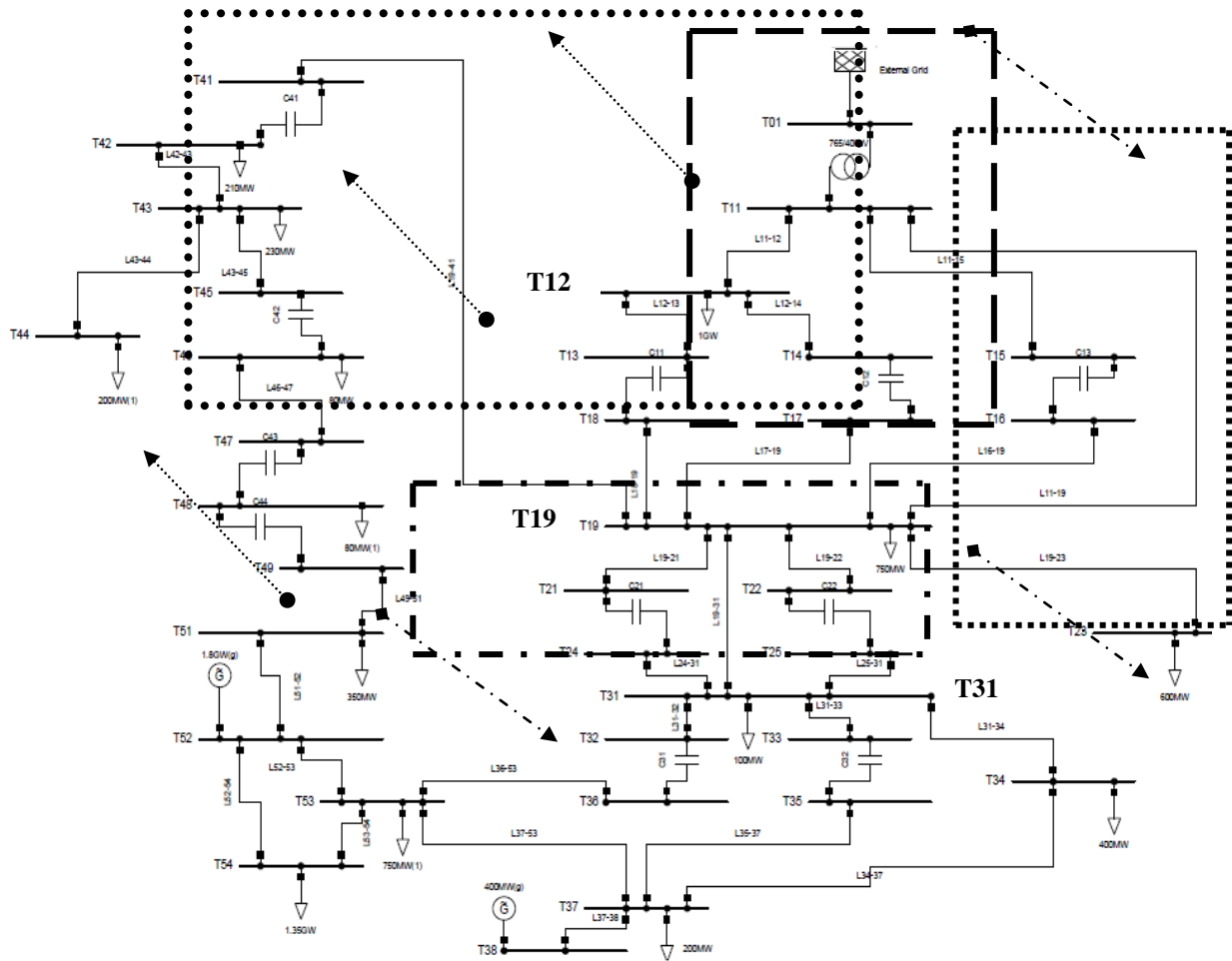
The failure data collected and published by the authors in [17] was applied to the test network components using (1).

$$f_{cRt} = \frac{NF_{Rt}}{NC_{Rt}} \quad (1)$$

Where:

f_{cRt} : failure rate of a component due to a specific threat in a given region or sub-region
 NF_{Rt} : number of failures, due to threat, in region or sub-region of influence

NC_{Rt} : number of components, in region or sub-region, exposed to given



Geographical regions and dominant external network risks
 Lightning - - - Birds - . . Bush Fires Pollution ◆ - -> Frontal region ●.....> Thunderstorm region

Fig. 1: Pseudo power network similar to part of the South African power grid

3.2 Transmission line failure models

The failures occurring every year between noon and 6 pm were analyzed. Three cases were considered for each component vulnerability model:

- Base case analysis: Deterministic model
- Region unspecific: Probabilistic models
- Region specific: Probabilistic models

Case 1: Base case models-deterministic

A base case analysis provides a set of values to be used for comparison with those obtained from other tests performed on a given system. This enables the evaluation of different action alternatives from a reliability view point. This base case analysis modelled line failures deterministically. It considered the sub-regions in which each external element had significant influence. Variation in severity of a given threat across the geographic regional boundary was not considered. The line failure data sets corresponding to the dominant external element in each sub-region were used to determine the average value of line failures due to each threat. All lines in a given sub-region and thus exposed to the same dominant external element, were assigned the same frequency and duration of

failure values. For lines in overlapping sub-regions (crossing more than one sub-region), average values were determined from the failure data sets of the corresponding sub-regions and summated. Table 2 presents the annual average frequency of failure derived in the selected time window.

Table 2: Average frequency of component failure due to different external elements

Network risk	All exposed components (failures/year)	Per component (failures/year)
Birds	7.2	0.8
Lightning	24.0	1.7
Bush Fires	38.2	4.2
Pollution	2.4	0.4
Birds and Lightning	(7.2+24.2) = 31.4	2.5

On average, birds and lightning cause more outages annually compared to the other threats in the time slot considered.

Case 2: Region unspecific models-probabilistic

This case also neglects variation in the two geographic regions. However, instead of using the average values, the frequency and duration of line outages were developed as PDFs. Dispersion in the line failure parameters, due to variability in the

occurrence of each external threat was thus considered. A single PDF was developed for each threat and applied to all lines in the network that are exposed to the given threat. The PDFs derived for the significant threats in the selected time slot are displayed in Fig. 2.

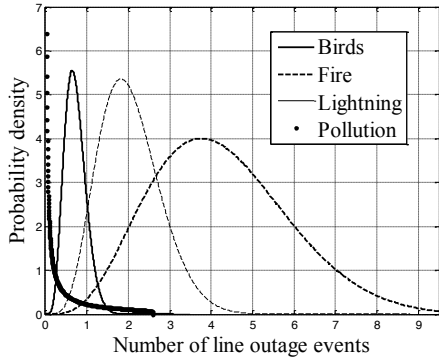


Fig. 2: Annual network threat PDFs for the noon to 6 pm time slot

Fig. 2 indicates that a line outage in the selected time window will more likely result from fire or lightning.

Case 3: Region specific models-probabilistic

This case considers external threat models that relate to the geographic regions. The models are developed based on the actual conditions in proximity of the affected component. This is more realistic compared to the two previous cases. For each threat, two failure models were thus derived and applied to affected components while taking into account their geographical locations. These are shown in Fig. 3

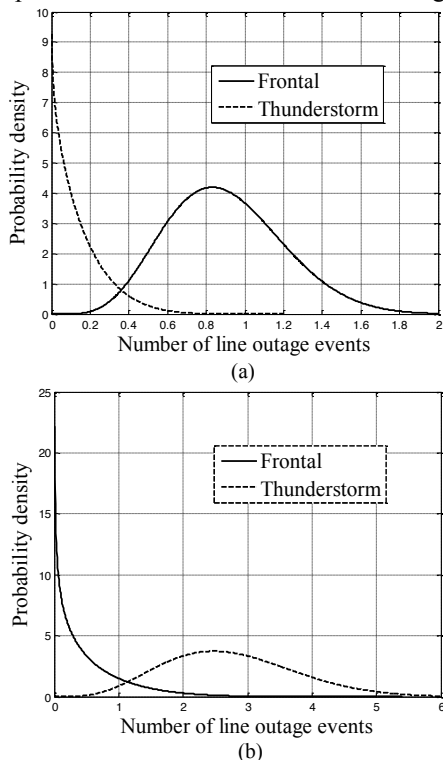


Fig. 3: Geographical based line failure PDFs for (a) birds (b) lightning

The shapes in Fig. 3 clearly show that the influence of a network threat on line outages varies between the two regions.

Fig. 4 shows the duration of failure PDF applied in Cases 2 and 3. The average of the duration parameter, 10 hours, was applied in the base case analysis.

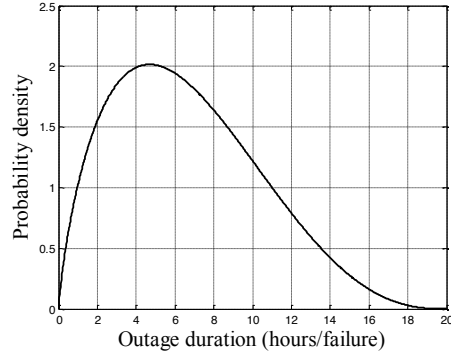


Fig. 4: Beta PDF model for component restoration time

4. SIMULATION RESULTS

The load point and system indices computed in each case include the Frequency of Load Curtailment (FLC) and Duration of Load Curtailment (DLC). The values for FLC computed were rounded to the nearest whole number e.g. 3.2 = (3 events/year) and 3.5 = (4 events/year). The load point results are presented in this section for three buses: T12, T1 and T31. The performance of load points T12 and T31 is affected by components that lie only in the frontal and thunderstorm regions respectively. Load point T19 on the other hand is affected by components in both regions. Analyzing corresponding indices of the three load points provides an indication of how the network performs in each region.

Table 3 presents the average values of the indices computed based on the failure models in cases 1 and 2.

Table 3: Comparison of average index values computed using models in cases 1 and 2

	FLC (events/year)		DLC (hours/year)	
	Base Case	1-year PDF	Base Case	1-year PDF
T12	5	6	29.6	64
T19	8	12	49.9	130
T31	11	14	67.1	155
System	31	48	185.5	545

The indices computed using each failure modelling approach indicate that the best and worst performing load points are T12 and T31 respectively. The analysis that applies Case 2 models (single annual region unspecific PDFs) however yielded significantly higher index values. This could be attributed the PDFs applying the full range of the failure parameter values. The indices can be further analyzed by comparing the distributions of the indices computed in each case. Fig. 4 shows a comparison of the index PDFs derived in each case.

It is clear that some of the Beta PDFs are shifted horizontally when the component failure parameters are modelled probabilistically. Using PDFs ensures that the selection of input failure parameter values was carried out while considering the likelihood of a parameter taking on a given value. The skewness of a given component parameter's PDF ensures that certain values are selected more in the analysis because the parameter is more likely to have such values. Unlike the base case, each reliability index computed thus exhibit a specific range with distinct minima and maxima.

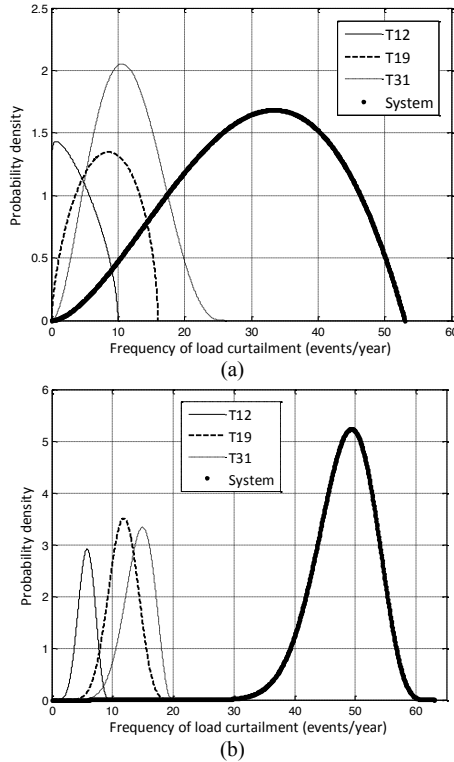


Fig. 5: FLC index PDFs derived based on inputs modelled as (a) average values (b) annual region unspecific PDFs

The base case analysis and the case with single annual PDFs, applied the same model to lines, irrespective of whether they lay in the frontal or thunderstorm regions. Unlike cases 1 and 2, the models in case 3 are based on the severity of a threat in each geographical region. The models are developed based on the actual conditions in the proximity of the affected line. Fig. 5 and 6 compare the FLC and DLC indices for T12 and T31 computed with and without regard for geographical regions.

A significant increase is noted in the indices computed for both load points. The shapes of the PDFs also change which affects the likelihood of a given index taking on different values. Consider indices compute for T31. From Fig. 5, the number of load curtailments events increases when regional based PDFs are applied. However, the likelihood of fewer load curtailments events also increases as seen from the lower tails of its FLC index PDFs. The

lower tails of the T31 DLC index PDFs in Fig. 6 almost overlap which shows that the likelihood of short load curtailments occurring is unaffected. The length of load curtailment events however increases when regional PDFs are applied.

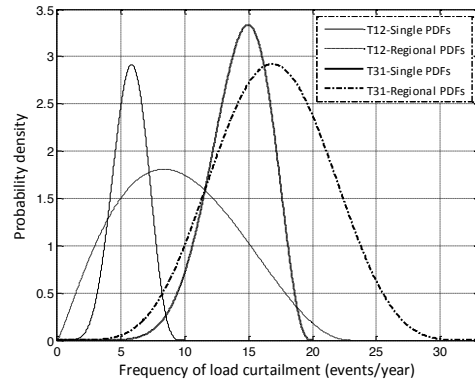


Fig. 6: Comparative FLC indices based on single and regionally based composite input PDFs

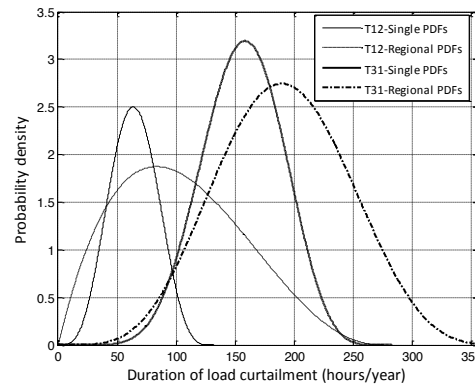


Fig. 7: Comparative DLC indices based on single and regionally based composite input PDFs

5. IMPLICATIONS OF THE RESULTS

Most of the software packages used by power utilities for reliability analyses require component parameters inputted as deterministic values. They also present the computed reliability indices in the same form. The results however showed that the representation of reliability inputs as PDFs is more comprehensive than the use of average deterministic values. This necessitates the refinement of failure data analysis. Incorporation of seasonal and time-of-day dependency allows planners to assess network failures in the context of other stochastic network parameters such as loading. As an example, maintenance practices can be scheduled more effectively into a time window that ensures the least impact on the network and its customers. The seasonal and time-dependent probabilistic modeling approach allows planners and operators to vary the risk of component failure based on expected conditions. The risk of failure in winter is higher due to increased stress on the network. The skewness of a given PDF can be changed to account for such elevation in risk of failure.

Description of reliability indices is improved when PDFs are applied. The full range of an index is

available. So what index value should be selected as a basis for decision making? A risk-based approach can be applied so that each index value has a level of risk or confidence attached. This allows the uncertainty induced in the decision making process to be quantified.

6. CONCLUSION

The input failure models applied in an analysis have a significant impact on the perception of a network's reliability. Deterministic models provide a single dimension to describing failure parameters. PDFs allow for a more realistic description of network parameters. They provide the full range of possible parameter values. PDFs also describe the dispersion and skewness of the underlying probability distributions of input failure parameters. This ensures that a network's reliability is assessed while accounting for the most and least likely failure events. Seasonal and time-dependent probabilistic models provide a means of accounting for stochastic elements that affect a network's reliability.

REFERENCES

- [1] D Cheng, D Zhu, R P Broadwater, S Lee, "A Graph Trace Based Reliability Analysis of Electric Power Systems with Time-Varying Loads and Dependent Failures", *Electric Power Systems Research* Vol.79, pp.1321-1328, 2009.
- [2] A M Koonce, G E Apostolakis, B K Cook, "Bulk Power Risk Analysis: Ranking Infrastructure Elements According to their Risk Significance", *Electrical Power and Energy Systems Journal*, Vol. 30, pp. 169-183, 2008.
- [3] M Mili, Q Qiu, "Risk Assessment of Catastrophic Failures in Electric Power Systems", *International Journal of Critical Infrastructure*, Vol. 1, No. 1, pp. 38-63, 2004.
- [4] S Blake, P Taylor, A Creighton, "Methodologies for the Analysis of both Short-term and Long-term Network Risks", *20th International Conference on Electricity Distribution*, Prague, June 2009.
- [5] R Billinton, R N Allan, *Reliability Evaluation of Power Systems*, Plenum Press, 1996.
- [6] "IEEE Standard Terms for Reporting and Analyzing Outage Occurrences and Outage States of Electrical Transmission Facilities", IEEE Standard 859-1987, 1988.
- [7] E Brostrom, J Ahlberg, L Söder, "Modelling of Ice Storms and their Impact Applied to a Part of the Swedish Transmission Network", *Power Tech*, Lausanne, pp. 1593-1598, 2007.
- [8] R E Brown, S Gupta, R D Christie, S S Venkata, R Fletcher, "Distribution System Reliability Assessment: Momentary Interruptions and Storms", *IEEE Transactions on Power Delivery*, Vol. 12, No. 12, pp. 1569-1575, 1997.
- [9] N Balijepalli, S S Venkata, C W Richter, R D Christie, V J Longo, "Distribution System Reliability Assessment due to Lightning Storm", *IEEE Transactions on Power Delivery*, Vol. 20, No. 3, pp. 2153-2159, 2005.
- [10] K Alvehag, L Söder, "A Reliability Model for Distribution Systems Incorporating Seasonal Variations in Severe Weather", *IEEE Transactions on Power Delivery*, Vol. 26, No.2, pp. 910-919, 2011.
- [11] Z Aydogmus, M Cebeci, "A New Dynamic Model of Polluted HV Insulators", *IEEE Transactions on Dielectrics and Electrical Insulation*, Vol. 11, No. 4, pp. 577-584, 2004.
- [12] R Herman, C T Gaunt, "Probabilistic Interpretation of Customer Interruption Costs (CIC) Applied to South African Systems", *11th 12th International Conference on Probabilistic Methods Applied to Power Systems*, Singapore, June 2010.
- [13] M Edimu, C T Gaunt, R Herman, "Probabilistic modelling of the effects of external network threats on transmission reliability assessment", *12th International Conference on Probabilistic Methods Applied to Power Systems*, Istanbul, June 2012.
- [14] M Edimu, C T Gaunt, R Herman, "Using Probability Distribution Functions in Reliability Analyses", *Electric Power Systems Research Journal*, Vol. 81, pp. 915-921, 2011.
- [15] R A González-Fernández, A M Leite da Silva, "Reliability Assessment of Time-dependent Systems via Sequential Cross-entropy Monte Carlo Simulation", *IEEE Transactions on Power Systems*, Vol. 26, No. 4, pp. 2381-2387, 2011.
- [16] M Edimu, K Alvehag, C T Gaunt, R Herman, "Performance of a Time-Dependent Probabilistic Approach for Bulk Network Reliability Assessment" Submitted to *IEEE Transactions on Power Systems*, 2012.
- [17] U J Minnaar, C T Gaunt, F Nicolls, "Characterization of Power System Events on the South African Transmission Power Lines", *Electric Power Syst. Research Journal*, Vol. 88, pp. 25-32, 2012.

INFLUENCE OF TEMPERATURE ON TIME DOMAIN REFLECTOMETRY IN SHIELDED POWER CABLES

L.S. Ndlovu S. Munilal and C. Nyamupangedengu

School of Electrical & Information Engineering, University of the Witwatersrand, Johannesburg, Private Bag 3, Wits 2050, South Africa, E-mail: Lalo.Ndlovu@students.wits.ac.za

Abstract: Time domain reflectometry (TDR) is a travelling wave technique that is widely used to locate defects in power cables. When used for partial discharge (PD) location under online conditions where the cable temperature can vary widely, there is a possibility of TDR errors introduced by temperature variations. TDR measurements on a 13 m long extruded dielectric cable were conducted at different temperature conditions of the cable. It was found that the velocity of propagation in the cable changed by 6.1% when the temperature of the cable was increased from 9°C to 75 °C. If the TDR calibration is done at 9°C a defect location error of 7% is introduced by increasing the cable temperature to 75°C. Temperature effects should therefore be factored in when making TDR measurements.

Keywords: TDR, temperature, power cable, partial discharges.

1. INTRODUCTION

Time domain reflectometry (TDR) is a technique of using the travelling wave phenomenon to locate points of impedance changes in a coaxial cable using the time of flight differences of pulses travelling in the cable. TDR is the most cost effective and widely used method of locating defects in a power cable [1]. While there have been extensive studies on factors that affect the accuracy of TDR such as the frequency dependent signal transmission characteristics of power cables [2-5], the effect of temperature on the cable signal transmission characteristics has not been given the same attention.

Steiner et al [2] mentioned the importance of cable temperature as a contributing factor towards TDR measurement errors. The researchers however toned down this problem on the account that power cables are usually buried at depths where temperature variations are minimal. While this rationale is valid for offline TDR measurements, the situation is significantly different for online conditions. Online partial discharge (PD) measurement is now a common practice [6]. There is a possibility that online PD measurements are taken at temperatures different from the cable temperature at which the TDR calibration would have been done. The cable temperature is a function of the current flowing in the cable which in turn varies widely depending on the load characteristics. In that regard, the effect of temperature on the TDR accuracy becomes imperative. Some researchers such as [7] have recognised the importance of understanding the influence of temperature on TDR. It is an indication of the growing interest in understanding the influence of temperature on the travelling wave transmission characteristics of shielded power cables.

This paper presents results of an investigation into the extent to which temperature variations in a power cable may affect the TDR measurement accuracy. An overview of the TDR principle and the temperature dependency is

presented in Section 2. The experimental procedure and results discussion are presented in sections 3 and 4 respectively and the paper concluded in Section 5.

2. THE PRINCIPLE OF TDR MEASUREMENTS AND THEORY ON TEMPERATURE DEPENDENCY

When a cable in a power system develops a fault, the attendant protection system operates to isolate the cable. The actual location of the fault on the cable has to be determined. The TDR method is usually employed to identify the location of the fault as illustrated in Figure 1. Furthermore, with the increasing importance of condition based maintenance practice, it is now imperative to identify and locate incipient power cable defects before they develop into power flow interruption faults. Most of these incipient faults produce PD signals. Detection and analysis of the PD signals give important information about the developing faults and this includes the location of the defects. The TDR technique is used to locate the PD source as illustrated in Figure 2.

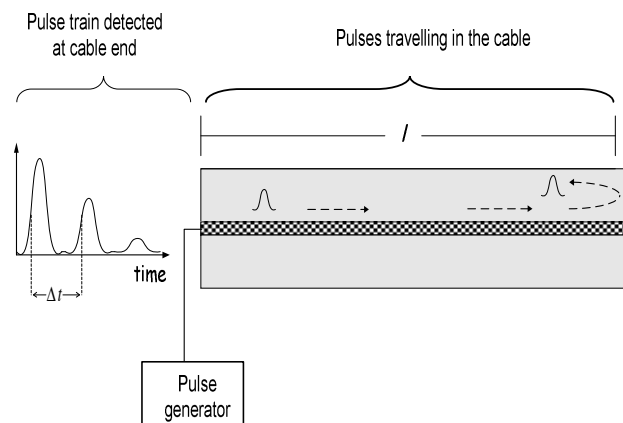


Figure 1: An illustration of externally injected pulses travelling in a power cable

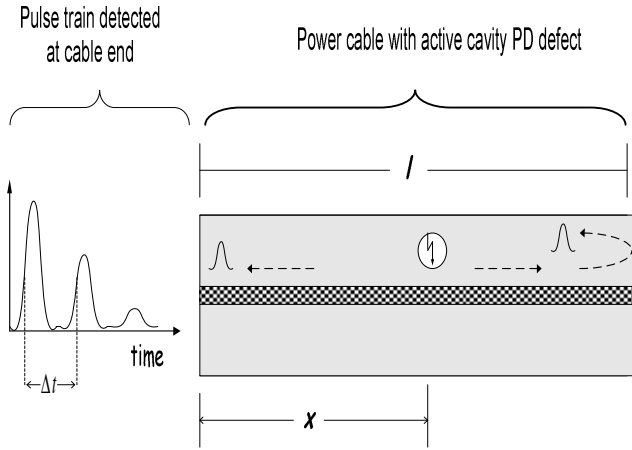


Figure 2: An illustration of PD pulses travelling in a power cable

In the case illustrated in Figure 1, the length of the cable l is given by equation 1 [5].

$$l = \frac{(VF \cdot c) \cdot \Delta t}{2} \quad (1)$$

Where:

- l = the cable length [m],
- c = the speed of light
- Δt = the time of flight difference between the incident and reflected pulses [s],
- VF = the velocity factor given by $VF = \frac{v}{c} = \frac{(l/\Delta t)}{c}$ and v is the velocity of pulse propagation in the cable [m/s].

In Figure 2, the defect is located a distance x from the cable-end and is calculated using equation 2 [5].

$$x = l - \frac{1}{2} \cdot (VF \cdot c) \Delta t \quad (2)$$

The term VF is determined through TDR calibration. The calibration method involves injecting a known pulse in a known cable length and calculating VF using equation 1 [1].

The temperature dependent behaviour of the TDR measurements can be attributed to the influence of temperature on the cable insulation permittivity as well as the semiconducting layers.

In similar work done by Dubickas et al [7], the effect of temperature on TDR measurements was reported. Their investigation focused on each of the three dielectric layers of an XLPE cable, that is, inner semiconducting layer, XLPE layer and outer semiconducting layer. The effect of temperature on the material characteristics of

each layer was investigated. It was reported that the real part of the complex permittivity of the semiconducting layers had a decrease of 0.7 to 3% when the temperature was increased from 20°C to 40°C and from 40°C to 60°C. It was then concluded that the pulse velocity in the cable increased with temperature [7].

The crosssectional geometry of the power cable is as shown in Figure 3. The equivalent high frequency model is as shown in Figure 4.

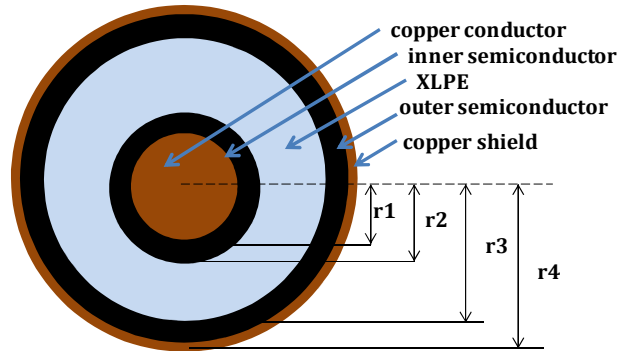


Figure 3: The cable structure

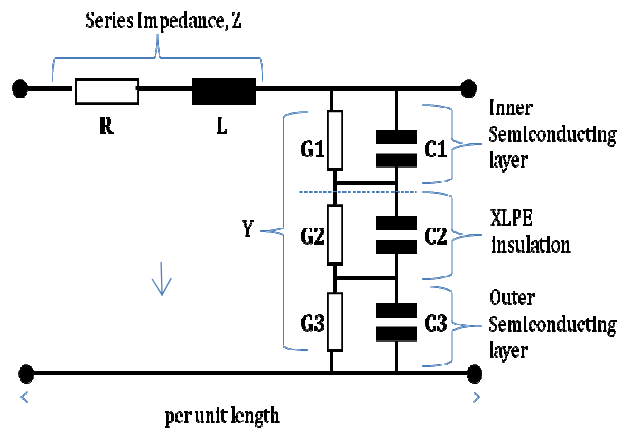


Figure 4: XLPE power cable model, adapted from [9].

It has been shown that the high frequency behaviour of the power cable is largely dependent on the shunt parameters. The admittance (Y), as expressed in equation 3, is made up of the semiconducting material and XLPE insulation. The admittance is a function of the capacitance (C) and dielectric losses or conductance (g).

$$Y = \frac{1}{\left\{ \frac{1}{Y_1} + \frac{1}{Y_2} + \frac{1}{Y_3} \right\}} \quad (3)$$

Where:

Y_1 , Y_2 and Y_3 are the admittances of the outer semiconducting layer, XLPE insulation and the inner semiconducting layers respectively. The capacitance C and conductance (g) of each layer are expressed as given in equations 4 and 5 respectively [9].

$$C_n = \frac{2\pi\epsilon_0\epsilon'(\omega)}{\ln\left(\frac{r_n}{r_{n-1}}\right)} \quad (4)$$

$$g_n = \frac{2\pi\epsilon_0\epsilon''(\omega)}{\ln\left(\frac{r_n}{r_{n-1}}\right)} = \frac{2\pi\sigma_n}{\ln\left(\frac{r_n}{r_{n-1}}\right)} \quad (5)$$

Where:

- ϵ_0 = permittivity of free space,
- $\epsilon'(\omega)$ = relative real part of the complex permittivity of the material,
- r_n = radius of the layer from the centre
- σ_n = conductivity

An inspection of the analytical expressions of the capacitance and conductance of the cable shows that the parameters that are susceptible to influence by changes in temperature are the real and imaginary permittivity. It has been reported by other researchers that the permittivity of cable semiconducting layers was in the order of 0.3% in the temperature range 20°C to 40°C but changed to about 7% when the temperature was increased to 60 °C [8]. Furthermore researchers that have investigated the relationship between dielectric losses in XLPE power cables and temperature changes in the cable reported significant increases in response to increase in temperature [10].

If the TDR calibration, from which the VF is derived, is performed at a temperature different from that when the time of flight measurements are taken, then there is a possibility of errors introduced in the TDR measurements due to temperature differences. A laboratory based experimental investigation was conducted to determine the extent to which temperature variations in a power cable affect the signal propagation velocity. The subsequent sections of this paper present the investigation method, results analysis and discussion.

3. THE EXPERIMENTAL PROCEDURE

3.1 Cable heating and cooling

To investigate the insulation properties of the cable under different temperature variations, the power cable was exposed to two extreme temperatures; 9°C and 75°C, and 25°C was the reference temperature. The cable temperature was lowered to 9°C by cooling the cable overnight in a walk-in coldroom. The TDR measurements were taken as the temperature rose to room temperature.

In order to heat up the cable for high temperature TDR

measurements, a current 550 A was continuously injected into the 95 mm² cross-linked polyethylene (XLPE) insulated power cable until the insulation reached a steady state temperature of 75°C. High current injection cable heating method was chosen among other possibilities as it simulates the real life application where a cable heats up due to the load current flow in the conductor. The flow chart diagram depicted in Figure 5 summarises the experimental procedure.

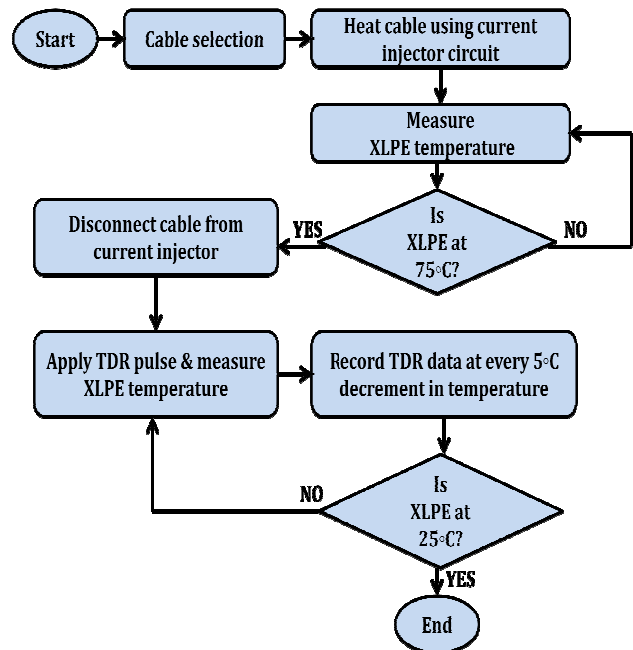


Figure 5: A flow chart of the experimental procedure

3.2 The TDR measurement setup

A pulse of 5 ns rise time, 20 ns width and 5 V magnitude was injected into a 13 m power cable from an Agilent digital signal generator. A RIGOL DS1064B digital oscilloscope was connected to the cable as shown in Figure 6. The waveforms of the incident and reflected pulses at different temperatures were displayed on the oscilloscope.

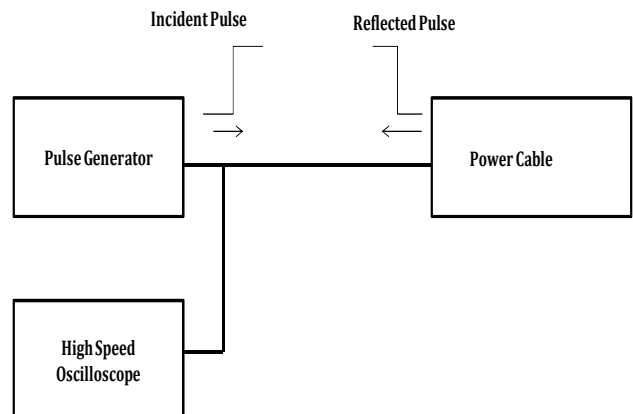


Figure 6: Block diagram of the TDR measurement setup

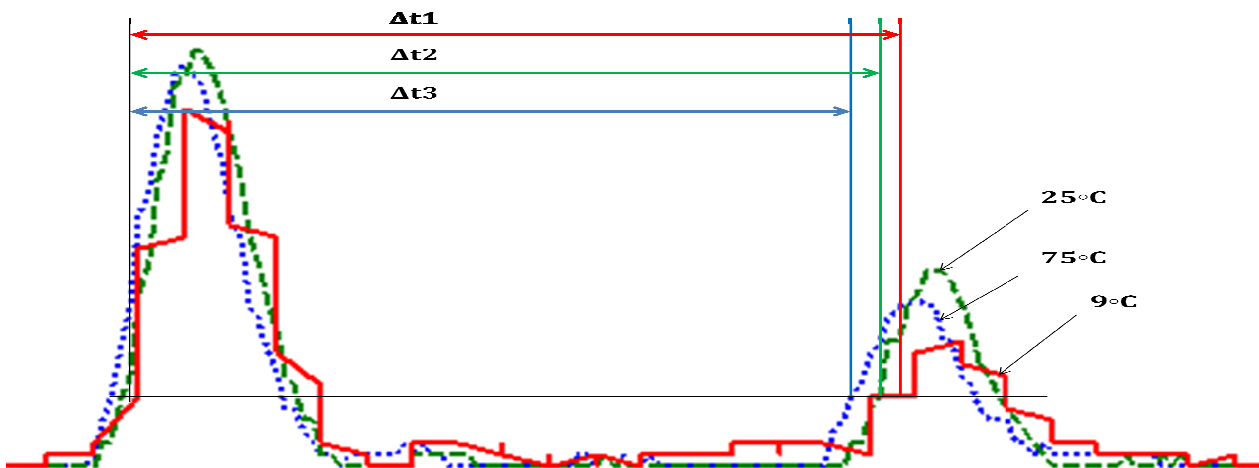


Figure 7: The incident and first reflected pulses at different temperatures in a 13 m cable.

4. THE MEASUREMENT RESULTS AND DISCUSSION

The detected incident and first reflected pulses at the three temperatures of the cable viz 75°C, 25°C and 9°C are shown in Figure 7. It can be seen that the reflected pulses are a function of temperature. Taking the reference pulses as those at room temperature (25 °C), the pulses shift to the right as the temperature decreases and to the left as the temperature increases.

The information obtained from the time domain pulses is used to determine fault location in power cables. The 1st and the 2nd reflected pulses are used to calculate the travel time of the pulse in the cable as shown in Figure 5. There are three waveforms on the diagram at different temperatures with different travel times.

Δt_1 , Δt_2 and Δt_3 are the travel times of the pulses at 9°C, 25°C and 75°C respectively. Using equation 1, the velocity factor and propagation speeds in the power cable at different temperatures are calculated and presented in Table 1.

Table 1: Travel times, velocity factors and travels speeds of the pulses at extreme temperatures.

Temp(°C)	Round_trip(ns)	Velocity Factor	Speed(m/s)
9	170	0.542	1.63E+08
25	164	0.562	1.69E+08
75	160	0.576	1.73E+08

The travel time or round trip time of the pulse at high temperature is shorter as compared to the lower temperature, as shown on the table. When the TDR technique is performed under normal atmospheric temperature of 25°C, the speed of the pulse is 56.2% of that of light; and this is typical for XLPE extruded power cables [8]. However, when the temperature of the cable

is lowered to 9°C the speed drops to 54.2% of the speed of light and when the temperature is raised to 75°C, the speed rises to 57.6% that of light.

For the 13 m cable, if the TDR measurements calibration are done at 25°C, the TDR calculated lengths of the cable at 9°C and 75°C give length values of 13.51 m and 13.35 m respectively. Physically the cable does not expand that much with increase in temperature. Table 2 shows the percentage errors introduced by temperature changes in the TDR calculated lengths. It is interesting to note that in real life cable circuits of lengths in the order of 1 km, a 7% error as determined in the present work would translate into a 70 m miss in defect location!

Table 2: Percentage errors and length errors of the pulses at extreme temperatures.

Temp(°C)	%error	length error(13m)	length error(1km)
9	3.6	0.51m	36m
25	0	0m	0m
75	2.4	0.34m	24m

It follows therefore that the admittance in the cable model changes in response to changes in temperature. The temperature dependent shift in position of the TDR pulses that was observed in the present work is therefore consistent with the theory.

5. CONCLUSION

The work reported in this paper shows that temperature changes in a power cable insulation affects the speed of pulse propagation in the cable. This phenomenon has implications on the accuracy of TDR measurements in power cables. It therefore may be necessary to take into account temperature conditions when performing TDR based measurements in power cables.

6. ACKNOWLEDGMENT

The authors would like to acknowledge with gratitude Eskom for their support of the High Voltage Engineering Research Group through TESP. They would also like to express gratitude to the Department of Trade and Industry (DTI) for THRIP funding and to thank the National Research Foundation (NRF) for direct funding of the research group.

7. REFERENCES

- [1] F.H. Kreuger, M.G. Wezelenburg, A.G. Wiemer and W.A. Sonneveld: "Partial discharge Part XVIII: Errors in the location of partial discharges in high voltage solid dielectric cables", *IEEE Electrical Insulation Magazine*, Vol. 9, No. 6, 1993, pp.15-22
- [2] J.P. Steiner, P.H. Reynolds and W.L. Weeks, "Estimating the location of partial discharges in cables", *IEEE Transactions on Electrical Insulation*, Vol. 27, No. 1, 1992, pp 44-51.
- [3] Zhifang Du, P.K. Willet and M.S. Mashikan, "Performance limits of PD location based on time-domain reflectometry", *IEEE Transactions on Dielectrics and Electrical Insulation*, Vol. 4, No. 2, 1997, pp 182-188.
- [4] W.E. Anderson, J. D. Ramboz, and A.R. Ondrejka, "The detection of incipient faults in transmission cables using time domain reflectometry techniques: Technical challenges", *IEEE Transactions on power apparatus and systems*, Vol. PAS-101, No. 7, 1982, pp 1928-1934.
- [5] H. Borsi, "Digital location of partial discharges in HV cables", *IEEE Transactions on Electrical Insulation*, Vol. 27, No. 1, 1992, pp 28-36
- [6] J. Veen, "Online signal analysis of partial discharges in medium-voltage power cables", PhD thesis, Technical University of Eindhoven, 2005.
- [7] V. Dubickas and H. Edin, "On-line Time Domain Reflectometry Measurement of Temperature Variations of an XLPE Power Cable." *IEEE Annual Report Conference on Electrical Insulation and Dielectric Phenomena*, 2006, pp. 47-50.
- [8] G.M Hashmi, R Papazyan and M. Lehtonen, "Determining wave propagation characteristics of MV XLPE power cable using time domain reflectometry technique", *Turk J. Elec. Eng & Comp Sci*, Vol. 19, No. 2, 2011, pp 207-219.
- [9] G. Mugala, "High Frequency Characteristics of Shielded Medium Voltage XLPE Cables", Doctoral Thesis, KTH University, Stockholm, Sweden, 2005
- [10] G. Tinamoto, M. Okashita, F. Aida and Y. Fujiwara, "Temperature dependence of $\tan \delta$ in polyethylene", *Proceedings of the 3rd International Conference on Properties and Applications of Dielectric Materials*, Tokyo, Japan, 1991, pp 1068-1071.

INTRODUCTION OF A MORE DETAILED CALCULATION OF GEOMAGNETICALLY INDUCED CURRENTS IN TRANSMISSION NETWORKS

D.T. Oyedokun*, M.N. Simon**, C.T. Gaunt***

University of Cape Town, Department of Electrical Engineering, Rondebosch, 7700, South Africa
 E-mail: * davoyedokun@ieee.org, ** magnaemsimon@gmail.com, *** ct.gaunt@uct.ac.za

Abstract: Geomagnetic storms lead to large fluctuations of the earth’s magnetic field which creates the Earth Surface Potential (ESP) inducing quasi-DC currents in electric power systems through the grounded neutral of power transformers. These currents are commonly referred to as Geomagnetically Induced Currents (GICs). The flow of GICs through transmission lines and transformers across the power network has great consequences. Since 1849, several methods have been used to calculate GICs flowing in transmission networks. This paper looks at some of these methods, analyses their merits and introduces a more detailed approach to the calculation on GICs in transmission networks. By incorporating transformer time constants into the line and transformer calculation of GICs – which incorporates the earth’s magnetic field data – the amount of GIC flowing in various parts of a specific network can be determined.

Keywords: Geomagnetically induced currents, GICs, transformers, transmission lines.

1. INTRODUCTION

Geomagnetically Induced Currents in power networks are the result of changing geo-magnetic field which is a consequence of a geomagnetic disturbance. During solar storms, enormous explosions of energy on the sun’s surface hurl waves of charged particles - called Coronal Mass Ejections (CMEs) - and the flow of plasma-called solar wind - through space, which may take several days to reach earth. The interaction of these charged particles with the earth’s magnetic field is known as a geomagnetic storm [1, 2]. Geomagnetic storms lead to large fluctuations of the Earth’s magnetic fields which induce quasi-DC currents in electric power systems earthed with neutrals of power transformers. These currents are commonly referred to as Geomagnetically Induced Currents (GICs) [1]. The flow of GICs through transmission lines and transformers across the power network has consequences some of which are discussed in [3, 4, 5].

In this paper, a novel way of calculating GICs is introduced. This method combines the plane wave model, network nodal admittance matrix approach to the network calculation [6] and incorporates for the first time, the transformer time constant which does not appear to have been considered in any previous calculations.

Software called “Tortoise” based on this new method has been written in Matlab. The name of the software reflects the complex nature of power networks and the gradual development of GIC calculation algorithms. The results obtained from this software shows good correlation with results from the

software written by Natural Resources Canada (NRCAN) and other South African algorithms.

2. CALCULATION OF GICs

The calculation of GICs flowing in transmission networks through transmission lines and the grounded neutrals of power transformers involves two major parts [7]. The first part is the geophysical response of the geo-electrical field to a given geomagnetic disturbance arising from ionospheric and magnetospheric currents. The second part is the calculation of GICs in the network from the geo-electrical field.

2.1 The geophysical problem: Electric field calculation

In this section - which covers the first part of GIC calculations - a review of previous work in the calculation of the geophysical problem will be presented. Over the last few decades, the calculation of GICs has evolved. In 1940, McNish derived a mathematical expression for earth’s electric field using the formula in equation 1[8]:

$$E = -\frac{\partial A}{\partial t} \quad (1)$$

where:

A= the magnetic vector potential of the auroral line current flowing in the atmosphere and
 E= the induced electric field

In this model, the conductivity of the earth was neglected which made it incomplete.

In 1966, the earth’s electric field was calculated by Kellogg [9] from Maxwell’s equation as:

$$\text{curl } E = -\frac{\partial B}{\partial t} \quad (2)$$

Where: E= the induced electric field

In this method, a plane downward propagating wave - towards the earth - was used to represent the magnetic field. Unlike the model by McNish, this model took the conductivity of the earth into consideration. However, McNish assumed that the conductivity of the ground was uniform [9, 10]. Details about the model can be found in [12].

In 1970, Alberton and Van Baelen [10] derived a mathematical relation between the changes in the magnetic field and the resulting earth surface potential which lead to the flow of GICs. Their method took into consideration the conductivity distribution of the earth and used a log of the measured earth's magnetic field. The auroral currents are modelled as a plane wave due to its distance from the earth and its direction of propagation. This assumption still holds in most publications [11, 12, 13, 14].

The electric field was calculated as:

$$E_0 = \text{Re}(E_y) \quad (3)$$

Where $E_y = \int_0^\infty E_y(v)dv$

$E_y(v)$ is defined in equation 4 as:

$$E_y(v) = \frac{J e^{j\omega t}}{\pi} e^{-vh} \frac{j\omega\mu_0 Z_s(v)}{j\omega\mu_0 + v Z_s(v)} \cos vx \quad (4)$$

Only the y component of the electric field was of interest because it corresponds to $z = 0$. Further reasons are given in [10].

In 2004, Viljanen et al [13] stated that in solving the geophysical problem, what is needed is a model of the magnetospheric-ionospheric current system as a function of time and the earth's conductivity structure. Then in theory, it will be possible to solve Maxwell's equations and boundary conditions for the earth's electric and magnetic fields. However in practice, sources are partially unknown. Even if the sources are known the solution path is very complex and time consuming which will become a significant drawback [15].

Other methods include the uniform plane wave model (UPWM), the spherical elementary current systems (SECS) method introduced and validated in 1997 by Amm and used by Viljanen [16] and the Complex Image Method (CIM) [15].

Uniform plane wave model

Viljanen and Pirjola [14] introduced the uniform plane wave model application to the calculation of induced electric field in transmission lines. The approach reduces the geomagnetic effect to two components of the electric field E_x and E_y . Due to the perpendicular relationship between magnetic and electric fields, E_x is calculated from B_y and E_y is calculated from B_x . This method was used to calculate GICs in the Southern African electricity transmission network in 2002 [17].

Spherical elementary current systems (SECS) method

Elementary currents are derived by fitting the model field to the measured field in spherical coordinate system [13, 18, and 19]. This approach was adopted in the calculation of GICs in Southern Africa [20]. The elementary ionospheric currents are placed in an equally spaced grid pattern over the area of interest as seen in figure 1.

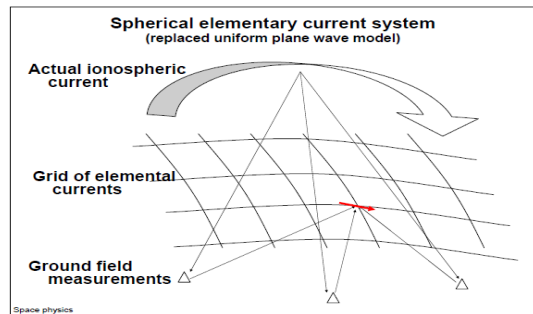


Figure 1: The SECS showing the ground field measurements and the grid of elementary current [20]

The Complex Image method (CIM)

The Complex Image method (CIM) has also been used to calculate the geophysical problem using a layered conductivity model of the earth. This method has been applied in Sweden [21] and in Southern Africa [22]. In 2003, Pulkkinen et al introduced a combination of SECS and CIM [23].

2.2 Network calculation

This section covers the second part of GIC calculations. Several methods have been proposed for the calculation of GICs in specific nodes and branches within a transmission network. Two methods will be covered in this paper. The first method is "a & b parameter" while the second method is based on power system nodal admittance which is explained by Boteler et al [24].

Method based on Network constants: a & b parameters

This method is based on a derivation by Lehtinen & Pirjola in 1985 [12] which calculates the network constants called a & b parameters for a defined network. The method is appropriate for uniform plane wave and uniform ground conductivity as explained in section 3.1. A representation of the network is given in equation 5 as:

$$I^e = (1 + Y^n Z^e)^{-1} J^e \quad (5)$$

Where Y = the network admittance
 Z = the earthing impedance matrix
 J^e = a column matrix of the electric field of 1V/km. This is expanded in [17].

The approach reduces to form equation 6 from which the GIC flowing in any node of the network can be defined as:

$$I_{GIC} = aE_x + bE_y \quad (6)$$

Where a = the evaluation of equation 5 using the eastward surface potential of 1V/km

b = the evaluation of equation 5 using the northward surface potential of 1V/km

The approach was applied in the GIC calculations for Southern Africa network in 2002 [17, 25].

Power system nodal admittance approach

Using source transformation – a combination of Thevenin’s and Norton’s theorems – to the induced voltage in figure 2, the induced voltage in the transmission line can be converted to an equivalent current source in parallel with the transmission line admittance. Applying Kirchoff’s current law, the total current at each node in the network can be determined. The nodal current represents the GIC flowing between the transformers and ground in the substation.

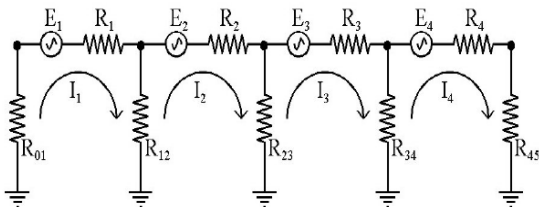


Figure 2: GIC modelled as an induced voltage in transmission line as [24]

3. INTRODUCING TRANSFORMER TIME CONSTANT TO GIC CALCULATIONS

The uniform plane wave and the power systems nodal admittance approach has been discussed in the previous section. A combination of the aforementioned methods and a novel incorporation of the transformer time constant forms a new tool which the authors are presenting. This is because various transformers within a transmission network will respond differently to the flow of geomagnetically induced currents. Amongst other transformer parameters, this response will be based on the resistance of the windings and the inductance of the transformer. The combination of these defines the transformer’s time response which governs the transformer’s transient response to changing induced electric field. The transient response of a transformer subject to fluctuations in the earth’s magnetic field is

the transformer’s reaction to the changing GIC levels with respect to time.

Figure 3 illustrates the difference between the prospective GIC value and the actual GIC value obtained as a function of the transformer’s response time.

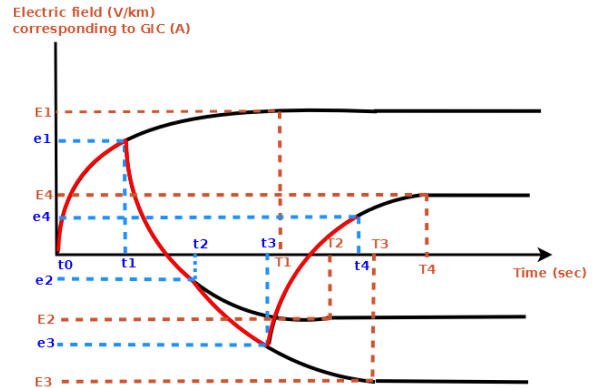


Figure 3: Different GIC values over time, the transformer’s response time and the time at which the GIC value changes.

In figure 3, E is the calculated induced voltage which corresponds to a prospective GIC value after time T , which is the transformer time constant. The actual GIC value reached at the time t , when the field changes correspond to e .

If $T > t$: the GIC in the transformer will never get to its calculated prospective peak value.

If $T < t$: the GIC in the transformer will always get to its calculated prospective peak GIC value over T .

The approach taken to solve this problem is to consider one of the windings as an inductor coil which has an exponential relationship between the rise in current and time as seen in equation 7.

$$I_{gic(t)} = I_{gic} (1 - e^{-\frac{t}{\tau}}) \quad (7)$$

Where I_{gic} = the prospective nodal GIC magnitude
 $I_{gic(t)}$ = the exact GIC magnitude as a function of the time the field changes
 τ = the transformer time constant

4. RESULTS FROM A TEST NETWORK

Let us consider an arbitrary test network with 10 nodes and 13 transmission lines, where each node represents a substation with one power transformer. Each power transformer has a response time of 4 minutes. The earth’s magnetic field was sampled at 2 minute intervals over 3 hours. Using the uniform plane wave method explained in section 2.1, 90 electric field values were obtained. I_{gic} was calculated using equation 6 and verified using the

power system nodal admittance approach in section 2. Figure 4 shows the GIC flowing through one of node without considering the transformer time constant.

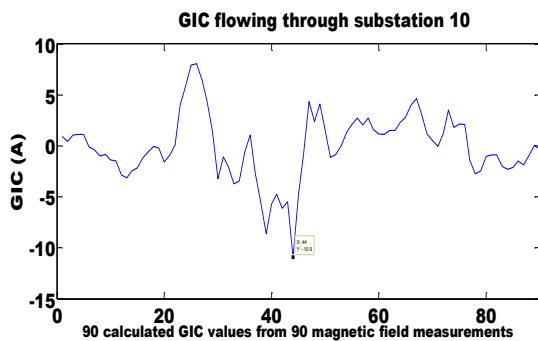


Figure 4: shows the GIC profile at the node without the transformer time constant

From figure 4, the magnitude of the maximum amount of GIC was found to be 10.89 A.

Figure 5 shows the GIC flowing through the same node after incorporating the transformer time constant within the calculation in tortoise (i.e., the software written based on this new approach).

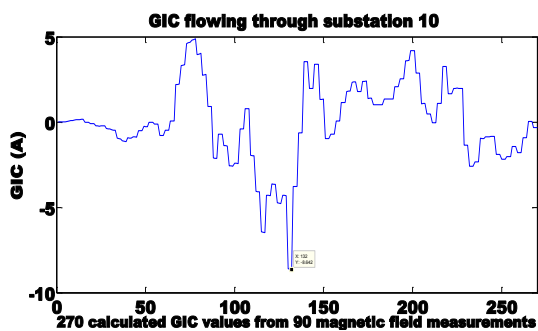


Figure 5: shows the GIC profile at the node with the transformer time constant taken into consideration

In figure 5, the magnitude of the maximum GIC reduced to 8.64 A which represents a 20.66 % reduction. The reason for this reduction is because: it takes about 4 minutes for the transformer to fully reflect the prospective amount of GIC (10.89 A). Since the field was sampled every 2 minutes, the actual amount of GIC will be less than the prospective amount of GIC.

5. CONCLUSION

A new approach to the calculation of GICs has been presented. This approach prevents an exaggeration of the expected GIC in a network. From the results the following conclusions are made:

- a) The time constant of all the transformers in the network is needed to determine the exact amount of GIC expected as a function of time.

- b) The sampling time of the earth's magnetic field must be chosen in relation to the time constant of the transformers in the network.

This is a work in progress. Further work, will include testing the software with the test case arranged for GICs calculations by R Horton et al [26] and adapting the algorithm to include SECS.

ACKNOWLEDGMENT

The authors would like to thank our research collaborators; Dr. P.J. Cilliers and Dr. Stefan Lotz at the space science directorate of the South Africa National Space Agency (SANSA).

REFERENCES

- [1] P. Kundur et al: "Definition and Classification of Power System Stability - IEEE/CIGRE Joint Task Force on Stability Terms and Definitions", IEEE Trans. on Power Systems, Vol.19,No. 2, May, 2004.
- [2] P. F de Toledo, et al: "Multiple Infeed Short Circuit Ratio- Aspects Related to Multiple HVDC into One AC Network", ABB Power Systems, HVDC Division, Sweden, 2005.
- [3] T. S. Molinski: "Why utilities respect geomagnetically induced currents". Journal of Atmospheric and Solar-Terrestrial Physics 64, 2002.
- [4] P. R. Price: "Geomagnetically Induced Current Effects on Transformers". IEEE transactions on power delivery, vol. 17, no. 4, October 2002.
- [5] M. Heindl, M. Beltle, D. Schneider, S. Tenbohlen, D.T. Oyedokun, C.T. Gaunt: "Investigation of GIC related effects on power transformers using modern diagnostic methods", ISH, Hannover, 2011.
- [6] D.H Boteler, L. Trichtchenko, R. Pirjola, P. Parmelee, S. Souksaly, A. Foss and L. Marti: "Real-time simulation of Geomagnetically induced currents", 7th International Symposium on Electromagnetic Compatibility and Electromagnetic Ecology, 26-29 June 2007.
- [7] R. Pirjola: "Review on the calculation of surface electric and Magnetic fields and of Geomagnetically induced Currents in ground-based technological systems", Surveys in geophysics 23: Kluwer academic publishers, Netherlands, pp. 71-90, 2002.
- [8] A. G. McNish: "Magnetic storms," EEI Bull, pp. 361-370, July 1940.
- [9] P. J. Kellogg: "Terrestrial effects of solar activity," *Proceedings Minn. Power Systems Conf.*, October 1966.

- [10] V. D. Albertson and J. A. Van Vaelen: "Electric and Magnetic Fields at the Earth's Surface Due to Auroral Currents," IEEE Transactions on Power Apparatus and Systems, vol. PAS-89, no. 4, pp. 578-584, April 1970.
- [11] A. Pulkkinen, A. Thomson E. Clarke, A. McKay: "April 2000 geomagnetic storm: ionospheric drivers of large geomagnetically induced currents. Annales Geophysicae. European Geosciences Union, 2003.
- [12] M. Lehtinen, and R. Pirjola: "Currents produced in earthed conductor networks by geomagnetically-induced electric fields", Annales Geophysicae, pp. 479-484, 1985.
- [13] A. Viljanen, A. Pulkkinen, O. Amm, R. Pirjola, T. Korja, and BEAR Working Group: "Fast computation of the Geoelectric field using the method of elementary current systems and planar Earth model", Annales Geophysicae. European Geosciences Union, 2004.
- [14] A. Viljanen and R. Pirjola: "Statistics on geomagnetically-induced currents in the Finnish 400 kV power system based on recordings of geomagnetic variations", Journal of Geomagnetism and Geoelectricity (ISSN 0022-1392), vol. 41, no. 4, pp. 411-420, 1989.
- [15] R. Pirjola: "Geomagnetically Induced Currents during magnetic Storms", IEEE transactions on plasma science, vol. 28, no. 6, December 2000.
- [16] A. Viljanen and R. Pirjola: "Magnetic environment: science of GIC", Presentation at the First European Space Weather Week, 2004.
- [17] J. Koen: "Geomagnetically Induced Currents and its Presence in the Eskom Transmission Network", MSc Thesis, University of Cape Town, South Africa, 2000.
- [18] T. A. Tjimbandi: "Geomagnetically Induced Currents in South Africa", Bsc Thesis, University of Cape Town, South Africa, 2007.
- [19] O. Amm: "Ionospheric elementary current systems in spherical coordinates and their application", Journal of Geomagnetism and Geoelectricity, 49, pp. 947-955, 1997.
- [20] E.H. Bernhardt, T.A. Tjimbandi, P.J. Cilliers, C.T. Gaunt: "Improved calculation of geomagnetically induced currents in power networks in low-latitude regions", Power Systems Computation Conference, paper 677, Glasgow, July, 2008.
- [21] R. Pirjola, D. Boteler, A. Viljanen and O. Amm: "Prediction of geomagnetically induced currents in power systems", Adv Space Res. Vol.26, No.1, pp 5-14, 2000.
- [22] C.M. Ngwira, A.A. Pulkkinen, L.A. McKinnell and P.J. Cilliers: "Improved modeling of geomagnetically induced currents in the South African power network". Space Weather 6, 2008.
- [23] A. Pulkkinen, O. Amm, A. Viljanen and BEAR Working Group: "Ionospheric equivalent current distributions determined with the method of spherical elementary current systems", Journal of geophysical research, vol. 108, pp.1053, 2003.
- [24] D.H. Boteler, L. Trichtchenko, R. Pirjola, P. Parmelee, S. Souksaly, A. Foss and L. Marti: "Real-time simulation of Geomagnetically induced currents", 7th International Symposium on Electromagnetic Compatibility and Electromagnetic Ecology, 26-29 June 2007
- [25] J. Koen and C.T. Gaunt: "Disturbances in the Southern African power network due to geomagnetically induced currents", Cigre session, Paris, August 2002.
- [26] R. Horton, D.H. Boteler, T. J. Overbye, R. J. Pirjola and R. Dugan: "A Test Case for the Calculation of Geomagnetically Induced Currents", IEEE Transactions on Power Delivery, Issue: 4, October, 2012.

INVESTIGATING THE PERFORMANCE OF FACTS DEVICES (SVCs) IN THE ESKOM NETWORK

L Matake*, AK Saha*

*University of KwaZulu-Natal, School of Engineering, Durban, South Africa.

Abstract. With the concept of FACTS technology, there are high possibilities that power transfer issues such as maximum power transfer and voltage instability can be solved. This paper discusses the technical theory of FACTS devices and most their effectiveness as voltage control equipment in the Eskom Holding SOC Limited's electrical power network. Special emphasis is put on SVCs. The performance of these devices was determined by examining the primary stability parameters of the system such as power angle, reactive power and voltage variations. The simulation results reveal that indeed the SVCs installed at Hydra and Muldersvlei substations are performing well both under normal and during emergency conditions. The results were validated by simulations of real events using the DIG-SILENT Power Factory V14.1 Software.

Key Words. FACTS; SVC; simulation; Digsilent Power Factory; Eskom; transient stability.

1. INTRODUCTION

Today's power systems are large, interconnected and involves thousands of buses and hundreds of generators. Environmental as well as economic factors primarily govern the installation of new power stations and to transport this power, new transmission line are often needed to meet the ever increasing load demand. Hence, there is an interest in better utilization of available capacities by installing flexible ac transmission systems (FACTS) devices [1-2]. FACTS technology can significantly improve the steady state as well as the transient performance of power systems, including power flow and voltage control, available transfer capability (ATC) enhancement, oscillation damping, and transient stability improvement [3].

IEEE defined FACTS devices as "alternating current transmission systems incorporating power electronic-based and other static controllers to enhance controllability and increase power transfer capability" [4].

Eskom Holdings SOC Limited has an extensive electrical network across South Africa. Due to rapid growth in the residential, commercial and industrial sector loads, the utility now faces challenges in maintaining the demand versus supply equilibrium and ensuring quality supply. Eskom has had to install FACTS devices in its networks in order to enjoy the advantages mentioned earlier on. The research questions that this paper seeks to answer are:

- Why, where and how has Eskom installed FACTS devices in its network?
- Are the devices performing optimally and serving their purposes?

This paper seeks to investigate and evaluate the technical performance of the installed FACTS devices installed in the Eskom network. The paper's outcome will be to provide recommendations to Eskom regarding improvement of the performance of these devices, where necessary in view of enabling the company to transform its network to suit the latest smart grid.

2 LITERATURE REVIEW

2.1 Origins of FACTS Devices

FACTS controller history began in the seventies, when Hingorani proposed the scheme of power compensation in electrical power systems using power electronic applications [3]. The concept of FACTS as a total network control philosophy was then introduced in 1988 by Dr. N. Hungarian from the Electric Power Research Institute (EPRI) in the USA. The significant impact that FACTS

devices make on transmission systems arises from their ability to affect high-speed control.

2.2 Functions and benefits of FACTS technology

The fundamental applications of FACTS-devices are:

- Power flow control: FACTS devices based on the progressive semiconductor technology control the power flow in the transmission lines and extending the loadability of the available transmission system and therefore mitigating congestion [5-6].
- Voltage (stability) control: IEEE defined Voltage stability as "the ability of a system to maintain voltage so that when load admittance is increased, load power will increase and so that both power and voltage are controllable" [7]. A possible outcome of voltage instability is loss of load in an area, or tripping of transmission lines and other elements leading to cascading outages. In this case, reactive power support must be provided. FACTS controllers, such as static var compensator (SVC) and (static synchronous compensator) STATCOM, can be used for this purpose [8].
- Interconnection of renewable and distributed generation: Eskom is in the process of integrating independent power producers (IPPs) in an effort to incorporate solar and wind generation to its generating pattern currently dominated by thermal power stations. The forthcoming 100MW Sere Wind power station in the Western Cape will be commissioned in October 2013. This shift to wind energy will inevitably lead to large wind turbine generators (WTGs) being integrated into electric power grids. By so doing, series reactive power compensation becomes necessary to alleviate problems of voltage instability. Series compensation is an effective means of increasing power transfer capability of an existing transmission network; however, it causes a detrimental phenomenon called sub-synchronous resonance (SSR) in electrical networks. FACTS provide an effective solution to alleviate SSR and thyristor-based FACTS controllers have been employed in the field for this purpose [9].

2.3 Types of FACTS devices

In general, three basic types of FACTS devices can be identified according to the electrical parameters that they

control, as shown in Table 1.0. For example, the SVC is used to control active and reactive line flows (P, Q) whilst the phase angle regulator is used to control active power flow (P). The SVC and the STATCOM control reactive power flow (Q). There are a total of nine SVCs in the Eskom network of which three of them are located in the Eskom’s Western grid, which is the region under consideration in this paper. The Western grid covers major centres including Cape Town. The author chose to analyse this part of the Eskom network because the grid is very far away from the generation pool in Mpumalanga, to the north west of the country, and hence the grid experiences severe voltage control problems.

Table 1.0: Types of FACTS Devices [10]

Type	Parameter Controlled	FACTS Device
Series and shunt (Type A)	P and Q	UPFC
Series (Type B)	P and Q	TCSC, Static phase-shifter, SSSC
Shunt (Type C)	Q	SVC, STATCOM

2.4 Performance records of SVCs in Eskom

The criteria to determine performance of SVCs used in this report were twofold:

- 1 levels of plant availability (how often the SVC is in service)
- 2 SVC’s dynamic response to system voltage (supplying or absorbing vars correctly) in emergency situations such as fault conditions. The V-Q sensitivity must be positive i.e., the bus voltage must increase as the reactive power injection at the bus is increased. The SVC must meet the reactive power required to restore voltage to above 0.95 level of nominal voltage within 15 seconds.

The author did a study to determine the plant availability levels of SVCs. Figures 1, 2 and 3 show the plotted graphs of performance levels of three of the nine SVCs connected in the Eskom network. Status 1 means the device is healthy and operational whilst status 0 means the FACTS device is offline and/or out of order. Based on this study, it can be seen that over a period of ten months from January to October 2012:

1. Hydra SVC 1 was non-functional for 43 days (86 % availability)
2. Hydra SVC 2 was non-functional for 10 days (97% availability)
3. Muldersvlei SVC was non-functional for 19 days (93% availability).

The major reasons recorded for the outages of these devices were, among others:

- a) The SVC device has developed a technical fault.
- b) SVC is undergoing a planned service

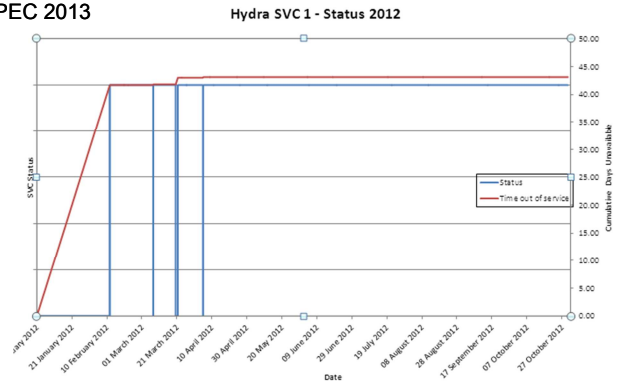


Figure 1 Hydra SVC1 performance

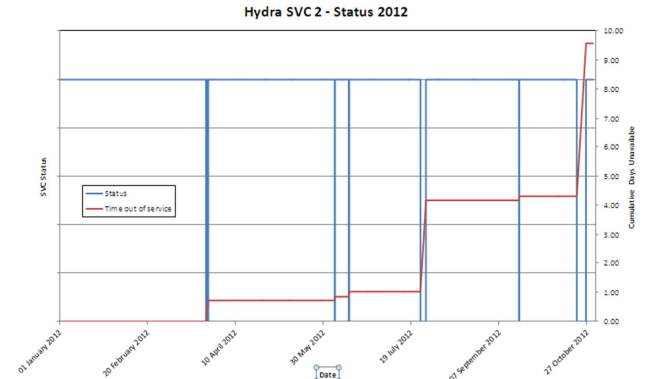


Figure 2 Hydra SVC2 performances

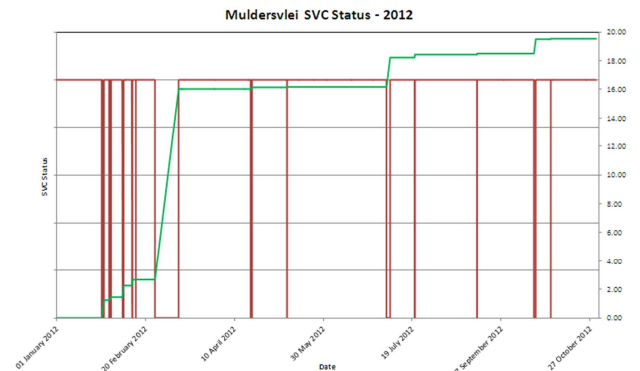


Figure 3 Muldersvlei SVC1 performances

The performance of these FACTS devices is very satisfactory as far as plant availability is concerned. To prove the good performances of the SVCs beyond doubt, Section 4 will show whether selected FACTS are performing optimally according to their set limits based on dynamic simulation results of real faults.

3 THEORETICAL ASPECTS OF FACTS DEVICES

3.1 Technology, theory and basic principles of reactive power compensation

To understand the technical aspects of FACTS, Figure 4 (a) is shown a model of a power transmission system and its equivalent phase diagram, which is simplified to economise on space. Two power grids are connected by a high voltage transmission line which is assumed to have no losses.

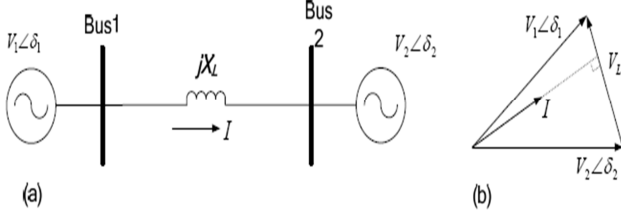


Figure 4 Power transmission system: 4(a) simplified model; 4(b) phase diagram [12]

The magnitude of the current in the transmission line is given by:

$$I = \frac{V_L}{X_L} = \frac{|V_1 \angle \delta_1 - V_2 \angle \delta_2|}{X_L} \quad (\text{Eq. 1.1})$$

The active and reactive components of the current flow at bus 1 are given by:

$$I_{d1} = \frac{V_2 \sin \delta}{X_L}, \quad I_{q1} = \frac{V_1 - V_2 \cos \delta}{X_L} \quad (\text{Eq. 1.2})$$

The active power and reactive power at bus 1 are given by:

$$P_1 = \frac{V_1 V_2 \sin \delta}{X_L}, \quad Q_1 = \frac{V_1 (V_1 - V_2 \cos \delta)}{X_L} \quad (\text{Eq. 1.3})$$

Similarly, the active and reactive components of the current flow at bus 2 can be given by:

$$I_{d2} = \frac{V_1 \sin \delta}{X_L}, \quad I_{q2} = \frac{V_2 - V_1 \cos \delta}{X_L} \quad (\text{Eq. 1.4})$$

The active power and reactive power at bus 2 are given by:

$$P_2 = \frac{V_1 V_2 \sin \delta}{X_L}, \quad Q_2 = \frac{V_2 (V_2 - V_1 \cos \delta)}{X_L} \quad (\text{Eq. 1.5})$$

The equations (1.1) through (1.5) depict that the active and reactive power or current flow can be regulated by controlling the following three variables: voltages, phase angles, and line impedance of the transmission system. The active power flow will reach the maximum when the phase angle δ is 90° . However, in practice, a small angle is used to keep the system stable from the transient and dynamic oscillations [13].

3.4 Configurations of the SVC

The IEEE definition of a SVC is "A shunt-connected static var generator or absorber whose output is adjusted to exchange capacitive or inductive current so as to maintain or control specific parameters of the electrical power system (typically bus voltage)". In principle the SVC consists of Thyristor Switched Capacitors (TSC) and Thyristor Switched or Controlled Reactors (TSR / TCR). The coordinated control of a combination of these branches varies the reactive power

During normal conditions, SVCs are operated with floating output so that rapid capacitive and inductive boost is available for severe disturbances. The SVC characteristic is illustrated in Figure 5

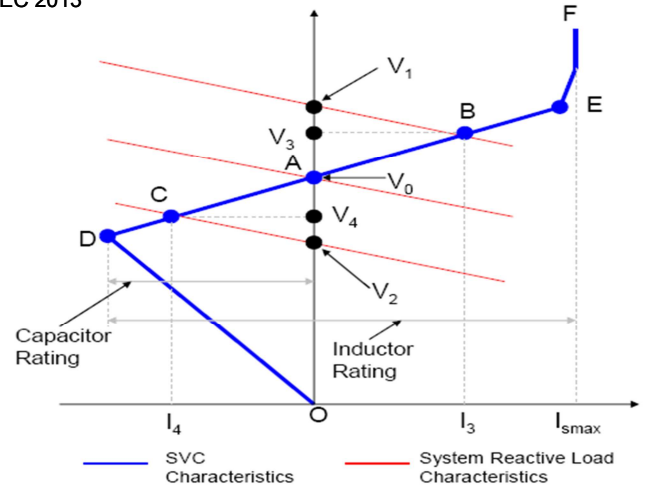


Figure 5: SVC Current-Voltage Characteristics [14]

- Line O-D: is capacitive (i.e. reactive power output, $Q_C = B_C V^2$)
- Line D-E: linear control range with slope K_S , the normal mode of operation is in this region (i.e. reactive power output, $Q(\alpha) = |B_C - B_L(\alpha)| V^2$). For this range of thyristor firing angles (α), the reactive power output of the SVC should vary between its maximum inductive MVar output (at $\alpha = 90^\circ$, corresponding to full conduction of its thyristors) to its maximum capacitive MVar output (at $\alpha = 180^\circ$, corresponding to zero conduction of its thyristors).
- Line E-F: inductive (i.e. reactive power output, $Q_L = |B_C - B_{Lmax}| V^2$)

where,

B_C is the full admittance of a capacitor

$B_L(\alpha)$ is the effective admittance of a controlled inductor

B_{Lmax} is the full admittance of an inductor

α is the thyristor gate firing angle.

I_{smax} is the maximum current that the inductor can handle.

Three system reactive load characteristics are considered in Figure 5 corresponding to three values of the source voltage (i.e. HV busbar where the SVC is connected to). The middle characteristics represent nominal system conditions, and are assumed to intersect the SVC characteristics at point A where $V = V_0$ and $I_S = 0$ (i.e. floating output) [14].

The reference voltage V_0 of the SVC is chosen such that, under normal operating conditions, SVC delivers close to zero reactive power so that the full control range of SVC is available for use during transient. For example, without the SVC the decrease in system load level will move (increase) the operating system voltage to V_1 (refer to Figure 5). However, with the SVC, the operating point moves to point B; by absorbing inductive current I_3 , the SVC holds the voltage to V_3 . Similarly, if the source voltage decrease (due to increase in system load level, the SVC holds the voltage at V_4 , instead of at V_2 without the SVC. The significance of K_S can best be explained as: If the slope, K_S , of the SVC characteristics were zero, the voltage would have been kept at V_0 for both cases considered above [14]. However, in the linear control range, the SVC voltage is not maintained constant usually. The slope of the control (droop) characteristics is positive (between 3 to 5%) and helps in

stable parallel operation of more than one SVC connected at the same or neighbouring buses and prevents SVC reaching the limits too frequently.

4 SIMULATION RESULTS AND DISCUSSION

DigSilent Powerfactory version 14.1 was chosen for this simulation because it is easy to use and caters for all standard power system analysis needs. To evaluate the performance of FACTS devices in the Eskom network, dynamic simulations were done whose results would show whether the installed devices are responding to disturbances correctly. The stability limit for transient and sustained voltage dips being investigated is that the SVCs should help to restore the bus voltage to above 0.95 levels within 5-15 seconds. In this paper, the dynamic behaviour of SVCs installed at Hydra 765 kV and Muldersvlei 400 kV substations in the Western region of Eskom was investigated.

4.1 Simulation setup procedures

The simulation approach was broken down into six chronological procedures as shown in Figure 7.

4.1.1 Identifying voltage dip incidents

This paper analyses two SLG faults on two different 400kV lines from major Eskom transmission substations. These two faults sourced from the Eskom Quality of Supply database form the basis of the investigation in this report. Two substations in the Western Grid were chosen. The reason for studying two faults at two different stations was to increase the level of confidence in the results; to enable the author to make a meaningful conclusion. The circuit configurations for both substations are similar before and after the fault. Appendices 1 and 2 show the voltage dip profiles, showing all phases for the Hydra-Droerivier 400 kV line and the Muldersvlei-Bacchus 400 kV line fault under investigation in this research. Figure 6a and 6b show the voltage and current profiles of one of the selected faults.

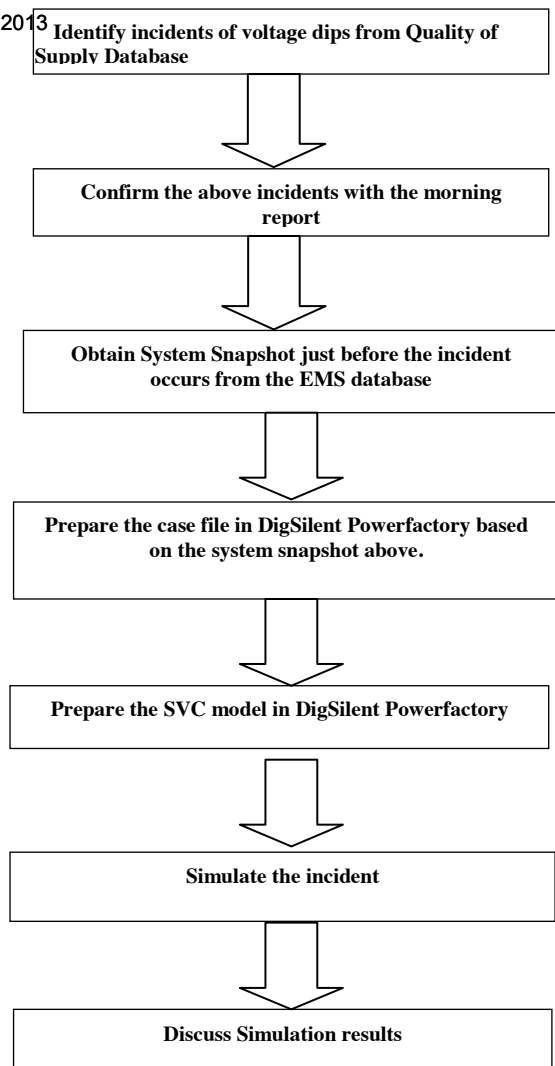


Figure 7 Simulation procedures

4.1.2 System snapshot and case -file

EMS is a database that keeps track of all events, statuses of network elements and loads. A five minute snapshot data immediately before the simulated faults occurred was taken for this study. This was to ensure that the study case file exactly resembles the state that the actual network was in terms of voltage at bus bars, line loading, etc. This was done to make the simulation scenario resemble that of the actual system.

4.1.3 DigSilent Powerfactory SVC modelling

For dynamic studies, the simulations will not run successfully without an SVC element correctly modelled. To do a load flow analysis using DigSilent Powerfactory version 14.1, the SVC element is modelled as shown in Figure 8. A Thyristor Controlled Reactor (TCR) of 500 Mvars together with a 250 MVar Manually Switched Capacitor (MSC) is used for the SVC. The linear control range of the SVC has a slope (droop) of 3%, as per Eskom’s stability analysis requirements.

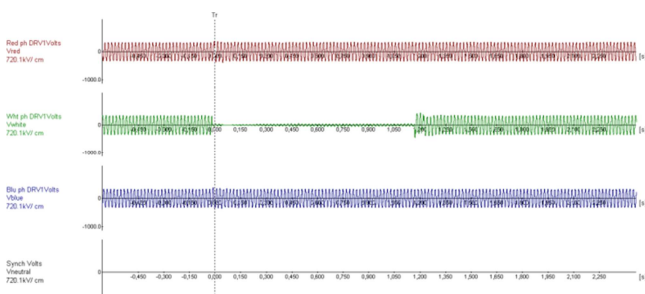


Figure 6a: Actual voltage profile before, during and after the SLG fault

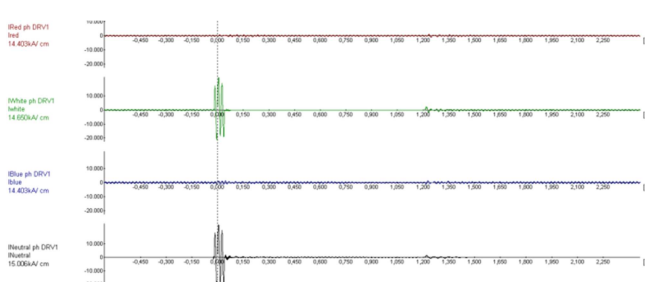


Figure 6b: Actual current profile before, during and after the SLG fault

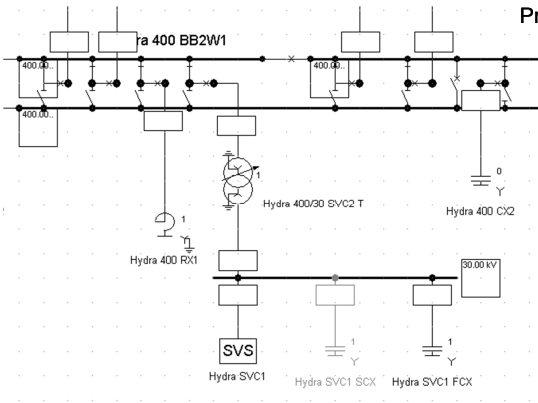


Figure 8 Modelling of SVC in DigSilent for load flow analysis.

The SVC is connected to the 400 kV bus bar, which it is controlling voltage via a step-up transformer. The reason for connecting the SVC on the LV/MV side of the transformer is to reduce the size and number of components required within the SVC. With proper co-ordination of the capacitor switching and reactor control, the reactive output of the SVC can be varied continuously between the capacitive and inductive ratings.

4.2 Simulations Results and Analysis

Transient stability analysis was performed for faults occurring in the Eskom system. The parameters measured were:

- a) Voltage magnitudes in p.u
- b) Voltage angles in degrees
- c) Reactive power response of the SVC in MVars

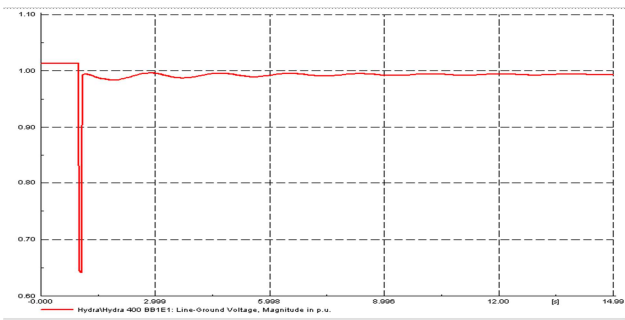


Figure 9a Simulated system voltage is restored to acceptable levels after the SLG fault.

Figure 9 shows that the SVC maintained voltage stability after a large disturbance due to the fault on the 400 kV Hydra-Droerivier transmission line. A similar voltage profile was obtained for the Muldersvlei-Bacchus line fault. The results of the simulation show that pre-fault voltage on the 400 kV busbar 1 at Hydra substation was 406 kV. During the fault, the voltage fell to as low as 323 kV, but the response of the two SVCs at Hydra lifted the voltage back to 398 kV and stabilised it to near 400 kV for over 15 seconds.

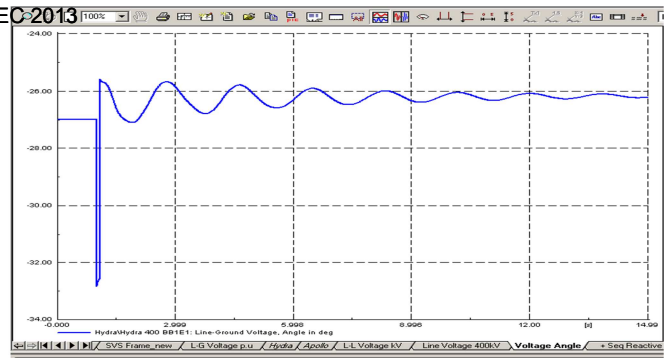


Figure 10 Simulated Hydra-Droerivier line Voltage-angle profile (deg.).

According to the basic power transmission equation

Real or active power transfer depends mainly on voltage angle. Steady state angle across a transmission line path between “voltage secure” busses should normally be less than 45° . In this case, the pre-fault voltage angle on the 400 kV bus bar at Hydra was 27° and then settled close to 26° in the post-fault equilibrium as Figure 10 shows.

Figure 11 shows how quickly the SVC responded to the voltage drop caused by the fault on the Hydra-Droerivier 400 kV line. Before the fault, the SVC was absorbing 217Mvars of reactive power to match the reactive power requirement at that equilibrium state. During the fault, when the 400 kV bus bar voltage was falling, the SVC dropped its absorption of reactive power so that the fall of the voltage due to the fault could be arrested by an additional availability of reactive power in the system.

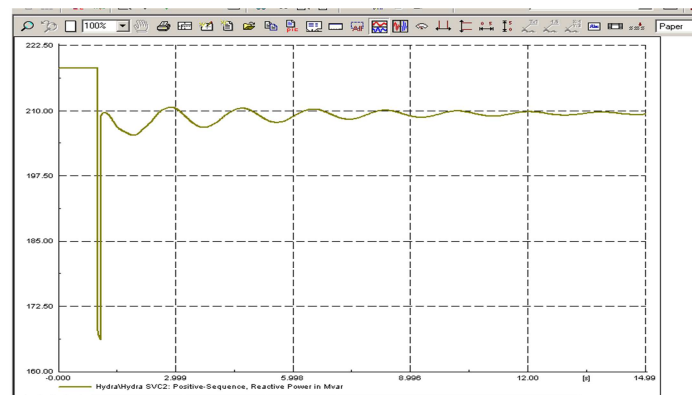


Figure 11 Simulated Positive Sequence Reactive Power response: Hydra-Droerivier line.

After the fault, it is clear that the SVC stabilised back to its steady state reactive power absorption of close to 210 Mvars. Its new equilibrium state of 210 Mvars is less than the pre-fault absorption due to more Mvars being required in the system after the voltage dip incident. The system would have become voltage unstable had the bus bar voltage magnitude decreases as the reactive power injection at the same bus is increased. In our case, according to the results of the simulations, it can be seen that the V-Q sensitivity measure was positive for the Hydra and Muldersvlei buses.

5 CONCLUSION

The author has presented his research on the performance of FACTS devices in the Eskom transmission network. The

simulation results have shown that the SVCs installed at two different substations responded correctly to 400kV real line faults of considerable fault currents.

General trends of the SVC control of the 400kV bus voltage are shown in appendix 3. This appendix clearly shows how the reactive power output of the SVC responds to the 400 kV bus voltages over a random 24- hour snap- shot. It reveals that, indeed, these FACTS devices are conforming well in accordance with Eskom and NERSA’s voltage control requirements and set limits of $\pm 5\%$ deviation from nominal or declared voltage at a customer busbar. However, the minimum voltage at any non-customer busbar may be allowed to reach 90% of the nominal after a contingency.

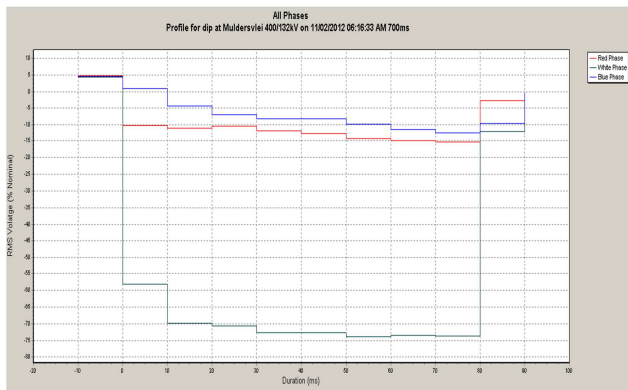
An SVC has been shown in this paper to be a suitable tool for dynamic reactive power support in high voltage transmission networks as it has been shown that bus voltages were restored to $\pm 5\%$ with 15 seconds after a disturbance. SVCs have been proven to have a capability for high speed, cycle-to-cycle control of vars thereby counteracting the often hazardous voltage depressions that follow in conjunction with line faults in the power grids. As Figure 9 shows, due to the SVC’s var absorption capability, it also effectively suppresses temporary over-voltages that appear upon fault clearing. Appendix 3, reiterates the fact that in steady-state conditions, the SVC at Hydra assists with accurate voltage control so that the 400 kV voltage profile of the Eskom grid is optimized.

ACKNOWLEDGEMENTS

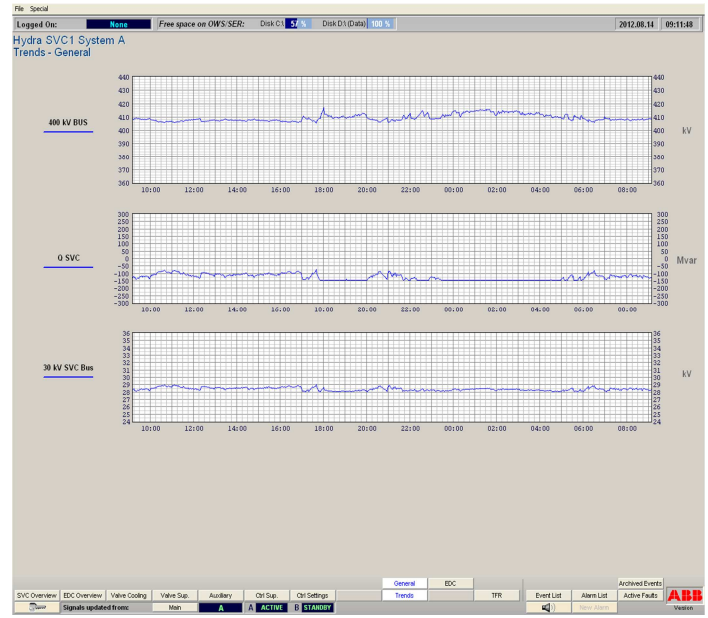
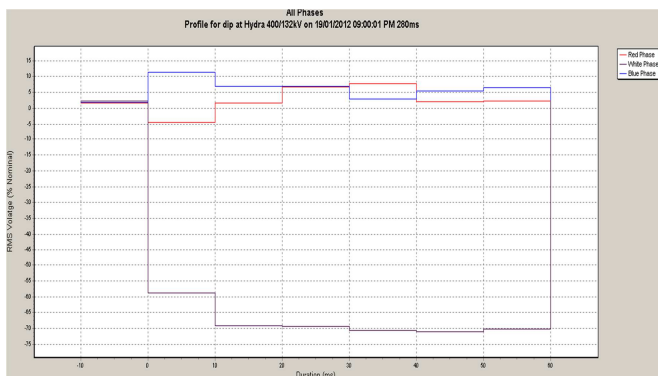
My gratitude goes to Dr.A K Saha, School of Engineering, UKZN Durban, SA, for his constant guidance, encouragement and assistance during this research.

APPENDICES

Appendix 1 Voltage dip profile, (all phases) for the Muldersvlei-Bacchus 400kV line fault [15].



Appendix 2 Voltage dip profile, (all phases) for the Hydra-Droerivier 400kV line fault. [15].



REFERENCES

- [1] S. N. Singh and A. K David, “Optimal Location of FACTS Devices for Congestion Management”, *Electric Power Systems Research.*, vol.58, pp. 71-79, July 2001.
- [2] A. Saha, P Das and A. K Chakraborty, “Performance Analysis and Comparison of Various FACTS Devices in Power System”, *International Journal of Computer Applications.*, vol.46, May 2012.
- [3] N.G. Hingorani and L. Gyugyi. “Understanding FACTS -Concepts and Technology of Flexible AC Transmission Systems”, *IEEE Press*, pp.245, 2000.
- [4] CIGRE, “FACTS Overview”, *IEEE Power Engineering Society.* 95 TP 108, April 1995.
- [5] M Dorostkar-Ghamsari, M Fotuhi-Firuzabad and F Aminifar, “Probabilistic Worth Assessment of Distributed Static Series Compensators”, *IEEE Trans. Power Delivery.*, vol.26, no. 3, pp. 1734-1743, July 2011.
- [6] H. Javaheri and R.G. Soloot, “Locating and Sizing of Series FACTS Devices Using Line Outage Sensitivity Factors and Harmony Search Algorithm”, *Energy Procedia 14-2nd International Conference on Advances in energy Engineering (ICAEE2011) (Science Direct)*, 2011
- [7] A. Wiszniewski, “New Criteria of Voltage Stability Margin for the Purpose of Load Shedding”, *IEEE Trans. Power Syst.*, vol.22, no. 3, pp. 1367, July 2007.
- [8] J. Zhu, K. Cheung, D. Hwang and A. Sadjadpour, “Operation Strategy for Improving Voltage Profile and Reducing System Loss”, *IEEE Trans. Power Syst.*, vol.25, no. 1, pp. 390, January 2010.
- [9] R.K. Varma, S.Auddy and Y.Semsedini, “Mitigation of Subsynchronous Resonance in a Series-Compensated Wind Farm Using FACTS Controllers”, *IEEE Trans. Power Syst.*, vol.25, no. 3, pp.1542, August 2010.
- [10] S. Haddad, A.Haddouche and H. Bouyeda, “The Use of FACTS Devices in Disturbed Power-Systems-Modelling, Interface, and Case Study”, *International Journal of Computer and Electrical Engineering*, vol.1, no.1, pp. 1793, April 2009.
- [11] [Discover the world of FACTS technology, Siemens Technical compendium]
- [12] N.G.Hingorani, L. Gyugyi, “Understanding FACTS, Concepts and Technology of Flexible AC Transmission Systems”, *IEEE Press 2000.*
- [13] L. Gyugyi, “Application Characteristics of Converter-based FACTS Controllers”, *IEEE Conference on Power System Technology*, Vol. 1, pp. 391 - 396, December 2000.
- [14] P. Kundur, “Power System Stability and Control”, McGraw-Hill, ISBN-13: 978-0-07-035958-1 (ISBN-10:0-07-035958-X, 1994.
- [16] Schauder, C.; Gyugyi, L. and others, *AEP UPFC project: Installation, Commissioning and Operation of the ±160MVA STATCOM.* Westinghouse Electr. Corp., USA, October 1998.
- [15] Eskom National Power Quality Database System-Data Viewer- Event Data. PQT Version 3.14, Copyright 1997, Developed by Eskom Enterprises (Pty) Ltd, TSI Division.

INVESTIGATION INTO THE PERFORMANCE OF PHASOR MEASUREMENT UNITS FOR POWER SYSTEM STABILITY APPLICATIONS – PRELIMINARY INVESTIGATIONS

B.W.D. Berry*, and K.J. Nixon****

* *Operations Planning, Eskom Transmission, Corner of Lake and Power Roads, Germiston, 1400, South Africa E-mail: brian.berry@eskom.co.za*

** *School of Electrical and Information Engineering, Private Bag 3, Wits 2050, South Africa E-mail: ken.nixon@wits.ac.za*

Abstract: Phasor measurement unit (PMU) technology has come to the forefront in terms of smart measurement of the power system in general. There has been extensive work done in this field which includes the publication of the IEEE C37.118 performance standard which has recently been revised. The question that remains however is whether these standards are satisfactory in ensuring adequate operation of the numerous Wide Area Monitoring System (WAMS) applications. This paper highlights some of the preliminary investigations into this question and overview of the methodology used to test this is explored.

Keywords: Phasor Measurement Unit (PMU), Wide Area Monitoring System (WAMS), synchrophasor, power system stability, IEEE C37.118.

1. INTRODUCTION

The modern era of power delivery is faced with many challenges due to decreased reserves, increased use of renewable generation, Flexible Alternating Current Transmission System (FACTS) devices, and changes in customer/load behaviour. In order to manage the risks introduced by these challenges, it is important to have near real time observability of the health of the power system [1]. Phasor Measurement Unit (PMU) technology provides high resolution, accurate measurement techniques which could be useful for power system monitoring however the link between the Intelligent Electronic Device (IED) accuracy and the end interpretation of the information is not clearly defined which could lead to complications or even invalid interpretation of the data. The aim of this work is therefore attempt to address and quantify this link to ensure that power system stability can be assessed in an accurate and practical manner.

2. UNDERSTANDING POWER SYSTEM HEALTH

The observability of power system health is divided into two categories: steady state and dynamic health.

2.1 Steady state health

Steady state health is fairly well understood and mitigated through contingency studies where the before and after states of multiple contingencies are determined using power simulation software. Traditionally this was done in an offline manner which is slow and inaccurate but advancements in this field are primarily focused around providing online analysis of contingency risks every few minutes [2]. Whilst this is not a new technology and has been implemented in many utilities, it can still benefit

from the use of PMU technology to improve the state estimator accuracy and speed [3].

2.2 Dynamic health

Dynamic health is defined by the ability of the power system to return to a state of equilibrium after disturbances. This is often referred to as power system stability and is divided into three categories as shown in Figure 1 below [4].

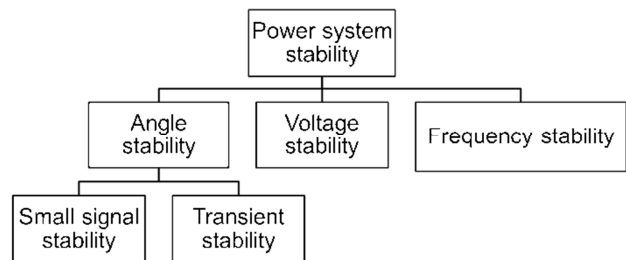


Figure 1: Basic categories of power system stability

Angular stability is of particular interest for this work as it is claimed to be accurately measured by PMU technology.

3. PMU MEASUREMENT TECHNOLOGY

One of the key benefits of PMU measurement technology is the use of highly accurate GPS timing to measure phase angle which can be compared over a wide area. This is done in the following way: the GPS time is used to construct a time reference (this is essentially the same over a wide area due to the high accuracy of GPS timing). This time reference is transmitted to the PMU via a 1 Pulse per Second (PPS) signal which is used to define the start of the second. The phase angle is then measured

as the angle difference between the start of the second and the peak of the wave as shown in Figure 2 [5].

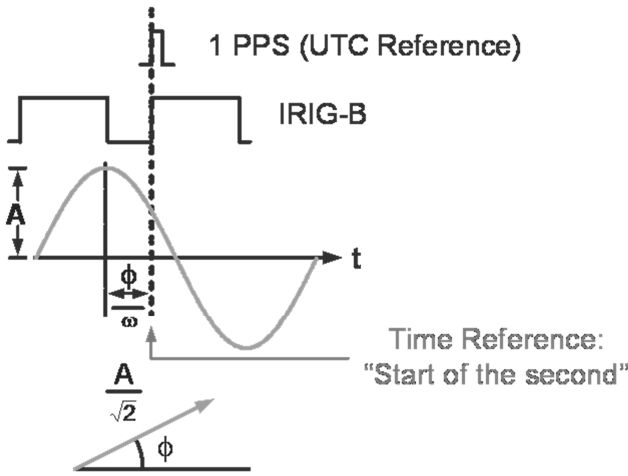


Figure 2: Phase angle measurement using a GPS time reference via the 1 PPS signal [5]

This time reference can then be replicated over each sample so that a relative angle can be calculated per frame. Therefore if the voltage is at synchronous frequency (i.e. 50 Hz) and the frame rate is a factor of this frequency (i.e. 10, 25 or 50 Hz) then the phasor would remain stationary. However if the frequency of the voltage signal was off nominal, the phasor would then rotate at a speed of $f_m - f_n$ where f_m is the measured frequency and f_n is nominal frequency [6].

This technique of phase angle measurement allows for the comparison of angles of a wide area. As per Figure 3 below, the difference between the voltage angles of bus 1 and 2 can be determined simply because they share the same time reference [6].

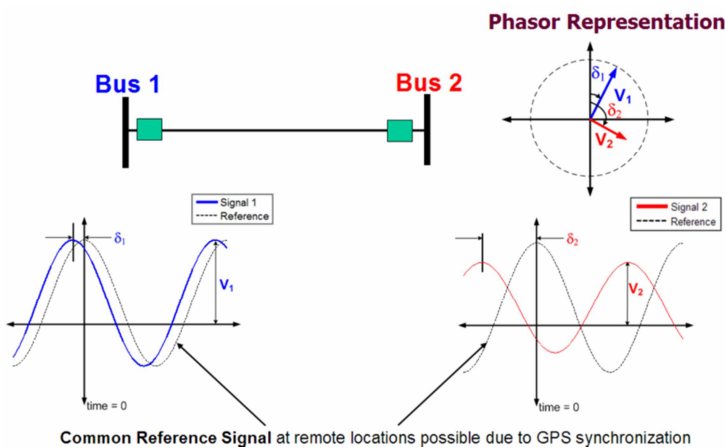


Figure 3: Voltage angle comparison over wide area [6]

Combining this measurement with high resolution reporting (up to 50 frames a second), makes this data extremely useful.

5. PMU PERFORMANCE

The standard which defines PMU performance, known as IEEE C37.118, was revised in 2011 but most vendors are currently still in the process of achieving full compliance with the predated 2005 standard [7].

The current C37.118 standard is divided into two parts, the first (C37.118-1) dealing with PMU measurements and performance and the second (C37.118-2) focusing on the protocol for data transmission [5, 8].

The C37.118-1 standard defines an error measurement metric which encompasses both the magnitude and phase error. This is known as the Total Vector Error and is defined as follows.

$$TVE = \sqrt{\frac{(X_r(n) - X_r)^2 + (X_i(n) - X_i)^2}{X_r^2 + X_i^2}}$$

Where $X_r(n)$ and $X_i(n)$ are the measured values, given by the measuring device, and X_r and X_i are the theoretical values of the input signal at the instant of time of measurement [5].

To elaborate, TVE is shown graphically in Figure 4. 1% TVE equates to an operational area within the circle which is contained by a $\pm 1\%$ magnitude and $\pm 0.573^\circ$ angle error tolerance [5].

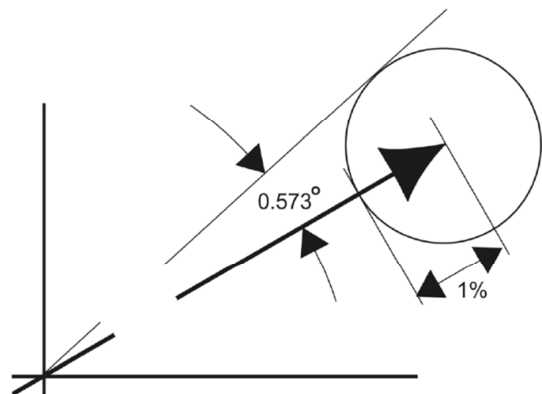


Figure 4: Total Vector Error (TVE) shown visually as an operational area of 1% magnitude and 0.573 degree angle tolerance [5]

The C37.118-1 also specifies an error calculation for both frequency and rate-of-change of frequency (ROCOF):

Frequency Measurement Error:

$$FE = |f_{true} - f_{measured}| = |\Delta f_{true} - \Delta f_{measured}|$$

ROCOF Measurement Error:

$$RFE = |(df/dt)_{true} - (df/dt)_{measured}|$$

The C37.118-1 standard defines performance in two parts: steady state and dynamic performance. These are clarified further below.

5.1. Steady State Performance

The steady state performance requirements are listed below:

1. Frequency accuracy
2. Magnitude accuracy (voltage and current)
3. Phase angle accuracy (voltage and current)
4. Harmonic rejection
5. Out-of-band interference (0-100 Hz oscillation acceptance/rejection)

5.2. Dynamic Performance

The dynamic performance requirements are listed below:

1. Modulation tests (amplitude and phase)
2. Frequency ramp test
3. Step tests (amplitude and phase)
4. Reporting latency test

6. WIDE AREA APPLICATIONS FOR PMU DATA

When the PMU data is consolidated into one central point, many application possibilities surface. Table 1 below lists a number of wide area applications that are currently required in the power industry [1]. These are categorised by the industry’s need for the application and the development time which is based on the deployment challenges such as the amount of PMUs required, telecommunications infrastructure and general application needs. It is important to note that whilst some of the listed industry needs could be achieved without PMU technology, it is beneficial for achieving these goals either quicker or more accurately.

Table 1: Wide area applications for PMU data

Description	Industry Needs	Time
Angle/Freq. Monitoring	Critical	Short term
Voltage Stability Monitoring	Critical	Short term
Thermal Overload Monitoring	Critical	Short term
State Estimation (Improvement)	Critical	Short term
Wide Area-PSS	Moderate	Short term
Power System Restoration	Critical	Short term
Post-event Analysis	Critical	Short term
SE boundary conditions	Critical	Medium term
Adaptive Protection	Moderate	Medium term
Congestion Management	Critical	Medium term
Real-time Control	Critical	Long term
Model Testing	Critical	Long term
Planned Power System separation	Critical	Long term

7. PROPOSED WORK

Whilst the IEEE C37.118-1 2011 standard is well defined, many vendors are not yet compliant with this or even its predecessor from 2005. The reason for this being that this standard is quite stringent and is aiming to cater for a wide variety of applications. This leads to a trade-off between steady state and dynamic performance. Steady state performance which deals largely with noise rejection requires long filter buffers which lead to delays in the dynamic response. Conversely, dynamic performance requires fast, accurate responses to disturbances but this inherently allows noise into the data signal [7].

This problem places the responsibility on the power utilities to define where the focus of accuracy will be. This task is challenging due to the variety of applications available to the utility and also the lack of understanding around the real performance requirements of each application.

This leads to some fundamental questions:

- *What performance is necessary for each application?*

Not all applications are the same and require different accuracies to perform correctly. It is important to define what accuracy is required for each application. This requires in depth analysis of the algorithms used to obtain the final results. This will include research around the algorithms as well as physical tests which will insert known signals into the PMU and compare results produced by the algorithms to the expected results.

- *What is the operating region of the PMU for each application?*

In order to define the correct test signal it is important to understand the realms of each application. This will once again involve research around theoretical expectations as well as statistical analysis of the phenomena in a real grid situation.

- *What is the effect of using multiple PMU vendors?*

The strength of PMU applications comes from being able to compare signals over a wide area. This has the added advantage that if the measurement contains an error this could have little effect since the same error will be repeated across all of the PMUs. This however will not be true if different vendors are used because there will be differences in the how the PMUs respond which could lead to comparative errors. It is important to understand and quantify these

errors. This will require the application of test signals across multiple PMUs from different vendors.

- *What is the real effect of small errors on the PMU side on the end result?*

Errors which seem relatively small on the PMU side could lead to larger errors on the final application result. For example, when using PMUs for line parameter estimation, a steady state accuracy of less than 1% TVE is required [7]. This will require testing of the algorithms with known signals. This could be done by applying a signal with a known error into the algorithm directly and observing the final error on the application output.

- *Can all of the wide area applications be met by one PMU type?*

Once the accuracy of each application is defined, each PMU's ability to meet these requirements can easily be defined by testing whether a single PMU (with a single set of preconfigured settings) can meet all of the requirements simultaneously.

8. TEST ENVIRONMENT CONSIDERATIONS

8.1. Practical Layout of WAMS Equipment

In practical applications, a WAMS would be connected in a manner similar to that shown in Figure 5 where the Central Phasor Data Concentrator (CPDC) condenses multiple streams into one to be used by multiple WAMS applications. This may vary slightly because of added Phasor Data Concentrators (PDCs) in the network path but the essential components are shown.

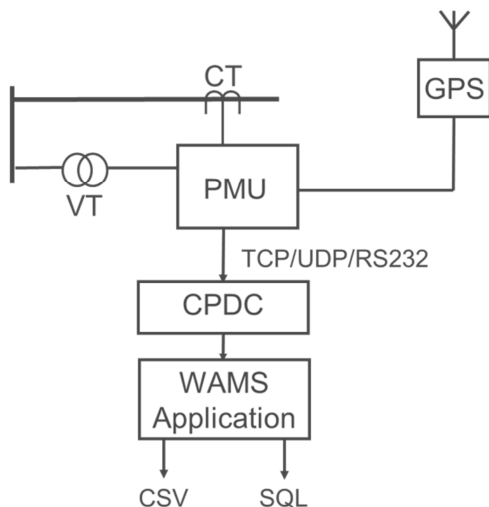


Figure 5: Practical connection of a PMU to a busbar and line via a CT and VT through to the central applications server

8.2. Instrument Transformer Accuracy Test Layout

Figure 6 shows the test layout for determining the accuracy of the current transformer (CT) and voltage transformer (VT).

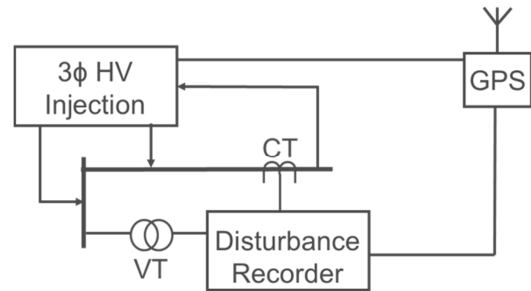


Figure 6: Test layout for determining CT and VT errors using simulated high voltage three phase signals

8.3. PMU Accuracy Test Layout

In order to test the errors produced by the PMU, instantaneous three phase values must be created and input into the PMU in real time. This layout is shown in Figure 7. It is best if the test set can be synchronised via the same GPS to ensure that the test signals are accurately compared.

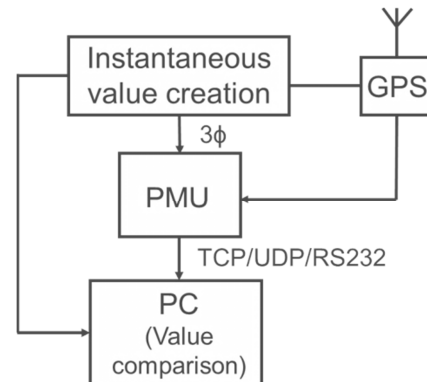


Figure 7: Test layout for determining PMU errors using simulated instantaneous values

8.4. WAMS Application Accuracy Test Layout

Once the PMU data errors have been quantified for all of the applications, these can be inserted into the WAMS application server as predefined error quantities in order to determine the effect on the final result. Figure 8 shows how a 'virtual PMU' (i.e. PMU data created via a simulated source) can be inserted directly into the CPDC providing it is in the C37.118 data format. The data can typically be exported from the application server via standard methods such as Comma Separated Values (CSV) file export or direct SQL database retrieval.

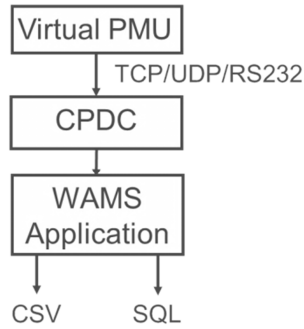


Figure 8: Test layout for determining the effect of PMU errors on the WAMS application

9. PRELIMINARY RESULTS

Some PMU accuracy tests have been completed for a single vendor using a standard secondary injection set. Whilst this is not of the highest precision, it is sufficient to determine conformance to the IEEE C37.118 standard. The precision of the Omicron CMC256 is < 0.03 % typ. (< 0.1 % guar.) for magnitude and < 0.02° typ. (< 0.1° guar.) for phase angle [8].

The results are summarised in tables below using the colour legend shown in Table 2.

Table 2: Colour legend for IEEE C37.118-1 2011 compliance

Legend		
Green – Passed requirement	Red – Failed to meet requirement	Grey – Not tested/

The following tests were done using a single vendor’s PMU using one setting configuration for all tests. These tests were all done using the highest available frame rate (i.e. 50 fps) and floating point measurement values.

9.1. Steady State Test Results

The results for the tests done in [9] are shown in the tables below. The test compliance is divided into two parts, the first is for TVE (shown in Table 3) and the second is the FE and RFE (shown in Table 4).

Table 3: TVE compliance for steady state tests

Accuracy Test	Requirement	
	P class	M class
	Max TVE (%)	Max TVE (%)
Frequency	1	1
Voltage magnitude	1	1
Current magnitude	1	1
Phase angle	1	1
Harmonic distortion	1	1
Out of band interference	None	1.3

The device was compliant for all tests except for the current magnitude test where the TVE requirement was exceeded at magnitude values of below 30 %. This is due to the current transformer used in the device and is a problem that is common amongst PMU vendors [7].

Table 4: FE and RFE compliance for steady state tests

Accuracy test	Requirements			
	P class		M class	
	Max FE	Max RFE	Max FE	Max RFE
Frequency	0.005 Hz	0.01 Hz/s	0.005 Hz	0.01 Hz/s
	0.005 Hz	0.01 Hz/s	0.005 Hz	0.01 Hz/s
Harmonic distortion	0.005 Hz	0.01 Hz/s	0.025 Hz	6 Hz/s
	0.005 Hz	0.01 Hz/s	0.005 Hz	2 Hz/s
Out-of-band interference			Max FE	Max RFE
	None	None	0.01 Hz	0.1 Hz/s

The filtering used on frequency is usually different to that used for current and voltage [7]. It is therefore possible to have non-compliance in terms of frequency error whilst not exceeding TVE. It is clear from Table 4 that the out of band interference test is non-compliant in terms of frequency. This is because the 2005 standard did not specify frequency accuracy and the filtering algorithm on frequency should therefore be improved to meet the recent 2011 requirement.

9.2. Dynamic Test Results

The results from the tests done in [10] are summarised in the tables below.

- Modulation Accuracy Test

As seen in Table 5, the TVE is below 3% for modulated frequencies of below 5 Hz (M class) and 2 Hz (P class).

Table 5: TVE compliance for modulation tests

Modulation Type	Requirement	
	P class	M class
	Max TVE	Max TVE
Amplitude	3 %	3 %
Phase	3%	3%

Table 6 shows that for a sample rate of 50 fps, the device maintains compliance for both FE and RFE.

Table 6: FE and RFE compliance for modulation tests

Modulation reference condition	Requirement			
	P class		M class	
	Max FE	Max RFE	Max FE	Max RFE
	Sample Rate > 20	0.06 Hz	3 Hz/s	0.3 Hz
Sample Rate ≤ 20	0.01 Hz	0.2 Hz/s	0.06 Hz	2 Hz/s

- Frequency Ramp Tests

The frequency ramp test requires that a 1 Hz/s ramp be applied to the voltage and current input values. It is clear from Table 7 that the FE remains within tolerance however the RFE value could not be determined due to the noise on the input signal. The noise on the input signal was due to the ramp consisting of discrete steps that were large enough to distort the ROCOF metric.

Table 7: FE and RFE compliance for the frequency ramp tests

Test Signal	Requirement			
	P class		M class	
	Max FE	Max RFE	Max FE	Max RFE
Frequency ramp	0.01 Hz	0.1 Hz/s	0.005 Hz	0.1 Hz/s

- Step Response Tests

Table 8 shows the TVE compliance for the step response tests. It is clear that this particular device setting passes for the M class requirements but not for P class. This is most likely due to the filter length used which is directly related to the response time. Therefore in order to achieve P class compliance, a filter of around 2 cycles or less would be required.

Table 8: TVE compliance for the step response tests

Step change	Requirement			
	P class		M class	
	Response time (s)	Delay time (s)	Response time (s)	Delay time (s)
Magnitude ± 10%	0.034	0.005	0.199	0.005
Angle ± 10°	0.034	0.005	0.199	0.005

Table 9 shows the FE and RFE compliance during the step tests. It is clear that RFE is non-compliant, however ROCOF is rarely used directly by applications and rather calculated centrally using the frequency signal, therefore this requirement may not require such stringent requirements [7].

Table 9: FE and RFE compliance for the step response tests

Step change	Response time requirement			
	P class		M class	
	Frequency (s)	ROCOF (s)	Frequency (s)	ROCOF (s)
Magnitude	0.07	0.08	0.130	0.134
Phase	0.07	0.08	0.130	0.134

10. CONCLUSION

The benefits and application possibilities of the synchrophasor technology are numerous and clear however the accuracy and performance requirements for these applications have not been explored extensively in a practical manner. The proposed work aims to quantify this error from the field equipment through to the application output. This information will help utilities to understand the limitations of the applications and thereby operate the power grids more effectively. An overview of the test bench required as well as some preliminary results from the PMU performance testing was discussed.

11. REFERENCES

- [1] D H Wilson et al., "Phasor-based wide area monitoring in the South African power system," *Energize*, pp. 32-38, June 2011.
- [2] Powertech Labs Inc. (2010, June) DSATools - VSAT Product Brochure. [Online]. http://www.dsatools.com/html/prod_vsats.php
- [3] JS Thorp AG Phadke, *Synchronized Phasor Measurements and Their Applications*, 1st ed., A Stankovic MA Pai, Ed.: Springer Science+Business Media, LLC, 2008.
- [4] P Kundur, *Power System Stability and Control*, 1st ed., MG Lauby NJ Balu, Ed.: McGraw-Hill, Inc., 1994.
- [5] Power System Relaying Committee, "IEEE Standard for Synchrophasor Measurements for Power Systems," IEEE Power & Energy Society, IEEE Std C37.118.1™ -2011, Dec 2011.
- [6] Performance & Standards Task Team (PSTT), "PMU System Testing and Calibration Guide," North American SynchroPhasor Initiative (NASPI), Dec 2007.
- [7] R Lira, D H Wilson, K Hay, and T Porrelli, "Performance Testing For Interoperability Of Phasor Measurement Units To Meet Application Requirements," in *International Protection Testing Symposium (IPTS)*, Brand, Austria, 2011.
- [8] Omicron, "Test Set CMC 256 Technical Data Sheet," V 4.5.1.0, 2012.
- [9] B Berry, "Eskom Verification of the WAMS PMU FAT of the 72B Firmware – Steady State Results," Eskom, Oct 2012.
- [10] B Berry, "Eskom Verification of Dynamic Results of the WAMS PMU FAT for the 72B Firmware," Eskom, Oct 2012.
- [11] Power System Relaying Committee, "IEEE Standard for Synchrophasor Data Transfer for Power Systems," IEEE Power & Energy Society, IEEE Std C37.118.2™ -2011, Dec 2011.

PROBABILISTIC METHODS APPLIED TO LOAD MODELLING IN RELIABILITY AND CUSTOMER INTERRUPTION COSTS EVALUATION

N. F. S. Ip Cho*, K. O. Awodele ** and R. Herman***

* Power System Group, Dept. of Electrical Engineering, University of Cape Town, Cape Town, South Africa, E-mail: *nicolas.ipcho@uct.ac.za **kehinde.awodele@uct.ac.za ***ronald.herman@uct.ac.za

Abstract: The work presented in this paper shows the impact of using deterministic and stochastic load models in reliability and customer interruption costs evaluation. The study focuses on probabilistic methods applied to the modelling of load in distribution power systems. The probabilistic approaches are compared to the deterministic, conventional methods. A description of four load models is provided in this paper and each model is developed and applied in a test system using loads data collected in South Africa. A sequential Monte Carlo Simulation technique is used to implement the models in MATLAB software. The aim is to demonstrate that using deterministic and stochastic techniques result in distinct results. Furthermore, this paper demonstrates that probabilistic methods provide a better representation of the actual load along with additional useful information that conventional techniques do not provide.

Keywords: customer interruption costs, distribution power system, deterministic, load modelling, probabilistic methods, reliability, stochastic

1. INTRODUCTION

Reliability and the costs of interruption that customers incur are important aspects to consider in planning for a distribution power system project. Reliability of power systems has become an increasing concern as power outages can have severe and direct socio-economic impacts. Therefore, the costs of interruptions should also feature as one of the cost elements when considering distribution planning projects. Utilities are trying to meet customer demands as economically as possible and at a reasonable level of supply reliability. Conventional deterministic methods have been used in the past by power utilities, however, these methods are not considered accurate representations of the actual customer load during an outage [1-6]. This paper presents probabilistic methods which are applied to load modelling in distribution power system. A comparative analysis is performed on existing load models to investigate the representativeness of actual load for each model and their respective modelling complexity and computation difficulty level. Traditional deterministic approaches are presented and utilized in this paper as base case and the results are compared to those of the stochastic approaches.

A deterministic model is defined as always producing the same output from a given starting condition or initial state. It therefore does not have any element of randomness involved in the development of future states. In contrast, subsequent states in a stochastic model are determined by both the process's predictable actions and by a random element. It is important to note that a model that uses any kind of time development (either deterministic or probabilistic) which is analysed in terms of probability deserves to be called a stochastic process. Several load models used in literature [1-6] have been

developed and implemented using a sequential Monte Carlo Simulation technique on a test system (Roy Billinton Test System, Bus 3) in MATLAB. The load models of interest in this paper are: (1) the average model, (2) the time varying model, (3) a stepped probabilistic model and (4) a Beta probability density function (PDF) Model.

2. LOAD MODEL ANALYSIS & CONCEPTS

Several load modelling techniques are used in literature for reliability or customer interruption costs (CIC) evaluation of power systems. A few of them are studied and described in this paper.

2.1 Average Load Model

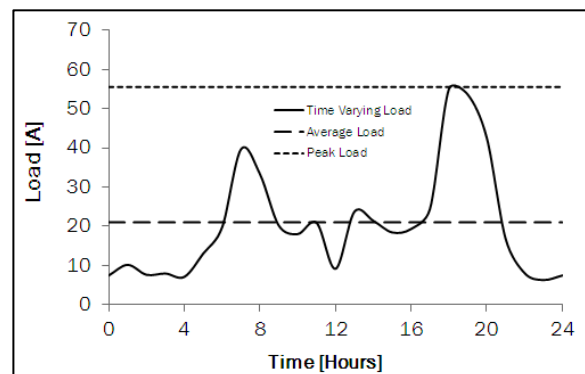


Figure 1: Example of a load profile showing the average load, the peak load and the time varying load.

The average load model is also known as a deterministic model and has been extensively used in reliability and CIC assessments in power systems [1-2, 7-11]. In general, the average values at the load points are used in

the reliability or CIC study. The average load model is described as only an approximation of the actual load in [1] and therefore is not considered an accurate representation. Customer load at a load point varies stochastically. In the average load model, the variation of load with time and the element of randomness in load usage are not portrayed when capturing interrupted load in a reliability study. The average load is illustrated in Figure 1.

2.2 Time Varying Load Model

The time varying load model is generally described as a more accurate representation of the actual load than the average load model [1-2, 8-11]. Although the time varying component is introduced in this approach, it is essentially a deterministic model as load interrupted during an outage at a specific time will be the same for future states and therefore does not contain any element of randomness when the interrupted load is concerned. However it is an improvement on the average load model since time, day and season are fundamental factors in determining the load loss during an outage. Figure 1 illustrates the difference in load variation using a 24 hour profile. However the more the factors (time of day, day of week, etc.) introduced, the more demanding are the data requirements and the more complex is the modelling procedure.

2.3 Stepped Probabilistic Load Model

The stepped probabilistic load model basically calculates probability values for intervals of the percentages of the peak load at a particular load point of the system [3-5]. The stepped load model is essentially modelled by grouping customer loads determined by the percentage of load intervals or clusters of load. The probability values are then calculated for each load interval or cluster. The number of steps used may vary and the more steps the loads are divided into, the more accurate will be the load representation.

This is also true for time varying loads where smaller time intervals (5min, 10min, etc.) used to model the load will result in a better accuracy. Table 1 shows an example of a step probabilistic load which uses a five-step load duration curve approximation method [4]. This method consists of getting a load duration curve and calculating the probability that the group of loads occur in a pre-defined period.

Table 1: Five-step load duration curve approximation [4]

Load Level (Peak)	Probability
90-100 %	0.001
80-90 %	0.025
70-80 %	0.040
60-70 %	0.097
< 60 %	0.837

For example, using a 24hr load profile, the probability that a load is interrupted during an outage is calculated by

weighing the amount of time that customer loads occur in a load interval (e.g. 90-100% of the peak load) over the total time (24 hours). Although the load modelling approaches in [3-5] may vary, the general concept is to group customer load into defined categories/groups and to calculate the probability of occurrence of each group.

2.4 Beta PDF Load Model

The probabilistic model using beta probability density functions can be applied to customer loads in reliability evaluations. A beta PDF approach is used in [6] to model the load for distribution systems. In this approach, the alpha and beta parameters are calculated from the load measurements obtained from [12] at 5 min intervals. The beta PDF is used in this assessment for the following reasons [6]:

- The customer loads are confined between 0 and the maximum, C, in the same way the Beta PDF is constrained to a finite base. C in this case is the circuit breaker limit.
- It can be negatively or positively skewed showing the shape of the customer load distribution, and the relative position of the mean, mode and median.
- Its parameters α and β can be easily found from existing data.

The stochastic nature of electrical loads makes statistical methods applied to load modelling very appropriate. In [13] light industrial loads are modelled stochastically by using probabilistic methods at a given time of occurrence. A similar concept is used in this paper using beta PDF to generate the load interrupted statistically at given time intervals using the sequential Monte Carlo simulation method.

3. TEST SYSTEM & DATA REQUIREMENTS

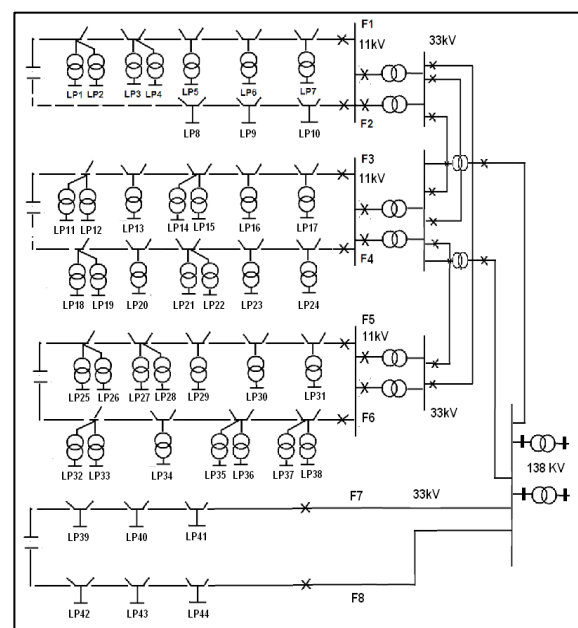


Figure 2: Bus 3 of the Roy Billinton Test System [14].

The test system used in this paper is illustrated in Figure 2. Due to number of components involved, only bus 3 of the Roy Billinton Test System (RBTS) is considered. RBTS is a distribution system consisting of 44 load points and a mix of residential and commercial customers. The reliability data required for this evaluation is available in [14], the load data were obtained from Herman and Gaunt [12] and the cost data in the form of customer damage functions for residential and commercial customers are available in [15]. A Failure Mode and Effect Analysis (FMEA) is performed on the RBTS to identify which load points in the system are affected when a component fails.

4. SIMULATION METHODOLOGY

The sequential Monte Carlo Simulation (MCS) technique is used to simulate the reliability and CIC evaluation of the RBTS. The simulation procedure for the MCS technique is available in [7] and it is used to design the simulation procedure which is written in MATLAB.

4.1 Time Reduction Technique

To reduce the computation time of the simulation performed for each load model, a reduction technique [2, 16] is used. The time reduction technique uses a stopping criterion as follows:

$$coefficient\ of\ variation = \frac{\sigma}{\mu\sqrt{N_s}} < \epsilon \tag{1}$$

Where:

σ = Standard deviation of the data series

μ = the mean of the data series

N_s = No of samples in the data series.

ϵ = Tolerance error

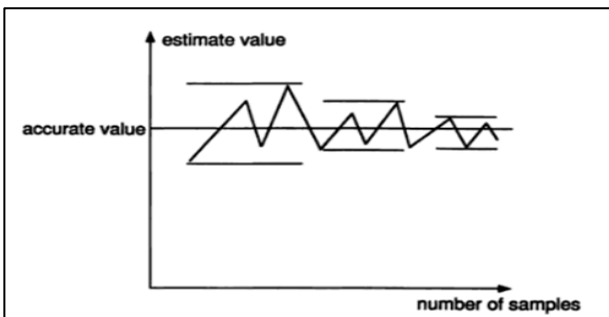


Figure 3: Convergence Process [16].

Figure 3 shows the convergence process occurring in the simulation as the number of simulation period increases. A tolerance error of 0.25% is used in each case study. In power system reliability evaluation, different reliability indices have different convergence speeds [16]. However a study in [16] shows that the coefficient of variation of the expected energy not supplied (EENS) index has the lowest rate of convergence. Therefore the coefficient of variation of the EENS is used as the stopping criterion for each simulation.

4.2 General Procedure (flowchart)

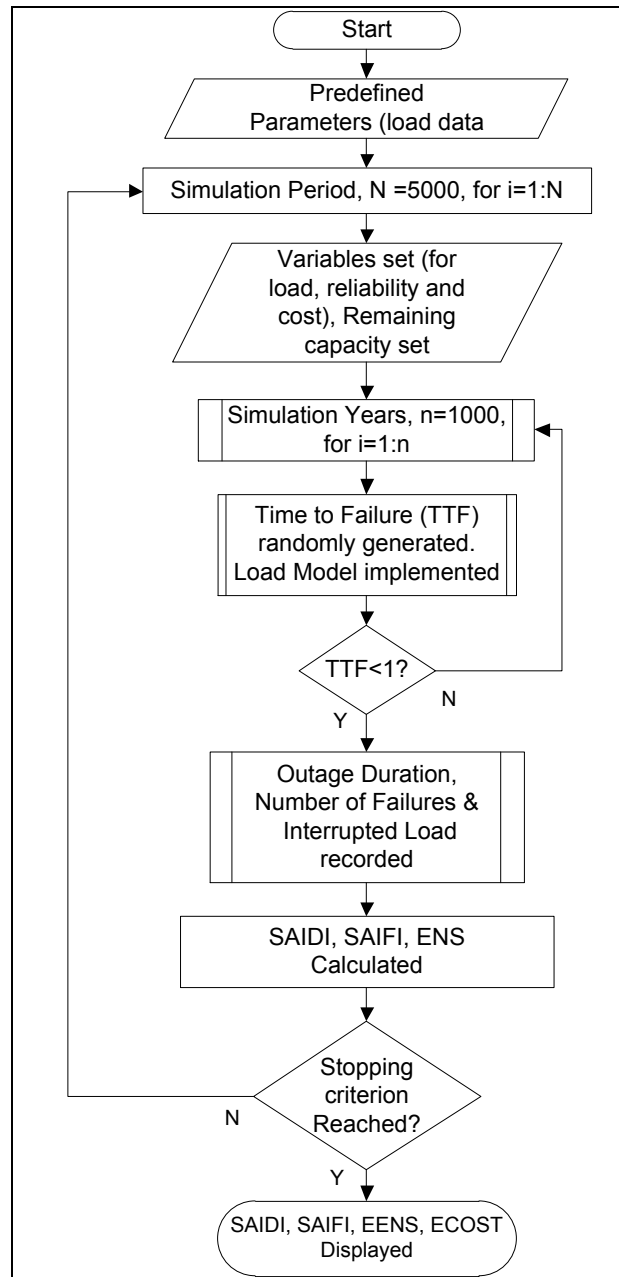


Figure 4: Simulation flow chart of the general procedure.

Figure 4 shows the flow chart which described the general simulation process implemented in MATLAB software package.

4.3 Computation Performance

With high performance computers made accessible and affordable, simulations are computed much faster than in the past. Therefore stochastic processes are more likely to be used in reliability and CIC evaluation than conventional techniques. The computation performance is also analysed along with the impacts of the load modelling technique used in each case.

5. APPLICATION OF LOAD MODELS

Several case studies are illustrated in Table 2 and the load, cost and reliability models for each case are shown. Average values for the cost and reliability models are consistently used in all the case studies while the load model is varied. The purpose is to obtain a comprehensive analysis of the impact of different load modelling approaches in a reliability or CIC evaluation.

Table 2: Case Studies

Case Studies	Load Model	Cost Model	Reliability Model
Case 1: Base Case	Average	Average	Average
Case 2	Time Varying	Average	Average
Case 3	Probabilistic	Average	Average
Case 4	Time varying & Probabilistic	Average	Average

The average load model is deterministic and is simple to model, however the approach does not adequately represent the customer load during an outage. In the time varying approach, the load is modelled as changing over time. However the method uses known values at hourly intervals and these values are repeated for future states. In contrast the stepped probabilistic load model assigns probability values to intervals of the percentage of the peak load. Each load modelling approach are described below as case studies 1-4.

5.1 Case Study 1: Base Case (Average Load)

The average load used in this paper is modelled deterministically and a single average value is assigned at each load point to represent the interrupted load.

5.2 Case Study 2: (Time Varying Load)

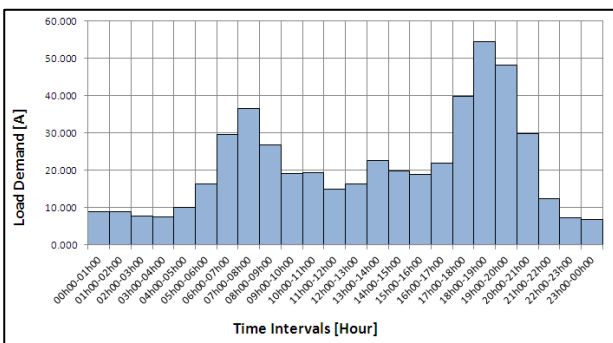


Figure 5: Variation of load over a 24 hour profile.

The time varying load is modelled as average values at hourly intervals of a 24 hours load profile at each load point. Load profiles are generated using the available loads data [12] for each load point.

A time parameter is introduced in the simulation and is randomly generated to simulate the time of day an outage occurs and the load at that time is used as the interrupted load as depicted in Figure 5.

5.3 Case Study 3: Stepped Probabilistic Load

Although the stepped probabilistic load is modelled by finding the probability for fixed intervals of the percentage of the peak load, predefined probability values are set along the time axis of a load duration curve and the equivalent percentage load levels are grouped to get several intervals of percentage load level of the peak load. An example of this is shown in Figure 6.

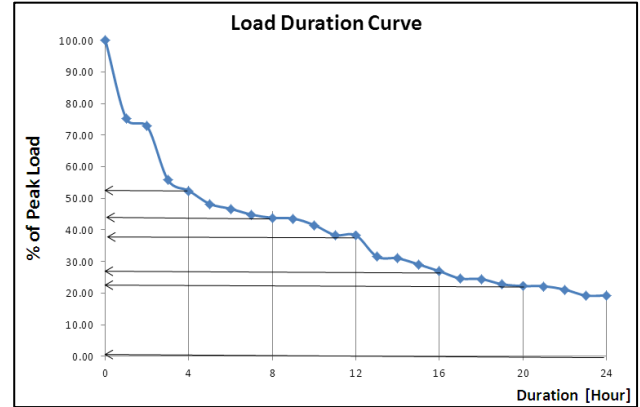


Figure 6: 24 hour load duration curve.

Therefore each interval of the percentage of the peak load has equal probability of one sixth for a total of 6 intervals. In the simulation, a uniform distribution is used to generate the load occurring in each interval randomly by finding the product of the probability of each interval (1/6) and the load value generated for each interval. The total load at that particular load point is found from summation of the product of each load level and probability, to get the interrupted load during an outage. The large number of steps along the duration axis taken will result in a more accurate representation of the actual load.

5.4 Case Study 4: Beta PDF Load

Case study 4 presents a combined time varying and beta probability density function fitted to the loads data [12] and the alpha and beta parameters are calculated at hourly intervals for each load point in the system. When an outage occurs, the alpha and beta parameters at time of occurrence are used for a particular load point to generate the interrupted load randomly using a beta probability density function. Figure 7 shows the variation of individual customer load at a load point in the system. The customer load varies with time and also from customer to customer. Therefore using the beta PDF model, the interrupted load that is generated considers both the customer load interrupted when an outage occurs at the time of the interruption as well as that based on the pattern of load usage of individual customers at a load point. These individual load values are generated randomly using the α and β parameters and the number of customers at a load point using the beta PDF and the summation of these loads are accounted for at the interrupted service point.

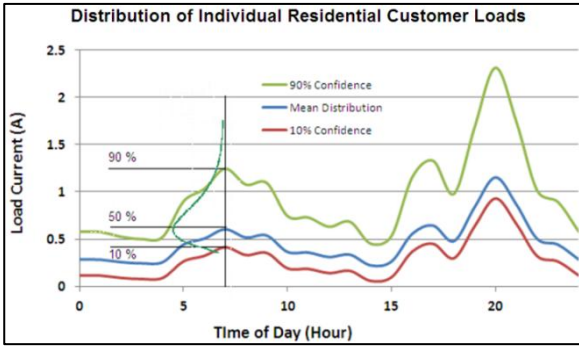


Figure 7: Beta PDFs with variation of individual loads.

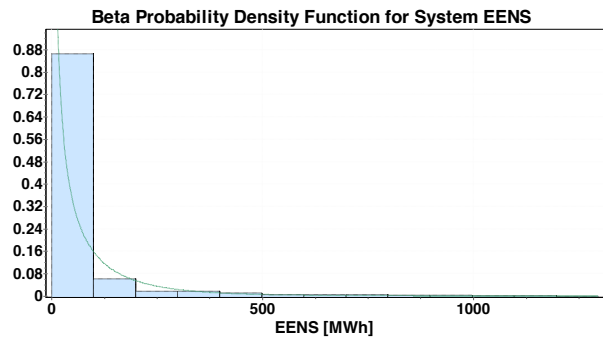


Figure 8: Beta PDF for system EENS.

6. SIMULATION RESULTS

The simulations are run for the four different load models individually with the assumption that if an outage occurs, feeders have enough capacity to fully supply each other when the normally open switch connecting them is closed. Therefore the load points that are not directly affected by a failed component in the system will only experience a switching time (usually the time taken to switch the tripped circuit breaker online) which is less than the repair time. The results for each case study were then captured and are shown below.

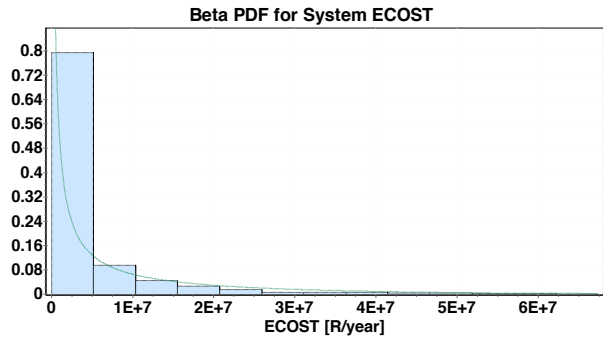


Figure 9: Beta PDF for system ECOST.

Table 3: EENS for each load model

Load Model	EENS [MWh/year]		
	Base Case	62.6942	
Case 1	65.3747		
Case 2	84.1262		
Case 3 mean	Risk Level		
	80%	50%	30%
	≤0.4843	≤13.2602	≤49.1471
	25%	20%	5%
	≤66.1164	≤88.9693	≤254.5566

Table 4: ECOST for each load model

Load Model	ECOST [Rand/year]x10 ⁶		
	Base Case	5.6445	
Case 1	5.8312		
Case 2	7.5594		
Case 3	Risk Level		
	80%	50%	30%
	≤0.00539	≤0.4458	≤3.436
	25%	20%	5%
	≤4.9783	≤7.1873	≤16.782

Table 5: SAIFI, SAIDI & simulation performance

Load Model	SAIFI	SAIDI [hr]	Processing Time [sec]
Base Case	0.2205	3.3474	40.09
Case 1	0.2206	3.4364	39.71
Case 2	0.2207	3.4533	53.05
Case 3	0.2201	3.4303	16.78

7. DISCUSSIONS

The values of SAIFI and SAIDI are very similar in all cases as an average reliability model is used throughout as shown in Table 5. The results obtained for the base case and case 1 are very similar as the load values used for the simulation are deterministic and therefore the outputs should in fact be close. However case 1, the time varying load model, does show a slightly higher expected energy not supplied (EENS) and expected costs of interruption (ECOST) than the base case due to the variation of load with time. Cases 2 and 3, in which the load is modelled stochastically using two distinct methods, result in a larger estimate of the EENS and ECOST. The load is stochastically modelled when it is generated in the simulation during an outage for each load point, where case 2 (stepped probabilistic model) uses probability values assigned to intervals of the percentage of the peak loads at the service points. A uniform distribution is applied to each interval and a value is randomly picked when calculating the interrupted load. For case 3, the values of EENS and ECOST are stored in vectors instead of additions per iteration, therefore removing the need for large number of simulations. The EENS and ECOST shown in the Tables 3 and 4 are the summation of individual load point EENS and ECOST values and the outcome is divided over the total number of years in the simulation to get the values of expected energy not supplied and expected costs of interruption in MWh/year and R/year respectively. The EENS and ECOST results for case 3 are much higher due to the way in which the load is modelled. It is also important to note that these values are much higher because the model does not use average values in

modelling the load nor probability values. Instead, individual customer loads are generated at each load point using the parameters α and β and C (found from historical load data) at hourly intervals for a 24 hour duration. Therefore the model considers both the time of interruption as well as the stochastic nature of the load. Again the values of EENS and ECOST are summed and divided by the number of years used in the simulation. Instead of using uniform distributions as case 2, the stochastic load at the time of interruptions are generated based on the customer's load pattern using a beta probability density function which can simulate various customer load profiles. Random individual loads are generated and summed to get a better estimate of the actual interrupted load. Additional information can be extracted from Figures 8 and 9, showing the beta PDF for the system's EENS and ECOST respectively, such as the average, minimum and maximum values in each distribution of individual load point EENS and ECOST.

8. CONCLUSIONS

The results obtained from simulations shows a clear difference in EENS and ECOST values when comparing the stochastic load models (stepped probabilistic and beta PDF) with the deterministic load models. As deterministic models do not take into consideration the randomness of customer load, the step probabilistic and the beta PDF load models can be considered to provide a better representation of the actual load. The results demonstrate that using average values and averages at hourly intervals does not portray accurately how and by how much (R/year) the customers are affected by interruptions. Therefore deterministic models are much simpler to model and faster to simulate and can be used to obtain a quick reference on what the energy not supplied and the expected cost of interruption in a power system would be on average. Alternatively, stochastic models can be used to obtain a better and more versatile representation of the actual load by providing the power system planner with values of EENS and ECOST associated with risk levels and by providing distributions for both variables.

9. REFERENCES

- [1] Peng Wang and Roy Billinton, "Time Sequential Distribution System Reliability Worth Analysis: Considering Time Varying Load and Cost Models", *IEEE Transactions on Power Delivery*, Vol. 14, No. 3, pp. 1046-1051, July 1999.
- [2] K. Alvehag, *Impact of Dependencies in Risk Assessment of Power Distribution Systems*. Licentiate Thesis Report. Stockholm, Sweden: Royal Institute of Technology, School of Electrical Engineering, Sept 2008.
- [3] Wenyuan Li, Jiaqi Zhou, Jiping Lu, and Wei Yan, "Incorporating a Combined Fuzzy and Probabilistic Load Model in Power System Reliability Assessment", *IEEE Transactions on Power Systems*, Vol. 22, No. 3, pp. 1386-1388, August 2007.
- [4] A. A. Chowdhury and D. E. Custer, "A Value-Based Probabilistic Approach to Designing Urban Distribution Systems", in *Proc. 8th International Conference on Probabilistic Methods Applied to Power Systems, Iowa State University, Ames, Iowa*, pp. 939-946, Sept. 2004.
- [5] Chanan Singh and Quan Chen, "Generation System Reliability Evaluation Using a Cluster Based Load Model", *IEEE Transactions on Power Systems*, Vol. 4, No. 1, pp. 102-107, February 1989.
- [6] R. Herman and C. T. Gaunt, "A Practical Probabilistic Design Procedure for LV Residential Distribution Systems", *IEEE Transactions on Power Delivery*, Vol.23, No.4, pp. 2247-2254, October 2008.
- [7] Roy Billinton and Peng Wang, "Teaching Distribution System Reliability Evaluation Using Monte Carlo Simulation", *IEEE Transactions on Power Systems*, Vol. 14, No.2, pp. 397-403, May 1999.
- [8] N.F.S Ip Cho and K.O. Awodele, "Load Modelling for Reliability and Customer Interruption Costs Evaluation", in *Proc. 19th South African Universities Power Engineering Conference*, Johannesburg, South Africa, pp. 108-113, Jan. 2010.
- [9] N.F.S Ip Cho and K.O. Awodele, "Impacts of using Average, Time Varying and Probabilistic Load Modelling on Customer Interruption Costs Evaluation in Power Systems", in *Proc. 20th South African Universities Power Engineering Conference*, Cape Town, South Africa, pp. 125-130, Jul 2011.
- [10] K. O. Awodele and N.F.S. Ip Cho, "Impacts of Different Load Models on Reliability Evaluation in Power Systems", *46th International Universities' Power Engineering Conference*, Soest, Germany, 5-8th Sept. 2011. Available: <http://ieeexplore.ieee.org/stamp/stamp.jsp?tp=&arnumber=6125570&tag=1>
- [11] K.O. Awodele and N.F.S. Ip Cho, "Investigating a Probabilistic Customer Interruption Costs and Energy Not Supplied Assessment for Electric Power Distribution Residential Customers", *10th IEEE Region 8 AFRICON Conference*, Livingstone, Zambia, 13-15 Sept. 2011. Available: <http://ieeexplore.ieee.org/stamp/stamp.jsp?tp=&arnumber=6072165>
- [12] R. Herman and C.T. Gaunt, "Direct and Indirect Measurement of Residential and Commercial CIC: Preliminary findings from South Africa Surveys", *PMAFS08*, Puerto Rico, June 2008.
- [13] P. Van Rhyn, J-H Pretorius and R. Herman, "Appropriate Statistical Load Models for Light Industrial Electrification", in *Proc. IASTED International Conference, Power and Energy Systems*, Crete, Greece, pp. 325-330. June 2011.
- [14] R. Billinton and S. Jonnavithula, "A Test System for Teaching Overall Power System Reliability Assessment", *IEEE Transactions on Power Systems*, Vol. 11, No.4, November 1996.
- [15] Michael Dijerenge, "Comparison of Customer Outage Cost Models in Quality Regulation of Electricity Distribution using Monte Carlo Simulations", *Thesis Report*, University of Cape Town, Department of Electrical Engineering, May 2009.
- [16] R. Billinton, and W. Li, "Reliability Assessment of Electric Power Systems Using Monte Carlo Methods", Plenum Press, 1994.

REVIEW OF BARE CONDUCTORS FOR OVERHEAD POWER TRANSMISSION

L P Luhlanga and A K Saha

University of KwaZulu Natal, School of Engineering.

Abstract. In parallel with the rapid growth of power transmission systems, notable changes on the types of conductor materials used for overhead power lines have occurred. This paper reviews the existing literature on the different types of bare conductors for overhead power transmission lines by pointing out the characteristics of the various conductor strands and the flexibility in line design obtained by varying the makeup of the conductors. The practical factors which govern the conductor applications such as sag control, corrosion and vibration resistance are discussed.

Key Words: Power transmission, overhead transmission line conductor materials, alloy, transmission capacity.

1. INTRODUCTION

The need to optimise power transfer in overhead transmission lines by cost-effective and environmentally friendly methods is directly linked with the choice of conductors [1]. Many innovative bare overhead power transmission line conductor designs have been developed to address the changing needs of power transmission. New alloys have been developed to provide increased conductivity, vibration resistance, low weight, high tensile strength, corrosion resistance and thermal resistance [2].

The selection of the optimum conductor type for a given transmission line design requires a complete understanding of the characteristics of all the available conductor types [3, 4, 5, 6]. The classifications of the conductors are based on the alloy combinations and the manufacturing processes used to develop the conducting and core materials of the conductor [7].

An example of a round wire, bare overhead stranded conductor is presented in Fig. 1, showing the conducting material and the core material. Several sizes and number of wire combinations (see Fig. 2) are available depending on the transmission application and manufacturing standards [7].

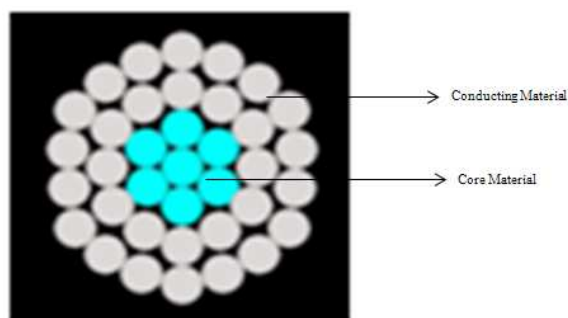


Fig. 1: Cross-section of a Typical Bare Overhead Conductor for Power Transmission

1.1 Conducting materials

The most used alloys for the conducting material are the 1350-H19 and 1350-OH series which consist of pure aluminium, and the 6201-T18 and 6201 series made of aluminium, magnesium and silicon alloy [8]. The latest developed alloy consists of aluminium, magnesium, silicon alloys with zirconium additions [9]. Proper controls of the alloying elements (Mg, Si and Zr) quantities are required to provide a compromise on the high strength-to-density ratio and good electrical conductivity. For instance, with the 6xxx series, an increase in the Mg and Si quantities causes an increase in strength but decreases the conductivity of the

alloy [10], whereas pure aluminium is more conductive, but has less strength compared to the alloyed material [11]. The aluminium-zirconium alloys are produced in order to increase heat resistance of the material. The poor thermal-resistant property of Al-Mg-Si alloys restricts higher operating temperature of all Aluminium alloy conductors [12]. Addition of Zr element increases the tensile strength and improves the ductility of the Al-Mg-Si alloy. Zr addition produces dispersion of fine Al_3Zr particles that slows down the recrystallization process, and hence increases the tensile strength [9, 12]. Aluminium alloys have superior corrosion resistance [9].

1.2 Core Materials

The most common core material is steel, chosen because of its availability and high tensile strength [7]. But new materials such as iron-nickel (Fe-36%Ni) alloy sometimes called invar; carbon/glass fiber polymer matrix and metal matrix composite have been developed [13]. These new core materials have lower coefficient of thermal expansion (CTE) than that of steel and provide low sag properties which help in increased power transfer capabilities [7]. The invar core is coated with a very thin layer of aluminium to increase the strength and to prevent corrosion. [13].

The carbon/glass fiber polymer matrix core is made of solid matrix with no voids. This solid polymer matrix core is composed of carbon fibers surrounded by an outer shell of boron-free E-glass fibers that insulates the carbon from the conducting material [14].

The metal matrix composite core is composed of stranded reinforced aluminium oxide fiber embedded in high-purity aluminium [7, 15]. The fiber reinforced metal matrix has strength similar to that of steel and weight similar to aluminium. The thermal expansion of the metal matrix core is less than that of steel and retains its strength at high temperatures [7, 15, 16, 17]. The wires have good corrosion resistance due to the compatibility between Aluminium and Aluminium oxide fibers, even at high temperatures with long thermal exposure [7].

The purpose of this paper is to present the available conducting material compositions to help utilities optimise conductor selection for a particular design based on specific conditions. The paper refers to published work for the available types of conductor materials and future developments, highlighting the properties of the conductors that offer flexibility for optimum transmission line designs.

2 CONDUCTOR TECHNOLOGIES

The international survey conducted by Cigre revealed that 82% of conductors installed by utilities worldwide are the Aluminium Conductor Steel Reinforced (ACSR) [18].

Hence, most of the conductor applications referred to in this paper are compared with the ACSR conductor. Some European countries showed preferences for All Aluminium Alloy Conductor (AAAC) and Aluminium Conductor Alloy Reinforced (ACAR) conductors in their newer lines. Special conductors such as Trapezoidal Wire (TW), Self-Damping Conductors (SDC), Aluminium Conductor Steel Supported (ACSS) and Twisted Aluminium pair (T2) conductors are used in North America [18]. The Japanese and Asian countries have installed High Temperature Low Sag conductors (HTLS) [18].

This section discusses the commercially available conductors. The profiles of these conductors are shown in Fig. 2.

2.1. ACSR Conductor

ACSR is the most common type of conductor used today [18]. It is composed of one or more layers of hard-drawn concentrically stranded 1350 aluminium wire with a high-strength galvanized steel core [7, 18, 19]. The core may be of a single wire or stranded depending on the size [7]. Because numerous stranding combinations of aluminium and steel wires may be used, it is possible to vary the proportions of aluminium and steel to obtain a wide range of current carrying capacities and mechanical strength characteristics [18].

The steel core may be furnished with three different coating weights of zinc. The "A" coating is the standard weight zinc coating. To provide better protection where corrosive conditions are present, heavier class "B" or "C" zinc coatings may be specified where "C" is the heaviest coating [7, 19].

2.2. ACSR/AW Conductor

ACSR/AW (Aluminium Conductor, Aluminium-Clad Steel Reinforced) conductor is similar to conventional ACSR except the core wires are high strength aluminium clad steel instead of galvanized steel [18, 19]. Aluminium-clad steel wire has a minimum aluminium thickness of 20 per cent of its nominal wire radius [19]. This cladding provides greater protection against corrosion than any of the other types of steel core wire, and it is applicable for use where corrosive conditions are severe [19]. ACSR/AW also has a significantly lower resistivity than galvanized steel core wire and may provide lower losses [18].

2.3. AACSR Conductor

AACSR (Aluminium Alloy Conductor Steel Reinforced) is an ACSR with the 1350 aluminium wires replaced by 6201-T81 aluminium alloy wires [7, 20]. The high tensile strength of the 6201-T81 wires combined with the high strength of steel provides an exceptionally high strength conductor with good conductivity [7]. AACSR conductors have approximately 40% to 60% more strength than comparable standard ACSR conductors of equivalent stranding, with only an 8-10% decrease in conductivity. [7] AACSR is available with all core types specified for use with standard ACSR [7, 18].

2.4. AAC Conductor

AAC (All Aluminium Conductors – 1350 H19) conductor is made up entirely of hard-drawn 1350 aluminium strands [7, 18, 19]. AAC is usually less expensive than other conductors, but is not as strong and tends to sag more when compared to ACSR conductor in particular [7, 18]. AAC conductors are most useful where electrical loads are heavy and where spans are short and mechanical loads are low [7, 18].

2.5. AAAC Conductor

A high strength AAAC conductor is composed entirely of 6201-T81 high strength Aluminium-Magnesium-Silicon Alloy wires concentrically stranded [7, 18, 20]. The alloy strength is comparable with that of ACSR [7]. It was developed to fill the need for a conductor with higher strength than that obtainable with 1350 aluminium conductors, but without a steel core [2]. AAAC conductor may be used where contamination and corrosion of the steel wires is a problem [21]. It has proven to be somewhat more susceptible to vibration problems than standard ACSR conductor strung at the same tension [7]. The disadvantages of using AAAC conductor are that it has lower breaking load capacity and limited self-damping properties compared to ACSR conductors [7]. The UK's assessment of the condition of the 275 and 400 kV Super-grid system showed that the major need for refurbishment of the existing lines is brought about by galvanic corrosion between the aluminium and steel, on ACSR conductors [10]. The homogeneity of aluminium alloy conductors gives, amongst other things, an improved corrosion resistance. Hence, AAAC was a major consideration in the UK's choices for the refurbishment programme [10].

2.6. ACAR Conductor

ACAR (Aluminium Conductor Alloy Reinforced) conductor consists of 1350 aluminium strands reinforced by a core of higher strength 6201 alloy [7, 18]. These 6201 reinforcement wires may be used in varying amounts allowing almost any desired property of strength/conductivity - between conductors using all 1350 wires and those using all 6201 wires to be achieved [7]. Strength and conductivity characteristics of ACAR are somewhere between those of a 1350 aluminium conductor and a 6201 conductor [21].

2.7. ACSR/SD Conductor

ACSR/SD (Aluminium Conductor Steel Reinforced - Self Damping) conductor may use either two layers of trapezoidal-shaped aluminium wires or two layers of trapezoidal-shaped aluminium wires and one layer of stranded round wires of hard-drawn 1350 aluminium [7, 18]. The steel core may be a single wire or stranded depending on the size of the conductor [18]. From a performance point of view, ACSR/SD conductor is similar to conventional ACSR except that it has self-damping characteristics [7]. That is, the conductor is designed to reduce aeolian vibrations. The damping occurs because of the interaction between the two trapezoidal layers and between the trapezoidal layers and the core [7, 18]. Special precautions and distinct procedures should be followed during stringing to avoid difficulties [7]. ACSR/SD conductor may be more expensive than conventional ACSR, but has the ability to be strung at higher tensions to reduce sag, which may result in economic advantages that offset its extra cost [7]. SDC conductors, have been used in North America for approximately 20 years and have a proven history of providing effective and cost competitive control of aeolian vibration without the use of additional hardware [22]. SDC conductors, have been used in North America for approximately 20 years and have a proven history of providing effective and cost competitive control of aeolian vibration without the use of additional hardware [23]. The lab and the outdoor tests performed by [23] showed that at very high tension, the amplitude of vibration of the SDC is well below the limit generally assumed to cause fatigue failures as compared to ACSR conductors. Also, the stress-strain graphs developed in [23] indicated identical behaviour under tensile loading, with ACSR curves.

2.8. ACSR/TW Conductor

As with ACSR/SD, the conductor layers of ACSR/TW (Trapezoidal Shaped Strand Concentric - Lay Stranded Aluminium Conductors, Steel Reinforced) are trapezoidal-shaped aluminium wires [7, 18, 19]. However, unlike ACSR/SD conductor, no gaps exist between layers ACSR/TW strands [19]. The compact trapezoidal-shaped wires result in an increased capacity for an equivalent standard range of ACSR conductor diameters [7, 19]. Also, for a given aluminium area, a smaller conductor diameter can be designed for ACSR/TW than for equivalent round-wire ACSR which results in reduced wind-on-wire load on the structure [7]. These are important advantages when existing transmission lines are considered for upgrading or reconductoring. Other advantages and improvements of ACSR/TW include corrosion resistance and lower temperature gradient [7, 19].

The use of ACSR/TW should be based on an economic evaluation to determine whether savings will be achieved in comparison with the use of conventional ACSR conductor [18]. Through comparing the power dissipation between TW 997.2 and ACSR 795 it was observed in [19] that the TW conductor has an internal damping of two to five fold compared to ACSR conductor for frequencies ranging from 10 to 50 Hz under a tension level of 25% RTS.

2.9. T2 Conductor

T2 (Twisted Pair Aluminium Conductor) conductors are invented by twisting two conventional (either ACSR or AAAC) conductors together [18, 19, 24]. This conductor helps to subdue mechanical oscillations caused severe wind and reduces galloping when the conductor is coated with ice [9, 16]. Central Iwo Power Co-operation (CIPCO) has 10 years of experience in using T2 conductors [25]. CIPCO's experience showed that the conductor costs just little more than ACSR conductor, can reduce the impact of ice and wind storms and minimize long term aeolian vibrations on transmission system without significant increase in operating or maintenance cost [25]. Also, rapid corrosion was experienced on the grade "A" galvanizing and so recommends the use of grade "B". Another bad experience was the irregular sub-conductor separations in the length of the wire caused by inadequate control at the factory. Special conductor stringing procedures are required [25].

2.10. Aero-Z Conductor [26]

Z-shaped profiled wires are used instead of conventional round wires. The last layer, virtually smooth, has small helical grooves created between the upper edges of the z-shaped wires with carefully chosen lay, depth and width for a significant reduction of the drag coefficient against strong winds. This reduction in drag coefficient induces lower stress on the support structures for an equal conductor diameter for maximum wind. Using compact conductors in any case reduces the reinforcements of the towers and foundations compared to what they would have been with conventional conductors. The large contact area between two z-shaped wires of a same layer constitutes an effective protection against seepage of the grease towards the outside of the conductor. The compact conductor, by contrast, maintains a constant level of protection against corrosion, thus guaranteeing slower ageing of the wires over time. The large surface of contact between the profiles also gives the Aero-Z better damping, which prevents galloping. [26].

2.11. HTLS Conductor

The conducting part of HTLS conductors are either developed using zirconium additions to aluminium to form

high thermal resistant alloys or fully annealed aluminium. The core of HTLS conductors can either be developed from invar (iron-nickel alloy) or metal matrix or composite [4, 5, 7].

The Al-Zr alloy is a hard aluminium alloy with properties and hardness similar to standard 1350-H19 aluminium [18]. However, the microstructure is designed to maintain strength after operating at high temperatures (210°C continuous and 240°C emergency) [7, 18] that when stressed, the Aluminium elongates and transfers the entire load to the conductor core [7, 16, 17, 18]. The core materials for HTLS conductors have low coefficient of thermal expansion for low sagging characteristics when compared to steel cores. A key characteristic of HTLS conductor core is the ability to control the knee-point temperature, the point where the load on the conductor shifts from the complete conductor to the core only. At temperatures exceeding this transition point, sag increase with temperature is reduced [17].

High temperature conductors are often used to uprate existing transmission lines, utilizing their decreased thermal expansion, higher allowable temperatures, or their higher cross-sectional area to increase ampacity without increasing final sag [16, 26]. Increases in allowable operating temperature correspond to significant increases in ampacity (conductor current carrying capacity) [4, 7, 8, 16, 17]. One benefit of HTLS conductors can be the avoided cost of replacing existing structures [4, 17]. The temperature ratings for these conductors can be limited by hardware, so extreme care should be used when specifying hardware and establishing operating temperature limits [7]. Also, the unique natures of these conductors result in the use of special precautions during stringing, such as special stringing blocks in certain locations and multiple grips when installing conductors with multi-layer annealed aluminium conductor strands [7, 18, 27].

ACCR (Aluminium Conductor Composite Reinforced) conductors are composed of heat resistant aluminium-zirconium alloy outer strands and aluminium oxide matrix core strands [5, 16, 18]. The core of the ACCR is composed of stranded fiber reinforced metal matrix, an aluminium oxide fiber embedded in high-purity aluminium [7]. The thermal expansion of the metal matrix core has less thermal expansion than steel and retains its strength at high temperatures [7, 17, 27]. ACCR conductors use similar stranding as ACSR. Because of the lightweight core, heat resistant outer and core strands, higher electrical conductivity, and lower thermal expansion for less sag, higher operating temperatures may be used with this conductor which leads to higher ampacity [7, 16, 17, 18]. ACCR conductors and hardware are usually rated up to 210°C continuous operating temperatures with 240°C for short term maximum operating temperature [17, 18].

ACCC (Aluminium Conductor Composite Core) are composed of trapezoidal wire of 1350 Aluminium stranded around the composite core [14, 18]. The 1350 Aluminium trapezoidal wires are fully annealed which make them softer compared to the hardened Aluminium wires used in some other conductors [14, 16, 18]. ACCC conductors are rated up to 180°C continuous operating temperatures with 200°C for short term maximum operating temperature. However, because of the softer temper of the Aluminium wires, the outer wires can be more susceptible to damage from improper installation and handling. Advantages of the ACCC design are two-fold [14]. Firstly, carbon fibers have an axial coefficient of thermal expansion that is slightly negative upon heating. Secondly, the tempered Aluminium wire used in the ACCC design has a significantly lower

resistivity than the 1350 H19 Aluminium used in the ACSR. Thus, the ACCC line will generate less heat than the steel reinforced designs, resulting in significantly less sag. The fully annealed aluminium also allows the ACCC lines to transmit 2-3 times more current than ACSR lines at equal temperatures [7, 18].

ACSS (Aluminium Conductor Steel Supported) conductor is similar to ACSR; however, the aluminium strands in ACSS are fully annealed and depends on the steel for its strength and sag characteristics [17]. ACSS conductors and hardware are usually rated up to 250°C or more continuous operating temperature, depending upon the coating on the steel core, without loss of strength [7, 16, 17, 18]. However, because of the softer temper of the aluminium wires, the outer wires can be more susceptible to damage from improper installation and handling [7].

(Z)TACSR (Aluminium-Zirconium Conductor Steel Reinforced) conductor is identical to conventional ACSR conductors [16, 17]. The aluminium alloy used in (Z)TACSR has a slightly higher electrical resistivity than standard hard-drawn aluminium, but in all other respects the two conductors are almost identical [16]. (Z)TACSR is not, by design, a low-sag conductor. It has the same thermal elongation behaviour as ACSR [16]. The main advantage of (Z)TACSR is that its aluminium alloy wires do not anneal at temperatures up to 150°C for TAL and 210°C for ZTAL - temperatures above 100°C would cause annealing of the aluminium strands in standard ACSR [16, 17]. (Z)TACSR can be used to uprate existing lines where some additional clearance is available.

(Z)TACIR (Aluminium-Zirconium Conductor Invar Reinforced) conductor has a conventional stranded construction identical to ACSR [18]. In place of the steel strands of (Z)TACSR, it has galvanised or aluminium-clad invar alloy steel wires for the core and extra thermal resistant (ZTAL) wires surrounding them. ZTAL resists annealing up to a continuous temperature of 210°C [17, 18]. The coefficient of thermal expansion of invar wire is around one third that of galvanised or aluminium-clad steel wire. The installation methods and accessories for the conductor are virtually the same as those used for conventional ACSR [18].

G(Z)TACSR (Gaped Aluminium Conductor Steel Reinforced) or Gap-type conductor has small gap between steel core and innermost shaped aluminium layer, in order to allow the conductor to be tensioned on the steel core only [4, 5, 8, 16, 17, 27]. This effectively fixes the conductor's knee-point to the erection temperature, allowing the low-sag properties of the steel core to be exploited over a greater temperature range [18]. The gap is filled with heat-resistant grease, to reduce friction between steel core and aluminium layer, and to prevent water penetration and aeolian vibrations [27].

Fig. 3 presents the alloy combinations of conducting and core materials used in each conductor type.

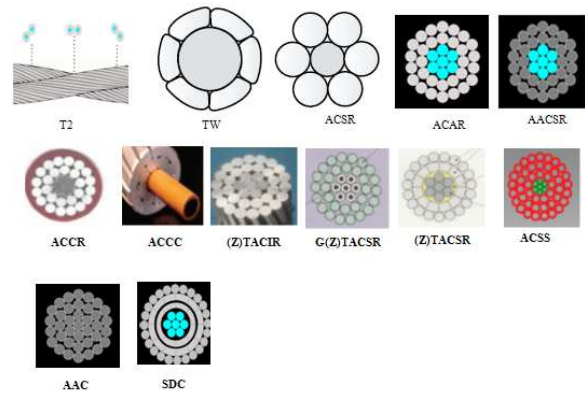


Fig. 2: Overhead power transmission conductors [28]

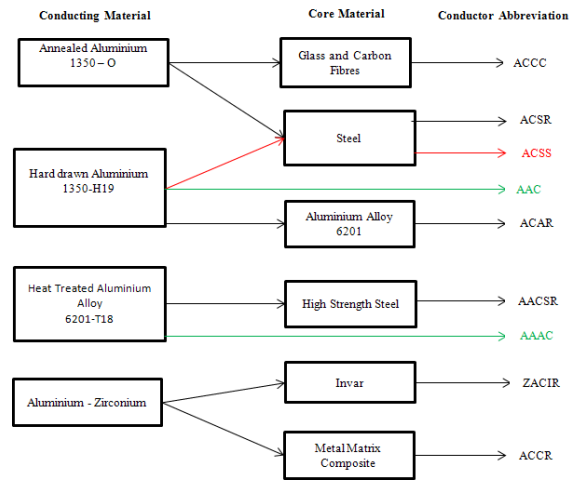


Fig. 3: Overhead Power Transmission Conductor Materials Combinations

3 FUTURE DEVELOPMENTS

Newer alloy developments with more improved mechanical and electrical properties based on thermal resistance and lower CTE than the existing alloys are underway. These include combinations of manganese, scandium and zirconium additions to the aluminium alloys containing magnesium and silicon for the conducting materials [29]. The available combinations of the conducting and core materials need to be further investigated to determine the best electrical and mechanical performing pair. For instance a combination of annealed aluminium and high strength steel or annealed aluminium and the metal matrix composite core need to be investigated and compared to the available combinations. Furthermore, self-damping and trapezoidal shaped HTLS conductors need to be developed and tested. So far only the ACCC, ACSS and the G(Z)ACSR conductors have been developed in trapezoidal shapes.

4 DISCUSSION OF REVIEW

4.1 Conductor Material Properties

Table 1 shows the electrical and thermal properties of the conductor materials. Table 1 reveals that fully annealed aluminium (1350-OH) has a high conductivity and high operating temperature than the other listed materials. Although the Hard-drawn aluminium (1350-T18) has a higher conductivity, it has the lower operating temperature. Aluminium zirconium based thermal resistant alloys have a good balance of conductivity and operating temperature following the fully annealed aluminium.

Table 1: Aluminium Types for Conductors [4, 16, 17]

Types of Aluminium	Conductivity (%IACS*)	Max. Operating Temp. (°C)
Hard Drawn (1350-H19)	61.2	80-90
6201-T18	53	80-90
Thermal Resistant (TAI) (Al-Zr)	60	150
Super Thermal Resistant (ZTAI) (Al-Zr)	60	210
Fully Annealed (1350-OH)	63	200-250

* IACS = International Annealed Copper Standard

Table 2 shows the mechanical properties of the conductor core materials. The polymer matrix core has the highest tensile strength and a very low coefficient of thermal expansion compared to the other cores. A high modulus of elasticity is given by the metal matrix core. Although the galvanised steel core has a low tensile strength, and a high CTE, it has the second highest modulus of elasticity.

Table 2: Core Types for Conductors [17]

Types of Core	Tensile Strength (MPa)	Modulus of Elasticity (GPa)	Thermal Expansion ($\times 10^{-6}/^{\circ}\text{C}$)
Galv. Steel	1230-1965	207	11.5
Al. Clad Steel	1515-1825	162-174	13.0 - 11.8
Galvanised Invar Steel	1030-1080	162	
Polymer core	2200	117	1.6
Metal Matrix	1300	216	6.3

4.2 Conductor Current Carrying Capacity

Fig. 4 presents the ampacity of the different conductors developed between the years of 1910 – to – 2000. From the figure it is shown that the HTLS conductors offer better ampacity compared to the ACSR and AAAC conductors. The ACSS conductor and the G(Z)TACSR conductors currently have the highest values of ampacity compared to all the available conductors. New conductor alloys are currently being researched and will have the highest ampacity in the future [29]. The G(Z)TACSR conductor's high ampacity is further enhanced by the trapezoidal shaped wires, that help increase the conducting surface area with a reduced overall conductor diameter.

4.3 Vibration and Corrosion Resistance

The SDC conductor designs allow for a small gap to exist between the conducting layer and the core [30]. The presence of these small clearances between layers divides the conductor into distinct components, each with its own natural frequency of vibration. Because these inter-layer

gaps are maintained even when the conductor is under tension, it follows that their vibration performances are independent of tension and thus they have improved self-damping properties than the mostly used round wire designs [31].

The inherent corrosion resistance of aluminium and its alloys is due to the thin-tough aluminium oxide coating that forms immediately after a fresh surface of metallic aluminium is exposed to air [32]. Instances where corrosion has appeared are usually traceable to connections between dissimilar metals subjected to moisture conditions [12]. As such, TW conductors are very good in corrosion resistance because there are no gaps between the aluminium strands as compared to round wire conductors.

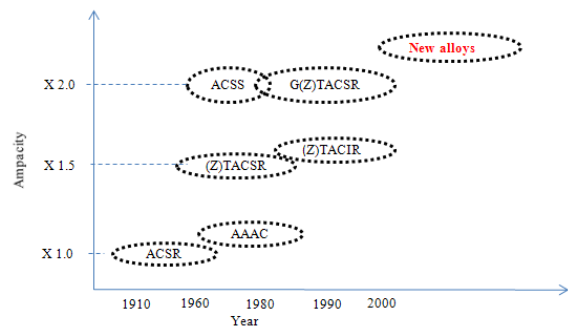


Fig. 4: Conductor Ampacity Comparisons

5 CONCLUSION

There is a wide variety of conductors that have been developed for specific power transmission applications. The size and the shape of the conductor are manipulated to provide increased current carrying capacity, corrosion resistance and vibration resistance. A good compromise between the tensile strength and electrical conductivity is achieved by the alloy combinations used for the conducting and core materials of the conductor. Compact and specially designed conductors such as the T2, TW, SDC, and Aero-Z conductors can be used to damp aeolian vibrations for very long spans. AAC and AAAC conductors can be used in high corrosive environments. The HTLS conductors offer better benefit to ACSR and AAAC conductors for operations at high temperatures. The main advantage of HTLS conductors is related to the fact that uprating is obtained without need to strengthen the towers. The available conducting material compositions help utilities to optimise conductor selection for a particular design based on the specific conditions. The modifications on the conductor materials can reduce; cost of land, difficulty in right-of-way acquisition, environmental impact associated with bare overhead power lines, conductor material degradation and fatigue due to unfavourable environmental operation conditions, conductor swing and sag [33, 34, 35]. Hence, the choice of a conductor for overhead transmission lines should depend on specific circumstances and conditions applicable to a project rather than mere standardization.

REFERENCES

- [1] A. R. Pettersson, W. Bronnvall, "A1 59 A Swedish Standard for Overhead Aluminium Alloy Conductors with 59% Conductivity (IACS)", IEEE Conference Proceeding, Sweden, Swedish State Power Board, 1988.
- [2] S. Karabay, "Modification of AA-6201 Alloy for Manufacturing of High Conductivity and Extra High Conductivity Wires with Property of High tensile stress after artificial aging heat treatment for all-aluminium alloy conductors", available online at www.sciencedirect.com, Material and Design section, 3 August 2005.

- [3] F.R. Thrash, "Transmission Conductors - A review of the design and selection criteria". A report compiled by Wire & Cable Technology Group, Southwire Company.
- [4] E. Mateescu, D. Marginean, G. Gheorghita, E. Dragan, I. A. Gal, C. Matea, "Uprating a 220 kV Double Circuit Transmission LINE in Romania; Study of the Possible Solutions, Technical and Economic Comparison", Paper accepted for presentation at IEEE Power Tech Conference, Bucharest, Romania, June 28th - July 2nd, 2009.
- [5] I. Albizu, A. J. Mazo'n, V. Valverde, G. Buigues, "Aspects to take into account in the application of mechanical calculation to high-temperature low-sag conductors", IET Generation, Transmission and Distribution, Vol. 4, Is. 5, pp. (631-640), 2010.
- [6] S. K. Salman, R. N. Allan, "Application of optimization techniques to the design of very-high-voltage power lines", IEEE Conference Proceeding, Vol.126, No. 6, June 1979.
- [7] N. A. Elgohary, "Design Manual for High Voltage Transmission Lines", U.S. Department of Agriculture, Bulletin 1724E-200, Rural Utility Services, U.S., 2009.
- [8] S. Karabay, M. Yilmaz, M. Zeren "Investigation of extrusion ratio effect on mechanical behaviour of extruded alloy AA-6101 from the billets homogenised-rapid quenched and as-cast conditions", Journal of Materials Processing Technology 160 (2005) 138-147, Available online: www.elsevier.com/locate/jmatprotec, accepted 20 May 2004.
- [9] W. Yuan, Z. Liang, C. Zhang, L. Wei, "Effects of La addition on the mechanical properties and thermal-resistant properties of Al-Mg-Si-Zr alloys based on AA 6201", Materials and Design 34 (2012) 788-792, Available online: www.elsevier.com/locate/matdes, 8 July 2011.
- [10] G. Davies, "Aluminium Alloy (6201, 6101A) Conductors", IEEE Conference Proceeding, British Alcan Conductor Ltd, UK, 1988.
- [11] S. N. Mohtar, M. N. Jamal, M. Sulaiman, "Relaxations of Metallurgy and TEM Analysis with Conductivity of Aluminum Conductor", National Power and Energy Conference Proceedings, Bangi, Malaysia, 2003
- [12] W. Yuan, Z. Liang, "Effect of Zr addition on properties of Al-Mg-Si Aluminium alloy used for all Aluminium alloy conductor", Materials and Design 32 (2011) 4195-4200, Available online: www.elsevier.com/locate/matdes, 27 April 2011.
- [13] S. Sakabe, N. Mori, K. Sato, Y. Miyake, A. Tanaka, "DEVELOPMENT OF EXTREMELY-LOW-SAG INVAR REINFORCED ACSR (XTACIR)", IEEE Transaction on Power Apparatus and Systems, Vol. PAS-100, No.4, April 198.
- [14] A. Alawar, E. J. Bosze, S. R. Nutt, "A Composite Core Conductor for Low Sag at High Temperatures", IEEE Transactions on Power Delivery, Vol. 20, No. 3, pp. (2193-2199), July 2005.
- [15] D.J. Johnson, T.L. Anderson, H.E. Deve, "A New Generation of High Performance Conductors", 3M, St Paul, MN 55144-1000, IEEE Conference Proceeding, 2001
- [16] D. A. Douglas, "A Practical Application of High Temperature Low Sag (HTLS) Transmission Conductors", Power Delivery Consultants Inc. June 11, 2004.
- [17] T. Kavanagh, O. Armstrong, "An Evaluation of High Temperature Low Sag Conductors for Uprating the 220kV Transmission Network in Ireland", UPEC2010 Conference Proceeding, September 2010.
- [18] Cigre SC B2 WG 12 "Conductors for the uprating of overhead lines", Technical Brochure published 2004.
- [19] J. M. Hesterlee, F. Ridley Thrash, E. T. Sanders, "Bare Overhead Transmission and Distribution Conductor Design Overview", IEEE Conference Proceeding, Paper No. 95 C1, pp. (C1-1 - C1-5), 1995.
- [20] S. N. Mohtar, M. N. Jamal, M. Sulaiman, "Analysis of All Aluminum Conductor (AAC) and All Aluminum Alloy Conductor (AAAC)", IEEE Conference Proceeding, pp.(409-412), 2004.
- [21] S. Karabay, F. K. Önder, "An approach for analysis in refurbishment of existing conventional HV-ACSR transmission lines with AAAC", Electric Power System research, available online at www.sciencedirect.com, 2 July 2004.
- [22] T. A. Jones, E. T. Cometa, J. C. Chan, "Comparative Stress-Strain Characteristics of ACSR and SDC Overhead Conductors", IET Conference Publications, Power Energy, and Industry Applications, 1988.
- [23] K. Munaswamy, A. Haldar, "Self-Damping Measurements of Conductors with Circular and Trapezoidal Wires", IEEE Transaction On Power Delivery, Vol. 15, No. 2, April, 2000.
- [24] G. C. Baker, "ACSR Twisted Pair Overhead Conductors", IEEE Rural Electric Power Conference (pp. B4-1 - B4-2), Louisville, KY, BICC General Cables Industries Inc., 2000.
- [25] M. W. Vogt, "T2 ACSR Conductors: Lessons Learned", IEEE Industry Application Magazine, May/June 1998.
- [26] P. Couneson, J. Lamsoul, D. Delplanque, T.H. Capelle, M. Havaux, X. Delreed, D. Guery, "Improving the Performance of Existing High-Voltage Overhead Lines by Using Compact Phase and Ground Conductors", Paper 22-209, CIGRE Session Paris, August, 1998.
- [27] S. P. Hoffman, M. J. Tunstall, "Maximizing the Ratings of National Grid's Existing Transmission Lines Using High Temperature, Low Sag Conductor", Paper 22-202, CIGRE Session Paris, August, 2000.
- [28] J. Parmar, "Types of Overhead Conductors" Retrieved November 23, 2012, <http://electricalnotes.wordpress.com>, posted on 20 March 2011.
- [29] W.W. Zhou, B. Cai, W.J. Li, Z.X. Liu, S. Yang "Heat-resistant Al-0.2Sc-0.04Zr electrical conductor", Materials Science and Engineering A 552 (2012) 353- 358, Available online: www.elsevier.com/locate/msea, 24 May 2012.
- [30] A.S. Richardson, "VIBRATION DAMPING REQUIRED FOR OVERHEAD LINES", IEEE Transactions on Power Delivery, Vol. 10, No. 2, April 1995
- [31] R. A. MONROE, R.L. TEMPLIN, "Vibration of Overhead Transmission Lines", Transactions A. I. E. E (1059-1073), December 1932.
- [32] S. R. Krishnamurthy, P. Selvan, "Use of AAAC in a distribution network - a strategy for energy and cost reduction", Power Engineering Journal, June 1995
- [33] K. Kopsidas, S. M. Rowland "A performance Analysis of Reconducting an Overhead Line Structure", IEEE Transaction on Power Delivery, Vol.24, No.4, October 2009.
- [34] G. Orawski, "Overhead lines - the state of the art", Power Engineering Journal (221-232), October 1993.
- [35] Ahmad Alawar, Eric J. Bosze, Steven R. Nutt "A Composite Core Conductor for Low Sag at High Temperatures", IEEE Transaction on Power Delivery, Vol.20, No.3, July 2005.

SHORT TERM LOAD FORECASTING FOR A LARGE INSTITUTION USING SUPPORT VECTOR REGRESSION

R. Clark* and W. Cronje†

* Faculty of Engineering and the Built Environment, Private Bag 3, Wits 2050, South Africa E-mail: ronald.clark@students.wits.ac.za

† Faculty of Engineering and the Built Environment, Private Bag 3, Wits 2050, South Africa E-mail: willie.cronje@wits.ac.za

Abstract: Short term load forecasting is an important aspect of the electricity management process as it allows operators to plan and implement mitigation strategies using a full knowledge of the day's expected load. This paper investigates the use of Support Vector Regression to model the complex non-linear relationship between a number of exogenous variables (temperature, insolation, type of day), the past load data and the current load value. The SVR model is trained using load data from the campuses of the University of the Witwatersrand. The results show that the system is highly accurate with a mean average error of only 3.44% which compares favourably to a number of other techniques. The system can thus be a beneficial component of any load management strategy.

Key words: load forecasting, time-series, support vector regression, real-time

1. INTRODUCTION

The matching of supply and demand is essential to the efficient and economical provisioning of electrical power. Although this is essentially a supply side issue, utility companies shift the burden onto the consumer by including additional charges in their electrical bill. Thus load management has become an important concern for both suppliers and consumers of electricity. The goal of load management strategies is to achieve more effective distribution and use of available power generation capacity by "intelligently" shaping aspects of the consumers' load usage. The most important factors include the total real energy used and the peak apparent load in a rolling 30 min interval.

However, load management measures are often difficult to implement as their efficacy is dependent on a quick trigger-to-response turnaround time. For example, a simple strategy to reduce the peak energy usage of a large institution may involve asking the staff to turn off their appliances once a certain peak value is reached. Although simple, this strategy is impractical as by the time the consumers respond to the power alert, the peak threshold will already have been exceeded.

This paper describes the design and implementation of a load forecasting technique that can be used to aid the load management process. The system is tested using load data from a large academic institution: the University of the Witwatersrand. The report is structured as follows. In Section 2. the Support Vector Regression (SVR) method is explained along with the criteria used to assess the performance of the prediction system. In Section 3., an overview of the forecasting algorithm and its implementation are provided. Then, in Section 4. the method used to train and test the system is described. Finally, the results are analysed and relevant conclusions

are drawn.

2. BACKGROUND

2.1 Support Vector Regression

Support Vector Machines (SVMs) are a class of algorithms that are typically used to perform classification in pattern recognition problems [1]. SVMs are very popular for a number of reasons including the absence of local minima, sparseness of the solution and their ability to handle non-linear relationships in the input data [2]. The Support Vector Machine is, however, not limited to classification problems and can be extended to perform regression.

Support Vector Regression (SVR) is characterised by the use of a cost function which ignores errors that are situated a certain distance ϵ from the true value [3]. Figure 1 illustrates a one-dimensional linear regression line that has been fitted using an epsilon loss function. The figure also shows the result of applying a mapping to the data points which transforms the non-linear relationship in the one-dimensional feature space to a linear relationship in the two-dimensional space. The quantity ξ represents the cost of the errors of the training data.

In the case of non-linear regression, the input data is mapped into a higher dimensional space, allowing a linear model to be fitted in the new space [2]. The mapping is denoted by $\phi(\mathbf{x})$ which represents the map to the higher dimensional space where the data are linearly separable.

By using the kernel function $\mathbf{K}(\mathbf{x}, \mathbf{x}_i) = \phi(\mathbf{x}_i)^T \phi(\mathbf{x})$, the decision function of the SVM can be represented by:

$$f(\mathbf{x}) = \sum_{i=1}^n \alpha_i y_i \mathbf{K}(\mathbf{x}, \mathbf{x}_i) + \mathbf{b} \quad (1)$$

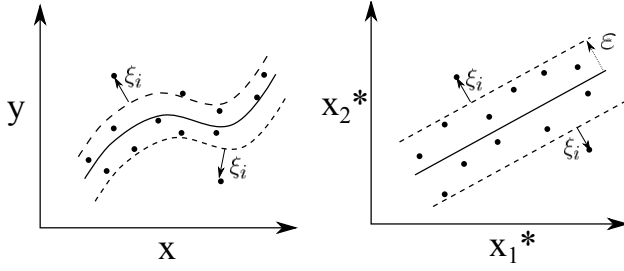


Figure 1: One dimensional non-linear regression [3]. The left axes depicts the original one dimensional input data with a non-linear relationship. The right axes shows the result of applying a non-linear transformation $\Phi(\cdot)$ to convert the data to a two-dimensional space, allowing a linear regression model to be fitted.

where $f(x)$ is the regression output, y_i is the output corresponding to the training data \mathbf{x}_i and \mathbf{x} is the input data to be processed. The loss function itself is defined by [3,4]:

$$L(y, f(\mathbf{x})) = \begin{cases} 0 & |y - f(\mathbf{x})| \leq \varepsilon \\ |y - f(\mathbf{x})| - \varepsilon & \text{otherwise} \end{cases} \quad (2)$$

The parameters α_i and b in Equation 1 are found during training which is performed by solving the following optimisation problem [3]:

$$\begin{aligned} \min_{w, b} \frac{1}{2} \|\mathbf{w}\|^2 + C \sum_{i=1}^n (\xi_i + \xi_i^*) \quad (3) \\ \text{subject to } \begin{cases} |y_i - f(x_i)| \leq \xi_i + \xi_i^* \\ \xi_i, \xi_i^* \geq 0 \end{cases} \end{aligned}$$

From Equation 3 it can be seen that SVM regression tries to minimise the loss function as well as keeping the complexity of the model (quantified by $\|\mathbf{w}\|^2$) as low as possible.

Many kernel functions exist but a well-performing kernel, used in many forecasting systems, is the radial basis function (RBF) [4]:

$$\mathbf{K}(\mathbf{x}, \mathbf{x}_i) = \exp(-\gamma \|\mathbf{x} - \mathbf{x}_i\|^2), \gamma > 0 \quad (4)$$

The constant C in Equation 3 is the penalty parameter of the error term. It determines the trade off between the complexity of the model and the extent to which deviations larger than ε from the optimal regression function are tolerated.

The constant ε in Equation 2 controls the size of the region outside of which outlying data points are penalised during training. Both of these parameters have a significant effect on the accuracy of the trained system and need to be

carefully set prior to the training process. The method used for selecting these parameters is mentioned in Section 2.2.

2.2 Tuning the SVR Parameters

There are two parameters that need to be set when using an RBF kernel: C and γ . The constant C is the penalty parameter of the error term and the constant γ in Equation 4 is a kernel parameter. Both of these values have a significant effect on the accuracy of the trained system and need to be carefully selected prior to the training process. The combination of parameters (C, γ) are chosen which best allow the prediction of new data. To automate this process, the grid-search method described in [3] was implemented as part of the training stage. This method does an exhaustive search using various pairs of (C, γ) values and selects the pair for which the highest cross-validation accuracy is obtained. As suggested in [2], exponentially growing values of C and γ are used during this process. This simple but naive brute force method was chosen in favour of more intelligent procedures for the reasons suggested by Ben-Hur et al. [5]. Firstly, the exhaustive search ensures that globally-optimal parameters are always obtained. Furthermore, the grid-search can be parallelised if needed and, because there are only two parameters, the computational time required by more advanced methods is likely to be similar to that of the grid-search [5].

2.3 Performance Criteria

Numerous criteria exist for quantifying the efficiency of load forecasting techniques. The most popular of these include maximum absolute error and peak error. These quantities are calculated as follows [6]:

1. The accumulated difference between the actual and predicted load values over a 24 hour period

$$MAPE = \frac{100\%}{N} \sum_{k=1}^N \left| \frac{e_n}{P(n)} \right| \quad (5)$$

2. The difference between the peak forecasted and predicted value over a 24 hour period

$$PE = \max \left\{ \frac{e_n}{P(n)} \right\} \quad (6)$$

where $e_n = P_{forecast} - P_{actual}$, $P_{forecast}$ is the predicted load value and P_{actual} is the actual load.

3. SYSTEM OVERVIEW

As illustrated in Figure 2, the load forecasting algorithm consists of two stages: a training stage and a forecasting stage. During the training stage the SVR model is created and optimised to best allow the prediction of new data during forecasting.

The input data consists of a time series of sampled weather, load and day-type information. These data is preprocessed

during normalisation so that all values lie in the $\{0, 1\}$ range.

The prediction module operates on normalised data to produce a single predicted load value. This process is repeated for 48 half-hour time periods to obtain a complete daily forecast.

After the prediction has been obtained, it can be used along with a suitable load management strategy to achieve the desired load profile.

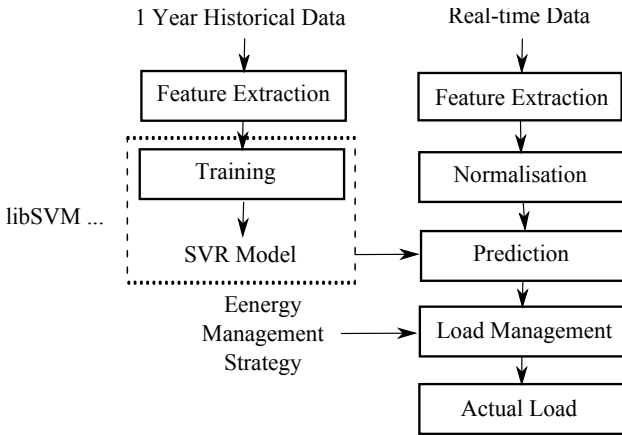


Figure 2: Overview of the load forecasting system

3.1 Prediction Model

Load forecasting is performed using SVR. The SVR method was chosen due to the high accuracy obtained for time series forecasting where it was shown to outperform other regression techniques such as Autoregressive Integrated Moving Average (ARIMA), artificial neural networks and self-organising polynomials [4, 7–9]. Although SVR training time is quadratic in the number of samples and thus often slow, the actual regression is very fast, can be performed in realtime and does not depend explicitly on the size of the training set [2, 5]. The libSVM library was used to implement and train the SVM for regression [2].

To implement SVR, a suitable Kernel function has to be selected, along with appropriate parameter values. The Radial Basis Function (RBF) was chosen as the kernel function. This is a well-performing kernel which is used in many forecasting systems.

3.2 Feature Selection

The half-hour load data for the University of the Witwatersrand between 2011 and 2012 is shown in Figure 3. From this Figure, a number of trends are evident. Firstly, the load curve is periodic with a frequency of 1/day, ie. the shape of the load profile is approximately the same for each day. The peak and average load during non-working days, however, are significantly lower than that during the week which suggests that the type of day has a significant effect on the load demand. Furthermore, the load decreases

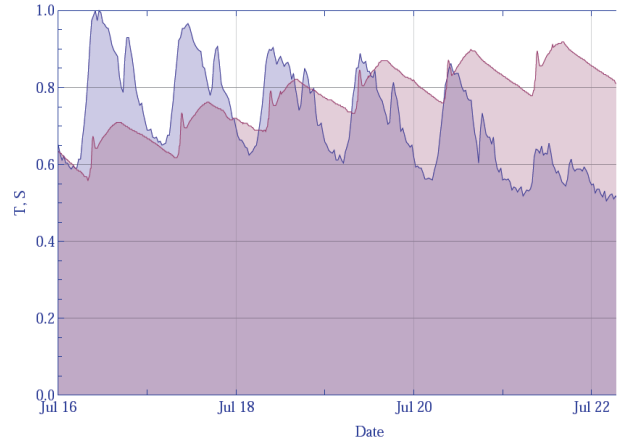


Figure 3: Load and temperature data for the University of the Witwatersrand Raikes road campus between July 16, 2012 and July 22, 2012.

with increasing temperature which, in itself, is directly correlated to the average insolation.

Here it is, however, important to draw a distinction between the short-term (hourly) and medium-term (daily) temperature trend. As the temperature is directly related to the intensity of the solar radiation, there exists a strong short-term correlation between temperature, insolation and load demand. On the other hand, the average daily temperature (with short term variations removed) is inversely related to the load. For example, if the average temperature for a day is low, more heaters will be used and the load demand will increase.

Using the factors mentioned above, the data passed to the SVR for prediction consists of the following features:

$$\mathbf{x}_{d,h} = [L_{d,h}, L_{d-1}, L_{d-7}, W_d, H_r, D_T, \bar{T}, \bar{I}, H_m] \quad (7)$$

where L_{d-1} is the load at the same time during the previous day, L_{d-7} is the load during the same day and hour the previous week, W_d is the day of the week, D_T is the type of day and \bar{T} and \bar{I} are the most recent 24-hour moving averages of insolation and temperature, respectively.

The output of the model is the predicted load for the next 30 min interval:

$$y_{d,h+1/2} = L_{d,h+1/2} \quad (8)$$

From Equation 4, it is evident that all the quantities apart from $L_{d,h}$ are available for a 24-hour ahead prediction. Subsequent values of $L_{d,h}$ are obtained by performing a rolling prediction.

4. TESTING METHOD

The SVR model was trained with historical load data from June 20, 2012 to November 3, 2012 obtained from the Raikes Road campus of the University of the Witwatersrand along with the corresponding temperature and insolation information recorded by on-campus data loggers.

5. RESULTS AND DISCUSSION

The results of the grid-search that was run prior to training are shown in Figure 4. In this case the optimal parameter values were found to be $C = 2^{10}$ and $\gamma = 2^{-2}$.

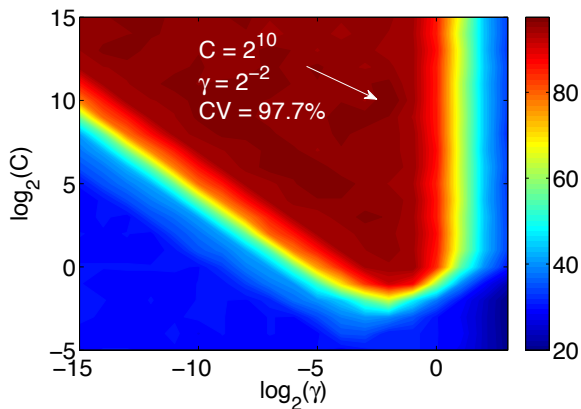


Figure 4: Result of the grid-search procedure carried out prior to training. The contour plot shows the cross validation accuracy obtained using various combinations of parameters. The highest cross validation accuracy is indicated by the arrow.

The contour plot presented in Figure 4 clearly illustrates the importance of selecting the correct training parameters for the SVR. For example, if the parameter values were blindly chosen as $C = 2^{-4}$ and $\gamma = 2^2$, then a cross-validation accuracy of only 24.5% would have been achieved, compared to the accuracy of 97.7% obtained using the grid-search method. This parameter search, although paramount to the performance of the system, is by far the most computationally-expensive aspect of the training process as it takes approximately 3m21s to complete a search of 399 points using an Intel 2.8 GHz Core2Quad CPU with 8 GB RAM. However, for the reasons described in Section 2.2, along with the high cross-validation accuracy that was achieved during training, this simple parameter tuning procedure is preferred.

The forecasting result obtained by applying the trained SVR model to unknown load data is shown in Figure 6. From Table 1 it can be seen that the model achieved high forecasting accuracies for the Raikes Road campus.

The maximum peak error that resulted during testing was 0.134 MW or 6.55% which occurred on a Monday. At current electrical tariffs, this corresponds to a R 27 675 underestimate of the peak demand charge. The most likely

cause of this error is the use of L_{d-1} as a feature, coupled with the fact that not enough holiday and weekend data was used to allow the SVR model to distinguish between the sharp increase in load from a non-working day (Sunday) to a working day (Monday).

A more detailed error analysis is presented in Figure 5 which shows that the errors closely fit a zero-mean normal distribution with a standard deviation of $\sigma = 0.07097$ MW. This means that an error as high as 6.55% is relatively uncommon as an error this large or greater only has a 0.6% chance of occurring. Furthermore, the algorithm is able to predict to an accuracy of 0.125 MW with a confidence of 99%.

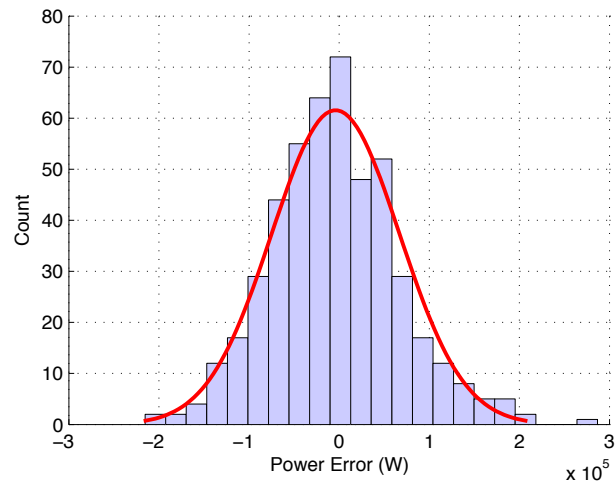


Figure 5: Plot of the error distribution along with an approximate Gaussian fit. The mean and standard deviation estimates are $\mu = -0.0034$ MW and $\sigma = 0.07097$ MW.

The MAE, which relates to the total average energy charge, is significantly less than the peak error. The actual MAE achieved was 3.44%. This value compares favourably to the 9.42% MAE reported by Yuan et al. using the LS-SVM method [9].

6. FUTURE WORK

Future work should focus on testing the system using data obtained from other institutions and on larger data sets which were not available during the time of publication. A more extensive set of features could also be used as the input to the SVR model, possibly increasing the accuracy. In order to eliminate the inclusion of redundant data in the feature set, dimensionality reduction techniques such as

Table 1: Results obtained during testing. The results are for data from the Raikes Road campus of the University of the Witwatersrand from November 4, 2012 to November 14, 2012. All values in MW.

Campus	Error	MAPE	Peak Error	MPE
Raikes Road	0.005	3.44%	0.134	6.55%

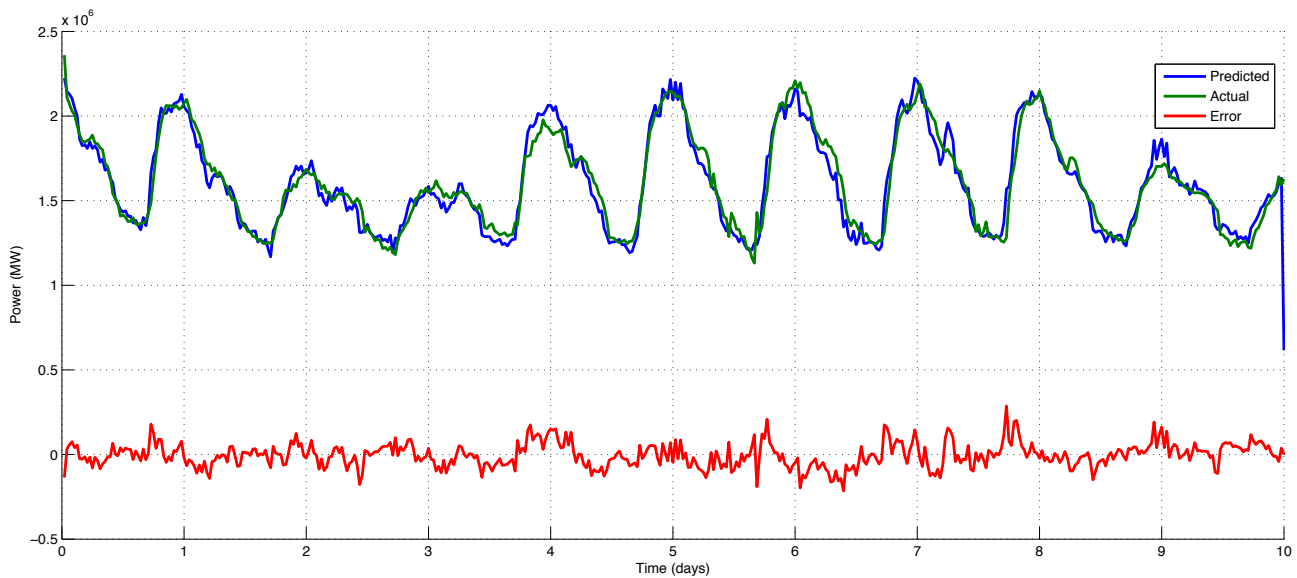


Figure 6: Comparison between the predicted load values and the actual values over a 10-day period. A plot of the error values is also shown. The days with significantly lower load are non-weekdays (Saturday, Sunday).

Principle Component Analysis (PCA) or Factor Analysis (FA) could be used to extract the information with the highest correlation to the load. Finally, the system should be tested in conjunction with a real load management strategy to assess its practical performance.

7. CONCLUSION

This paper presents an SVR-based load forecasting method for predicting load values 24-hours ahead in 30min intervals. The method was implemented and tested using load data from the University of the Witwatersrand. The results are very promising and show that the method has a high prediction accuracy. It is suggested that the system be used with a real load management strategy to quantify the benefits that can be obtained by its inclusion.

ACKNOWLEDGEMENTS

The authors would like to thank Ivan Hofsjer from the University of the Witwatersrand for his valuable input and suggestions.

REFERENCES

- [1] Xie Feixiang, Huang Mei, Zhang WeiGe, and Li Juan. Research on electric vehicle charging station load forecasting. In *Proceedings of the 2011 International Conference on Advanced Power System Automation and Protection (APAP)*, 2011.
- [2] Chih-Chung Chang and Chih-Jen Lin. Libsvm: A library for support vector machines. *ACM Transactions on Intelligent Systems and Technology*, 2:2701–2707, 2011.
- [3] John Shawe-Taylor and Nello Cristianini. *Support Vector Machines*. Cambridge University Press, 2000.
- [4] Xueming Yang. Comparison of the ls-svm based load forecasting models. In *Proceedings of the 2011 International Conference on Electronic & Mechanical Engineering and Information Technology*, 2011.
- [5] A. Ben-Hur and J. Weston. A users guide to support vector machines. Technical report, Department of Computer Science. Colorado State University, 2010.
- [6] Craig Stuart Carlson. Fuzzy logic load forecasting with genetic algorithm parameter adjustment. Master's thesis, University of the Witwatersrand, 2012.
- [7] Shu Fan, Yuan-Kang Wu, Wei-Jen Lee, and Ching-Yin Lee. Comparative study on load forecasting technologies for different geographical distributed loads. In *Proceedings of the 2011 Power and Energy Society General Meeting*, 2011.
- [8] Yaohui Bai, Jiancheng Sun, Jianguo Luo, and Xiaobin Zhang. Forecasting financial time series with ensemble learning. In *Proceedings of 2010 International Symposium on Intelligent Signal Processing and Communication Systems (ISPACS)*, 2010.
- [9] Jinsha Yuan, Yinghui Kong, and Yancui Shi. Online forecasting of time series using incremental wavelet decomposition and least squares support vector machine. In *Proceedings of the 2009 Asia-Pacific Power and Energy Engineering Conference (APPEEC)*, 2009.

TRANSMISSION GRID EXPANSION IN UGANDA: A PROPOSED PLANNING PROCESS

S. Mugisa* and C.T. Gaunt*

University of Cape Town, Department of Electrical Engineering, Private Bag X3 Rondebosch 7701.

Abstract: There is a strong call for increase in transmission capacity to meet the increasing electricity demand. This requires a corresponding increase in transmission investment. In addition to being very expensive, transmission grid expansion is further hindered by environmental, social and political constraints. These constraints have slowed down transmission grid expansion. This paper proposes the use different transmission technology options as demonstrated elsewhere and quality decision making to minimize constraints faced by transmission grid expansion. In contrast to traditional planning that assesses alternative planning solutions by finding a solution with least cost, the proposed methodology considers all conflicting and multiple objectives faced by grid expansion by use of a multi criteria decision making (MCDM) model. To demonstrate the proposed methodology, a worked example is performed on a test transmission expansion project in Uganda.

Keywords: Transmission planning, Transmission technologies, Quality decision making, Multi criteria decision making (MCDM) models

1. INTRODUCTION

An increase in transmission capacity directly implies increase in transmission investment [1]. In addition to being very expensive, transmission grid expansion is further troubled by environmental, social and political constraints. These constraints lead to many transmission projects to be delayed or even cancelled [2].

Uganda is a developing country in East Africa and only 6-9% of the total population of Uganda has access to electricity, majority of whom live in urban areas [3]. Figure 1 shows the annual maximum demand from 1954-2012 [4]. From the Figure 1, it's evident that Uganda has an increasing electricity demand.

Uganda also has considerable unexploited energy resources for energy production. For example it has a total hydro potential of approximately 2200MW but currently only exploits 416MW. Therefore, the potential to meet this growing demand is available [4]. However, in the last three decades there has been minimal transmission investment in the country [1].

The TSO in Uganda (UETCL) released a 10-year Grid Investment Plan (GIP) 2008-2023 to meet the proposed programmes for system expansion. The new power transmission plan aims at improving electricity transmission to meet national economic and social development objectives.

The lack of transmission investment in the past and the need for it, have led to network congestions, which in turn lead to loss of reliability and network quality. This goes against one of UETCL's missions that is, "to dispatch, transmit quality and reliable bulk power in a viable and efficient manner [1]." This has generally slowed down economic and social development of Uganda. The transmission system is one of the major

parts of the electricity power industry and a good transmission plan is, therefore, always essential [5].

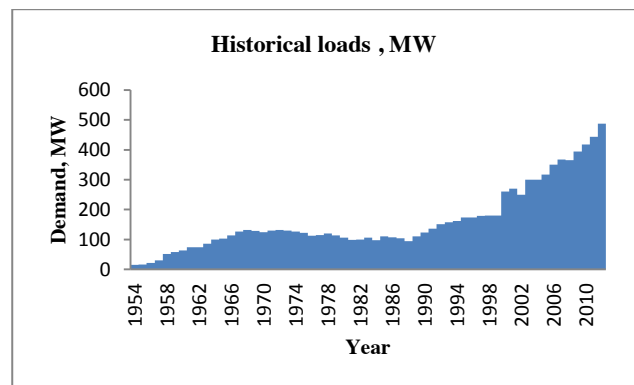


Figure 1: Annual maximum demand from 1954-2012

2. TRANSMISSION PLANNING

Planning is a decision-making process that seeks to identify the available options and determine which is best. Applied to electric utility planning, the process seeks to identify the best schedule of future resources and actions to achieve the utility goal [3, 6].

Transmission network planning is a very complex process and recent trends and challenges make it even more complicated. For the case of Uganda, before the electricity market liberalization, in a centrally managed power system the system operator (UEB) controlled the whole power system. The transmission network was then expanded with the aim to minimize both generation and transmission costs, while meeting static and dynamic technical constraints to ensure a secure and economically efficient operation.

Nowadays, there are increasing concerns over issues like environmental impact, social welfare and political

influence [1, 2, 4, and 7]. In addition to this, many electricity power industries, including Uganda, are now restructured and liberalized. These combined are stimulating a paradigm shift in planning for the industry by creating more multiple and conflicting decision criteria and more uncertainties as well.

Conventional techniques (e.g. least cost planning) fail to integrate all these multiple criteria making them inadequate. This results into poor quality decisions and in turn delays in transmission project implementation or even in extreme cases, can lead to project failure.

These constraints have also slowed down transmission grid expansion in Uganda. Uganda in the last three decade has had minimal investment in transmission infrastructure and in fact in 2008, 80% of the overhead lines were more than 45 years old.

the use of different transmission technologies other than AC overhead lines can minimize some constraints faced in transmission expansion [2]. This could also find application in Uganda as discussed next.

3. APPLICATION OF TECHNOLOGIES SPECIFICALLY FOR UGANDA

AC overhead lines are the standard solution for grid expansion in Uganda but it can be argued that different technology options can overcome many obstacles that proposals for OHLs face. To overcome or minimize some of the obstacles faced, selection of an appropriate technology would be vital in the transmission planning process.

Overbuilding can be defined as building a line to match a longer term forecast than the short term or the current forecast. Overbuilding a line now will reduce long-term costs by avoiding the much higher costs of building two smaller lines. It will also further reduce the delays and opposition associated with transmission-line siting by eliminating these costs for the now unneeded second line [8].

Uprating is generally understood as increasing the transmission capacity of existing transmission lines. The options available for uprating are as follows: increasing the voltage or increasing the current [9]. Smaller costs and less environmental impact when compared to a new transmission line are very attractive for the case of Uganda with financial and environmental constraints. Uprating a circuit from one system voltage to the next is feasible mainly at lower voltages because older circuits (110,115 and 138kV) were often conservatively designed [9]. Therefore, Uganda with mainly lower voltage lines (66 and 132kV) and old lines (40-50 yrs) can take advantage of these conservative designs as well. In this respect, the dissertation assumes a successful voltage feasibility studies for the analysis.

Advanced technologies (e.g. FACTS and HVDC) offer the hope of better control of transmission flow and voltages. Such improved control would permit the system to be operated closer to her thermal limits, thereby

expanding transmission capabilities without increasing its footprint. Less environmental and technical constraints will be faced, thus reducing the fights about transmission siting. Unfortunately, these advanced technologies are still too expensive for wide spread application in Uganda, although they may be economical in niche applications. They are promising for future applications like RES integration (wind and solar) and long distance interconnection.

The transmission planning process has to deal with multiple and often conflicting objectives. Each objective of the process is important and if poorly considered will lead to poor decision making, a poor plan and ultimately failure to attain the planning goals [3]. This calls for quality decision making.

4. QUALITY DECISION MAKING

The success of a project is directly related to the quality of the decision underlying the project. A quality decision can be defined as being, “well considered, justifiable and explainable” [10]. In addition to this, Bakker [11] identified that uncertainties need also to be acknowledged.

MCDM is a generic term for all methods that exist for helping people making decisions according to their preferences, in cases where there is more than one conflicting criterion [10]. Using MCDM can be said to be a way of dealing with complex problems by breaking the problem into smaller pieces. Transmission network planning being a decision making problem with both multiple decision makers and multiple decision criteria, can find application of MCDM models.

4.1 MCDM

The MCDM process generally consists of three steps:

- The structuring of the decision making problem
- The acquisition of preference information
- The aggregation of preferences to obtain a unified value across multiple criteria

The MCDM models have different strengths depending on the decision to be made. For this research project, the MCDM chosen is the SMART. The main reason for choosing SMART is that, it has been used in numerous fields whose strength resides in its ability to structure a complex, multi-personal, multi-attribute, and multi-period problem hierarchically. It has also been applied in electricity network planning [12]. The linear utility function used by SMART is

$$V(\mathbf{a}) = \sum_{i=1}^m w_i v_i(\mathbf{a}) \quad (1)$$

where w_i is the scaling value (weight) assigned to the i^{th} of m criteria, and $v_i(\mathbf{a})$ is a partial value function reflecting alternative \mathbf{a} 's performance on criterion i . The partial value function must be normalized to some convenient scale (e.g. 0–100). Using Eqn.1, a total value score $V(\mathbf{a})$ is found for each alternative \mathbf{a} . The alternative with the highest value score is preferred.

It should be noted that weighting of criteria is a difficult task and is open to criticism, as it includes a strong subjective component. Many different methods have been proposed for assessing criteria weights.

4.2 Uncertainty in decision making

For a quality decision making, uncertainties need to be acknowledged. Bakker [11] identifies that, “lack of uncertainty acknowledgement in the decision-making process as one of the major causes of electrification project failure in developing countries.”

There are two types of uncertainty, hard and soft, based on Davidson’s conceptions of reality and previous work by a variety of authors [11].

In hard uncertainty 1) the set of all possible outcomes of an action is unknown and can only be hypothesized, or 2) if all the outcomes are known, the probability distributions of all the outcomes are unknown or not fully definable. Examples of hard uncertainties include effectiveness of institution, corruption, human inertia to change, and political uncertainty.

Soft uncertainty or risk is used to define situations where all the possible outcomes of an action, as well as the outcomes’ probability distributions, are known, and are therefore falls within the area of immutable reality. The methodology will acknowledge both the soft and hard uncertainties.

5. METHODOLOGY

The proposed process begins with a clear identification of the purpose of the transmission plan, followed by a comprehensive assessment of the current situation. This situation analyses provides a firm basis for assessing future conditions, problems, constraints and potential solutions (including other transmission technologies). The MCDM assesses the various transmission alternatives that might solve the identified problems and constraints. The planning methodology goes further to acknowledge the hard uncertainties that the planning process faces. A final decision is made guided by the results from the MCDM model.

5.1 MCDM Analysis

Structure the hierarchy: The first step of the MCDM is to structure the problem as a decision hierarchy. This is perhaps the most creative part of decision making that has a significant effect on the outcome.

Select evaluation criterion: To allow each planning solution to be assessed, evaluation criteria need to be identified. The next sub-sections discuss the evaluation criteria used:

Environmental Impact criterion (EIC): The goal is to minimize the environmental effect (social environment and natural environment). That is to say, minimize the impact on settlement (settlement areas, cultural assets, and real assets), recreational use (fields and grassland), landscape (view places) and areas of unspoiled nature (forestry). The method that will be adopted for this criterion is to consider the total surface area occupied by

the tower footing (ROW inclusive) and the span of the new or modified transmission technology to represent the likely environmental impact for each circuit route [12].

Cost Criterion (CC): The goal of this criterion is to identify from the selected transmission technologies that satisfy the basic electric criteria, the option with a least economic and financial impact. The method that is going to be adopted here is to calculate the capital cost. Capital cost is an important factor when assessing alternative planning solutions. This is a summation of the costs involved in implementing each of the options selected plus any ongoing costs related to implementation or other operational aspects associated with the network. The cost of each option will either be expressed as a current cost or as a future worth equivalent at the end of the planning period, converted using the present-worth calculation [12].

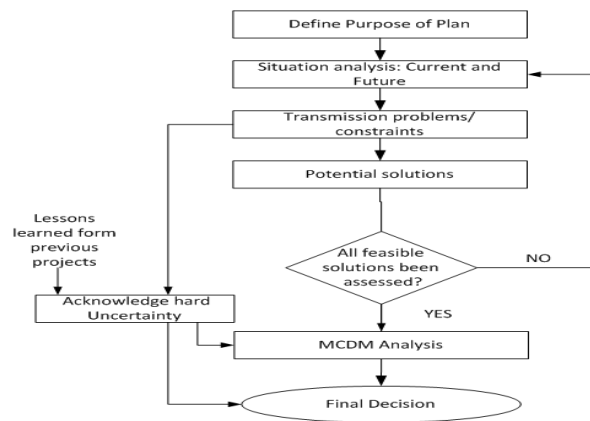


Figure 2: Proposed planning methodology for this dissertation

Reliability Criterion (RC): The reliability criterion adopted in this dissertation is the expected energy not supplied (EENS), and this will be calculated as described below [13];

$$EENS = \sum U_f \cdot P_f \quad (2)$$

Where; U_f is the probability of being in a failure state f i.e. unavailability in hr/yr and P_f is the power not supplied during the failure state f in MW .

The EENS value will provide a quantitative prediction of the system performance, and also provide a way of constantly evaluating the respective and relative reliability levels of alternatives proposed. The goal of this criterion is to identify the alternative with least EENS value.

The values from each criterion are compared with one another against the criterion goal by normalising to a convenient scale (i.e. 0-1). This develops single dimension utilities by converting measures into value functions (utilities) that can be used in Eqn.1.

Weighting the criteria: Not all criteria will be equally important. User preference weights allow the designer to

stress some criteria over others. For example, some utilities may be forced to stress cost very heavily over others because of very limited resources while other utilities may prefer more reliable designs [12]. The user preference weights represent the users concerns under different circumstances, thus is subjective. It is also perhaps the most contentious issue associated with the MCDM techniques as the chosen weight values will have direct impact on the resulting solution score.

Elicitation of weights can be difficult, several methods have been proposed for reducing the burden of the process. One of the proposals has been the based on the rank order centroid (ROC) weights [14]. Barron and Barret [14] found that ROC captures a substantial portion of the information content of totally precise weights and compared to other approximation methods, ROC is clearly and overwhelmingly the most efficacious. In this light, the dissertation will adopt the ROC weighting method to estimate the weights.

In the ROC method, weights are assessed based on the rank order of the criteria importance. The rank order will be determined by the decision maker based on the objective/ goal of the process. The ROC assigns weights as follows, w_1 is the most important objective, w_2 is the weight of the second most important objective and so on. For k objectives, the weight of the k^{th} attribute is:

$$w_k = (1/k) \sum_{i=k}^k (1/i) \quad (3)$$

Aggregating weights and the value functions: The model used is an additive model (Eqn.1), the total score for each alternative being the sum of the weighted value scores for all the criteria for the alternative. In other words, the total decision score for each alternative is then determined using linear additive –value function to sum the individual scores of each criterion [12].

Therefore, the alternative with the lowest weighted score is considered as the most desirable among the assessed alternatives since it faces least constraints (i.e. 0-least constraint and 1- more constraint).

Sensitivity analysis: To ensure that the decision process is indeed robust, a sensitivity analysis will be performed on the criteria ranks [12]. It's going to take the form of changing the rank position of different criterion and see what effect it has on the overall weighted score.

5.2 Acknowledgment of hard uncertainty

The soft uncertainties are made explicit are acknowledged in the MCDM model.

Bakker and Gaunt [15] used an uncertainty checklist as a means of making uncertainties explicit in electrification projects, thus increasing the quality of decision making, and ultimately the success of the project. This makes potentially hidden project uncertainties explicit without restoring to subjective numerical methods. That said, the dissertation goes further to try improve the quality of the planning process and ultimately the success of the project by acknowledging hard uncertainties and to do this, proposes the use of an uncertainty checklist; created from

literature and lessons learned from failures and problems on previous transmission expansion projects.

The final step is to make the decision or recommendations based on the results of the MCDM analysis. This will be a quality decision.

6. CASE STUDY

Currently, Uganda and Kenya are interconnected via a double-circuit 132kV line from Tororo (Uganda) to Lessos (Kenya). The transfer capacity of the line is 118MW. A recent power transfer forecast gives the estimate maximum possible transfer between each two countries over the period 2013-2038 as 794MW [16].

The GIP 2008-2023 proposed another interconnection between Uganda and Kenya. The line will have a transfer capacity of 300MW and the earliest year of commissioning is 2014. SNC-Lavalin and PB [16], also propose construction of yet another 220kV line from Bujagali to Lessos to meet the increased capacity. Its transfer capacity is expected to be 440MW and the earliest year of commission is 2023. This is illustrated in the Table I and Fig.3.

Using SIL values of typical AC OHLs and the St. Claire curve, the capacity of the proposed new AC technology are calculated.

6.1 Proposed alternatives

Alternative one (A1), is proposed in SNC-Lavalin and PB [16] and uses only AC OHLs. This paper proposes other alternatives that could have been considered for this interconnection.

Table I: Existing, under construction, and proposed interconnection between Uganda and Kenya

Project	Voltage, kV	Distance, km	Capacity, MW	Configuration	Status
Uganda-Kenya	132	254	118	double-cct	Existing
Uganda-Kenya	220	254	300	double-cct	Funds secured
Uganda-Kenya	220	254	440	double-cct	Proposed

Alternative two (overbuilding): This option assumes that the electricity demand in Uganda will keep increasing as shown in Figure I. In Figure-I, it's clear that there was a decrease in demand from 1978 to 1986. This is mainly due to political instability in the country at the time. But since 1990 to date, the demand has been increasing due to the political stability. Therefore the process assumes political stability in order to be a viable option.

The dissertation proposes construction of one double 345kV circuit instead of two 220kV AC OHLs. This will be alternative two, **A2**. The aim is to achieve less environmental impact, cheaper costs in the long run and of course boost regional power trade.

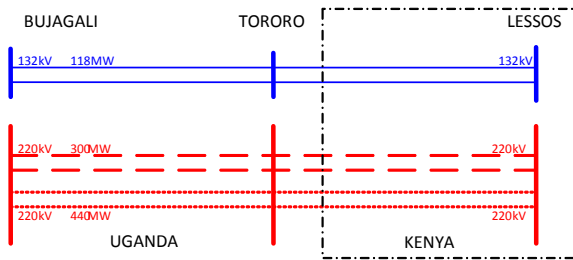


Figure 3: Kenya- Uganda interconnection

Alternative three (uprating): After the construction of the 220kV in 2014, assuming a successfully voltage uprating feasibility study, the dissertation proposes refurbishment of the old already existing 132kV line by replacing the conductor and voltage uprating and construction of a 132kV line. This will be alternative three, **A3**. The aim here is to achieve cheaper costs by uprating than construction of the 220kV line.

7. EVALUATION AND RESULTS

This chapter shows the application of the methodology on the case study identified. This leads to a set of results which will be presented.

7.1 MCDM Analysis

Structure the decision hierarchy:

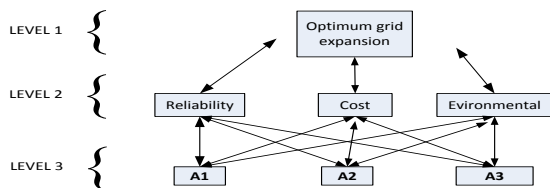


Figure 4: Transmission alternatives decision hierarchy

Weighting the criteria: In order to estimate, the ROC method requires the rank order of the criteria importance. This is going to be determined based on the project objective. The rank order for this case is as follows:

Rank 1 is the cost criterion. This is because Uganda is a developing country with limited resources, so minimizing cost of any project is a key issue that is considered greatly

Rank 2 is the reliability criterion. This is because in the GIP 2008-2023, the objective of the proposed projects is to build a robust network, enhance transfer capacity, improve reliability and quality of power supply, and provide capacity for regional power trade. Also transmitting reliable bulk power is one of the missions of UETCL. Therefore, reliability will be ranked second because it's one of the major objectives of the transmission grip expansion.

Environmental impact criterion is ranked 3rd. This is because the route of the line has proximity to mainly low socially, ecologically and archeologically sensitive areas. Table 2 summarizes the weights of our criteria.

Aggregating the weights and the value functions: The weighted scores of each alternative are summarised in the Table 3.

Table 2: Criteria preference weights

Rank	Criteria	ROC weights
1	Cost	0.6111
2	Reliability	0.2778
3	Environment	0.1111

Table 3: Summary of the weighted scores

Criterion	Weights	Normalized Scores		
		A1	A2	A3
Cost	0.6111	0.4161	0.2131	0.3708
Environment	0.1111	0.3929	0.2142	0.3929
Reliability	0.2778	0.2901	0.4198	0.2901
Total	1			
Total, WS		0.3785	0.2706	0.3508

8. DISCUSSION OF RESULTS

From Table 3, A1 and A3 performed best in terms of the reliability criterion. A2 performed best in both environment and cost criteria. In the weighted scores, A2 is the most optimum solution followed by A3 and in last place A1.

A2 will avoid construction of two transmission lines where only one line could have done the job. Economies of scale in transmission investment argue for overbuilding, rather than under building, transmission. It is substantially cheaper per GW-km to construct a higher voltage line than lower voltage line (it is cheaper in the long run too). Higher voltage line also requires less land per GW-mile, which should reduce opposition from local landowners and environmentalist bodies. Also, building a larger line now eliminates the need to build another line in several years. This situation can eliminate the need for another potentially bruising and expensive fight over the need for and location of another line. In addition, the availability of suitable land on which to build can only go down and get more expensive to acquire as in the future, as populations grow and economies expand. On the other hand, overbuilding reduces the reliability of the network and increases financial risk to transmission owners.

A3 performed second best. A3 uses line uprating which can be cheaper depending on the feasibility studies compared to building new AC OHL lines. Although, uprating has a limitation that it requires already existing infrastructure in order to be applicable. Uprating can lead to substantial saving of transmission investment. This will be highly beneficial to a developing country especially one with old transmission infrastructure and low voltage lines like Uganda.

A1, uses only AC OHL, it should be noted that this still has wide application especially in rural electrification and is the cheaper option in such a case.

The process also acknowledges hard uncertainties by use of an uncertainty checklist. Therefore, we assume measures are put in place to overcome the impact of these hard uncertainties. For example for the issue of corruption, the decision makers to come up with an audit trail that would reduce loop holes that corrupt officials take advantage of. The process also assumes that the projects have the support of government or the donors that are funding the project.

9. CONCLUSION

The proposed planning process is more comprehensive and rigorous giving an all-round consideration for transmission expansion planning. It uses an MCDM model which makes explicit a coherent family of criteria, integrates all the multi criteria, provides structure, encourages multidimensional perspective (instead of focusing mainly on the financial dimension), and also provides a common terminology for discussion throughout the decision making process.

MCDM models have been used and tested in electricity utility planning. They have proved to have the ability to structure a complex, multi-person, multi-attribute and multi-period problem hierarchically. It was discovered that evaluating all planning problems simultaneously can provide substantial benefits to utilities, not only in terms of improving the desirability of possible solutions but also by potentially deferring network investment. It was also discovered that the models have the ability to make strategic planning decisions relating to both the whole network and also particular planning problems.

The process ensures both hard and soft uncertainties are acknowledged. The soft uncertainties are acknowledged in the MCDM model and the hard uncertainties are by use of an uncertainty checklist. The checklist is used to make more apparent a wide range of possible uncertainties and focuses attention of the decision making process on where measures are required to reduce the impact of hard uncertainty. The use of the MCDM model and uncertainty acknowledgement improves the quality of the decision making process.

Finally, the process also encourages use of different mature transmission technologies that are already being used elsewhere in the world other than AC OHLs. This is because of the addition benefits they have and fewer constraints they face. Therefore, depending on the type of project different technologies have added advantages and can tackle some of the constraints encountered by AC OHLs. Therefore, these approaches properly considered are capable of assisting TSO decision makers to make a quality decision. In turn this will better the success of transmission projects because the negative impact of the unconsidered criteria is prevented or reduced.

Decision aiding however can't be forced upon the decision maker. The TSO in Uganda being government

owned, where electricity service delivery represents political capital and favour. Decision makers positioned within this landscape might have little motivation to implement a decision aiding process that will lead to a more transparent decision with an audit trail.

10. REFERENCES

- [1] UETCL, "Corporate Business Plan, 2008-2013" Uganda Electricity Transmission Company, February 2008
- [2] Buijs P, Bekaert D, Cole S, Hertem D.V, Belmans R, "Transmission investment problems in Europe: Going beyond standard solutions" Energy Policy, Vol. 39, Issue 3, March 2011.
- [3] Willis H. L, "Power Distribution Planning Reference Book" Marcel Dekker, New York, 1997
- [4] ERA, "System statistics" <http://www.era.or.ug/> : 10/10/2012
- [5] Lee C W, Ng S.K.K, Zhong J, Wu F.F, "Transmission Expansion Planning From Past to Future," Power Systems Conference and Exposition, IEEE PES, 2006
- [6] Gonen T, "Electric Power Transmission System Engineering, Analysis and Design" New York: John Wiley and Sons, 2006
- [7] Akampurira E, Root D, Shakantu W, " Stakeholder perceptions in the factors constraining the development and implementation of public private partnerships in the Uganda electricity sector" Journal of Energy in South Africa, Vol 20, No.2, May 2009
- [8] Hirst E, Kirby B, " Key Transmission Planning Issues", The Electricity Journal, Volume 14, Issue 8, October 2001,
- [9] Barthold L.O, Douglass D.E and Woodford A.D, " Maximizing the capability of existing AC transmission lines" Cigre Technical Programme, Paris, 2008.
- [10] Belton V, Stewart T.J, "Multi-criteria Decision Analysis; An Integrated Analysis" Boston: Kluwer Academic Publications, 2002
- [11] Bekker B, "Decision aiding in off-grid electrification projects: the role of uncertainty acknowledgement and objectives alignment" PhD thesis Electrical Engineering, University of Cape Town, February 2010.
- [12] Espie P, Ault G.W, Burt G, McDonald J.R, (2003), "Multiple Criteria Decision Making Techniques Applied to Electricity Distribution System Planning" IEEE Proceedings Generation, Transmission, Distribution Vol. 150 September, 2003
- [13] Billinton R, Allan R, "Reliability evaluation of engineering systems; concepts and techniques," (book) Second edition, Plenum Press, New York, ISBN-0-306-44063-6, 1992
- [14] Barron, F.H., B.E. Barret, "Decision quality using ranked attribute weights," Management Science, 42: 1515-1523,1996
- [15] Bekker B., Gaunt C.T, "Sustainable rural electrification projects through a multi-criteria informed logical framework approach," Cigre SC-C6(COLL 2007)...IWD, 2007
- [16] SNC-Lavalin, Parsons Brinckerhoff, "Regional power system master plan and grid code study; Final master plan report, Volume 1,2,3 and 4 and Executive summary " East African Power Pool (EAPP) and East African Community (EAC), May 2011

Topic G

Renewable and alternative energy

ASSESSING THE ECONOMIC VIABILITY OF THE MOLTEN SALT POWER TOWER CONCENTRATED SOLAR POWER WITH THE NATIONAL ENERGY REGULATOR OF SOUTH AFRICA RENEWABLE ENERGY FEED-IN TARIFF SCHEME

C. Chukwuka* and K.A. Folly**

* Faculty of Engineering and the Built Environment University of Cape Town, Private Bag X3, Rondebosch 7701, South Africa, E-mail: oluchux@yahoo.com.

** Faculty of Engineering and the Built Environment University of Cape Town, Private Bag X3, Rondebosch 7701, South Africa E-mail: komla.folly@uct.ac.za

Abstract: The need to diversify the energy generation capacity of South Africa has led to the introduction of the Renewable Feed-in Tariff (REFIT) by the National Energy Regulators of South Africa (NERSA). In this paper, we did an economic study of the Molten Salt Power Tower Concentrated Solar Power with the Systems Advisor Model (SAM). Using the parameters specified by the NERSA draft document of March 2011 we studied the effects of the nameplate capacity, loan rate, debt fraction, analysis period and the thermal energy storage on the levelized cost of electricity (LCOE). Hence, we compared the LCOE obtained with the REFIT tariff.

Key Words: Solar multiple, concentrated solar power, systems advisor model, national energy regulators of South Africa, Renewable Energy Feed-in tariff, capacity factor, molten salt energy storage

1. INTRODUCTION

South Africa plays a leading role in energy generation, transmission and distribution in Africa. Recent increase in the price of fossil fuels such as coal leads to higher price of electricity. Eskom, the South African utility is looking at other cleaner and renewable means of generating electricity. Concentrated solar power has the potential of producing low cost, clean and reliable electricity. This paper begins with an introduction of solar energy concept. The section 2 is an overview of the concentrated solar power technology and Systems Advisor Model (SAM). Section three covers simulation of the plant and section four deals with the systems analysis and discussions.

2. OVERVIEW

The literature review is done in two parts. The first part is the overview of the plant while the second part is the overview of the software used for the simulations.

2.1 Concentrated Solar Power

The molten salt power tower concentrated solar power plant basically contains the solar collectors that focus the incident solar rays on a central receiver shown in figure 1. The incoming solar radiation is converted to heat by the receiver; this heat is stored in the molten salt. The amount of heat energy stored by the salt is determined by the size of the tanks measured in hours of thermal energy [1]. From the

Salt tanks steam is generated and sent to the turbine for onward conversion to electricity.

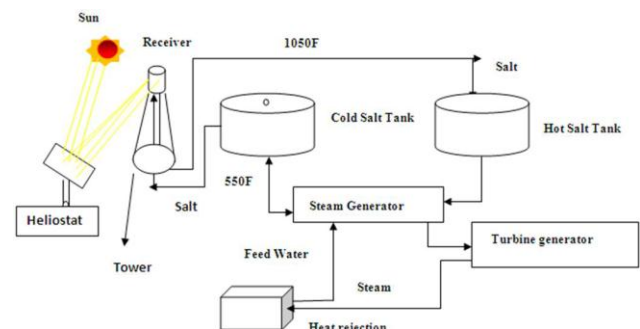


Figure 1: The Block diagram of the Molten Salt Power Tower Concentrated Solar Power Plant [2]

There are currently different designs of CSP: the parabolic trough which is by far the most developed, the Fresnel type, Stirling dish and the power tower type which is known for its high efficiency because of its ability to reach very high temperatures up to 2000deg Celsius.

2.2 Systems Advisor Model (SAM)

SAM, originally called the ‘Solar Advisory Model’ was developed by the National Renewable Energy Laboratory in collaboration with Sandia National Laboratories in 2005 [3]. It was first used internally by the U.S. Department of Energy’s Solar Energy Technologies Program for systems-based analysis of

solar technology improvement opportunities within the program. The first public version was released in August 2007 as version 1, making it possible for solar energy professionals to analyze photovoltaic systems and concentrated solar power parabolic trough systems in the same modeling platform using consistent financial assumptions. Since 2007, two new versions have been released each year. Adding new technologies and financing options. In 2010, the name changed to ‘Systems Advisor Model’ to reflect the addition of non-solar technologies.

The Department of Energy, National Renewable Energy Laboratory and Sandia continue to use the model for program planning and grant programs. Since the first public release, over 35,000 people representing manufacturers, project developers, academic researchers and policy makers have downloaded the software. Manufacturers use the model to evaluate the impact of efficiency improvements or cost reductions in their products on the cost of energy from installed systems. Project developers use SAM to evaluate different system configurations to maximize earning from electricity sale. Policy makers and designers use the model to experiment with different incentive structure.

SAM requires inputs describing the weather at the system’s location, information about the project’s cost and the financial assumptions and specifications of the system’s performance characteristics.

SAM’s input variables are populated with sample default values which are

- Weather Data which include; wind speed, temperature, snow cover all in TMY2 or TMY3 or EPW formats
- Financial and Economic inputs variable are projects finances such as the analysis period equivalent to the system lifetime, discount rate, inflation rate, loan amount and loan rate
- Incentives: types of incentives can be modeled by SAM are tax credits and incentive payments. Tax credits are provided by government while incentives can be provided by government and any willing body. Here in South Africa, the following incentives are obtained namely: Renewable Energy Feed-in-tariff (Refit); energy efficiency programs/projects under South African Revenue Service (SARS); National Energy Regulator of South Africa (NERSA) R5.4billion project; Critical Infrastructure Grant of the Department of Trade and Industry; Renewable Energy Finance and Subsidy office grant; Renewable Energy market Transformation (REMT) [4]
- System performance : SAM simulates the hourly performance of the power system using the hourly weather data and hence the hourly electrical output estimates and then adds 8760 hourly values to calculate the systems total annual output

- Costs: SAM calculates the cash flow and resulting metrics based on two categories of costs. Capital cost accounts for the cost of installing components and the balance-of-system components, operation and maintenance cost accounts for the recurring costs

The outputs are levelized cost of energy, Power purchase price, rate of return and other financial targets, Payback period and net present value, Hourly, monthly and annual average predictions of the system performance including net electric output and efficiencies, annual cash flow table with cost details and customizable graphs.

The levelized cost of electricity (LCOE) in cents per kilowatt-hour accounts for a project’s installation, financing, tax, and operating costs and the quantity of electricity it produces over its life. The LCOE makes it possible to compare alternatives with different project lifetimes and performance characteristics. The real LCOE accounts for the effects of inflation over the life of the project. The nominal LCOE excludes inflation from the calculation [NREL 2011].

$$\text{Real LCOE} = \frac{\sum_{n=0}^N \frac{C_{\text{AfterTax},n}}{(1+d_{\text{nominal}})^n}}{\sum_{n=1}^N \frac{Q_n}{(1+d_{\text{real}})^n}} \quad \text{----- (1)}$$

Where:

- Q_n (KWh) = the electricity generated in year n
- N = the analysis period in years
- $C_{\text{AfterTax},n}$ = the after tax cash flow in year n
- d_{real} = the discount rate
- d_{nominal} = the nominal discount rate

The nominal discount rate can be calculated based on the values of the real discount rate and the inflation rate as shown in equation 2

$$d_{\text{nominal}} = (1 + d_{\text{real}})(1 + e) - 1 \text{----- (2)}$$

Where:

- d_{nominal} = the nominal discount rate expressed as a fraction
- d_{real} = the real discount rate expressed as a fraction
- e = the inflation rate expressed as a fraction [NREL 2011]

3. INPUTS

3.1 Climate

The climate input page shows detailed weather information of the location of the plant. In this case,

Cape Town weather data is selected. The weather data of Cape Town is shown in table 1.

Table 1: Weather Data of Cape Town

Location Details	
City	Cape Town
Time zone	GMT+2
Elevation	47m
Latitude	-33.98
Longitude	18.6 deg
Annual Weather Data Information	
Direct Normal Irradiance (DNI) kWh/m ²	1923.9
GlobalHorizontalIrradiance kWh/m ²	1900.7
Dry-bulb temperature deg C	16.5
Wind speed (m/s)	5.1

3.2 REFIT Parameters

The input parameters used in these simulations are based on the draft document of Review of Renewable Energy Feed-in-Tariff (REFIT) of the National Energy Regulator of South Africa (NERSA) consultation paper March 2011[5]. The exchange of R8.60 to \$1 is used.

In 2007, the terms of the Act, the energy regulator commissioned a study on the Renewable Energy Feed-in-tariffs (REFITs) to support renewable energies in South Africa. The Feed-in tariffs (FITs) would be based on levelized cost of electricity (LCOE). The term of the Power Purchase Agreement (PPA) is to be twenty years and is to be reviewed every year for 5 years of implementation and every 3 years thereafter and the resulting tariffs will apply to only new projects.

In March 2009, the first REFIT tariffs were announced for wind, small hydro, landfill-to-gas and CSP (parabolic trough with 6hr storage). In October 2009, the second REFIT tariffs were announced for CSP (parabolic trough without storage), PV, solid biomass, biogas and CSP (Tower with 6hrs storage). In March 2011, the REFIT tariffs were revised, proposing to reduce tariffs between 7.3 to 41.5%. In August 2011, the ‘REBID’ was announced with 5 bidding windows: November 2011, March/August 2012, and March/August 2013. The initial total renewable energy allocation (RE) was increased from 1250MW to 3725MW [6]

The US-based costs from SAM are used and the results are converted to the South African Rand for the simplicity of the model. Inflation is assumed to be constant because inflation forecasting is not covered in this journal.

The power purchase agreement (PPA) which in South African context is the Renewable Energy Feed-in Tariff (REFIT). NERSA approved term is 20 years. The tax rate is fixed at 28%. The REFIT escalation is given by the formula

$$REFIT_{j+1} = Capex_{2011} + (FOM_j + VOM_j + FUEL_j)X \left(1 + RSA_{CPI_j}/100 \right) \quad \text{----- (3)}$$

Where:

j = calendar year ≥ 2011

$REFIT_j$ = PPA tariff in year j

$CAPEX_{2011}$ = capital expenditure, Capex, R/kWh

FOM = Fixed Operation and Maintenance in year j , R/kWh

VOM = variable operation and Maintenance in year j , R/kWh

RSA_{CPI_j} = Actual South Africa CPI for year j [NERSA pp. 25, 2011]

The REFIT escalation exclusively reduced to operation and maintenance hence the non-escalated part of the tariff losses value in real terms. ZAR inflation proceeds over the REFIT lifetime. The investors and lenders would have to enter into long term currency hedges like ZAR-USD or ZAR-EUR. The ZAR-USD exchange rate benchmark is ZAR7.4 to \$1 while the cost of hedging would be included in the operation and maintenance cost [NERSA REFIT pp.24 2012]. Some investors (such as the SASTELA) suggest that the tariff should balance the forex shock thereby enabling and mobilizing both local and foreign debt finance and equity investment [7]. The Southern African Solar Thermal and Electricity association (SASTELA) is an umbrella that unites solar companies in the Southern African region. Some their participants are EMVELO, DBSA, IDC, SIEMENS, Exxaro, Areva, University of Stellenbosch, EARTH, quartile capital, Sol Africa, Abengoa Solar, Group five, Sessa, Standard bank, Alstom, Bridge capital and Built Africa.

3.3 Real Discount Rate

The real discount rate refers to the factor used in the present value calculation that indicates the time value of money thereby equating current and future costs. According to the Energy Department document on the input parameters, the discount rate should be set at real (after inflation) rate of 8% per annum [8,9].

Other technical inputs are the Tower system costs like the direct capital costs which include the site improvements, heliostat field etc. The indirect capital costs are owners, land costs and the rest. The total installed cost and the operation, annual performance and maintenance cost are worked out by SAM.

3.4 Operation and Maintenance

The levelized Fixed Operations and Maintenance cost FOM for the CSP with 6 hours storage is R0.16/kWh [NERSA pp. 29 2011]. Levelized fuel is R0.0029/kWh and variable O & M levelized (VOM) is 0.0 for 2012 are shown in table 2

Table 2: Operation and Maintenance Cost Adjustments with CPI

CSP CPI adjustments	2011	2012	2013
CAPEX R/kWh	1.24	1.24	1.24
FOM R/kWh	0.15	0.16	0.17
Fuel R/kWh	0.0027	0.0029	0.0030
VOM	0.00	0.00	0.00
Total	1.39	1.40	1.41

The REFIT escalation is hereby calculated as ratio of increase in LCOE from 2009 to 2010 to 2011 which is equal to 1.006%

3.5 Solar Multiple/ Capacity Factor

Solar Multiple (SM) is the ratio of the receiver’s design thermal output to the power block’s design thermal input.. For systems with no storage, the solar multiple should be close to or equal to one. NERSA specifies capacity factor of 40% which corresponds with the solar multiple of 3.2 and thermal storage (TES) of 6 hours as shown in figure 2.

The capacity factor (cf) of a plant is the ratio of the actual amount of energy produced over the maximum energy that it can produce if the plant was to operate at full load hourly round the year (i.e. 8760hrs). Or the ratio of the system’s predicted electrical output in the first year of operation to the output had the system operated at its nameplate capacity. Cf is given by the equation 4

$$cf = \text{Net annual Energy}(kW) / 8760 \left(\frac{h}{yr}\right) \text{----- (2)}$$

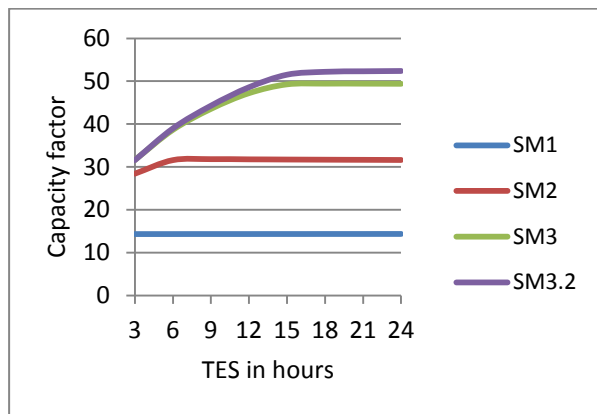


Figure 2: TES versus capacity factor

3.6 Optimization of the Power Tower

The power tower optimization simplifies the task of choosing values for the relatively large number of input parameters required to specify the power tower solar field and receiver. Because the heliostat field is typically the most capital intensive part of the power tower project, often accounting for 30-40% of the total installation cost, optimizing the heliostat field is

a critical step in minimizing overall project cost. The optimization wizard searches for a set optimal system parameter values where the optimal system is defined as the one that results in the lowest levelized cost of energy. In this case where the solar multiple of 3.2 gives us the capacity factor of over 50% we set the solar multiple tab in the optimization wizard to 3.2 and run the optimization. Then set the thermal energy storage to 15 hours and then run the rest of the simulations to obtain the results shown section 4

3.7 Analysis period

The analysis period is the number of years covered by the analysis. This is typically equivalent to the project or investment life and it is the number of years in the projects cash flow. The term of the Power Purchase Agreement (PPA) which is the analysis period is 20years [NERSA pp13, 2011]. Figure 3 shows the general relationship between the LCOE and the analysis period. The longer the analysis period the smaller the LCOE

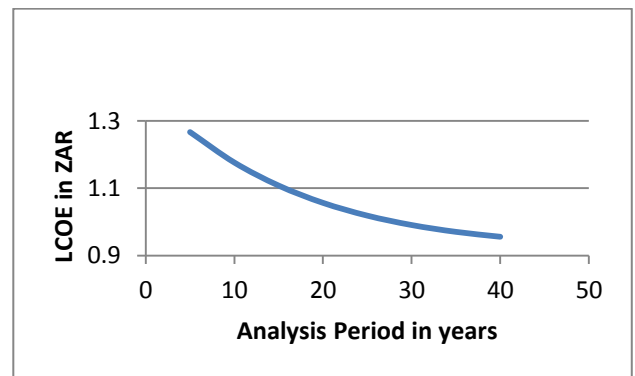


Figure 3: the variation of LCOE with the analysis period

Table 3 Summary of the Inputs

Inputs	values
Climate	Cape Town
Nameplate Capacity	100MW
Inflation Rate	5% [10]
Real discount rate	8%
Loan Term	20
Debt Fraction	70%
Solar Multiple	3.2
Thermal Storage (TES)	15hrs
First year PPA Price	0.162
PPA Escalation Rate	1.006%
Condenser type	evaporation
Tax Rate	28%
Loan Rate	6% [11]

4. RESULT

Table 4: The Summary of the Output

Metric	Cost (1USD=ZAR8.6)
Total Direct Cost	R7,077,000,000
Total Installed Cost	R8,281,000,000
Total Installed Cost per Capacity	R82,560/kW
Net Annual Energy	451,561,665kWh
First year PPA price	R1.39/kWh
LCOE Real	R1.05/kWh
After Tax Net Present value(NPV)	R197,000,000
Gross to Net conversion Factor	0.89
Debt Fraction	70%
Capacity Factor	51.6%
Annual Water Usage	1,217,669m3
Total Land Area	2711.89 acres

per net capacity value on the system cost page and the capacity factor reported in the result [NREL2011]

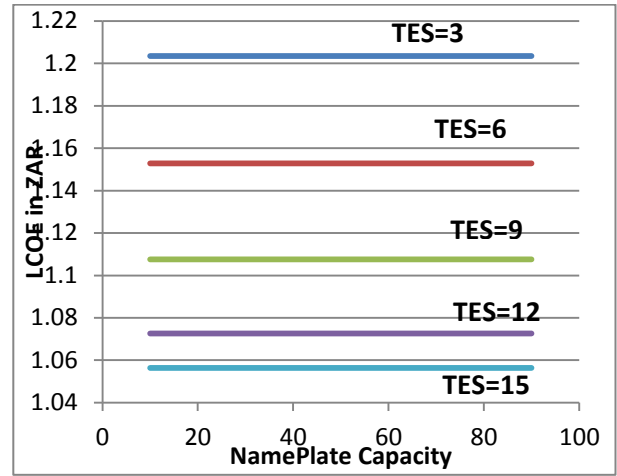


Figure 6: Analysis of the LCOE with the Nameplate capacity

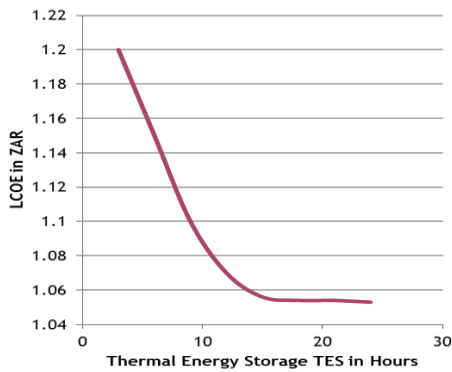


Figure 4: Variation of LCOE with TES

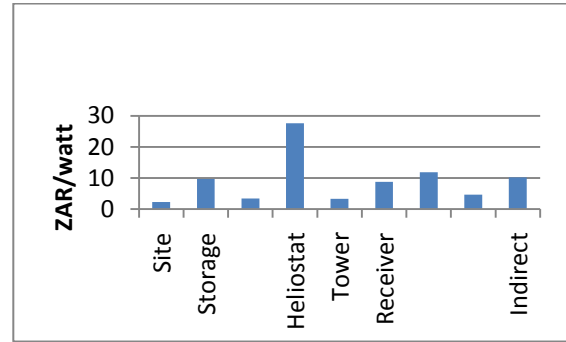


Figure 7: Cost per watt of the CSP components

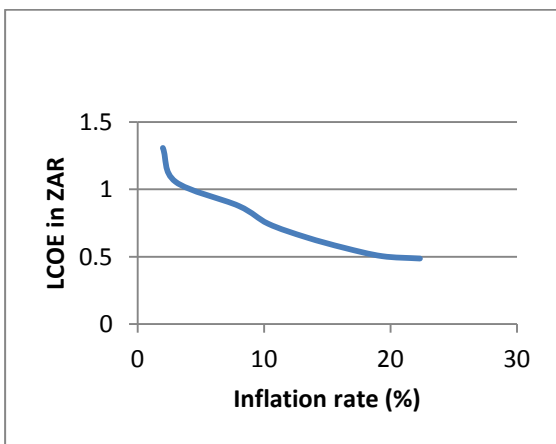


Figure 5: Variation of LCOE with the inflation Rate

The power cycle's nominal capacity, calculated as the product of the design gross output and estimated gross to net conversion factor. SAM uses this value to calculate the system's rated capacity for capacity related calculations, including the estimated total cost

It is worthy of noting that at different predetermined levels of thermal energy storage the CSP power tower LCOE shows no sensitivity to the changes in the nameplate capacity which was increased from 10MW to 1000MW. Figure 7 shows the cost per watt of the components of the plant. The power plant cost only accounts for about 14% of the total cost of the installation no surprise the changes in the sizes of the power plant does not account for much change in the overall LCOE shown in figure 6. This is particularly important when determining the economic size of the CSP plant.

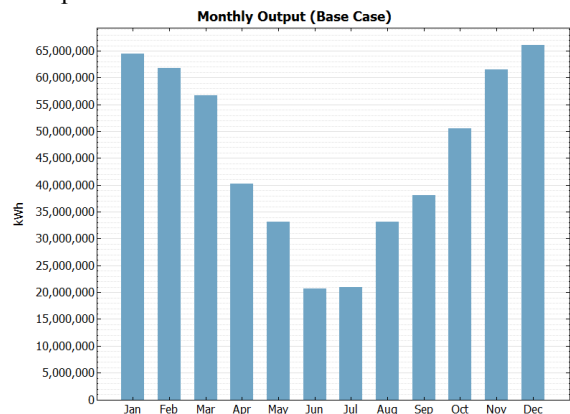


Figure 8: Monthly Energy Output

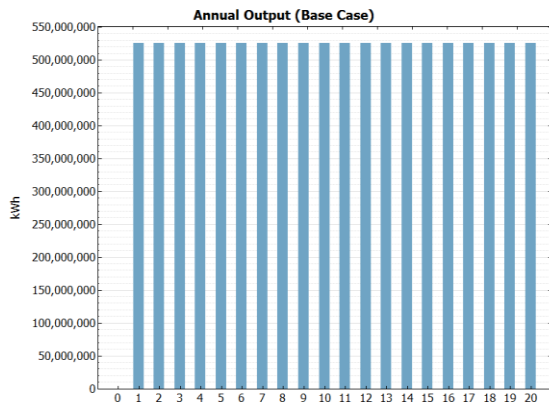


Figure 9: Annual Energy Output

5. DISCUSSION

The REFIT document recommends the sale price agreement of electricity for each technology for the 20 year term. For the CSP with 6hr storage, the REFIT price is R1.408 per kWh [NERSA pp.25]. In this case, we set the first year power purchase agreement (PPA) to R1.406/kWh, escalation to 1.006%/yr and the resulting LCOE is R1.05/kWh. This is about 40% mark up from the REFIT price. The capacity factor is 51% about 10% higher than the NERSA benchmark capacity factor which is 40%. The thermal energy storage (TES) is set to 15hrs. REFIT recommended TES is 6hrs but this would mean a lower capacity factor and higher LCOE. The smart way to increase the capacity factor would be by increasing the solar multiple from the default 1.9 to 3.2 as shown in figure 9 after which we increase the TES to 15hrs which is the lowest point on the LCOE/TES curve in figure 16 and 17. This suggests that running the plant as a base load configuration. Figure 8 shows the monthly energy output which is minimal in winter months of June and July. Figure 9 shows the annual energy output of the plant and it is constant for the analysis period which is 20 years. Both the annual energy produced and the total installed capacities are higher than that of a plant with a lower capacity factor. But this plant much economical.

The plant LCOE showed no sensitivity to the nameplate capacity when the LCOE was simulated for between 10 to 100MW of Nameplate capacity. This therefore suggests that smaller plants sizes such as 10MW could make more economic sense. The round trip efficient of the plant is about 13% which is very low compared with that of the best photovoltaic panels (about 40%). Other issues such as funding is dealt with by the Department of Environment Request for proposal (RPF) Green funding in South Africa [12, 13]

CONCLUSION

This study clearly reveals that the molten salt power tower type concentrated solar power is a feasible technology in the Cape Town area of South Africa and the NERSA REFIT scheme is suitable for renewable energy projects such as the CSP studied in this paper.

REFERENCES

- [1] Sargent and Lundy LLC Consulting group: "Assessment of parabolic trough and power tower solar technology cost and performance forecasts", National Renewable Energy Laboratory; pp. 1-6, October 2003.
- [2] Sandia Report: "Software and Codes for Analysis Concentrating Solar Power Technologies", pp. 8, December 2008
- [3] National Renewable Energy Laboratory: *Systems Advisor Model Help files*, December 2011.
- [4] M. Mathekgan: *Clean Energy*, Department of Energy, pp. 19, 2010
- [5] NERSA Consultation Paper: *Review of Renewable Energy feed-in Tariffs*, National Energy Regulator of South Africa (NERSA), pp. 1-32, March 2011.
- [6] R. Meyer: "The South African REFIT: Solar Resource Assessment options for Solar Developers", Centre for Renewable and Sustainable Energy Studies, University of Stellenbosch, pp. 3, 2010.
- [7] P. Ndebele: "REFIT REVIEW Consultation Hearing", Southern Africa Solar Thermal and Electricity Association (SASTELA), pp. 15, May 2011.
- [8] S3: Discount rate-Integrated Resource plan: IRP 2010 Parameter, pp.1, 2010.
- [9] S. Petsa: "Evaluation of Renewable Energy Feed-in Tariff Scheme in South Africa", MSc. Program in Sustainable Energy Planning and Management, Aalborg University pp. 28-32, 2011.
- [10] Statistics South Africa: "Monetary Policy Review", South Africa Reserve Bank, pp. 3, May 2012.
- [11] Nedbank: "Economic Commentary", March 2012.
- [12] Department of Environmental Affairs: "Green Fund: Request for Proposals", Environmental Affairs, Development Bank of Southern Africa (DBSA), September. 2012.
- [13] P. Du Plessis: "The Potential of Solar process heat for South African Industry", University of Cape Town, Energy Research Centre, pp. 53-54, 2011.

DESIGN OF A PROTOTYPE ULTRA-CAPACITOR SOLAR PANEL STREET LIGHT

A.E van Niekerk* and R Gouws*

* North West University, Faculty of engineering, Private Bag X6001, Postpoint 288, Potchefstroom, 2531, South Africa Email: elizabethniekerk@gmail.com

Abstract: The purpose of the paper is to describe and discuss the design of a prototype ultra-capacitor solar panel street light. The effect of ultra-capacitors as an energy storage device in a solar panel street light is evaluated. The design is designed to evaluate three systems of energy storage devices: 1) where a solar panel charges a battery, 2) where a solar panel charges an ultra-capacitor bank and 3) where a solar panel charges a battery and ultra-capacitor bank to obtain the most efficient energy storage device and evaluate the different devices. The evaluations show that batteries provide a constant supply to the load, while ultra-capacitors charge and discharge with a linear curve. The results show that it is too expensive to replace batteries with ultra-capacitors, but a combination of these devices will be a good solution as the ultra-capacitor bank can extend a battery's life time.

Keywords: Ultra-capacitors, energy management, photovoltaic, programmable logic controller.

1. INTRODUCTION

Solar panel street lighting was initially used in areas where electricity was not available. Renewable energy (solar light) is a good solution to provide electricity to such places. Solar panel street lights can save electricity if implemented in streets or parking lots.

For this project, ultra-capacitors were included in a prototype solar panel street light as an energy storage device to evaluate its energy efficiency and if it could contribute to the energy storage of solar panel street lights. The solar panel normally charges batteries in a solar panel street light. These batteries normally have a life time of 2 - 3 years, and normally require some maintenance [1]. PV systems require batteries with a life cycle of about 3 000 cycles [2]. It is therefore crucial to investigate and invest in the project to improve the current energy storage of solar panel street lights. Ultra-capacitors can contribute towards energy storage for solar panel streetlights. Ultra-capacitors has a life time of 1 000 000 cycles and about 7 – 10 years [1].

For this project three different energy storage solutions were built and evaluated: 1) where the battery is the energy storage device, 2) where the ultra-capacitor is the energy storage device and 3) where the battery and the ultra-capacitors is the energy storage device. One with a battery as energy storage, a second system with an ultra-capacitor bank as energy storage and the third system was a combination of a battery and the ultra-capacitor bank as energy storage. The following provides an overview of the main components for a solar panel street light:

- Solar panel: Solar panels produce and provide electricity by converting the energy coming from the sun into electricity. There are different solar panels available and each designed for a purpose. Suitable solar panels

must be chosen for specific tasks and factors like bad weather conditions must be taken into consideration.

- Control unit: It is the circuitry that controls the solar power system. The purpose of a solar controller is to prevent batteries from overcharging and also to prevent back flow of current from the batteries to the solar panels. Most present controllers also have the advanced of preventing the battery to fully discharge. A solar charge controller is found between the solar panels and the batteries and must feed the batteries with the needed voltage and amperage coming from the solar panels. A Programmable Logic Controller (PLC) can also be used and programmed to install all functions above such as a solar charge controller.

- Energy storage: Batteries are normally used as energy storage devices for solar panel street lights. The solar panel charges the battery and at night the battery will discharge to provide energy to the light. In bad weather the batteries must be able to provide energy to the street light. Low-maintenance or maintenance-free batteries are used.

In the development super capacitors also known as ultra-capacitors will be included as an energy storage device. A battery's life time can expand by placing an ultra-capacitor bank in parallel with the battery or the battery can just be replaced by an ultra-capacitor bank. Examples where batteries and ultra-capacitors are placed in parallel is in Hybrid-electrical Vehicles (HEV) or Electrical Vehicles (EV) [3]. Ultra-capacitors are also used as primary energy storage in toys, emergency devices, cordless tools etc. If ultra-capacitors can expand the life time of a battery or eliminate this problem, less maintenance will be required and thus less maintenance cost will be required in solar panel street lights.

• Load: Different lamps are available for the usage of solar street lights’ loads, such as LEDs, Compact Fluorescent Lamps, High Intensity Discharge lamps, Low Pressure Sodium lamps or Metal Halide lamps. The most suitable and effective light will obviously be used for the appropriate and suitable function.

2. MATERIALS AND METHOD

2.1 Materials

A brief overview on the design proposal is given below in figure 1 and each component is discussed below.

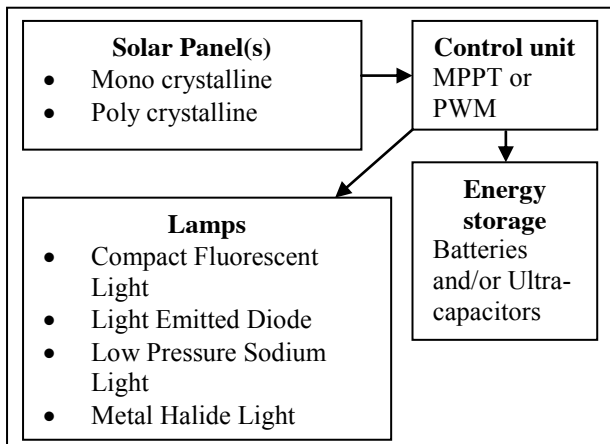


Figure 1: Design proposal of a prototype solar panel street light

Solar panels: Mono crystalline solar panels are a bit more efficient than poly crystalline solar panels although poly crystalline solar panels cheaper are than mono crystalline solar panels.

Control unit: The control unit will control the solar power system. The main two and popular control units available are Pulse-Width-Modulated (PWM) or Maximum Power Point Tracking (MPPT) controllers.

Energy storage: Sealed lead acid batteries and gel batteries are currently very popular to use. It is recommended that deep-cycle batteries are used for solar electric systems. To improve the current product, the energy storage device will also contain an ultra-capacitor bank. Ultra-capacitors are available in different sizes and have different manufactures. Currently there are not ultra-capacitors available in South-Africa and it will be ordered from overseas. A integrate kit will also be necessary to integrate the ultra-capacitors with one another. Both of these components will be bought. A comparison between ultra-capacitors and batteries can be seen in table 1 [4].

Table 1: Comparison between ultra-capacitors and batteries.

Ultra-capacitors	Batteries
Low energy	High energy
High power	Low power
Fast charge and discharge time	Long charge and discharge time
Operating temperature: -40°C to 65°C	Operating temperature: 20°C to 60°C
“Unlimited” cycle life, 1 000 000 cycles	Hundreds/thousands cycles
Low equivalent series resistance	Higher internal resistance
Fully discharge	Deep-cycle batteries 50%-80%
Efficiency: 95%-98%	Efficiency: 70%

Lamp: Different lamps are available for the usage of solar street lights as mentioned above.

2.2 Method

Figure 2 provides a brief overview on how the design and calculations will follow on one another.

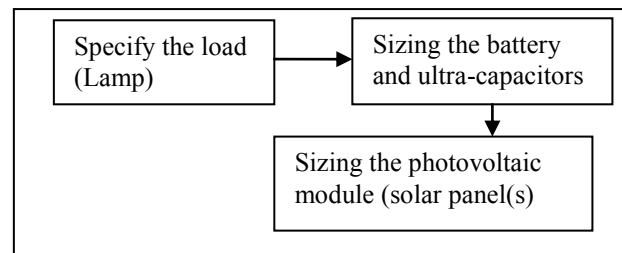


Figure 2: Design method

Load demand: The load will be considered as 6 W including all other factors necessary. Therefore the total load demand is given below:

$$\text{Load demand} = 6 \text{ W} \times 10 \text{ hours per day} = 60 \text{ Wh/day}$$

Sizing the battery: The battery’ capacity can be obtained by the following calculations by using a nominal battery voltage of 12 V:

$$\text{Load demand} \times 1.25 \text{ (a loss factor)} = (x \text{ number}) \text{ Wh/day}$$

The battery capacity (A/h):

$$\frac{(x \text{ number}) \text{ Wh/day} \times 3 \text{ (cloudy and rainy days)}}{0.8 \text{ (20\% deep discharging)} \times 12 \text{ (nominal battery voltage)}}$$

(1)

It was decided to choose the advanced VRLA 7 A/h battery and thus it will let the load burn for about 5 hours. Therefore the load demand (6 W) for 5 hours, will be 30 Wh/day.

Sizing the ultra-capacitors: Ultra-capacitors usually used for solar systems are in the range of 650 F – 3000 F. Ultra-capacitors of 1200 F – 3000 F were considered. As ultra-capacitors only have a rated voltage of 2.7 V it is needed to place ultra-capacitors in series for a 12 V solar panel system in this case. The number of cells to put in series and the total capacitance to be placed in series are calculated with equation 2 and 3 respectively.

$$\# \text{ series cells} = \frac{V_{\max}}{V_r} \quad (2)$$

Where V_{\max} is the maximum working voltage and V_r is the ultra-capacitor's rated voltage.

$$C_{\text{total}(i)} = \frac{C_{\text{cell}}}{\# \text{ series}} \quad (3)$$

Where $C_{\text{total}(i)}$ is the total series capacitance and C_{cell} the capacitance of a cell.

To obtain how long ultra-capacitors will be able to let the light shine in seconds, dt , can be evaluated by the following formulas:

$$\begin{aligned} C_{\text{total}(i)} &= (i_{\text{avg}}) \left(\frac{dt_i}{dV} \right) + (i_{\text{avg}})(R) \\ &= (i_{\text{avg}}) \left(\frac{dt_i}{dV} \right) + (i_{\text{avg}}) \left(\frac{\tau_i}{C} \right) \end{aligned}$$

(4)

or

$$dt = \frac{C_{\text{total}(i)}}{i_{\text{avg}}} \times dV \quad (5)$$

Where i_{avg} is the average current, dt the time in seconds the ultra-capacitor will operate and dV the voltage drop.

By calculating and evaluating the cost in dollar per minute it was obtained that the 3000 F ultra-capacitor will be the most cost efficient. It was decided to order 6 x 3000 F ultra-capacitors.

Sizing the solar panel: There are many aspects to consider when sizing a solar panel, such as: hours of sun per day, load demand, solar radiation in the area and the mounting angle of the solar panel for optimal solar radiation.

Firstly it is important to obtain the amount of power per day that will be demanded from the solar panel by the system. Thus the calculations are as follows: load demand (W/h) x 1.3 (energy losses caused by the system) = $(x_2 \text{ number})$ Wh/day (must be provided by the solar

panels). The lowest solar radiation in Potchefstroom is 3.64 kWh/m²/day, which were used for the calculations [5].

Watt-peak rating of the solar panels needed (kWh/day):

$$\frac{(x_2 \text{ number}) \text{ kWh/day}}{3.276 \text{ (solar panel generation factor)}} \quad (6)$$

The solar panel generation factor is the collection efficiency of the solar panels multiplied by the lowest monthly solar radiation in a year. To obtain the amount of solar panels needed, are clarified by the following formula: Wh/day (watt-peak rating) / (solar panel size of choice) = photovoltaic modules. Therefore only one 30 W solar panel will be needed.

Sizing the solar regulator / controller: To evaluate the size of the solar regulator is as follows:

Determine its charge current:

$$C_c = \frac{30 \text{ W (power output of solar panel)}}{12 \text{ V (nominal battery voltage)}} = 2.5 \text{ A} \quad (7)$$

Determine its maximum charge current:

$$C_{c\max} = C_c \times 1.2 \text{ (safety factor)} = 3 \text{ A} \quad (8)$$

Thus, a solar regulator with a maximum charge current of 3 A must be obtained. Looking at the prices and the features of the regulators, it was decided to obtain the Steca Solum 6.6 F solar regulator as it has the most features and it is simple to install.

Programmable Logic Controller: A PLC was used for the solar system where the battery and the ultra-capacitor bank were used as a combination for energy storage. The xLogic SuperRelay (PLC) that was used was programmed with xLogic software. The software includes logic building blocks to program the device. The xLogic SuperRelay was programmed with the basic function blocks AND, OR and NOT. The PLC let the ultra-capacitors charge to 12 V and discharges to 6 V as the lights turn off at 6 V as ultra-capacitors can be discharged to 0 V. It let the battery charge to 13 V and discharges to 11 V. The xLogic SuperRelay let the ultra-capacitor bank discharges first and then the battery.

All the components sized above were used in each of the three systems except for the PLC was only used as described above.

3. RESULTS

The tests results shown below were recorded from 24 – 28 September 2012. No cloudy or rainy days were present and the solar panel was perfectly placed to obtain the most solar radiation possible. It was simulated in PVsyst® that a solar panel mounting angle of 28° are necessary in Potchefstroom.

3.1 Battery as energy storage

The system containing a battery as energy storage gave a constant charging and discharging voltage curve as expected.

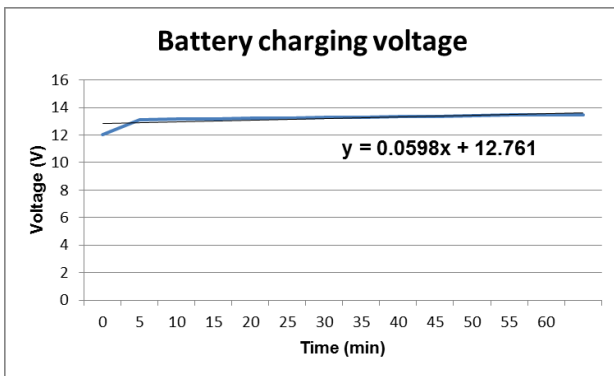


Figure 1: Battery charging voltage curve.

The battery’s discharging curve is being displayed in the figure below. As can see the battery gave an overall constant supply voltage with a slightly decrease in the battery’s voltage over time until the battery supply is being cut off by the solar regulator to protect the battery from deep discharging. The Steca Solum 6.6 F solar regulator is designed to cut a 12 V battery’s voltage off between 11.2 V – 11.6 V during discharging. Thus the measurements show that the solar regulator indicated a weak battery voltage at about 11.8 V and the light stop shining. The light has shone for 5.5 hours (330 min) as indicated on the graph below.

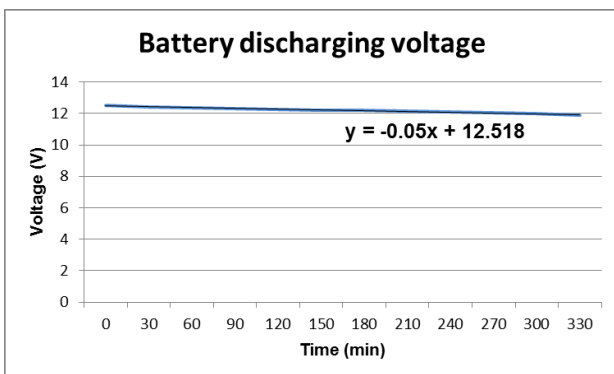


Figure 2: Battery discharging voltage curve.

The battery’s discharging load current was measured 0.45 A – 0.47 A for the full discharging period. Therefore it also indicates that a battery gives a constant energy supply and let the light shine with a slight change in

brightness throughout the discharging period. It can be seen on the graph and the linear equation that the discharging curve of the battery is minimal and has a gradient of -0.05.

3.2 An Ultra-capacitor as energy storage

The figures below shows the charging and discharging voltage curves of the ultra-capacitor bank used.

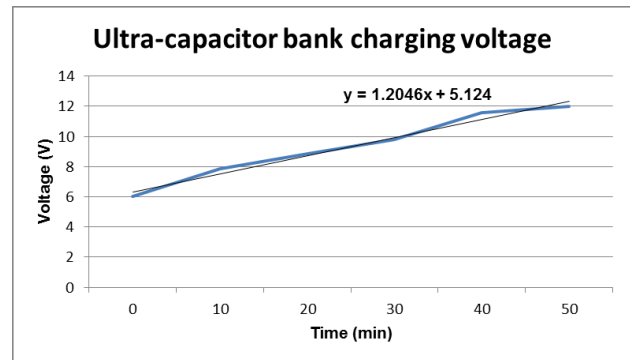


Figure 3: Measured charging voltage.

In the graph above it can be seen that the ultra-capacitor bank only charge in 50 minutes, which is one of ultra-capacitor’s greatest advantages. The charging time for ultra-capacitors is much faster than for batteries.

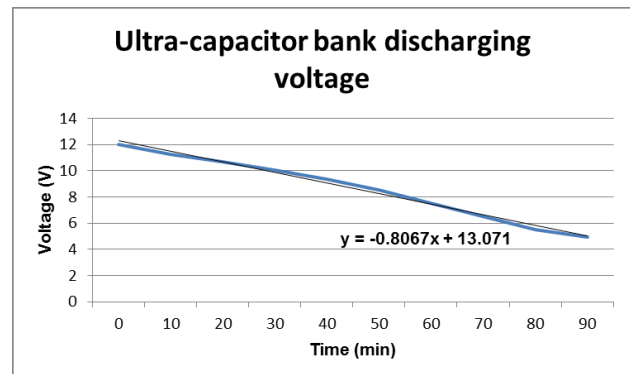


Figure 4: Measured discharging voltage.

When looking at the two figures above it can be seen that the charge and discharge curves results into two linear curves. As it is a characteristic of ultra-capacitors that the charge and discharge curves is linear, it can be said that the ultra-capacitor bank operate normally in the system. In the figure above it can be seen that the ultra-capacitor bank discharges until about 4 V before the lights switches off, but as from 6 V – 4 V the lights intensity are very weak. Thus for efficient lighting the ultra-capacitors discharges for about 75 minutes when it reaches 6 V.

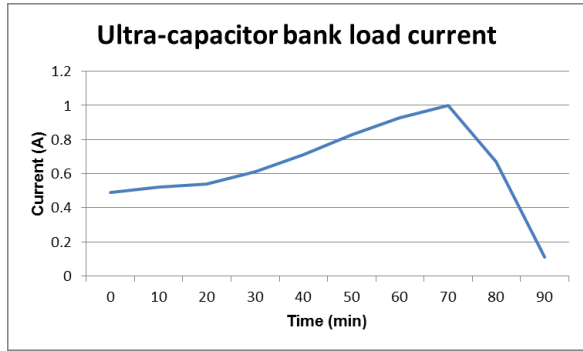


Figure 5: Measured load current.

Figure 7 shows that the load current at the beginning of the discharging period is 0.5 A as expected with 12 V energy and a load demand of 6 W. As the voltage of the ultra-capacitor bank drops, the current increases until there is not enough energy left to provide the load with and the current drops. Thus the current drop states the fact that the light intensity from 6 V – 4 V are very weak. Therefore the lights will be efficient until the ultra-capacitor bank reaches 6 V. The highest current the 6 W load can demand is 1 A that was reached at 6 V when comparing figure 6 and figure 7.

3.3 A battery and an ultra-capacitor bank as energy storage

A photo of the prototype battery and ultra-capacitor bank solar panel street light is shown in figure 8. In this figure the ultra-capacitors, solar panel, battery, PLC and light can be seen. A PLC is used to control the system as described under heading 2.2, “Method”.

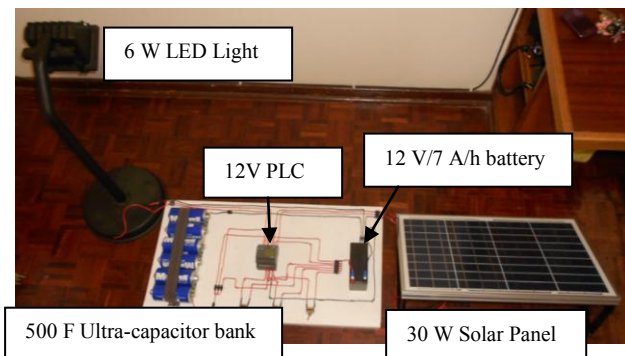


Figure 8: Solar light with a battery and ultra-capacitor bank as energy storage.

The charging and discharging voltage curves of the combination system is seen below.

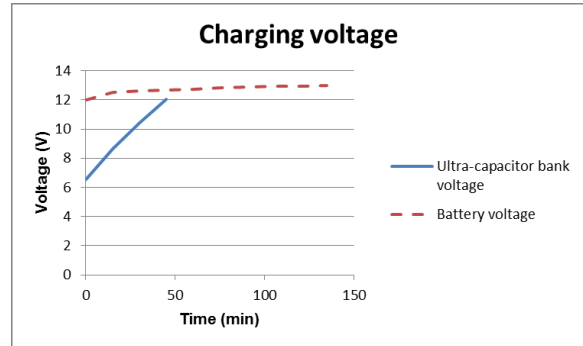


Figure 9: Charging voltage curve of a battery and ultra-capacitor.

The battery and the ultra-capacitor bank charges at the same time until the ultra-capacitor bank is fully charge as indicated in the figure above. After about 50 minutes the battery charges alone for another 90 minutes until fully charged while the ultra-capacitor bank is fully charge at 12 V within 50 minutes.

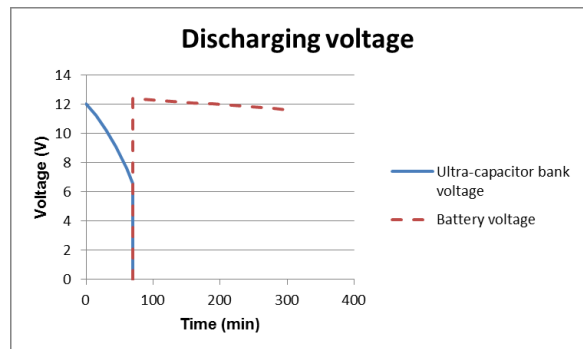


Figure 10: Discharging voltage curve of a battery and ultra-capacitor.

The ultra-capacitor bank discharge just above 6 V in about 80 minutes and then the PLC switches from the ultra-capacitor bank to the battery. In the switching time the light goes off for a split second until relay 4 is opened and relay 3 is closed of the PLC for discharging the battery until just above 11 V.

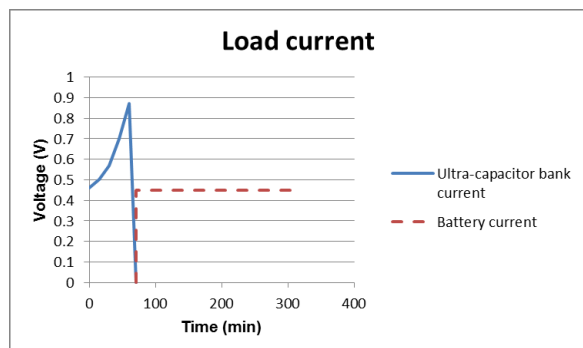


Figure 11: Load current of the battery and ultra-capacitor bank.

The figure above represents the current drawn from the energy storage device by the load. Again it can be seen that if the voltage drop in the ultra-capacitor bank the current increases and the battery provides a constant load

current for the load. This system let the light shine for about 5 hours. This is because the ultra-capacitor bank switches off at 6 V in about 80 minutes and the battery are only charge to 13 V and not higher as in the battery system as evaluated earlier.

3.4 Economical evaluation

The greatest characteristic of ultra-capacitors is there long life time of about 1 000 000 life cycles towards thousands of life cycles compared to batteries. Ultra-capacitors also have a life time of 10 years at rated voltage (2.7 V) and room temperature (25°C). Normally batteries are being discharge to an 80% charge and therefore PV systems required 3 000 life cycles of batteries [2]. The battery that was used has a life time of 5 years.

If considering the life cycles of each energy storage device discussed above, one ultra-capacitor bank will be used when batteries would have been used and replaced for several times. It can be calculated that ultra-capacitors have $(1\ 000\ 000 / 3\ 000) = 333.33$ life times more than required PV batteries.

If only ultra-capacitors are being used for energy storage, it would be very expensive. The ultra-capacitor bank cost almost R 7 000 without the import tax payment. The ultra-capacitor bank only let the light shine for about 90 minutes. Therefore if looking at figure 12 below it indicates what an ultra-capacitor bank will cost to let the light shine for only 12 hours (720 min) without considering bad weather conditions when back-up power is needed for 3-5 days.

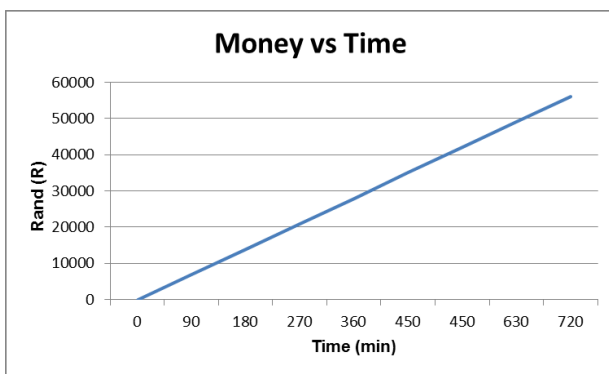


Figure 12: The cost of ultra-capacitors for 12 hours.

4. CONCLUSION

The evaluations preformed in this paper were done to develop and extend solar panel street light technology. A prototype solar panel street light was built, since it was too expensive to build a standard size solar panel street light. The aim was to evaluate three systems with three different energy storage devices (battery and/or ultra-capacitors). The systems include a 30 W solar panel, 12 V / 7 A/h battery, 500 F ultra-capacitor bank, a solar regulator, a PLC and a 6 W LED load. The first system evaluated was the system with the battery as energy

storage. As expected it gave a constant energy supply to the load for a period of 5.5 hours, as shown in figure 4. The second system evaluated was the system with the 6 ultra-capacitors in series as energy storage. A total of 6 ultra-capacitors were used in series to provide the required 12 V. The results obtained shows that the ultra-capacitors charged to 12 V within 50 minutes and for efficiency lighting it discharged in about 70 - 80 minutes.

It is shown that the cost of replacing batteries with ultra-capacitors is very high. Although ultra-capacitors have a very long life time of about 1 000 000 life cycles the initial cost to install such a system will be unrealistic when considering it for a standard solar panel street light. When a standard solar panel street light must be implemented it is very important to include backup energy for rainy and cloudy days and thus such a system's funds would be even more.

When considering the third system (battery and ultra-capacitor bank combination), it can be seen that the life time of the battery can be extended by including ultra-capacitors. As ultra-capacitors have about 333.33 life time more than batteries, it will cost R 37 666.25 to replace the batteries for the life time of the ultra-capacitors. Therefore ultra-capacitors can be used together with batteries and ultra-capacitors can provide a solar panel street light's load for the first half or quarter of a night. If the ultra-capacitor discharging time represented a half or quarter night time it would just let the battery discharge to about 96% or 92% charge respectively (less than 10% discharge), but the battery can be used when bad weather conditions is present and a long discharging time is needed.

5. REFERENCES

- [1] RichardsonRFPD "Ultracapacitors", Internet: www.richardsonrfpd.com/Pages/Products-End-Category.aspx?productsCategory=10120&gclid=CNva8_eBrACFYwQfAodcGJnUA, [Accessed on November 22, 2012].
- [2] Y. Chang, X. Mao, Y. Zhao, S. Feng, H. Chen and D. Finlow, "Lead-acid battery in the developments of renewable energy systems in China," *Journal of Power Sources*, vol. 191, pp. 176 -183, Feb. 2009.
- [3] S. Pay and Y. Baghzouz, "Effectiveness of Battery-Supercapacitor combination in Electric Vehicles," in *IEEE Bologna Power Tech Conference*, 2003.
- [4] "Product Guide, Maxwell Technologies Boostcap Ultracapacitors." Internet: www.maxwell.com/products/uiltracapacitors/docs/1014627_boostcap_product_guide.pdf, 2009, [Accessed on Nov. 22, 2012].
- [5] Sustainable energy for environment and development programme, "Exploring LED Street Lighting," *Urban seed update*, vol. 2, no. 3, Sept. 2008.

FLY ASH RESISTIVITY PROFILING FOR COAL FIRED POWER STATIONS USING ESP FILTRATION

G. Chauke and R. Gouws

North-West University, Faculty of Engineering, Private Bag X6001, Potchefstroom, 2520, South Africa.

Email: Chaukegv@eskom.co.za

Abstract: Electrostatic precipitators (ESP) are, used in coal-fired power plants for the removal of particulate emissions. Fly ash resistivity is a primary parameter in the collection of particulate emissions. ESP systems operating with high or low resistivity ash find it difficult to effectively and efficiently collect fly ash, as high resistivity ash results in back-corona discharge, whilst low resistivity results in particle re-entrainment into the flue gas stream. The purpose of this paper is to investigate and obtain a fly ash resistivity profile for existing power plants in South Africa. Ash samples obtained from power plants are, tested making use of an, ash resistivity test oven in accordance with IEEE standard 548-1984. This paper discusses the preliminary experimental results, to determine the resistivity profile in which power plant ESP's are operating. The electrical efficiency of the ESP system is, evaluated based on the obtained resistivity profiles.

Keywords: Electrostatic precipitator, fly ash, resistivity, back-corona, re-entrainment

1. INTRODUCTION

South Africa generates majority of its electricity supply by mean of fossil fuel power stations. The burning of coal has a negative impact on the environment as the gases exhausted from the boiler contain chemical substances, which are harmful to the environment [2, 3]. This is, mainly due to the low-grade quality coal that is, used during combustion. South African power plants, burn low-grade coal, with high ash content that ranges between 28 and 42%. The grade of coal is, determined by the quantity of the combustible (volatile) and non-combustible (ash) matter and sulphur content contained in the coal, i.e. coal of calorific value averaging at 14MJ/kg and 38.3% ash content is, deemed as a low-grade coal [1]. Ash is the non-combustible material present in coal and thus a bi-product during the combustion process. This bi-product exists in two forms, coarse and fly ash. Coarse ash is easily collected in the boiler, whilst, fly ash is, collected by means of electrostatic precipitators or fabric filter bags. The collection of fly ash or particulate emissions minimises air pollution from industrial processes.

Particulate emissions limit are set at 75mg/Nm³, monitored continuous (hourly). A chief air pollution control officer (CAPCO) is, appointed by the department of environmental affairs to ensure that operating plants are, in compliance with legislation.

Failure to operate within the set limits is a taken as non-compliance and results in penalties and the regulator may withdraw the plants operating licence. Thus, in cases where plants exceed the set emissions limit, they are required to reduce production in order to reduce emissions levels to acceptable set standards. The department is in the process to, further reduce this limit to a stringent 50mg/Nm³ by the year 2020 and with existing plants struggling to achieve the, current 75mg/Nm³ limit [3, 6]. Thus, particulate emission has become a major problem that needs to be, addressed by industry in order to operate within the means of the law. Optimizing the operating and collection efficiency of particulate collection systems has become a necessity.

Power plants mainly use Electrostatic precipitators (ESP's) or Fabric Filter plants/ Bags (FFP's) to collect and reduce particulate dust emissions. It has been, found that these systems can achieve collection efficiencies up to 99% under ideal operating conditions [4, 5]. This paper focuses on ESP's installed in coal-fired power plants and profiling fly ash resistivity for different power plants. The resistivity profile is, used to evaluate the influence of different resistivity's on the ESP operating parameters.

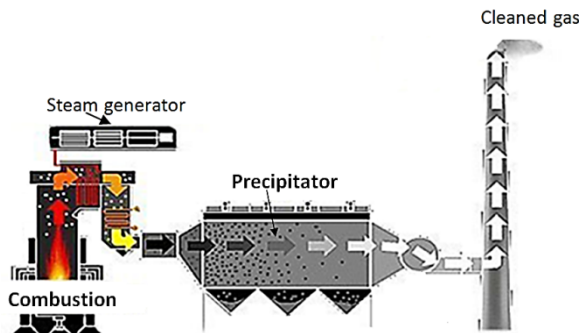


Figure 1: Flue gas filtration in coiler combustion process [11]

Figure 1, demonstrates the application of an ESP. Flue gas filtration is achieved means of electrical forces. The system is, made up of a discharge electrode and two collector plates/ electrodes on either side of the discharge electrode forming horizontal ducts.

The discharge electrode connected to a high voltage DC supply in order to produce the corona discharge needed for ionization. The ionization excites the electron in the inter-electrode vicinity resulting in electron collisions cause an electron avalanche. The electrons, attach themselves to the suspended dust particle in the flue gas stream. The dust particles subsequently attain a negative charge and thus repelled by the electric field toward the collecting plate. The collected dust burden retained in the collector plate until a rapping process dislodges it into ash hoppers. The rapping process is a periodic hammering system, knocking off the collected ash from the collector plate and collected for disposal[4, 5].

2. MATERIALS AND METHOD

The methodology and materials used in obtained the presented results are, discussed in this section.

2.1 Ash resistivity profiling

Ash resistivity is a primary parameter in the effective collection of fly ash. It is dependent on a wide range of factors, such as coal quality and the combustions process. These factors determine the chemical composition of the produced ash.

ESP's have been design to operate at an optimum resistivity of at 1×10^8 to 1×10^{11} Ω -cm [4 and 5] for effective ESP performance (fly ash particles are charged and collected with high efficiency). Thus, any resistivity outside this range results in ineffective

ESP collection, as the ash may fall in the range of low or high resistivity. Particle collection requires the particles to be, charged and retain the charge long enough in order to be, repelled by the electric field established in the inter-electrode spacing for collection.

Low resistivity ash, below 1×10^8 Ω -cm, is difficult to precipitate and collect. The reduced resistivity has been, found to be mainly due to the presence of metallic particles and un-burnt carbon in ash. The effect of low resistivity ash during precipitation is that, it easily attains a charge during the ionization process but tends to; rapidly lose the charge before collection. The charged particles need to retain a charge long enough to migrate to the collector plate and the loss of charge results particle re-entrainment. Particle re-entrainment occurs when particles re-enter the flue gas stream and are not collected, exiting into the atmosphere. Similar problem exists for high resistivity ash, as particles do not easily attain a charge and thus cannot be, collected. The problem of high resistivity was, solved with flue gas treatment to reduce the resistivity; the most effective and commonly used flue treatment is SO_3 injection into the flue gas stream.

The Southern research institute [7 - 9] was at the forefront in conducting research on the measuring of ash resistivity. IEEE Standard 548-1984 was, published as a guideline on conducting ash resistivity measurements on ash in controlled laboratory environment. Laboratory testing is, conducted making use of an, ash resistivity test oven. Prior to testing, the ash sample must be analysed for elemental composition, particle size distribution, and particle density.

The ash resistivity oven is, constructed such that it operates in conditions similar to those in fully, operational ESP plants. The oven parameter inputs are moisture, nitrogen, oxygen, and temperature conditions in which the ash is, exposed too during normal operating conditions.

Figure 2and 3shows the experimental set-up that is, applied in conducting ash resistivity measurements with connected gas cylinders to be, adjusted to model the operating conditions or parameters.

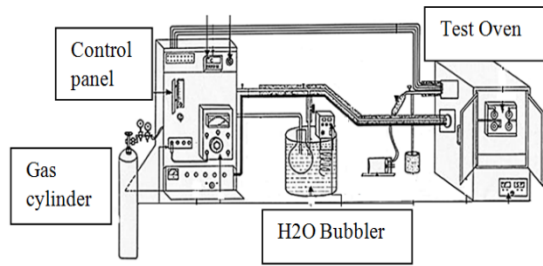


Figure 2: Fly ash resistivity, test set-up apparatus [10]

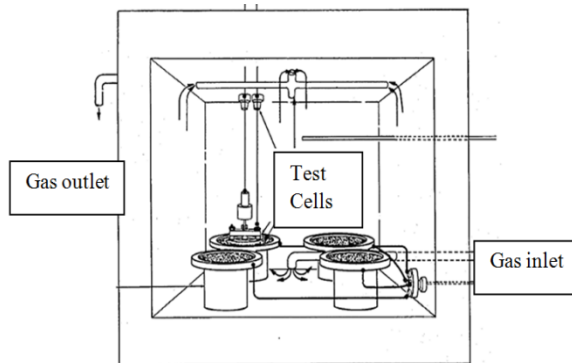


Figure3: Resistivity test oven, test electrode arrangement [7]

The measurements are, taken for descending temperatures, decrements of 30 °C from 215 °C to 95 °C. Current measurements are, taken at every temperature set point for an applied voltage. An alternative test procedure with incrementing temperature is as follows [7 - 9]:

- The collected sample is, firstly sieved making use of a 180-µm sieve.
- The resistivity-measuring cell is, firstly weighed without the ash sample.
- The sieved samples are, packed into the resistivity measurement cell and weighed.
- Care is, taken to insure that the sample is evenly ,distributed throughout the measurement cell.
- The resistivity, measuring cell with the ash sample is, placed inside the temperature-controlled chamber.
- The voltage lead and the electrometer are, connected to the measuring cell; a thermocouple is, connected to the measuring cell.
- Place the disc electrode on surface of the dust sample
- Set the temperature of the chamber to a temperature 215 °C, the setup is, left to run overnight.
- A nitrogen flow is, introduced during the heating up process, overnight.

- The other gases, CO₂, O₂, and moisture are, introduced into the chamber and allowed to reach equilibrium over a period of 2 hours.
- Without the voltage supply connected, leakage or induced current is, measured from the different cells and recorded.
- This leakage current is due to residual charge that is, obtained and retain by the ash elements in the heating process.
- A voltage supply is, introduced to each cell for a period of 60 seconds and 12 current measurements are, recorded.
- The recorded currents are, averaged out, to get a fair representation of the actual current that flows through the sample.
- This procedure is, repeated with every temperature decrement.
- The resistivity is determined by solving for equation 2; knowing the test electrode's dimensions and dust layer thickness, with the recorded current and voltage values.

Resistivity is, defined by the following formulation:

$$\rho_R = \frac{R \cdot A}{l} \quad (1)$$

Whereby, the ash resistivity (ρ_R) in *ohm-cm* is expressed as a function of the resistance (R), obtained by making use of Ohm's law ($R = \frac{V}{i}$), A being the area of the collector plate/ disc and the dust layer thickness (l). Substituting ohm's law, gives the following expression that can used to determine the ash resistivity:

$$\rho_R = \frac{\Delta V \cdot A}{i \cdot l} \quad (2)$$

The obtained resistivity results are, plotted as a function of the different temperature set points. An, additional test is conducted whereby for a fixed temperature, the voltage is incremented until spark over occurs, whilst taking current measurements with every voltage increment. The voltage reading recorded before spark over occurs, is, taken as the electrical breakdown voltage of the dust layer, and is used in determining the resistivity as a function of varying electric field.

2.2 High resistivity effects on ESP's

The collected ash, during precipitation accumulates on the grounded collector plate. When, the dust layer builds up on the ESP collector plate, the resistivity also increases. The potential difference between the discharge electrode and collector plate builds up due to the increased resistivity, as leakage current is

restricted from flowing to ground. This restriction results in collected charged particle not being able to dissipate their charge through the collector plate and thus leading to a charge build-up on the dust layer. The build-up of positive surface charge increases to the point of electrical breakdown, resulting in back-corona. Back-corona is an abnormal gaseous discharge that occurs at the collector electrode and takes place in the presence of corona discharge. The back-corona discharge occurs when the electric field across the dielectric layer is higher than its breakdown strength [12]. Equation 3, describes the positive electric field that is, created due to charge build-up and acts to reduce the overall negative electric field established by the discharge electrode.

$$E_l = j\rho \quad (3)$$

This phenomenon is undesired, as the positive corona discharge also results in the collected dust particles being, dislodged. The dislodged particles are, re-entrained into the flue gas stream. Thus, reduces the collection efficiency of the system.

3. RESULTS

In this section, preliminary laboratory experimental results obtained from two power plants presented, and discussed.

Ash elementary analysis is, conducted on the ash samples. Table 1 lists the elemental composition of the fly ash samples. The elemental composition of the ash is not, used in the determination of the resistivity, though it is given that the composition influences the resistivity. No model accurate model is available that correlates the elementary composition to the resistivity for South African coal and ash. The samples have small percentage deviations in their elemental composition.

Table 1: Fly ash elemental composition

% Elemental Composition	Sample A	Sample B
Silicon (SiO ₂)	53.4	54.8
Aluminium (Al ₂ O ₃)	27.5	25.4
Iron (Fe ₂ O ₃)	3.6	3.8
Titanium (TiO ₂)	1.5	1.4
Phosphorous (P ₂ O ₅)	0.28	0.44
Calcium (CaO)	6.5	7.4
Magnesium (MgO)	1.3	1.5
Sodium (Na ₂ O)	0.3	0.2
Potassium (K ₂ O)	0.8	1.1
Sulphur (SO ₃)	2.6	0.5

Test preparations involve the weighing of the ash samples in order to determine the packing density of each cell. Ash samples have different particle size distributions, which influence their respective packing densities. Table 2, represents the masses obtained for samples A and B. The packing densities of the two samples vary slightly, and this is mainly due to the variation in particle size distribution of the samples.

Table 2: Test cell dimensions and mass measurements

Sample A					
Cell #	Dia. (mm)	Dish mass (g)	Dish + dust mass (g)	Dust mass (g)	Packing density (g/cm ³)
1	76.2	99.3	121.1	21.80	0.99
2	70	116.7	135.8	19.10	1.03
3	70	118.8	135.8	17.00	0.89
4	70	115.9	135.2	19.30	0.99
Average				19.30	0.98
Sample B					
Cell #	Dia. (mm)	Dish mass (g)	Dish + dust mass (g)	Dust mass (g)	Packing density (g/cm ³)
1	76.2	99.4	111.7	12.30	0.56
2	70	116.9	135.4	18.50	1.00
3	70	118.9	139.6	20.70	1.09
4	70	116.0	122.0	18	0.93
Average				19.07	1.00

The test oven has been set-up with gas flow inputs and the oven gas composition is determined from plant operating conditions. Table 3, list the gas composition and flow set-up for the test oven as determined from plant operating conditions. The gas pressures are, regulated at 400 kPa for the duration of the test.

Table 3: Gas flows used during testing

Gas	Flow (ml/min)
Nitrogen (N ₂)	8.7
Carbon dioxide (CO ₂)	13.8
Oxygen (O ₂)	4.6

The gas flow and temperature conditions were, allowed to settle for a period of 24 hours before testing could commence. The obtained results for both samples are as follows.

3.1 Resistivity profile at 2KV, sample A

The results show the average resistivity of the four test cells tested at 2 kV voltage supply. Figure 4, graphically illustrates the resistivity profile of sample

A. It is, noted that at 0% moisture the resistivity is high, whereas with 7% moisture, the resistivity is decreased. Moisture provides a surface conduction path for current to flow through, hence the reduction in the sample's resistivity. The lowest resistivity observed at 95 °C but at 1.28×10^{12} this is, deemed as high resistivity ash. South African power plant ESP's operates in temperature region of 115 °C to 150 °C, and based on the results, the resistivity is high at this range of temperatures for sample A.

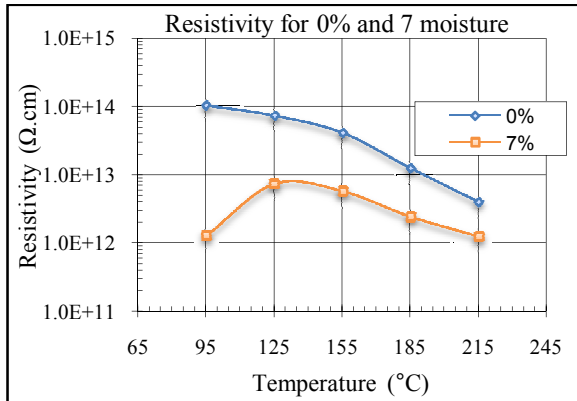


Figure 4: Resistivity profile at 0% and 7% moisture

Table 4, lists the calculated resistivity results as obtained for sample A. The reduction in resistivity when moisture is, introduced into the test oven is most significant at low temperatures and this may be caused by condensation in the system allowing more current to flow through the sample.

Table 4: Sample-A experimental results

Oven Temp. (°C)	95	125	155	185	215	
Sample A						
0% H ₂ O	I (A)	2.01×10^{-10}	2.85×10^{-10}	5.17×10^{-10}	1.69×10^{-9}	5.31×10^{-9}
	ρ_R	1.03×10^{14}	7.31×10^{13}	4.09×10^{13}	1.24×10^{13}	3.96×10^{12}
7% H ₂ O	I (A)	1.62×10^{-8}	2.82×10^{-9}	3.63×10^{-9}	8.59×10^{-9}	1.66×10^{-9}
	ρ_R	1.28×10^{12}	7.34×10^{12}	5.69×10^{12}	2.41×10^{12}	1.24×10^{12}
% ρ_R Reduction	98.76	89.97	86.09	80.51	68.67	

3.2 Resistivity profile at 2KV, sample B

Sample B's resistivity has a similar profile to that of sample A, for 0% and 7% moisture. At 0% Moisture and low temperature the resistivity is at its highest, whereas, with 7% moisture and low temperature is at its lowest and within the stipulated ESP operating range. This highlights the importance of moisture in an ESP system, for the reduction of the ash resistivity

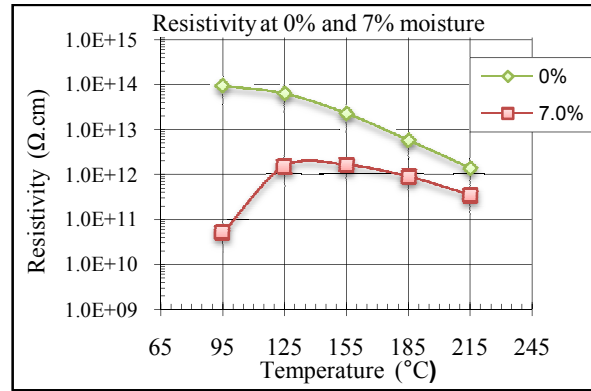


Figure 5: Sample B, resistivity profile at 0% and 7% moisture

The calculated experimental results for sample B presented in table 5. The results exhibit a similar pattern to those obtained for sample A, with the highest resistivity reduction observed at lower temperatures.

Table 5: Sample B experimental results

Oven Temp. (°C)	95	125	155	185	215	
Sample B						
0% H ₂ O	I (A)	1.06×10^{-6}	1.33×10^{-8}	1.21×10^{-8}	2.22×10^{-8}	5.65×10^{-8}
	ρ_R	9.31×10^{13}	6.26×10^{13}	2.26×10^{13}	5.75×10^{12}	1.38×10^{12}
7% H ₂ O	I (A)	4.87×10^{-6}	3.21×10^{-8}	1.87×10^{-8}	3.07×10^{-8}	7.55×10^{-8}
	ρ_R	5.06×10^{10}	1.50×10^{12}	1.63×10^{12}	8.97×10^{11}	3.48×10^{11}
% ρ_R Reduction	99.95	97.60	92.76	84.40	74.71	

3.3 Sample result comparison

The samples had a similar elementary percentage composition. Thus, are, expected to exhibit similar resistivity profiles. Figure 6, illustrates the difference in resistivity profiles for both ash samples.

Sample A has a lower resistivity profile for 0% moisture at higher temperature as compared to that of sample B. However, sample B appears to have a lower resistivity profile when moisture is, introduced into the gas stream. The introduction of moisture, acts to coat the surface of the ash particles and thus reducing the resistivity of the ash samples. The reduction in resistivity means that, in ESP's more ionic current flows and improves the retention of the collected ash. However, the attained resistivity at 7% moisture can, be classified as high resistivity.

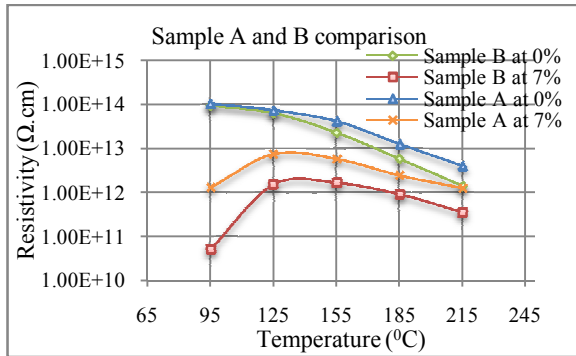


Figure 6: Sample A and B resistivity profiles

The desired resistivity range for efficient ESP operation/ collection has been determined to be 1×10^8 to 1×10^{11} Ω -cm [4 and 5]. The above, obtained results indicate that South African power plants operate with high ash resistivity, when the ash has only been conditioned by moisture. The desired resistivity is achieved at low temperatures, but ESP's operate at temperatures averaging at 110 $^{\circ}$ C to 150 $^{\circ}$ C.

4. CONCLUSION

The preliminary results of samples A and B, indicates that South African ash has high resistivity for moisture conditioning. The desired resistivity range for efficient ESP operation is 1×10^8 to 1×10^{11} Ω -cm. The desired resistivity is achieved at low temperatures, but ESP's operate at temperatures averaging at 110 $^{\circ}$ C to 150 $^{\circ}$ C. The high resistivity results indicate that the ESP's for both sample are operating under back-corona effects. Thus, difficult to achieve the set emissions limit of 75 mg/Nm^3 due to particle re-entrainment resulting from, the high resistivity.

Further studies will be, conducted, making use of SO_3 treatment. SO_3 treatment will be, investigated to quantify the reduction in resistivity. The resistivity at 125 $^{\circ}$ C and 155 $^{\circ}$ C must be, reduced below 1×10^{11} Ω .cm for efficient precipitator collection.

5. REFERENCES

1. Integrated resource plan of 2010 (IRP 2010) [online], available: www.energy.gov.za/IRP/irp%20files/INTEGRATED_RESOURCE_PLAN_ELECTRICITY_2010_v8, accessed: June, 26, 2012
2. R von Grunewald and Y Scorgie (May 2008), "Air quality impact assessment for the proposed new coal-fired power (Vaal south) in the northern free state", Report No.: APP/06/NMS-02 Rev 1.3 [online], Airshed Planning Professionals (Pty

- Ltd, Available: <http://www.saaqis.org.za>. [May 1, 2012]
3. The department of environmental affairs, National air quality offices news volume 5: issue 4 [online], Available: <http://www.saaqis.org.za>. [May 1, 2012]
4. H.White. *Industrial electrostatic precipitation*, London, UK: Addison-Wesley, 1963.
5. K. Parker, *Electrical operation of electrostatic precipitators-IEE power & energy series; no. 41*, London, The Institute of Engineering and technology (2003). [online] Available: www.epri.com. [March 28, 2012]
6. Department of Environmental affairs. National environmental management: air quality act, 2004 (act no. 39 of 2004) [online], available: <http://www.saaqis.org.za>, accessed: May, 10, 2012
7. IEEE Criteria and Guidelines for the Laboratory Measurement and Reporting of Fly Ash Resistivity, IEEE Standard 1224/1327/1224.1/1NT, 1994
8. G. B. Nicholas and S. M. Banks, *Test methods and apparatus for conducting resistivity measurement, report no. 3121-III*, Alabama, The Southern research institute, 1977
9. H. W. Spencer. *Electrostatic precipitators: Relationship between resistivity, particle size and spark-over, report no. EPA-600/2-76-144*, Alabama, The Southern research institute, 1976
10. A. Chandra et al. (2006). "Investigations on fly ash resistivity: Development of empirical relations based on experimental measurement", *Centre for Energy Studies, Indian Institute of Technology Delh.* [Online]. Available: www.isesp.org/. [May 28, 2012]
11. Neundorfer Inc, [online] http://www.neundorfer.com/knowledge_base/electrostatic_precipitators.aspx, accessed: May, 25, 2012
12. A. Jaworeket al. (2006). "Laboratory studies of back-discharge in fly ash, " *Journal of Electrostatics*, [On-line]. vol. 64. pp. 326-337, Available: www.elsevier.com/locate/elstat [June 25, 2012]
13. S. Masuda and A. Mizuno. (1977). "Basic studies on back discharge mode and streamer propagation, Fourth International Clean Air Congress". [On-line]. Paper no.V-47, pp. 73-75. Available: www.elsevier.com/locate/elstat. [June 18, 2012]

OPERATIONAL STUDY ON LOW TEMPERATURE AND HIGH TEMPERATURE PEM FUEL CELLS

C. de Beer*, P. Barendse*, P. Pillay*, B. Bullecks** and R. Rangeswamy**

* Department of Electrical Engineering, University of Cape Town, Rondebosch, Cape Town, South Africa, 7701. E-mail: c.debeer@uct.ac.za.

** Department of Chemical Engineering, Texas Tech University, Lubbock, Texas, United States, 79409

Abstract: This paper presents a comparative study on the operation and performance of Low Temperature (LT) Proton Exchange Membrane (PEM) and High Temperature (HT) PEM fuel cells. The differences in the chemical compositions of the fuel cell components and operational requirements are presented. The dependence on temperature and the resulting change in performance are experimentally analysed and the captured performance curves are presented and discussed for the purpose of practical implementation.

Keywords: Fuel Cell, Flow Fields, Proton Conduction, Flooding

1. INTRODUCTION

Fuel cells are electrochemical energy converters that can directly generate electrical power by converting the potential chemical energy in the reactant gasses to DC voltage and current. A number of different types of fuel cells have been developed, each utilising a unique material or chemical solution as the electrolyte to facilitate the internal chemical reactions [1]. These include the Direct Methanol fuel cell, Alkaline fuel cell, Solid Oxide fuel cell, Molten Carbonate fuel cell, Phosphoric acid fuel cell and the Proton Exchange Membrane fuel cell.

The PEM fuel cell has been developed up to the point where commercial systems are available, and are mainly used in the small scale backup power supply and automotive markets. These systems have a high power density, efficiency and relatively quick start-up times [1]. The main focus of research, to further commercialization, has been cost reduction, reliability and improvements in material performance. Most PEM fuel cells make use of a Nafion membrane that must be humidified to ensure proton conductivity. These cells typically operate in a temperature range between 60°C and 80°C. As a result the water flow in the gas channels is considered to be in a two-phase state, meaning both liquid and vapour phase. The low operating temperature and the humidification requirement gives rise to water management issues within the fuel cell assembly.

In order to improve performance and mitigate the water management issues, PEM fuel cells have been developed that operate at higher temperatures. These HT PEM fuel cells require different materials to withstand the operating conditions. The most viable membrane material developed up to date is polybenzimidazole (PBI) [2]. To enable proton conduction, the membrane must be doped with phosphoric acid. The typical operating temperatures of HT PEM systems range between 120°C and 180°C. At these temperatures the acid becomes immobile and the

water generated can be assumed to be in vapour phase only [3].

This paper presents a study on both LT PEM and HT PEM fuel cells. The differences in the assembly of the two types of PEM fuel cell systems are discussed and the problems with each are highlighted. In particular, the dependence on temperature and resulting change in output power is experimentally investigated. It is shown that the liquid water present in the LT PEM fuel cell causes a drop in performance and the mechanisms involved are discussed.

2. PEM FUEL CELL OPERATION

The PEM fuel cell uses a solid polymer as the electrolyte that allows protons to flow while blocking the electrons, forcing them to flow through the external circuit as shown in Fig. 1. For normal PEM fuel cells the Nafion based membranes must be humidified to enable proton conduction. This is achieved either by direct liquid hydration or by humidification of the gas streams [4], [5].

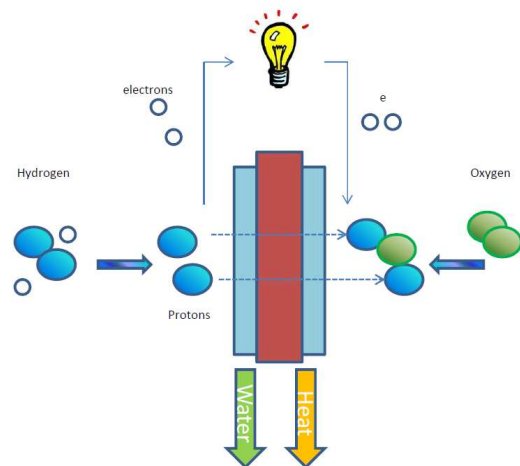


Figure 1: Schematic of the PEM fuel cell reaction.

High purity hydrogen is utilized as the primary fuel and is fed into the anode side of the fuel cell. The introduction of impurities such as CO or sulphides can cause poisoning of the catalyst and a drop in performance. Oxygen must be fed into the cathode side of the fuel cell and can be in a pure form as in Hydrogen/Oxygen fuel cells or in a normal air mixture in Hydrogen/Air fuel cells. The latter, requires an increased amount of catalyst in the cathode side as well as an increased flow rate in order to maintain the same performance as in the pure Oxygen counterpart as the partial pressure of Oxygen is now reduced.

A schematic of the physical structure of the fuel cell assembly is presented in Fig. 2. The membrane electrode assembly consists of the polymer membrane situated between the catalyst layers. The catalyst layers consist of a carbon support with finely dispersed platinum particles [1]. This doping mechanism increases the effective surface area of the platinum resulting in an increase in chemical reactivity during the fuel cell reaction. The catalyst layers are fabricated onto the gas diffusion layers (GDL), these layers are typically manufactured from a carbon cloth or a carbon fibre matrix. The GDL must be electrically conductive and allow the reactant gasses to diffuse to the catalyst layers.

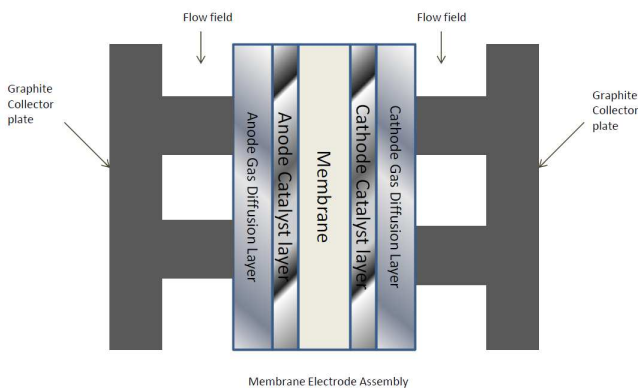


Figure 2: Schematic of the PEM fuel cell assembly.

The complete Membrane Electrode Assembly (MEA) is clamped between the two graphite bipolar plates that act as the current collectors. Etched into the plates are the flow fields that allow the reactant gasses to flow across the surface area of the diffusion layers. Many different types of flow field patterns have been developed in order to increase electrical conductivity and gas diffusion surface area while trying to minimise water droplet formation.

3. EXPERIMENTAL SETUP

In order to demonstrate the performance of both a PEM and HT PEM fuel cell, two assemblies were constructed for testing purposes.

3.1 LT PEM fuel cell assembly

The LT PEM fuel cell MEA consisted of a Nafion 112 membrane with a carbon/platinum catalyst. The surface area of the MEA was 25cm² and was compressed between two graphite bipolar plates with parallel flow fields. A photograph of the bipolar plates with the flow fields is presented in Fig. 3. The cell assembly was heated with cartridge heaters situated in the end plates. The heaters were controlled with a dedicated temperature controller between 70°C and 80°C with a deviation less than 0.5°C from the chosen set point.

During operation, the cell was fed with compressed air on the cathode side and research grade hydrogen on the anode side. Testing was conducted on a Scribner associates test bench. The humidifiers were heated to specific temperatures to avoid or accelerate flooding of the cell. The gas transfer lines were heated to a set temperature of 80°C.

3.2 HT PEM fuel cell assembly

The HT PEM fuel cell assembly consisted of a phosphoric acid doped PBI membrane with a carbon/platinum catalyst. The surface area of the cell was 45cm² and was compressed between two graphite bipolar plates with quad serpentine flow fields. The bipolar plate utilized is presented in Fig. 4. The cell assembly was heated using two cartridge heaters in the end plates using a dedicated temperature control system. The temperature was varied between 140°C and 180°C during operation.

The humidifiers were bypassed during operation as the membrane does not require additional humidification to enable proton conduction. The gas transfer lines were heated to 85°C during operation.

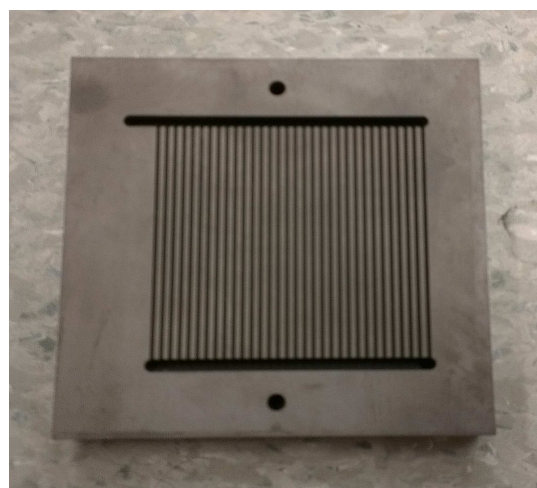


Figure 3: Graphite bipolar plate with parallel flow fields.

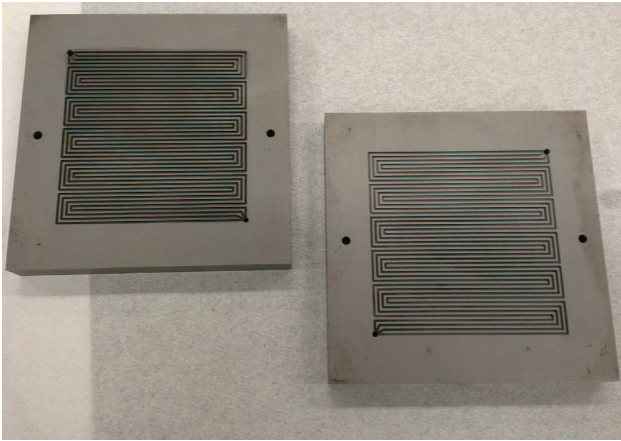


Figure 4: Graphite bipolar plates with quad serpentine flow fields.

4. RESULTS AND DISCUSSION

The performance of a fuel cell can be characterised by a polarization curve. A typical curve and the associated loss regions are shown in Fig. 5. In order to start the reaction, a finite amount of energy is required and results in the initial voltage drop, known as the activation loss. The linear voltage loss results from the internal resistance of the membrane and other cell components. The final loss mechanism is known as the mass transport loss or the concentration loss and results from the limitation on the transportation of gas to the reaction sites at high cell currents.

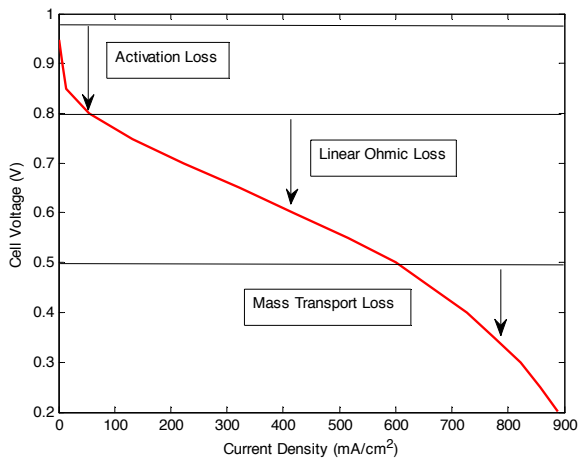


Figure 5: Polarization curve and associated loss regions.

The results captured demonstrate the dependence on temperature and the resulting change in output power for the PEM and HT PEM fuel cells. The 25cm² PEM fuel cell assembly was fed with hydrogen and air at constant flow rates. The load current was varied and the corresponding output voltage captured to generate the polarization curves. Fig. 6 presents the curves for the PEM fuel cell at 75°C and 80°C. The activation, linear ohmic and concentration regions are clearly visible in the plot. The drop in performance for only a 5°C change in temperature is substantial.

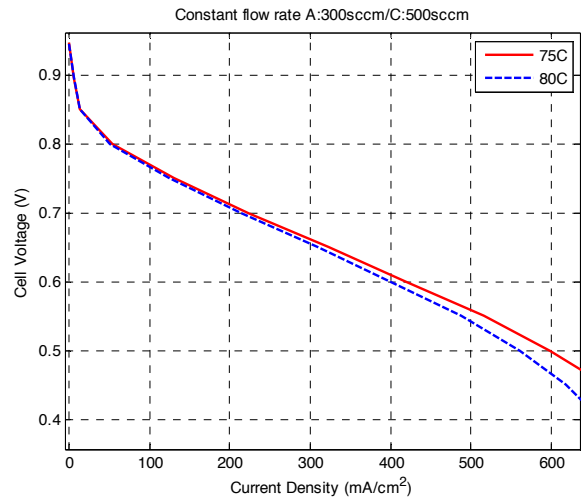


Figure 6: Polarization curves of a PEMFC at different operating temperatures.

The 45cm² HT PEMFC was tested across a temperature range of 140°C to 180°C. An increase in temperature results in an increased power output as shown in Fig. 7. The ability of this type of fuel cell to run at higher operating temperatures creates a number of advantages that can be utilised in a complete power supply system. This includes operating with hydrogen generated from a reformer without the need of a CO scrubbing phase as the HT PEM cell has a greater tolerance for CO in the gas stream. The other operational advantage is the use of the fuel cell in the combined heat and power (CHP) system. These systems not only use the output power of the fuel cell but also make use of the heat generated to assist with the heating functions in a residential or commercial environment [6]-[8].

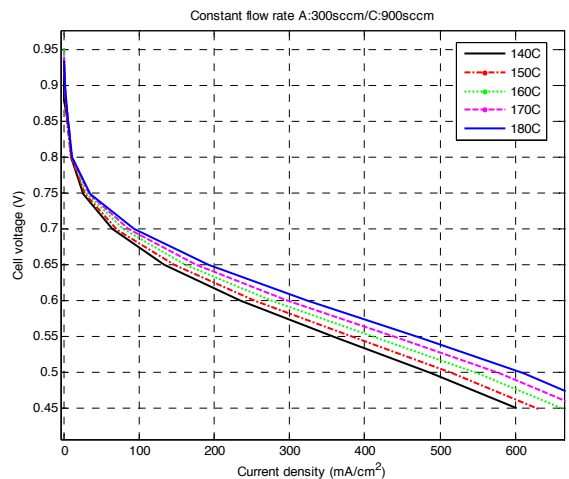


Figure 7: Polarization curves of a HT PEMFC at different operating temperatures.

As stated previously, the major disadvantage of running the PEM fuel cell below 100°C is the presence of liquid water in the gas streams. The liquid water penetrates the gas diffusion layer and restricts the flow of reactants to the catalyst sites and results in a drop in output power.

This fault mechanism is known as flooding [4]. Many factors contribute to the flooding mechanism. One of major concerns is the design of the flow field pattern. The proper design of these flow fields has been a major point of research and has resulted in many computational fluid dynamics (CFD) analyses and resulting models [5]. The most standard flow pattern is the parallel flow field and contributes to the flooding mechanism. The PEM cell assembly tested utilised normal parallel flow fields and the resulting flooding that occurs during operation was captured.

Fig. 8 presents the output current density of the cell for a constant voltage of 0.55V over a period of 300 seconds. The output current decreases at almost a linear rate during the first 150 seconds as flooding takes place in the gas diffusion layer. Water droplets form inside the flow fields and block the flow of the reactant gasses. Once the droplet reaches sufficient size and weight the gas pressure might dislodge it and force it out of the flow field. This results in a sudden increase in output current density as the fuel cell recovers. The captured results for this phenomenon are clearly visible in the magnified results of Fig. 9. The parallel flow fields utilized in this test were particularly susceptible to water droplets blocking gas flow and effectively causing part of the MEA to become inactive.

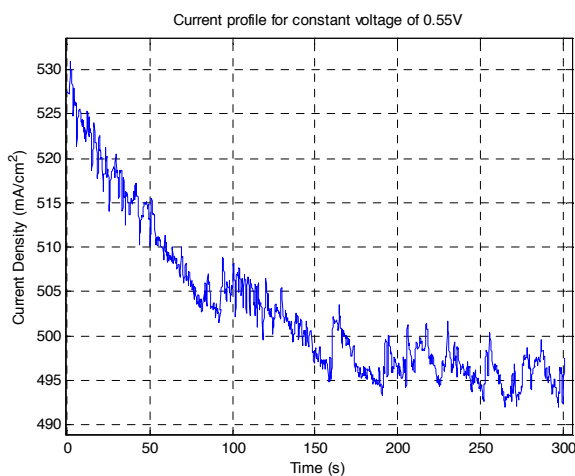


Figure 8: Current density captured during constant voltage test.

The flooding mechanism is accelerated during extreme humidification of the gas streams. Many of the current fuel cell systems make use of online gas humidifiers that are controlled by varying the temperature. For flooding to occur, the humidifier must be run at a temperature higher than the cell temperature, while drying will take place if the humidifier temperature is lower than that of the cell. During operation of the cell, the internal generation of water on the cathode side is greater at higher current densities. Running the humidifiers at a single temperature set point for different cell current densities will thus result in flooding if the internal water management of the cell is not properly managed.

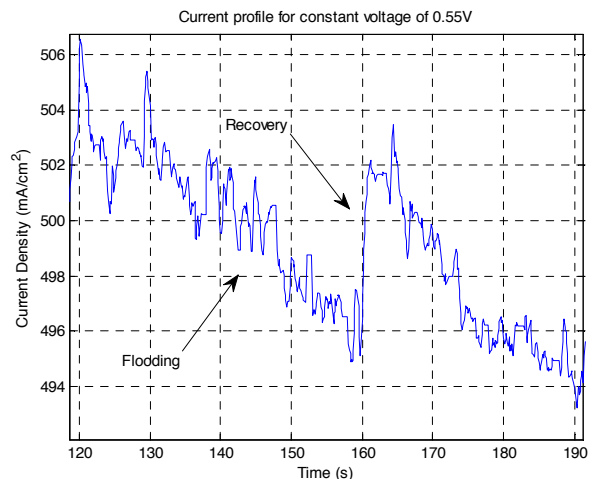


Figure 9: Current density captured during constant voltage test, magnified at recovery.

Because the HT PEM fuel cell operates at elevated temperatures, the discussed water management problems associated with the normal PEM fuel cells are not present. There are however other factors that increase the operational complexity of these systems. The increased operating temperatures accelerate the degradation mechanisms associated with the carbon/catalyst layers. The system also requires a longer time to reach operating temperature during start-up and to cool down during shut down.

5. CONCLUSION

This paper presents the differences in performance for variation in temperature for PEM and HT PEM fuel cells. The differences in the assembly of the two types of cells are presented and discussed. In particular, the major problem in the operation of the normal PEM fuel cells, known as flooding, is discussed and the experimental drop in electrical performance is presented. The reduction in output current density due to electrode flooding and water droplet formation and recovery is clearly visible in the obtained experimental plots. The design of the flow pattern of the flow field and the role it plays in the flooding mechanism is discussed.

6. REFERENCES

- [1] F. Barbir, *PEM Fuel Cells Theory and Practice*, Elsevier, 2005.
- [2] Jianlu Zang et al., "High Temperature PEM Fuel Cells", *Journal of Power Sources*, Vol. 160, pp 872-892, 2006.
- [3] A. Su, Y.M. Ferng, J. Hou, T.L. Yu, "Experimental and numerical investigations of the effects of PBI loading and operating temperature on a high-temperature PEMFC", *International Journal of Hydrogen Energy*, Vol. 37 pp. 7710-7718, 2012.

- [4] Hui Li et al., "A review of water flooding issues in the proton exchange membrane fuel cell", *Journal of Power Sources*, Vol. 178, Jan 2008.
- [5] N. Yousfi-Steiner et al., "A review on PEM voltage degradation associated with water management: Impacts, influent factors and characterization", *Journal of Power Sources*, Vol. 183, April 2008.
- [6] A.D Hawkes and M. A. Leach, "Cost-effective operating strategy for residential micro-combined heat and power", *Energy*, vol. 32, no. 5, May 2007, pp. 711-723.
- [7] J. Harrison and S. Redford, "Domestic CHP: What are the potential benefits?," *EA Technology for the Energy Saving Trust*, Capenhurst, Chester, Tech. Rep. CH1 6ES, 2001.
- [8] M. Houwing, R.R. Negenborn and B. de Schutter, "Demand Response with Micro CHP Systems." *Proceedings of the IEEE*, vol. 99, 1, pp. 200, Jan. 2011.

PROBABILISTIC METHODS FOR RENEWABLE ENERGY SOURCES SUPPLYING VARIABLE LOADS – ADDITION OF GRID CONNECTION

E. Namanya* and C. T. Gaunt*

* *Department of Electrical Engineering, University of Cape Town, Private Bag, Rondebosch, 7701, South Africa, South Africa E-mail: ct.gaunt@uct.ac.za and nmemm001@myuct.ac.za*

Abstract: Solar homes have become a popular technique in rural electrification in South Africa. Given the stochastic nature of solar availability, these solar homes are only effective during days of high solar irradiation. This paper explores the possibility of adding a low current capacity grid connection to solar PV system, as a Hybrid Renewable Energy System (HRES), in a single household system (SHS) application using probabilistic methods. The method used is an extension of the optimization model, presented in a 2009 report to analyse the performance of a Hybrid Wind Solar Power System (HWSPS). It is extended to assess the effect of the grid connection addition on the reliability and sizing of the solar PV system. A model for grid connection, based on its capacity and failure rate, and an on/off based charge control algorithm was added to the existing model and the system simulation process established for Monte Carlo Simulations using MATLAB® program. A reliability study simulation is carried out using the Adequacy Confidence index (ACI), a reliability index used in the model. The effect of several variations in the HRES components was tested in several simulations. Using a desired level of reliability (i.e. specified ACI), the system was optimally sized for different battery sizes and cost added to produce financial optimization results.

Keywords: hybrid renewable energy systems; system sizing; reliability; weak grid connection

1. INTRODUCTION

South Africa has an abundant supply of sunshine hence the increased proposals to use solar PV as energy source in rural electrification and other applications such as solar homes. In the Eastern Cape, for instance, 7300 solar homes have been installed by KwaZulu Energy Services (KES), a subsidiary of French Power utility EDF, with each household system having between 55 – 65 Wpeak capacities [1].

However, this source is weather dependent and varies in availability whereas the load demand varies according to the demands of the customer. Most of the country is grid-connected through Eskom's electrification activities and the choice between use of PV or grid depends on factors such as location and classification type of customer [2]. There is room for development and use of both solar and grid connection in a hybrid system. Although the conventional grid connection to rural areas is a very expensive venture, a small grid connection may be added to the renewable energy (RE) system to compensate for the unavailability of solar resource. In this report, we explore an approach to answering the questions: "How small a grid connection can be added to a solar system to achieve a desired level of reliability cost effectively and is it a worthwhile venture?"

Extensive study and research has been carried out to assess Hybrid Renewable Energy Systems (HRESs) in regards to their performance and optimization. Many models and approaches based on the basic power model have been presented to assess HRES performance based upon specific design situations or scenarios [3] [4] [5] [6].

A more general model of HRES was proposed to which an approach was taken with the inclusion of uncertainty, to investigate the adequacy and reliability of a Hybrid Solar/Wind Power System (HSWPS). This model was also used to optimally size the solar PV and wind components, as well as the battery sizing requirements to supply the load with required confidence. This general model can be used and extended to include HRES assessment for a variety of combinations of intermittent (e.g. renewable), dispatchable (e.g. diesel generators) or grid sources of supply of energy [7].

2. GENERAL MODEL OF POWER SYSTEM WITH RENEWABLE ENERGY

In [7], a general model was proposed to analyse the performance of various configurations of HRESs. The schematic diagram of a general power system, shown in Figure 1, is used in the model. The model unifies a wide variety of combinations of different power sources – intermittent (i.e. renewable energy sources e.g. solar, wind), dispatchable (i.e. diesel generators) and grid supply. It allows for the variation in the load and can also be refined to include losses in the battery, which is not perfectly efficient. The model can be applied to very simple installations such as single households and be extended to include many sources, each of different characteristics and reliability. The model allows comparisons to be made for a consistent level of adequacy and reliability of the total supply, and with appropriate confidence in the model, giving greater meaning to the financial optimization of the combinations. This model

adds onto the basic power system by taking into account the variation of the load and modelling its uncertainty [7].

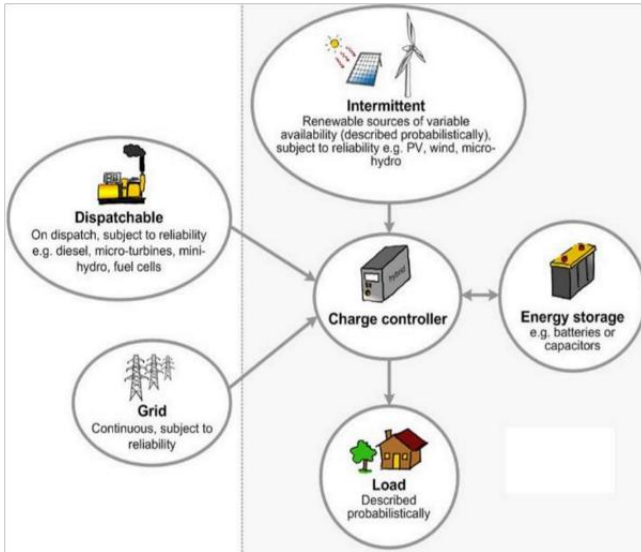


Figure 1: Schematic diagram of General Power System

This general model is used in this paper to investigate the possibility of adding a small grid connection to a solar PV/Battery system in regards to system reliability and optimization.

3. SYSTEM DESCRIPTION

The Figure 2 shows the solar PV/Battery system with a small grid connection supplying a single rural household load. The system is based in the Lucingweni village area in the Eastern Cape in South Africa. The solar PV panel provides power when the solar irradiance levels are high. This energy supplies the load and the excess is used to charge the battery. The grid connection supplies energy from the grid to charge the battery when it is below a desired level of capacity. The charge controller controls the movement of energy in the system, according to its algorithm.

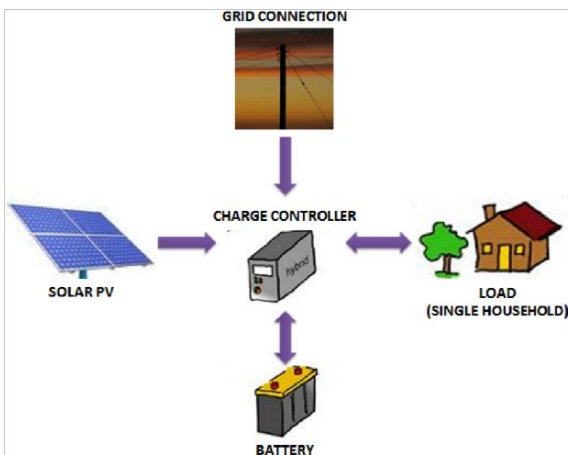


Figure 2: Schematic of HRES - Solar PV/Battery system with small grid connection

4. HRES MODEL

4.1 Solar PV system model

Many probability distributions have been used to model solar and wind such as beta distribution for solar. These distributions are mostly focused on the total energy availability during an extended period. This model, however, is concerned with the variability of the energy source during typical days of the year. Since there were no data for solar irradiation for the Lucingweni site, the resource data was obtained by normalizing hourly measurement data from similar locations (Durban for solar irradiation and East London for wind). Estimation software was then used to obtain the power output profile per kWpeak installed for one year at the Lucingweni site [7].

The power from the PV panel, covering area A_{PV} for a particular level of solar irradiance, I_{PV} is given in equation (1) below:

$$P_{PV} = A_{PV} \times I_{PV} \tag{1}$$

4.2 Load model

A Beta probability distribution function was used to model small groups of customers. However for a large number of customers (larger than 30) the load current distribution tends towards a Gaussian or normal distribution with an overall group mean μ_N and variance σ^2_N [7].

The variation in the load distribution may then be described by equation (2) below, as indicated in report [7]:

$$I_N = \mu_N + Z(\sigma_N) \tag{2}$$

Where Z is obtained from the Gaussian tables (e.g. $Z = 1.28$ for a 90% level of confidence).

Although the normal distribution is suitable for a large number of customers, it is worthwhile to note that its infinite limits may lead to sampling impractical load figures for example, in a house with a 60 A circuit breaker, the load currents modelled using Gaussian distribution may lead to sampling values of current above 60 A. A beta distribution may be better distribution to model the load because of its closed finite limits.

4.3 Grid Connection model

A grid connection has two operating states, normal operating state and failure state. When representing the characteristic of a grid connection, the basic parameter used is its Forced Outage Rate (FOR). Similar to the probabilistic model of generation with consideration of FORs, the FOR can be useful in expressing the outage rate of a grid connection to model the uncertainty in the grid connection [8].

A two-state model for the grid connection is obtained by modelling the FOR. FOR is denoted as q and the

transmission line capacity as c , as shown in equation (3) [9].

$$P(X = x_i) = \begin{cases} 1 - q & x = c \\ q & x = 0 \end{cases} \quad (3)$$

4.4 Battery model

The battery is sized to supply and meet the load demand when the solar PV is not sufficient to meet the load. The battery sizing parameter considered in this project is the rated battery capacity and the model is based on the Battery State of Charge (SOC), similar to the model in the paper [3].

Assumptions made to the battery model include:

1. The battery discharge efficiency is 70% accounting for losses of 30% while the battery charging efficiency is 100% (ideal)
2. The maximum SOC, SOC_{max} is equal to the nominal rating of the battery
3. The system conversion components (inverters) are 100% efficient
4. The battery lifetime (discharge cycles) is infinite

The battery SOC at a time (hour) t is given by:

Without grid connection:

$$SOC(t) = [SO(t - 1)\alpha + E_{PV}(t)] - E_{Load}(t) \quad (4)$$

With grid connection:

$$SOC(t) = [SO(t - 1)\alpha + E_{GRID}(t)] - E_{Load}(t) \quad (5)$$

The SOC is subject to constraints

$$SOC_{min} \leq SOC(t) \leq SOC_{max} \quad (6)$$

Where:

SOC_{min} and SOC_{max} is minimum and maximum battery charge quantity respectively $SOC(t) =$ Battery State of Charge at hour, t

$SOC(t - 1) =$ Battery State of Charge at the previous hour

$E_P(t) =$ Energy from solar PV at hour, t

$E_{GRID}(t) =$ Energy from grid connection at hour, t

$E_{Loa}(t) =$ Load demand at hour, t

$\alpha =$ Battery discharge efficiency

4.5 Charge Control Algorithm

The charge controller algorithm dictates the mode of operation of the system, specifically the direction flow of energy in the system. It maintains the highest possible SOC in the battery whilst avoiding overcharging and undercharging. The algorithm used in this project is based on the on/off algorithm, used by majority of the charge controllers.

The 4 modes of operation in the system based on the battery SOC, as described as follows:

Mode 1 – Battery Fully Charged

$$(SOC(t) = SOC_{max})$$

Here, the charge controller disconnects the battery from the PV panels and prevents any flow of energy to the

battery to avoid over charging. The charge controller allows flow of energy out of the battery (discharging) to supply excess load demand, which cannot be met by the PV.

Mode 2 – Battery SOC above Specified Threshold Capacity

$$(SOC_{threshold} \leq SOC(t) \leq SOC_{max})$$

The charge controller allows charging in case of any surplus energy (when PV power exceeds load demand) or discharging of the battery to supply excess demand (when load demand exceeds available PV power).

Mode 3 – Battery Below Specified Threshold Capacity

$$(SOC_{threshold} \geq SOC(t) \geq SOC_{min})$$

The charge controller allows connection to the grid to charge only up to the threshold capacity as it discharges to supply the excess load demand or is being charged using surplus energy from the available PV.

Mode 4 – Battery at minimum charge

$$SOC(t) = SOC_{min}$$

The charge controller disconnects the load from the battery and prevents further flow of energy from the battery to avoid over discharging. The charge controller allows flow of energy to the battery (charging) from the grid connection and PV panel.

Figure 3 shows the simplified charge controller algorithm implemented in this system. It categorises the system operation in 4 modes.

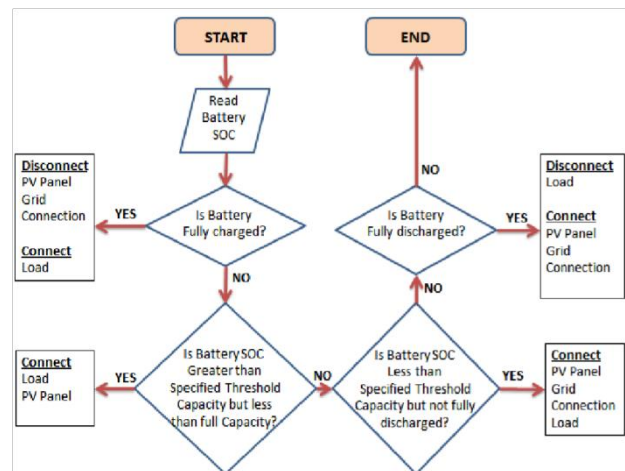


Figure 3: Simplified Charge Controller Algorithm

5. OPTIMAL SIZING CRITERIA FOR HRES

In the existing literature in the area of HRES, there have been various methods for assessment of these HRESs. In this paper, the solar PV/Battery system with a weak grid connection system is assessed based on reliability. Optimization is carried out based on the desired reliability. The overall methodology used in this study is shown in Figure 4 below. It comprises simulating the system process for 50 years using the Monte Carlo Simulation (MCS), because of its ability to handle uncertainty in complex models.

5.1 Reliability Criteria Based on Adequacy Confidence Index (ACI) technique

In this study, the HRES reliability is expressed in terms of a reliability index - Adequacy Confidence Index (ACI). ACI can be defined as the maximum number of hours per year at a specified confidence level the system will not supply the load (i.e. load demand exceeds the power generated) for a large number of simulations. The MCS developed mimics the system process for each hour in 50 years. An outage hour is obtained through the battery SOC in that a negative value for the battery SOC indicates both the PV and battery, trickled charged by grid connection, cannot fully supply the load. For example, if there are less than 100 hours of outage in 45 out of the 50 simulations, the ACI of the system is described as 90% confidence in less than 100 outage hours.

5.2 HRES Optimization

The system is then optimized based on the desired reliability required by the planner. The system optimization is done for both capacity and cost perspectives. For these simulations, the system is optimized for a given number of outage hours at a specified confidence index. For capacity optimization, the solar PV and grid connection is optimized for different battery capacities. For preliminary financial optimization, the capital costs of the system components are added onto the capacity optimization to add financial meaning to the optimization.

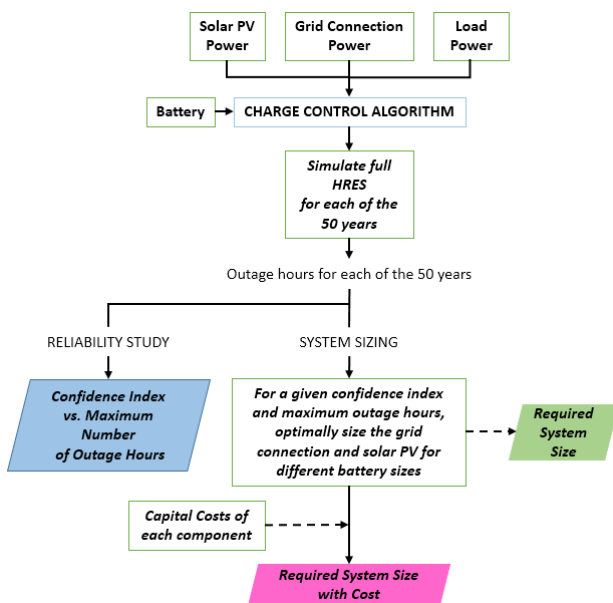


Figure 4: Flow chart showing overall system simulation process and methodology

6. RESULTS AND DISCUSSION

6.1 Base Case Configuration

The methodology above has been applied to analyse a solar PV/Battery system with a small grid connection designed

to supply a single rural household or solar home system (SHS). The technical characteristics include 300Watt solar PV panel, 1800 Wh battery system [10]. A 2-A grid connection, with no failures, is added to the system.

6.2 Reliability Study

Figure 5 shows that the addition of a small grid connection improves the reliability of the PV–Battery System. The system without a grid connection has more outages because of its reliance on a single source of energy (the sun), which is continuously varying throughout the year.

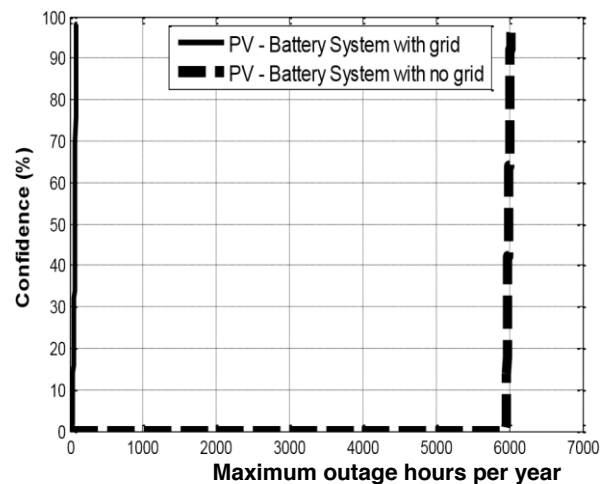


Figure 5: Reliability Study of PV/Battery system with or without grid connection

Addition of the small grid connection helps to compensate for times when the solar PV is not available (low irradiance levels) by trickle charging the battery when its capacity is below the set threshold level of 80%. The grid connection acts as an extra back up to the solar system with the battery.

6.3 Capacity Optimization

Figure 6 shows that an increased system (solar PV and grid current) capacity is required for to achieve higher system reliability i.e. less number of outage hours. To maintain the reliability desired (i.e. number of outage hours at desired confidence level), the addition and increase of a grid connection current capacity can reduce the size/capacity of solar PV installed for a specified battery capacity. The capacity of PV, grid current and battery in the base case were more than adequately sized because of high battery losses (30%). Employing batteries with high efficiency (10% battery loss) and low grid failure rate allows for smaller system sizes to achieve desired reliability. Large battery capacities allow for reduced solar PV and grid connection currents to achieve same level of desired reliability or system adequacy.

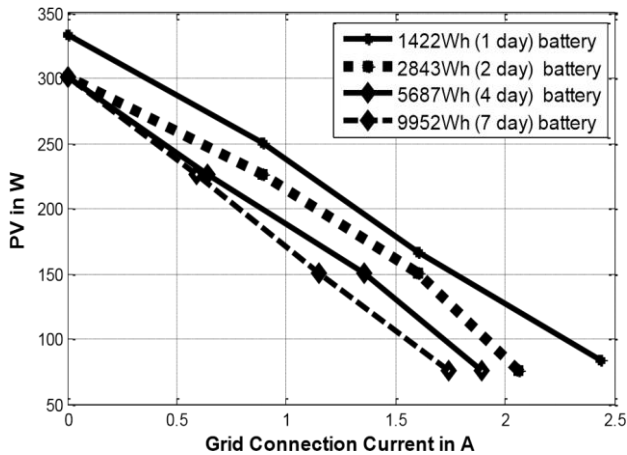


Figure 6: Combination of PV, grid current and battery needed in CS needed for 90% confidence in less than 100 hours of outage for SHS

It is also observed that addition of the grid connection reduces the required PV capacity for different battery capacities. Increasing the grid connection capacity allows the designer to have a smaller solar PV capacity installed and still attain the required reliability (i.e. maximum outage hours at specified confidence level).

6.4 Preliminary Financial Optimization

The ACI can also be used to optimize the system from a capital costs perspective to achieve a desired reliability in terms of maximum hours of outage acceptable. From this, the combination, of lowest cost, providing the same level of reliability (system adequacy) can be found. Figure 7 shows that the smallest battery capacity (1-day) configuration has higher costs more than the 2-day battery because it requires higher PV capacity to maintain the same levels of system adequacy.

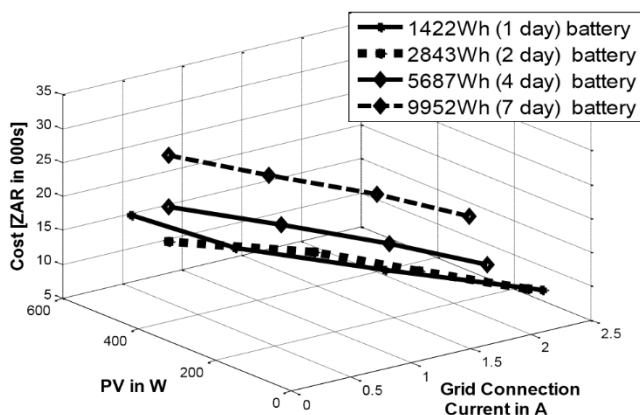


Figure 7: Financial Optimization Results (only Capital Costs) for CS needed for 90% confidence in less than 100 outage hours

However, the 7-day battery has the highest costs because of the cost of the battery (energy storage). The optimal

choice of system configuration can be chosen in between these two extremes.

6.5 Significance of Threshold Capacity Adjustment

Figure 8 shows that increasing battery threshold capacity improves system reliability. This is because of the small battery size used, which means that a high battery threshold capacity allows charging from the grid connection to maintain the high battery charge. This allows the battery to adequately satisfy the excess load demand.

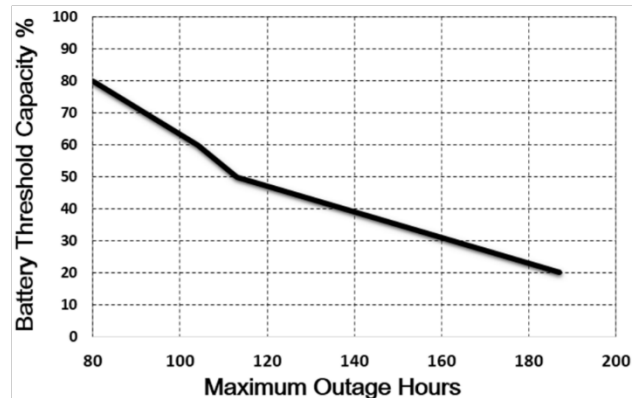


Figure 8: Effect of variation of Threshold Capacity

However, it is important to know that although decreasing the threshold improves system reliability and it comes at increased cost of use of grid connection.

7. CONCLUSIONS

The optimization model used in [7] was successfully extended to analyse the adequacy of a different type of HRES (i.e. solar PV–grid connection–battery system) and allow for optimization of the combinations for a required number of outage hours with appropriate confidence.

The possibility of small grid extension to solar PV systems would be a welcome option to the solar home systems in that it improves the reliability and capability. A small capacity (mean current around 2A) grid connection can be added to homes only for purposes of charging the battery below a set threshold capacity, which allows for smaller capacity solar PV panels and battery size to be used. It also reduces the overall cost of system making solar homes affordable for customers. With a grid connection, the threshold which dictates the level at which the grid connection comes in to top up the battery can be adjusted to limit the energy obtained from the grid connection. This is very useful as it allows for different energy requirements with different battery capacities used e.g. small battery sizes require higher threshold at which the grid connection comes in to top up while large battery sizes used may allow for a much lower threshold capacity set meaning less energy is drawn from the grid.

The grid connection capacity need not exceed a mean of 2 A to enable maximum and effective use of the free clean PV energy. A balance in capacity is reached such that the grid connection current is not enough to be used to meet the normal daily load demand but is enough to trickle

charge the battery to keep it at a high level of charge. This brings importance to a low current capacity grid connection and dispels the notion of thought that conventional grid connection (for current capacities in the order of 20 A and 60 A) is the only way of reliable electrification. As it is expensive or not worthwhile to connect some rural areas to the main grid due to various reasons, a cheaper option of using low current in a small conductor to improve reliability can be used and create a “win-win” situation for both consumers and the power utility or government.

8. REFERENCES

- [1] I. Esterhuizen, “KES submits proposal to continue KZN solar electrification project,” *Creamer Media's Engineering News*, 4th October 2012.
- [2] Barnard, D.W., 2011. *Renewable Energy and Rural Electrification: South Africa Experience*. [Online] Available at: http://www.energy.gov.za/files/media/presentations/2011/20111206_WolseyBarnard_RE_electrificationPresentationv2.pdf [Accessed 15 August 2012].
- [3] A. Celik, “Techno-economic analysis of autonomous PV–wind hybrid systems using different sizing methods,” *Energy Conversion and Management*, vol. 44, no. 12, p. 1951–1968, 2003.
- [4] Y. Katsigiannis, P. Georgilakis and E. Karapidakis, “Multiobjective genetic algorithm solution to the optimum economic and environmental performance problem of small autonomous hybrid power systems with renewables,” *IET Renewable Power Generation*, vol. 5, no. 4, pp. 404-419, 2010.
- [5] S. Ashok, “Optimised model for community-based hybrid energy system,” *Renewable Energy*, vol. 32, no. 7, p. 1155–1164, 2007.
- [6] H. Yang, L. Lu and J. Burnett, “Weather data and probability analysis of hybrid photovoltaic-wind power generation systems in Hong Kong,” *Renewable Energy*, vol. 28, no. 11, p. 1813–1824, 2003.
- [7] C. Gaunt, R. Herman and B. Bekker, “Probabilistic Methods for Renewable Energy Sources and Associated Electrical Loads for Southern African Distribution Systems,” in *CIGRE/IEEE PES Joint Symposium*, Calgary, 2009.
- [8] S. Lee and L. Min, “Probabilistic Transmission Congestion on Forecasting,” *University of California CIEE*, California, 2008.
- [9] X.-F. Wang, Y. Song and M. Irving, *Modern Power Systems Analysis*, 2009 ed., New York: Springer, 2008.
- [10] EEMB Company Ltd, “Solar Home System Specification EEM ET-300,” EEMB Company Ltd, 2011. [Online]. Available: <http://www.eemb.com/pdf/EEMB%20ET300%20%20.pdf>. [Accessed 24 September 2012].

RECONFIGURABLE SOLAR ARRAY FOR IMPROVING EFFICIENCY OF A POWER CONVERTER

M.R.Looi, M.M. Wu, J.I. Braid

Abstract: A reconfigurable solar array for a small solar-powered vehicle is presented. The performance of the system is measured by the improvement of efficiency of the DC-DC power converter for supplying a 300W, 24V Permanent Magnet DC motor. The switching matrix, consisting of 12 nodes and 11 MOSFETs, allow the 24V, 16V, 12V output voltage configurations to be utilised. A marginal increase (less than 2%) is measured for systems under 60W, and that the switching matrix has higher losses at higher output power. The reconfigurable solar array is recommended for systems with high voltage and low current specifications.

Key words: reconfigurable solar array, adaptive solar array, electrical array reconfiguration, load matching.

1. INTRODUCTION

With the escalation of energy crisis over the recent years, extensive research has been devoted to increasing the efficiency of photovoltaic (PV) systems. The attempt to minimise the losses while providing maximum power transfer is of significant importance in this field of research. As commercial solar panels are produced with defined voltage specifications (12, 24, 48V), the use of a DC-DC converter is inevitable in extracting the user desired voltage from the fixed voltage. However, this additional sub-system introduces more losses. This challenge is prominent in systems where PV panels are directly coupled to the load, due to the lack of energy storage system.

A buck converter is a switch mode power supply used to convert the high output voltage from the PV array to the lower user-desired voltage. Fig. 1a depicts the relationship between the efficiency and the duty cycle of a traditional buck converter system. The losses of a buck converter is inversely proportional to the duty cycle, therefore, for most efficient operation, the duty cycle is to be kept as close to 100% as possible. This is achieved by allowing the input voltage to be as close to the output voltage as possible via a reconfigurable array. Fig. 1b compares the efficiency of the reconfigurable array to a traditional array with a constant resistance load. It shows that for a traditional array, the system is inefficient at low output voltages, and that it is possible to obtain a higher average efficiency by reconfiguring the PV array.

A reconfigurable PV array, consists of multiple smaller PV modules, known as nodes, which are interconnected by a network of switches. A desired configuration of the nodes is achieved by controlling the combination of the switches by allowing the nodes to be connected in series or in parallel. The V-I characteristic of the array can be modified over a wide output range, whilst keeping the output of each module relatively constant.

This paper investigates a reconfigurable PV array as a final

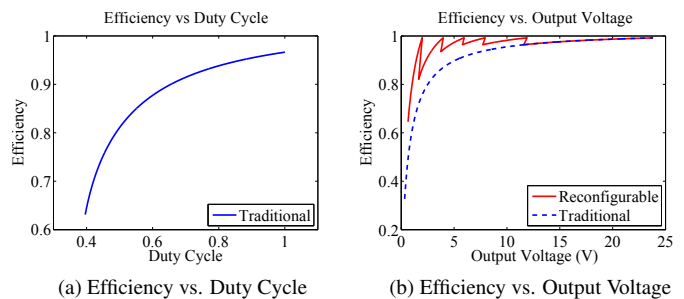


Figure 1: Performance of a Buck Converter

year student project, where the success of the project is not based on an increase of system performance, but rather the contributions made to this field of research. A brief background is presented, while the detail of the system design considerations is followed by the comparison between a traditional and reconfigurable array.

2. PROJECT BACKGROUND

It is noted in [1] that the performance of a solar-powered system is not only dependent on the weather conditions and the panel degradation, but is also strongly dependent on the PV system configuration. This section summarises the existing reconfigurable arrays in mitigating the challenges facing current PV systems.

Different methods have been developed to condition a PV system to operate near its optimal operating point [2], where the typical method is the implementation of a Maximum Power Point Tracker (MPPT) [3]. An alternative is the method of reconfiguring the connection of solar cells to achieve a certain electrical condition. In [1], the reconfiguration of the solar modules is presented to improve the system efficiency for partially-shaded cells. Similarly, [4] proposes a switching matrix that connects an adaptive solar bank to a larger, fixed PV system under shading conditions. In [5], an $m \times n$ solar matrix design is proposed to maximise the available power by

matching solar modules to the operating conditions, based on insolation and shading.

Another variation of the reconfigurable array aims at producing a higher output power via load matching. In [6], the author suggests that since the VI-characteristics of the load is independent of the array characteristics, the interconnections may be selected to suit the load. Electrical Array Reconfiguration Controller (EARC) is utilised in direct-coupled water pump systems, where the switching is based on the insolation level and the current requirements of the motor [7]. An EARC that is made appropriate for a photovoltaic car is presented in [8], where the array configuration is determined by the state of driving. A series connected array is used for accelerating state where a high voltage is required; on the other hand, a parallel connected array is configured to provide a high starting torque [8].

3. PROJECT FRAMEWORK

The focus of the project is aimed at improving the efficiency of the buck converter in supplying a constant power load for a direct-coupled system. As a measure of performance, the reconfigurable array is compared to the traditional array. The success of the project is primarily based on the improvement of efficiency of the buck converter via the use of power electronics as the switches to reconfigure the PV array. In addition, it is necessary to identify the conditions where the proposed system is deemed feasible. Through an extensive literature survey of reconfigurable solar array solutions, the system specifications are defined by highlighting the assumptions and constraints.

3.1 Constraints and Specifications

Other than the time constraint of six weeks, the availability of the materials poses significant limitation in the choice of system design. As a result, the system specifications are governed by the following constraints:

- The limited use of electronic components due to a budget and availability constraints.
- Due to the unavailability of solar wafers and manufacturing equipments, the solar cells as the nodes for the matrix were emulated with bench top power supplies. As a result, the maximum node current capacity is limited at 3A.

The system specifications were determined to have a voltage and power capacity at a minimum of 300W at a maximum of 24V.

3.2 Assumptions

The project is developed as a proof-of-concept, the detailed design choices (such as the MOSFET model, cable size, etc) that do not have a fundamental significance in the

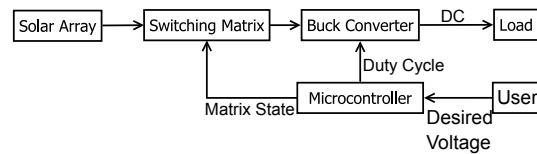


Figure 2: System Block Diagram

engineering solution are selected based on availability, cost and the ease of implementation. Solar cells operating at an ideal capacity, would allow the bench-top power supplies to be used for testing— (at 4V, 3A). In addition, each solar cell is considered identical, hence equal current-sharing between the solar modules is assumed.

4. DESIGN CONSIDERATIONS AND IMPLEMENTATIONS

For a conventional, direct-coupled solar system, the output voltage of the solar array is stepped down to the user-desired voltage via a buck converter, where the duty cycle is determined by a microcontroller. The operation of the reconfigurable solar array system is depicted in Fig. 2. The microcontroller obtains the desired voltage that the user defines and subsequently reconfigures the matrix into the corresponding states depending on the requirements. This switching process is where an increase in efficiency is achieved. A Pulse Width Modulated (PWM) signal is sent to the buck converter, which steps down the output voltage of the solar matrix by changing the duty cycle, matching the output of the buck converter to the user-desired voltage.

Since the performance is assessed by comparing the reconfigurable array to the traditional array, designs that are common to the two are not a priority. As a result, the buck converter is only designed to handle the system specifications and to allow the ease of interface with the solar array. To achieve a significant amount of decrease in losses for the buck converter, the choice of switching matrix topology as well as the auxiliary driving circuit is to be carefully evaluated as there are substantial losses associated to the switches. In addition, the design of the PV array architecture defines the operating regions of the system.

4.1 Solar Array Architecture

A reconfigurable solar array consists of multiple smaller solar modules, which is henceforth referred to as a “node”. The nodes are the smallest composition unit within the array, and the specifications of the nodes determine the capability of the system performance. The structure of the solar array is based on two parameters: the number of nodes and the relative size of each node.

The choice of the number of nodes installed is a tradeoff between complexity, flexibility, cost, efficiency and the average utilisation of installed capacity. The utilisation of installed capacity is referred to as the ratio of the

number of nodes being used to the total installed capacity at various configurations. A 100% of utilisation factor implies that all the solar cells installed are being utilised at all configurations. Flexibility of the system is of importance, and it can be achieved by smaller node sizes, more nodes as well as more configurations. A simple system implies that the number of nodes is to be reduced without compromising the flexibility. With an increase in the number of nodes, the flexibility increases, but the cost and efficiency decrease as more circuitry and hence losses are required to switch between the different voltage configurations. The optimal number of nodes is one which has the highest number of factors, where the number of configurations increases. This implies that the increase in flexibility is at the expense of higher complexity. Complexity is therefore the limiting factor when choosing the number of nodes.

The primary design decision of choosing the optimal node size is based on the complexity introduced. As a result, identical sized nodes are chosen to simplify construction, design and testing of the system [9]. The current sharing between identical nodes is simpler to control. In addition, the full output voltage of the solar array can be utilised when the nodes are connected in parallel [9]. The size of the node refers to the solar module's voltage and current capability, and is therefore limited by constraints described in Section 3.1. Although it is preferable to have a smaller node size to allow for a more flexible system, a balance must be achieved to reduce complexity while maintaining the flexibility.

A 12 node system is selected as the most optimal, as it results in the highest number of factors with the least amount of nodes. The configurations that can be achieved include placing 1, 2, 3, 4, 6 and 12 nodes in series, where this number is multiplied by the node voltage size, which will result in the output voltage of the solar array. Initially, the node voltage is selected to be at 2V to allow all the configurations to be used. Upon further investigations, by only selecting the middle three configurations (3, 4, and 6), the minimum duty cycle is increased from 50% to 66%. This configuration is desirable since efficiency is inversely proportional to the duty cycle. This implies that instead of a 2V scaling factor, the 4V scaling factor is to be used as illustrated in Fig. 3. The relative node size is based on the required output voltage specification and current constraint, and is designed to be at 4V, 3A. As a result, the proposed reconfigurable PV array has the voltage configurations of 12, 16, 24V.

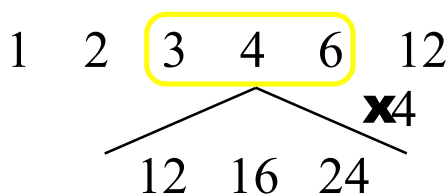


Figure 3: 12 Node, with 4V Node Voltage

Due to the research and development nature of this

project, prototyping and testing is essential in validating each design decision. As a result, a unique 3-layered switching matrix topology is implemented to create a robust and adaptive solution. The switching matrix topology is designed to allow maximum flexibility for the interconnection of the solar modules, the switching circuit and the buck converter, as illustrated in Fig. 4. The logic signal is sent to the driving circuit to connect the solar modules in various series and parallel configurations, where the array output voltage is the input to the buck converter.

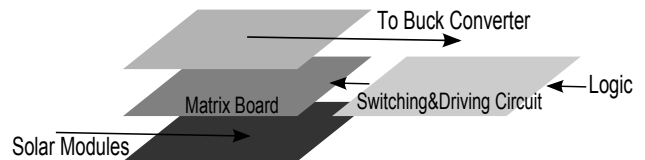


Figure 4: Switching Matrix Topology

4.2 Switching Board Topology

The switching board topology is the arrangement of the nodes in relation to one another. The layout of the nodes also contributes to the flexibility of the connection of nodes, the number of switches required, and the type of switches. By using a matrix layout, as opposed to a linear topology as proposed in [9], the flexibility is increased as it allows non-adjacent nodes to be connected. In addition, the number of switches can be further reduced by replacing non-essential switches with fixed wires, which are identified as the switches that are either entirely on or off for the various configurations. Although this design reduces the number of switches, the disadvantage is that since each node is presented with a different voltage potential at the various configurations, the driving of the semiconductor switches must be carefully designed.

The proposed matrix topology (Fig. 5) reduces the number of switches by four in comparison to a linear topology, promoting simplicity and efficiency of both the switching and driving circuit. In addition, this architecture benefits from its modular nature that further allows the expansion of the modules if needed. By connecting two identical matrices in series, the output voltage can be doubled, while the current capacity can be increased via a parallel connection. The 4×3 matrix board comprises of two sets of terminal blocks, allowing the connection for both the solar modules and the switching matrix, where the simplified circuit diagram is shown in Fig. 5.

4.3 Electronic Switching

The use of electronic devices to switch the configuration of the nodes allows the configuration of the solar array to be controlled by a microcontroller. Complexity in the driving circuit and the associated losses between the connection points (load side) of the switch are the primary deciding factors in selecting the switching device. Since MOSFETs are preferred in low voltage and low power applications (<

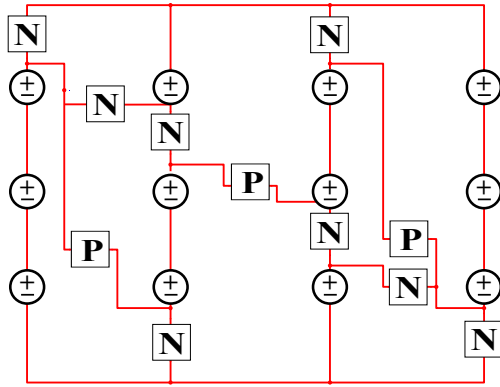


Figure 5: Switching Matrix Circuit

250V, < 500W), it is preferred over IGBTs that typically operate at high voltages. Solid-State Relays (SSR) are expensive and include higher losses than MOSFETs. As a result, the decision lies between electromechanical relays and MOSFETs. The MOSFET losses are only present when it is conducting in the forward direction, and is quantified by $P_{loss} = i^2 R_{ds(on)}$. As a result, the losses are proportional to the current. On the other hand, the losses of a relay are constant throughout its on-state, independent of the power within the system. This dynamic characteristic of the MOSFET is preferable since the system is required to operate over a wide range of power.

A switching matrix using semiconductors as switches to connect power sources in various configurations, is shown in Figure 5. Two semiconductor devices are considered: the P-channel MOSFET and the Back-to-Back N-channel MOSFET, where the placement of the FETs are determined by the voltage potential at the node as well as the current direction required. P-channels are placed between each string as shown in Fig. 5, where bi-directional current is not present. Rather than using a blocking diode, a back-to-back N-channel design is implemented to prevent the reverse current flow when the MOSFET is required to be in an off state. The losses associated with a blocking diode is defined by its forward voltage drop ($V_D = 0.7$), while the losses in a MOSFET are quantified by the drain-source on-resistance ($R_{ds(on)} \approx m\Omega$). Although the drive circuit for a back-to-back N-MOSFET is far more complex, the efficiency of the system is significantly increased.

The challenges of high-side driving is alleviated through the implementation of an optocoupler with an isolated power supply, as shown in Fig. 6. The voltages on D_1 and D_2 become sequence independent, implying that both D_1 and D_2 can be connected to a higher potential since bi-directional current is restricted. Although this has the drawback of doubling the losses, the total loss using two N-channels are less than using a single P-channel since the $R_{ds(on)}$ are typically smaller in N-channels. By independently tying the sources and the gates of the two MOSFETs together, only a single driving circuit is needed, as opposed to two separate driving circuits.

The isolated power supply that is required to feed the output side of the optocoupler is achieved by a transformer and rectifier, which is modelled as a 9V battery in Fig 6. The transformer is excited with a 5V, 62.5kHz signal, and with a 1:2 turns ratio. The output of the transformer is rectified with a full-wave rectifier IC, where the negative end is then connected to the output emitter of the optocoupler. The positive end is used to drive the gate voltage, where a 100kΩ current-limiting resistor is used to tie the gate and source together. This connection between the gate and source allows $V_s = V_g$ during the off state of the MOSFET, when the isolated power supply is not connected. The problem of high side driving is no longer a concern and since the source and gate terminals are driven by the external circuit, where the MOSFET can be placed in any location in the matrix, obtaining a much more flexible and adaptive circuit.

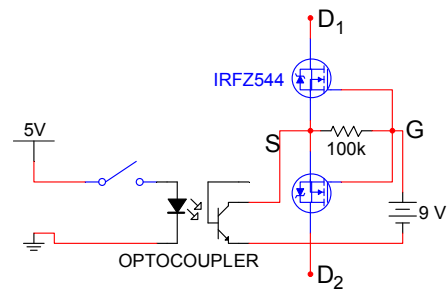


Figure 6: Back-to-Back N-channel Drive Circuit

4.4 Final Design Implementation

The switching board was built on veroboard that caters for 12 nodes, which required 11 MOSFETs to achieve three different configurations (12, 16, 24V). To incorporate the ease of installation and to enhance re-usability, the switching board only consisted of wire buses and terminal blocks. The semiconductor switches and driving circuits were mounted on an external veroboard, which allowed for a smoother testing and debugging process. The nodes were made easily detachable in order to switch to the traditional setup during testing. The traditional switching board was implemented by using the same veroboard design, but replacing all electronic switches with the fixed 24V connection.

5. RESULTS

This section presents the experimentally measured results, where the same quantification scheme is used to assess the improvements of the proposed solution. A MATLAB script was developed prior to the experiments, where the simulated results for constant power test are shown in Fig. 7. Two sets of tests were performed to validate the simulation as well as to quantify the performance of the reconfigurable array by comparing its performance to a traditional array.

Firstly, the ideal reconfigurable array, where there are no switching losses, are compared to a traditional array. This

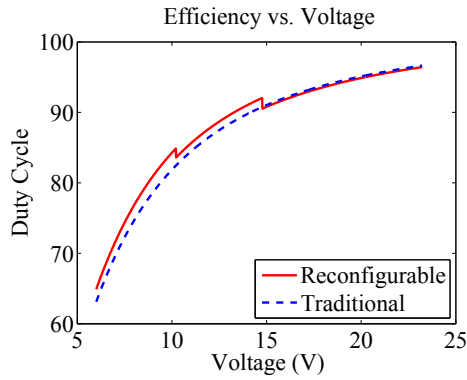


Figure 7: Simulated Constant Power Test Results

serves as a proof of feasibility prior to the construction of the electronic switching. The experiment was conducted with the use of a single power supply to emulate the entire reconfigurable array, where the switching of each state is performed manually. The nominal efficiency of a traditional array is found to be around 90%, where an increase of over 2% was measured for all the tests conducted. This indicates that the reconfigurable array is worth pursuing.

Secondly, the system described in Section 4. was tested, including all the switching and driving circuit with the microcontroller actuating the process. An individual 5V power source is used to supply the auxiliary circuit, where the current was carefully monitored and recorded to represent the driving circuit losses, as seen in Table 1. In addition, the power required to drive the transformer is 10.23mW, contributing to the losses involved in the auxiliary circuit. It can be seen that the losses for the auxiliary circuit are proportional to the number of MOSFETs being switched on. The results are shown in Fig. 8 for various constant power loads.

Table 1: Microcontroller and Driving Circuit Losses at Various Configurations

Configurations	12V	16V	24V
# of MOSFETs on	6	5	4
Losses (mW)	660mW	365mW	372mW

6. DISCUSSION

The constructed system is a prototype version of the proposed system, where the circuit parameters and system implementation can be further optimised. The MATLAB script was developed based on the theoretical model, and it is shown that the experimental results (Fig. 8) closely follow the simulated results (Fig. 7). This provides validation of the feasibility of the reconfigurable array, while raising the confidence level of the obtained results. This section discusses the performance of the system through quantitative and qualitative analysis by assessing the results.

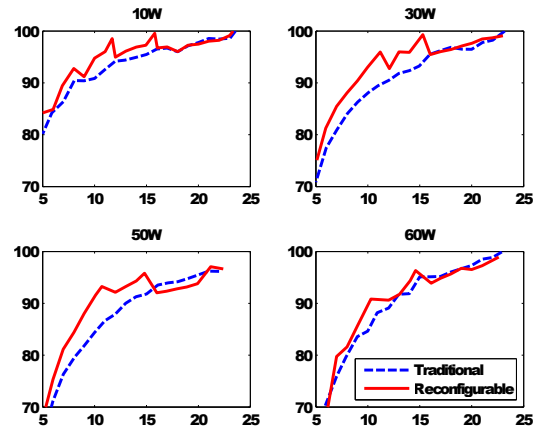


Figure 8: Constant Power Test for Traditional Solar Array vs. Ideal Reconfigurable Solar Array

6.1 Efficiency Analysis

Table 2: Comparison between Traditional and Ideal Reconfigurable Solar Array under Constant Power

Tested Power	Traditional Efficiency (%)	Reconfig. Efficiency (%)	Efficiency Increase (%)
10W	93.73	95.36	1.63
30W	90.69	93.27	2.58
50W	87.13	89.67	2.53
60W	90.42	90.81	0.38

The average efficiency for the various power loads are calculated and shown in Table 2. The results demonstrated a marginal increase in the overall efficiency. Over the range of tested constant power loads, the reconfigurable array improved the efficiency by an average of 1.78%. The calculation of efficiency is based on the voltage and current readings from analogue meters, which both provides a very coarse resolution. Therefore, measurement errors are present in the results. The ammeter with a scale reading up to 10A has an accuracy of $\pm 0.05A$, and the voltmeter with a scale reading up to 30V has an accuracy of 0.1V.

The constructed system was tested under various constant power conditions, and the results show that the average efficiency of both traditional and reconfigurable arrays, decreases as the power required increases. This is because the buck converter loss is proportional to the current, with the occurrence common to both systems. The important point to note is that although there is an average increase in efficiency by using the reconfigurable array, it is in fact less efficient at the high output voltage range compared to the traditional array, especially as the power increases. As output power increases, the current that flows through the MOSFETs and the driving circuit also increases. As a result, more losses are dissipated in the switching circuit.

A distinct efficiency increase is seen in Fig. 8 when the

array reconfigures. Due to the inevitable losses in the circuit, although the duty cycle is at unity, the efficiency of the system is not. Another interesting point is that even though the duty cycle is 100% at all 12, 16, 24V, the efficiency decreases at lower voltages. This is due to the inverse proportionality of the voltage and current at constant power. At lower voltages, the current increases to maintain the power, resulting in higher losses.

Most importantly, there is only an average efficiency increase of 0.38% at 60W. This means that with the increase in current, the losses dissipated in the switching circuitry negate the benefits of the array reconfiguration. Since output power beyond this cannot be tested due to the power supply constraints, the validity of the reconfigurable system cannot be tested for higher power levels.

Since the performance of the reconfigurable array is dependent on the operating conditions, it is most beneficial to allow the reconfiguration to occur at regions where the load is most frequently operated. For instance, different configurations can be employed for different types of loads. Although it may not be beneficial to use the proposed voltage configurations (12, 16, 24V) for loads that operate predominantly at lower voltages, a different configuration such as 6, 8, 12V can be used.

During the component selection of MOSFETs, the cheapest and the most available IC's were used. It is possible to further increase the efficiency of the reconfigurable array with the use of MOSFETs having a lower on-resistance.

6.2 Flexibility of the Switching Matrix

The modular topology can be easily expanded to increase the current and/or voltage capabilities of the PV generator by preserving the matrix structure. In addition, the matrix design can be used to switch any type of power sources as well as loads due to its robust nature. For a battery-coupled system, a separate matrix (with the same structure) may be used to interconnect the batteries during charging conditions. Moreover, for loads that do not require smooth voltage inputs, the buck converter may be entirely eliminated by having sufficient nodes for each discrete operating condition of the loads.

6.3 Optimal Operation Criteria

In order to maximise the benefits of a reconfigurable solar array that is directly coupled to the load, the following conditions must be met:

- To improve efficiency, a high voltage and low current system specification is essential. As with conventional solar-powered systems, the losses in the switching circuit are dependent on the current; therefore, it is beneficial to have low currents to minimise power losses.

- The voltage configurations are to be chosen to cater for the specific types of loads, based on the voltage ranges where the load is most frequently operated.

6.4 Future Work

Partial shading effects can be addressed by a reconfigurable solar array. With the use of a microcontroller and current sensors at each node, the switches within the matrix can be controlled to ensure the current through each node is equal. This entails the redesign of the matrix board topology to increase the flexibility of the system, allowing more paths for the current to flow. The reconfigurable solar array is not limited to solar cells, as any power source can be used. If batteries were used as nodes, battery charge equalisation is a possible application.

The reconfigurable solar array is required to supply dynamic loads, which implies that the power demand of the load must be met. Due to the limited physical space and lack of storage in a direct-coupled system, both efficiency and power transfer is of importance. To obtain the maximum power transfer, the load must operate at the maximum power point of the solar array. This is more challenging for a direct coupled system, with the power converter acting either as a variable speed drive or a MPPT. In a direct coupled system, a user controlled MPPT can be employed, which visually indicates the optimal speed to drive the motor at the MPP of the solar array. As a reconfigurable solar array has a dynamic V-I characteristic, the feasibility study of load matching can be conducted. To ensure a quality match, the load line is to coincide with the array's maximum power line, allowing the load to derive maximum power from the PV generator at all time. For example, either the type of load can be re-chosen or the PV generator can be re-sized to ensure a better correlation to the maximum power points.

A more holistic assessment of the quality of the system can be achieved by obtaining the results for the reconfigurable array at more power levels. It is then possible to extrapolate the performance of an unknown load at a known power rating. More tests to investigate the behaviour of the reconfigurable array under various loaded conditions can be conducted.

7. CONCLUSION

A reconfigurable solar array was designed, implemented and optimised for a 300W, 24V PMDC motor. The performance of a reconfigurable solar array was compared and contrasted with a traditional array, where both simulation and experimental testings were conducted. The efficiency of a buck converter could be improved via a reconfigurable solar array. However, this increase in performance is only beneficial in specific output voltage ranges, where the efficiency increases significantly at the point of reconfiguration, while other regions present only a marginal increase and even a decrease in efficiency. To fully utilise the benefits of a reconfigurable solar array,

a high voltage and low current system specification is recommended. In addition, the system should be designed to reconfigure at the regions where the load is most frequently operated. The reconfigurable array has the potential to address other problems encountered with solar panels, such as load matching for maximum power transfer and partial shading.

REFERENCES

- [1] M.A. Chaaban, M. Alahmad, J.Neal, J. Shi, C. Berryman, Y. Cho, S. Lau, H. Li, A. Schwer, Z. Shen, J. Stansbury, and T. Zhang. "Adaptive Photovoltaic System". In *IECON 2010 - 36th Annual Conference on IEEE Industrial Electronics Society*, pages 3192–3197, Nov 2010.
- [2] L.A.R. Tria, M.T. Escoto, and C.M.F. Odulio. "Photovoltaic Array Reconfiguration for Maximum Power Transfer". In *TENCON 2009 - 2009 IEEE Region 10 Conference*, pages 1–6, jan. 2009.
- [3] T. Esum and P.L. Chapman. "Comparison of Photovoltaic Array Maximum Power Point Tracking Techniques". *Energy Conversion, IEEE Transactions on*, 22(2):439–449, june 2007.
- [4] N. Dzung and B. Lehman. "An Adaptive Solar Photovoltaic Array Using Model-Based Reconfiguration Algorithm". *Industrial Electronics, IEEE Transactions on*, 55(7), july 2008.
- [5] G. Velasco-Quesada, F. Guinjoan-Gispert, R. Pique-Lopez, M. Roman-Lumbreras, and A. Conesa-Roca. "Electrical PV Array Reconfiguration Strategy for Energy Extraction Improvement in Grid-Connected PV Systems". *Industrial Electronics, IEEE Transactions on*, 56(11):pp. 4319–4331, nov. 2009.
- [6] O.E. Ibrahim. "Load Matching to Photovoltaic Generators". *Renewable Energy*, 6(1):pp. 29 – 34, 1995.
- [7] A.K. Mulpur Z. Salameh and F. Dagher. "Two-stage electrical array reconfiguration controller for PV-powered water pump". *Solar Energy*, 44(1):pp. 51 – 56, 1990.
- [8] Y. Auttawaitkul, B. Pungsiri, K. Chammongthai, and M. Okuda. "A Method of Appropriate Electrical Array Reconfiguration Management for Photovoltaic Powered Car". In *Circuits and Systems, 1998. IEEE APCCAS 1998. The 1998 IEEE Asia-Pacific Conference on*, pages 201–204, nov 1998.
- [9] D.J. Walters. "The Design and Implementation of Multi-Node Converters". Master's thesis, University of Witwatersrand, School of Electrical and Information Engineering, 2009.

SOUTH AFRICAN COAL AND ITS ABRASIVENESS INDEX DETERMINATION: AN ACCOUNT OF CHALLENGES

N. Tshiongo and A. Mulaba-Bafubiandi

University of Johannesburg, Faculty of Engineering and the Built Environment, School of Mining, Metallurgy and Chemical Engineering, Department of Metallurgy, Minerals Processing and Technology Research Centre, South Africa, POBOX 526, Wits 2050, South Africa

Abstract: It is the main aim of electricity generators to produce electricity at the lowest cost possible. And the challenge currently remains on receiving constant coal quality parameters that will increase the efficiency of existing electricity generation process without installations experiencing severe wear of the facility using pulverised coal. Coal characterisation and classification is done based on the proximate and ultimate analysis to determine the coal quality parameters that includes; ash content, moisture, coal composition, Hardgrove grindability index and abrasiveness index. These are a few required physical and chemical compositions that are important for coal utilisation for combustion in electricity generation plants. This work investigates the effect of quartz and pyrite content on the abrasiveness index, which is the main problem in electricity generation as coals of a higher abrasiveness index value tend to be abrasive to equipment's and parts of the plant. The wearing off of electricity generating plant equipment's results in frequent plant maintenance and equipment replacements that increased operational cost. A lack of irreparability in the values of abrasiveness index of South African coal samples tested using the Yancey, Geer and Price (YGP) method has been investigated, and this study will attempt to find a holistic integration of coal properties (pyrite and quartz) leading to the abrasive behaviour of coal. And holistic account of challenges faced by electricity producers when using highly abrasive South African coal will be made.

Keywords: coal, Abrasiveness index, Coal properties, Holistic integration, Coal composition, Coal characterisation

1. INTRODUCTION

Coal has been in the past years and will continue to be the main source of fuel for electricity generation here in South Africa and in the world. Coal is the most abundant source of fuel as compared to oil and gas reserves, and in South Africa coal is used to generate ±75% of electricity. Coal is composed of organic components and inorganic constituents heterogeneously distributed as a result of the sedimentary and post-sedimentary conditions [1], [2]& [3]. The organic matter that is also known as the macerals is responsible for all coal benefits including the energy output during combustion. The inorganic matter also referred to as mineral matter can give rise to many problems that includes industrial, environmental, technological also in combustion processes. These inorganic components contributed very little to the value of coal during its utilisation as they form ash residues, they intend to be diluents and replacement the useful and combustible organic matter [2].

The mineral matter is also the source of unwanted abrasion, stickiness, corrosion or pollution that are associated with coal usage [2]. Technological properties of coal can be predicted from the rank, maceral, and chemical composition of the coals. This study gives an account of challenges that are experienced during the investigations of the abrasiveness index of South African coal. The relationship of abrasiveness index and the quartz and pyrite content of coal is evaluated.

2. SOUTH AFRICAN COAL FIELDS.

South Africa ranks number seven on the top ten coal producers in the world at 282 million metric tonnes of coal produced yearly as per the table below. South Africa produces 98% of the total coal produced in Africa per annum, and the remaining 2% is from all the other African countries that produce coal.

Table 1: World production of coal per annum

Country	Capacity
PR China	3471Mt
USA	1004Mt
India	585Mt
Australia	414Mt
Indonesia	376Mt
Russia	334Mt
South Africa	253Mt (282Mt: 2012)
Germany	189Mt
Poland	139Mt
Kazakhstan	117Mt

There has been a huge demand of coal properties and quality in the overall industrial utilisation of coal. Electricity can be produced using all ranks of coals, but due to the demand of good quality coals; most electricity generators utilises poor quality coal with low calorific value [4]. The most aspect that affects the efficiency of coal utilization is the abrasive and corrosive behaviour of coals due to the mineral matter contained in the coal matrix.

Table 2: Summary of South African coal characterisation

The changes that can be noted are the mines that were abandoned at this time has since reopened and

Coal analysis (wt% dry basis)	Coal ¹ (Int)	Coal ² (Int)	Coal ³ (Highveld)	Coal ⁴ (Highveld)	Coal ⁵ (Kusile Power Station)	Coal ⁶ (Witbank)	Coal ⁷ (Natal)	Coal ⁸ (Ermerlo)	From this work (Ave)
<i>Proximate analysis</i>									
Ash	13.70	16.68	22.0	26.5	40.1	12.1	15.5	10.0	20.88
Volatile Matter	34.94	22.85	29.0	26.1	21.5	33.6	12.2	33.8	31.86
Fixed Carbon	51.36	60.85	29.0	47.0	35.4	51.8	70.4	49.6	43.47
<i>Ultimate analysis</i>									
Carbon	70.22	68.1	-	-	-	82.3	86.5	78.8	80.21
Hydrogen	4.90	3.49	-	-	-	5.3	4.1	5.0	5.52
Nitrogen	1.39	1.69	-	-	-	2.0	2.3	1.1	1.60
Total Sulphur	1.01	0.54	-	-	-	0.8	1.5	0.3	0.67
Oxygen	8.78	7.47	-	-	-	9.6	5.6	14.8	11.99
Moisture	-	2.44	-	-	-	2.5	1.9	6.6	3.79

Figure 1 below shows the abundant coal fields of South Africa and their geographic positioning. The figure was constructed a couple of years back (C.J Vorster, 2003), but there has been little change and it is therefore still applicable in this date.

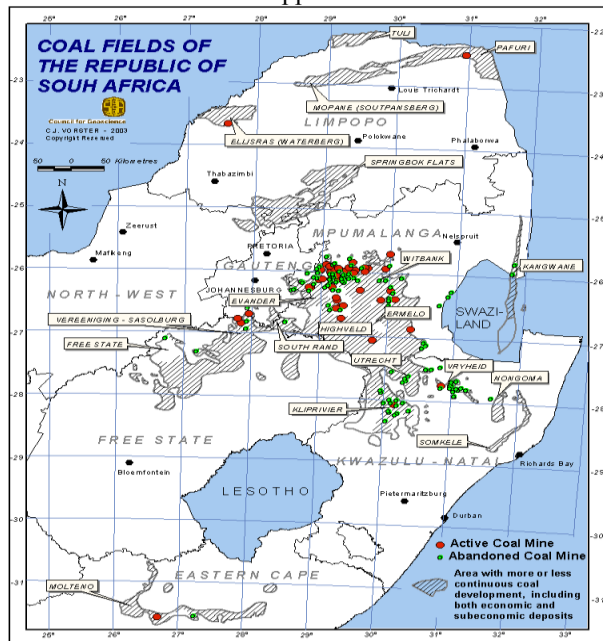


Figure 1: Geological coal fields of South Africa

¹ [20]; ² [21]; ³ [5]; ⁴ [5]; ⁵ [4]; ⁶ [3]; ⁷ [3]; ⁸ [3]

are currently in operation like Vele coal mine in Limpopo province. South African coal is concentrated mostly in Limpopo, Mpumalanga, Free State, Kwazulu-Natal and Eastern Cape provinces with most collieries concentrated around Witbank, Ermelo and Secunda towns in Mpumalanga.

Most of the Gondwana coals, used for electricity generation, are generally found to be associated with a high amount of mineral matter. South African coals are classified as medium rank C bituminous coals which are inertinite-rich with high mineral matter content [3]& [5]. Coals of this rank have great density, hardness and abrasion resistance and they have higher durability [4]

Low rank coals like sub-bituminous and lignite cannot be used conveniently because of low calorific value and high tendencies of spontaneous combustion, but these kinds of coals find usage in electricity generation.

3. ELECTRICITY GENERATION FROM SOUTH AFRICAN COAL

Eskom is currently burning 110 million metric tonnes of coal to produce electricity yearly with 70 million metric tonnes export and 50 million tonnes used for synthetic fuels [5]. The balance from the 282 million metric tonnes is used for other industrial uses including domestic utilization.

Eskom is a South African electricity generator with 13 coal fires power stations, which is also the biggest electricity generator in Africa. Eskom generated 237 291 GWh net electricity per annum in 2011/12, in which 218 212 GWh (92%) was produced from coal. To produce this amount of

power, 125 Million tons of coal was burnt. Producing electricity using coal has many stages involved like transporting coal by conveyor belts from the mine to the bunkers. Coal is then fed to cause coal bin then sent to rotating drums, where it is crushed and milled to fine dust. The pulverised coal is blown by a steam of air into the boiler. The mineral matter undergo chemical changes (loss of water of crystallization) and physical changes (minerals accrete to form hollow spheres) during combustion in the boiler [6]. All the parts that get in contact with coal as stated above are likely to experience wearing due to abrasive South African coals. Greater wear is found on the breakers, transfer points, silos, pulverisers and coal piping [7] amongst many other parts.

4. METHODOLOGY

4.1 Coal characterisation and classification

South African coals from different collieries around the country are used for this work. The coal samples were tested and analysed using proximate and ultimate analysis. The results were used to classify and characterised coal samples from different areas into different groups according to their physical and chemical properties. These results were compared with results obtained from various international and national previous researches on South African coal characterisation.

4.2 Abrasiveness index determination

Abrasiveness index of South African coal samples are identified using YGP method. This is done by placing 4kg of coal sample in a mill and mechanically rotating the sample with a steel blade of a certain mass and shape that stir up the sample during rotation. The weight of the blade is measured before and after stirring up the coal sample. AI is the measure of how the coal sample abrades the equipment during its processing and utilization, and this value is measured by the change in mass loss of the blade. AI is measured in milligrams of wear blades per kilograms of coal processed.

5. RESULTS, DISCUSSION AND FINDINGS

5.1 Coal characterisation and classification

South African coals have been characterised in previous work conducted locally and internationally and the results is summarised on the table below.

Coal classification uses the rank as one parameter to classify coal, but classification cannot be done on only one measured parameter or property as this

becomes insufficient information to classify coal. Primary parameters used to classify coals are fixed carbon (dry, mineral matter-free basis) for high rank coals and gross calorific value (moist, mineral matter-free basis) for lower rank coals. Bituminous and anthracite coals are classified on the basis of volatile matter (dry, mineral matter-free basis) and coking properties [8]. Table 3 above shows parameters that were used to characterised and classify coal samples. The most commonly used parameters used to identify coal rank are the C, H, volatile matter and calorific value [9].

Most of the classifications that are done did not specify the list of important parameters to be considered. Some of the values identified for coal parameters are not on the general coal properties range for different coal ranks. All the coals listed on the table are classified as high volatile bituminous coal, but they all have different values in all parameters and in some of them the range becomes too wide. Depending on what parameters are considered first, South African coals can be characterised as rank High Volatile Bituminous C to Low Volatile Bituminous.

The behaviour of macerals towards combustion is affected more by the coal rank than their types. The inertinite composition of the Gondwana coals is considered to be less reactive but have also shown good burning characteristics, and low-rank inertinite can have better burning characteristics than the high-rank vitrinites [10].

5.2 Abrasiveness index determination

Coal quality is traditionally determined by parameters such as calorific value, ash and sulphur content. The main minerals in coal are clays, quartz, sulphides, sulphates and carbonates, but the trace minerals contribute greatly to the overall chemistry of coal [11]. Most trace elements in coal are associated with mineral matter. The presence of pyrite (FeS_2) in coal contributes to not only environmental pollutions via sulphur emissions but also problems related to coal utilization due to trace elements it contains [12].

Abrasiveness index of coal is a function of the mineral matter characteristics, and the mineral matter that is harder than mild steel is the ones that determine the abrasiveness index. The nature of pyrite and quartz minerals (Table 3) in terms of size, shape and degree of inclusion can vary with coal samples. The mineral matter that are released during grinding (excluded) would be the only ones that affects abrasive behaviour of coals, whereas those mineral matter that remains in the coal particles (included) would not render the coal to be abrasive [13].

Table 3: Abundant minerals found in the suit of power station coals [14]

Mineral Name	Chemical Formula	Hardness (Mohs' scale)
Quartz	SiO ₂	7.0
Pyrite	FeS ₂	6.0-6.5
Mild Steel		5.0-5.0
Siderite	FeCO ₃	4.0-4.5
Dolomite	CaMg(CO ₃) ₂	3.5-4.0
Ankerite	Ca(Mg,Fe)(CO ₃) ₂	3.5-4.0
Calcite	CaCO ₃	3.0
Muscovite	KAl ₃ Si ₃ O ₁₀ (OH) ₄	2.5-3.0
Kaolinite	Al ₂ Si ₂ O ₅ (OH) ₄	2.0-2.5
Illite	As muscovite, but with Fe and Mg replacement	1.0-2.0

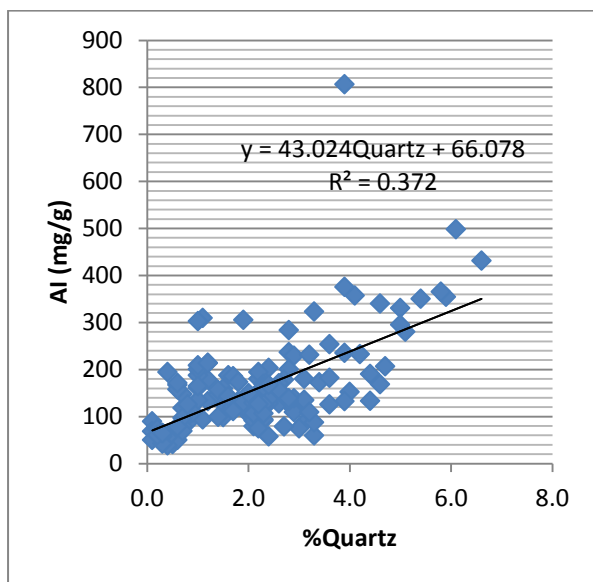


Figure 2: Plot of abrasion index versus quartz of the Witbank coal.

Figure 2 above show the relationship between AI and quartz content of the Witbank coal samples. The AI shows a positive relationship with quartz with a very broad but positive trend in the plot. But the correlation between the two properties is very low at 0.37; this is an indication that there are other factors apart from quarts that affect the value of the AI.

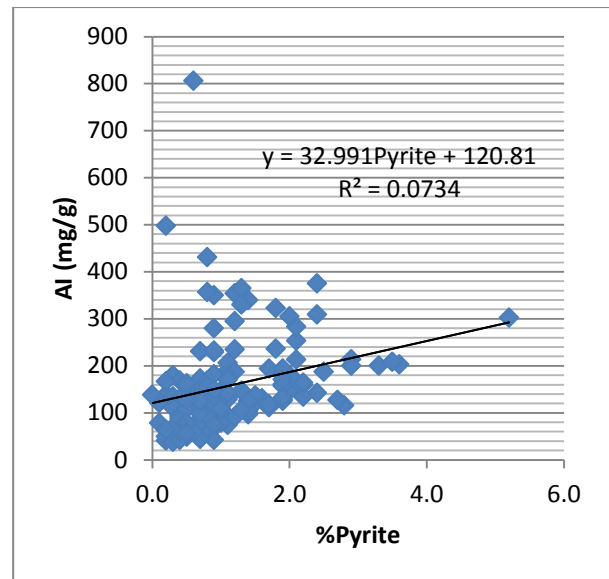


Figure 3: Plot of abrasion index versus pyrite of the Witbank coal.

Figure 3 above show the relationship between AI and pyrite content of the Witbank coal samples. Even though the two variables have a positive relationship, the trend is too broad. The correlation between AI and pyrite content is low at 0.07 and if it is compared with that of quartz at 0.37 it can be clearly be depicted that quartz has more effected on the abrasive behaviour of Witbank coals that pyrite.

Prior investigations [13] on the relationship of quartz and pyrite have suggested quartz to be 2-5 times more abrasive that pyrite on the wt% basis in coal. Quartz has been found to be a mineral matter on the surface of coal particle grains and more abrasive the pyrite which is include in the coal particle grain covered in the soft clays and the coal matrix. This is supported by the plots above. Apart from the positioning and location of the mineral matter in a coal particle grain, the particle shape and the degree of liberation affects the AI coal and the equipment used in electricity generation

Previously done work didn't attribute the wear at the plant to a specific coal while different coals were tested for the AI values. If the quartz contents are contained in large phases that are situated on the outside of the coal particle, the AI value will tend to be higher and vice versa if the quartz contents are in the inside of the coal particle.

Chemical and physical properties of freshly mined coal are changed with oxidising conditions, physical and chemical weathering occurs in the presence of elemental oxygen during coal storage. These changes on the properties of coal caused by weathering include increase in oxygen and volatile matter and decrease in calorific value, and such changes may also be accompanied by surface area

and pore size distribution variations [15], which then also affect its utilisation in technological processes. Mastelerz et al. (2009) found that there is an increase in carbon content while there is a decrease in moisture, Ash %, CV and volatile matter when a proximate analysis (wt% on dry, ash free basis, daf) of coal is done prior and after 13month storage which allowed time for coal oxidation.

There has not been an indication of storage conditions (time and conditions) that was employed before the AI test was done, oxidation affects coal properties and these properties affect the resulting AI value. This can be the reason for lack of repeatability in the AI values. There are common variations that can be causes of lack of repeatability on the AI value when the tests are done in different laboratories, and they can be summarised as follows;

- Sample preparation at the different testing laboratories can be different.
- Moisture content (some moisture would be lost during the handling and transportation stages) and this is not noted before the test is done. Some moisture is lost during the test and this has not been accounted for.
- Irregularities of the blades and associated wears, the shape of the blades would change as it is utilised and this should be considered when the same coal sample is tested repeatedly.
- Experimental conditions and the methods used to test for AI, even though YGP method of testing is employed the experimental conditions have to be documented, this includes the laboratory conditions and the weather during the test.

All the above should be considered so that conclusions on the lack of AI repeatability can be drawn.

6. WAY FORWARD

Characterization of South African coals shows that these coals can be classified as low volatile to high volatile bituminous C rank as they contain a wide range of values for the properties that are used for characterizing coal in different ranks. Coal rank can change from one part to another in the same coalfield and hence differenced in the characterization of coal in table 3. With high challenges associated with high abrasive South African coals, it is advisable to pre-treat the coal

and reduce the mineral matter content using processes like Biodesulphurization [16](bacterial removal of sulphur that forms part of pyrite), Demineralization [17] (removal of minerals contained in coal), microwave pre-heating [18] and also alkaline oxidation (which removes a considerable amount of sulphur from coal) [19].

7. ACKNOWLEDGEMENTS

The data that is used for this study is secondary data. I would like to thank all people who collected the data and everyone that has shared their input on this work.

8. REFERENCES

- [1] A. Alastuey, A. Jimenez, F. Plana, X. Querol and I. Suarez-Ruiz, "Geochemistry, mineralogy, and technological properties of the main Stephanian (Carboniferous) coal seams from the Puetollano Basin, Spain," *International journal of coal geology*, vol. 45, pp. 247-265, 2001.
- [2] C. R. Ward, "Analysis and significance of mineral matter in coal," *international Journal of coal Geology*, vol. 50, pp. 135-168, 2002.
- [3] S. V. Vassilev and C. G. Vassileva, "a new approach for the combined chemical and mineral classification of the inorganic matter of coal. 1. Chemical and mineral classification systems," *Fuel*, vol. 88, pp. 235-245, 2009.
- [4] S. B. Mishra, S. P. Langwenya, B. B. Mamba and M. Balakrishanan, "Study on surface morphology and physicochemical properties of raw and activated South African coal and coal fly ash," *Physics and Chemistry of the Earth*, vol. 35, pp. 811-814, 2010.
- [5] N. Malumbazo, N. J. Wagner and J. R. Bunt, "The petrographic determination of reactivity differences of two South African inertinite-rich lump coals," *Journal of analytical and applied pyrolysis*, vol. 93, pp. 139-146, 2012.
- [6] D. O. Moumakwa and K. Marcus, "Tribology in coal-fired power plants," *Tribology International*, vol. 38, pp. 805-811, 2005.

- [7] D. Tinkner and R. W. Majer, "Design considerations for pulverised coal fired boilers combusting Illinois basin coals," in *Electric Power*, Chicago, Illinois, USA, 2005.
- [8] R. G. Left and T. C. Ruppel, "Coal, Chemical and Physical properties," *Encyclopedia of energy*, vol. 1, pp. 411-423, 2004.
- [9] S. V. Vassilev, K. Kitano and C. G. Vassileva, "Some relationships between coal rank and chemical and mineral composition," *Fuel*, vol. 75, pp. 1537-1542, 1996.
- [10] N. Choudhury, S. Biswas, P. Sarkar, M. Kumar, S. Ghosal, T. Mitra, A. Mukherjee and A. Choudhury, "Influence of rank and macerals on the burnout behaviour of pulverised Indian coal," *International Journal of Coal Geology*, vol. 74, pp. 145-153, 2008.
- [11] S. M. Pollock, F. Goodarzi and C. L. Riediger, "Mineralogical and elemental variation of coal from Alberta, Canada: an example from the No. 2 seam, Genesee Mine," *International Journal of coal geology*, vol. 43, pp. 259-286, 2000.
- [12] A. Kolker, "Minor element distribution in iron disulfides in coal: A geochemical review," *International Journal of Coal Geology*, vol. 94, pp. 32-43, 2012.
- [13] J. J. Wells, F. Wigley, D. J. Foster, W. H. Gibb and J. Williamson, "The relationship between excluded mineral matter and the abrasion index of a coal," *Fuel*, vol. 83, pp. 359-364, 2004.
- [14] J. J. Wells, F. Wigley, D. J. Foster, W. R. Livingston, W. H. Gibb and J. Williamson, "The Nature of mineral matter in coal and the effects on erosive and abrasive behavior," *Fuel Processing Technology*, vol. 86, pp. 535-550, 2005.
- [15] M. Mastalerz, W. Solano-Acosta, A. Schimmelmann and A. Drobniak, "Effects of coal storage in air on physical and chemical properties of coal and on gas adsorption," *International Journal of Coal Geology*, vol. 79, pp. 167-174, 2009.
- [16] A. Moran, J. Cara, N. Miles and C. Shah, "Biodesulphurization of coal: behaviour of trace elements," *Fuel*, vol. 81, pp. 299-304, 2002.
- [17] A. Demirbas, "Demineralisation and desulphurisation of coals via column froth flotation and different methods," *Energy Conversion and Management*, vol. 43, pp. 885-895, 2002.
- [18] E. Lester and S. Kingman, "The effect of microwave pre-heating on five different coals," *Fuel*, vol. 83, pp. 1941-1947, 2004.
- [19] K. Liu, J. Yang, J. Jia and Y. Wang, "Desulphurisation of coal via low temperature atmospheric alkaline oxidation," *Chemosphere*, vol. 71, pp. 183-188, 2008.
- [20] I. Prieto-Fernandez, J.-C. Luengo-Garcia and M. Alonso, "Determination of moisture in coal, in the case of discontinuous transport, using condensers," *Fuel Processing Technology*, vol. 75, pp. 129-140, 2002.
- [21] J. Barroso, J. Ballester, L. M. Ferrer and S. Jimenez, "Study of coal ash deposition in an entrained flow reactor: Influence of coal type, blend composition and operating conditions," *Fuel Processing Technology*, vol. 87, pp. 737-752, 2006.
- [22] M. D. Casal, A. I. Gonzalez, C. S. Canga, C. Barriocanal, J. J. Pis, R. Alvarez and M. A. Diez, "Modifications of coking coal and metallurgical coke properties induced by coal weathering," *Fuel Processing Technology*, vol. 84, pp. 47-62, 2003.

THE CHALLENGES OF SUSTAINABLE ENERGY DEVELOPMENT IN DEVELOPING NATION - A CASE STUDY OF NIGERIA

O. A. MAFIMIDIWO*, and A. K. SAHA**

*University of Kwazulu-Natal, Department of Electrical Engineering, Durban, South Africa.

** University of Kwazulu-Natal, Department of Electrical Engineering, Durban, South Africa.

Abstract. The two-fold energy challenge in the 21st century facing the developing and emerging economies are first, the need to meet the needs of billions of people who still lack access to basic, modern energy services while the second is the need to simultaneously participate in a global transition to clean, low-carbon energy systems with particular focus on Biomass energy. Both needs of this challenge demand urgent attention. Using Nigeria as a case study reveals further that there is still the need for the generality of people to have access to reliable, affordable and socially acceptable energy services which is a pre-requisite to alleviating extreme poverty and meeting other societal development goals. The paper considers the sustainable alternative sources of energy in Nigeria which are otherwise not properly harnessed and briefly highlights the energy prospects in Nigeria. It also outlines some of the challenges militating against the sustainable energy development particularly in Nigeria and proffered ways towards achieving sustainable energy development.

Key Words: Biomass, Emissions, Energy services, Developing Nation, Sustainable energy.

INTRODUCTION

The developing nation has underdeveloped energy infrastructures. The ever increasing demand and meager supply of energy in the developing nation has been a great challenge to her development. The energy problems of the developing world are both serious and widespread. This situation is becoming critical, with increasing population not balanced by an adequate energy development programme. The incessant power generation failure has grossly affected the economy, seriously slowing down development in rural and sub-rural settlements, with present energy policy mainly benefiting the urban dwellers. Lack of access to sufficient and sustainable supplies of energy affects as much as 90% of the population of many developing countries.

Some two billion people are without electricity and a similar number remain dependent on fuels such as wood, sawdust, crop residues, animal dung, charcoal to cook their daily meals. Without efficient clean energy, people are hindered in their efforts to engage effectively in productive activities or to improve their quality of life or standard of living.

Dominating the traditional use of biomass in developing countries is firewood for cooking. The record has it that Fuelwood accounts for some 10% of total biomass use in the world. It provides some 20% of rural household consumption in Latin

America and about 50% in Africa. (Foundation for Alternative Energy (FAE), Slovak). Traditional cooking techniques are inefficient (the three-stone hearth), likewise the charcoal-making techniques. In addition charcoal is two to five times denser than wood with the same energy yield.

THE NIGERIA ENERGY CHALLENGE

Nigeria's energy need is on the increase, and her increasing population is not balanced by adequate energy development programme. The present urban-centered energy policy is deplorable, as cases of rural and sub-rural energy demand and supply do not reach the center stage of the country's energy development policy. A recent survey at a settlement in Lambe, an outskirts in Ogun State part of Nigeria reveals that some people in most settlements still depend on burning wood and traditional biomass for their energy needs, causing great deforestation as seen in Figure 1 below, emitting greenhouse gases, and polluting the environment, thus, creating global warming. Access to electricity supply seems to be a luxury as most homes depend more often than not, on locally made lamps or fossil fuel powered generating sets as alternative to electric light which is hardly available

Harmful Effects of Current Cooking Fuels and Technologies

The harmful effects are considered in the following areas:

Health - It is estimated that indoor air pollution causes about 36% of lower respiratory infections and 22% of chronic respiratory disease [1]

The World Health Organization (WHO) estimates that 1.5 million premature deaths per year are directly attributable to indoor air pollution from the use of solid fuels. That is more than 4 000 deaths per day, more than half of them children under five years of age. More than 85% of these deaths (about 1.3 million People) are due to biomass use, the rest due to coal.

Women and children suffer most from indoor air pollution because they are traditionally responsible for cooking and other household chores, which involve spending hours by the cooking fire exposed to smoke.

Young children are particularly susceptible to disease, which accounts for their predominance in the statistics for premature deaths due to the use of biomass for cooking.

The prevalence of indoor air pollution is significantly higher where income is below \$1 per day per capita [2]. As well as being much more dependent on biomass, poor households rely on low-quality cooking equipment and live in poorly ventilated housing, exacerbating the negative health impact, as there is incomplete combustion and non-dissipation of smoke

Environment - Inefficient and unsustainable cooking practices can have serious implications for the environment, such as land degradation and local and regional air pollution. Charcoal, on the other hand, is often inefficient and can lead to localized deforestation and land degradation around urban centers.

The Burden of Fuel Collection - In developing regions reliant on biomass, women and children are responsible for fuel collection, a time-consuming and exhausting task. Women can suffer serious long-term physical damage as fuelwood collection time has a significant opportunity cost, limiting the opportunity for women and children to

improve their education and engage in income-generating activities. Many children, especially girls, are withdrawn from school to attend to domestic chores related to biomass use, reducing their literacy and restricting their economic opportunities.

CONVENTIONAL ENERGY SOURCES

Modern energy services promote economic development by enhancing the productivity of labour and capital. More efficient technologies provide higher-quality energy services at lower costs and free up household time, especially that of women and children, for more productive purposes.

The conventional energy sources such as coal, natural gas and crude oil have been the mostly used energysources and these produce harmful emissions, thereby making them environmentally unfriendly as seen in Figure 2 below. These sources also deplete and do not produce adequate and consistent power for national consumption; the cost of maintenance also is capital intensive. Moreover, the energy needs of the countries of the world are progressively increasingly above what is supplied.

The developing world has uneven fossil resource but it is blessed by nature with more evenly distributed underdeveloped renewable and sustainable energy sources. Unfortunately the availability of these renewable energysources is not adequately harnessed to their benefits. In the developing world, the standard of living still requires improvement. One of the major steps required to bring about this change is the need to transform the energy distribution of the developing world today. This step will further protect the environment and natural life supporting systems. The energy that is sustainable is the energy that is renewable because this energy will meet the needs of the present without compromising the ability of future generations to meet their needs.

The technologies that promote sustainable energy include renewable energy sources such as hydroelectricity, solar energy, wind energy, Biomass, geothermal energy, wave power and tidal power. However, until the full benefits in renewable sustainable energy are made available, attainable and affordable to the general masses, the developing nations stand at risk of perpetual penury.



Figure 1 Wood fuel for cooking



Figure 2 Energy waste/Environmental pollution

SUSTAINABLE ENERGY PROSPECTS IN NIGERIA

It was reported that Nigeria receives a huge amount of solar radiation, has abundant wind energy resources, and large deposits of fossil fuel, as well as enormous hydro-power resources from Niger and Benue Rivers. However, of these about 80% of hydro-power remains untapped, the total 5.5KW-

hr/m²/day of solar radiation is not utilized and wind energy resources remain unexploited [3]

The table1 below shows the available energy resources in Nigeria

Table 1: Energy Resources of Nigeria, Source: Renewable Energy Master Plan (2005), Sambo (2009)

Resource type	Energy carriers	Reserves	Production level
	Crude oil	36.2 billion barrels	Producing 2.2million bbl/day
	Natural gas	187 trillion SCF	7.1 billion SCF/day
	Coal and lignite	2.7 billion tonnes	0
	Tar sand	32 billion barrel of oil equivalent	NA
Renewable Energy	Large hydropower	11,250MW	1,938MW (167.4million MWh/day)
	Small hydropower	3,500MW	30MW (26 million MWh/day)
	Solar radiation	3.5 – 7.0 KWh/m ² /day	>240 kwp or 0.01 million MWh/day
	Wind	2 -4 m/s at 10m height	-

	Biomass (fuel wood)	11 million hectares of forest and wood land	0.11 million tonnes/day
	Biomass (Animal wastes)	245 million tonnes	NA
	Energy crops & farm residues	72 million hectares of Agric land	NA

GENERAL OBSTACLES TO INVESTMENT IN ALTERNATIVE ENERGY IN NIGERIA

The key general obstacles to investment in alternative sustainable energy in Nigeria can be summarized as follows:

- (i) Drastically Reduced Returns Due to Infrastructure Constraints - The cost of doing business in Nigeria is generally high as a result of poor infrastructures. This include: poor quality and unreliable supply of power; poor transportation infrastructure; ineffective communication facilities; etc. All these usually lead to erosion of the profit margins. The Federal Government of Nigeria is aware of this barrier, especially its impact on foreign direct investment and as such government efforts have consistently focused on alleviating these barriers through the implementation of policy
- (ii) Legal Uncertainties - According to World Bank report [4], Nigeria is ranked 108 out of 178 countries categorized in terms of the ease of doing business in the countries. The report provides quantitative indicators on business regulations and the protection of property rights that can be compared across 17 economies Legal uncertainties in terms of property rights, contract law, lackof international investment treaties, intellectual property concerns are at low levels and need to be beefed-up in order to attract foreign investors to do business in and with Nigeria.
- (iii) Uncertain Evolution of Governance - Governance in Nigeria about a decade ago

initiatives that directly and indirectly mitigates these issues.

- (iv) Political Risks – When compared to 5-10 years ago, Nigeria is relatively politically stable with a few rumbles here and there. One of the few hotspots is the ethnic rumbles such as in the Niger Delta Area where militant activities such as kidnapping for extortion are sending negative signals to potential foreign investors. While the political stability is gaining ground now, another issue of threat on security matter is now of great concern. However, the government is not relenting to seek a solution to this through dialogue and consultation with all concerned parties.

constituted a hindrance to the flow of investment into the country. Corruption, dysfunctional bureaucracy, Non-independent judiciary, among others, all contributed to make the country a pariah nation in those times and foreign direct investment became a trickle.

- (v) Lack of a Level Playing Field – There is the need to transform energy market to an effective and inefficiently functioning one by the removal of hidden subsidies and internalizing external cost. Without addressing these needs it might be impossible for renewable energy technologies to compete favorably for market shares with the already established convectional energy.

Lack of a Renewable Portfolio Standard (RPS) – There is the need to set up firm and realistic portfolio standards for clean energies. A Clean Energy Portfolio Standard (CEPS) refers to minimum targets of clean energy contents of the overall energy supply to specific areas. Essentially, a policy should be put in place that will require that a certain percentage of annual electricity and thermal energy use in the country comes from clean energy

(vi) Lack of a Renewable Portfolio Standard (RPS) - There is the need to set up firm and realistic portfolio standards for clean energies. A Clean Energy Portfolio Standard (CEPS) refers to minimum targets of clean energy contents of the overall energy supply to specific areas. Essentially, a policy should be put in place that will require that a certain percentage of annual electricity and thermal energy used in the country comes from clean energy.

(vii) Barriers to Gas-Flare-to-Energy Projects in Nigeria – In spite of the appreciable endowment of natural gas resources in Nigeria and the fact that natural gas is a relatively cleaner energy compared to petroleum and other fossil fuels, associated natural gas is still being flared. Flaring of this clean energy resource is still occurring in a country that is characterized by frequent power shortages, and where many of the finished goods that can be produced from the flared gas as feedstock are still being imported.

BIOFUEL POTENTIAL IN NIGERIA

From the perspective of available land and wide range of biomass resources, Nigeria has significant potential to produce biofuels and even become an international supplier. Bioenergy feedstock is not only abundant in Nigeria, it is also widely distributed [5] Table 2 below shows available quantity of biomass resources in Nigeria while Table 3 shows the current ethanol production in the country.

At the moment, potential crops for biofuel

production in the country are cassava, sugarcane, rice and sweet sorghum for bioethanol; palm oil, groundnut, and palm kernel for biodiesel because of their high yield and current production output in the country as illustrated in Figure 3. Nigeria is the largest producer of cassava in the world and has the largest capacity for oil palm plantation which serves as a great source for biodiesel [5]. It is interesting to mention that Nigeria could also be a major player in the biofuel industry given the enormous magnitude of various waste/residues (agricultural, forestry, industry and municipal solid) available in the country.



Figure 3 Plants for Biomass fuel production

Biofuel may be of special interest in many other developing countries like Nigeria for several reasons. Climate in many of the countries are well suited to growing biomass. Biomass production is inherently rural and labor-intensive.

Table 2: Biomass resources and estimated quantities in Nigeria (2004) - Source (Sambo, 2009)

Resource	Quantity (million tonnes)	Energy value (' 000 MJ)
Fuel wood	391,000	531,0000
Agro-waste	11.2444	147.7000
Saw dust	1.8000	31.4333
Municipal solid waste	4.0750	

Biofuel Potential in Nigeria

From the perspective of available land and wide range of biomass resources, Nigeria has significant potential to produce biofuels and even become an international supplier. Bioenergy feedstock is not only abundant in Nigeria, it is also widely distributed [5].

Table 6 shows the current ethanol demand in the country. At the moment potential crops for biofuel production in the country are cassava, sugar cane rice and sweet sorghum for bioethanol; palm oil, groundnut, and palm kernel for biodiesel because of their high yield and current production output in the country. Nigeria is the largest producer of cassava in the world and has the largest capacity for oil palm plantation which serves as a great source for biodiesel [6]. It is interesting to mention that Nigeria could also be a major player in the biofuel industry given the enormous magnitude of various waste/residues (agricultural, forestry, industry and municipal solid) available in the country.

Table 3: Current ethanol production in Nigeria

Source: ECN- NDP.

Name of Company	Plant location	Feedstock	Installed capacity
Alconi/Nosak ^a	Lagos	Crude ethanol(imported)	43.8
UNIKEM ^b	Lagos	Crude ethanol(imported)	65.7
Intercontinental Distilleries	Ota-Idiro	Crude ethanol(imported)	9.1
Dura clear	Bacita	Molasses/cassava	4.4
Allied Atlantic Distilleries	Sango Ota	Cassava	10.9
Total			133.9

CONCLUSION

The review critically focuses on biomass resources currently available in Nigeria, and the potential to utilize them for the production of various types of biofuel. The review shows that a variety of biomass resources exists in the country, and that there is also immense opportunity for their conversion to various types of biofuels using different biomass conversion technologies that are currently available. Nigeria has immense potential for energy crops cultivation and the production of bioethanol and biodiesel. The existing database shows that Nigeria ranks very high in terms of production of the major energy crops such as soybean, palm oil, sesame and cassava.

The availability of different types of agricultural

crop residues, forest residues and wood processing waste in Nigeria makes them potential biofuel feedstocks (lignocellulosic feedstocks), particularly for the production of second generation biofuels. Also, the organic portion of municipal solid waste (MSW), together with animal manure could play a major role as potential cellulosic feedstocks for the production of biogas.

Nigeria has the capacity to be a leading exporter of biofuels. The adoption of biofuel can ease the financial strain relating to the heavy burden of fossil fuel subsidy and also enhance local livelihood within the production chains [6]. With the very high potential for biofuel production, the Government as well as private investors should take steps towards investing in agriculture for the production of energy crops and the establishment of biofuel processing plants in Nigeria.

The current energy outlook is very challenging. Whether governments are chiefly concerned with the economic growth, environmental protection or energy security or not, it is clear that a simple continuation of current energy trends would have many undesirable consequences in the short run or face global threats to human well-being on the long run, if left unchecked.

For effective energy hybrid, there is the need to create a mixed energy supply of the yet untapped renewable energy resources with that of the abundant non-renewable fossil fuel, including the massive quantities of gas being wasted from crude oil exploitation.

RECOMMENDATION

Nigeria should strive for a well-rounded energy mix, combining the available renewable energy with the non-renewable fossil fuel. The gas being flared at the different crude oil refining sites could be used to generate abundant electric power for the nation instead of being wasted with deleterious impact of burning on the environment. The government also needs to develop capacities and develop the infrastructure for harvesting wind for power generation from sites within regions having high wind capacity, trapping the abundant solar energy freely available in the nation, increase the capacities of the present hydro-power stations and also establish various power stations that will use the natural gas from crude oil exploitation to drive turbines for electricity generation.

All the energy thus generated should be fed into the national grid, creating adequate mix of energy

from the different sources and having a compact energy development process which will be suitable, sustainable, constantly available, environmentally friendly and economically viable in the long term national energy plan. Furthermore, There is the need for the legislative arm of the government to back up the measures and policies already put in place to increase the attractiveness of the country as a destination for clean energy investment. These include the development of the Renewable Energy Master Plan for the country and the enactment of a strong Bio-fuel Policy.

REFERENCES

- [1]. Abila N. Biofuels adoption in Nigeria: A Preliminary Review of Feedstock and Fuel Production Potential, Dept. of Industrial Management, University of Vaasa, Vaasa, Finland. pp 1-11, (2010).
- [2] Brew-Hammond, Abeeku, —Rural Energy Poverty and the Environment: A Case for Bio-Fueled Multi-Functional Platforms. I Energy and the Environment, Technology Policy Briefs Volume 1 Issue 4, 2002. United Nations University/Institute for New Technologies.
- [3]. Adekoya, L.O. and A.A. Wind energy potential of Nigeria, *Renewable Energy*, 1992, 2(1), 35-39.
- [4] Anozie A.N., Bakare A.R., Sonibare J.A. and Oyebisi T.O. "Evaluation of cooking energy cost, efficiency, impact on air pollution and policy in Nigeria", *Energy*, Vol.32, Issue 7, July 2007, 1283-1292;
- [5] ECN- UNDP. Energy Commission of Nigeria and United Nations Development Programme. Renewable energy master plan: Final draft report available on [<http://www.iceednigeria.org/REMP%20Final%20Report.pdf>, 17 June 2007]
- [6] *Research Journal in Engineering and Applied Science* (ISSN: 2276-8467) Pg 149-155 A comprehensive Review of Biomass Resources and Biofuel Production Potential in Nigeria
- [7] Fagbenle, R.O. and T.G. Karayiannis. The wind energy resources of Nigeria, *International Journal of Energy Research*, 1994, 18 (5), 493-508, (1994).
- [8] Hermann, S. A. Solar manifesto, James and James LTD, London, 2001, 1-22. (2001)
- [9] Sorensen, H.A. Energy conversion systems, Wiley, USA, 1983, 485-491, (1983)

Index

A

Adlam, F., 2
 Almeida, J. A., 69
 Andriambeloson, J. A., 33
 Atkinson-Hope, G., 8, 157, 176, 182
 Awodele, K.O., 188, 228

B

Barandse, P., 146
 Barendse, P., 270
 Berry, B.W.D., 222
 Bokoro, N.P., 152
 Braid, J.I., 281
 Bredekamp, A.J., 8
 Brummer, H.L., 22
 Bullecks, B., 270

C

Chauke, G., 264
 Chetty, L., 16, 44, 80
 Chetty, N. K., 44
 Chisepo, H.K., 37
 Chukwuka, C., 252
 Clark, R., 240
 Coetzer, G. C. M., 33
 Cornish, D.R., 57
 Cronje, W.A., 86, 194, 240

D

d'Almaine, G. F., 62
 de Beer, C., 270
 Doorsamy, W., 86
 du Plessis, N., 104

E

Edimu, M., 200

F

Folly, K. A., 252

G

Gaunt, C.T., 29, 37, 75, 200, 211, 245, 275
 Gouws, R., 92, 104, 127, 258, 264
 Gumede, M., 62

H

Harris, R.T., 51, 133
 Herman, R., 200, 228

I

Ip Cho, N.F.S., 228

J

Joannou, A.L.J., 140

K

Kamper, M.J., 98, 110
 Kasangala, F.M., 157
 Khan, A., 146
 Khan, M.A., 146
 Kühn, C., 116

L

Looi, M.R., 281
 Luhlanga, L.P., 234

M

Mafimidiwo, O.A., 294
 Matabaro, M.J., 176
 Matake, L., 216
 McAfee, C.W.I., 22
 Meru, A.M., 183
 Modisane, T., 169
 Mugisa, S., 245
 Mulaba-Bafubiandi, A.F., 288
 Munilal, S., 206
 Mutize, C., 122
 Mvuyana, S., 169

N

Namanya, E., 275
 Naude, M. I., 194
 Ndlovu, L.S., 206
 Nixon, K.J., 22, 69, 222
 Ntshamba, N.,
 Nyamupangadengu, C., 57, 206

O

Oberholster, R.J., 2
Oyedokun, D.T., 29, 37, 211

P

Pentz, D.C., 140
Phetha, W.M., 16
Phipps, W., 51, 133
Pillay, P., 270
Potgieter, J.H.J., 98
Pretorius, J.H.C., 152

R

Randewijk, P.J., 116
Rangeswamy, R., 270
Reader, H. C., 33
Roberts, A.G., 51, 133
Russell, E., 51

S

Saha, A.K., 216, 234, 294
Sandt, M., 133
Shabalala, M.B., 163

Shuma-lwisi, M.V., 163, 194

Simon, M.N., 29, 211

Singh, Y. , 80

Smit, N. D., 69

Stemmet, W.C., 176

Stephen, R.G., 75

Swart, B., 2

T

Tshiongo, N., 288

V

Van Coller, J.M., 169

van Jaarsveldt, H., 92

van Niekerk, A.E., 258

Villet, W.T., 110

Visser, T.C., 127

W

Wang, R-J., 122

Wu, M.M., 281